Proceedings
PRO 128

Proceedings of the International Conference on Sustainable Materials, Systems and Structures (SMSS2019)

Novel Methods for Characterization of Materials and Structures

Edited by
Ivan Gabrijel
Christian Grosse
Marijan Skazlić

RILEM Publications S.A.R.L.

International Conference on Sustainable Materials, Systems and Structures (SMSS 2019)

Novel Methods for Characterization of Materials and Structures

International Conference on Sustainable Materials, Systems and Structures (SMSS 2019)
Novel Methods for Characterization of Materials and Structures
20-22 March 2019 – Rovinj, Croatia

Published by RILEM Publications S.A.R.L.
4 avenue du Recteur Poincaré 75016 Paris - France
Tel : + 33 1 42 24 64 46 Fax : + 33 9 70 29 51 20
http://www.rilem.net E-mail: dg@rilem.net

ISBN: 978-2-35158-217-6, Vol 5. 978-2-35158-227-5
e-ISBN: 978-2-35158-218-3

RILEM, The International Union of Laboratories and Experts in Construction Materials, Systems and Structures, is a non-profit, non-governmental technical association whose vocation is to contribute to progress in the construction sciences, techniques and industries, essentially by means of the communication it fosters between research and practice. RILEM's activity therefore aims at furthering the knowledge of properties of materials and performance of structures, at defining the means for their assessment in laboratory and service conditions and at unifying measurement and testing methods used with this objective.

RILEM was founded in 1947, and has a membership of over 900 in some 70 countries. It forms an institutional framework for co-operation by experts to:

- optimise and harmonise test methods for measuring properties and performance of building and civil engineering materials and structures under laboratory and service environments,
- prepare technical recommendations for testing methods,
- prepare state-of-the-art reports to identify further research needs,
- collaborate with national or international associations in realising these objectives.

RILEM members include the leading building research and testing laboratories around the world, industrial research, manufacturing and contracting interests, as well as a significant number of individual members from industry and universities. RILEM's focus is on construction materials and their use in building and civil engineering structures, covering all phases of the building process from manufacture to use and recycling of materials.

RILEM meets these objectives through the work of its technical committees. Symposia, workshops and seminars are organised to facilitate the exchange of information and dissemination of knowledge. RILEM's primary output consists of technical recommendations. RILEM also publishes the journal *Materials and Structures* which provides a further avenue for reporting the work of its committees. Many other publications, in the form of reports, monographs, symposia and workshop proceedings are produced.

International Conference on Sustainable Materials, Systems and Structures – SMSS 2019

Novel Methods for Characterization of Materials and Strutures

Rovinj, Croatia
20-22 March 2019

Edited by
Ivan Gabrijel
Christian Grosse
Marijan Skazlić

RILEM Publications S.A.R.L.

CONFERENCE SPONSORS

RILEM Publications

The following list is a summary of global RILEM Publications, sorted by series. Each publication is available in printed version and/or in online version.

RILEM PROCEEDINGS (PRO)

PRO 1: Durability of High Performance Concrete (ISBN: 2-912143-03-9); *Ed. H. Sommer*

PRO 2: Chloride Penetration into Concrete (ISBN: 2-912143-00-04); *Eds. L.-O. Nilsson and J.-P. Ollivier*

PRO 3: Evaluation and Strengthening of Existing Masonry Structures (ISBN: 2-912143-02-0); *Eds. L. Binda and C. Modena*

PRO 4: Concrete: From Material to Structure (ISBN: 2-912143-04-7); *Eds. J.-P. Bournazel and Y. Malier*

PRO 5: The Role of Admixtures in High Performance Concrete (ISBN: 2-912143-05-5); *Eds. J. G. Cabrera and R. Rivera-Villarreal*

PRO 6: High Performance Fiber Reinforced Cement Composites - HPFRCC 3 (ISBN: 2-912143-06-3); *Eds. H. W. Reinhardt and A. E. Naaman*

PRO 7: 1st International RILEM Symposium on Self-Compacting Concrete (ISBN: 2-912143-09-8); *Eds. Å. Skarendahl and Ö. Petersson*

PRO 8: International RILEM Symposium on Timber Engineering (ISBN: 2-912143-10-1); *Ed. L. Boström*

PRO 9: 2nd International RILEM Symposium on Adhesion between Polymers and Concrete ISAP '99 (ISBN: 2-912143-11-X); *Eds. Y. Ohama and M. Puterman*

PRO 10: 3rd International RILEM Symposium on Durability of Building and Construction Sealants (ISBN: 2-912143-13-6); *Eds. A. T. Wolf*

PRO 11: 4th International RILEM Conference on Reflective Cracking in Pavements (ISBN: 2-912143-14-4); *Eds. A. O. Abd El Halim, D. A. Taylor and El H. H. Mohamed*

PRO 12: International RILEM Workshop on Historic Mortars: Characteristics and Tests (ISBN: 2-912143-15-2); *Eds. P. Bartos, C. Groot and J. J. Hughes*

PRO 13: 2nd International RILEM Symposium on Hydration and Setting (ISBN: 2-912143-16-0); *Ed. A. Nonat*

PRO 14: Integrated Life-Cycle Design of Materials and Structures - ILCDES 2000 (ISBN: 951-758-408-3); (ISSN: 0356-9403); *Ed. S. Sarja*

PRO 15: Fifth RILEM Symposium on Fibre-Reinforced Concretes (FRC) - BEFIB'2000 (ISBN: 2-912143-18-7); *Eds. P. Rossi and G. Chanvillard*

PRO 16: Life Prediction and Management of Concrete Structures (ISBN: 2-912143-19-5); *Ed. D. Naus*

PRO 17: Shrinkage of Concrete – Shrinkage 2000 (ISBN: 2-912143-20-9); *Eds. V. Baroghel-Bouny and P.-C. Aïtcin*

PRO 18: Measurement and Interpretation of the On-Site Corrosion Rate (ISBN: 2-912143-21-7); *Eds. C. Andrade, C. Alonso, J. Fullea, J. Polimon and J. Rodriguez*

PRO 19: Testing and Modelling the Chloride Ingress into Concrete (ISBN: 2-912143-22-5); *Eds. C. Andrade and J. Kropp*

PRO 20: 1st International RILEM Workshop on Microbial Impacts on Building Materials (CD 02) (e-ISBN 978-2-35158-013-4); *Ed. M. Ribas Silva*

PRO 21: International RILEM Symposium on Connections between Steel and Concrete (ISBN: 2-912143-25-X); *Ed. R. Eligehausen*

PRO 22: International RILEM Symposium on Joints in Timber Structures (ISBN: 2-912143-28-4); *Eds. S. Aicher and H.-W. Reinhardt*

PRO 23: International RILEM Conference on Early Age Cracking in Cementitious Systems (ISBN: 2-912143-29-2); *Eds. K. Kovler and A. Bentur*

PRO 24: 2nd International RILEM Workshop on Frost Resistance of Concrete (ISBN: 2-912143-30-6); *Eds. M. J. Setzer, R. Auberg and H.-J. Keck*

PRO 25: International RILEM Workshop on Frost Damage in Concrete (ISBN: 2-912143-31-4); *Eds. D. J. Janssen, M. J. Setzer and M. B. Snyder*

PRO 26: International RILEM Workshop on On-Site Control and Evaluation of Masonry Structures (ISBN: 2-912143-34-9); *Eds. L. Binda and R. C. de Vekey*

PRO 27: International RILEM Symposium on Building Joint Sealants (CD03); *Ed. A. T. Wolf*

PRO 28: 6th International RILEM Symposium on Performance Testing and Evaluation of Bituminous Materials - PTEBM'03 (ISBN: 2-912143-35-7; e-ISBN: 978-2-912143-77-8); *Ed. M. N. Partl*

PRO 29: 2nd International RILEM Workshop on Life Prediction and Ageing Management of Concrete Structures (ISBN: 2-912143-36-5); *Ed. D. J. Naus*

PRO 30: 4th International RILEM Workshop on High Performance Fiber Reinforced Cement Composites - HPFRCC 4 (ISBN: 2-912143-37-3); *Eds. A. E. Naaman and H. W. Reinhardt*

PRO 31: International RILEM Workshop on Test and Design Methods for Steel Fibre Reinforced Concrete: Background and Experiences (ISBN: 2-912143-38-1); *Eds. B. Schnütgen and L. Vandewalle*

PRO 32: International Conference on Advances in Concrete and Structures 2 vol. (ISBN (set): 2-912143-41-1); *Eds. Ying-shu Yuan, Surendra P. Shah and Heng-lin Lü*

PRO 33: 3rd International Symposium on Self-Compacting Concrete (ISBN: 2-912143-42-X); *Eds. Ó. Wallevik and I. Níelsson*

PRO 34: International RILEM Conference on Microbial Impact on Building Materials (ISBN: 2-912143-43-8); *Ed. M. Ribas Silva*

PRO 35: International RILEM TC 186-ISA on Internal Sulfate Attack and Delayed Ettringite Formation (ISBN: 2-912143-44-6); *Eds. K. Scrivener and J. Skalny*

PRO 36: International RILEM Symposium on Concrete Science and Engineering – A Tribute to Arnon Bentur (ISBN: 2-912143-46-2); *Eds. K. Kovler, J. Marchand, S. Mindess and J. Weiss*

PRO 37: 5th International RILEM Conference on Cracking in Pavements – Mitigation, Risk Assessment and Prevention (ISBN: 2-912143-47-0); *Eds. C. Petit, I. Al-Qadi and A. Millien*

PRO 38: 3rd International RILEM Workshop on Testing and Modelling the Chloride Ingress into Concrete (ISBN: 2-912143-48-9); *Eds. C. Andrade and J. Kropp*

PRO 39: 6th International RILEM Symposium on Fibre-Reinforced Concretes - BEFIB 2004 (ISBN: 2-912143-51-9); *Eds. M. Di Prisco, R. Felicetti and G. A. Plizzari*

PRO 40: International RILEM Conference on the Use of Recycled Materials in Buildings and Structures (ISBN: 2-912143-52-7); *Eds. E. Vázquez, Ch. F. Hendriks and G. M. T. Janssen*

PRO 41: RILEM International Symposium on Environment-Conscious Materials and Systems for Sustainable Development (ISBN: 2-912143-55-1); *Eds. N. Kashino and Y. Ohama*

PRO 42: SCC'2005 - China: 1st International Symposium on Design, Performance and Use of Self-Consolidating Concrete (ISBN: 2-912143-61-6); *Eds. Zhiwu Yu, Caijun Shi, Kamal Henri Khayat and Youjun Xie*

PRO 43: International RILEM Workshop on Bonded Concrete Overlays (e-ISBN: 2-912143-83-7); *Eds. J. L. Granju and J. Silfwerbrand*

PRO 44: 2nd International RILEM Workshop on Microbial Impacts on Building Materials (CD11) (e-ISBN: 2-912143-84-5); *Ed. M. Ribas Silva*

PRO 45: 2nd International Symposium on Nanotechnology in Construction, Bilbao (ISBN: 2-912143-87-X); *Eds. Peter J. M. Bartos, Yolanda de Miguel and Antonio Porro*

PRO 46: ConcreteLife'06 - International RILEM-JCI Seminar on Concrete Durability and Service Life Planning: Curing, Crack Control, Performance in Harsh Environments (ISBN: 2-912143-89-6); *Ed. K. Kovler*

PRO 47: International RILEM Workshop on Performance Based Evaluation and Indicators for Concrete Durability (ISBN: 978-2-912143-95-2); *Eds. V. Baroghel-Bouny, C. Andrade, R. Torrent and K. Scrivener*

PRO 48: 1st International RILEM Symposium on Advances in Concrete through Science and Engineering (e-ISBN: 2-912143-92-6); *Eds. J. Weiss, K. Kovler, J. Marchand, and S. Mindess*

PRO 49: International RILEM Workshop on High Performance Fiber Reinforced Cementitious Composites in Structural Applications (ISBN: 2-912143-93-4); *Eds. G. Fischer and V.C. Li*

PRO 50: 1st International RILEM Symposium on Textile Reinforced Concrete (ISBN: 2-912143-97-7); *Eds. Josef Hegger, Wolfgang Brameshuber and Norbert Will*

PRO 51: 2nd International Symposium on Advances in Concrete through Science and Engineering (ISBN: 2-35158-003-6; e-ISBN: 2-35158-002-8); *Eds. J. Marchand, B. Bissonnette, R. Gagné, M. Jolin and F. Paradis*

PRO 52: Volume Changes of Hardening Concrete: Testing and Mitigation (ISBN: 2-35158-004-4; e-ISBN: 2-35158-005-2); *Eds. O. M. Jensen, P. Lura and K. Kovler*

PRO 53: High Performance Fiber Reinforced Cement Composites - HPFRCC5 (ISBN: 978-2-35158-046-2); *Eds. H. W. Reinhardt and A. E. Naaman*

PRO 54: 5th International RILEM Symposium on Self-Compacting Concrete (ISBN: 978-2-35158-047-9); *Eds. G. De Schutter and V. Boel*

PRO 55: International RILEM Symposium Photocatalysis, Environment and Construction Materials (ISBN: 978-2-35158-056-1); *Eds. P. Baglioni and L. Cassar*

PRO56: International RILEM Workshop on Integral Service Life Modelling of Concrete Structures (ISBN 978-2-35158-058-5); *Eds. R. M. Ferreira, J. Gulikers and C. Andrade*

PRO57: RILEM Workshop on Performance of cement-based materials in aggressive aqueous environments (e-ISBN: 978-2-35158-059-2); *Ed. N. De Belie*

PRO58: International RILEM Symposium on Concrete Modelling - CONMOD'08 (ISBN: 978-2-35158-060-8); *Eds. E. Schlangen and G. De Schutter*

PRO 59: International RILEM Conference on On Site Assessment of Concrete, Masonry and Timber Structures - SACoMaTiS 2008 (ISBN set: 978-2-35158-061-5); *Eds. L. Binda, M. di Prisco and R. Felicetti*

PRO 60: Seventh RILEM International Symposium on Fibre Reinforced Concrete: Design and Applications - BEFIB 2008 (ISBN: 978-2-35158-064-6); *Ed. R. Gettu*

PRO 61: 1st International Conference on Microstructure Related Durability of Cementitious Composites 2 vol., (ISBN: 978-2-35158-065-3); *Eds. W. Sun, K. van Breugel, C. Miao, G. Ye and H. Chen*

PRO 62: NSF/ RILEM Workshop: In-situ Evaluation of Historic Wood and Masonry Structures (e-ISBN: 978-2-35158-068-4); *Eds. B. Kasal, R. Anthony and M. Drdácký*

PRO 63: Concrete in Aggressive Aqueous Environments: Performance, Testing and Modelling, 2 vol., (ISBN: 978-2-35158-071-4); *Eds. M. G. Alexander and A. Bertron*

PRO 64: Long Term Performance of Cementitious Barriers and Reinforced Concrete in Nuclear Power Plants and Waste Management - NUCPERF 2009 (ISBN: 978-2-35158-072-1); *Eds. V. L'Hostis, R. Gens, C. Gallé*

PRO 65: Design Performance and Use of Self-consolidating Concrete - SCC'2009 (ISBN: 978-2-35158-073-8); *Eds. C. Shi, Z. Yu, K. H. Khayat and P. Yan*

PRO 66: 2nd International RILEM Workshop on Concrete Durability and Service Life Planning - ConcreteLife'09 (ISBN: 978-2-35158-074-5); *Ed. K. Kovler*

PRO 67: Repairs Mortars for Historic Masonry (e-ISBN: 978-2-35158-083-7); *Ed. C. Groot*

PRO 68: Proceedings of the 3rd International RILEM Symposium on 'Rheology of Cement Suspensions such as Fresh Concrete (ISBN 978-2-35158-091-2); *Eds. O. H. Wallevik, S. Kubens and S. Oesterheld*

PRO 69: 3rd International PhD Student Workshop on 'Modelling the Durability of Reinforced Concrete (ISBN: 978-2-35158-095-0); *Eds. R. M. Ferreira, J. Gulikers and C. Andrade*

PRO 70: 2nd International Conference on 'Service Life Design for Infrastructure' (ISBN set: 978-2-35158-096-7, e-ISBN: 978-2-35158-097-4); *Ed. K. van Breugel, G. Ye and Y. Yuan*

PRO 71: Advances in Civil Engineering Materials - The 50-year Teaching Anniversary of Prof. Sun Wei' (ISBN: 978-2-35158-098-1; e-ISBN: 978-2-35158-099-8); *Eds. C. Miao, G. Ye, and H. Chen*

PRO 72: First International Conference on 'Advances in Chemically-Activated Materials – CAM'2010' (2010), 264 pp, ISBN: 978-2-35158-101-8; e-ISBN: 978-2-35158-115-5, *Eds. Caijun Shi and Xiaodong Shen*

PRO 73: 2nd International Conference on 'Waste Engineering and Management - ICWEM 2010' (2010), 894 pp, ISBN: 978-2-35158-102-5; e-ISBN: 978-2-35158-103-2, *Eds. J. Zh. Xiao, Y. Zhang, M. S. Cheung and R. Chu*

PRO 74: International RILEM Conference on 'Use of Superabsorsorbent Polymers and Other New Addditives in Concrete' (2010) 374 pp., ISBN: 978-2-35158-104-9; e-ISBN: 978-2-35158-105-6;
Eds. O.M. Jensen, M.T. Hasholt, and S. Laustsen

PRO 75: International Conference on 'Material Science - 2nd ICTRC - Textile Reinforced Concrete - Theme 1' (2010) 436 pp., ISBN: 978-2-35158-106-3; e-ISBN: 978-2-35158-107-0;
Ed. W. Brameshuber

PRO 76: International Conference on 'Material Science - HetMat - Modelling of Heterogeneous Materials - Theme 2' (2010) 255 pp., ISBN: 978-2-35158-108-7; e-ISBN: 978-2-35158-109-4;
Ed. W. Brameshuber

PRO 77: International Conference on 'Material Science - AdIPoC - Additions Improving Properties of Concrete - Theme 3' (2010) 459 pp., ISBN: 978-2-35158-110-0; e-ISBN: 978-2-35158-111-7; *Ed. W. Brameshuber*

PRO 78: 2nd Historic Mortars Conference and RILEM TC 203-RHM Final Workshop – HMC2010 (2010) 1416 pp., e-ISBN: 978-2-35158-112-4; *Eds J. Válek, C. Groot, and J. J. Hughes*

PRO 79: International RILEM Conference on Advances in Construction Materials Through Science and Engineering (2011) 213 pp., e-ISBN: 978-2-35158-117-9; *Eds Christopher Leung and K.T. Wan*

PRO 80: 2nd International RILEM Conference on Concrete Spalling due to Fire Exposure (2011) 453 pp., ISBN: 978-2-35158-118-6, e-ISBN: 978-2-35158-119-3; *Eds E.A.B. Koenders and F. Dehn*

PRO 81: 2nd International RILEM Conference on Strain Hardening Cementitious Composites (SHCC2-Rio) (2011) 451 pp., ISBN: 978-2-35158-120-9, e-ISBN: 978-2-35158-121-6; *Eds R.D. Toledo Filho, F.A. Silva, E.A.B. Koenders and E.M.R. Fairbairn*

PRO 82: 2nd International RILEM Conference on Progress of Recycling in the Built Environment (2011) 507 pp., e-ISBN: 978-2-35158-122-3; *Eds V.M. John, E. Vazquez, S.C. Angulo and C. Ulsen*

PRO 83: 2nd International Conference on Microstructural-related Durability of Cementitious Composites (2012) 250 pp., ISBN: 978-2-35158-129-2; e-ISBN: 978-2-35158-123-0; *Eds G. Ye, K. van Breugel, W. Sun and C. Miao*

PRO 85: RILEM-JCI International Workshop on Crack Control of Mass Concrete and Related issues concerning Early-Age of Concrete Structures – ConCrack 3 – Control of Cracking in Concrete Structures 3 (2012) 237 pp., ISBN: 978-2-35158-125-4; e-ISBN: 978-2-35158-126-1; *Eds F. Toutlemonde and J.-M. Torrenti*

PRO 86: International Symposium on Life Cycle Assessment and Construction (2012) 414 pp., ISBN: 978-2-35158-127-8, e-ISBN: 978-2-35158-128-5; *Eds A. Ventura and C. de la Roche*

PRO 87: UHPFRC 2013 – RILEM-fib-AFGC International Symposium on Ultra-High Performance Fibre-Reinforced Concrete (2013), ISBN: 978-2-35158-130-8, e-ISBN: 978-2-35158-131-5; *Eds F. Toutlemonde*

PRO 88: 8th RILEM International Symposium on Fibre Reinforced Concrete (2012) 344 pp., ISBN: 978-2-35158-132-2, e-ISBN: 978-2-35158-133-9; *Eds Joaquim A.O. Barros*

PRO 89: RILEM International workshop on performance-based specification and control of concrete durability (2014) 678 pp, ISBN: 978-2-35158-135-3, e-ISBN: 978-2-35158-136-0; *Eds. D. Bjegović, H. Beushausen and M. Serdar*

PRO 90: 7th RILEM International Conference on Self-Compacting Concrete and of the 1st RILEM International Conference on Rheology and Processing of Construction Materials (2013) 396 pp, ISBN: 978-2-35158-137-7, e-ISBN: 978-2-35158-138-4; *Eds. Nicolas Roussel and Hela Bessaies-Bey*

PRO 91: CONMOD 2014 - RILEM International Symposium on Concrete Modelling (2014), ISBN: 978-2-35158-139-1; e-ISBN: 978-2-35158-140-7; *Eds. Kefei Li, Peiyu Yan and Rongwei Yang*

PRO 92: CAM 2014 - 2nd International Conference on advances in chemically-activated materials (2014) 392 pp., ISBN: 978-2-35158-141-4; e-ISBN: 978-2-35158-142-1; *Eds. Caijun Shi and Xiadong Shen*

PRO 93: SCC 2014 - 3rd International Symposium on Design, Performance and Use of Self-Consolidating Concrete (2014) 438 pp., ISBN: 978-2-35158-143-8; e-ISBN: 978-2-35158-144-5; *Eds. Caijun Shi, Zhihua Ou, Kamal H. Khayat*

PRO 94 (online version): HPFRCC-7 - 7th RILEM conference on High performance fiber reinforced cement composites (2015), e-ISBN: 978-2-35158-146-9; *Eds. H.W. Reinhardt, G.J. Parra-Montesinos, H. Garrecht*

PRO 95: International RILEM Conference on Application of superabsorbent polymers and other new admixtures in concrete construction (2014), ISBN: 978-2-35158-147-6; e-ISBN: 978-2-35158-148-3; *Eds. Viktor Mechtcherine, Christof Schroefl*

PRO 96 (online version): XIII DBMC: XIII International Conference on Durability of Building Materials and Components (2015), e-ISBN: 978-2-35158-149-0; *Eds. M. Quattrone, V.M. John*

PRO 97: SHCC3 – 3rd International RILEM Conference on Strain Hardening Cementitious Composites (2014), ISBN: 978-2-35158-150-6; e-ISBN: 978-2-35158-151-3; *Eds. E. Schlangen, M.G. Sierra Beltran, M. Lukovic, G. Ye*

PRO 98: FERRO-11 – 11th International Symposium on Ferrocement and 3rd ICTRC - International Conference on Textile Reinforced Concrete (2015), ISBN: 978-2-35158-152-0; e-ISBN: 978-2-35158-153-7; *Ed. W. Brameshuber*

PRO 99 (online version): ICBBM 2015 - 1st International Conference on Bio-Based Building Materials (2015), e-ISBN: 978-2-35158-154-4; *Eds. S. Amziane, M. Sonebi*

PRO 100: SCC16 - RILEM Self-Consolidating Concrete Conference (2016)**,** ISBN: 978-2-35158-156-8; e-ISBN: 978-2-35158-157-5

PRO 101 (online version): III Progress of Recycling in the Built Environment (2015), e-ISBN: 978-2-35158-158-2; *Eds I. Martins, C. Ulsen and S. C. Angulo*

PRO 102 (online version): RILEM Conference on Microorganisms-Cementitious Materials Interactions (2016), e-ISBN: 978-2-35158-160-5; *Eds. Alexandra Bertron, Henk Jonkers, Virginie Wiktor*

PRO 103 (online version): ACESC'16 - Advances in Civil Engineering and Sustainable Construction (2016), e-ISBN: 978-2-35158-161-2

PRO 104 (online version): SSCS'2015 - Numerical Modeling - Strategies for Sustainable Concrete Structures (2015), e-ISBN: 978-2-35158-162-9

PRO 105: 1st International Conference on UHPC Materials and Structures (2016), ISBN: 978-2-35158-164-3, e-ISBN: 978-2-35158-165-0

PRO 106: AFGC-ACI-fib-RILEM International Conference on Ultra-High-Performance Fibre-Reinforced Concrete – UHPFRC 2017 (2017), ISBN: 978-2-35158-166-7, e-ISBN: 978-2-35158-167-4; *Eds. François Toutlemonde & Jacques Resplendino*

PRO 107 (online version): XIV DBMC – 14th International Conference on Durability of Building Materials and Components (2017), e-ISBN: 978-2-35158-159-9; *Eds. Geert De Schutter, Nele De Belie, Arnold Janssens, Nathan Van Den Bossche*

PRO 108: MSSCE 2016 - Innovation of Teaching in Materials and Structures (2016), ISBN: 978-2-35158-178-0, e-ISBN: 978-2-35158-179-7; *Ed. Per Goltermann*

PRO 109 (2 volumes): MSSCE 2016 - Service Life of Cement-Based Materials and Structures (2016), ISBN Vol. 1: 978-2-35158-170-4, Vol. 2: 978-2-35158-171-4, Set Vol. 1&2: 978-2-35158-172-8, e-ISBN : 978-2-35158-173-5; *Eds. Miguel Azenha, Ivan Gabrijel, Dirk Schlicke, Terje Kanstad and Ole Mejlhede Jensen*

PRO 110: MSSCE 2016 - Historical Masonry (2016), ISBN: 978-2-35158-178-0, e-ISBN: 978-2-35158-179-7; *Eds. Inge Rörig-Dalgaard and Ioannis Ioannou*

PRO 111: MSSCE 2016 - Electrochemistry in Civil Engineering (2016), ISBN: 978-2-35158-176-6, e-ISBN: 978-2-35158-177-3; *Ed. Lisbeth M. Ottosen*

PRO 112: MSSCE 2016 - Moisture in Materials and Structures (2016), ISBN: 978-2-35158-178-0, e-ISBN: 978-2-35158-179-7; *Eds. Kurt Kielsgaard Hansen, Carsten Rode and Lars-Olof Nilsson*

PRO 113: MSSCE 2016 - Concrete with Supplementary Cementitious Materials (2016), ISBN: 978-2-35158-178-0, e-ISBN: 978-2-35158-179-7; *Eds. Ole Mejlhede Jensen, Konstantin Kovler and Nele De Belie*

PRO 114: MSSCE 2016 - Frost Action in Concrete (2016), ISBN: 978-2-35158-182-7, e-ISBN: 978-2-35158-183-4; *Eds. Marianne Tange Hasholt, Katja Fridh and R. Doug Hooton*

PRO 115: MSSCE 2016 - Fresh Concrete (2016), ISBN: 978-2-35158-184-1, e-ISBN: 978-2-35158-185-8; *Eds. Lars N. Thrane, Claus Pade, Oldrich Svec and Nicolas Roussel*

PRO 116: BEFIB 2016 – 9th RILEM International Symposium on Fiber Reinforced Concrete (2016), ISBN: 978-2-35158-187-2, e-ISBN: 978-2-35158-186-5;

PRO 117: 3rd International RILEM Conference on Microstructure Related Durability of Cementitious Composites (2016), ISBN: 978-2-35158-188-9, e-ISBN: 978-2-35158-189-6; *Eds. Changwen Miao, Wei Sun, Jiaping Liu, Huisu Chen, Guang Ye and Klaas van Breugel*

PRO 118 (4 volumes): International Conference on Advances in Construction Materials and Systems (2017), ISBN Set: 978-2-35158-190-2, Vol. 1: 978-2-35158-193-3, Vol. 2: 978-2-35158-194-0, Vol. 3: ISBN:978-2-35158-195-7, Vol. 4: ISBN:978-2-35158-196-4, e-ISBN: 978-2-35158-191-9; *Ed. Manu Santhanam*

PRO 119 (online version): ICBBM 2017 - Second International RILEM Conference on Bio-based Building Materials, (2017), e-ISBN: 978-2-35158-192-6; *Ed. Sofiane Amziane*

PRO 120 (2 volumes): EAC-02 - 2nd International RILEM/COST Conference on Early Age Cracking and Serviceability in Cement-based Materials and Structures, (2017), Vol. 1: 978-2-35158-199-5, Vol. 2: 978-2-35158-200-8, Set: 978-2-35158-197-1, e-ISBN: 978-2-35158-198-8; *Eds. Stéphanie Staquet and Dimitrios Aggelis*

PRO 121 (2 volumes): SynerCrete18: Interdisciplinary Approaches for Cement-based Materials and Structural Concrete: Synergizing Expertise and Bridging Scales of Space and Time, (2018), Set: 978-2-35158-202-2, Vol.1: 978-2-35158-211-4, Vol.2: 978-2-35158-212-1, e-ISBN: 978-2-35158-203-9; *Ed. Miguel Azenha, Dirk Schlicke, Farid Benboudjema, Agnieszka Knoppik*

PRO 122: SCC'2018 China - Fourth International Symposium on Design, Performance and Use of Self-Consolidating Concrete, (2018), ISBN: 978-2-35158-204-6, e-ISBN: 978-2-35158-205-3

PRO 123: Final Conference of RILEM TC 253-MCI: Microorganisms-Cementitious Materials Interactions (2018), Set: 978-2-35158-207-7, Vol.1: 978-2-35158-209-1, Vol.2: 978-2-35158-210-7, e-ISBN: 978-2-35158-206-0; *Ed. Alexandra Bertron*

PRO 124 (online version): Fourth International Conference Progress of Recycling in the Built Environment (2018), e-ISBN: 978-2-35158-208-4; *Eds. Isabel M. Martins, Carina Ulsen, Yury Villagran*

PRO 125 (online version): SLD4 - 4th International Conference on Service Life Design for Infrastructures (2018), e-ISBN: 978-2-35158-213-8; *Eds. Guang Ye, Yong Yuan, Claudia Romero Rodriguez, Hongzhi Zhang, Branko Savija*

PRO 126: Workshop on Concrete Modelling and Material Behaviour in honor of Professor Klaas van Breugel (2018), ISBN: 978-2-35158-214-5, e-ISBN: 978-2-35158-215-2; *Ed. Guang Ye*

PRO 127 (online version): CONMOD2018 - Symposium on Concrete Modelling (2018), e-ISBN: 978-2-35158-216-9; *Eds. Erik Schlangen, Geert de Schutter, Branko Savija, Hongzhi Zhang, Claudia Romero Rodriguez*

RILEM REPORTS (REP)

Report 19: Considerations for Use in Managing the Aging of Nuclear Power Plant Concrete Structures (ISBN: 2-912143-07-1); *Ed. D. J. Naus*

Report 20: Engineering and Transport Properties of the Interfacial Transition Zone in Cementitious Composites (ISBN: 2-912143-08-X); *Eds. M. G. Alexander, G. Arliguie, G. Ballivy, A. Bentur and J. Marchand*

Report 21: Durability of Building Sealants (ISBN: 2-912143-12-8); *Ed. A. T. Wolf*

Report 22: Sustainable Raw Materials - Construction and Demolition Waste (ISBN: 2-912143-17-9); *Eds. C. F. Hendriks and H. S. Pietersen*

Report 23: Self-Compacting Concrete state-of-the-art report (ISBN: 2-912143-23-3); *Eds. Å. Skarendahl and Ö. Petersson*

Report 24: Workability and Rheology of Fresh Concrete: Compendium of Tests (ISBN: 2-912143-32-2); *Eds. P. J. M. Bartos, M. Sonebi and A. K. Tamimi*

Report 25: Early Age Cracking in Cementitious Systems (ISBN: 2-912143-33-0); *Ed. A. Bentur*

Report 26: Towards Sustainable Roofing (Joint Committee CIB/RILEM) (CD 07) (e-ISBN 978-2-912143-65-5); *Eds. Thomas W. Hutchinson and Keith Roberts*

Report 27: Condition Assessment of Roofs (Joint Committee CIB/RILEM) (CD 08) (e-ISBN 978-2-912143-66-2); *Ed. CIB W 83/RILEM TC166-RMS*

Report 28: Final report of RILEM TC 167-COM 'Characterisation of Old Mortars with Respect to Their Repair (ISBN: 978-2-912143-56-3); *Eds. C. Groot, G. Ashall and J. Hughes*

Report 29: Pavement Performance Prediction and Evaluation (PPPE): Interlaboratory Tests (e-ISBN: 2-912143-68-3); *Eds. M. Partl and H. Piber*

Report 30: Final Report of RILEM TC 198-URM 'Use of Recycled Materials' (ISBN: 2-912143-82-9; e-ISBN: 2-912143-69-1); *Eds. Ch. F. Hendriks, G. M. T. Janssen and E. Vázquez*

Report 31: Final Report of RILEM TC 185-ATC 'Advanced testing of cement-based materials during setting and hardening' (ISBN: 2-912143-81-0; e-ISBN: 2-912143-70-5); *Eds. H. W. Reinhardt and C. U. Grosse*

Report 32: Probabilistic Assessment of Existing Structures. A JCSS publication (ISBN 2-912143-24-1); *Ed. D. Diamantidis*

Report 33: State-of-the-Art Report of RILEM Technical Committee TC 184-IFE 'Industrial Floors' (ISBN 2-35158-006-0); *Ed. P. Seidler*

Report 34: Report of RILEM Technical Committee TC 147-FMB 'Fracture mechanics applications to anchorage and bond' Tension of Reinforced Concrete Prisms – Round Robin Analysis and Tests on Bond (e-ISBN 2-912143-91-8); *Eds. L. Elfgren and K. Noghabai*

Report 35: Final Report of RILEM Technical Committee TC 188-CSC 'Casting of Self Compacting Concrete' (ISBN 2-35158-001-X; e-ISBN: 2-912143-98-5); *Eds. Å. Skarendahl and P. Billberg*

Report 36: State-of-the-Art Report of RILEM Technical Committee TC 201-TRC 'Textile Reinforced Concrete' (ISBN 2-912143-99-3); *Ed. W. Brameshuber*

Report 37: State-of-the-Art Report of RILEM Technical Committee TC 192-ECM 'Environment-conscious construction materials and systems' (ISBN: 978-2-35158-053-0); *Eds. N. Kashino, D. Van Gemert and K. Imamoto*

Report 38: State-of-the-Art Report of RILEM Technical Committee TC 205-DSC 'Durability of Self-Compacting Concrete' (ISBN: 978-2-35158-048-6); *Eds. G. De Schutter and K. Audenaert*

Report 39: Final Report of RILEM Technical Committee TC 187-SOC 'Experimental determination of the stress-crack opening curve for concrete in tension' (ISBN 978-2-35158-049-3); *Ed. J. Planas*

Report 40: State-of-the-Art Report of RILEM Technical Committee TC 189-NEC 'Non-Destructive Evaluation of the Penetrability and Thickness of the Concrete Cover' (ISBN 978-2-35158-054-7);
Eds. R. Torrent and L. Fernández Luco

Report 41: State-of-the-Art Report of RILEM Technical Committee TC 196-ICC 'Internal Curing of Concrete' (ISBN 978-2-35158-009-7); *Eds. K. Kovler and O. M. Jensen*

Report 42: 'Acoustic Emission and Related Non-destructive Evaluation Techniques for Crack Detection and Damage Evaluation in Concrete' - Final Report of RILEM Technical Committee 212-ACD (e-ISBN: 978-2-35158-100-1); *Ed. M. Ohtsu*

Report 45: Repair Mortars for Historic Masonry - State-of-the-Art Report of RILEM Technical Committee TC 203-RHM (e-ISBN: 978-2-35158-163-6); *Eds. Paul Maurenbrecher and Caspar Groot*

Report 46: Surface delamination of concrete industrial floors and other durability related aspects guide - Report of RILEM Technical Committee TC 268-SIF (e-ISBN: 978-2-35158-201-5); *Ed. Valérie Pollet*

Conference Chairs

Marijana Serdar, University of Zagreb, Faculty of Civil Engineering, Croatia

Ivana Banjad Pečur, University of Zagreb, Faculty of Civil Engineering, Croatia

Honorary President of Scientific Committee

Dubravka Bjegović, University of Zagreb, Faculty of Civil Engineering, Croatia

International Scientific Committee of Segment on Novel Methods for Characterization of Materials and Structures

Dimitrios Aggelis
Sofía Aparicio Secanellas
Marko Bartolac
Violeta Bokan Bosiljkov
William Peter Boshoff
David Corbett
Sinan Turhan Erdoğan
Ivan Gabrijel
Jacek Golaszevski
Christian Grosse
Nenad Gucunski
Neil Hoult
Ioannou Ioannis
Wim Stenfert Kroese
Markus Kruger
Eric Landis
Thorsten Leusmann
Andrzej T. Moczko
Ernst Niederleithinger
Mato Pavlović
Thomas Schumacher
Dalibor Sekulić
Tomoki Shiotani
Marijan Skazlić
Radoslav Sovjak
Gregor Trtnik
Neven Ukrainczyk
Mario Uroš
Luca Valentini
Herbert Wiggenhauser

Organizing Committee of Segment on Novel Methods for Characterization of Materials and Structures

Ivan Gabrijel, University of Zagreb, Faculty of Civil Engineering, Croatia

Christian Grosse, Technische Universität München, Germany

Marijan Skazlić, University of Zagreb, Faculty of Civil Engineering, Croatia

Contents

Preface

The RILEM International Conference on Sustainable Materials, Systems and Structures (SMSS 2019) was organised by the Faculty of Civil Engineering University of Zagreb as a supporting event of the RILEM Spring Convention in Rovinj, Croatia. These events are held in the year the Faculty of Civil Engineering in Zagreb celebrated its 100 year anniversary of its founding, making 2019 the ideal year to host such an important international event. The purpose of the conference was to bring together scientists, practitioners, members of technical committees and users of technical recommendations, to jointly discuss and envision the future of sustainable development of materials, systems and structures in a holistic, global way.

The SMSS 2019 conference had participants from 50 countries, from Argentina to United States of America, who presented a total of 290 papers. The conference was sponsored by 10 international industrial partners, supported by 6 international organisations of scientists and practitioners and organised with the support of 4 governmental bodies. A total of 450 contributions were reviewed by more than 150 prominent reviewers from different fields. The events organizing committee consisted of 16 local members and 6 invited international members.

As part of the ***RILEM SMSS 2019 conference***, the goal of the segment *Novel Methods for Characterization of Materials and Structures* was to compile papers which were oriented towards promoting approaches that provide new insight into material properties or structural behaviour. Topics of the segment deal with methods for characterisation of materials at a microstructural level, methods for monitoring age-dependant processes in cement based materials, experimental techniques supported by numerical analysis, new applications of existing methods, non-destructive testing methods, methods for on-site inspection and monitoring and novel approaches in the design of concrete structures.

The Editors wish to thank the authors for their efforts to produce and deliver papers of the highest standard. We are certain that these Proceedings will be a valued reference for research topics in this important field and that it will, together with the other volumes from the SMSS conference, form a suitable base for discussion and suggestions for future development and research.

Ivan Gabrijel (University of Zagreb, Croatia)
Christian Grosse (Technische Universität München, Germany)
Marijan Skazlić (University of Zagreb, Croatia)

International Conference on Sustainable Materials, Systems and Structures (SMSS 2019)
Novel Methods for Characterization of Materials and Structures
20-22 March 2019 – Rovinj, Croatia

ULTRASONIC MONITORING OF STRUCTURAL CONCRETE ELEMENTS

Ernst Niederleithinger (1)

(1) Bundesanstalt für Materialforschung und -prüfung (BAM), Unter den Eichen 87, 12205 Berlin, Germany

Abstract

Ultrasonic transmission measurements are used to monitor concrete elements since decades, mostly on a laboratory scale. Recently, coda wave interferometry, a technique adapted from seismology, has been introduced to civil engineering experiments. It can be used to reveal subtle changes in concrete samples and even large construction elements without having a transducer directly at the location where the change is taking place. The methodology works best with embedded transducers to avoid coupling issues or excessive environmental influence. These transducers can be used for newly built and existing structures. Meanwhile, several experiments in the lab and at realistic structures have been performed. Recently, large concrete beams have been equipped with a network of transducers and loaded until failure. Using code wave interferometry, it was possible to visualize stress fields and damaged areas. This paper gives an overview of the state of the art, recent results achieved at BAM and a task list for further results and development.

Keywords: Ultrasound, Monitoring, Embedded Transducers, Coda Wave Interferometry, Cracks, Stress, Concrete

1. INTRODUCTION AND STATE OF THE ART

Due to the aging infrastructure, monitoring of concrete structures is of utmost importance in many countries. A large variety of sensors and data processing methods is used to assess loads, structural health, load capacity, and remaining lifetime [1].

Ultrasonic methods are well established in structural concrete investigations (echo methods, imaging) or material testing (mostly transmission methods) [2]. This paper focuses on the latter. It has been shown that changes in the insonificated material due to temperature, any kind of degradation, damage or stress lead to small changes in the ultrasonic signals. Time of flight (TOF) measurements are standardized for examination of concrete quality and strength estimation [3]. They are used on a regular basis in so-called CIF tests to examine the

freeze-thaw resistance of concrete. In addition, as an example of recent research, it was shown, that the change of the velocity ultrasonic p-waves, picked by TOF, is an excellent indicator for fatigue damage [4]. Unfortunately, TOF measurements have a limited sensitivity to changes. If the damage is not located in the direct line of sight between transmitter and receiver, it cannot be detected at all. However, an indication for a change in the material or structure might show up in the amplitude, frequency or other features of the recorded signals.

The propagation of elastic waves in concrete structures can be divided into four regimes, depending on their frequency f and wavelength λ and their relation to the size of the structure L, size of microstructure features (inhomogeneities as aggregates, cracks) d and intrinsic absorption characteristic length la [5]:

- Low frequency regime ($\lambda > L$)
- "Standard" frequency, single scattering regime ($d < \lambda < L < la$)
- Mesoscopic frequency, multiple scattering regime ($\lambda < d < L < la$)
- High frequency, attenuation regime ($\lambda > la$)

As d is normally spread over a certain range, there is an overlap between the different ranges. The low frequency range is used in modal analysis or guided wave investigations. For ultrasonic echo measurements, the standard range is used. In this paper, we are focusing on the mesoscopic range. According to Fröjd & Ulriksen [6] 50 kHz to 150 kHz is a useful frequency range for this regime in practical applications on concrete.

In the 1970s geophysicists considered the use of diffuse tail of earthquake waves (the "coda"), resulting from multiple scattering, to examine changes in the earth's crust [7]. The development of very sensitive evaluation techniques has resulted in lots of applications mainly in earthquake and volcano research. The most used technique, coda wave interferometry (CWI, [8]), was as well applied in the investigation of rock samples or in mining environments. This technique aims to retrieve information on alterations in the investigated material by comparing measurements to a reference. As travel paths are much longer in the late part of the signal, any change in wave speed will have a greater influence (phase lag) in the coda (Figure 1). Unavoidable, the area of influence increases significantly, leading potentially to a reduced number of transducers required to monitor a specific volume and a reduced spatial resolution at the same time.

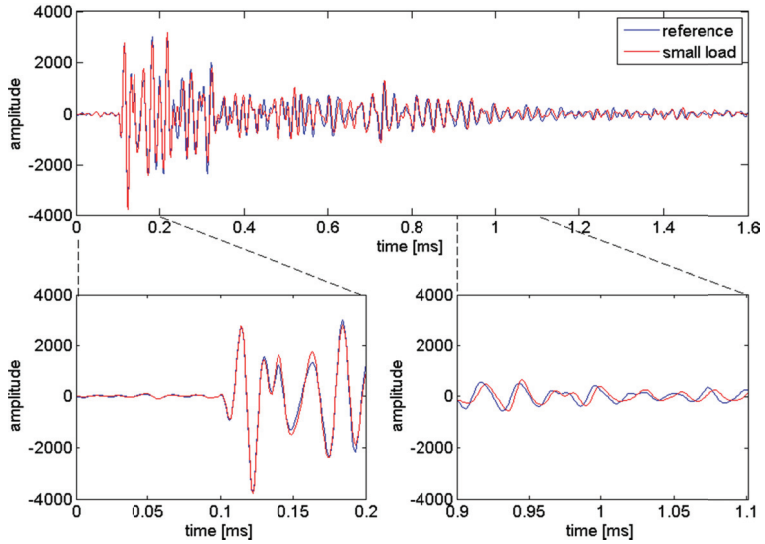

Figure 1: Changes in an ultrasonic signal caused by a weak perturbation (here: small tensional load on a concrete model). From [21].

CWI evaluates selected time windows of the signal either by shifting (doublet technique, [9]), or time axis scaling (stretching technique, [10]). Other methods, e.g. based on Taylor expansion [11], are faster but less accurate. Calculation of cross correlation of the shifted/stretched signal against the reference is repeated for a predetermined set of velocity variations until the highest cross correlation coefficient is retrieved. The velocity change at this point is taken as the apparent velocity change in the area of influence. If the velocity change is not homogeneous in this area (e.g. inhomogeneous load or development of cracks), the cross correlation at this point will be less than one, often also indicating irreversible changes (deterioration).

It was only straightforward to extend the geophysical approach to civil engineering. Since the early 2000s, a couple of research groups, mainly in the USA, France and Germany, have used CWI to investigate various alterations in concrete, mostly on a lab scale. Published research includes studies on (see, e.g., the review of by Planes & Larose [5]):

- compressional load (Figure 2)
- tensional load
- temperature
- moisture

An example (concrete sample under uniaxial load, [12]) is shown in Figure 3. However, in most cases it is so far hard to characterize the nature of the change or to localize the affected volume precisely. Data from ultrasound transmission experiments in concrete include direct, scattered and reflected waves, thus carrying information about material parameters as well as micro- and macrostructure. Specific Information about a specific parameter is often almost impossible to extract. The measurements contain information from larger volumes or entire construction elements. Ways to compensate temperature influence have been proposed by Zhang et al. [13] or Fröjd et al. [14], but most are hard to implement in practice. Separation of different kind of changes is still an unsolved challenge. One of the current shortcomings

might be that CWI is not systematically combined with other feature extraction techniques and/or non-ultrasonic technologies to exploit its full potential.

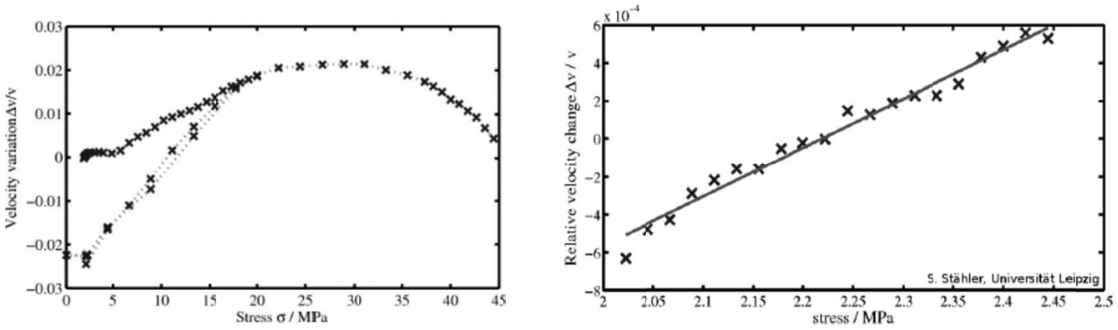

Figure 2: Change of ultrasonic velocity in a concrete cube under uniaxial load. Left: Nonlinear effects in a two-cycle load test until failure. Right: Linear relationship in a limited, small load regime in the same experiment. From [12].

An alternative to the evaluation of conventional ultrasonic impulse data was proposed by Fröjd et al. [15]. He uses continuous monofrequent waves and detects phase shifts (related to velocity change) induced by alterations in the material using lock-in amplifiers. This method seems to have advantages in the lab (very high accuracy), but applicability in the field have yet to be evaluated.

Localization algorithms have been proposed to allow pinpointing the spatial distribution of changes in the material from data of ultrasonic transducer networks. Most are based on the groundbreaking work of Pacheco & Snieder [16], but have been refined later. The state of the art is to calculate sensitivity kernels based on radiative transfer theory and to invert for the spatial distribution either of velocity change or decorrelation [17]. The results for lab samples [18] as well as for structural elements tested in the lab [19][20] have shown the large potential of this approach (Figure 3). However, they are limited to simple geometries (cuboids) and are computationally very expensive. Simplified approaches have been shown by Fröjd et al. [14] and Niederleithinger et al. [21], based on spatial averaging of the parameters obtained by each transducer pair. They seem to be able to provide an estimate of the spatial distribution of parameters but have difficulties to pinpoint localized changes exactly and quantitatively. A reliable technique applicable in real structures with limited computational resources has yet to be found.

Related research has been focused on the investigation and evaluation of nonlinear elasticity in concrete using ultrasound ("nonlinear ultrasound", e.g. [22][23]). Main purpose is to identify cracking by using effects as opening and closing cracks by high amplitude ultrasonic waves and analyzing the resulting frequency spectra at a receiver. Frequency shifts over time or components having the two times the source frequency can be observed. Various potential applications have been demonstrated in lab environments, e g. detection of carbonation or alkali silica reaction (ASR), e.g. [24][25][26][27][28]. One approach is to combine both CWI and nonlinear ultrasonics by using a low frequency, high amplitude pump wave in addition to a conventional ultrasonic transmitter-receiver setup [29][30][31]. While these approaches showed potential to identify micro- and macro-cracks in specific applications, a practical use in monitoring of significant volumes in large structures has not been demonstrated yet.

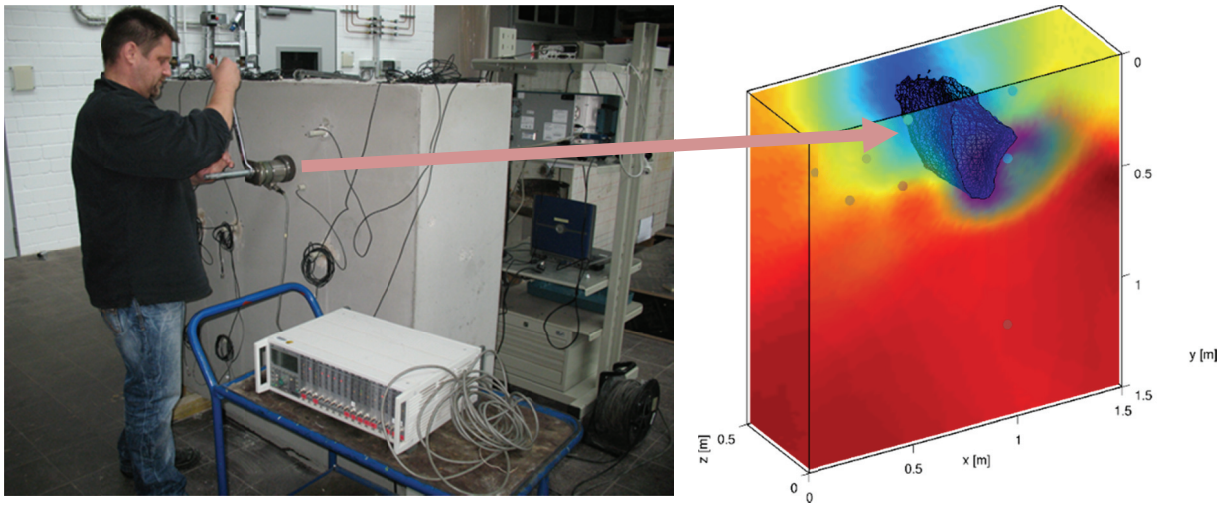

Figure 3: Spatial evaluation of CWI measurement from a network of ultrasonic transducers in a concrete specimen subjected to local compressional load. Right: Color code decorrelation image. Red: no change. Blue large change. Mesh: Isoface of significant change, co-located with compressional load. From [20].

All ultrasonic features determined (velocities, amplitudes, correlation, coherence, nonlinear parameters) are indirectly related to engineering parameters as high strain elastic moduli, load capacity or others. So far the only way for a "translation" are site and object specific calibrations, mostly performed on samples taken during concreting or by coring [3][12][19]. The possibilities for establishing relations based on large laboratory programs, combinations of features and methods or data driven approaches using additional sensors (other than ultrasonic) are not yet fully explored. In most publications, the results are limited to feature maps or volumes, displaying the distribution of certain ultrasonic parameters.

2. RECENT WORK AT BAM

The involvement of the author in CWI research started in 2008 triggered by a cooperation with the University of Leipzig [12]. A small concrete cube was subjected to uniaxial load and monitored using point contact transducers at BAM to calibrate experiments at a newly constructed bridge. Using CWI, the linear relationship between stress and velocity change (acoustoelastic effect) had been shown for certain (small loads) as well as the nonlinear effects for loading/unloading as well as failure scenarios (Figure 2).

The work continued with more detailed research on the acoustoelastic effect [32], partly using CWI, but TOF measurements of surface waves as well [33][34]. It could be shown, that both technologies have the potential to detect load induced reversible changes and damages in large scale lab experiments. In parallel, investigations on the influence of temperature have been carried out [35].

A large-scale concrete model ("All Inclusive") was built at the BAM test site Horstwalde to perform long term experiments with various innovative sensors technologies to detect several types of changes, induced by stress, moisture, temperature or corrosion. The model was used to evaluate an early stage coda wave imaging technique in the frame of a cooperation with Prof. Roel Snieder of Colorado School of Mines (Figure 4, [35]).

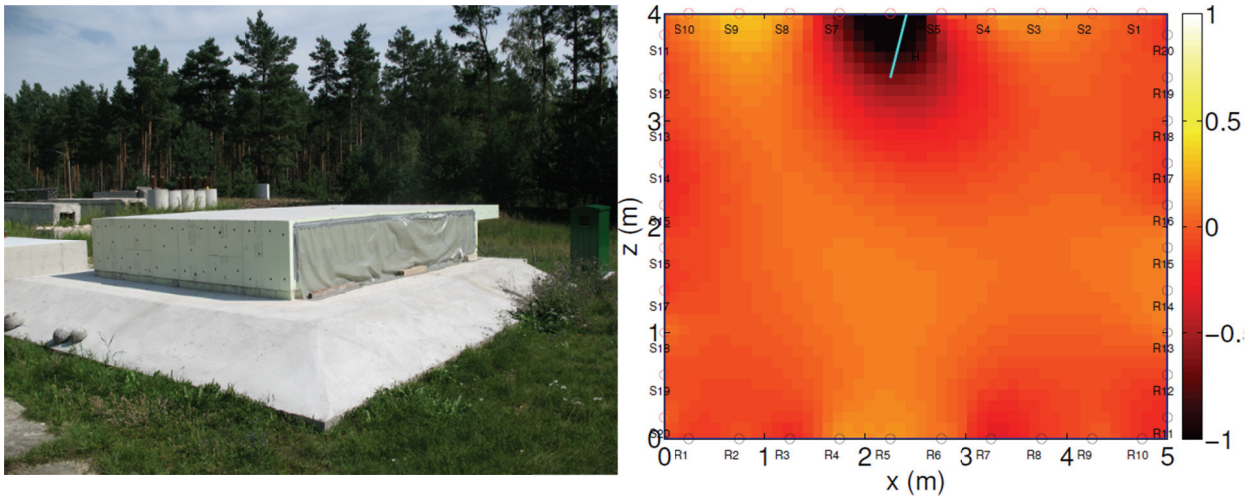

Figure 4 Left: Experimental concrete slab "All inclusive" at BAM-TTS, Horstwalde. Right: Horizontal cross-section with color-coded ultrasonic velocity changes (%) due to heating a cartridge (positioned at the blue line), imaged by 40 transducers on the perimeter and decorrelation tomography [36].

At the same time, work has been started to improve the ultrasonic measurement setup in terms of robustness, reliability and sensitivity. In the frame of the Russian-Turkish-German research project UNeCom several improvements have been made and a first field installation at a bridge close to Izmir, Turkey, has been set up. Main outcome of this study was a novel ultrasonic transducer for embedment in concrete, applicable both before and after concreting (Figure 5, left, [37]). While other developments in this field have been reported (Figure 5, right, [38][39][40]), this transducer seems to be more robust, reliable and easy to apply in real structures.

Figure 5: Left: Transducer used by BAM in current experiments [21][20][36][37], mounted to reinforcement using 3D-printed custom made clips.

Meanwhile other installations have been set up, e. g. in a bridge close to Gliwice, Poland (now used as a reference object in the EC MSC ITN project INFRASTAR) or a tunnel cover

in Munich (potential reference object for the proposed research group). BAM also performed research on simplified, affordable ultrasonic data acquisition systems.

From 2011 to 2014, the group participated in the BMBF Geotechnologien project MIIC (coordination by Christoph Sens-Schönfelder, then with University of Leipzig). BAM's part was to provide an experimental setup, to acquire ultrasonic datasets and to validate if a novel technology could pinpoint localized load quite accurately [20] (Figure 3).

Recently, the group has monitored several load tests on released size bridge girders at RWTH Aachen in a joint project funded by the German Road Research Institute (BASt). With a limited number of transducers and a much simplifies localization techniques it was possible to map stress fields at various load levels [21]. The correlation between the position and shape of areas with a large drop in velocity and the recorded crack patterns in the experiment (Figure 6) as well as in FE simulation (Figure 7) was significant. As the change of the ultrasonic signals exceeded the amount traceable by a fixed reference, a moving reference approach was introduced.

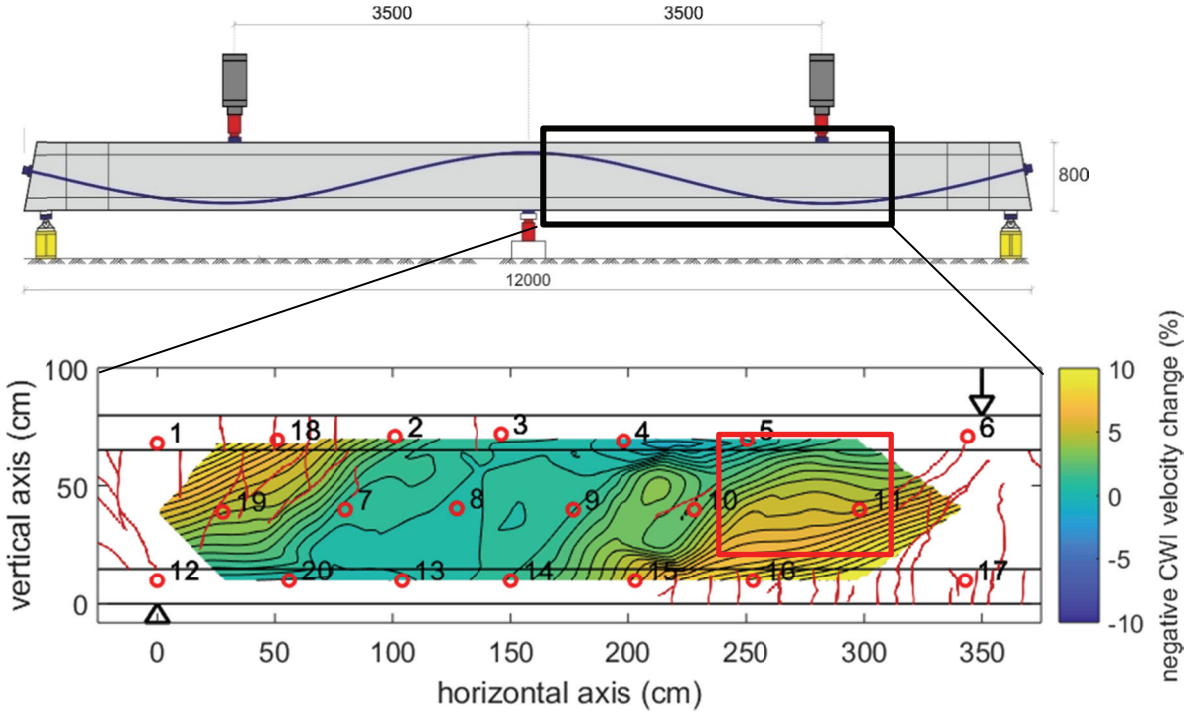

Figure 6. Velocity changes revealed by CWI evaluation of data from embedded ultrasonic transducer network in a bridge girder subjected to 1250 kN load (arrow: hydraulic jack, triangle: support). Red lines: cracks visible at surface. Red rectangle: surface covered by paint for digital image correlation (no cracks visible) [21].

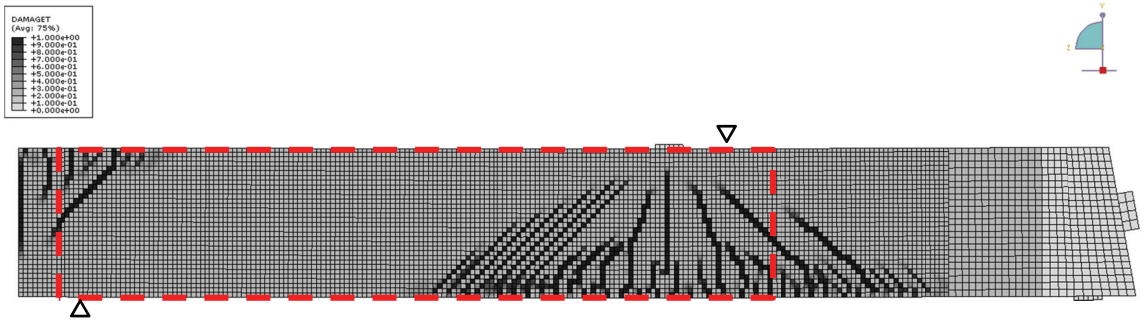

Figure 7. FE simulation of cracks ("damage parameter") at 1250 kN load. Abaqus, M. Herbrand, RWTH Aachen University. Red rectangle: area displayed in Fig. 7. From [41]

3. SUMMARY AND OUTLOOK

Sensing techniques based on the evaluation of the coda (diffuse tail) of ultrasonic signals will potentially fill several gaps in the toolbox available for monitoring concrete structures. There are proven indications that these techniques

- have a better resolution, meaning that smaller changes in a structure can be detected than by conventional ultrasonic monitoring techniques,
- have a greater areal sensitivity than conventional ultrasonic techniques, meaning that larger volumes can be monitored with fewer sensors, and,
- are sensitive to a great variety of influence factors, leading to the detectability of several kinds of damages.

Several research groups have discovered this huge potential, invented by and already practically used by geophysicists for examination of changes in the earth's crust in seismic studies, for civil engineering in the years following the last millennium. However, before any substantial practical application, several gaps in this technology must be filled:

- Gaps in basic understanding of the physical connection between certain loads and damages on one side and the features obtained by CWI or related methods on the other
- Lack of generic methods to separate different loads and environmental effects on the ultrasonic features, with or without combination with other sensing methods
- Lack of generic procedures to translate the ultrasonic features into material/structural parameters, with or without combination with other sensing methods
- Lack of science-based rules for set up of devices, distribution of transducers as well as measurement parameters
- Lack of localization procedures, which overcome the limitations of the current available ones.

REFERENCES

[1] Karbhari, V. M.; Ansari, M. (Eds.); *Structural Health Monitoring of Civil Infrastructure Systems*. Woodhead Publishing, Cambridge, UK, 2009, ISBN 978-1-84569-392-3.

[2] McCann, D.M, M.C Forde. „Review of NDT Methods in the Assessment of Concrete and Masonry Structures“. *NDT & E International* 34, Nr. 2 (März 2001): 71–84. https://doi.org/10.1016/S0963-8695(00)00032-3.

[3] Deutsches Institut für Normung DIN e.V.: DIN EN 12504-4: Prüfung von Beton in Bauwerken - Bestimmung der Ultraschallgeschwindigkeit, Beuth, 2004.

[4] Thiele, M.. Experimentelle Untersuchung und Analyse der Schädigungsevolution in Beton unter hochzyklischen Ermüdungsbeanspruchungen. BAM-Dissertationsreihe, Band 140. Berlin: Bundesanstalt für Materialforschung und -prüfung (BAM), 2016.

[5] Planès, T., E. Larose. „A Review of Ultrasonic Coda Wave Interferometry in Concrete“. *Cement and Concrete Research* 53 (November 2013): 248–55. https://doi.org/10.1016/j.cemconres.2013.07.009.

[6] Fröjd, P., P. Ulriksen. „Frequency Selection for Coda Wave Interferometry in Concrete Structures“. *Ultrasonics* 80 (September 2017): 1–8. https://doi.org/10.1016/j.ultras.2017.04.012.

[7] Aki, K., B. Chouet. „Origin of coda waves: Source, attenuation, and scattering effects“. *Journal of Geophysical Research* 80, Nr. 23 (1975): 3322. https://doi.org/10.1029/JB080i023p03322.

[8] Snieder, R. „The Theory of Coda Wave Interferometry“. *Pure and Applied Geophysics* 163, Nr. 2–3 (Februar 2006): 455–73. https://doi.org/10.1007/s00024-005-0026-6.

[9] Poupinet, G., W. L. Ellsworth, J. Frechet. „Monitoring Velocity Variations in the Crust Using Earthquake Doublets: An Application to the Calaveras Fault, California“. *Journal of Geophysical Research: Solid Earth* 89, Nr. B7 (10. Juli 1984): 5719–31. https://doi.org/10.1029/JB089iB07p05719.

[10] Sens-Schönfelder, C., U. Wegler. „Passive image interferometry and seasonal variations of seismic velocities at Merapi Volcano, Indonesia“. *Geophysical Research Letters* 33, Nr. 21 (1. November 2006). https://doi.org/10.1029/2006GL027797.

[11] Liu, S., J. Zhu, Z. Wu. „Implementation of Coda Wave Interferometry Using Taylor Series Expansion“. *Journal of Nondestructive Evaluation* 34, Nr. 3 (September 2015). https://doi.org/10.1007/s10921-015-0300-1.

[12] Stähler, S., C. Sens-Schönfelder E. Niederleithinger. “Monitoring Stress Changes in a Concrete Bridge with Coda Wave Interferometry.” *JASA* 129, no. 4 (2011): 1945.

[13] Zhang, Y., O. Abraham, V. Tournat, A. Le Duff, B. Lascoup, A. Loukili, F. Grondin, O. Durand. „Validation of a Thermal Bias Control Technique for Coda Wave Interferometry (CWI)“. *Ultrasonics* 53, Nr. 3 (März 2013): 658–64. https://doi.org/10.1016/j.ultras.2012.08.003 .

[14] Fröjd, P., und P. Ulriksen. „Detecting Damage Events in Concrete Using Diffuse Ultrasound Structural Health Monitoring during Strong Environmental Variations“. *Structural Health Monitoring*, 26. März 2017, 147592171769987. https://doi.org/10.1177/1475921717699878.

[15] Fröjd, P., und P. Ulriksen. „Continuous Wave Measurements in a Network of Transducers for Structural Health Monitoring of a Large Concrete Floor Slab“. *Structural Health Monitoring: An International Journal* 15, Nr. 4 (Juli 2016): 403–12. https://doi.org/10.1177/1475921716642139.

[16] Pacheco, C., R. Snieder. „Time-lapse travel time change of multiply scattered acoustic waves“. *The Journal of the Acoustical Society of America* 118, Nr. 3 (2005): 1300. https://doi.org/10.1121/1.2000827.

[17] Planès, T., E. Larose, L. Margerin, V. Rossetto, C. Sens-Schönfelder. „Decorrelation and Phase-Shift of Coda Waves Induced by Local Changes: Multiple Scattering Approach and Numerical

Validation“. *Waves in Random and Complex Media* 24, Nr. 2 (3. April 2014): 99–125. https://doi.org/10.1080/17455030.2014.880821.

[18] P., Thomas, V. Rosseto, E. Larose, L. Margerin. „Locating a small change in a multiple scattering environment (LOCADIF): Application to monitoring concrete“. *The Journal of the Acoustical Society of America* 128, Nr. 4 (2010): 2375. https://doi.org/10.1121/1.3508438.

[19] Zhang, Y., T. Planès, E. Larose, A. Obermann, C. Rospars, G. Moreau. „Diffuse Ultrasound Monitoring of Stress and Damage Development on a 15-Ton Concrete Beam“. *The Journal of the Acoustical Society of America* 139, Nr. 4 (April 2016): 1691–1701. https://doi.org/10.1121/1.4945097.

[20] Niederleithinger, E., C. Sens-Schönfelder, S. Grothe, H. Wiggenhauser. “Coda Wave Interferometry Used to Localize Compressional Load Effects on a Concrete Specimen.” In *Proceedings of 7th EWSHM*. Nantes, France, 2014.

[21] Niederleithinger, E., X. Wang, M. Herbrand, M. Müller. „Processing Ultrasonic Data by Coda Wave Interferometry to Monitor Load Tests of Concrete Beams“. *Sensors* 18, Nr. 6 (19. Juni 2018): 1971. https://doi.org/10.3390/s18061971.

[22] Payan, C., V. Garnier, J. Moysan. „Potential of Nonlinear Ultrasonic Indicators for Nondestructive Testing of Concrete“. *Advances in Civil Engineering* 2010 (2010): 1–8. https://doi.org/10.1155/2010/238472.

[23] Shokouhi, P., J. Riviere, P.-Y. Le Bas, T. J. Ulrich. „Nonlinear Acoustic Testing for Concrete Materials Evaluation“. *Materials Evaluation* 75, Nr. 3 (2017).

[24] Payan, C., V. Garnier, J. Moysan, P. A. Johnson. „Applying nonlinear resonant ultrasound spectroscopy to improving thermal damage assessment in concrete“. *The Journal of the Acoustical Society of America* 121, Nr. 4 (2007): EL125-EL130. https://doi.org/10.1121/1.2710745.

[25] Kim, G., J.-Y. Kim, K. E. Kurtis, L. J. Jacobs, Y. Le Pape, M. Guimaraes. „Quantitative Evaluation of Carbonation in Concrete Using Nonlinear Ultrasound“. *Materials and Structures* 49, Nr. 1–2 (Januar 2016): 399–409. https://doi.org/10.1617/s11527-014-0506-1.

[26] Jin, J., M. G. Moreno, J. Riviere, P. Shokouhi. „Impact-Based Nonlinear Acoustic Testing for Characterizing Distributed Damage in Concrete“. *Journal of Nondestructive Evaluation* 36, Nr. 3 (September 2017). https://doi.org/10.1007/s10921-017-0428-2.

[27] Ju, T., J. D. Achenbach, L. J. Jacobs, M. G., J. Qu. „Ultrasonic Nondestructive Evaluation of Alkali–silica Reaction Damage in Concrete Prism Samples“. *Materials and Structures* 50, Nr. 1 (Februar 2017). https://doi.org/10.1617/s11527-016-0869-6.

[28] Kim, G., G. Loreto, J.-Y. Kim, K. E. Kurtis, J. J. Wall, L. J. Jacobs. „In Situ Nonlinear Ultrasonic Technique for Monitoring Microcracking in Concrete Subjected to Creep and Cyclic Loading“. *Ultrasonics* 88 (August 2018): 64–71. https://doi.org/10.1016/j.ultras.2018.03.006.

[29] Hilloulin, B., Y. Zhang, O. Abraham, A., F. Grondin, O. Durand, V. Tournat. „Small Crack Detection in Cementitious Materials Using Nonlinear Coda Wave Modulation“. *NDT & E International* 68 (Dezember 2014): 98–104. https://doi.org/10.1016/j.ndteint.2014.08.010.

[30] Legland, J.-B., B. Hilloulin, O. Abraham, A. Loukili, F. Grondin, O. Durand, V. Tournat. „Monitoring of the Healing in Cementitious Materials Using Nonlinear Coda Wave Modulation“. In *International Symposium Non-Destructive Testing in Civil Engineering (NDT-CE)*. Berlin, Germany, 2015. http://www.ndt.net/article/ndtce2015/papers/096_legland_jean-baptiste.pdf.

[31] Legland, J.-B., Y. Zhang, O. Abraham, O. Durand, V. Tournat. „Evaluation of Crack Status in a Meter-Size Concrete Structure Using the Ultrasonic Nonlinear Coda Wave Interferometry“. *The Journal of the Acoustical Society of America* 142, Nr. 4 (Oktober 2017): 2233–41. https://doi.org/10.1121/1.5007832.

[32] Shokouhi, P., A. Zoëga, H. Wiggenhauser. “Nondestructive Investigation of Stress-Induced Damage in Concrete”. *Advances in Civil Engineering* 2010 (2010): 1–9.

[33] Shokouhi, P., A. Zoega, H. Wiggenhauser, G. Fischer. „Surface Wave Velocity-Stress Relationship in Uniaxially Loaded Concrete“. *ACI Materials Journal* 109, Nr. 2 (2012). https://doi.org/10.14359/51683700.

[34] Zoega, A., P. Shokouhi, H. Wiggenhauser. „Propagation Time of Elastic Surface Waves on Concrete Specimens under Uniaxial Loads“. *Journal of Structural Engineering* 36, Nr. 1 (o. J.): 11–15.

[35] Niederleithinger, E., C. Wunderlich. „Influence of small temperature variations on the ultrasonic velocity in concrete“. In *Proceedings of QNDE 2012*, 390–97. Denver, 2012. https://doi.org/10.1063/1.4789074.

[36] Kanu, Chinaemerem. „Time-lapse monitoring of localized changes within heterogeneous media with scattered waves“. PhD thesis, Colorado School of Mines, 2014.

[37] Niederleithinger, E., J. Wolf, F. Mielentz, H. Wiggenhauser, S. Pirskawetz. „Embedded Ultrasonic Transducers for Active and Passive Concrete Monitoring“. *Sensors* 15, Nr. 5 (27. April 2015): 9756–72. https://doi.org/10.3390/s150509756.

[38] Song, G., H. Gu, Y.-L. Mo. „Smart aggregates: multi-functional sensors for concrete structures—a tutorial and a review“. *Smart Materials and Structures* 17, Nr. 3 (1. Juni 2008): 033001. https://doi.org/10.1088/0964-1726/17/3/033001.

[39] Yan, Shi, Haoyan Ma, Peng Li, Gangbing Song, und Jianxin Wu. „Development and Application of a Structural Health Monitoring System Based on Wireless Smart Aggregates“. *Sensors* 17, Nr. 7 (17. Juli 2017): 1641. https://doi.org/10.3390/s17071641.

[40] Zhao, J., T. Bao, S. Chen, T. Kundu. „Smart Aggregate-Piezoceramic Patch Combination for Health Monitoring of Concrete Structures“. *Journal of Sensors* 2016 (2016): 1–7. https://doi.org/10.1155/2016/3270916.

[41] Niederleithinger, E.; Herbrand, M.; Müller, M. „Monitoring von Querkraftversuchen an Spannbetondurchlaufträgern mit Ultraschall und Codawelleninterferometrie (Monitoring of shear tests on prestressed concrete continuous beams using ultrasound and coda wave interferometry)“. Bauingenieur 2017, 11, pp. 474–481.

International Conference on Sustainable Materials, Systems and Structures (SMSS 2019)
Novel Methods for Characterization of Materials and Structures
20-22 March 2019 – Rovinj, Croatia

STANDARDISED EXPERIMENTAL TECHNIQUES AND NOVEL MICRO-DESTRUCTIVE METHODS FOR THE ASSESSMENT OF LIME MORTAR PROPERTIES

Loucas Kyriakou (1), Magdalini Theodoridou (1, 2) and Ioannis Ioannou (1)*

(1) Department of Civil and Environmental Engineering, University of Cyprus, Nicosia, Cyprus

(2) School of Engineering, Cardiff University, Cardiff, Wales, United Kingdom

Abstract

The ongoing research community interest in the assessment of lime mortars renders the need for further study on their physico-mechanical characteristics timely. Relevant standardized experimental methods are predominantly destructive and demand extensive sampling and controlled laboratory conditions. In contrast, novel micro-destructive techniques may be used in either the laboratory or in-situ, with minimal intervention to the original structure.

In this study, two micro-destructive techniques, based on the measurement of either the scratching or drilling resistance force, were used to assess the mechanical properties of a range of laboratory designed and produced lime mortars. Data was collected on various hydrated and hydraulic lime mortar samples optimized with the addition of nanosilica and nanotitania. A statistical approach was used to correlate the results of the micro-destructive testing methods with the results of standardized tests implemented to assess the uniaxial compressive strength, flexural strength and dynamic Young's modulus of elasticity of the mortars under study.

The results confirm the potential of the two aforementioned micro-destructive techniques in assessing the mechanical properties of lime mortars. Therefore, the use of either the scratching or drilling resistance measurement is recommended in cases where sampling is limited due to the importance of a historic structure.

Keywords: lime mortars, micro-destructive techniques, scratch tool, DRMS, mechanical properties

1. INTRODUCTION

The restoration of heritage masonry buildings requires knowledge of the mechanical properties of the materials used; this is considered mandatory for all experts in the field of

engineering. For the assessment of the aforementioned properties, a standardized procedure is recommended. This usually demands sampling and is primarily destructive. The introduction of micro-destructive techniques that have a minimally invasive character for the assessment of the mechanical properties of monumental building materials is considered unavoidable in the field of cultural heritage conservation, in order to preserve the history and cultural value of the structure under examination. The aim of providing such knowledge is to establish a database for making decisions in planning correct interventions of restoration and preservation of existing vernacular buildings and structures of cultural importance.

Two micro-destructive techniques have recently been developed and used in order to evaluate the mechanical properties of building materials: these are the scratching and drilling tests. The main concept of these techniques lies with determining the resistance of materials to cutting or drilling; the latter is related to their mechanical properties. The fundamental principles and the theoretical approach of both techniques are described by Dagrain et al. [1].

A number of researchers have used the aforementioned techniques in order to investigate various stone properties [2, 3, 4]. However, only limited work has been published on historical mortars, mainly for conservation purposes [5, 6, 7, 8].

In this study, a wide collection of laboratory designed and produced lime mortars with various binders, aggregates and additives, have been subjected to a series of laboratory standardized tests in order to determine their mechanical properties at different curing ages. The same samples have also been tested using the innovative micro-destructive techniques of scratching and drilling to further investigate their mechanical behaviour. The sound correlations between the results obtained from the standardized tests and the micro-destructive methods applied suggest that the latter may be applied for the determination of the properties of historic and laboratory lime mortars.

2. MATERIALS AND METHODS

2.1 Materials and sample preparation

Twelve lime-based mixtures were designed and produced in the laboratory with a constant workability (165±5 mm) and binder/aggregate ratio (1/3). The latter was chosen based on its prevalence in previously analyzed ancient and traditional lime composites from Cyprus [9]. Four of the mixtures were produced with either hydrated or hydraulic lime and served as reference mixtures, whilst the rest were optimized with either nanosilica (nSi) or nanotitania (nTi). In the hydrated lime mixtures, the binder consisted of 100% CL80 hydrated lime (A) supplied by Hellenic Mining Public Co., while in the hydraulic lime mixtures the binder consisted of 100% natural hydraulic lime 3.5 (Chaux Blanche Naturelle) (H), supplied by Lafarge. The aggregate fraction in all mixtures consisted either of a local reef limestone sand (M) with approximately 80% dolomite and 20% calcite, or a local calcarenite sand (L) with calcite (up to 60%), albite (25%), quartz (15%) and chlorite (traces) [10], both with 0-2 mm particle size.

The nanosilica used in the mixtures was a lightweight white powder with high concentration of SiO_2 (up to 99.5%), supplied by Elkem. Its particle size was <1 μm, while its specific surface area was approximately 30 m^2/g. The nanotitania (Aeroxide® TiO_2 P25) was a lightweight hydrophilic white powder with high concentration of TiO_2 (> 99.5%) provided by Evonic Industries; its average particle size was 21 nm, while its specific surface area was

50±15 m^2/g. Both nano-additives were added at a mere 3% w/w in replacement to the binder. This diminutive percentage was intentionally chosen in order not to alter significantly the traditional nature of the composites and to maintain costs at reasonable levels. The nanomaterials were added to the mixtures in an aqueous suspension following a 15 min sonication using an ultrasonic bath.

The fresh mortars were cast in standardized prismatic 40x40x160 mm steel molds. The hydraulic lime mixtures were additionally covered with a glass surface to avoid instant loss of humidity. All specimens were demolded 3 days after casting. The hydrated mortar specimens were cured in open air, while the hydraulic mortars were covered with water-saturated burlap in closed plastic containers; both types of mortars were stored in the same constant temperature (23±5 °C) room. Different curing times (28, 90 and 180 days) were set for all specimens, in order to determine their mechanical performance.

2.2 Experimental tests

Three prismatic specimens were used in order to evaluate the dynamic modulus of elasticity of the mortars, through sound speed propagation measurements, using a Portable Ultrasonic Non-Destructive Indicating Tester. The same prismatic specimens were also used for testing the materials under flexural load (three-point bending), in accordance with the procedure described in EN 1015-11 [11]. Compression strength tests were performed on the two half-prisms obtained from each specimen after the flexural tests.

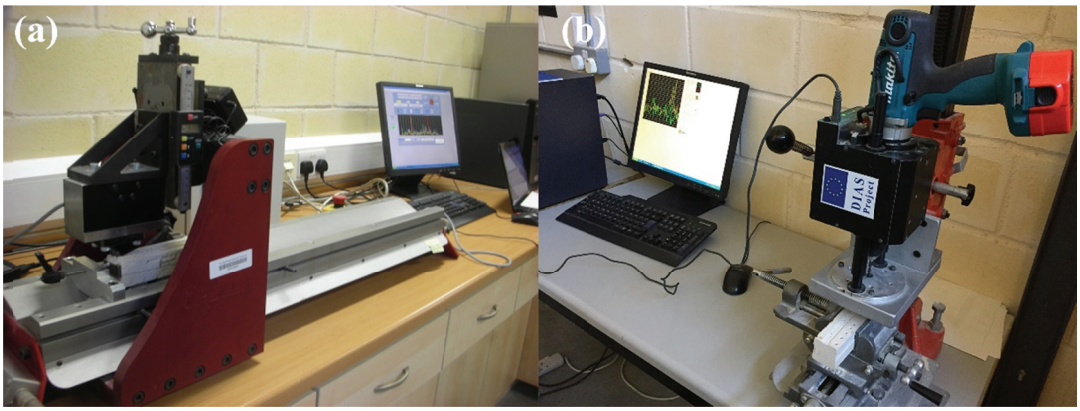

Figure 1: Micro-destructive test equipment: (a) scratch tool; (b) DRMS.

For the assessment of the material's mechanical performance, two micro-destructive tests were additionally performed; the scratching (Figure 1a) and the DRMS (Figure 1b) tests. Using the scratch tool, supplied by Epslog Engineering, measurements were performed with a 10 mm wide diamond compact (PDC) cutter. During the test, the cutter traced successive grooves (depth from 0.05 mm to 0.30 mm) on the surface of the test specimen (see Figure 2a), whilst recording continuously the tangential and normal components of the total force applied on it. The output of the test was the intrinsic specific energy [MPa], determined by linear regression on the cutting test data plotted in a graph presenting the tangential force acting on the cutter vs. the cross-sectional area of the cut. With the Drilling Resistance Measurement System (DRMS), supplied by Sint Technology, measurements were performed using a 5 mm diameter twist diamond drill bit. The rotational speed was 600 rpm, while the penetration rate and depth were 10 mm min^{-1} and 10 mm respectively. Five holes were drilled on each sample

(see Figure 2b) for the determination of the average drilling resistance, i.e. the force [N] recorded in reaction to the weight or thrust acting on the drill bit.

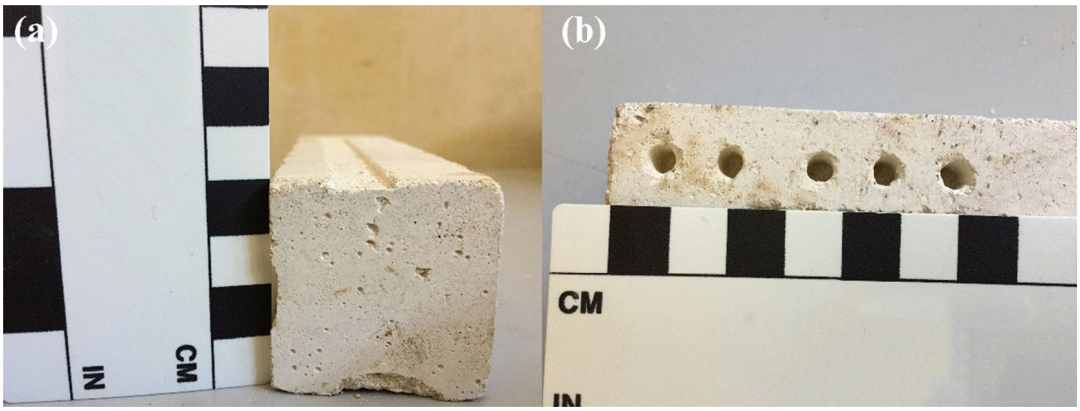

Figure 2: Output of micro-destructive tests: (a) scratching groove; (b) drilling holes.

3. RESULTS AND DISCUSSION

The results from the standardized laboratory and the non-standardized micro-destructive tests on the composites hereby investigated are summarized in Table 1.

Correlation analyses were applied to investigate whether the results from the standardized methodologies relate with the intrinsic specific energy derived from the scratching test and the drilling resistance measured by the DRMS. It needs to be noted that no selection of data has been made in order to optimize the best fit of the trend-lines in favor of the regression analysis. All relations with correlation coefficient values (R^2 parameter values) ≥ 0.85 were considered to show strong independence between the mortar properties, while those with correlation coefficient values > 0.70 were considered statistically significant.

The results of the scratching test, expressed by the intrinsic specific energy, vs. the drilling resistance force are plotted in Figure 3. Even though the correlation coefficient (R^2=0.66) is marginally statistically significant, this relation confirms that the two non-destructive techniques work on the same principle. Both methods use forces that relate to the mechanical properties of the material and the technological parameters applied on the tool [12]; consequently, they can be considered complementary to each other.

Table 1: Mechanical properties of laboratory composites measured at 28, 90 and 180 days after casting. M: local reef limestone sand, L: local calcarenite sand, A: hydrated lime, H: hydraulic lime, nSi: nanosilica, nTi: nanotitania

Mixture	Flexural Strength (MPa)			Compressive Strength (MPa)			Dynamic Modulus of Elasticity (GPa)			Scratch Resistance (MPa)			Drilling Resistance (N)		
	28d	90d	180d	28d	90d	180d	28d	90d	180d	28d	90d	180d	28d	90d	180d
MA	0.81	0.90	0.91	2.64	3.43	3.53	4.44	4.24	4.34	n/d	4.24	4.34	0.50	0.69	0.88
MAnSi	0.70	1.08	1.21	3.52	4.39	5.33	4.28	4.93	5.24	7.76	9.09	9.22	2.02	2.98	1.98
MAnTi	0.45	0.74	0.75	2.62	3.19	3.37	3.31	4.17	4.39	6.17	6.29	3.44	0.70	0.77	1.80
LA	0.79	0.80	0.95	2.66	3.22	3.53	4.62	4.17	4.49	n/d	2.84	2.89	0.87	0.50	0.64
LAnSi	0.97	1.12	1.37	4.39	5.00	6.09	5.43	5.69	5.93	6.73	7.73	8.67	1.29	2.09	1.85
LAnTi	0.74	0.95	1.00	2.90	3.50	3.53	4.50	4.38	5.45	3.05	3.02	4.29	0.74	1.13	0.71
MH	0.97	1.42	1.66	4.22	6.28	7.34	10.05	11.99	12.54	5.85	8.68	9.62	1.60	2.57	3.76
MHnSi	1.48	1.89	2.31	6.41	8.00	8.64	13.08	14.93	14.12	9.89	11.02	14.60	1.92	2.40	4.83
MHnTi	0.79	1.50	1.70	3.79	5.51	6.49	8.49	9.60	11.26	5.63	9.42	10.35	1.97	2.90	3.25
LH	0.78	1.55	1.88	4.47	6.49	7.65	10.04	12.85	12.74	8.23	10.80	12.31	1.20	2.45	3.89
LHnSi	1.44	2.09	2.50	6.70	8.60	9.89	14.22	16.12	16.51	10.87	13.18	19.47	1.86	1.98	3.67
LHnTi	0.99	1.83	1.96	4.66	5.68	7.95	10.23	11.84	12.69	8.85	10.17	12.39	1.02	2.57	3.60

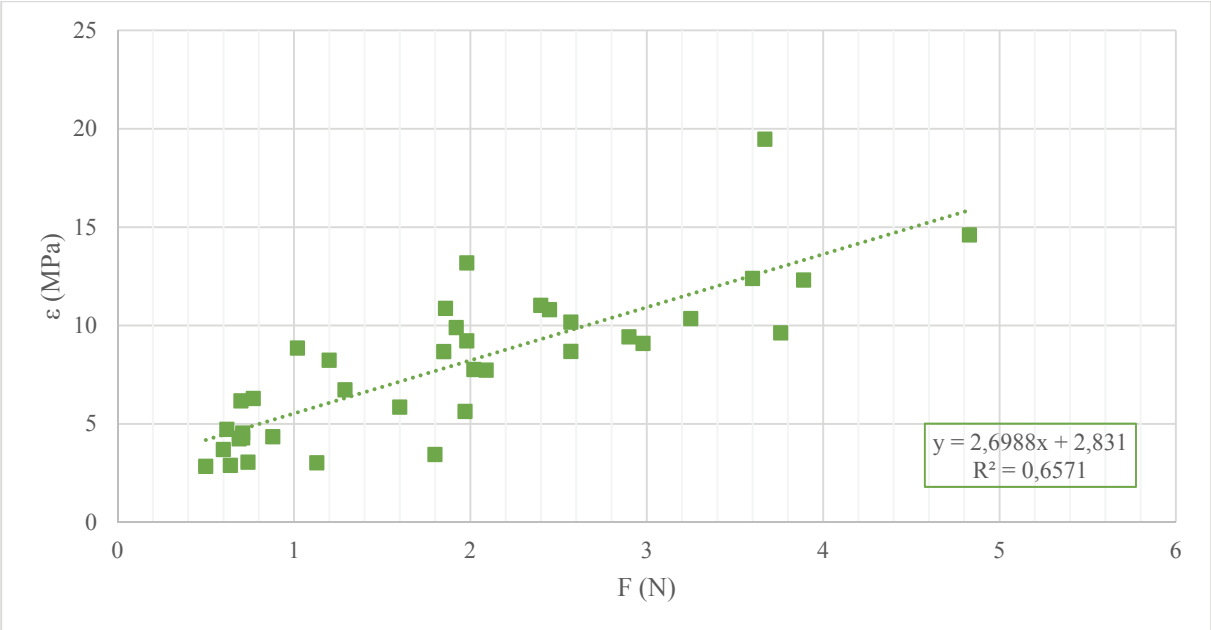

Figure 3: Correlation of the scratching test results, expressed by the intrinsic specific energy (ε), with the DRMS test results.

A strong correlation coefficient (R^2=0.86) is noted in Figure 4a for the linear relation between the intrinsic specific energy and the uniaxial compressive strength (UCS). This strong linear relation is in line with other published data [7, 13]. According to Van Parys et al. [5, 13] and Dagrain et al. [14] a strong correlation (R^2~0.99) between the intrinsic specific energy and the conventional values of the standardized UCS test exists for mortars. However, these results were based on a limited number of samples. Our extended collection of samples confirms that the scratch tool can be efficient for the indirect, micro-destructive estimate of the compressive strength of homogeneous and cohesive mortars. This technique, though, may not be applicable on mortars presenting severe inhomogeneity [13].

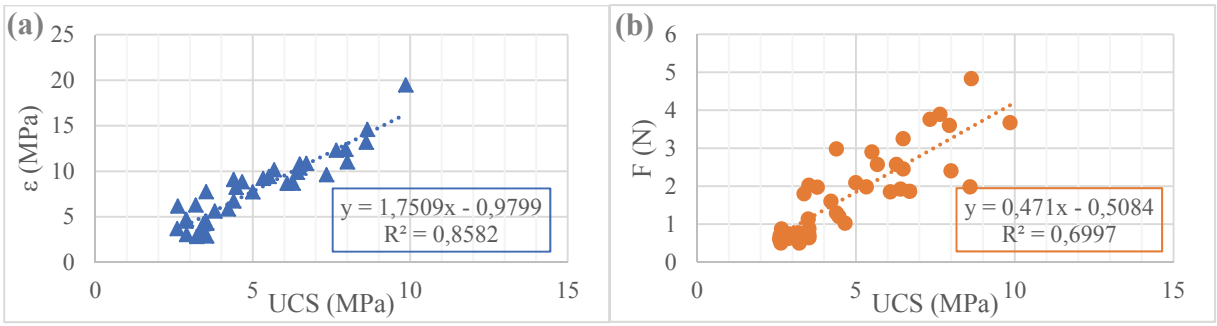

Figure 4: Correlation of the uniaxial compressive strength (UCS) with (a) the scratching test results, expressed by the intrinsic specific energy (ε) and (b) the DRMS results.

A significant correlation coefficient (R^2=0.70) is also noted in Figure 4b for the relation between the drilling resistance and the UCS. Again, it needs to be noted that this correlation coefficient was derived from the analysis of a variety of lime mortars with different mix designs, binders, aggregates, admixtures and curing times.

In Figure 5, the results suggest a linear relation between the intrinsic specific energy and the drilling resistance with the flexural strength (FS), with statistically significant correlation coefficients (R^2 values equal to 0.79 and 0.70 respectively). It should be noted that a similar comparison or correlation has never been established before in the literature. The results are in line with those provided by Theodoridou and Ioannou [15], who suggested that the scratch tool and the DRMS may be used to assess the mechanical performance of relatively weak traditional composite materials, such as lime mortars.

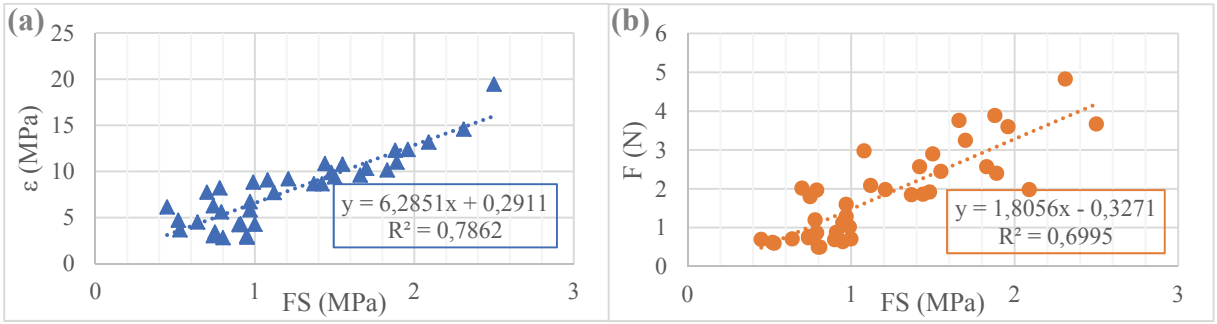

Figure 5: Correlation of the flexural strength (FS) with (a) the scratching test results, expressed by the intrinsic specific energy (ε) and (b) the DRMS results.

In Figure 6a, a statistically significant correlation coefficient (R^2=0.71) is noted for the linear relation between the intrinsic specific energy and the dynamic Young's modulus of elasticity (E_{dyn}); again no such correlation has previously been established with drilling resistance. A safe determination of the E_{dyn} can be of a great importance, since there is a relation between the propagation velocity of ultrasonic wave pulses and the mechanical properties of mortars [16]. The relationship between the drilling resistance and E_{dyn} is also linear (Figure 6b), albeit not very strong; this is likely attributed to the inhomogeneity of the samples under investigation.

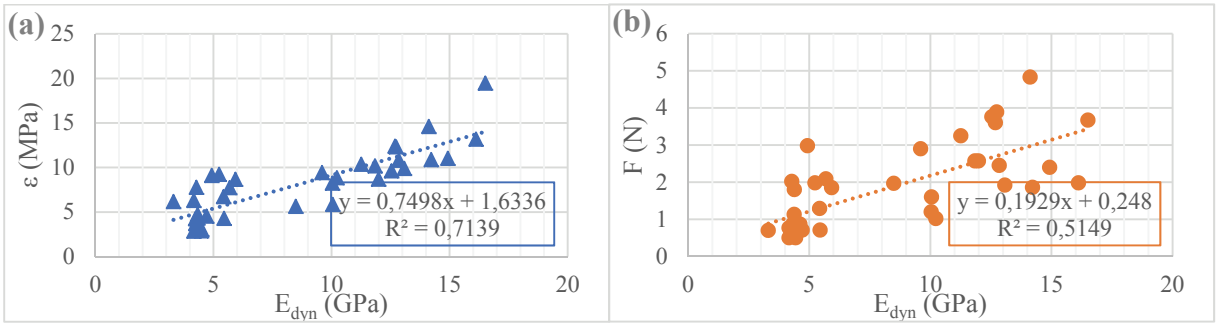

Figure 6: Correlation of the dynamic Young's modulus of elasticity (E_{dyn}) with (a) the scratching test results, expressed by the intrinsic specific energy (ε) and (b) the DRMS results.

4. CONCLUSIONS

An investigation for the correlation of the results of the innovative micro-destructive techniques of scratching and drilling with the mechanical properties of lime-based composites, determined through laboratory standardized tests, has been presented in this paper. The results validate the potential of both aforementioned micro-destructive techniques to assess the mechanical performance of lime mortars, based on their intrinsic specific energy and drilling resistance. This is confirmed by the strong/relatively strong correlation coefficients observed despite the variety in mix designs (i.e. type of binder, aggregates and additives) of the specimens used.

It is worth noting that the portability of both micro-destructive techniques allows their application on-site; hence the relationships hereby observed could be used for a quick in-situ evaluation of the mechanical properties of lime mortars. Furthermore, their micro-destructive nature would have only a minor effect on the specimens or the structure itself; therefore, both techniques could easily be used for the characterization of historic mortar fragments, overcoming any limitations in sampling that may derive from the study of monuments.

ACKNOWLEDGEMENTS

The authors (LK) would like to acknowledge financial support from the University of Cyprus.

REFERENCES

[1] Dagrain, F., Descamps, T. and Benoit, P., 'Less-destructive testing of masonry materials: A comparison between scratching and drilling approaches', Proceedings of the 8th International Masonry Conference, Dresden, Germany, 2010.

[2] Theodoridou, M., Dagrain, F. and Ioannou, I., 'Micro-destructive cutting techniques for the characterization of natural limestone', *Int. J. Rock Mech. Min.* **76** (2015) 98-103.
[3] Richard, T., Dagrain, F., Poyol, E. and Detournay, E., 'Rock strength determination from scratch tests', *Eng. Geol.***147-148** (2012) 91-100.
[4] Chen, J., Feng, Y., Zeng, Y., Han, Y., Wang, Y. and Niu, C., 'Continuous rock drillability measurements using scratch tests', *J. Petrol. Sci. Eng.* **159** (2017) 783-790.
[5] Van Parys, L., Dagrain, F., Coudyzer, C. and Datoussaïd, S., 'On-site determination of compressive strength for historical mortars with the scratching test: method and preliminary results', Proceedings of the 10th Canadian Masonry Symposium, Banff, Alberta, Canada, 2005.
[6] Dagrain, F., Demelenne, M. and Scaillet, J., 'Wide-scale program on the suitability of mortar formulations for interventions on heritage buildings in the Walloon Region', Proceedings of the 8th International Masonry Conference, Dresden, Germany, 2010.
[7] Dagrain, F., Descamps, T. and Scaillet J., 'The scratching test, an alternative technique for determining strength properties of historical mortars', Proceedings of the HMC08 – Historical Mortars Conference, Lisbon, Portugal, 2008.
[8] Del Monte, E. and Vignoli, A., 'In situ mechanical characterization of the mortar in masonry buildings with DRMS', Proceedings of the SACoMaTiS 2008 – Symposium on On Site Assessment of Concrete, Masonry and Timber Structures, Varenna, Como Lake, Italy, 2008.
[9] Theodoridou, M., Ioannou, I. and Philokyprou, M., 'New evidence of early use of artificial pozzolanic material in mortars', *J. Archaeol. Sci.* **40** (2013) 3264-3269.
[10] Fournari, R., Ioannou, I. and Vatyliotis, D., 'A study of fine aggregate properties and their effect on the quality of cementitious composite materials', in 'Engineering Geology for Society and Territory Vol. 5', 2015 (Springer International Publishing, Switzerland, 2015) 33-36.
[11] European Committee of Standardization, 'Methods of test for mortar for masonry. Determination of flexural and compressive strength of hardened mortar, EN 1015-11', 1999.
[12] Ioannou, I., Theodoridou, M., Modestou, S., Fournari, R. and Dagrain, F., 'Use of non-standardised micro-destructive techniques in the characterization of traditional construction materials', Proceedings of the EGU General Assembly Conference, Vienna, Austria, 2013.
[13] Van Parys, L. and Dagrain, F., 'Scratching test applied for on-site determination of compressive strength on historical mortars', Proceedings of the 7th National Congress on Theoretical and Applied Mechanics - NCTAM, Mons, Belgium, 2006.
[14] Dagrain, F. and Germay, C., 'Fields applications for the scratching tests', Proceedings of the Eurock 2006 - International Society for Rock Mechanics and Rock Engineering, Liege, Belgium, 2006.
[15] Theodoridou, M. and Ioannou, I., 'Novel applications of micro-destructive cutting techniques in cultural heritage', in 'Emerging Technologies in Non-Destructive Testing VI', Brussels, 2015 (CRC Press Taylor & Francis Group, London, 2016) 499-504.
[16] Cikrle, P., Adámek, J. and Stehlík, M., 'Ultrasonic testing of properties of mortars', Proceedings of the 4th International Seminar on Structural Analysis of Historical Constructions, Padova, Italy, 2004.

CARACTERIZATION OF THE ADHESION OF FRESH TO EARLY-AGE CONCRETE

T. Craipeau (1, 2), A. Perrot (1), F. Toussaint (2), T. Lecompte (1)

(1) Institut de Recherche Dupuy De Lôme, Centre de recherche Christian Huygens, Lorient, France

(2) LafargeHolcim Research Center, Lyon, France

Abstract
Cement and water reaction induces Le Chatelier contraction. This phenomenon creates a decreasing of pore water pressure creating suction which increases granular stress on a contact surface, as a formwork.

A specific device has been developed in order to control pore water pressure and therefore to reproduce water suction in the material. Therefore, the use of an inert material allows to avoid hydrates physical bonding to a contact surface and to mimic water consumption. The aim is to quantify the effect of pore water pressure on friction increase and on rheological properties.

Keywords: adhesion, interface, friction, pore water pressure, cement material

1. INTRODUCTION

Interfaces between concrete and formwork are present in many applications. The concrete behaviour at the interface is crucial especially during the first hours of hydration. During this period, water consumption from the cement hydration induces a negative pore water pressure. This increases the apparent cohesion of the mix and the friction on the formwork [1]. When the latter is moving, for example during slipforming process where the formwork is continuously lifted, this adhesion to the formwork can create damages to the surface affecting the durability of the structures. It is assumed that the risk for surface damage increases with friction [2].

The aim of the present paper is to understand the phenomena which affect the adhesion and the friction at the interface between the concrete building up and steel formwork. More precisely, the objective is to quantify the relative influence of the pore water pressure and the hydrates physical bonds to the surface under controlled negative water pressure conditions. In order to isolate the effect of the pore water pressure, the experiments were conducted on an inert material and on mortar before hydrates formation.

2. CONCRETE / FORMWORK INTERFACE ZONE

In slipforming process, the formwork is continuously lifted stepwise; as a matter of fact it is impossible to use demolding oil as used on classical steel formwork. The experiments of this paper focus on the interface zone because it has been shown [3] that the microstructure of the steel/concrete interface (SCI) defers from the microstructure in the bulk of the material. At first approximation the SCI can be assumed similar to the interfacial transition zone (ITZ) between cement paste and inert aggregate particles [4].

The approximate thickness, and the heterogeneity, of the ITZ is comparable to the size of cement grains. The porosity of the ITZ appears to remain higher than the porosity of the bulk cement paste. Moreover, this steel/concrete interface differs depending on W/C ratio and the fines concentration. Those differences are very apparent with a high W/C ratio. Globally, the steel/concrete interface W/C ratio and concrete porosity are higher than in the bulk material [5].

3. PORE WATER PRESSURE

It has been shown that suction increases with mortar setting [1]. This evolution induces drastic changes on the mechanical behavior at the interface [2] (adhesiveness, suction, shear stress) and thus the mortar interface properties are modified. At fresh state, material behaviour is governed by colloidal interactions. Small attractive forces will reduce the mean distance between particles and the system becomes compact. As the cement hydration continues, the particles are gradually interlocked (hydrates formation) and finally form a solid structure [6].

At a given age (hydration degree), the solid particles percolate and can therefore transfer the stress to their weight or other applied stresses due through the freshly formed solid network [7].

The stress between the particles is called the **effective stress** (named σ'). Tests show that there is a linear correlation between the friction that occurs and the effective stress [1]. The effective stress is the difference between the concrete **normal stress** (named σ) and the **pore water pressure** (named u_w); according to **Terzaghi equation**.

$$\sigma = \sigma' + u_w \tag{1}$$

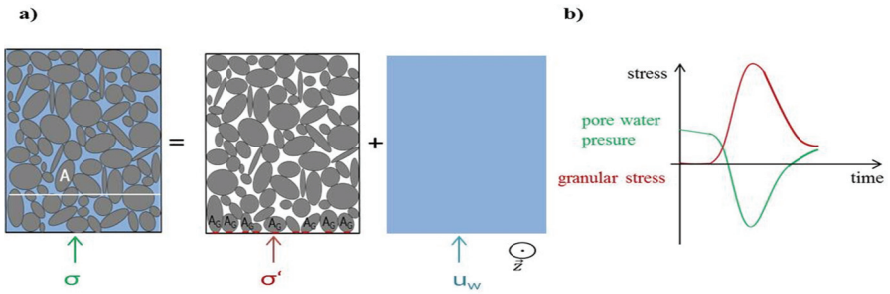

Figure 1. Terzaghi equation illustration.

Tests show that the pore water pressure variations can be considerably larger than the normal stress variation in a slipform. Therefore, pore water pressure variations are mainly responsible for friction increasing. The **percolation of air** between panel and concrete will

induce the disappearance of suction force and as a result, the friction will be reduced. Pore water pressure will be back positive due to non-continuity of the pore water system [2] [8] (Figure 1).

4. EXPERIMENTAL PROCEDURES

4.1 Materials and mixing procedure

Two materials are formulated for the experiments. A mortar for the first device described in paragraph *4.2 Vertical shear stress device*, and an inert material for the second device described in *4.3 Capillary water controlled device*.

The mortar is made with a Portland cement (CEM I 52.5N PM-ES CP2 NF) and 37v% of a fine sand (PE2LS 0/0.315µm) to help the mixing (also to reduce heating during mixing). A low Water/Cement ratio (W/C=0.3) is used to reduce strongly the pore water pressure. In order to obtain a low W/C ratio and a good rheology, a common polycarboxylate plasticiser admixture was used: Glenium 27 from BASF (0.063wt%/cement). In the fresh state, the mortar is fluid (slump ASTM is 260 mm), and its air volume fraction is 2.7%.

The designed mortar was prepared with a Perrier mixer with the same mixing protocol in order to ensure tests reproducibility. The sand was first mixed with part of the water at low speed (140 rpm) during 1 minute. Then, after a waiting period of 4 minutes, cement is introduced and mixed at low speed during 1 minute. The rest of water is introduced during 30 seconds at low speed. Finally, the material is mixed at high speed (180 rpm) during 2 minutes.

The inert mix was formulated to be similar than the mortar: cement volume fraction was replaced by a limestone and the admixture quantity was adjusted in order to obtain the same fluidity (0.046wt%/binder). Sand fraction remained constant. The mix was prepared with the same protocol than the mortar.

Two devices used for the experiments will be described. The first one gathers multiple physical phenomena in order to be representative of the real process [9]. The second one aims to pilot and observe specific phenomena in order to isolate physical phenomena and understand the origin of the friction.

4.2 Vertical shear stress device

The first device consists of a parallelepiped box, filled with mortar. One face of the box, attached to a traction machine, can be moved and is made of a material that represents the formwork interface. A load cell allows to measure the global interfacial shear load (Figure 2). It is also equipped with pore pressure sensors [5] and force transducers to estimate those critical physical parameters. It allows to improve the understanding of the impact of suction on granular/interfacial friction and to assess its relative influence on the total stress. The advantage of this apparatus is to benefit from total lifting amplitude of 380 mm. For each lifting step, the lifting speed is 1 $mm.s^{-1}$ for a move of 5 mm. The time at rest is 565 seconds between each step. The average lifting speed is then 0.5 $mm.min^{-1}$. The total test lasts around 12 hours, which is representative of industrial applications.

This device permits to observe the friction globally. Cement hydration induces simultaneous hydrates creation and water consumption as presented in the Figure 3.

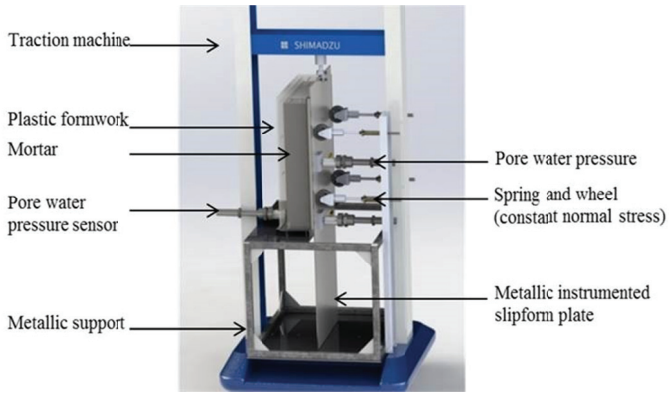

Figure 2. Vertical shear stress device developed to study slipforming operations.

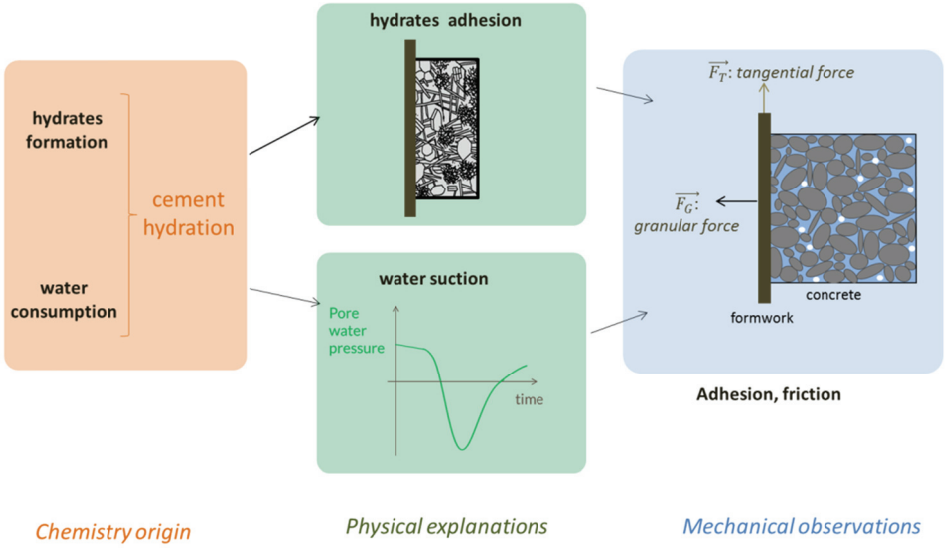

Figure 3. Friction origin

In order to study the phenomenon more in depth, we developed another specific device. This device was designed to study the effect of pore water pressure (suction) on mortar interfacial behavior.

4.3 Capillary water controlled device

The second device is composed of a small cylindrical box where the material is under controlled negative pressure. The objective is to measure shear stress evolution of the material under pore water negative pressure to simulate the effect of cement hydration. The measuring cell is placed on a rheometer with a vane tool to observe the yield stress or with a smooth cylindrical tool to characterize tribology properties. The measuring cell is 50 mm high and 50 mm diameter (Figure 4) to guaranty the homogeneity of the material. The system is equipped with two pressure volume controllers (GDS ELDPC), one for inducing water pressure decrease (by water removing) and the other for measuring the pressure at 90° location and at the height of the tools. The size of the chamber can be small because the experiments are conducted with small grains mix (gap between blades and chamber 10 times larger than the diameter of the bigger particles [10]). In the vertical shear stress device we observe the

friction created by both the bonding of the hydrates and the increasing of the effective granular stress (which increases with water consumption). This device is complementary to the vertical shear stress device because it will permit to separate the adhesion phenomena created by pore water pressure and the hydrates physical bonds to the metallic surface [6]. This small device allows to monitor the pore water pressure without the creation of hydrates because experiment are conducted on an inert material and secondly on the cementitious material before the hydrates formation. This device also allows comparing the material cohesion (yield stress) with its adhesion to a given support.

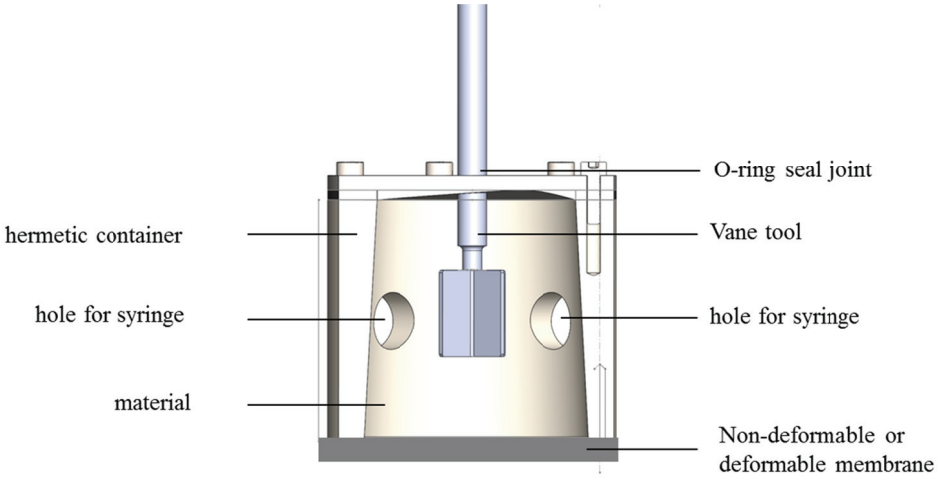

Figure 4. Controlled pressure device to measure shear stress

This device has similarities with [10], that developed a set-up to measure simultaneously torque and pore water pressure for concrete sample (so the chamber size is larger to avoid aggregates effect and especially the pore water pressure is measured whereas in our device pore water pressure can be controlled).

Protocol

The two different tools are used: a vane tool and a cylindrical tool (see Figure 5). The height of both tools is 18 mm and 18 mm diameter. The rotation speed is calculated to be equivalent to the vertical shear stress device (0.5 mm.min^{-1}). The tool circumference is 56.5 mm, therefore the speed of measurement is **0.0088 rpm.**

Shear stress

Torque (M_0) is measured thanks to a rheometer. Then shear stress (σ_0) is calculated for both tools (h: height, d: diameter of the tool) assuming that the shear surface described by the tool rotation are similar cylindrical surface:

$$\sigma_0 = \frac{2}{\pi d^3\left(\frac{h}{d}+\frac{1}{3}\right)}.M_0 \qquad (2)$$

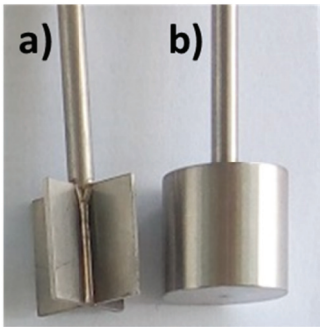

Figure 5. Photo of a) Vane tool b) Cylindrical tool

Control of the pore water pressure

Two pressure/volume controllers are used in the device. They are filled with de-aerated water. Those two controllers are used to record pressure during the test. In the vertical shear stress device, the effective stress increases when the pore water pressure decreases. The relevant zone of interest is identified during the period when the pore water pressure is decreasing from 0 to around -20 kPa. The protocol of the test begins with a rheometer measurement at atmospheric pressure. Then, water pressure was set to -16 kPa, and rheometer measurement was conveyed at this negative pressure. At the end of the test, a last measurement was carried out at 0 kPa pressure in order to evaluate the impact of the O-ring joint which can induce unwanted friction stress (that is corrected by a blank before test).

Two configurations

Two different configurations of the device have been developed. The first one is a non-deformable and the second one is a deformable box (see Figure 4). The objective is to study the difference between the two devices. The non-deformable box should not allow for volume variation of solid skeleton, used as the reference whereas the deformable membrane (situated at the bottom of the box) should allow to increase the effective stress (in example: one can think about a coffee box or coffee bag under pressure, in the first case the coffee grains can move whereas in the deformable coffee bag, with negative pressure, grains are confined by increasing the solid volume content).

Mecanisms

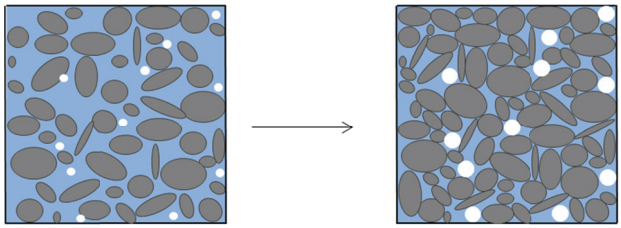

Figure 6. "Soft" state to "hard" state concrete transition behaviour

Fresh concrete may be visualized as particles of inert aggregate which are held or suspended in a deformable matrix of cement paste and air bubbles [11]; this means that under atmospheric pressure grains are like suspended, then, when pore water pressure becomes negative called limit between ”soft “ suspension and “ hard “ suspension where the aggregates

contact network appears [10]. After this "hard state" capillary pressure can only cause comparatively little compaction. When grains percolation is reached, the grains are pushed together to form chains and increase the particle friction force [12].

Therefore the effect of entrapped air is mostly dominant because the volume of air bubbles will increase. Air plays the role of expansion cavities (see Figure 6). This last phenomenon can be study when using a non-deformable container.

5. PRIMARY RESULTS

Primary results were obtained with its deformable device on the inert mix with the vane tool. A blank of the joint friction with water was subtracted to the curves (Figure 7).

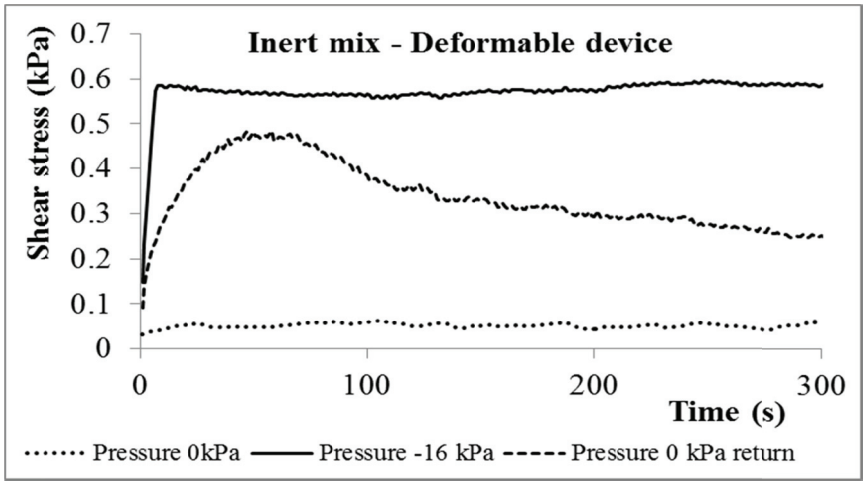

Figure 7. Shear stress (Vane tool 18 mm) of the inert material in the deformable device at 0, -20 and 0 kPa water pressure

At 0 kPa (atmospheric) pressure, the shear stress of the material is very low. Under pressure (-16 kPa), the shear stress increases to an average of 0.6 kPa. After the test, shear stress was measured at 0 kPa again. The material seems to have been compacted because the shear stress is higher than the first one obtained at 0 kPa.

Those results need to be confirmed using the un-deformable container, as water has been removed resulting in a higher solid contain and that the shear stress is observed with a higher solid content material.

With this device, the experiments were conveyed only on the inert material; for the following of the study, the mortar will be study to observe if there is an effect of the hardening of the concrete.

6. CONCLUSION AND PERSPECTIVES

Specific devices have been designed to study the adhesion phenomenon of fresh to early age concrete. A first experiment tool allows measuring the friction of a fresh mortar during the 12 first hours of hydration. Pore water pressure is a key parameter because it seems to be mainly at the origin of friction on concrete/formwork interface. A more specific device was developed in order to take into account only pore water pressure effect (without hydrate bonding) by using an inert material. Two types of container were used: a deformable which

allows water transfer and a non-deformable one. First experiments show an increase of shear stress with a decrease of pore water pressure.

Further experiments on the non-deformable container will be explored to confirm the increasing of yield stress by negative water controlled pressure. The tribology properties will be also considered in the following study.

ACKNOWLEDGEMENTS

The authors warmly thank Alexandre Menguy who made the drawings of the experimental device, and Cédric Juge who helped with the development of the pressure control device.

REFERENCES

[1] Fossä, K. T. Slipforming of Vertical Concrete Structures. Friction between Concrete and Slipform Panel. (Fakultet for ingeniørvitenskap og teknologi, 2001).
[2] Hammer, T. A., «The use of pore water presure to follow the evolution from fresh to hardened concrete », 2006 (e-ISBN: 2351580028) RILEM Publications SARL.Conference, London, September, 1965 (Cement and Concrete Association, London, 1968) 59-81.
[3] U. M. Angst et al., « The steel–concrete interface », Mater. Struct., vol. 50, no 2, avr. 2017.
[4] Scrivener KL, Crumbie AK, Laugesen P (2004). The interfacial transition zone (ITZ) between cement paste and aggregate in concrete. Interface Sci 12(4):411–421.
[5] M. Martin, « Etude de la texture de la surface coffrée des parements verticaux en béton », Université Laval, 2007.
[6] F. H. Wittmann, « On the action of capillary pressure in fresh concrete », Cem. Concr. Res., vol. 6, no 1, p. 49–56, 1976.
[7] S. Ghourchian, M. Wyrzykowski, et P. Lura, « A poromechanics model for plastic shrinkage of fresh cementitious materials », Cem. Concr. Res., vol. 109, p. 120‑132, juill. 2018.
[8] V. Slowik, T. Hübner, M. Schmidt, et B. Villmann, « Simulation of capillary shrinkage cracking in cement-like materials », Cem. Concr. Compos., vol. 31, no 7, p. 461‑469, août 2009.
[9] T. Craipeau, T. Lecompte, F. Toussaint, A. Perrot, Evolution of concrete/formwork interface in slipforming process (2019) RILEM Bookseries, 19, pp. 12-23.
[10] T. Lecompte, A. Perrot, V. Picandet, H. Bellegou, et S. Amziane, « Cement-based mixes: Shearing properties and pore pressure », Cem. Concr. Res., vol. 42, no 1, p. 139‑147, janv. 2012.
[11] A. Alexandridis, N.J. Gardner, “Mechanical Behavior of Fresh Concrete”, Cem. Concr. Res., vol.11, 1981, p. 323-339.
[12] C.S. Campbell, Granular material flows — an overview, Powder Tech. 162 (2006) 208–229.

International Conference on Sustainable Materials, Systems and Structures (SMSS 2019)
Novel Methods for Characterization of Materials and Structures
20-22 March 2019 – Rovinj, Croatia

AIR-COUPLED FERROELECTRET ULTRASONIC TRANSDUCERS FOR NONDESTRUCTIVE TESTING OF WOOD IN THROUGH TRANSMISSION AND REFLECTION MODE

Konrad J. Vössing (1), Mate Gaal (1) and Ernst Niederleithinger (1)

(1) Bundesanstalt für Materialforschung und –prüfung, Germany

Abstract

The demand for nondestructive testing (NDT) methods of wood-based materials (WBM) that are able to automatically scan large areas is increasing. Air-coupled ultrasound (ACU) is used to detect flaws without having to provide contact to the surface or otherwise affect the object. Using through transmission, it is possible to detect even small voids and missing adhesive. If only one side of an object is accessible, the reflection mode is applicable at the expense of a reduced resolution and penetration depth. Novel ferroelectret transducers with a high signal-to-noise ratio (SNR) enable an accurate flaw detection while at the same time being cost effective. The transducers made of cellular polypropylene (PP) are suitable for ACU testing due to their extremely low Young's modulus and low density which result in a favorable acoustic impedance for the transmission of ultrasonic waves between the transducer and air. Thus, defects such as delamination, rot, and cracks can be detected. Successful tests were performed under laboratory conditions with frequencies from 90 kHz to 200 kHz. Ultrasonic quality assurance for wood is an important attempt to increase the acceptance of wooden structures and towards sustainability in civil engineering in general.

Keywords: Air-coupled ultrasound, Cellular polypropylene, Defect detection, Nondestructive Testing, Wood

1. INTRODUCTION

The challenge for nondestructive testing (NDT) is to identify hidden damage in timber without altering the functional properties of the elements under investigation so that appropriate measures can be taken address any deficiencies. Often, damage of timber is caused by manufacturing errors or incorrect applications during its service life. Common defects in practice which lead to complaints and repairs are delamination, cracks, and branchiness [1].

Like conventional ultrasound, air-coupled ultrasound (ACU) is non- hazardous, fast, and less expensive than most other techniques. This noncontact technique can scan large areas within a short time. ACU is quite suitable for characterizing wood and wood products because their lower mass density means a more favorable acoustic impedance for the transmission of ultrasonic waves [2]. Ultrasonic transducers have been made traditionally made from piezoceramic materials [3].

This paper presents nondestructive imaging based on a new type of ACU transducers that are focused on the internal inspection of wood by through transmission and reflection mode.

2. MATERIALS AND METHODS

2.1 Cellular Polypropylene transducers

The inspection presented in this article was performed with air-coupled transducers that utilize charged cellular polypropylene (PP) [4]. Charged cellular polymers are called ferroelectrets or sometimes piezoelectrets, as they have ferroelectric, and thus, piezoelectric properties respectively. Charged PP films (e.g. from EMFIT Ltd.) have a nominal thickness of 70 μm (actual thickness 80-90 μm), a density of about 330 kg/m^3, and an extremely low Young's modulus of about 1 MPa at their resonance frequency, which is between 200 and 300 kHz when glued to hard backing [5, 6]. Therefore, cellular PP has an exceptionally low acoustic impedance of about 0.03 MRayl against the 30 MRayl of piezoelectric materials commonly used as transducers. These features provide good matching to air, so that it requires no matching layers like conventional air-coupled transducers.

2.2 Experimental setup

For transmission measurements, the sample was placed between the transmitter and the receiver which were moved by an automated scanning system (USPC 4000 AirTech by company Ingenieurbüro Dr. Hilger) over the surface in a meandric pattern. At the same time, the data acquisition device displayed the signal amplitude and the time of flight (TOF) as a composite image (so called C-Scan) (Fig.1a). The separate transmitter and receiver were located on one side of the specimen so that the reflected pulse could be received (Fig.1b). We call this configuration reflection mode. The transducers were separated by an aluminum-foam-aluminum partition to avoid direct sound transmission. The aperture was pressed by rubber bands continuously on the surface. The incidence angle of the transducers was 3° and the distance to the sample 65 mm. The grid of the scan was 1.05 mm and the propagation direction radial/ tangential to the surface.

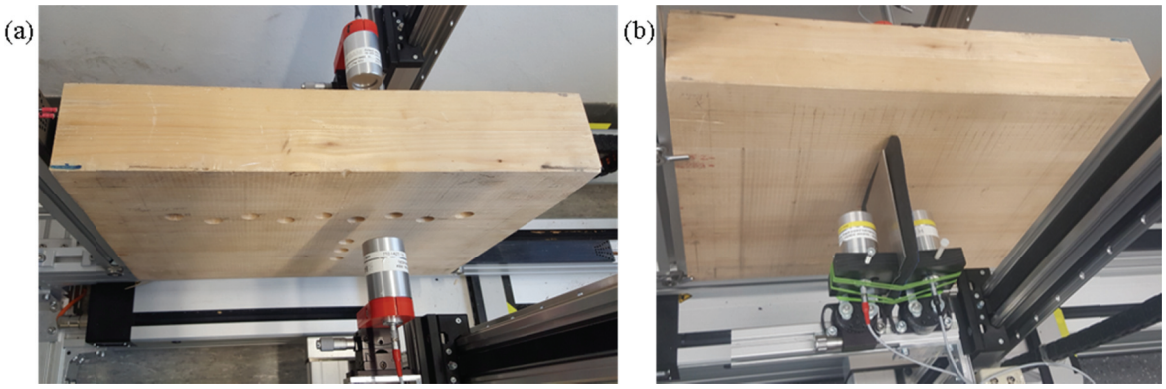

Fig. 1: Experimental setup in transmission (a) and reflection mode (b) with spruce specimen

2.3 Test sample preparation

Various wood-based materials were used as test materials to examine the new measurement technology. The samples were the most frequently used materials that fulfill high safety requirements, such as glulam, laminated veneer lumber (LVL), and plywood. These kinds of products are composed of several layers of wood glued together. In order to assess the potential of ACU for NDT, artificial defects, for example, wrong adhesives, drillings, and cuts, were inserted in the reference samples.

The measurement results collected on a sample of a glued laminated timber are shown as an example. The specimen "Glulam 1" (Fig. 1) out of spruce (picea) has a wood moisture of 9 % (50 % rel. air humidity, 24°C.) and a density of 470 kg/m^3. The glulam has the dimensions of 500 × 400 × 90 mm^3 and is composed of 16 square timbers stuck together. At the bottom, 12 drillings are located at various depths and shapes. They range from 10 mm to 50.1 mm and have either blind holes or countersinks.

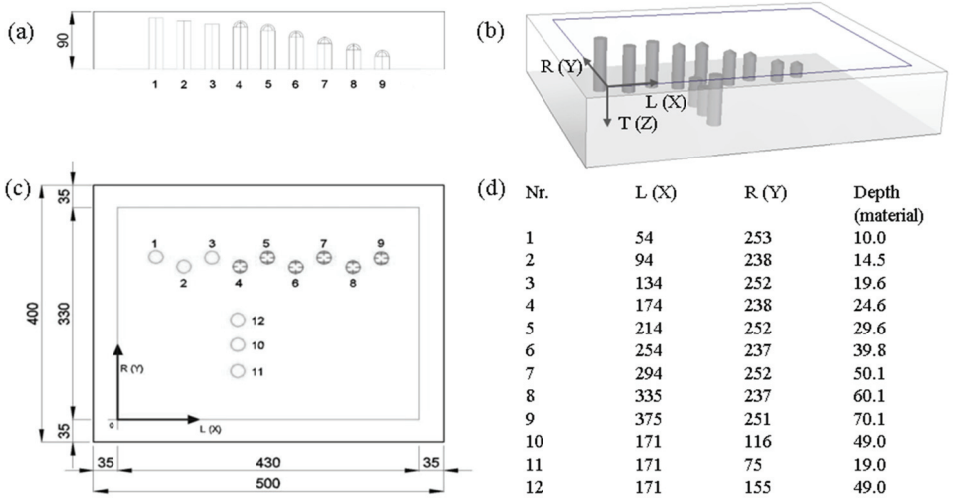

Nr.	L (X)	R (Y)	Depth (material)
1	54	253	10.0
2	94	238	14.5
3	134	252	19.6
4	174	238	24.6
5	214	252	29.6
6	254	237	39.8
7	294	252	50.1
8	335	237	60.1
9	375	251	70.1
10	171	116	49.0
11	171	75	19.0
12	171	155	49.0

Figure 2: Principal setup of the specimen Glulam 1 with 12 test-drillings on the bottom in lateral view (a), top view (b) and 3D view (c). The coordinate system shows the measuring field. Location information of the 12 drillings and their depth in mm can be taken from the tabular data (d).

3. RESULTS AND DISCUSSION

Previously published measurements in transmission mode have shown that cellular PP transducers allow the detection of delamination, glued joints, knots, and wood degradation by fungi & insect attack. Due to the improved signal to noise ratio, the amplitude of the receiving signal is up to three times higher than from commercially available ACU transducers. Thus, measurements in reflection mode are possible and lead to comparable results to point contact transducers with the advantage of being up to 200 times faster. In through transmission samples with thicknesses as great as 300 mm can be scanned.

Fig. 3 shows two measurements of the specimen Glulam 1 in reflection mode and through transmission. In reflection mode, the drillings 1–3 and 10-12 can be located because of their position near the surface and their blind hole shape. With increasing depth, the attenuation is increasing, too, so that the other drillings cannot be seen. Moreover, countersinks lead to an enhanced scatter of the signal.

The anisotropy of the wood has in reflection mode a doubled influence on the ultrasonic signal due to a doubled sound path. The result is a distorted scan caused by different sound velocities in all three anatomic directions. Another challenge are the surface waves which overlap the backwall echo of the specimen.

In through transmission, all drillings can be detected. Even the glueline of the individual battens and the fiber orientation can be seen. Using the imaging results of the transmission measurements, the depth of the holes can be determined by the color value analysis.

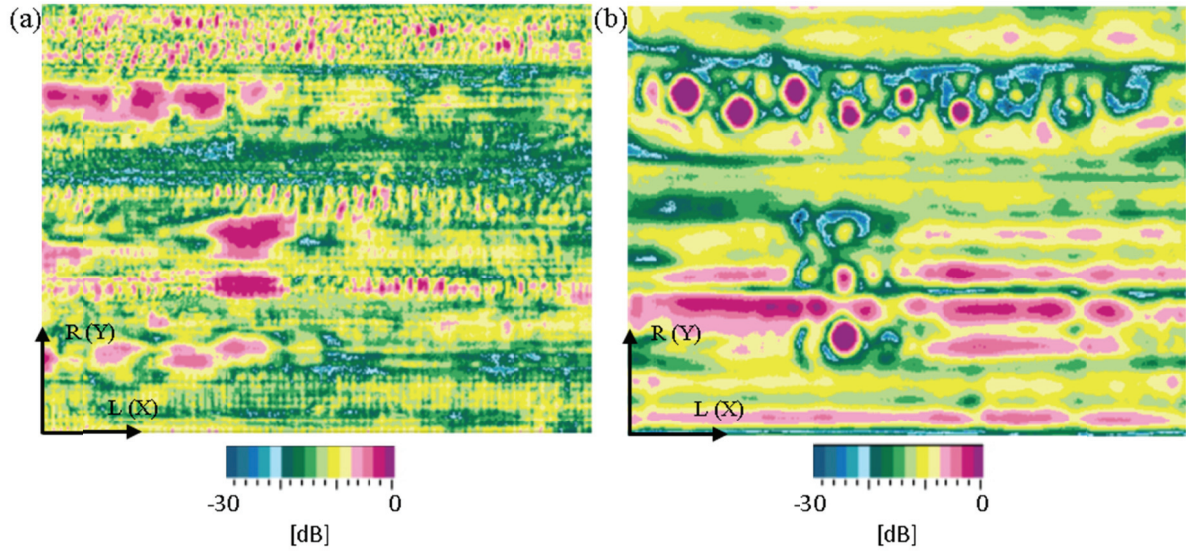

Fig. 3: Ultrasonic imaging results with frequencies of 130 kHz with reflection mode (a) and in through transmission (b). The measurement shows the amplitude in dB.

Fig. 4 shows for comparison ultrasonic imaging results collected with point contact transducers previously at BAM. The data were acquired using the device "Acsys A1220" and were processed by a so-called synthetic aperture focusing technique (SAFT) reconstruction in 3D [7]. The results are comparable to the ACU results in reflection mode. A SAFT-reconstruction takes a lot of time. Therefore, this technique is only applicable for small components. The demonstrated ACU-technique can deliver results in real time. Therefore, it

is applicable for continuously testing during production of wood-based materials. To verify the results, a radiogram was taken to visualize all defects and the wood texture.

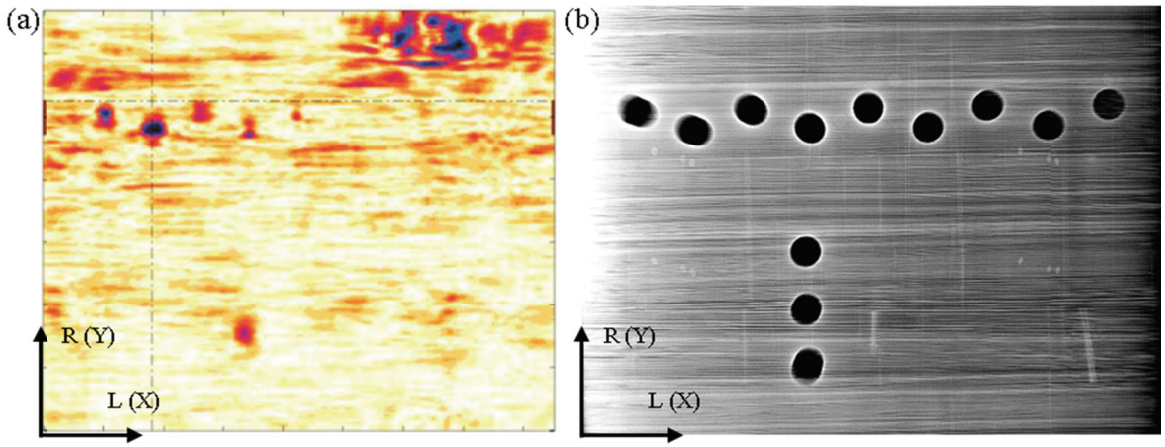

Fig. 4: Ultrasonic echo imaging results (reflection amplitudes) with point contact transducers (courtesy of Dr. Krause, BAM 8.2) (a). Radiograph of the test specimen with an exposure time of 3 min (b). From [7].

11. CONCLUSIONS

Cellular Polypropylene (PP) transducers are a promising new type of transducers for air-coupled ultrasound (ACU) testing. They allow for regular and reliable inspection and the possibility to detect delamination, rot, and cavities in timber structures so that suitable remediation can be initiated. These transducers have many advantages – they are powerful, non- hazardous, and their production is simple. The receiving signal is up to three times higher than from piezoceramic transducers. Therefore, cellular PP transducers can produce inspection results where piezocomposite transducers fail due to a lower signal to noise ratio. The measurements are possible in both through transmission and in reflection mode. The reflection mode was shown to be applicable in principle, but flaw detection capability is limited.

ACKNOWLEDGEMENTS

The first author's research work is funded by the Cusanuswerk, Episcopal Study Sponsorship.

REFERENCES

[1] Bucur, V., 'Delamination in Wood, Wood Products and Wood-Based Composites' (Springer Netherlands, Dordrecht, Heidelberg, London, New York, 2011).
[2] Chimenti, D.E., 'Review of air-coupled ultrasonic materials characterization', *Ultrasonics* **54** (2014) 1804–1816.
[3] Kunkle, J., Vun, R.Y., Eischeild, T., Langron, M., Bhardwaj, N., Bhardwaj, M., in: Secondary 'Phenomenal advancements in transducers and piezoelectric composites for non-contact ultrasound and other applications', ed Group, T.U. (Berlin, Germany, 2006).

[4] Paajanen, M., Lekkala, J., Kirjavainen, K., 'ElectroMechanical Film (EMFi) - a new multipurpose electret material', *Sensors Actuators, A Phys.* **84** (2000) 95-102.
[5] Döring, J., Bovtun, V., Gaal, M., Bartusch, J., Erhard, A., Kreutzbruck, M., Yakymenko, Y., 'Piezoelectric and electrostrictive effects in ferroelectret ultrasonic transducers', *J. Appl. Phys.* **112** (2012) 6.
[6] Gaal, M., Bovtun, V., Stark, W., Erhard, A., Yakymenko, Y., Kreutzbruck, M., 'Viscoelastic properties of cellular polypropylene ferroelectrets', *J. Appl. Phys.* **119** (2016).
[7] Krause, M., Mayer, K., Ballier, G., Borchardt, K., Chinta, P., Effner, U., Milmann, B., Müller, S., Nowak, T., in: Secondary 'Hochgenaue Strukturerkennung von Holzbauteilen mit 3D-Ultraschall', (Forschungsinitiative Zukunft Bau, Stuttgart, 2014).

International Conference on Sustainable Materials, Systems and Structures (SMSS 2019)
Novel Methods for Characterization of Materials and Structures
20-22 March 2019 – Rovinj, Croatia

METHODS OF EVALUATING WORKABILITY FOR CONCRETES REINFORCED BY DIFFERENT FIBER TYPES

Veronica Guerini (1), Antonio Conforti (1), Giovanni Plizzari (1) and Shiho Kawashima (2)

(1) Department of Civil, Environmental, Architectural Engineering and Mathematics, University of Brescia, Italy

(2) Department of Civil Engineering and Engineering Mechanics, Columbia University, New York, USA

Abstract

Fibers are effective for supplementing or replacing conventional reinforcement in non-structural and structural elements, i.e. industrial floor, road pavements, beams (shear reinforcement), slabs and tunnel linings. Although there are several benefits to using fibers as spread reinforcement, it is well-known that any type of fiber will reduce the workability, i.e. compactability, mobility and stability. In addition, there can be challenges in dispersion, where fibers entangle and result in non-uniform distribution in the concrete. The aim of this paper concerns the study of the influence of steel (rigid) and macro-synthetic (non-rigid) fibers on the fresh properties of concrete, i.e. workability and air content, as well as resultant mechanical performance. Four fiber types at two volume fractions (0.5% and 1.0%) were studied in a base concrete with a water-to-cement ratios equal to 0.45 by using the slump test, DIN flow table test and air content meter. Experimental results show that rigid and non-rigid fibers lead to different effects on the fresh properties. In addition, the combination of the slump test and DIN flow table test can give quantitative and qualitative information about the influence of fibers on concrete workability. Finally, an additional parameter for the DIN flow table test is proposed for quantifying any potential preferential flow direction.

Keywords: Workability, Slump, Steel fibers, Polypropylene fibers, Fiber Reinforced Concrete

1. INTRODUCTION

In comparison to the numerous studies present in the literature about the hardened properties of Fiber Reinforced Concrete (FRC), only a relatively small number of studies are focused on its workability [1, 2, 3, 4]. In addition, the majority of these studies are focused on

steel fibers [1, 2, 3], while macro-synthetic fibers were studied only in [4]. In these studies, different test methods were adopted to measure the fresh properties related to workability, including slump, Vebe test, inverted cone test, compacting factor test, DIN flow table test and rheometers. The slump test (also called the Abram's cone) was developed in the U.S. around 1910 for plain concrete (PC) [5]. Due to its simplicity, it is the most commonly used method for both PC and FRC, even if it only provides a measure of concrete consistency. Slump test can not provide a good index of workability in terms of placeability and compactability of FRC under vibration [6]. In the case of vibrated FRC, the Vebe test (developed around 1940 for PC [7]) is more suitable. However, the slump test is still the most used method on the building site, while Vebe test is more popular in the laboratory. In addition, the Vebe test is applicable only to low workability and stiff concretes, which are in general to be avoided for typical casting since concrete mobility and pumpability are required. Concerning the other tests, the compacting factor test measures the degree of compaction for a standard amount of work, while the inverted cone and DIN flow table tests allow for measuring concrete flowability. It is worth mentioning that the DIN flow table test, which was developed for PC by Graf in 1933 [8], is commonly used in several countries for evaluating the workability of concrete on-site. Finally, rheometers (which are generally used for normal and high strength mortars) are rarely used to characterize the rheological parameters of concretes.

rarely used to characterize the rheological parameters for concretes but instead more for normal and high strength mortars with fiber addition.

The present manuscript evaluates the fresh properties of FRC mixes. Two steel (rigid) and two macro-synthetic (non-rigid) fibers with similar aspect ratios were studied in a base concrete varying fiber volume fraction (0, 0.5, 1.0%) in order to evaluate the influence of rigid versus non-rigid fibers on the fresh properties. The fresh properties were evaluated by the slump test and DIN flow table test in order to analyze the possible integration of these two methods to control FRC workability on-site.

2. MATERIAL PROPERTIES

The effect of fibers on the fresh properties was studied on a base concrete C50 with a mean cylindrical compressive strength of about 50 MPa and water-to-cement ratio (w/c) of 0.45. The mix proportion of the base concrete was developed by following the Absolute Volume Method of Concrete Mix Design provided by American Concrete Institute (ACI) [9]. Table 1 shows the mix design of the concrete C50

Table 1: Mix design of base concrete C50.

Concrete C50	
Sand 0-4.75 [kg/m^3]	730
Coarse aggregate 4.75-25 [kg/m^3]	992
Maximum Aggregate Size [mm]	25
Cement Type	Type I
Cement Content [kg/m^3]	429
Water-Cement Ratio	0.45
Superplasticizer (% of cement content)	0.11

Four fiber types (Figure 1) were added to the base concrete:

- two rigid fibers having a hooked end shape: steel fibers s1 (35 mm long, diameter of 0.54 mm, tensile strength of 1345 MPa) and steel fibers s2 (60 mm long, diameter of 0.92 mm, tensile strength of 1100 MPa);
- two non-rigid macro-synthetic fibers: crimped polypropylene fibers p1 (40 mm long, diameter of 0.75 mm, tensile strength of 450 MPa) and embossed polypropylene fibers p2 (54 mm long, diameter of 0.81 mm, tensile strength of 552 MPa).

These fibers were added to concrete in two different volume fractions (V_f): 0.5% and 1.0%.

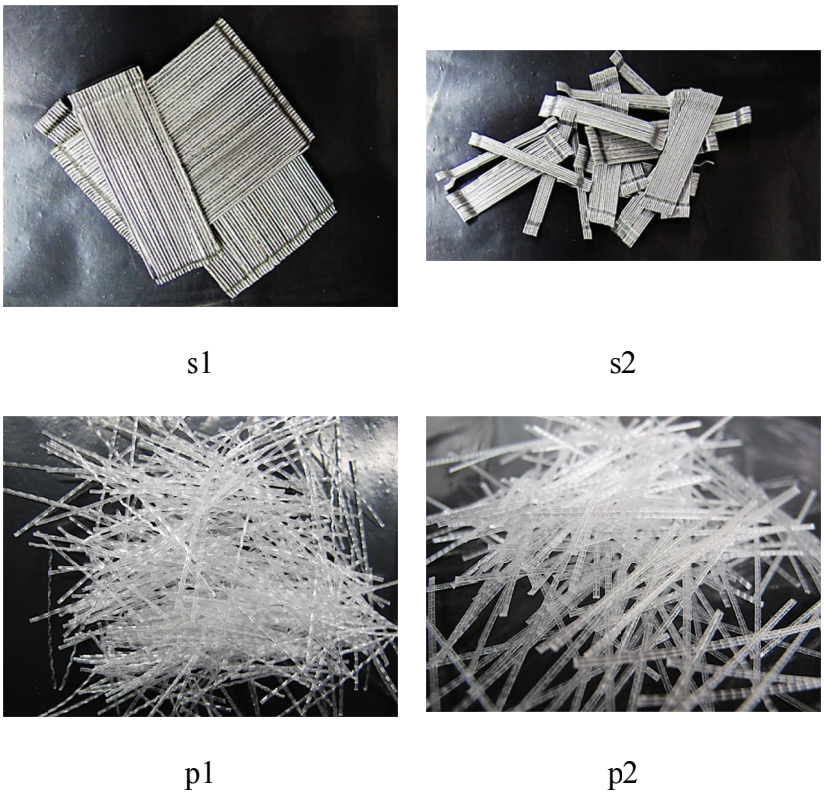

Figure 1: Steel fibers (s1, s2) and macro-synthetic fibers (p1, p2) used in this study.

Therefore, nine different concrete matrices were investigated: one PC, four Steel Fiber Reinforced Concrete (SFRC) and four Polypropylene Fiber Reinforced Concrete (PFRC). All the necessary information is included in the concrete designations, e.g. designation C50-p1-0.50% refers to a base concrete C50 reinforced by p1 fibers at a volume fraction of 0.50%.

3. TEST METHOD

For each mix design, three batches were prepared and the slump test, DIN flow table test and air content measurement were performed on each batch. After initial measurements, which capture any loss in workability caused by fiber addition as compared to the control (PC), each mix was modified by adding polycarboxylate-based SP until a slump of 18 ± 2 cm was restored. The DIN flow table test and air content measurement were performed on the

modified mix, then cast into molds immediately after to produce samples for mechanical testing. This allowed for comparing mechanical properties (minimizing possible different fiber orientation) of FRCs with similar slump, as well as flow properties and air content. All mixes were prepared by using a laboratory rotary concrete mixer. The mixing protocol consisted of the following steps:

- Dry-mix the sand, coarse aggregate and fibers for 90 seconds;
- Addition of cement. Mix for 90 seconds;
- 90 seconds of rest;
- Addition of liquid (water + superplasticizer listed in Table 1) in the mixer. Mix for 5 minutes. The mixture is then ready for evaluating workability and air content.
- Addition of additional superplasticizer to obtain PC consistency (slump of 18 ± 2 cm). Mix for 2 minutes. The mixture is then ready for casting.

The experimental setups of the adopted experimental tests are summarized in Figure 2.

Properties of fresh concrete

Air content

Slump test

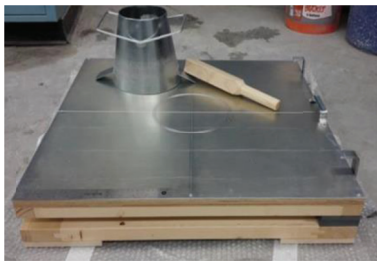

DIN flow table test

Properties of hardened concrete

Compressive strength

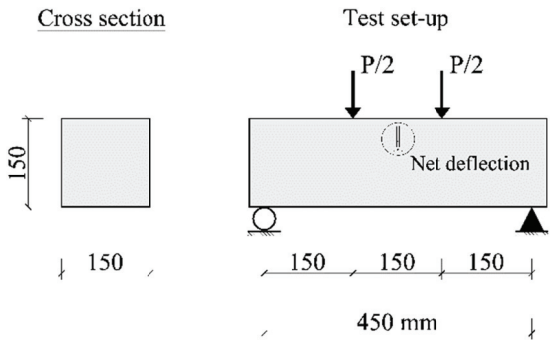

Four point bending test (ASTM C1609 [10])

Figure 2: Test methods to evaluate both fresh and hardened properties of PC and FRC.

4. HARDENED STATE PROPERTIES

Concretes C50 was characterized by an overall mean compressive strength of approximately 51.1 MPa with a coefficient of variation (CV) equal to 0.03. This result indicates that the fiber addition, either rigid or non-rigid, did not influence the compressive strength in the range of fiber content considered.

Concerning the flexural properties, the overall mean values of f_l was 6.13 MPa (CV = 0.03), while the residual flexural tensile strength and toughness values vary as a function of fiber type (with CV ranging between 0.03 to 0.32). Furthermore, residual flexural tensile strength results exhibited more variability than toughness results and, overall, similar values were observed in both steel and macro-synthetic fibers. A clear hardening behavior in bending was observed only for steel fibers s1 and s2 at V_f = 1%, while macro-synthetic fibers always exhibited a softening behavior characterized by a sharp drop after the peak load followed by residual strength. Figure 3 shows the mean value of $f_{150,3.00}$ exhibited by the different fibers.

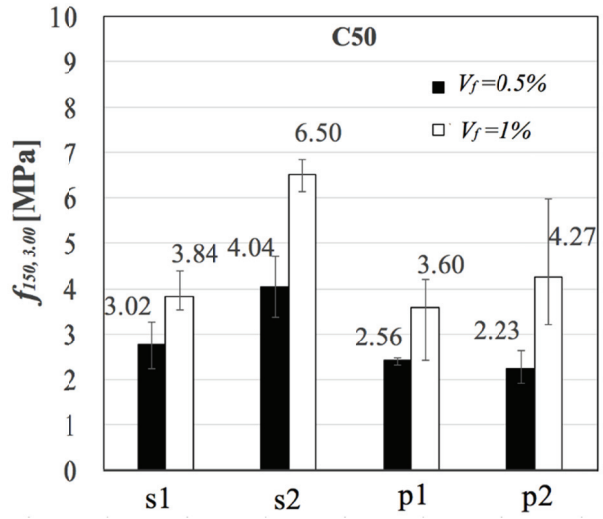

Figure 3: Residual strength at a deflection of 3.00 mm (ASTM C1609 [10]).

5. FRESH STATE PROPERTIES

First of all, it is interesting to discuss the air content in order to verify one of the potential negative influences of fibers. Both steel and macro-synthetic fibers led to a slight increase in air content and its variability, as well as an increase in air content with V_f. However, results show that macro-synthetic fibers more adversely affected air content than steel fibers. At V_f = 0.5%, SFRC was characterized by a similar air content as PC while PFRC exhibited an increase in air by up to 0.5%. With V_f = 1%, air content increased by up to 0.5% with steel fibers and up to 0.7% with macro-synthetic fibers as compared to PC. Even so, up to V_f = 1%, for both fiber types the increase in air was marginal, indicating that fiber influence was negligible in the base concrete systems investigated. This has positive implications as in the majority of structural and non-structural applications of fibers, the adopted values of V_f are generally not greater than 1%. Still, it would be interesting in future studies to investigate the effect of fibers on air content for V_f values greater than 1% or in different base concrete systems for more specialized applications.

Regarding concrete consistency, Figure 4 shows slump reduction as a function of fiber type and content. As expected, a noticeable slump reduction due to fiber addition was observed, indicating stiffer, less workable mixes. A similar trend was observed by other researchers studying different concretes and fiber types [3, 11]. In addition, considering the CV values, it can be observed that the addition of fibers not only reduced slump, it also increased variability. In fact, increase in V_f resulted in an increase in the slump scatter – the CV reached a max of 0.28 for V_f =1%. This indicates that at a given w/c ratio, the reliability of the slump test is less for FRC systems as compared to PC systems, likely due to greater heterogeneity of the material.

Comparing rigid versus non-rigid fibers, it is apparent in Figure 4 that non-rigid fibers led to a smaller reduction in consistency of about 15% as compared to rigid fibers.

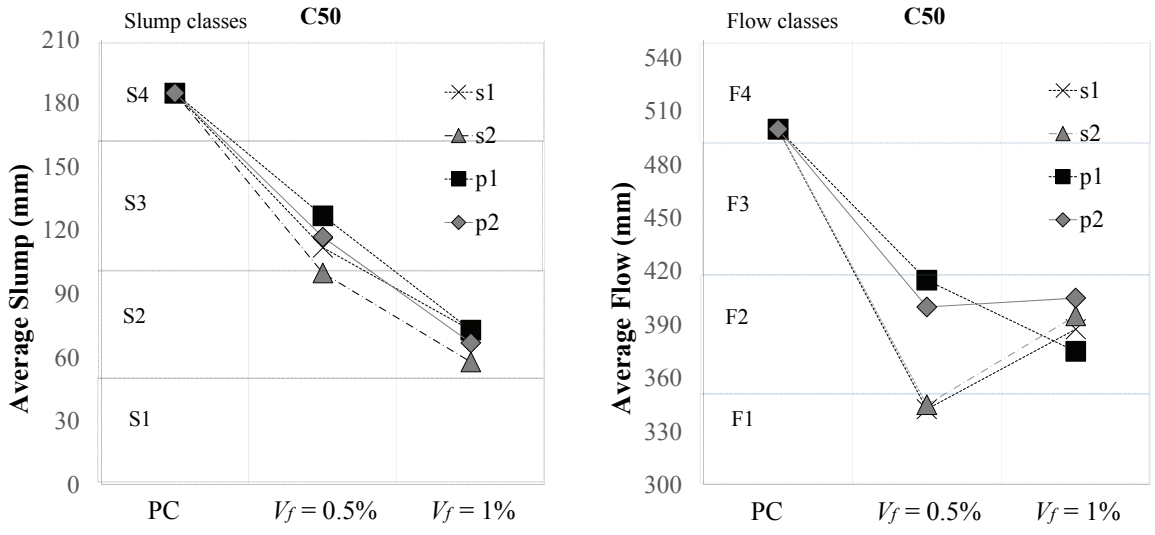

Figure 4: Influence of fibers on slump (left) and flow reduction (right).

Figure 4 shows also the DIN flow table test results in terms of average flow vs. fiber content. It can be observed that both steel and macro-synthetic fibers significantly reduced concrete flowability (by up to 35%) and increased average flow variability as compared to the base concretes. It should also be noted that the CV values for the DIN flow table test were generally smaller than those observed in the slump test. Although the steel fibers had a more adverse effect on flowability than the macro-synthetic fibers up to V_f=0.5%, there was no measurable difference between the mixes at V_f=1%. In fact, an unexpected trend of the mean flow value, which is the average between the minimum and the maximum flow diameter, was observed for C50 mixes with s1, s2 and p2. For these mixes, average flow increased from V_f=0.5% to V_f=1%, indicating an apparent increase in flowability with increase in fiber content. This unexpected trend was generally more evident in the case of the steel fibers. Upon visual inspection of the flow, it is evident that the flow shape changes from circular to elliptical with increased fiber content. The presence of an elongated flow shape in FRC can be attributed to preferential flow due to fiber alignment in one direction and limited flow in the orthogonal direction due to fiber interlocking. Thus, for FRC systems the average flow

diameter alone is not sufficient to quantify flowability and must be supplemented with an additional parameter to take into consideration the eccentricity of the final flow shape. In order to quantify this phenomenon, a new experimental parameter was introduced for FRC:

$$\rho = L_{min}/L_{max} \quad (1)$$

where L_{min} and L_{max} are the minimum and the maximum flow diameter, respectively. The closer the ratio is to 1 the more circular the shape of the flow.

In order to better understand the importance of this parameter, the experimental results of the DIN flow table test are summarized in Table 2, reporting also the ρ ratios and corresponding CV in brackets. It is worth mentioning that the CV of the ρ values are low, indicating good repeatability of the measurements. As expected, PC exhibited ρ values equal to or slightly lower than 1, thus uniform, circular flow. It is also shown that both fiber types led to ρ ratios lower than that of PC, with steel fibers resulting in lower values than macro-synthetic fibers. This indicates that macro-synthetic fibers resulted in more circular final flow shapes than steel fibers. The flexibility of the macro-synthetic fibers likely helped to maintain a more uniform concrete flow, while the rigid steel fibers interlocked and resulted in preferential flow in one direction. Therefore the proposed parameter can provide valuable information when implementing the DIN flow table test, where ρ ratio can give information about preferential direction of flow caused by the presence of fibers.

Table 2: Slump flow and ρ ratio for PC and FRC with different fiber types.

	0.5%	1%
PC	500 ρ=0.99 (0.01)	
s1	343 ρ=0.80 (0.02)	388 ρ=0.72 (0.05)
s2	345 ρ=0.84 (0.03)	395 ρ=0.72 (0.10)
p1	415 ρ=0.98 (0.01)	375 ρ=0.97 (0.00)
p2	400 ρ=0.93 (0.03)	405 ρ=0.90 (0.04)

6. CONCLUSIONS

- The influence of fibers on the air content is negligible up to 1% of volume fraction both in case of steel and macro-synthetic fibers;
- Concrete workability was overall more affected by steel fibers than macro-synthetic ones, as indicated by the results of both the slump and DIN flow table tests;
- Concrete flow behavior differed between SFRC and PFRC mixes. This may be attributed to the steel fibers re-orienting and interlocking, resulting in flow in a preferential direction and the final spread forming an elongated shape;

- DIN flow table test should be supplemented in case of FRC with an additional parameter – the ratio between the diameters along the two axes of symmetry (ρ) – to describe any potential preferential flow direction.

ACKNOWLEDGEMENTS

The Authors are grateful to BASF Construction Chemicals and Euclid Chemical for the materials provided, as well as the technical support by the staff of Carleton Laboratory at Columbia University. Furthermore, a special acknowledgement goes also to the University of Brescia for the economic support during the period of the project.

REFERENCES

[1] Hughes, B.P. and Fattuhi, N.I., 'The workability of steel-fiber-reinforced concrete', *Magazine of Concrete Research.* **28**(96) (1976) 157-161.
[2] Johnston, C.D., 'Measures of the Workability of Steel Fiber Reinforced Concrete and their Precision. Cement', *Concrete and Aggregates.* **6**(2) (1984) 74-83.
[3] de Figueiredo, A.D. and Ceccato, M.R., 'Workability analysis of steel fiber reinforced concrete using slump and Ve-Be test', *Materials Research.* **18**(6) (2015) 1284-1290.
[4] Pasini, F., Garcia, T., Gettu, R. and Agulló, L., 'Experimental study of the properties of flowable fiber reinforced concretes', Proceedings of the sixth RILEM International Symposium (BEFIB 2004) Varenna, Italy, (2004).
[5] EN 12350-2, 'Testing fresh concrete – Part 2: Slump-test', (2009).
[6] Mehta, K.P. and Monteiro, P.J.M., 'Concrete: Microstructure, Properties and Materials', McGraw-Hill, ISBN 0071797874, (2005) p. 659.
[7] Bahrner, V., 'Ein Neue Schwedisches Konsistenzpruefgerat', *Zement.* **29**(9) (1940) 102-106.
[8] Graf, O., 'Experiments of the behavior of Reinforcement in Concrete of Various Compositions', *Deutscher Ausschuss für Eisenbeton.* **71** (1933) 37-60.
[9] ACI Committee 211, 'Standard Practice for Selecting Proportions for Normal, Heavyweight, and Mass Concrete (ACI 211.1-91)', American Concrete Institute, (1991) p. 38.
[10] ASTM C1609, 'Standard Test Method for Flexural Performance of Fiber-Reinforced Concrete (Using Beam With Third-Point Loading)', American Standard, (2012).
[11] Bayasi, M.Z. and Soroushian, P., 'Effect of steel fiber reinforcement on fresh mix properties of concrete', *ACI Material Journal.* **89**(4) (1992) 369-374.

International Conference on Sustainable Materials, Systems and Structures (SMSS 2019)
Novel Methods for Characterization of Materials and Structures
20-22 March 2019 – Rovinj, Croatia

CELL DESIGN AND CHARACTERISATION OF CEMENT HYDRATION BY IMPEDANCE SPECTROSCOPY

Aldo F. Sosa Gallardo (1), John L. Provis (1)

(1) Department of Materials Science and Engineering, University of Sheffield, S1 3JD, United Kingdom

Abstract

The hydration of cement is a complex process which has been assessed by numerous researchers using different analytical tools and techniques. However, despite the progress achieved and the knowledge obtained over several decades, there are still areas not fully understood about this process. The aim of this study is therefore to assess alternating current impedance spectroscopy (ACIS) as a cement characterisation technique by the comparison of different electrochemical cell designs, including calibration. The results show the importance of the correct cell design selection, as this strongly affects the impedance measurements, parasitic effects, and data interpretation.

Keywords: Cement hydration, ACIS, Parasitic effects, Cell design.

1. INTRODUCTION

The early stage of hydration of Portland cement is not fully understood, as cement is a multiphase material that in contact with water triggers different simultaneous reactions, release of heat, the formation of hydrated products, and complex microstructure development [1]–[4]. The understanding of cement hydration and its kinetics, dielectric response, and microstructural development is of great importance to improve its early and final properties and applications.

Over the last decades, ACIS has been used in numerous investigations to assess the cement hydration process and correlate the dielectric response of cement to the microstructure development and features. However, ACIS is not fully accepted by the research community as information obtained at high frequencies at early hydration ages is restricted due to different limitations such as parasitic and electrode effects, the high conductivity of the cement paste, and the risk of misinterpretation of data due to these difficulties [5]–[8].

ACIS is a non-destructive, sensitive and powerful technique which is capable of measuring the electrical response of a system as a function of frequency and time, by applying a perturbation amplitude. The information obtained is often represented as complex impedance

plots or Nyquist plots. This represents both the material bulk response and the material-electrode response, from which it is possible to obtain the resistivity of the material. The impedance values that appear below the Z' axis intercept are identified as parasitic effects.

The electrochemical cell design and experimental procedure for in situ analysis of cements require significant caution, which is often overlooked, as the parasitic effects (e.g. inductance effects) and experimental procedure can affect the impedance measurements, leading to the misinterpretation of data and erroneous measurements [5], [9]–[12]. The purpose of this study is to investigate these effects and to provide guidance for appropriate experimental protocols.

2. MATERIALS AND METHODS

2.1 Cell design

A two-electrode cell design was made by attaching two threaded electrodes with hard plastic adhesive to the bottom of a plastic container. Figure 1 illustrates the experimental cell-design specifications, and the connections to a Metrohm AutoLab (PGSTAT204) impedance spectrometer connections.

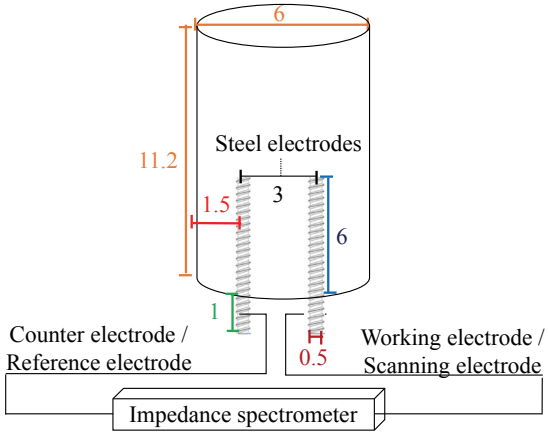

Figure 1: ACIS experimental cell-design (scale in cm).

2.2 Sample preparation

Samples were hand mixed for 3 min at ~ 25 °C by mixing white Portland cement (wPc, Blue Circle Snowcrete, CEM I 52.5R) with distilled water at a water/cement ratio of 0.45. Cement pastes were transferred into the cell and vibrated for 2 min to reduce the level of air bubbles.

2.3 Instrumental analysis

The Nyquist plot, which relate the imaginary and real impedance of the sample, was obtained by measuring 50 data points per cycle, applying a frequency range of 100 Hz to 1 MHz, a perturbation amplitude of 10 mV, and current range of 1 mA. Each sample measurements were obtained every 5 min using the potentiostat during the first 24 hrs after mixing.

2.4 Experimental procedure

The experimental procedure was divided into four stages. The first stage assessed the system linearity, potentiostat leads effects, and the electrode attachment. The second stage

assessed electrode effects such as surface area, material, and positioning. A custom cell design was selected by the evaluation of the previous stages. Table 1 shows the specification for stages one and two.

Table 1: Specifications of the parameters assessed

Stage	Parameter	Specification
1	Electrode attachment	Hard plastic adhesive and stainless-steel nuts
	System linearity	Perturbation amplitude (mV): 1 and 10
	Leads effects (cm)	- Position: vertical, horizontal, and height - Length: 150, 200 and 250
2	Surface area (cm)	- Diameter: 1, 0.5 and 0.3 - Length: 1,2, 4, 6 and 7 - Texture: threaded and flat
	Material	Stainless steel and mild steel
	Positioning (cm)	- Electrode separation 1.5, 3 and 6 - Electrode position: bottom, top, vertical and horizontal

The third stage consisted of the calibration of the custom cell design and ACIS measurement correction, considering the impedance response of the sample and the cell short circuit parasitic response (without cement) as additive quantities in the final ACIS measurement. Finally, the fourth stage assesses the hydration process of cement at early ages by using the selected custom cell design, and applying calibration-correction measurements.

3. RESULTS AND DISCUSSION

The information obtained in all experimentation at high frequency ranges, without applying the cell calibration and measurement corrections, was affected by parasitic effects at early hydration ages. These parasitic effects were due to the high conductivity of the cement paste at an early age, the state of the aqueous phase, limited solid phase microstructure development, and the parasitic effects produced by the experimental components (i.e. leads, electrodes and device).

3.1 Electrode attachment

The results show the impedance response of both electrode attachment methods, 5 min (representing early age) and 24 hrs (longer ages) after mixing. It was possible to observe lower parasitic effects at high frequencies at both ages for electrodes that were attached by hard plastic adhesive, while the electrodes that were attached by stainless steel nuts showed higher parasitic effects due to an increase of current flux lines, surface area, and the decrease of uneven electrode separation [13]–[15]. The emergence of a semicircular arc is more noticeable at longer ages, an effect that is related to the water consumption, the pore network and the microstructure evolution during cement hydration [16], [17].

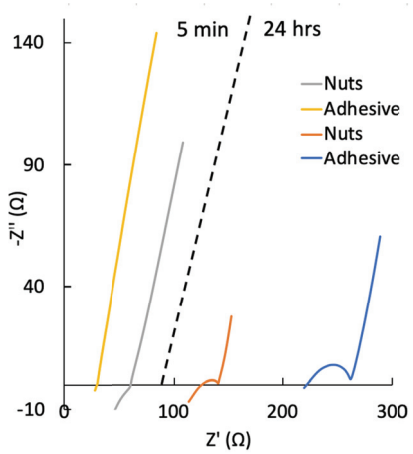

Figure 2: Cement impedance response to different electrode attachment methods.

3.2 System linearity

To verify the linearity of the ACIS response, and the sensitivity of the system, the raw impedance response of the cement system at early age was obtained by comparing two perturbation amplitudes (10 mV and 1 mV). The results were represented by Lissajous (Figure 3) and resolution plots, in which the impedance response at 10 mV, showed a high current and potential resolution, and linear response of the system. However, the impedance response at 1mV showed a strong non-linear response and low resolution because the measurements were affected by noise, polarisation effects and charge-transfer resistance [18]–[21].

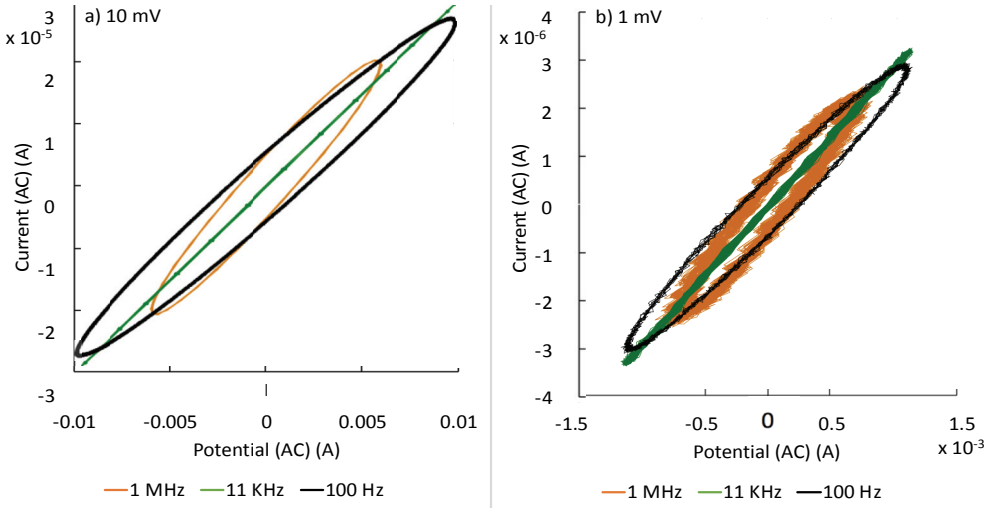

Figure 3: Lissajous plots for wPc at different perturbation amplitudes.

3.3 Leads effects

The leads connected from the potentiostat to the electrochemical cell are one of the main sources of noise and parasitic effects. Therefore, in order to verify the lead grounding, shielding, and effect of the lead length on the impedance measurements, different parameters such as lead alignment, position and length were assessed. The results showed an increase in the parasitic effects due to an amplitude drop as the lead length increases, consistent with the literature [14], [22], [23].

3.4 Electrode effects

Figure 4 shows the effect on the impedance measurements as the electrode surface area (i.e. dimeter, texture and length) changes. It was observed that, at both hydration ages, the parasitic effects rise as the electrode area increases. As the electrode surface area changes, the response of the double layer capacitance, electron transfer resistance, current dispersion and the rate of reactions between the electrode and the cement sample will change, leading to differences in the impedance response [11], [24]–[27]. It was also observed that the electrode texture has a small impact on the impedance measurements.

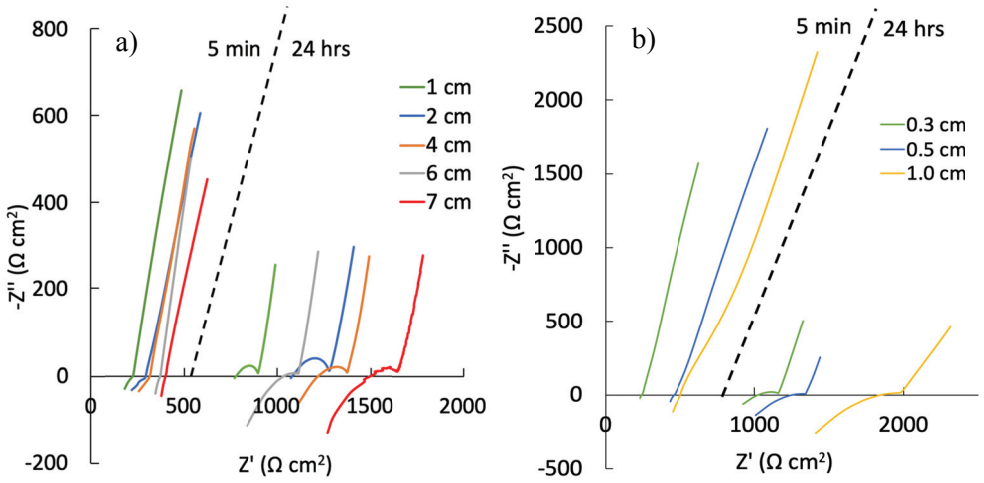

Figure 4: Electrode surface effects on impedance measurements: a) length, b) diameter.

Figure 5a shows the impedance response of cement at different stages of hydration using different electrode materials. Mild steel electrodes show a semicircular arc, the loss of parasitic effects, and higher impedance values at high frequencies. These differences in the impedance response are due to the formation of a protective iron oxide film generated by the pH of the cement paste passivating the mild steel electrodes. Conversely, the chromium-rich oxide film on the stainless steel electrodes is more stable [28]–[31].

Figure 5b shows the influence of the electrode separation on the impedance measurements, where the parasitic effects are affected as the positions of the electrodes change. The effect of the electrode position on the impedance measurements is related to the sample geometry, contraction propagation, thermal cracking of cement, and the current distribution through the sample [26], [32]–[36].

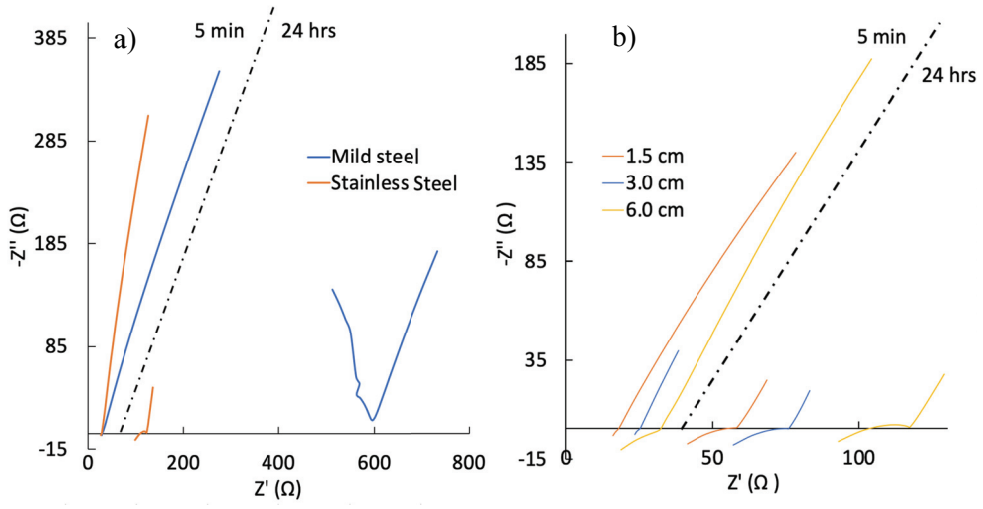

Figure 5: Effect of electrode material (a), and electrode separation (b), on impedance measurements

3.5 Calibration and measurement correction

The calibration and measurement correction were carried out by measuring the impedance response of the short circuited custom cell design selected (without sample). The parasitic effects produced by the experimental design (i.e. cell, leads and electrodes) resulted in a "pipe" shaped plot (below the Z' plane). The short circuit measurement obtained was considered as an additive correction to the impedance response of the cement systems tested. After the measurement correction, the impedance spectra at high frequency showed a semicircular arc above the Z' plane followed by the ACIS measurement correction (calibration of the cell).

3.6 White Portland cement characterisation by ACIS

The final cell design specifications involved the use of threaded stainless steel electrodes of 6 cm length and 3 cm diameter, separated by 3 cm from each other. The measurements were obtained using 10 mV as a perturbation amplitude. The impedance response of cement was obtained every 5 min during the first day, 10 min during the second day, 15 min during the third day, and 20 min during the last 20 hours.

Figure 6 shows the impedance response of cement system during 92 hrs after mixing. At early hydration ages, the resistivity and impedance values are small due to the high conductivity of cement paste. The parasitic effects were eliminated during the first 3.5 hrs. However, directly after this, the parasitic effects suddenly appeared due to the dissolution of C_3S and C_2S increasing the ionic strength (and thus conductivity) of the paste, which was followed by the nucleation of C-S-H, initial crystallisation of CH and the release of heat, which also have an impact on the dielectric properties of cement. At 15 hrs the parasitic effects started to decrease, until they disappeared at 30 hrs due to the microstructure development, pore structure partial closure, and reduced free water content. At longer ages the semicircular arc at high frequency starts to rise progressively as the resistivity keeps increasing, while reaction rates, microstructure and pore network development start to slow down [1], [2], [4], [37], [38].

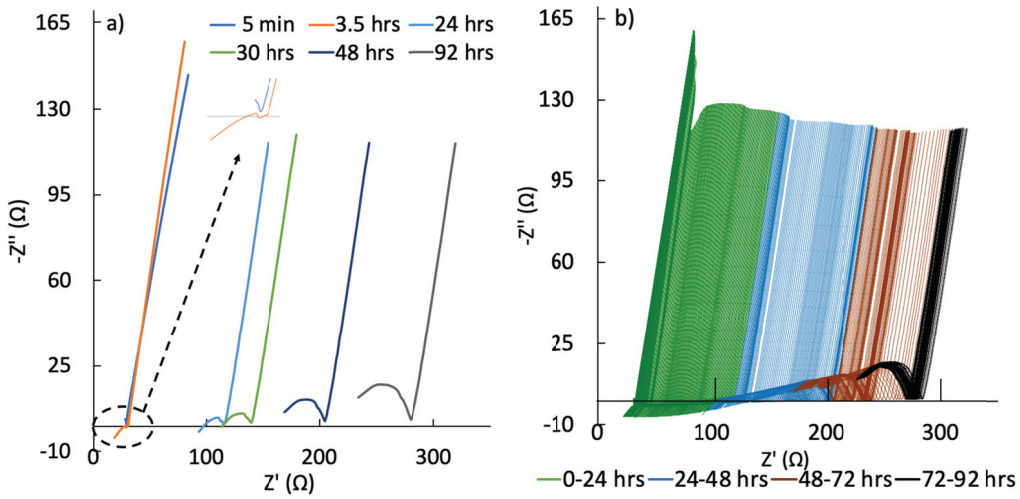

Figure 6: Cement ACIS response during the first 92 hours after mixing: a) selected ACIS spectra; b) waterfall plot of all ACIS spectra

4. CONCLUSIONS

This investigation demonstrates the importance of the cell design selection and the experimental procedure, as these can raise parasitic effects and noise, and lead to complications that can give rise to misinterpretation of data. The use of ACIS as a characterisation technique for the hydration of cement can provide valuable information related to dielectric properties, microstructure development, reaction rate and kinetics of cement. The emergence of parasitic effects, cement impedance response and its interpretation need further investigation.

ACKNOWLEDGEMENTS

This study was funded by the Science and Technology Council of Mexico (Consejo Nacional de Ciencia y Tecnología, CONACYT), and the European Union through the 7th Framework Programme (European Research Council Starting Grant #335928). We thank Prof. Derek C. Sinclair for very valuable discussion in the development and implementation of this work.

REFERENCES

[1] P. K. Mehta and P. J. M. Monteiro, *Concrete: microstructure, properties, and materials*, 3rd ed. California: McGraw-Hill, 2006.
[2] P. C. Hewlett, *Lea's Chemistry of Cement and Concrete*, 4th ed. Oxford: Elsevier, 1998.
[3] B. Kohlhaas, *Cement Engineers' Handbook*, 4th ed. Wiesbaden; Berlin: Bauverlag, 1983.
[4] H. F. W. Taylor, *Cement chemistry*, 2nd ed. London: Thomas Telford, 1997.
[5] T. O. Mason, S. . Ford, J. D. Shane, J.-H. Hwang, and D. D. Edwards, "Experimental limitations in impedance spectroscopy of materials systems," *Adv. Cem. Res.*, pp. 143–150, 1998.
[6] G. Hsieh, T. O. Mason, and L. R. Pederson, "Experimental limitations in impedance spectroscopy: Part II. Electrode artifacts three point measurements on Pt/YSZ," *Solid State Ionics*, pp. 203–212, 1996.
[7] J. H. Hwang, K. S. Kirkpatrick, T. O. Mason, and E. J. Garboczi, "Experimental limitations in

impedance spectroscopy: Part IV. Electrode contact effects," *Solid State Ionics*, pp. 93–104, 1997.
[8] R. Spragg, C. Villani, K. Snyder, D. Bentz, J. Bullard, and J. Weiss, "Factors that influence electrical resistivity measurements in cementitious systems," *Transp. Res. Rec.*, vol. 2342, pp. 1–12, 2013.
[9] X.-Z. Yuan, C. Song, H. Wang, and J. Zhang, *Electrochemical impedance spectroscopy in PEM fuel cells*. London: Springer, 2010.
[10] J. R. Macdonald and W. B. Johnson, *Impedance spectroscopy theory, experiment, and applications*, Second. Wiley, 2005.
[11] M. E. Orazem and B. Tribollet, *Electrochemical impedance spectroscopy*. Hoboken: Wiley, 2008.
[12] B. Christensen *et al.*, "Impedance spectroscopy of hydrating cement based materials: measurement, interpretation, and application," *J. Am. Ceram. Soc.*, vol. 77, no. 11, pp. 2789–2804, 1994.
[13] C. R. Paul, "Partial Inductance," *IEEE EMC Soc. Newsletters*, no. 226, pp. 34–42, 2010.
[14] S. J. Shah, "Field wiring and noise considerations for analog signals," *Natl. Instruments Corp.*, pp. 1–22, 2001.
[15] O. Reid, F. S. Saleh, and E. B. Easton, "Determining electrochemically active surface area in PEM fuel cell electrodes with electrochemical impedance spectroscopy and its application to catalyst durability," *Electrochim. Acta*, vol. 114, pp. 278–284, 2013.
[16] D. E. Macphee, D. C. Sinclair, and S. L. Stubbs, "Electrical characterization of pore reduced cement by impedance spectroscopy," *J. Mater. Sci. Lett.*, vol. 15, pp. 1566–1568, 1996.
[17] S. L. Cormack, D. E. Macphee, and D. C. Sinclair, "An AC impedance spectroscopy study of hydrated cement pastes," *Adv. Cem. Res.*, vol. 10, no. 4, pp. 151–159, 1998.
[18] B. Hirschorn, B. Tribollet, and M. E. Orazem, "On selection of the perturbation amplitude required to avoid nonlinear effects in impedance measurements," *Isr. J. Chem.*, pp. 133–142, 2008.
[19] A. Yerokhin, E. V. Parfenov, C. J. Liang, V. R. Mukaeva, and A. Matthews, "System linearity quantification for in-situ impedance spectroscopy of plasma electrolytic oxidation," *Electrochem. commun.*, vol. 27, pp. 137–140, 2013.
[20] J. J. Giner-Sanz, E. M. Ortega, and V. Pérez-Herranz, "Harmonic analysis based method for perturbation amplitude optimization for EIS measurements," *J. Electrochem. Soc.*, vol. 164, no. 13, pp. H918–H924, 2017.
[21] A. Lasia, *Electrochemical impedance spectroscopy and its applications*. New York: Springer, 2014.
[22] Chomerics, "EMI shielding theory & gasket design guide," in *EMI shielding engineering handbook*, pp. 191–220.
[23] BioLogic Science Instruements, "Precautions for good impedance measurements," 2010. [Online]. Available: http://www.bio-logic.net/wp-content/uploads/20101105-application-note-5.pdf.
[24] X. Jiang, S. Nešić, and F. Huet, "The effect of electrode size on electrochemical noise measurements and the role of chloride on localized CO2 corrosion of mild steel," in *NACE international*, 2009, no. 09575, pp. 1–17.
[25] N. Ogihara, Y. Itou, T. Sasaki, and Y. Takeuchi, "Impedance spectroscopy characterization of porous electrodes under different electrode thickness using a symmetric cell for high-performance lithium-ion batteries," *J. Phys. Chem.*, vol. 119, pp. 4612–4619, 2015.
[26] H. Zhou, R. D. Tilton, and L. R. White, "The role of electrode impedance and electrode geometry in the design of microelectrode systems," *J. Colloid Interface Sci.*, vol. 297, no. 2, pp. 819–831, 2006.
[27] S. Mohtashami, "Electrochemical properties of flexible electrodes for implanted neuromuscular excitation applications," Thesis, McMaster University, 2011.

[28] B. Li, Y. Huan, and W. Zhang, "Passivation and corrosion behavior of P355 carbon steel in simulated concrete pore solution at pH 12.5 to 14," *Electrochem. Sci.*, pp. 10402–10420, 2017.
[29] V. A. Alves and C. M. A. Brett, "Characterisation of passive films formed on mild steels in bicarbonate solution by EIS," *Electrochim. Acta*, vol. 47, no. 13–14, pp. 2081–2091, 2001.
[30] A. Nishikata, Y. Ichihara, and T. Tsuru, "An application of electrochemical impedance spectroscopy to atmospheric corrosion study," *Corros. Sci.*, vol. 37, no. 6, pp. 897–911, 1995.
[31] J. Hu, D. A. Koleva, J. H. W. De Wit, P. Petrov, and K. Van Breugel, "Corrosion performance of carbon steel in micelle-containing cement extract," *ECS Trans.*, vol. 28, no. 24, pp. 113–121, 2010.
[32] H. Cesiulis, N. Tsyntsaru, A. Ramanavicius, and G. Ragoisha, "The study of thin films by electrochemical impedance spectroscopy," in *Nanostructures and thin films for multifunctional applications*, Springer, 2016, pp. 3–43.
[33] R. Ahmed and K. Reifsnider, "Study of influence of electrode geometry on impedance spectroscopy," *Int. J. Electrochem. Sci*, vol. 6, pp. 1159–1174, 2011.
[34] F. Zhang *et al.*, "Reference and counter electrode positions affect electrochemical characterization of bioanodes in different bioelectrochemical systems," *Biotechnol. Bioeng.*, vol. 111, pp. 1931–1939, 2014.
[35] W. Yan, S. Hong, and R. Chaoshi, "Optimum design of electrode structure and parameters in electrical impedance tomography," *Physiol. Meas.*, vol. 27, no. 3, pp. 291–306, 2006.
[36] Corporate Circular, "Horizontal reinforcement for crack control in walls and wall type piers," *Bridge technical direction BTD2007/11*. [Online]. Available: http://www.rms.nsw.gov.au/business-industry/partners-suppliers/documents/technical-directions/btd2007_11.pdf.
[37] G. Renaudin, A. Mesbah, B. Z. Dilnesa, M. Francois, and B. Lothenbach, "Crystal chemistry of iron containing cementitious AFm layered hydrates," *Curr. Inorg. Chem.*, vol. 2, pp. 1–10, 2015.
[38] P. Navi and C. Pignat, "Simulation of cement hydration and the connectivity of the capillary pore space," *Adv. Cem. Based Mater.*, vol. 4, no. 2, pp. 58–67, 1996.

International Conference on Sustainable Materials, Systems and Structures (SMSS 2019)
Novel Methods for Characterization of Materials and Structures
20-22 March 2019 – Rovinj, Croatia

TESTING OF NEW ACCELERATED METHOD FOR DETERMINATION OF CHLORIDE THRESHOLD VALUES FOR CORROSION INITIATION IN REINFORCED CONCRETE

Søren Lundsted Poulsen (1) and Henrik Erndahl Sørensen (1)

(1) Danish Technological Institute, Taastrup, Denmark

Abstract

The so-called "chloride threshold value" may be defined as the minimum concentration of chloride that is able to initiate corrosion of the steel embedded in a reinforced concrete structure. This value is a crucial input parameter for service life modelling of concrete structures exposed to chlorides, e.g. structures located in marine environments or near roads regularly exposed to de-icing salts during winter seasons. Unfortunately, a commonly accepted test method for determination of chloride threshold values is still lacking, and most recently, the effort of RILEM TC 235-CTC failed to provide such a method. This paper presents the preliminary results from a test of a new experimental approach for measuring chloride threshold values in concrete. The principle of the method is to utilize an externally applied electrical field to accelerate the ingress of chloride ions from an exposure solution into the specimens. The moment of corrosion initiation is detected by a significant drop in the electrochemical potential of the steel bars, which is continually measured during the testing. After observation of corrosion initiation, the chloride threshold value is determined by measuring the chloride concentration at the depth of the steel bar in the given specimen.

Keywords: Chloride threshold value, corrosion initiation, service life modelling, concrete durability, accelerated test method**.**

1. INTRODUCTION

The chloride threshold value is a crucial parameter for service life modelling of reinforced concrete structures subjected to chlorides, e.g. structures in marine environments or near roads regularly exposed to de-icing salts during winter seasons [1]. This parameter is defined as the minimum chloride concentration at the depth of the reinforcement that can initiate corrosion of the steel. Even small variations of the chloride threshold values used for service life modelling may result in significantly shorter or longer estimated service life for a given concrete structure.

Unfortunately, a generally accepted test method for determination of chloride threshold values in concrete does currently not exist.

Chloride threshold values reported in the literature generally display a large scatter, partly because numerous different experimental approaches have been used to obtain the chloride threshold values [2]. This underlines the need for a reliable and commonly accepted method for determination of chloride threshold values. A RILEM committee (TC 235-CTC) was established back in 2009 with the purpose of developing such a method. After thorough discussions, the committee agreed on an accelerated test method based on open circuit measurements on rebars in concrete specimens exposed to a chloride solution. A Round Robin test involving 12 participating laboratories was subsequently carried out to test the proposed method, but eventually the effort of the RILEM committee failed to provide a reliable test method.

Based on work by Castellote et al. [3], Andrade and Rebolledo [4], Yang [5] and Yang et al. [6], Polder et al. [7] has recently proposed a new method for determination of chloride threshold values for corrosion initiation of steel embedded in mortar. The principle of the method is to utilize an externally applied electrical field to accelerate the ingress of chloride ions from an exposure solution into mortar specimens. The moment of corrosion initiation is then detected by a significant drop in the electrochemical potential of the steel bars, which is continually measured during the testing. After observation of corrosion initiation, the chloride threshold value is determined by measuring the chloride concentration at the depth of the steel bar in the given specimen.

In this paper, we present the preliminary result from an on-going investigation, where a slightly modified version of the method suggested by Polder et al. [7] is applied to determine the chloride threshold values in specimens of real concrete rather than mortar.

2. EXPERIMENTAL

2.1 Principle of test setup

The principle of the applied test method is to expose a specimen of concrete with a single embedded bar of reinforcing steel to one-sided chloride ingress until corrosion initiation is registered. The chloride ingress is accelerated by applying a low DC voltage (6 V) across the specimen. This is obtained using a copper cathode placed in a pond of 10% NaCl solution on the top of the specimen and a stainless steel anode placed in demineralised water on the opposite site of the specimen (Fig. 1).

A reference electrode (ERE20 electrode based on manganese dioxide) is placed in the demineralised water to continually monitor the potential of the steel bar in the concrete specimen.

At regular intervals (four times a day) the DC voltage is switched off for 1 hour to observe the “off” potential of the steel. A drop of >200 mV between two consecutive periods of “off” potential measurements is interpreted as an indication of corrosion initiation. The steel potential is monitored continuously, i.e. both when the DC voltage is turned on and off. After registration of corrosion initiation, the voltage is switched off and the specimen is removed from the test setup as soon as possible. Subsequently, the chloride threshold value is determined by measuring the chloride concentration at the depth of the reinforcing steel.

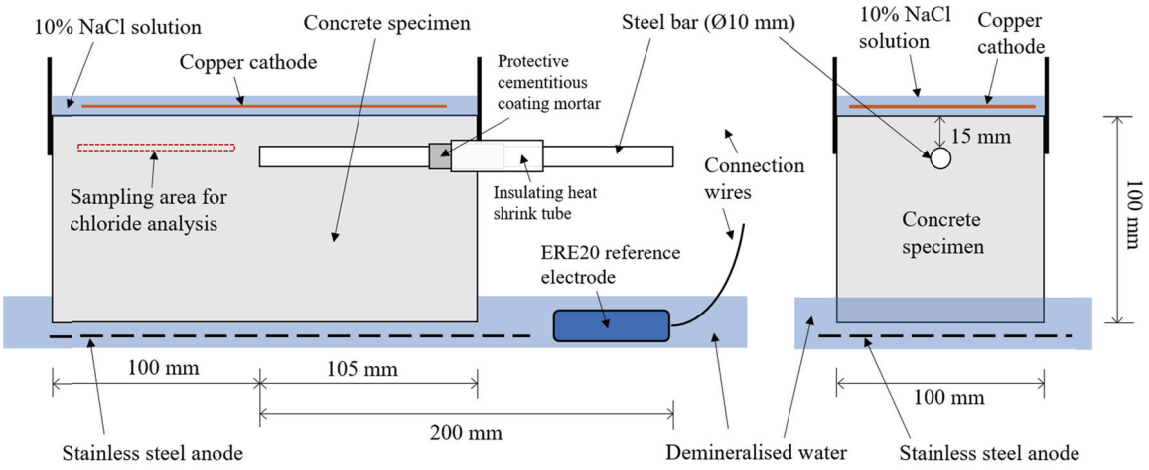

Fig. 1. Experimental setup for accelerated measurement of chloride threshold values in concrete.

2.2 Preparation of test specimens

A total of ten concrete specimens (205 x 100 x 100 mm) each with a single bar of reinforcing steel (Ø10 mm) without ribs were produced using the concrete mix design given in Table 1. Five of the specimens were produced with a concrete cover layer of 10 mm above the steel bar (specimens labelled 1_10mm, 2_10mm, … and 5_10mm) and the remaining five specimens were produced with a cover layer of 15 mm (specimens labelled 6_15mm, 7_15mm, … and 10_15mm). The general design of the specimens is shown in Fig. 1.

Prior to casting of the specimens, all steel bars were chemically cleaned by immersion in a chemical cleaner solution ($HCl:H_2O$ = 1:1 + 3 g/l urotropine) for 5 minutes and subsequent treatment in an ultra-sonic bath for 3 minutes.

Prior to testing, an epoxy coating was applied to all sides of the specimens except the top and bottom surfaces. Furthermore, a rubber sheet was applied around the top surface to form a pond on each specimen.

Table 1: Mix design for concrete specimens with water/cement ratio of 0.5.

Constituent	
Low-alkali sulphate-resistant Portland cement (CEM I 42.5 N)	380 kg/m^3
Fine aggregates (0-2 mm sand)	793 kg/m^3
Medium aggregates (4-8 mm granite)	984 kg/m^3
Superplasticizer (Glenium SKY 631)	1.2 kg/m^3
Water	189.1 kg/m^3
Air	2.6 %
Total	2347 kg/m^3

2.3 Measurement of chloride threshold value

After registration of corrosion onset the chloride concentration was measured at the depth of the reinforcing steel to determine the chloride threshold value. This was achieved by means of profile grinding around the depth of the steel bar. The position of the sampling area is shown in Fig. 1. Material was grinded off in 0.5 mm thick layers parallel to the chloride exposed surface at depths going from 1.5 mm above the steel bar to 1.5 mm below the steel bar. The chloride content of each layer was subsequently determined according to the procedure given in DS 423.28, which is similar to NT BUILD 208 [8]. The chloride contents were measured using potentiometric titration rather than Volhard titration. Finally, the chloride threshold value was determined by linear interpolation between the two points in the resulting chloride profile being closest the depth of the steel bar.

3. RESULTS

At the time of writing, we have only obtained test results for two of the prepared specimens (6_15mm and 7_15mm). In Fig. 2 the measured "off" potentials for these two specimens are presented. The average measured "off" potential is approximately -235 mV and -205 mV for specimen 6_15mm and 7_15mm, respectively. For both specimens, the test period included some periods, where the DC voltage was turned off for more than 1 hour, e.g. weekends with no available personnel to remove the specimen from the test setup in case of corrosion initiation. This was done to avoid a situation, where corrosion initiation was followed by an extended period with continued accelerated chloride ingress, which would result in a chloride content at the depth of the steel bar not representing the true value at the time of corrosion initiation.

Corrosion initiation was observed after about 14 days for both specimen 6_15mm and 7_15mm. This was indicated by a drop of the "off" potential of about 350 mV for specimen 6_15mm and 410 mV for specimen 7_15mm.

After registration of corrosion onset, the specimens were removed from the test setup and the chloride concentration around the depth of the steel bars were measured (Fig. 3), which resulted in chloride threshold values of 0.22 and 0.26 wt% of concrete for specimens 6_15mm and 7_15mm, respectively. This corresponds to 1.34 and 1.59 wt% of binder for specimens 6_15mm and 7_15mm, respectively.

Besides the measurement of chloride contents, the steel bars were also removed from the concrete specimens for visual inspection to make sure that the observed drops in measured steel potentials were indeed associated with visual signs of corrosion onset. This was the case for both specimens. An example of visual observation of corrosion onset in terms of pitting corrosion is given in Fig. 4.

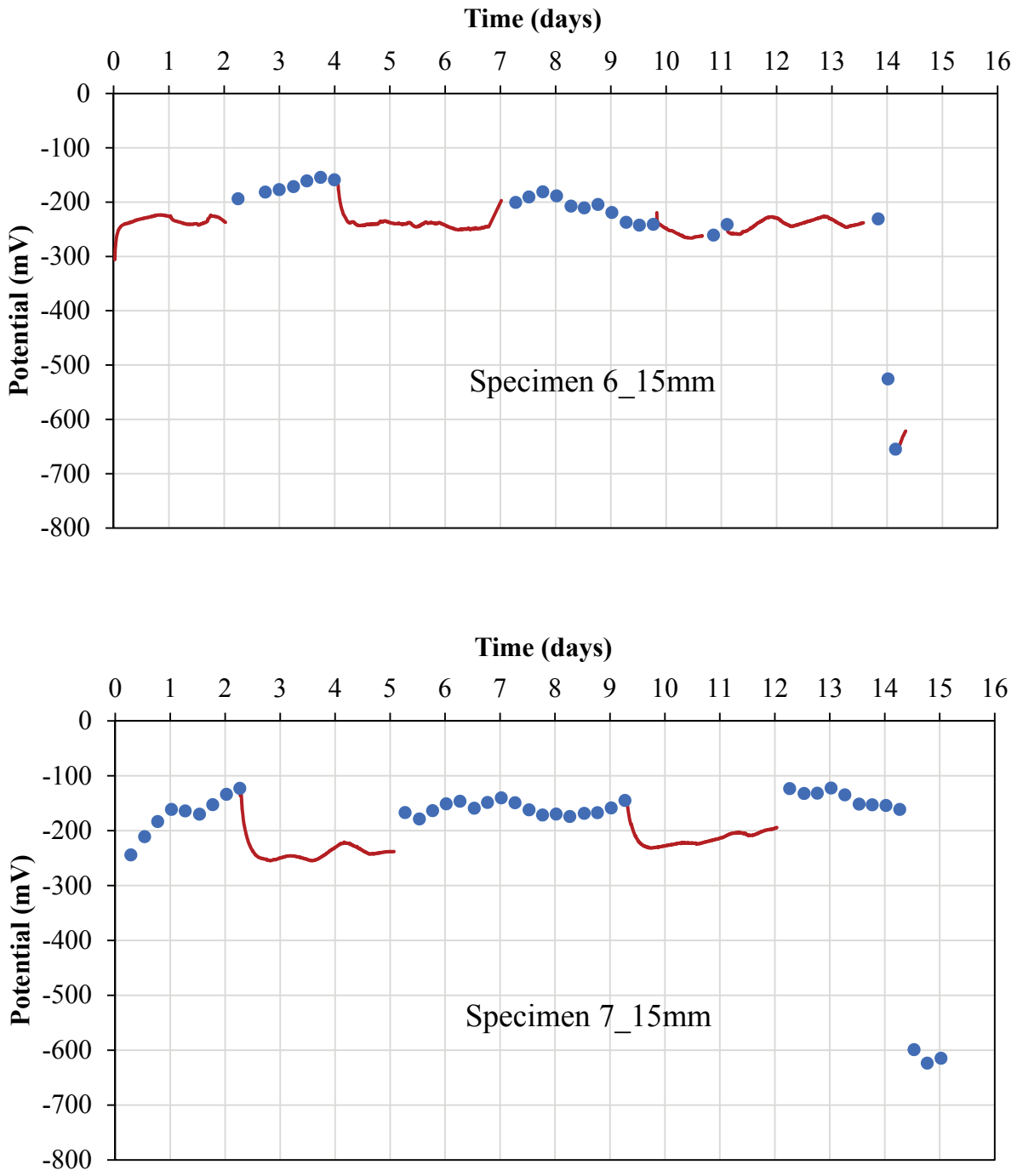

Fig. 2. Measured steel potentials for specimens 6_15mm and 7_15mm. Only the "off" potentials are shown in the figures. The blue dots represent data from periods, where the DC voltage has automatically been turned off four times a day for 1 hour. Each dot is the potential measured at the end of each 1 hour period, where the DC voltage has been turned off. The red curves are continuous measurements from periods, where the DC voltage has been switched off for a longer period of time.

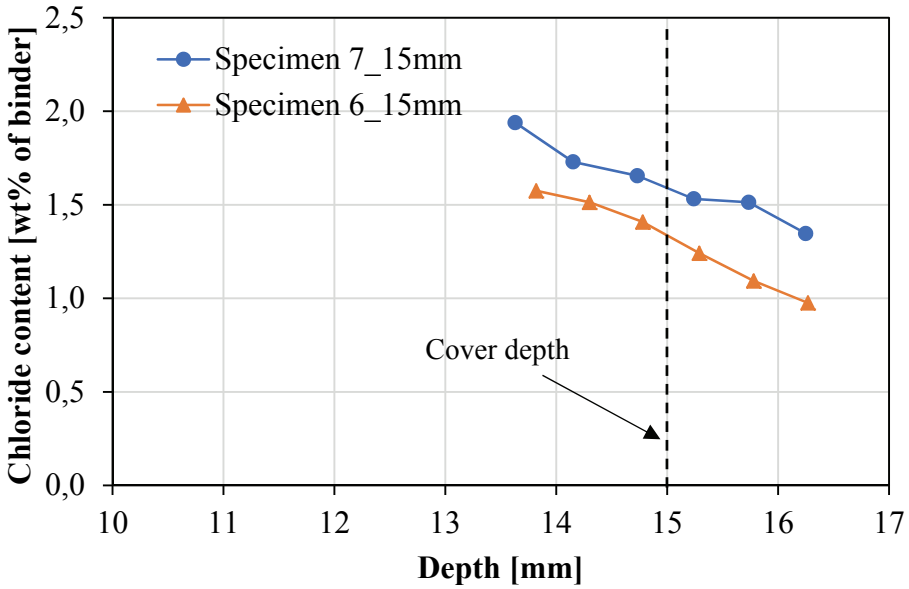

Fig. 3. Chloride contents around the depth of the steel bar in specimens 6_15mm and 7_15mm measured after registration of corrosion initiation.

4. DISCUSSION

The chloride threshold value measured for specimen 7_15mm (1.59 wt% of binder) is 0.25 wt% higher than the one measured for specimen 6_15mm (1.34 wt% of binder). Maybe part of this difference can be explained by the fact that specimen 6_15mm was removed somewhat quicker from the test setup than specimen 7_15mm after occurrence of a significant drop in the measured steel potential, i.e. chloride was allowed to penetrate the concrete cover layer for a longer period after corrosion initiation for specimen 7_15mm than for specimen 6_15mm. Ideally, the specimens should be removed from the test setup immediately after the decisive potential drop, but this was not practically possible with the applied method. Further investigations will be initiated to examine the importance of this short period after the potential drop for the determined chloride threshold value. For instance, we plan to carry out experiments, where the DC voltage is switched off at some point closely before corrosion initiation is expected to occur. In this way, the chloride ingress will be due to a slower diffusion process rather fast migration in the last period before corrosion initiation, thus reducing the risk of obtaining a chloride threshold value that is too high due to unwanted chloride ingress after corrosion initiation.

The chloride threshold values presented in this paper are in good agreement with data from Sørensen et al. [9], where chloride threshold values were obtained from concrete blocks naturally exposed to seawater at a field exposure site located in Rødbyhavn, Denmark. These chloride threshold values were estimated by comparison of the corrosion state of imbedded steel anodes and corresponding measurements of chloride content at the anode depth. They found that the chloride threshold value was at least 1.4 wt% of binder and not more than 1.7

wt% of binder for a concrete produced with a binder of 100% low-alkali sulphate-resistant Portland cement and a water/cement ratio of 0.40, i.e. a concrete that is close in composition to the one used in the present investigation. The agreement between these data from field experiments and the chloride threshold values determined in the laboratory using accelerated chloride ingress supports the validity of the proposed test method. Similarly, there is a good agreement between the chloride threshold values presented in this paper and data in Table 10.2.6:1 in the HETEK report by Nilsson et al. [10], where a chloride threshold value of 1.5 wt% of binder is specified for concrete with a binder of 100% ordinary Portland cement and a water/cement ratio of 0.5.

The validity and applicability of the proposed test method will be further examined through continued laboratory experiments carried out using the remaining test specimens described in section 2.2.

Fig. 4. Example of pitting corrosion (location indicated by the red circles) observed in specimen 7_15mm. The picture shows the specimen after it has been split into two parts to visually inspect the embedded steel bar after registration of a significant drop in the measured steel potential.

5. CONCLUSIONS

- An investigation has been initiated to test the validity and applicability of a new experimental method for measuring chloride threshold values for initiation of reinforcement corrosion in concrete.
- Preliminary results suggest that the proposed method can be applied for accelerated determination of chloride threshold values.
- So far, the investigation has resulted in measured chloride threshold values of 1.34 and 1.59 wt% of binder for concrete specimens with a binder of 100% Portland cement and a water/cement ratio of 0.5.

REFERENCES

[1] Bertolini, L., Elsener, B., Pedeferri, P., Redaelli, E. and Polder, R.B., 'Corrosion of Steel in Concrete: Prevention, Diagnosis, Repair, 2nd Edn (Wiley-VCH Verlag GmbH & Co KGaA, Weinheim, 2013).

[2] Angst, U., Elsener, B., Larsen, C.K. & Vennesland, Ø., 'Critical chloride content in reinforced concrete – A review', Cem. Conc. Res. 39 (12) (2009) 1122-1138.

[3] Castellote, M., Andrade, C. and Alonso, C., 'Accelerated simultaneous determination of the chloride depassivation threshold and of the non-stationary diffusion coefficient values', Corros. Sci. 44 (11) (2002) 2409-2424.

[4] Andrade, C. and Rebolledo, N., 'Accelerated evaluation of corrosion inhibition by means of the integral corrosion test', Proceeding of the ICCRRR, Cape Town, South Africa, 2012 (Taylor & Francis Group) 132-133.

[5] Yang, Z., 'Modified hydrotalcites as smart additives for improved corrosion protection of reinforced concrete', PhD. Thesis, (Delft University of Technology, 2015).

[6] Yang, Z., Polder, R.B., Mol, J.M.C., Andrade C., 'The effect of two types of modified Mg-Al hydrotalcites on reinforcement corrosion in cement mortar', Cem. Conc. Res. 100 (2017) 186-202.

[7] Polder, R.B., Put, M.v. and Peelen, W.H.A., 'Accelerated Testing for Chloride Threshold of Reinforcing Steel in Concrete', in: 'Where Technology and Engineering Meet', Proceedings of the 2017 fib Symposium, Maastricht, The Netherlands, 12-14 June 2017 (Springer International Publishing AG, 2018) 2066-2073.

[8] NT Build 208, 'Concrete, Hardened: Chloride content by Volhard titration', edition 3, Nordtest, 1996. Available at http://www.nordtest.info.

[9] Sørensen, H.E., Poulsen, S.L. and Jönsson, U., 'Chloride threshold values from concrete blocks exposed at Rødbyhavn marine field exposure site', Proceedings of *fib* Symposium 2016 on Performance-Based Approaches for Concrete Structures, Cape Town, South Africa, 21–23 November 2016.

[10] Nilsson, L.-O., Sandberg, P., Poulsen, E., Tang, L., Andersen, A., Frederiksen, J.M., 'HETEK, A system for estimation of chloride ingress into concrete, Theoretical background' (Danish Road Directorate, 1997).

International Conference on Sustainable Materials, Systems and Structures (SMSS 2019)
Novel Methods for Characterization of Materials and Structures
20-22 March 2019 – Rovinj, Croatia

ASR PERFORMANCE TESTING OF AIR ENTRAINED CONCRETE EXPOSED TO EXTERNAL ALKALIS

Karolina Gibas (1), Michał A. Glinicki (1), Mariusz Dąbrowski (1), Daria Jóźwiak-Niedźwiedzka (1), Aneta Antolik (1) and Kinga Dziedzic (1)

(1) Institute of Fundamental Technological Research, Polish Academy of Sciences, Warsaw, Poland

Abstract

The risk of occurrence of deleterious alkali-silica reaction (ASR) in concrete should be properly minimized in major highway pavements and bridges. Real-life experiences show that even in concrete made with aggregates potentially not susceptible to ASR, it may occur under unfavourable conditions of external alkali supply at wet conditions and heavy traffic load. An experimental investigation was performed to study the susceptibility of selected Polish mineral aggregates to ASR at external alkali supply. The test method „60°C concrete test with external alkali supply" covered by draft procedure RILEM AAR-12 was implemented at IPPT PAN laboratory. Air entrained concrete specimens were exposed to cyclic temperature changes and wet-dry exposure as well as NaCl solution exposure. Several combinations of coarse crushed aggregate and fine natural aggregate were tested in concrete designed as for heavy duty highway pavement. SEM evaluation of microstructure of concrete with glacial deposit aggregate revealed visible alkali-silica gel. The effects of fine aggregate on the expansion of concrete were also revealed.

Keywords: air entrained concrete, alkali-silica reaction, cyclic exposure, external alkali, highway pavement

1. INTRODUCTION

The issue of susceptibility of some mineral aggregates to the reaction with alkali hydroxides in concrete is still valid, despite numerous worldwide studies and publications [1]. The alkali-aggregate reaction occurs between the pore solution of concrete and the reactive minerals in aggregate grains, eventually leading to excessive expansion and cracking of concrete elements. ASR research on Polish mineral aggregates revealed reactivity of certain sands and gravels containing opal and chalcedony, sandstone, silica limestone and dolomite [2-4]. The expansion of cement mortar or concrete specimens with the tested aggregate depends on the content of potassium and sodium in cement. The impact of external alkalis

was demonstrated using the climate simulation concrete prism test [5] and such a test was used successfully to evaluate job mixtures for pavements.

For the ASR performance testing of concrete the "60°C concrete test with external alkali supply" method was developed at the German VDZ Institute [6]. The method involves cyclic exposure of concrete specimens to wetting-drying, soaking in solution of sodium chloride, while the temperature change takes place within the range from 20°C to 60°C. It has been recently included in RILEM AAR-12 draft procedure. The test method allows to evaluate the resistance to alkali-silica reaction of concrete mixtures for the moisture classes WA (concrete element exposed to extraneous moisture and to external supply of alkalis by de-icing agents) and WS (concrete element exposed to extraneous moisture, to external supply of alkalis by de-icing agents and to fluctuating loads – concrete pavements of motorway constructions) [7].

The "60°C concrete test with external alkali supply" method was implemented at the Institute of Fundamental Technological Research, Polish Academy of Sciences to assess the risk of ASR reactions in domestic aggregates in concrete [5]. The paper describes preliminary results of ASR performance tests on air entrained concrete containing crushed granite and aggregates crushed from glacial deposits in the northern part of Poland. The expansion tests with external alkali supply are compared with the standard expansion testing of mortar specimens in 1 N NaOH solution at 80°C.

2. EXPERIMENTAL SECTION

2.1 Materials and specimens

Air-entrained concrete containing crushed coarse aggregates and siliceous sand was tested (Table 1). Portland cement CEM I 42.5R was used, with an alkali content of Na_2O_{eq}=0.58%. The water-to-cement ratio was selected following an assumed limiting value adequate for slip-formed concrete highway pavement to be exposed to XF4 aggressive environment.

Concrete mixes contained domestic aggregates with maximum grain size of 16 or 22 mm. The grain size distribution of aggregates was set according to Polish standards for concrete highway pavements. The content of fine aggregates was 30%. Air entraining admixture was used to obtain the target fresh air content of 5% to 7%.

The mixes were manufactured using a laboratory mixes of 50 litres capacity. Concrete prisms 75x75x285 mm with steel studs were made of each mix for ASR performance testing. Companion cube specimens were also manufactured for standard compression testing.

Table 1: Composition and properties of fresh and hardened concrete mixture

Mixture Designation	GD1_QS	GD2_QS	G1_QS	G2_QS	G3_QS
Type of Cement	CEM I 42.5R				
Cement [kg/m^3]	360				
w/c	0.45				
Coarse aggregate	Glacial deposit 1, 2-16 mm	Glacial deposit 2, 2-16 mm	Granite 1, 2-16 mm	Granite 2, 2-16 mm	Granite 3, 2-22 mm
Fine aggregate	Natural quartz sand, 0-2 mm				
Fresh air content, A [%]	6.2	4.6	7.2	5.5	6.7
Slump [mm]	180	180	130	140	150
Compressive strength, $fc2_8$ [MPa]	42.6	48.1	41.6	44.5	42.4

2.2 Test methods

The petrographic analysis of minerals in aggregate grains was performed using RILEM AAR-1 Recommendation. Thin sections of aggregate grains were prepared with a thickness of 20±2 μm. The petrographic analysis was focused on characterisation of potentially reactive forms of silica using Olympus BX51 microscope with digital colour camera and automatic moving table Prior ES11BX/B.

Fresh mix properties were tested using standard EN methods (the slump, the fresh air content). After 28 days of curing the compressive strength of concrete on 100 cubes was tested according to PN-EN 12390. The air void content in hardened concrete was measured on polished flat sections using Image Pro 7 digital analysis of microscopic images according to PN-EN 480-11.

The ASR performance test consists of pre-storing specimens for 28 days and an alternating storage for 140 days.

Pre-storage: After casting, the prisms were protected from moisture loss and stored in the moulds at 20±2°C for 1 day. After demoulding the prisms were stored in a water bath for 20 days at the temperature of 20±2°C. The prisms were inserted into sealed containers and were placed in the thermostatic chamber (the reactor) for 6 days at a temperature of 60±2°C and a minimum relative humidity of 98%. Then stored 1 day in an unopened condition in a room with 20±2°C. At the age of 28 days the zero measurement of the mass and the length of specimens were taken.

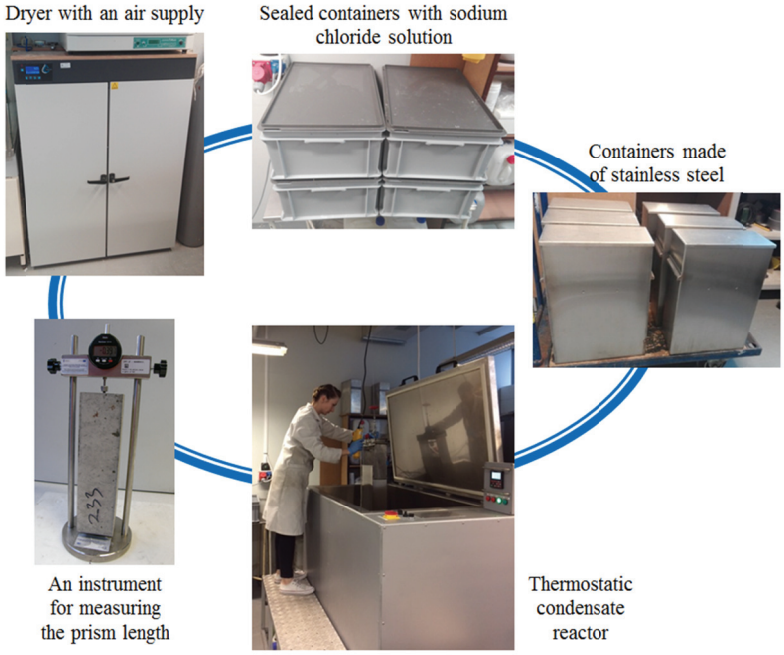

Figure 1: Alternating storage of concrete prisms with external alkali supply

Alternating storage: At the age of 28 days the prisms were exposed to the alternating storage condition. The single cycle lasted for 14 days and it was repeated 10 times. After the zero length measurement, the prisms were placed in a dryer at 60±5°C with an air supply for 5 days, Figure 1. Then the prisms were removed from the dryer to cool off and to be placed in containers with 3% NaCl solution at 20±2°C for 2 days. Afterwards the prisms were placed

over a water bath in a sealed container. The container was placed in the reactor for 6 days at 60±2°C and RH ≥ 98%. Containers removed from the reactor were stored in an unopened condition at 20±2°C for 1 day. Then the mass and the length of prisms were determined at the laboratory environment at 20±2°C and RH=65±5%. The alternating storage was continued until the specimens reached the age of 168 days following their preparation. The concrete has sufficient resistance to the alkali-aggregate reaction when the final expansion is less or equal to 0.30 mm/m.

Accelerated mortar bar test (ASTM C1260/RILEM AAR-2) was used to evaluate the ASR expansion potential on specimens exposed to 1 N NaOH solution at 80°C during 14 days. In accordance with these standards, if after 14 days of testing the expansion of the mortar bars is lower than 0.10%, the aggregate may be considered non-reactive, and above 0.20% is highly reactive. Three mortar bar specimens 25×25×285 mm were prepared using Portland cement CEM I 42.5R (Na2Oeq=0.88%) for each aggregates, which were processed by crushing and sieving to the appropriate specified by standard gradation.

Identification of alkali-silica gel was performed on polished sections with an area of 45x30 mm, cut from concrete prisms after 10 cycles of the alternating temperature exposure and out of mortar specimens after 14 days of the exposure to 1N NaOH solution at 80°C. The microstructure of mortar and concrete was observed using Scanning Electron Microscope (SEM) with Energy Dispersive X-Ray Analysis (EDX) [8]. Specimens were tested using Zeiss sigma VP microscope, in the backscatter mode using an acceleration voltage of 20 kV.

3. TEST RESULTS

The total air content (A) in hardened concrete specimens was measured and it was higher than 4.6% and smaller than 7.2%. The dispersion of the air content between concrete mixtures with different aggregate type was probably caused by a dust fraction of rocks. A large proportion of dust fraction causes the absorption of air entraining admixture and thus reduces its effectiveness. The compressive strength after 28 days of curing was from 42 MPa to 48 MPa (the average values for three specimens).

A variety of rock types was identified in crushed aggregate grains from glacial deposits: limestone, granite, diorite, sandstone, mudstone, spongiolite, quartzite and siliceous rock (chalcedony-rich rocks). Each of aggregates from glacial deposits contained quartz in its pure form, strained quartz and quartz crystals smaller than 60 μm and thus classifying as microcrystalline material. According to the RILEM classification this corresponds to the Class II of reactivity potential. All granites mainly consisted of plagioclase, albite and K-feldspar, quartz and biotite. The strained quartz and microcrystalline quartz were also present in granite aggregates as well as myrmekitic quartz which can increase the potential for ASR [8].

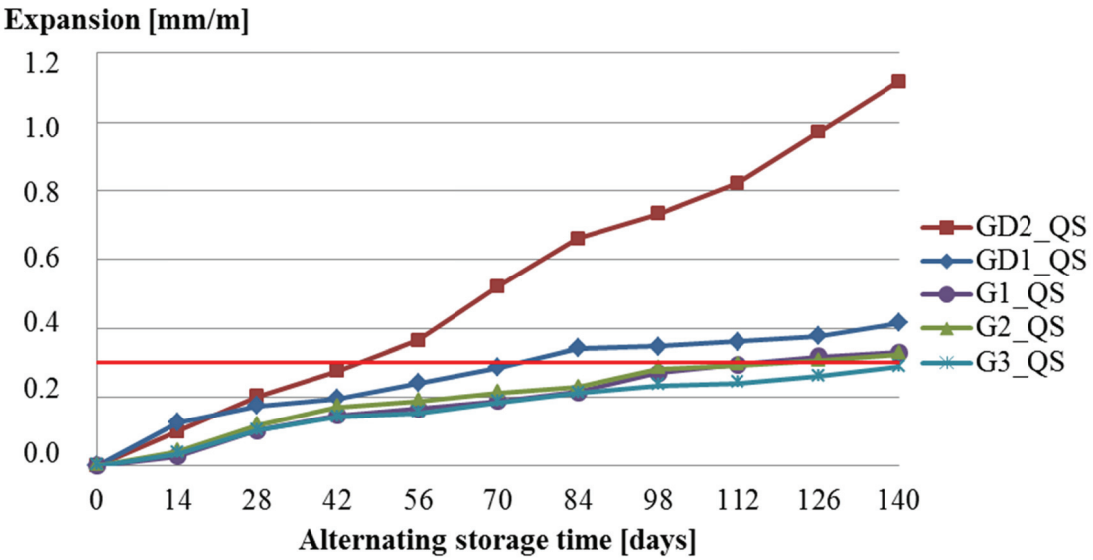

Figure 2: The expansion of concrete prisms in time during ASR performance testing with external 3% NaCl solution exposure

The relative increase of the length of concrete specimens in time is presented in Figure 2. The horizontal axis covers the time of 10 exposure cycles of specimens to alternating temperature, moisture and external alkalis. The mass of specimens increased over time: the mass gain was from 0.7% to 1.4%.

The ASR reactivity of single aggregates evaluated in accordance with ASTM C1260/RILEM-AAR-2 recommendation is shown in Figure 3.

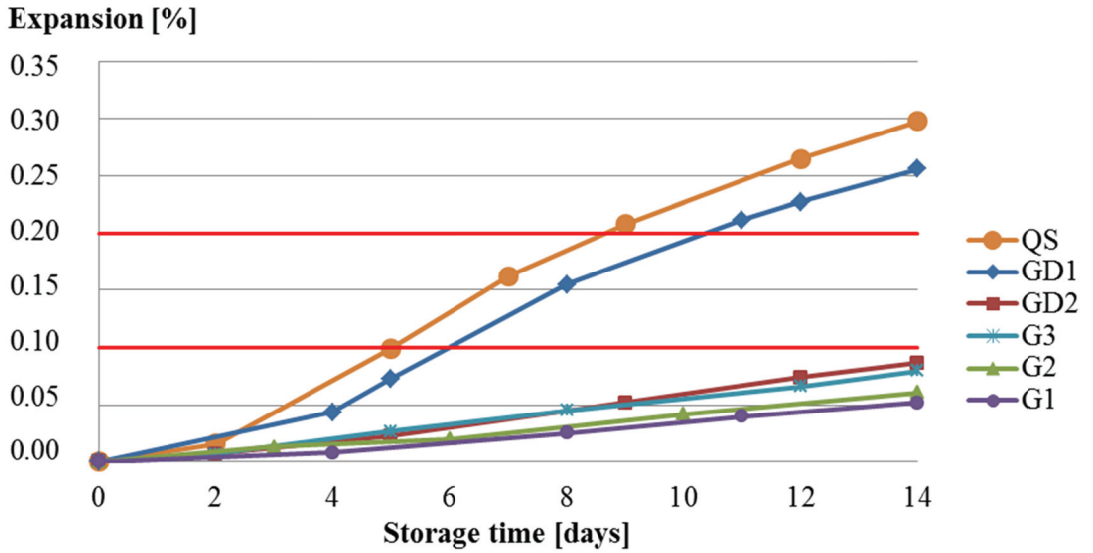

Figure 3: The expansion of mortar specimens in time in 1M NaOH solution at 80°C following ASTM C1260 procedure and RILEM AAR-2 recommendation

Examples of SEM images of specimens containing crushed aggregate from glacial deposit 1 after the termination of VDZ and ASTM tests are shown in Figures 4 – 5 along with EDS spectra at selected locations. Some cracks in the matrix were present in concrete specimens the most severe cracking was observed in concrete with aggregates from glacial deposits. ASR gel of typical composition was found; it was filling cracks and air-voids in air entrained concrete specimens.

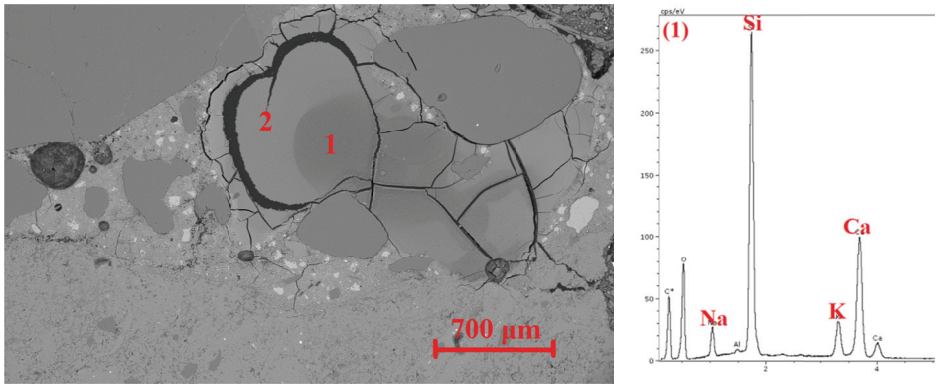

Figure 4: The microstructure of concrete with glacial deposit aggregate (GD1_QS) after VDZ test with visible alkali-silica gel (1)(2); the scale bar is 700 µm

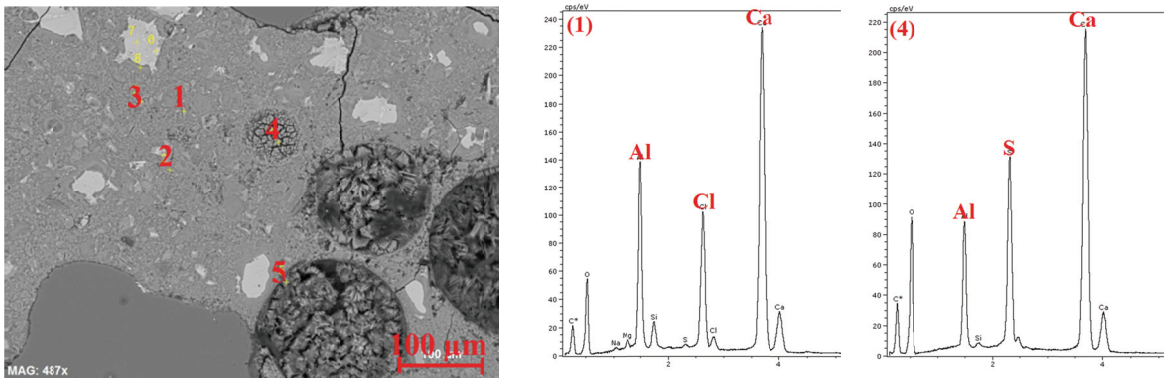

Figure 5: The microstructure of concrete with glacial deposit aggregate (GD1_QS) after VDZ test with visible Friedel's salt in cement matrix (1)(2)(3) and ettringite deposit in air-voids (4)(5); the scale bar is 100 µm

4. TEST ANALYSIS

The ASR reactivity of single aggregates was evaluated using ASTM C1260/ RILEM AAR-2 (Figure 3). Specimens containing crushed aggregate from glacial deposit 1 demonstrated the greatest expansion, above 0.25% after 14 days of storage in NaOH solution. Also the natural quartz sand exhibited a clear potential for ASR since the final expansion of mortar bars was about 0.298%. These aggregates can be considered as potentially harmful, reacting with sodium and potassium hydroxides in concrete pore solution. The other four coarse aggregates can be considered innocuous as indicated by modest final expansion of specimens.

The prolonged exposure of concrete specimens to cyclic changes of temperature and moisture, and external alkali supply resulted in steady increase of specimen length. For most

concrete mixes made with the combination of siliceous sand and crushed coarse aggregates the final expansion was above 0.30 mm/m (Figure 2). Only concrete specimens with granite 3 aggregate after 10 cycles showed the final expansion of 0.29 mm/m, slightly below the limiting value. The highest length increase was observed for concrete specimens made with crushed aggregate from glacial deposit 2 (1.12 mm/m).

To confirm that such a large expansion was caused by the formation of an expansive alkali-silica gel in concrete and mortar specimens, the microstructure was examined using SEM_EDX after termination of the VDZ and ASTM tests. ASR gel of typical composition was found. The weakest aggregate grains were completely or almost entirely replaced by alkali-silica gel. Many of the aggregate particles were found to contain cracks filled with alkali-silica gel from which is penetrated to the cement matrix (Figure 5). The chemical analysis in microsurface revealed that it was Si-Ca-K-Na gel. The chemical composition didn't differ from the range of composition known from the literature [9-13]. The ratios of Na/Si, K/Si, Ca/Si, (Na+K)/Si were 0.27, 0.03, 0.52, 0.31, respectively, i.e. within the range characteristic for ASR gel. The alkali-silica gel partially or completely filled the air-voids. After the exposure of concrete specimens to NaCl solution, ettringite appeared in the air-voids and Friedel's salt in the matrix (Figure 5).

The crushed coarse aggregate classified as innocuous using the data in Figure 3 when combined with QS sand exhibited quite substantial expansion during the concrete performance testing. The significant reactivity of fine aggregate clearly contributed to the length increase of concrete. That is a demonstration of the significance of sand reactivity in evaluation of such aggregate combinations.

5. CONCLUSIONS

The following conclusions can be drawn:

- The cyclic „60°C concrete test with external alkali supply" test method covered by draft procedure RILEM AAR-12 was effective to reveal the influence of domestic aggregate combinations on expansion of concrete specimens. The expansion of air entrained concrete specimens containing siliceous sand and crushed aggregate from glacial deposits or granite aggregate reached 0.287 to 1.119 mm/m when exposed to external 3% NaCl solution.
- Extensive amounts of ASR gel, identified using SEM-EDS, was found in specimens showing the largest length increase. The gel was filling the air-voids and replaced some aggregate grains.
- The exposure of concrete specimens to alternating temperature, moisture and 3% NaCl solution resulted in an increased occurrence of Friedel's salt and ettringite in the matrix.
- For the investigated range of slowly reacting mineral aggregates the results of concrete performance tests are broadly consistent with the prediction based on accelerated mortar bar tests.

ACKNOWLEDGEMENTS

This paper is part of the Project "Alkali-Aggregate Reactivity of Domestic Aggregates" funded by the National Centre for Research and Development (NCBiR) and the General Directorate for National Roads and Highways (GDDKiA) in Poland in 2016-2019.

REFERENCES

[1] Sims, I. and Poole, A.B., 'Alkali-Aggregate Reaction in Concrete: A World Review', CRC Press (2017).
[2] Góralczyk, S. and Kukielska, D., 'Analiza jakości krajowych kruszyw', *Prace Naukowe Instytutu Górnictwa Politechniki Wrocławskiej. Konferencje* **121** (50) (2008) 95-103.
[3] Naziemiec, Z. and Pabiś-Mazgaj, E., 'Preliminary evaluation of the alkali reactivity of crushed aggregates from glacial deposits in Northern Poland', *Roads and Bridges – Drogi i Mosty* **16** (3) (2017) 203-222. doi: 10.7409/rabdim.017.014
[4] Jóźwiak-Niedźwiedzka, D., Gibas, K. and Glinicki, M.A., 'Petrographic identification of reactive minerals in domestic aggregates and their classification according to RILEM and ASTM recommendations', *Roads and Bridges – Drogi i Mosty* **16** (3) (2017) 223-239. doi: 10.7409/rabdim.017.015
[5] Giebson, C., Voland, K., Ludwig, H.M. and Meng, B., 'Alkali-silica reaction performance testing of concrete considering external alkalis and preexisting microcracks', *Structural Concrete* (2017) 1–11. doi: 10.1002/suco.201600173
[6] Müller, Ch., Borchers, I. and Eickschen, E., 'Erfahrungen mit AKR-Prüfverfahren: Hinweise zur Ableitung praxisgerechter Bewertungskriterien für Performance- und WS-Grundprüfungen', *Beton* **62** (10) (2012) 397-406.
[7] Borchers, I. and Müller, Ch., 'Praxisgerechte Prüfung der Alkaliempfindlichkeit von Betonen für die Feuchtigkeitsklassen WF und WA in AKR-Performance-Prüfungen', Betontechnische Berichte 2013-2015, (VDZ Düsseldorf 2016) 39-48.
[8] Jóźwiak-Niedźwiedzka, D., Antolik, A. and Glinicki, M.A., 'Investigation of potential for alkali-silica reaction in granitic aggregates', in RILEM Proceedings PRO 125the, 4th International Conference on Service Life Design for Infrastructures (SLD4), Delft, August, 2018 (2018) 131-134.
[9] Fernandes, I., 'Composition of alkali–silica reaction products at different locations within concrete structures', *Materials Characterization* **60** (7), (2009) 655–668.
[10] Çopuroğlu, O., 'Microanalysis of crystalline ASR products from a 50 year-old concrete structure'. Proceedings of 14th Euroseminar on Microscopy Applied to Building Materials, Denmark (2013).
[11] Peterson, K., Gress, D., van Dam, T.and Sutter, L., 'Crystallized alkali–silica gel in concrete from the late 1890s', *Cement and Concrete Research* **36** (8) (2006) 1523–1532.
[12] Gholizadeh-Vayghan, A. and Rajabipour, F., 'The influence of alkali–silica reaction (ASR) gel composition on its hydrophilic properties and free swelling in contact with water vapour', *Cement and Concrete Research* **94** (2017) 49–583.
[13] Hou, X., Kirkpatrick, R.J., Struble, L.J. and Monteiro, P.J., 'Structural investigations of alkali silicate gels', *J. Am. Ceram. Soc*. **88** (4) (2005) 943–949.

International Conference on Sustainable Materials, Systems and Structures (SMSS 2019)
Novel Methods for Characterization of Materials and Structures
20-22 March 2019 – Rovinj, Croatia

A COMPARATIVE STUDY BETWEEN HARDENED CEMENT PASTES AND CONCRETE OXYGEN DIFFUSION COEFFICIENT

M. Boumaaza (1), B. Huet (1), Ph. Turcry (2), C. Gehlen (3), A. Aït-Mokhtar (2)

(1) LafargeHolcim research center, 95 rue du Montmurier, 38291 Saint Quentin Fallavier, France

(2) Laboratoire des Sciences de l'Ingénieur pour l'Environnement (LaSIE), UMR 7356 CNRS, Université de La Rochelle, Avenue Michel Crépeau, 17042 La Rochelle, France

(3) Centre for building materials (cbm) Technical University of Munich, Arcisstraße 21, 80333 Munich, Germany

Abstract

Experimental studies on cementitious materials transport properties are commonly performed on concrete specimens of a thickness equivalent to at least three times the maximum size of the aggregate in the sample. These specimens require long periods of time to obtain a uniform moisture distribution prior testing, while conditioning and testing thin cement paste samples can be carried out in limited time. Therefore, this paper presents an experimental comparison between oxygen effective diffusion coefficient of three concrete mixes and their equivalent hardened cement pastes. Concrete and hardened cement paste (HCP) specimens are tested after conditioning at three relative humidity levels (33%, 55% and 93%). Mixes with additions of fly ash, limestone and slag are tested. Some key parameters including the total porosity, the water saturation degree and the aggregate volume fraction of the tested materials are assessed. It is noticed that oxygen diffusion coefficient decreased with the sample's water saturation degree for both concrete and HCP, although concrete specimen water content is found to be lower than HCP samples at the same relative humidity of preconditioning. A correlation between the diffusion coefficient measured on concrete and cement paste specimens is discussed.

Keywords: gas diffusivity, concrete, hardened cement paste, water saturation, oxygen

1. INTRODUCTION

In the context of the durability of reinforced concrete structures, assessing the transport behavior of aggressive species is of high importance [1]. Concrete degradation mechanisms involve very often the ingress of gaseous species such as oxygen and carbon dioxide by a diffusive transport [2]. In the case of carbonation, which is widely recognized as a significant cause of corrosion of the reinforcement in concrete [3], atmospheric carbon dioxide (CO_2)

penetrates the concrete through its porous network where it dissolves in the pore water and reacts with different phases of the cement paste [4]. Therefore, carbonation in concrete is directly dependent on the transport of CO_2 through the material.

Previous works in the literature [5][6][7] showed that transport properties of cementitious materials are highly dependent on their degree of water saturation. Hence, the experimental determination of concrete transport properties at all hydric states is necessary so that a meaningful representation of real environment can be made.

When investigating the transport properties of concrete specimen, French standards [8] require testing concrete specimen of two times the cover thickness (50mm) or a thickness equivalent or bigger than three times the maximum size of the aggregate in the specimen. These specimens are assumed to be representative of the structure's property of interest. Nevertheless previous works in the literature showed that a thickness of at least 10 times of the maximum size of the aggregate present in the concrete is required to ensure reliable results [9].

From a practical point of view, testing 50 mm concrete samples is very time-consuming. For example an ordinary Portland cement mortar specimen of 50 mm thickness reaches moisture equilibrium at 55% relative humidity (20°C) after 6 months [7], while a 3mm hardened cement paste sample requires only four weeks to reach water under the same environment [6]. Furthermore, in the case of gas diffusivity measurement, it is known that the diffusion time is proportional to the square value of the sample thickness [10]. Hence a diffusion test of a 5mm thick specimen is a 100 times faster than a specimen of 50mm.

A rapid and convenient way to test cementitious materials at different hydric states is to employ thin specimen. However, our previous works [11] show that oxygen diffusion coefficient varies slightly with the concrete specimen thickness at both the dry state and after conditioning at 93% RH, which could be due to the fact that the tested specimens are not representative. On the other hand, employing hardened cement pastes (hcp) is of high convenience: the tests can be performed in limited time since thin specimen are used without experiencing huge size effects [5]. Indeed, cement grain sizes range from less than a micron up to 100 microns, while aggregates are several orders of magnitude larger. Plus, the cement paste fraction of mortar or concrete usually contributes for the greatest part of the porosity and thus determines their transport properties to a great extent [5].

Nevertheless, the comparison between concrete specimens and HCP transport properties is not widely addressed nor entirely understood. For this reason, the aim of this paper is to investigate this issue in a greater depth. Therefore, an experimental campaign is carried out on three concrete mixes and their corresponding HCP. After conditioning at three relative humidity levels (RH), specimens of these materials are tested to oxygen diffusivity. Basic material properties such as water porosity, air content and water saturation degree of the tested materials are measured. A comparison between oxygen diffusion coefficients measured on concrete and HCP specimens is discussed.

2. MATERIALS AND METHOD

2.1 Concrete specimen

In this study, three concrete mixes are prepared using Portland cement (CEMI type), fly ash, limestone and slag. The mixes are made with an effective water-per-binder ratio of 0.6 for mixes 2 and 3 and 0.4 for mix 1; the total water-per-binder ratio that includes the water fixed

by the aggregates is significantly large (Table 1) because the water absorption by aggregates is close to 3%. These concrete's cement and additions dosage, the aggregate volume fraction and an average of the total water porosity determined by water soaking under vacuum following the French standard NF P18-459 are shown in Table 1. The dry mass of the samples is given by oven-drying at 105°C, and the total porosity is computed following equation (1), where m_0 is the dry mass of the sample, m_{sat} is themass in the open air of the water-saturated sample and m_{hydro} is the hydrostatic weight, mass of the water-saturated sample by immersion in water under a vacuum for 48h.

$$\phi = \frac{m_{sat} - m_0}{m_{sat} - m_{hydro}} \quad (1)$$

The maximum aggregate size present in these tested concrete specimens is 22mm. Concrete mixes are cast into 110*220 mm moulds, demoulded after 24h and stored at 100% relative humidity for 90 days. The tested specimens are discs of 8 mm thickness with a diameter of 110mm. These samples are sawn from 220 mm height cylinder. For each concrete mix and conditioning relative humidity, four replicates are prepared. These specimens are stored in relative humidity controlled climate chambers at 33%, 55% and 93% RH by means of saline solutions with soda lime in order to avoid carbonation of the samples during the conditioning. Moisture equilibrium of these specimens is reached after 5 months (moisture equilibrium criteria: mass variation less than 0.05% in a week). Mixes 1 and 3 replacements of cement by limestone and slag, respectively exceed by 10% the values required by NF EN 206-1, while mix n°2 replacement of cement by fly ash corresponds to the maximum value accorded by the French concrete standards NF EN 206-1 for all exposure classes (except XF4). These mixes are tested in order to investigate the influence of the replacement of cement by a high percentage of mineral additions on gas diffusivity.

Table 1: Mix-design parameters of the three tested concrete

Concrete index	1	2	3
Total W/B	0.5	0.67	0.74
Total W/C	0.8	0.9	1.9
Effective W/B	0.4	0.6	0.6
Air content (%)	0.9	1.9	1.5
Mineral addition type	Limestone	Fly ash	Slag
Aggregate volume fraction (%)	62.8	69.7	70.8
Mineral additions (% binder)	40	30	60
Cement dosage (kg/m^3)	270	223	119
Addition dosage (kg/m^3)	190	95	179
Total porosity (%)	16.8	16.9	18.6

2.2 Hardened cement paste samples

Paste mixtures are prepared using the effective water-per-binder ratios corresponding to the tested concrete (0.6 for mixes 2 and 3 and 0.4 for mix 1). Cement pastes are cast in plastic cylindrical molds of diameter 40 mm and height 100 mm and rotated for 24h. The pastes are demolded afterwards and stored at 100% relative humidity for 90days. Thin discs of 3mm

thickness are sawn using a precision saw. The slices are then equilibrated at 93%, 55% and 33% RH in climate chamber with salt solutions and soda lime to avoid carbonation of the HCP during the conditioning. Moisture equilibrium time varies from 4 to 6 weeks depending on the relative humidity of the exposure.

Table 2: Mix-design parameters of the tested HCP

HCP index	1	2	3
Total W/B	0.4	0.6	0.6
Air content (%)	1.06	0.14	0.74
Addition type	Limestone	Fly ash	Slag
Mineral additions (% binder)	40	30	60
Total porosity (%)	53	54	53

2.3 Oxygen diffusivity measurement

The oxygen diffusion coefficient is measured using an experimental setup developed during our previous works [6][12]. The test device is designed to determine oxygen effective diffusion coefficient of hardened cement pastes and concrete specimen conditioned under different RH. The main element of the experimental setup is the diffusion cell also called "downstream chamber". The diffusion cell is placed inside a relative humidity controlled chamber also referred to as "upstream chamber. The cell is flushed with nitrogen at the beginning of each test. One face of the sample is exposed to the internal volume of the cell and the other face to the RH controlled air of the upstream chamber.

Oxygen diffuses successively through the sample into the cell where O_2 concentration is measured by a gas sensor. The effective diffusion coefficient of oxygen is determined by the numerical fitting of the accumulation curve to Fick's second law taking into account the transient regime.

3. RESULTS

3.1 Water saturation degree

The water saturation degree of the tested concretes and HCP is determined in the desorption state at three RH: 33%, 55% and 93% using the following equation:

$$S_r = \frac{m - m_0}{m_{sat} - m_0} \quad (2)$$

where m is the mass at equilibrium, m_0 the dried mass, and m_{sat} the saturated mass. The HCP and concrete specimens saturated mass is determined by water soaking under vacuum for 24h and 48h respectively. The dry mass is obtained after drying the samples in the oven at 105°C as required by the French standard NF P18-459.

Figure 1 shows that the water saturation degree at different relative humidity of conditioning depends on the specimen composition. For mix 3, HCP samples are 10% more water saturated than concrete specimens at 33% and 55% RH while they are 20% more water saturated at 93% relative humidity. Limestone concrete specimens (mix 1) are more water saturated than their corresponding HCP at all RH.

However results for the mix number 2 which contain fly ash are less consistent. At 33% and 55% RH the degree of water saturation of HCP is 10% and 6% respectively lower than for concrete specimens, while it is 20% higher at 93% RH.

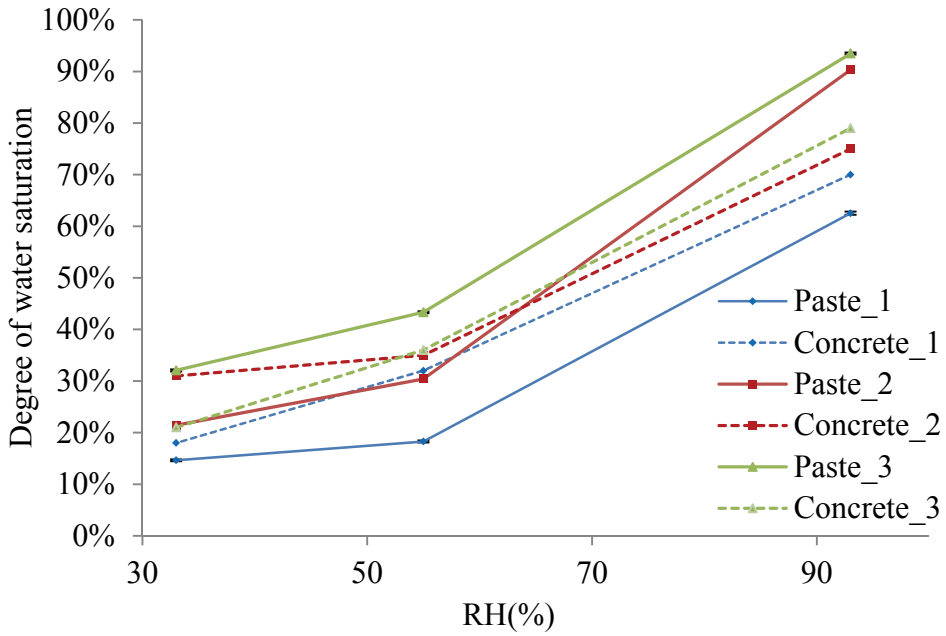

Figure 1: HCP and concrete water saturation degree at different RH in desorption

The total porosity of the cement paste present in these concrete specimens can be calculated from equation (3), where ϕ_c , $\phi_p$and f are the total porosity of concrete, the porosity of HCP in concrete and the aggregates fraction, respectively. This equation could also include aggregate and air contributions to concrete porosity which are not observed in pure paste.

$$\phi_c = \phi_p(1 - f) \tag{3}$$

Using equation (3) the calculated total porosity in HCP present in the concrete 1, 2 and 3 are 45.2%, 55.7% and 63.7% respectively while the corresponding HCP of these concrete total porosities are 53.8%, 54% and 53%.

For mixes 2 and 3 the higher porosity of the HCP present in the tested concrete explains the lower water content in the concrete samples. Moreover, the presence of porous aggregate-paste interfacial transition zones (ITZ), in which the porosity is higher than that of the cement paste causes the moisture storage of concrete specimen to be less important [14]. Finally, porous aggregates with pore sizes larger than the one of the paste could be still desaturated at 93% RH.

However for limestone mix 1 the HCP present in the concrete specimen is 8.6% less porous than its corresponding HCP which explains the lower water saturation degree for HCP1.

3.2 Concrete vs. cement paste diffusivity

Table 3 shows the oxygen effective diffusion coefficients $D_{e,O2}$ of the concrete specimens and their corresponding HCP. As expected, the oxygen diffusion coefficient of pastes and concretes decreases from one (mix1) to three (mix2) orders of magnitude with the relative humidity of conditioning [6]. This is explained by the fact that the relative humidity of preconditioning determines the water saturation degree of the tested specimen (Fig.1), which is directly related to the percentage of pores available to gas transport and their pore sizes.

Table 3: Concrete and HCP diffusion coefficient at different RH

Mix	RH(%)	HCP $D_{e,O2}$(m²/s)	Concrete $D_{e,O2}$(m²/s)	$\frac{D_{e,O2}^{Concrete}}{D_{e,O2}^{HCP}}$
1	33	$3.17 \cdot 10^{-7}$	$2.20 \cdot 10^{-7}$	0,7
	55	$2.67 \cdot 10^{-7}$	$8.30 \cdot 10^{-8}$	0,3
	93	$1.94 \cdot 10^{-8}$	$1.30 \cdot 10^{-8}$	0,7
2	33	$9.50 \cdot 10^{-8}$	$2.40 \cdot 10^{-7}$	2,5
	55	$5.22 \cdot 10^{-8}$	$7.50 \cdot 10^{-8}$	1,4
	93	$6.24 \cdot 10^{-11}$	$3.10 \cdot 10^{-8}$	496,8
3	33	$1.49 \cdot 10^{-8}$	$2.06 \cdot 10^{-7}$	13,8
	55	$6.92 \cdot 10^{-9}$	$8.80 \cdot 10^{-8}$	12,7
	93	$2.58 \cdot 10^{-10}$	$3.50 \cdot 10^{-8}$	135,7

Results from Table 3 show that for the mix 1, oxygen diffusion coefficients of concrete specimens are lower than $D_{e,O2}$ of their corresponding HCP. This could be explained by the fact that concrete specimen (mix 1) are more water saturated than HCP 1 and contain less entrained air.

Figure 2 shows that concrete specimen diffusivities are higher than the diffusivities of their equivalent HCP at the three RH of conditioning for mixes 2 and 3.

This could be explained by the influence of entrained air, aggregate-paste interfacial transition zone, aggregate porosity and liquid saturation in the concrete specimen. Indeed previous works of Wong et al [15] proved that air entrainment increases gaseous diffusivity by up to a factor of 3 regardless of the w/c ratio, curing age and conditioning regime.

In addition to that, the previous work of Larbi et al [16] on the influence of aggregates content on tritiated water diffusivity in mortars show that when the sand content exceeds 50% more air voids are created in the material leading to high diffusivity, which is in agreement with the results shown on Figure **2** since the aggregate volume fraction of the tested concrete specimen exceeds 60% for all mixes. $D_{e,O2}$ of concrete do not follow a simple linear mixing rule using paste diffusivity such as equation (3), which is valid for low (<0.5) aggregate volume fraction [15]. The higher diffusivity of concrete 3 samples is a consequence of their lower degree of water saturation comparing to their corresponding HCP. This lower degree of water saturation would be consistent with a contribution of aggregate to porosity. Indeed the water absorption by aggregate is larger than the one of mix 1 and 2 as seen whereas a similar aggregate volume fraction and air content is observed for all mixes.

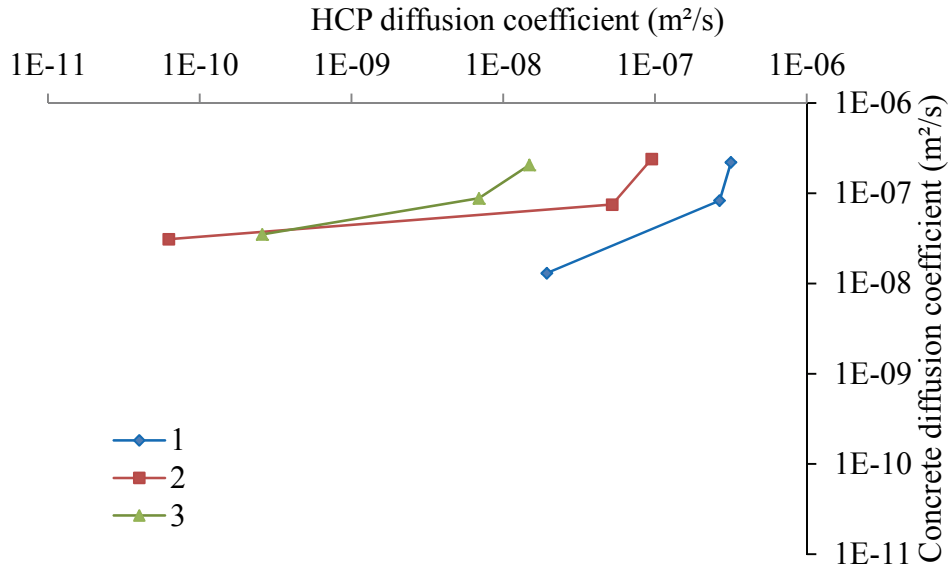

Figure 2: Concrete vs HCP oxygen diffusion coefficient

4. CONCLUSIONS

This study focused on an experimental investigation of the oxygen diffusivity in concrete specimens and their corresponding HCP conditioned at different relative humidity levels. Mixes blended with limestone, fly ash and slag are tested. From the results, it can be concluded that:

- HCP can have 100 times lower diffusion coefficients than the one of their equivalent concrete for the highest RH (93%); nevertheless in dry conditions (33% RH), diffusion coefficients of both HCP and concrete are in the same range.
- The desorption isotherms of the cement paste and concrete highlights the effect of aggregates on the moisture storage capacity and thus on the oxygen diffusivity.
- A correlation is observed between $D_{e,O2}$ of tested concrete specimen and there equivalent HCP.

To extend the correlation between HCP and concrete for water desorption isotherm and gas diffusivity, further work would be needed on other concrete mixes to highlight the role of air, ITZ, aggregate volume fraction and sorptivity.

REFERENCES

[1] Z. Yu, 'Microstructure Development and Transport Properties of Portland Cement-fly Ash Binary Systems', PhD thesis Wuhan University of Technology, 2015.
[2] R.J. Millington, 'Gas Diffusion in Porous Media', *Science*. **130** (1959) 100–102.
[3] B. Huet, V. L'hostis, G. Santarini, D. Feron, H. Idrissi, 'Steel corrosion in concrete: Determinist modeling of cathodic reaction as a function of water saturation degree', *Corros Sci*. **49** (2007) 1918–1932.

[4] W. Ashraf, 'Carbonation of cement-based materials: Challenges and opportunities', *Constr Build Mater*. **120** (2016) 558–570.
[5] J. Sercombe, R. Vidal, C. Gallé, F. Adenot, 'Experimental study of gas diffusion in cement paste', *Cem Conc Res*. **37** (2007) 579–588.
[6] M. Boumaaza, B. Huet, G. Pham, P. Turcry, A. Aït-Mokhtar, C. Gehlen, 'A new test method to determine the gaseous oxygen diffusion coefficient of cement pastes as a function of hydration duration, microstructure, and relative humidity', *Mater Struct*. **51** (2018).
[7] H.S. Wong, N.R. Buenfeld, M.K. Head, 'Estimating transport properties of mortars using image analysis on backscattered electron images'., *Cem Conc Res*. **36** (2006) 1556.
[8] Association Française de normalisation, XP P18-463, 2011.
[9] H.S. Wong, M. Zobel, N.R. Buenfeld, R.W. Zimmerman, 'Influence of the interfacial transition zone and microcracking on the diffusivity, permeability and sorptivity of cement-based materials after drying', *Mag Concr Res*. **61** (2009) 571–589.
[10] J. Crank, 'The Mathematics of Diffusion' , 2nd Edn (Clarendon, Oxford, 1975).
[11] M. Boumaaza, B. Huet, P. Turcry, C. Gehlen, A. Aït-Mokhtar, D. Heinz, 'Influence of carbonation and concrete specimen size on gas diffusion', in 'SynerCrete'18', Proceedings of an international conference, Portugal, October, 2018.
[12] M. Boumaaza, B. Huet, P. Turcry, A. Aït-Mokhtar, C. Gehlen, D. Heinz, 'Gas diffusivity test method development : effect of cement paste saturation degree and concrete specimen thickness', in: '12th Fib International PhD Symposium in Civil Engineering' 2018, Proceedings of an international conference, Czech republic, August, 2018.
[13] N. Issaadi, A. Nouviaire, R. Belarbi, 'Moisture characterization of cementitious material properties : Assessment of water vapor sorption isotherm and permeability variation with ages', *Constr Build Mater*. **83** (2015) 237–247.
[14] H.S. Wong, A.M. Pappas, R.W. Zimmerman, N.R. Buenfeld, 'Effect of entrained air voids on the microstructure and mass transport properties of concrete', *Cem Conc Res*. **41** (2011) 1067–1077.
[15] B. Larbi, W. Dridi, P. Dangla, P. Le Bescop, 'Link between microstructure and tritiated water diffusivity in mortars : Impact of aggregates', *Cem Conc Res*. **82** (2016) 92–99.

International Conference on Sustainable Materials, Systems and Structures (SMSS 2019)
Novel Methods for Characterization of Materials and Structures
20-22 March 2019 – Rovinj, Croatia

PARAMETER ESTIMATION IN FIBER REINFORCED CONCRETE

Ivica Kožar (1), Neira Torić Malić (1), Silvija Mrakovčić (1) and Danijel Simonetti (1)

(1) Univeristy of Rijeka Faculty of Civil Engineering, Croatia

Abstract

This paper presents application of a novel method for parameter estimation in a stochastic model of fiber reinforced concrete. Fiber reinforced concrete (FRC) is a new material with increasing application. Numerical model of FRC is not so well established as that of ordinary concrete. It is even more truth for procedures for material parameter estimation. Deterministic model of FRC has to deal with a large number of fibres and identification from that type of model is generally difficult.

In this work we present a stochastic model of FRC based on the fiber bundle model. Fiber bundle model allows introduction of a probability distribution function into the model and simple performance of Monte Carlo experiments. Introduction of order statistics and the Levenberg – Marquardt procedure leads to formulation of the inverse model that permits identification of material parameters. Numerical examples illustrate the properties and stability of the proposed method.

Keywords: fiber reinforced concrete, stochastic model, fiber bundle model, parameter estimation, Monte Carlo experiments

1. INTRODUCTION

Deterministic models of materials where we assume that every material parameter could be described exactly have dominated the last century. When industry started to deal with very small and very large structures it became evident that properties could vary significantly within the material. One of the first evidence of the importance of the stochastic approach to material modelling is the emergence of the scaling low in materials [1].

Parameters in a deterministic model usually represent some physical quantity and are easily identified as a material property. Formulation of a stochastic material model requires careful choice of parameters since parameters do not have to represent a physical quantity. In most cases one can not simply assign stochastic property to a parameter in a forward model since those parameters are not well exposed (they are hidden inside the mathematical formulation of a model). E.g., nonlinear finite element models apply linearization and iterative solution procedure and it is tedious to assign stochastic properties to material

parameters inside the model. That has been considered and the fiber bundle model (FBM) is adopted here as a model for fiber reinforced concrete. Fibers in a fiber bundle model do not represent physical fibers in a fiber reinforced concrete but are merrily a suitable parameterization for the stochastic model.

Stochastic model is transformed into a statistical by assigning a known probability distribution to one or more model parameters. One of the advantages of the stochastic model of material is its ability to perform error propagation analysis in a natural and simple way through Monte Carlo experiments. In the same way it is possible to simulate errors in measurement. Numerical experiments with a statistical model are much more similar to the real experiments with materials or structures.

Generally, a nonlinear model requires well defined parameters to produce output that reflects experimental results. Unfortunately, adjustment of parameters is a tedious task. The best way is to identify parameters from experimental results. Usually, parameters could not be measured directly (especially when they do not represent physical properties of a material) and an inverse procedure is required. Inversely formulated model is a procedure obtained from the original ("forward") model so that unknown parameters are explicitly formulated. Obtaining an inverse procedure is not simple because naïve formulations tend to be unstable and amplify the measurement error [2].

Procedure for parameter estimation in a statistical model has been described in [3 Here we present an extension of the presented procedure as we apply elastic-plastic force-displacement law for individual fibers in a bundle.

2. FIBER REINFORCED CONCRETE

There is a very short description of the fiber reinforced concrete (FRC), more detailed insight can be found e.g., in [4]. FRC comprises a concrete matrix with embedded fibers of different materials. In our analysis we are using only steel fibers. In Fig.1 one could see X-Ray image of a FRC sample [5] and a cross-section of a 3D stochastic computer model. Stochastic model employs the normal distribution with given mean fiber density and variance resulting in a slightly different fiber distribution in each simulation.

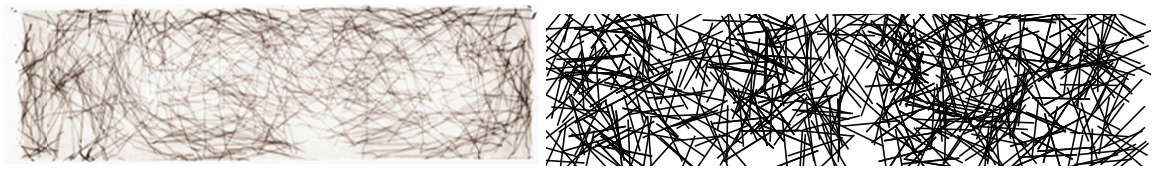

Figure 1: FRC sample beam 4x4x16 cm, a) X-Ray image, b) 3D computer model

Mechanical properties of the FRC are strongly influenced by the bond-slip relationship between the (steel) fiber and the cement matrix. Namely, when bearing capacity of the FRC specimen is exceeded it breaks in such a manner that fibers do not break but are instead pulled out of the matrix.

2.1 Laboratory experiments

Laboratory experiments provide the data for parameter estimation. In Fig.2 there is the experimental set-up for determination of the force-displacement diagram of a single fiber.

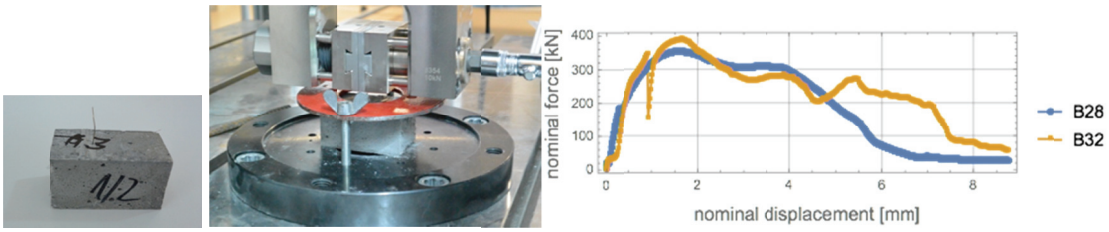

Figure 2: Experimental set-up, a) sample, b) pulling-out of a fiber, c) force-displacement diagram for two embedment depths

Experiments have been performed for various embedment depths of fibers and repeated for a number of samples. Blue coloured diagram has been chosen as a representative shape of the force – displacement law for fiber pull-out.

2.2 Fiber bundle model

Fiber bundle model appeared long time ago [6] in textile industry and latter made its way into physics of materials [7] and engineering [8,9,10]. Basic idea of the model is that material can be represented as a collection fibers of different orientation and statistically distributed properties, e.g., length or cross section of each fiber. Various stochastic distributions could be applied depending on the property that is addressed, like normal or uniform distribution for length or cross section properties or cosine distribution if fiber orientation is to be considered. Each bar behaves according to a deterministic but simple force – displacement (or stress - strain) law, as depicted in Fig.3

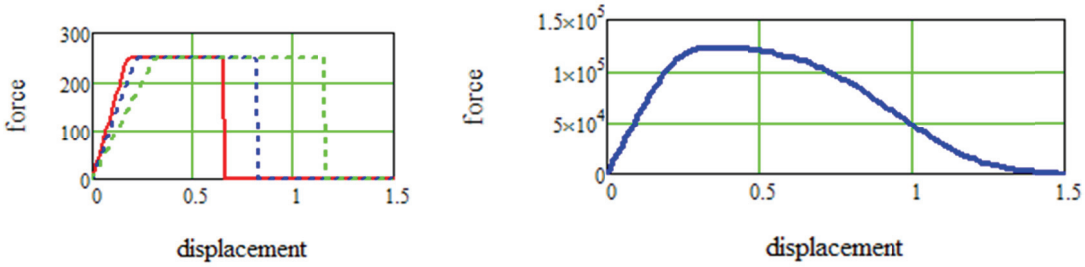

Figure 3: Force – displacement law for a) single bars, b) bundle of bars

Force – displacement relation for each bar has a simple form but it depends on the stochastic parameter. For length as a stochastic parameter and elastic-plastic bar behaviour it reads

$$P_i(\delta, i) = \begin{cases} \dfrac{EA}{L_i}\delta \; if \; \dfrac{\delta}{L_i} < d_0 \\ \dfrac{EA}{L_i} d_0 \; if \; \dfrac{\delta}{L_i} \geq d_0 \wedge \dfrac{\delta}{L_i} < d_t \\ 0 \; otherwise \end{cases} \tag{1}$$

Behaviour of the whole bundle is obtained through summation

$$F_b(\delta) = \sum_i P_i(\delta, i) \tag{2}$$

In the above equations δ and i are bar displacement and index number, respectively. L and EA are bar length and axial stiffness, respectively. F_t and d_t represent force and displacement threshold.

Combining a large number of bars with stochastic parameters various force – displacement relations could be obtained.

3. PARAMETER ESTIMATION

Behaviour of nonlinear models with several parameters is usually very complex and influence of parameters should be carefully investigated. In the case of unknown parameters, procedures for their estimation should be carefully devised since numerical instabilities commonly occur.

3.1 Significance of parameters

Choice of the stochastic distribution has a great influence on the force – displacement behaviour. Fig.4 illustrates the influence of change of the mean value of the fiber length and its variance (see Eq.1)

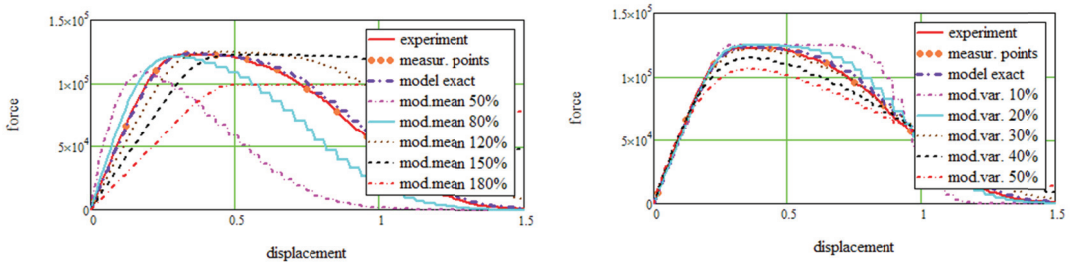

Figure 4: Dependance of the load – displacement law on the change of, a) mean value of fiber length, b) variance change of fiber length

3.2 Inverse model

In this case of forward stochastic model it turned out that the inverse model is obtained applying the Levenberg – Marquardt procedure. More about the Levenberg – Marquardt procedure, its limitations and presentation of an alternative method can be found in [11]. Minimisation of the required parameter is formulated as an iterative procedure

$$\Delta_\sigma = \frac{\sum_{im}\left[F_{\delta,im} - F_u(\delta_{im}, \sigma, \mu, F_t)\right] X_{\sigma,im}}{\sum_{im}\left(X_{\sigma,im}\right)^2} \tag{3}$$

In the Eq.3 im is the measurement index, Δ_σ is change of any parameter, F_δ is the measured value, F_u is the expected value and X_σ is sensitivity of the parameter, $X_\sigma = {\partial F_u}/{\partial\sigma}$. Update of the parameter is additive.

4. NUMERICAL EXPERIMENTS

The purpose of numerical experiments is to produce data for evaluation of the inverse procedure. Basically, numerical experiments should mimic real laboratory experiments.

In our experiment we are simulating pull-out of a steel fiber from the concrete block under displacement control, i.e., loading is in the form of given displacements and the force is produced from the model.

Since the material model is stochastic in nature, each experiment produces a slightly different result as parameters of the model vary according to the given probability distribution of parameters.

Finally, a series of load - displacement curves is obtained; they are the basis for parameter identification. We will assume that initial parameter values that produced the resulting load - displacement curves are not known and will try to determine their value using the inverse procedure.

4.1 Monte Carlo experiment

Our forward statistical model assumes normal distribution of fiber length and as a consequence each fiber has different threshold displacement for elastic and elastic-plastic limits (see Fig.3). However, threshold strains d0 and dt are prescribed as deterministic values.

Statistical model allows Monte Carlo experiments, so, we have varied parameter values using normal distribution for given mean and variance. The resulting load - displacement curves are presented in Fig.5 along with the corresponding curve obtained using order statistics.

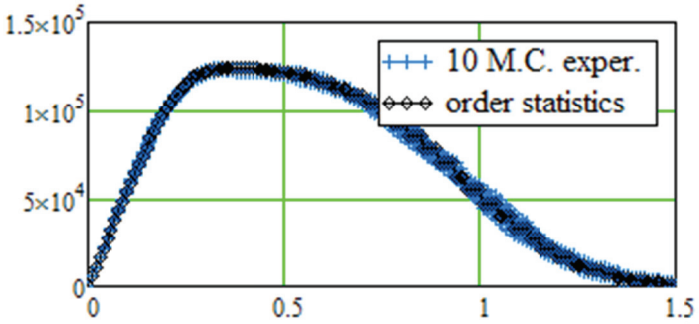

Figure 5: Force-displacement diagram for Monte Carlo numerical experiment for pulling-out of a fiber

It is clear that the order statistics gives results within 10 Monte Carlo experiments and can be used in the inverse model for parameter estimation.

4.2 Parameter estimation

Parameter estimation is performed using Eq.3 where order statistics replaces the expected values. We are estimating value of four parameters: the fiber length mean, the fiber length variance and the elastic and elastic-plastic strain thresholds. Those are parameters that enable the complete formulation of the forward statistical model and production of new load - displacement curves.

The procedure is iterative, a starting values for parameters are assumed and an algorithm produces a correction. Initial values are additively updated and the procedure is repeated as long as the correction is greater that the given bound.

4.3 Sensitivity analysis

We have not performed the complete sensitivity analysis here but only present some results as an indicator of the accuracy that could be achieved. Fig.6 presents error in measurement.

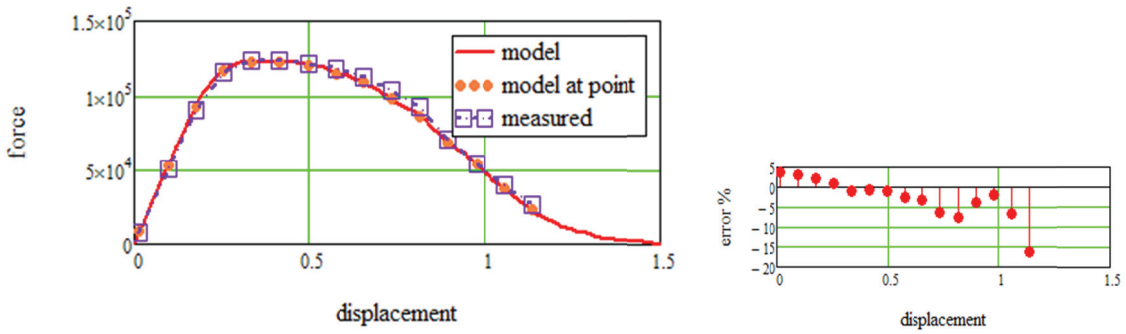

Figure 6: Error in measurement, a) in the force – displacement curve, b) relative in %

It is important to note that relative measuring error increases for large displacements since the nominal value of force is very low; there should be no measuring points.

Table 1 presents numerical results in parameter estimation using the Levenberg – Marquardt procedure.

Table 1: Numerical results in parameter estimation

Number of bins	No. of measuring points	L - mean	L - variance	Strain elastic threshold
50	15	0.5 %	-0.05 %	-0.07 %
100	15	1.56 %	-0.21 %	-0.46 %
50	25	-0.17 %	-0.52 %	-0.56 %
100	25	0.14 %	-0.05 %	-0.29 %

In all experiments number of iterations in the Levenberg – Marquardt procedure was between 5 and 11. One can conclude that increase in number of measuring points should be accompanied with an increase in the number of bins.

5. CONCLUSIONS

The paper presents application of a novel method for parameter estimation in a stochastic model of fiber reinforced concrete (FRC). Deterministic models are not suited for FRC and we present a stochastic model based on the fiber bundle model that allows introduction of a probability distribution function into the model. Such a model allows simple performance of Monte Carlo experiments thus mimicking the laboratory experiments.

Single fibers in the fiber bundle model behave according to elastic-plastic law and the obtained global force – displacement law is similar to the one from pull-out experiments.

Estimation of material parameters of the model is made possible by introducing the order statistics and the Levenberg – Marquardt procedure. It has been shown that the presented inverse formulation leads to efficient and stable procedure for parameter estimation.

Numerical examples have demonstrated that the number of measuring points and the number of bins in order statistics have to be in correlation.

ACKNOWLEDGEMENTS

This research has been supported by Croatian Science Foundation under the project 9068.

REFERENCES

[1] Ožbolt, J., Li, Y.J., Kožar, I. 'Microplane Model for Concrete with Relaxed Kinematic Constraint', Int. J. Solid. Struct. **38**(16) (2001), 2683-2711.
[2] Kerschen, G., Worden, K., Vakakis, A.F., Golinval, J.C., 'Past, present and future of nonlinear system identification in structural dynamics', Mech Syst Signal Process. **20** (2006) 505–592
[3] Kožar, I., Torić Malić, N., Rukavina, T., 'Inverse model for pullout determination of steel fibers', Coupled Systems Mechanics **7** (2018) 197-209.
[4] Jansson, A., Lofgren, I., Lundgren, K. and Gylltoft, K., 'Bond of reinforcement in self-compacting steel-fibre-reinforced concrete', Magazine of Concrete Research **64**(7), (2012) 617–630
[5] Kalinčević, S. (2016), "Determination of homogeneity of steel fibers in concrete specimens using computational tomography", M.Sc. Dissertation, supervisor Ivica Kožar, University of Rijeka, Rijeka, Croatia.
[6] Daniels, H.E., 'The statistical theory of the strength of bundles of threads', Proc. R. Soc. Lond. A **183** (1945) 405-435.
[7] Moral, L., Gomez, J.B., Moreno, Y. and Pacheco, A.F., 'Exact numerical solution for a time-dependent fibre-bundle model with continuous damage', J. Phys. A: Math. Gen. **34** (2001) 9983–9991.
[8] Mishnaevsky, L., 'HIERARCHICAL COMPOSITES: Analysis of damage evolution based on fiber bundle model', Composites Science and Technology **71** (4) (2011) 450-471.
[9] Raischel, F., Kun, F. and Herrmann, H.J., 'Continuous damage fiber bundle model for strongly disordered materials', Phys. Rev. E **77** (2008) 046102-046111.
[10] Salviato, M. and Bažant, Z.P., 'The asymptotic stochastic strength of bundles of elements exhibiting general stress–strain laws', Probabilistic Engineering Mechanics **36**, (2014) 1-7.
[11] Lozzi-Kožar, D., Kožar, I., T., 'Estimation of the eddy thermal conductivity for Lake Botonega', Engineering Review **37**(3) (2017) 322-334.

International Conference on Sustainable Materials, Systems and Structures (SMSS 2019)
Novel Methods for Characterization of Materials and Structures
20-22 March 2019 – Rovinj, Croatia

REALTIME READJUSTMENT OF THE RHEOLOGICAL PROPERTIES OF SCC BY AN EXPERT SYSTEM

Ivan Parić (1), Wolfgang Kusterle (1)

(1) OTH Regensburg, Germany

Abstract

SCC mixes may sometimes not fulfil fresh concrete requirements due to variances in constitutive materials. Instead of an adjustment by experienced lab staff, the use of a real-time expert system has been investigated. For this reason, a ball rheometer measures the fresh concrete directly after the mixing process, during a short break. The viscosity and the dynamic yield point are determined.

These rheological parameters describe the consistency and thus the casting ability and consequently the quality of the SCC. In future an automated expert system shall use this data for a necessary adjustment of the mix.

During the test series the mix designs of the well working SCC's were modified by using deviating water content. Subsequently, using the rheological data, water, superplasticizer or stabilizing agents were added to the mix, trying to reach proper workability again. The graphs for the changing rheological properties as a function of the respective amount of initial water content and additional water dosage or admixture dosage were generated and analysed for the mixes of two precast plants. This data is the input for the knowledge base, which is used by the expert system. Up to now the data is used for a manually dosage**,** the automated first version is under progress. The presented results show that a successful readjustment is possible in most cases.

Keywords: SCC, fresh concrete properties, workability, readjustment, expert system

1. INTRODUCTION

Rheology is an important property of self-consolidating concrete (SCC). However, concrete rheology is a complex phenomenon, which is difficult to define with a few parameters or by a single testing procedure [1]. Workability testing is one of the important early quality tests for all concrete structures. For SCC, maintaining the workability within given numbers for a defined time is essential for a fast and effective casting process.

Rheological tests of SCC may be performed using one-point tests, as given in EN 12350-8 to 11, which will not give exact rheological numbers, or by using costly stationary concrete rheometers. Testing takes time and results are not available during mixing process.

Rheological measurements in the mixer will give more reliable data regarding workability than one-point tests [1]. Figure 1 shows, how the physically data from rheological measurements can be used by an expert system to reach an ongoing proper workability of SCC.

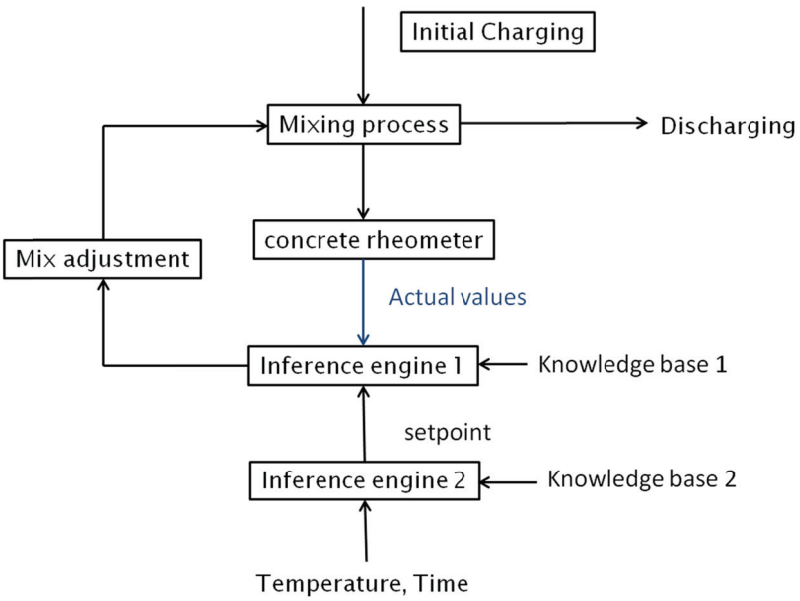

Figure 1: Flowchart for an expert system in SCC production [2].

The data of the knowledge base 1 (see section 2) give the target value for the rheological parameters and information for correcting measures. The inference engine creates an instruction in case of a deviation of the rheological parameters. The knowledge base 2 deals with the influence of time and temperature. It is not addressed in this paper. More information on the used rheometer and the measuring procedure are given in [3].

1.1 Rheometer used and Measurement profile

The results presented in this paper were investigated during a Bavarian research project. [4] Investigations were done in two precast plants with two different SCC mixes and in the laboratory of the OTH Regensburg. During these tests the knowledge base 1 (figure 1) for both mixes was created. In this way it was possible to define areas of workability, which will give best performance. The knowledge bases of two mixes were tested in some manual and finally in automated readjustment tests. The configuration of the rheometer is different for the two mixes. This leads to different absolute values in the respective results.

The used rheometer was a ball rheometer, which tested the unsheared concrete during half a rotation. The setup of the rheometer in the mixer can be seen in figure 2. The measurement profile is visible in figure 3. Dynamic yield stress and viscosity could be determined within one minute. The determined values are relative values, as a correlation to absolute values is tricky [5] and not necessary for the given purpose. The term dynamic yield stress is used for

the necessary torque in phase 1 (Fig.3) that is needed to keep the material flowing with a defined velocity [6]. The viscosity reported here is always the relative viscosity determined by the Bingham model.

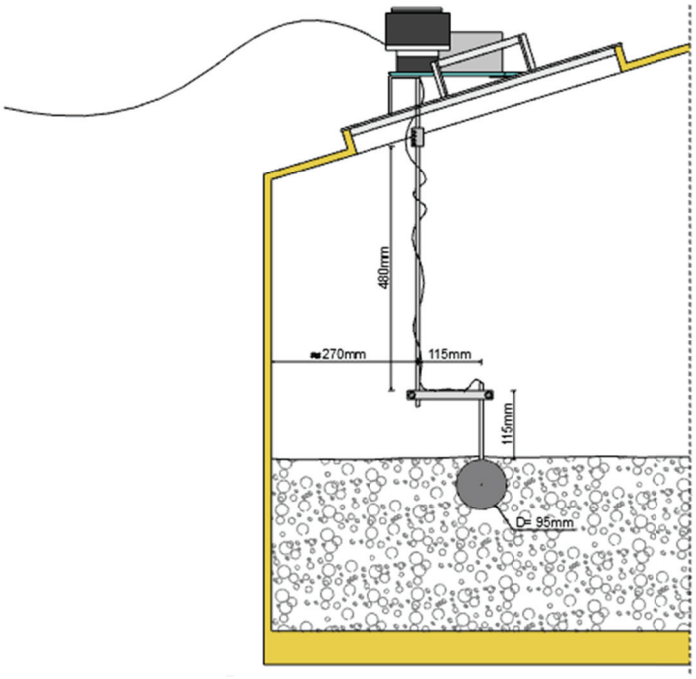

Figure 2: Ball rheometer measuring in the Eirich laboratory mixer

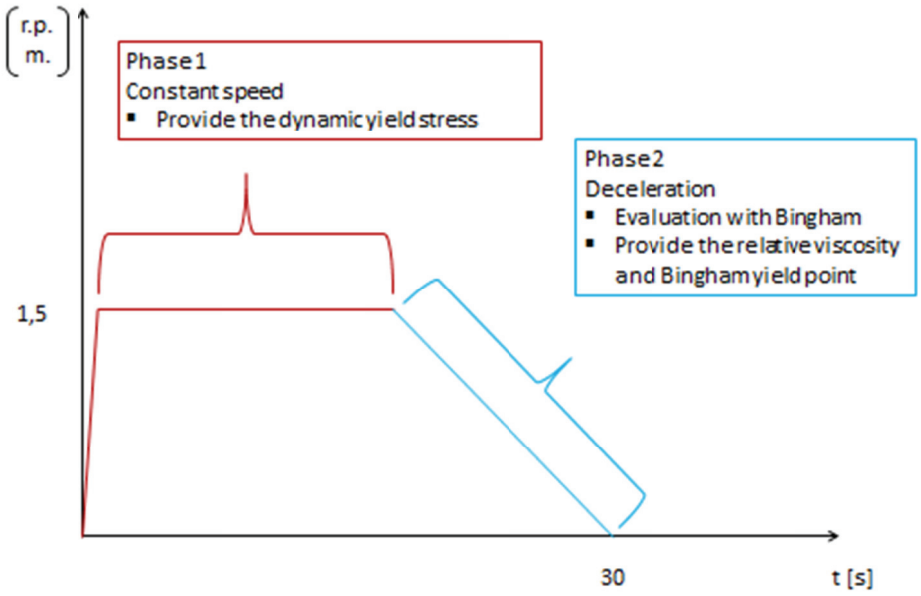

Figure 3: Used measuring profile with max. 1.5. r.p.m. In tests alternatively 1.0 and 2.0 r.p.m. have been used

2. TESTS FOR CREATING A KNOWLEDGE BASE 1

During the test series the mix designs of SCC's [7,8] were modified by using deviating water content from before defined target values.. Subsequently, water, superplasticizer or stabilizing agents were added to the mix. The graphs for the changing rheological properties as a function of the respective amount of initial water content and additional water dosage or admixture dosage were generated and analysed for the mixes of two precast plants. In this chapter data produced for the knowledge base 1, are presented for one specific mix only**.** Knowledge-base 2 is not addressed in this paper. Firstly, the changes in consistency with a rising water amount in one single test are demonstrated in figure 4. The mixture was produced with insufficient water content. Then, two times the amount of 10.4 l/m³ water was added, this equals each time a change in the w/c ratio of 0.02.

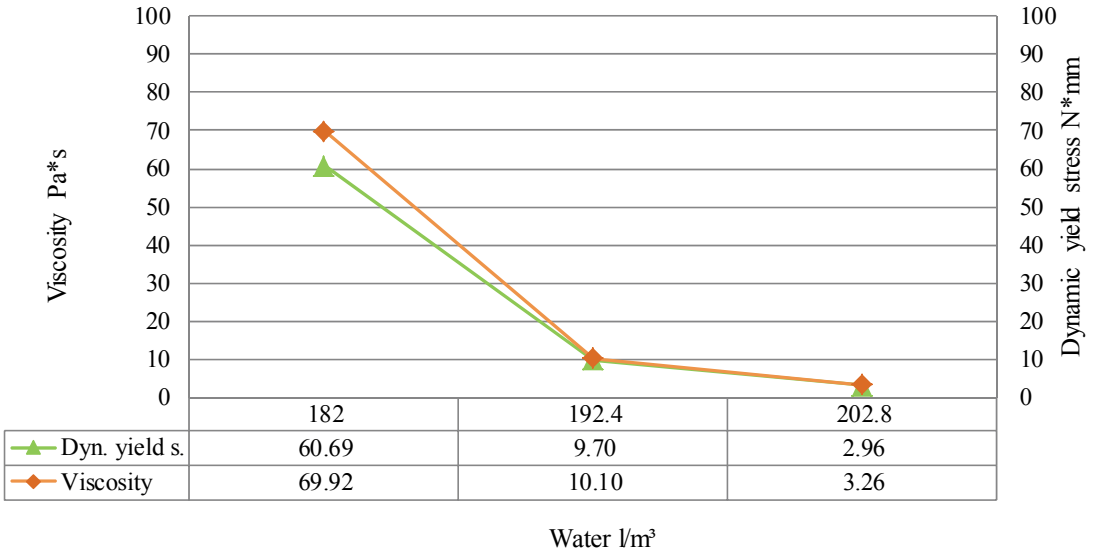

Figure 4: Adjustment with additional water - initial water amount 182.0 l/m³

By pure chance numbers of viscosity and dynamic yield stress are for this test quite similar. Similar investigations were done with superplasticizer and different stabilizers. These results are also part of the data for the knowledge base 1. Examples are shown in figure 5 and 6 respectively.

Figure 5 shows again a mixture that was produced intentionally with too little water. In three subsequent steps additional superplasticiser was added to the mix. At an additional dosage between 0.2 % and 0.4 % by mass of cement the rheological properties would correspond with a well working SCC.

In figure 6 the influence of a stabilizer addition to a mixture with an intentional excess of water is presented. The graphs may be different, when using other stabilizer types. But an adjustment of the rheological properties is mostly possible. However, many stabilizer types are sensitive to mixing energy and mixing time.

Finally, all the experiences in the lab and precast plants show an optimum of workability for the here presented mix of precast plant 1 and test set-up by the value 20 for the dynamic yield stress and the viscosity.

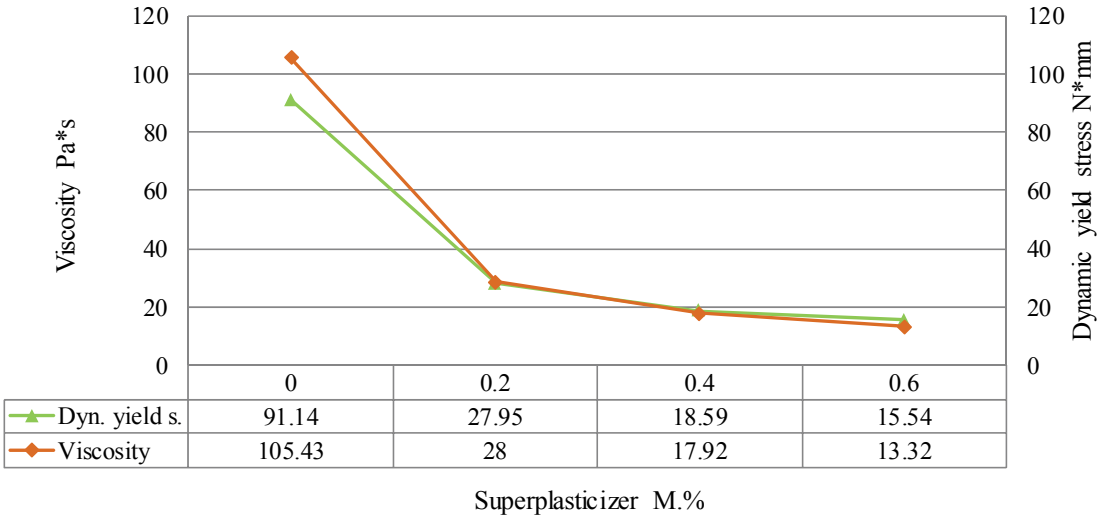

	0	0.2	0.4	0.6
Dyn. yield s.	91.14	27.95	18.59	15.54
Viscosity	105.43	28	17.92	13.32

Figure 5: Stepwise adjustment with additional superplasticizer-dosage

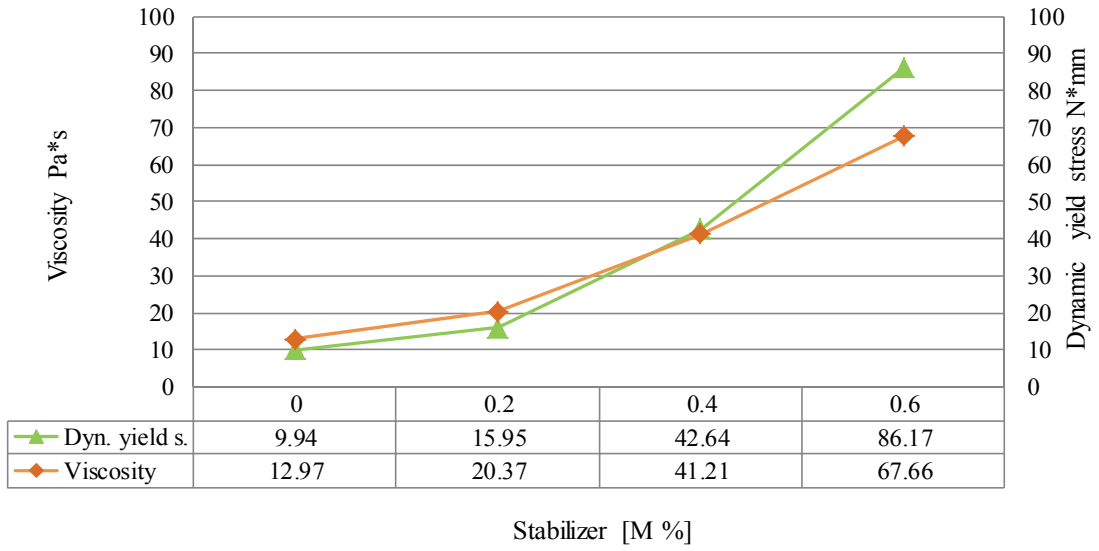

	0	0.2	0.4	0.6
Dyn. yield s.	9.94	15.95	42.64	86.17
Viscosity	12.97	20.37	41.21	67.66

Figure 6: Stepwise adjustment with stabilizer

3. MANUAL ADJUSTMENT

For the following tests the SCC's mixtures were produced intentionally too stiff. Using the data from the knowledge-base first steps of a successful direct correction are shown in figure 7 by the means of water and figure 8 by the means of superplasticiser.

The dosages used in figure 7 and 8 were predetermined by using the knowledge-base in a simplified way. The dynamic yield stress values from the online display of the rheometer were used, which are a good indicator for comparison with the knowledge-base. The amount of water in figure 7 and the respective amount of superplasticizer in figure 8 is calculated manually using the data base from many tests, described by examples in chapter 2.

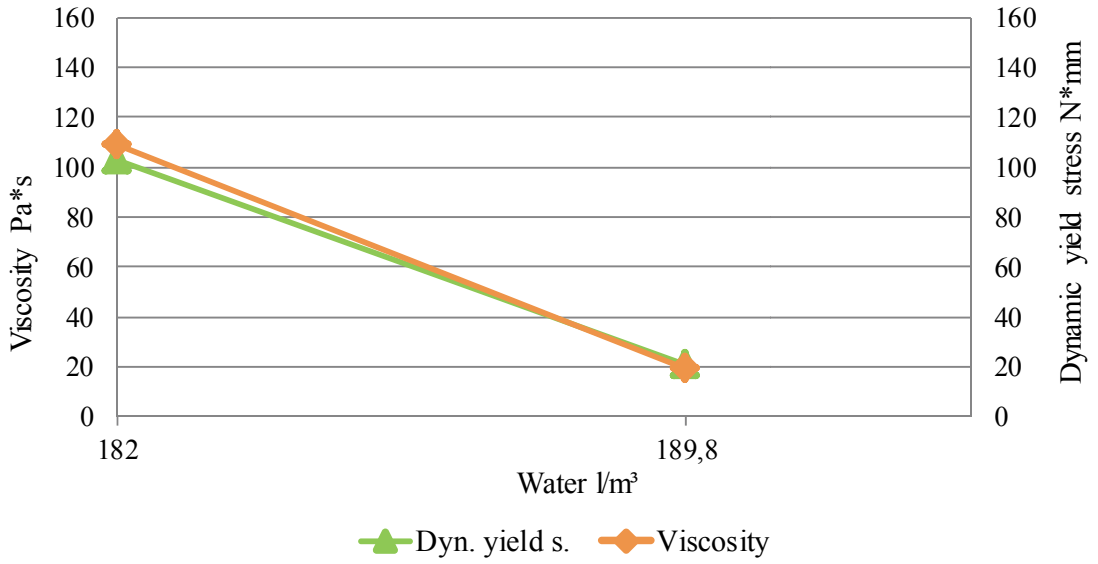

Figure 7: Test readjustment of a mixture with water. Starting point 182 l/m³ which led to a too stiff mix

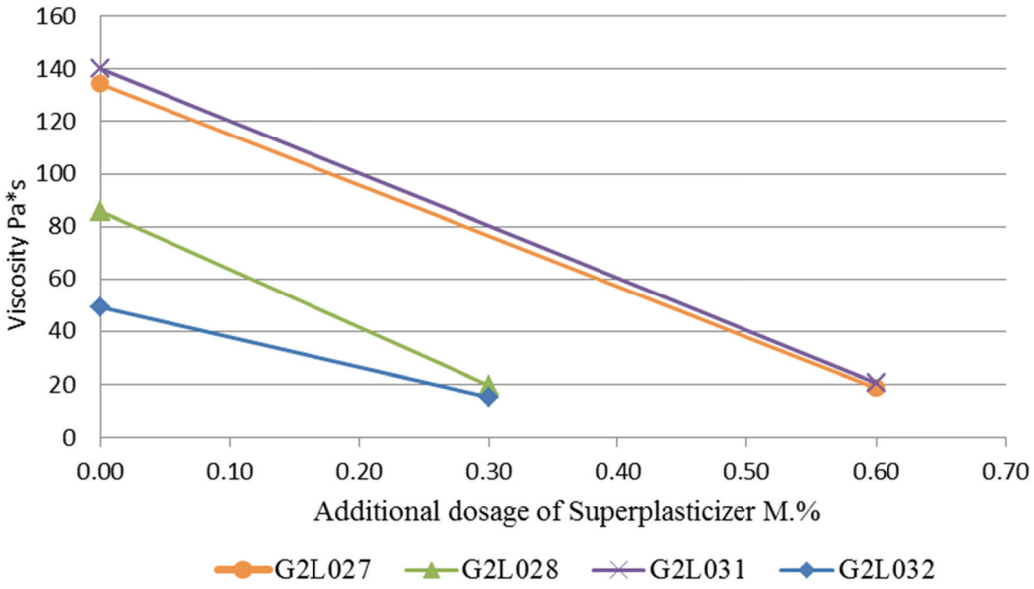

Figure 8: Four tests with direct readjustment of SP. Starting point were somewhat too stiff mixes with a given amount of SP. Then different additional dosages of SP have been added. In all four cases the target value could be reached within one adjustment.

These and further first manual calculated readjustment results showed to be a promising approach, worth going on. Therefore, the expert-system for calculating the readjustment was automatized and user-friendly installed in an app.

4. AUTOMATED READJUSTMENT WITH AN EXPERT SYSTEM

The knowledge from numerous tests on the rheological behaviour was used to build a new expert system, including, knowledge base and inference engine. An example for a successful readjustment with water, using the new expert system is given in figure 9.

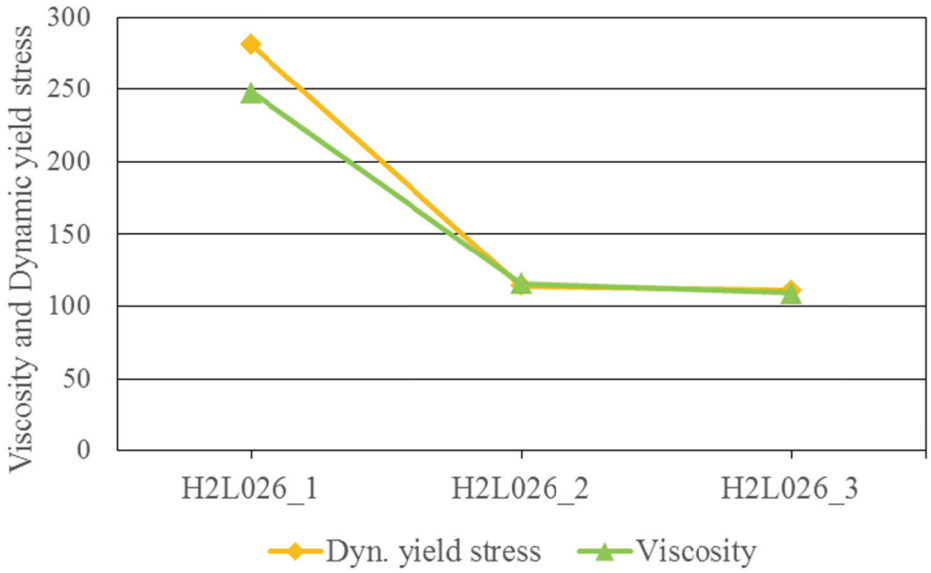

Figure 9: Readjustment by expert system with information about the test and measurement number. SCC mix design from plant 2.

The expert system evaluates the first measurement (H2L026_1) and gives the advice to add 0.2 l water to the 40 l mixture, which corresponds to 5.0 l/m³ (H2L026_2) and the repetition (H2L026_3). The ideal value for the viscosity and the dynamic yield stress is 115 for the mix from plant 2. (This corresponds for the selected measurement profile and SCC to a slump-flow of 625 mm and a v funnel time of 19 sec) The correction fits very well. The third measurement approved the result by a repetition of the test within a short time.

6. CONCLUSIONS AND OUTLOOK

Tests with a ball rheometer on various SCC mixtures, distinguished only in small quantities of water content, show accurate and reliable results. With this rheometer tests were performed with deviating water content and different correction measures. With the help of stabilizers, it is possible to readjust a mix which is too soft and tends to segregation. With superplasticizer or, if possible with small amount of water, too stiff mixes may be readjusted. The data of tests in laboratory and two precast plants was collected in a knowledge-base. An expert system uses this knowledge-base and the inference engine calculates the necessary amount of the materials for the corrections. The first tests using an automated processed expert system were promising. The amount of the necessary constitutive material (water, superplasticizer or stabilizer) could be predetermined and the rheological properties of the mix achieved the target values.

ACKNOWLEDGEMENTS

The project AZ-1182-15 is funded by the Bavarian Research Foundation. Many thanks to the partners in the project, Schleibinger Testing Systems, Godelmann, Hemmerlein Ingenieurbau and Rohrdorfer Zement for their support.

REFERENCES

[1] Khrapko, M., 'Aufrechterhaltung der erforderlichen Verarbeitbarkeit von SVB', (Maintaining the required workability of SCC). BetonWerk international, Vol. 2, Nr. 2/2012 (2012).

[2] Paric, I. and Kusterle, W., 'Selbstverdichtender Beton mit zeitnaher Aussteuerung der Mischungszusammensetzung im Betonmischer' (Self-compacting concrete with real-time control of the mix composition in a concrete mixer), research proposal, OTH Regensburg, (Regensburg, 2015).

[3] Paric, I., Fleischmann, F., Greim, M. and Kusterle, W., 'The Determination of Rheological Properties of "High Slump concrete" and SCC - The Advantages of a Modified Online Ball Measuring System', in Greim et al (Eds.), 'Rheologische Messungen an Baustoffen 2016', Proceedings of an International Conference, Regensburg, March 2016, (Tredition, Hamburg, 2016) 247-264.

[4] Bayerische Forschungsstiftung (Bavarian Research Foundation), 'SVBA – Selbstverdichtender beton mit zeitnaher Aussteuerung der Mischungszusammensetzung im Betonmischer', Project AZ-1182-15, (Munich, June 2016).

[5] Fleischmann, F., Ein Beitrag zur Bestimmung der Rheologischen Eigenschaften Selbstverdichtender Betone mit dem Kugel-Messsystem (A contribution to the determination of the Rheological Properties of Self-compacting concrete with the ball-measuring system). PhD-thesis Ruhr University Bochum and OTH Regensburg (2014)

[6] Fleischmann, F.; Greim, M., Kusterle, W.: The Assessment and Control of the Rheological Properties of Self-Compacting Concrete in a Concrete Mixer. In: Roussel, N; Bessaies-Bey, H. (Eds.): Rheology and Processing of Construction Materials. Proc. of the 7th RILEM International Conference on Self Compacting Concrete and of the 1st RILEM International Conference on Rheology and Processing of Construction Materials. September 2-4, 2013, Par is, RILEM Publication Proceedings S.A.R.L, PRO 90.

[7] Reuter, C. and Stepper, H., 'Zeitnahe Aussteuerung der rheologischen Frischbetoneigenschaften von selbstverdichtendem Beton durch Betonzusatzmittel und Wasser', Bachelor-thesis, OTH Regensburg (Regensburg, 2018).

[8] Härteis, J. and Höcherl, St., 'Untersuchung, Beurteilung und zeitnahe Aussteuerung der rheologischen Frischbetoneigenschaften von selbstverdichtenden Beton', Bachelor-thesis, OTH Regensburg, (Regensburg, 2018).

International Conference on Sustainable Materials, Systems and Structures (SMSS 2019)
Novel Methods for Characterization of Materials and Structures
20-22 March 2019 – Rovinj, Croatia

MONITORING MODAL PARAMETERS AND EXTERNAL LOADS OF WIND TURBINES FOR REMAINING USEFUL LIFE ANALYSIS

Max Botz (1), Georg Harhaus (1) and Christian U. Grosse (1)

(1) Chair of Non-destructive Testing, Technical University of Munich, Germany

Abstract

In this contribution a method for remaining useful life (RUL) analysis based on fatigue of wind turbine (WT) structures is presented. The method combines real measurement data and high-fidelity models. Here we focus on the input parameters from measurements: modal parameters and external loads, which are determined by operational modal analysis of vibration data and by applying Euler-Bernoulli beam theory to tower wall strains. Results from monitoring a large onshore wind turbine (3 MW, 142 m hub height) with a hybrid tower structure constructed of concrete (lower section) and steel (upper section) are presented. The modal parameters from measurement and FE-model match and the calculated external loads are plausible.

Keywords: Remaining useful life, remaining service life, wind turbine monitoring, operational modal analysis, model validation, load calculation, rotor thrust

1. INTRODUCTION

Wind turbines generally have a design life of 20 years. An extended design life seems feasible for various components and is desirable from an economic and ecological point of view [1]. However it can only be realized after an evaluation which involves reanalysis or inspections [2]. During the MISTRALWIND-project (Monitoring and Inspection of Structures at Large Wind Turbines) a method for estimating the remaining useful life (RUL) for WT support structures was developed and tested in cooperation with project partners (see Acknowledgements). A general overview of the procedure is depicted in Figure 1. The procedure is based on the continuous measurement of loads acting on the structure, that are applied to a validated finite-element-model (FE-model). The model delivers material stresses over time at critical (highly stressed) areas, based on the measured loads. From these stress signals, load cycles are counted using rainflow counting for different load levels. The number of stress cycles for different load levels are compared to material properties and by using a damage accumulation approach, local damage and RUL can be estimated.

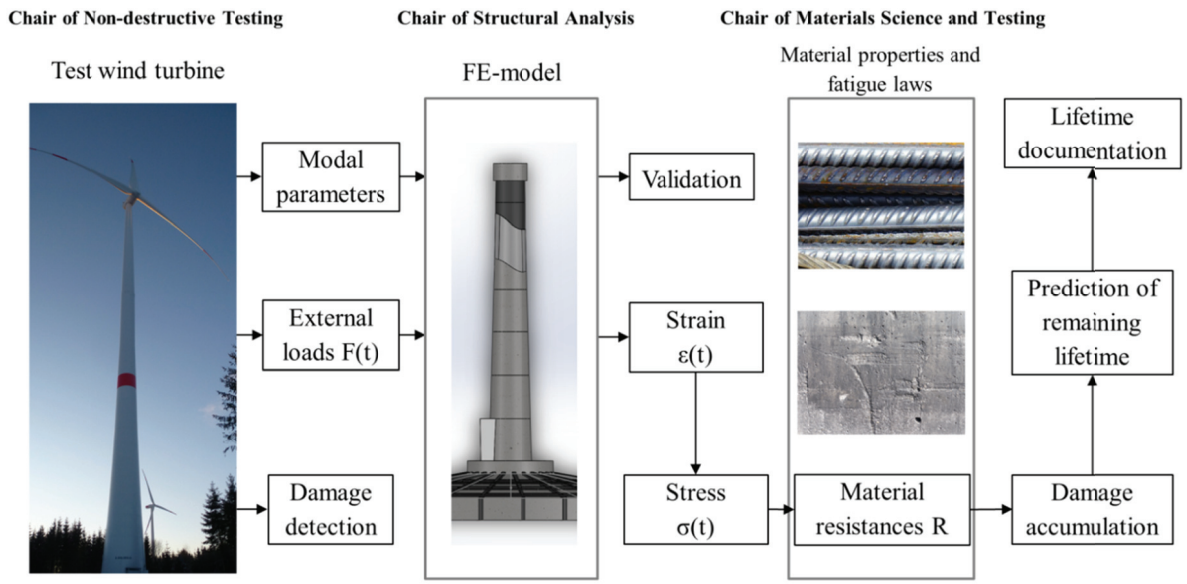

Figure 1: MISTRALWIND concept for remaining useful life analysis

The critical (highly stressed) areas were identified by analysing the stress distribution in the FE-model from typical loads and by visual inspection. Connecting elements were assumed to be uncritical as they are regularly inspected.

This paper focuses on the determination of the measured inputs for the described approach: modal parameters and external loads. Further project activities are described by Geiss et al. [3]. To determine the input parameters, a stationary monitoring system was installed at a functional WT. In the following sections, the WT and the monitoring system, as well as data processing are described. Finally, results are shown and explained, and future work is outlined.

2. TESTING ENVIRONMENT AND MONITORING SYSTEM

The wind turbine evaluated is a 3 MW direct-drive Siemens turbine with a Max Bögl hybrid tower [4] designed for low wind speed locations (IEC 3A). To achieve high revenues under these conditions, the WT has a large hub height of 142.5 m and rotor diameter of 113 m. The hybrid tower consists of two sections, a lower section, 79 m high, constructed of prefabricated concrete elements with external prestressing, to which an upper steel section is connected up to the final hub height of 142.5 m. On the left side of Figure 1, a photo of the WT is shown.

The monitoring system installed in the tower during the MISTRALWIND-project consists of a conventional and a fiber optic measurement system (named FOS in Figure 2). They are connected via CAN-bus (Controller Area Network). The conventional measurement system enables a modular setup with three data acquisition units (DAQ). Different types of sensors are deployed as shown in Figure 2: accelerometers, seismometer, temperature sensors and strain gauges (electric and fiber optic). For strain measurements, multiple sensors are required at a cross-section to capture the deformation. In the steel section (at DAQ2 and 3) three full bridges offset by 90 ° are installed measuring vertical strain (Figure 2, sg1-3). At one position shear is measured in ±45 ° orientation to the tower axis. At the tower base, strains are

measured using the fiber optical measurement system. Additional details on the setup are described by Botz, et al. [5]. Further short-time measurements were conducted with confirming results [6, 7].

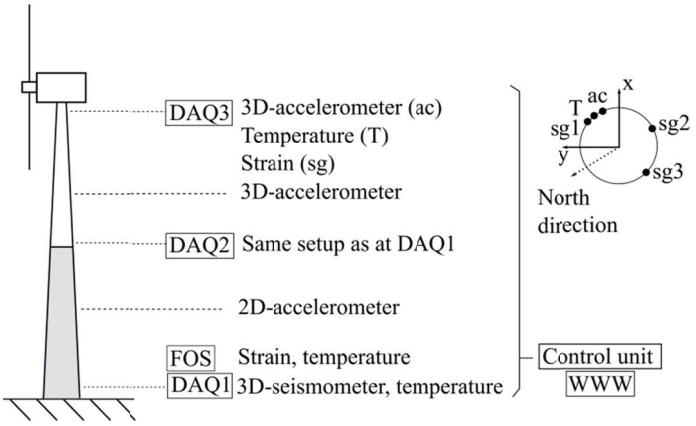

Figure 2: Setup of monitoring system at test wind turbine

3. METHODS FOR DATA ANALYSIS

3.1 External loads

Fatigue is caused by cyclic or repetitive loads acting on the structure. The major loads are determined based on strain measurements in the steel section of the tower at DAQ2. Applying these measured loads to the FE-model, stresses at arbitrary locations can be calculated and thus the cumulative fatigue and RUL of the structure. The first major load acting on the structure is the rotor thrust force that acts perpendicular to the rotor plane due to the incoming wind flow. It induces a bending moment in the structure that increases towards the tower base. The eccentric centre of mass of the nacelle induces a counter moment (M_N in Figure 3a). For the WT evaluated, this is the second major load acting on the structure. Additional smaller loads due to skewed inflow or the generator torque counter moment are neglected. Temperature effects on strain measurements are compensated. Loraux and Réthoré [8, 9] used a similar approach to calculate rotor thrust based on tower strain measurements.

The nacelle moment is constant over time, but acts in different directions depending on the yaw-angle (orientation of the nacelle). The moment can be determined using strain signals during an untwisting cables event in which the nacelle rotates 360 ° with constant angular speed. The event generally takes place during standstill of the WT and in low wind speed conditions. In this case the nacelle moment rotating around the tower axis is the dominant acting load. The start of the yaw-motors induces an impulse resulting in tower vibrations. As expected, the plot of the measured strains at DAQ2 during the untwisting cables event exhibits a sinusoidal shape with superimposed vibrations (Figure 3b). Based on the amplitude of the sinusoidal strain signal of $\varepsilon \approx 80\ \mu m/m$, the nacelle moment M_N can be calculated using the elastic modulus E of the steel tower and the local section modulus W:

$$M_N = M_{SG} = \varepsilon * E * W \approx 5\ MNm \quad (1)$$

Euler-Bernoulli beam theory can be applied due to the high slenderness ratio of the tower, neglecting shear deformations. The untwisting cables event is a recurring uniform load event. As such it can also be used for sensor offset determination and sensor health monitoring.

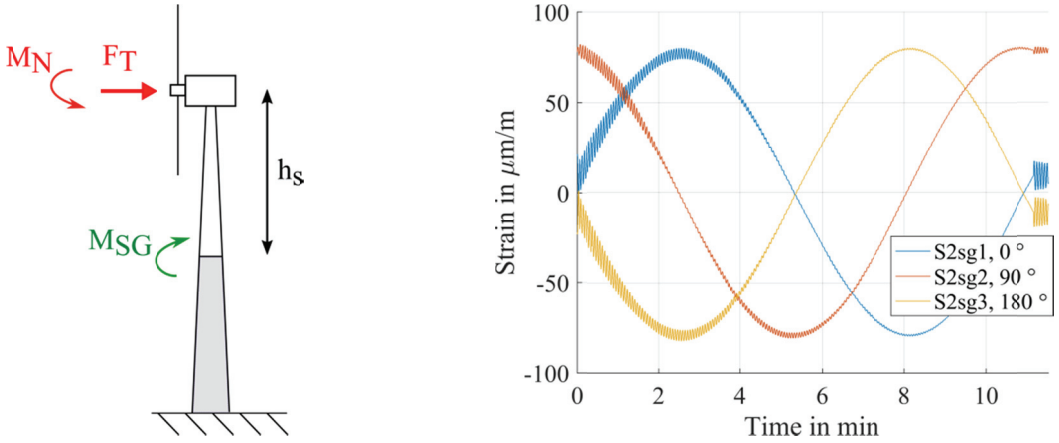

Figure 3: (a) Scheme of major external loads (red) and measured load (green); (b) vertical tower wall strain at DAQ2 during untwisting cables event on 17/07/2018, 00:34

The rotor thrust force is time-varying, depending on environmental and operational conditions (wind speed, rotor speed, pitch angle etc.). Neglecting the nacelle moment, the rotor thrust force F_T can be determined from the bending moment M_{SG} in the cross section where the strain gauges are mounted (near DAQ2) and the distance to the force application point (assumed to be rotor axis) h_S.

$$F_T(t) = \frac{M_{SG}(t)}{h_S} \tag{2}$$

The influence of the nacelle moment is removed by using the relationship between yaw-angle and strain values during the untwisting cables event. The moment resulting from the thrust force is calculated using the same relationship as in Equation (**1**) with compensated strain values ε_{comp}.

$$M_{SG}(t) = \varepsilon_{comp}(t) * E * W \tag{3}$$

The vector of the moment, and thus its magnitude and direction, is calculated using two strain gauges offset by 90 °. Thrust force and nacelle moment are both acting perpendicular to the rotor plane; to apply them in the FE-model, they are transformed from a nacelle-fixed coordinate system to a tower-fixed one.

3.2 Operational Modal Analysis

The RUL-estimation method described in Section 1 is only valid if the FE-model reproduces the WT accurately. For that purpose a detailed FE-model was constructed by project partners of the chair of structural analysis at TUM, using shell elements and considering geometric nonlinearities [3, 6]. To confirm the resemblance of dynamic properties as well as mass and stiffness distribution, the modal parameters are compared. Operational

modal analysis (OMA) is deployed to determine the modal parameters of the test WT using vibration data. In contrast to experimental modal analysis, no information on the excitation force is required, the regular excitation forces during operation or idling are sufficient. There are different OMA methods; we applied the covariance based stochastic-subspace-identification technique (SSI-COV) that delivers reasonable results for this application [10-12]. To ensure the validity of the FE-model, we want to monitor the modal parameters of the structure continuously. Therefore we implemented a method [6] for automated OMA, based on Neu, et al. and Reynders, et al. [13, 14], that enables evaluation of large datasets and considers environmental and operational conditions (EOCs). At this time, the automated OMA method is being improved; in this contribution only results from analysing one typical dataset are presented.

4. RESULTS

4.1 External loads

The procedure used to calculate the external loads from tower strains, explained in Section 3.1, is demonstrated using a one-hour dataset starting on 28/07/2018, 13:00. In this period, the WT is operating under partial and full load and generates a power output of 500 kW to 3 MW. Figure 4a shows the varying power output together with further operational data which are obtained from the Supervisory Control and Data Acquisition System (SCADA) that is part of any WT. The resulting vertical tower wall strain during operation at DAQ2 in the steel section of the tower at a height of 80 m is shown for all three circumferential positions in Figure 4b.

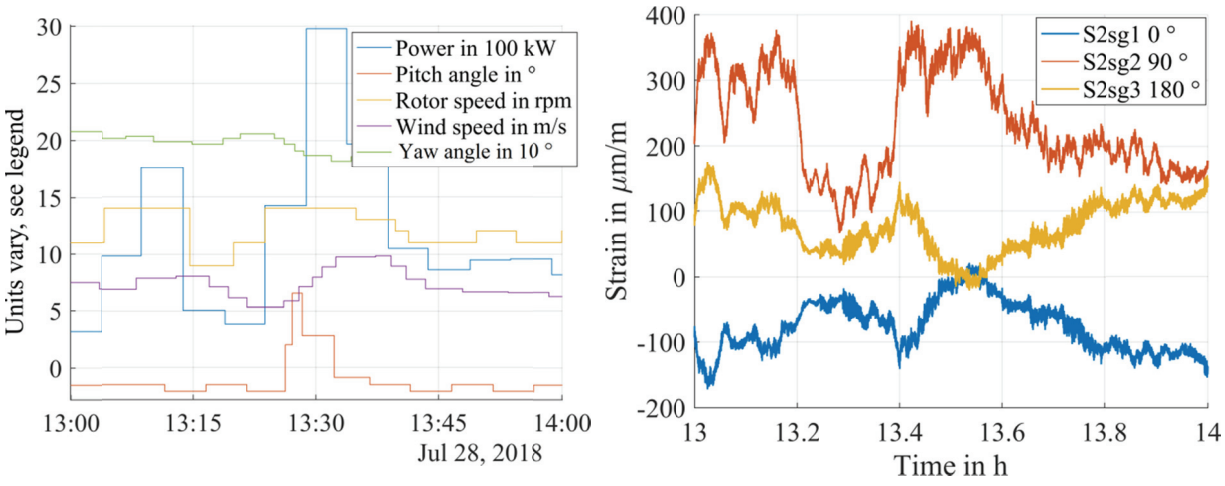

Figure 4: (a) SCADA parameters during 1 h dataset, on 28/07/2018, 13:00; (b) strain data from sensors at 0 °, 90 ° and 180 ° at DAQ2 in the same period

As expected, the signal from opposing strain gauges (sg1 and sg3) is inverted. Strain levels at sg2 are three times higher than at sg1 and sg3, which means that the nacelle is approximately oriented in the direction of sg2, which is the south direction. This observation corresponds to the yaw-angle from SCADA-data (yaw-angle ≈ 180 °, 0 ° equals north direction). The strain magnitude during operation is significantly higher than during the untwisting event (see Figure 3b). The rotor thrust force is consequently dominating the load scenario; this ratio increases in direction of tower bottom. The rotor thrust force calculated

from the strain data at DAQ2 (depicted in Figure 4b), as well as from fiber optic strain measurements at the base of the tower, is plotted together with the power output in Figure 5.

The resulting rotor thrust forces from electrical and optical strain measurements match. The optical measurements produced slightly lower force values. Also a correlation between the force and the power output can be seen, but due to the coarse temporal resolution of the SCADA data, the significance is limited. Loraux [8] calculated the rotor thrust force of a 2 MW wind turbine, obtaining similar values. Due to simplifications and assumptions during the calculation process and due to measurement uncertainties that have not yet been quantified, the results serve as an estimation of the external loads. For testing the presented concept for RUL analysis of WT structures this is sufficient for the moment.

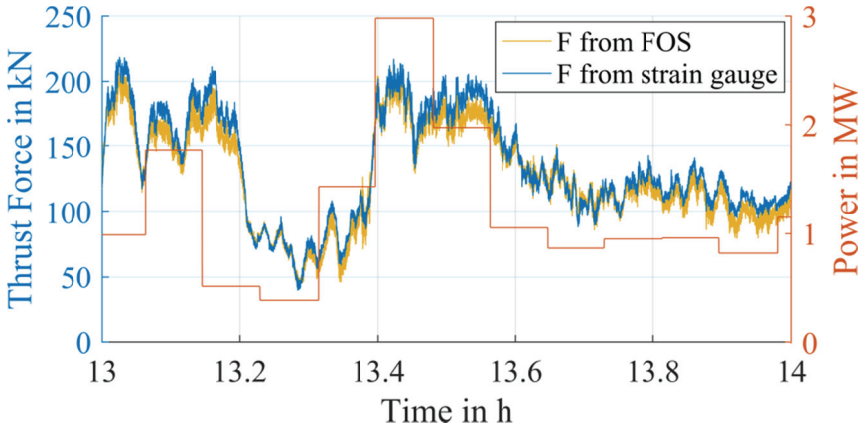

Figure 5: Rotor thrust force from strain gauges and FOS and power output in observed period

4.2 Modal parameters

The modal parameters of the WT are demonstrated by analysing a representative 10 min dataset (starting 21.01.2018, 03:50) using data from three 3D vibration sensors (two accelerometers and one seismometer) that are installed next to the DAQ1-3 (see Figure 2). In that period the WT is in a suitable stationary operating condition, which is idling with blades pitched in a feathered position (pitch angle > 80 °). During the process of SSI-COV OMA, state space models of different model orders are created and fitted to the data. The result is a stabilization diagram that is depicted in Figure 6. It shows the poles of the state-space models for different model orders. The poles are evaluated regarding their stability: if their corresponding frequency, damping, mode shape and further parameters do not change more than a fixed limit with rising model order, a pole is considered stable. An actual vibration mode of the regarded system is characterized by a high number of stable poles.

A vibration mode can originate from the tower, but also from the rotor or from a coupling effect. The vibration modes at 0.5, 1.5, 2.8, 4.5 Hz most likely stem from rotor vibrations. By looking at different datasets and comparing them to the results from the FE-model of the tower, the actual modal parameters of the WT tower can be deduced. The results are listed in Table 1. The names of the modes reflect their mode shape orientation: a bending mode in rotor plane is called side-side mode (SS); in opposite direction it is called a fore-aft mode (FA). As expected, closely spaced modes occur in SS and FA direction up to the third mode order. For the fourth mode order only one mode is detected by OMA. The FE-model cannot

predict these modes as the nacelle is modelled as a point mass. The FA-modes from OMA are compared to the eigenfrequencies of the FE-model, because the influence of the rotor is assumed to be smaller in this direction, as the blades are in a feathered position. For the second bending mode, three possible modes are detected; one of them is probably a coupled rotor-tower mode. The eigenfrequencies and the mode shapes from measurements at the WT and from the FE-model match; the maximum discrepancy in eigenfrequency is 7 %.

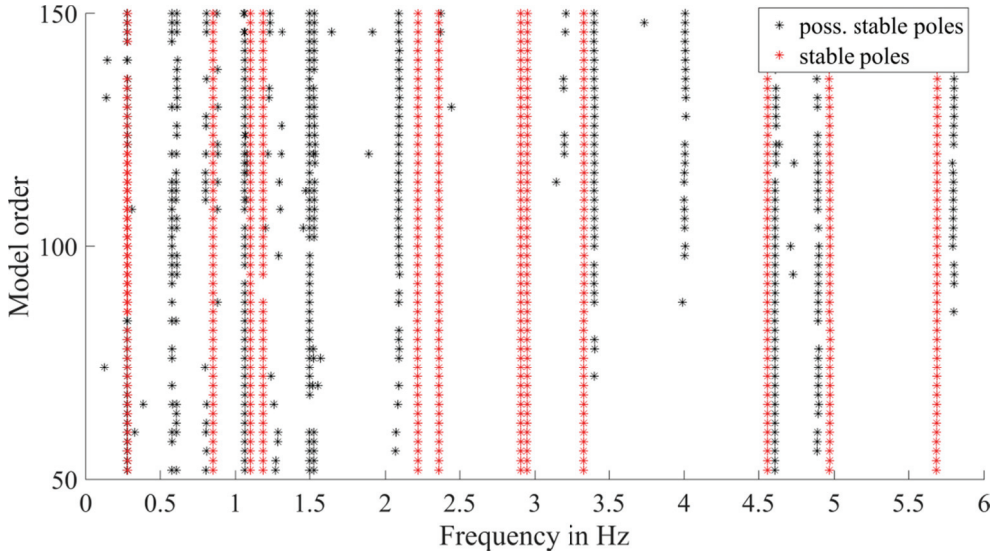

Figure 6: Result of OMA: stabilization diagram for 10-min dataset from jan 2018

Table 1: Modal parameters from OMA (frequency and damping) and FE-model (frequency)

Eigenmode	OMA f in Hz	OMA D in %	FEM f in Hz	Difference
FA1	**0.274**	**0.35**	**0.273**	**0 %**
SS1	0.277	0.62		
FA2a	**1.063**	**0.48**	**1.138**	**7 %**
SS2	1.100	0.28		
FA2b	1.184	0.51		
SS3	3.333	0.70		
FA3	**3.401**	**0.28**	**3.207**	**6 %**
FA/SS4	**5.688**	**0.58**	**5.495**	**3 %**

5. CONCLUSIONS

The method for RUL-analysis for WT support structures developed in the MISTRALWIND-project was described. The procedure for determination of the input parameters for the RUL-estimation method was explained: modal parameters via operational modal analysis and external loads via Euler-Bernoulli beam theory. Results from applying these methods on monitoring data of a full-size WT with a hybrid concrete-steel tower were discussed: Modal parameters from measurements and the FE-model match. The calculated

external loads seem reasonable. Next steps for load calculation are further plausibility checks using simulations and quantification of measurement uncertainties. Evaluation of long-term data is scheduled.

ACKNOWLEDGEMENTS

The authors would like to thank the German Federal Ministry for Economic Affairs and Energy for funding the MISTRALWIND-project under grant number 0325795, the project partners (Chair of Structural Analysis and Chair of Materials Science and Testing at TUM, IABG mbH, Siemens AG, Otto Lutz) for good collaboration and Max Bögl AG for providing access to the test wind turbine.

REFERENCES

[1] Jacobsen, M.Z., 'Review of solutions to global warming, air pollution, and energy security', *Energy & Environmental Science*. **2**(2009) 148-173.
[2] DNV GL, 'Guideline for the Continued Operation of Wind Turbines', 2009.
[3] Geiss, C.T. et al., 'The Mistralwind Project—Towards a Remaining Useful Lifetime Analysis and Holistic Asset Management Approach for More Sustainability of Wind Turbine Structures', 11th International Workshop on Structural Health Monitoring (IWSHM), 2017, Stanford.
[4] Bögl, S., Hierl, M. and Knitl, J., 'Tower comprising an adapter piece and method for producing a tower comprising an adapter piece', 2016.
[5] Botz, M., Oberlaender, S., Raith, M. and Grosse, C.U., 'Monitoring of Wind Turbine Structures with Concrete-steel Hybrid-tower Design', 8th European Workshop on Structural Health Monitoring (EWSHM), 2016, Bilbao, Spain.
[6] Botz, M., Raith, M., Emiroglu, A. and Grosse, C.U., 'Monitoring of Wind Turbine Structures using Stationary Sensors and Short-term Optical Techniques', 11th International Workshop on Structural Health Monitoring (IWSHM), 2017, Stanford.
[7] Wondra, B., Botz, M. and Grosse, C.U., 'Wireless monitoring of structural components of wind turbines including tower and foundations', *Journal of Physics: Conference Series*. **753**(7)(2016).
[8] Loraux, C., 'Long-term monitoring of existing wind turbine towers and fatigue performance of UHPFRC under compressive stresses', 2017, EPFL Lausanne: Lausanne, Switzerland.
[9] Réthoré, P.-E., 'Thrust and wake of a wind turbine: Relationship and measurements', in Department of Wind Energy, 2006, DTU.
[10] Devriendt, C. et al., 'Structural health monitoring of offshore wind turbines using automated operational modal analysis', *Structural Health Monitoring*. **13**(6)(2014) 644-659.
[11] Oliveira, G., Magalhães, F., Cunha, Á. and Caetano, E., 'Development and implementation of a continuous dynamic monitoring system in a wind turbine', *Journal of Civil Structural Health Monitoring*. **6**(3)(2016) 343-353.
[12] Botz, M., Zhang, Y., Raith, M. and Pinkert, K., 'Operational Modal Analysis of a Wind Turbine during Installation of Rotor and Generator', 7th International Operational Modal Analysis Conference (IOMAC), 2017, Ingolstadt.
[13] Neu, E., Janser, F., Khatibi, A.A. and Orifici, A.C., 'Fully Automated Operational Modal Analysis using multi-stage clustering', *Mechanical Systems and Signal Processing*. **84**(2017) 308-323.
[14] Reynders, E., Houbrechts, J. and De Roeck, G., 'Fully automated (operational) modal analysis', *Mechanical Systems and Signal Processing*. **29**(2012) 228-250.

International Conference on Sustainable Materials, Systems and Structures (SMSS 2019)
Novel Methods for Characterization of Materials and Structures
20-22 March 2019 – Rovinj, Croatia

MICROWAVE MONITORING METHOD FOR DETECTING THE HYDRATION PROCESS OF CONCRETE

A. Dollase (1), U. Möller (1), L. Nietner (1)

(1) University of Applied Sciences Leipzig, Germany

Abstract

The knowledge about the development of compressive strength of concrete is important for various construction tasks. Therefore, the demand for non-invasive testing methods rises, which allow a reliable, in-situ strength determination. The contribution introduces a new microwave method for continuous monitoring of hydration process in concrete, which can be used to evaluate the development of compressive strength non-destructively. Based on the measured data a calibration model can be created for different water/cement-ratios, additives in concrete and different cement types of the concrete. This calibration model allows to predict the strength development by using microwave data measured continuously and non-destructively.

Keywords: microwave, concrete, monitoring, strength development

1. INTRODUCTION

The knowledge about the development of compressive strength of concrete is important for various construction tasks. A proven destructive method consists of producing separate specimen during the construction of the building, which are examined as needed by using standardized pressure tests (EN 12390 parts 1-4). This procedure is very time-consuming. Furthermore, the compressive strength results of the laboratory tests have only limited applicability compared to the development of strength in external weather conditions.

Compared to moisture measurement in chemical inert building materials, the process of water retention is very complicated in materials like concrete. Physical and chemical properties and crystallization processes play a major role in the structural development. Different chemical and physical bondings of water molecules are present in parallel and their ratio is changing time dependent. Therefore, a microwave monitoring method is used to determine the hydration process of concrete.

2. BASICS OF THE MICROWAVE METHOD

The Microwave Method belongs to the dielectric measurement methods, which depends on the dielectric properties of water. The relative permittivity of water amounts to about 80. The permittivity of most solids, including the building materials, is substantially smaller, it is in the range of 3 to 6. Additionally to the polarizability of the water its dielectric losses can be used for measuring the water content with microwaves. On this basis small quantities of water can be measured.

The used microwaves-measuring technology (measuring frequency: 2.45 GHz) is based on the reflection principle. That means, the power of the sent and the reflected wave are measured. The ratio of these is the basis for the so-called moisture index. The main contribution to the reflection of the microwaves is from the free and physically bound water in the building material. Chemically bound water changes the dielectric properties of the building material itself and therefore the reflective quality of the microwave. Both of these effects result in a specific calibration for materials like concrete.

3. MICROWAVE METHOD FOR DETECTING THE HYDRATION PROCESS

To investigate the hydration process of concrete a sealed plastic formwork was developed (figure 1). This formwork allows a lateral application of the microwave sensor and at the same time a sealing of the test material. With the help of a cover the test material is protected against evaporation. The sensor is applied to the test material via a special flange.

In addition the temperature of the concrete was measured, which allows a compensation of the temperature influence on the microwave signal.

With the help of a measuring PC the microwave signals were logged. The measurement is done continuously, and begun directly after pouring the concrete into the formwork. The measurement signals are logged time-resolved by a special software. The measuring interval has been adapted programmatically to the hydration process. At the beginning a measuring interval of 1 hour and at the end of the measurement an interval of 24 hours was chosen. Throughout a test series 65 single measurements for a period of 7 days were logged.

Analysing the monitored microwave data allowed to draw conclusions on the properties of the concrete.

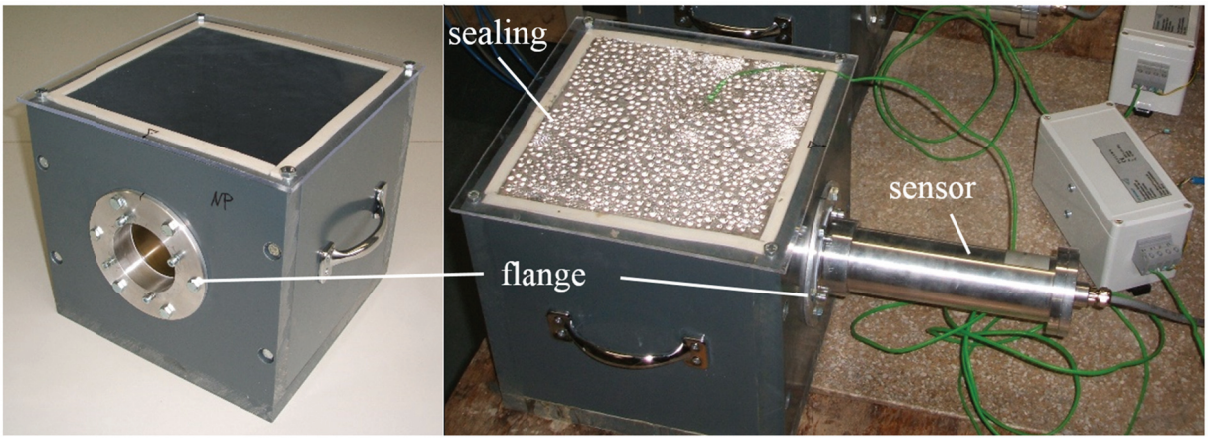

Figure 1: Equipment to monitor the hydration process of concrete on a laboratory scale

4. INVESTIGATION OF THE HYDRATION PROCESS OF CONCRETE WITH DIFFERENT WATER RATIOS (W/C-RATIOS)

The investigation of the hydration process of concrete was done with the help of the monitoring system described above. In 9 series of experiments water/cement-ratios (w/c) of 0.45, 0.50 & 0.55 and a Portland cement (CEM I 42.5 R) were used. The measurements took place in a test climate with a temperature of 20±2°C and 65±5% of relative humidity.

Simultaneous with the microwave measurement a compressive strength test (according to EN 12390 parts 1-4) was carried out. Aberrantly to the storage agreed in the norm, the test specimens were sealed and stored in the same climatic conditions as the microwave measurement setup. With these proceedings a comparability of the microwave investigation and the compressive strength test is given.

The detected microwave signals were evaluated by using the change of a special microwave parameter, which is the minimum of a resonance curve (*ΔMinFI*). The progress of the parameter *MinFI* shows, that for different w/c-ratios the change of this parameter is quite systematical (figure 2 a)). For a w/c-ratio of 0.45 the change in moisture index is about 6000. For a w/c-ratio of 0.50 the change is 5000 and for 0.55 it is 4800.

A comparison of the measured values of the parameter (*ΔMinFI*) and the compressive strength shows, that there is a direct correlation between both values (figure 2 b)). This means that the change in the parameter (*ΔMinFI*) is independent from the use of the water to cement ratio. This makes it possible to create one calibration model for all used w/c-ratios. The calibration model allows to predict the compressive strength from the change of the detected microwave signals continuously and non-destructively.

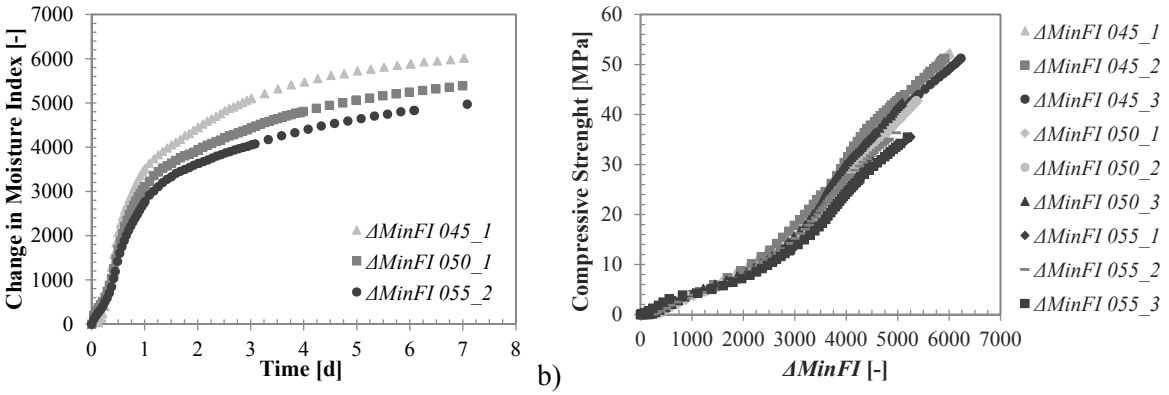

a) b)

Figure 2: Change in moisture index during the hydration process a) and a comparison of the measured compressive strength and the change of the parameter *ΔMinFI* b)

5. CALCULATION MODEL

The direct correlation of the parameter (*ΔMinFI*) and the compressive strength of the concrete can described with equation 1. This equation is similar to known mathematical functions witch describe the development of the compressive strength by other authors ([7], [8], [9]). Only a linear term is included, which allows to calculate the compressive strength from the change of the parameter (*ΔMinFI*).

$$f_c\,(\Delta MinFI) = A \cdot e^{-150 \cdot \left(\frac{\Delta MinFI \,\cdot\, 0.2}{135}\right)^{B}} + C \cdot \Delta MinFI \tag{1}$$

The factors A, B und C can be found with a regression analysis. For the test series with different w/c-ratios the calculation model is:

$$f_c\,(\Delta MinFI) = 38.20 \cdot e^{-150 \cdot \left(\frac{\Delta MinFI \,\cdot\, 0.2}{135}\right)^{-2.71}} + 0.0038 \cdot \Delta MinFI \tag{2}$$

In figure 3 the calculation model with the middle- and the maximum deviation is shown. The middle deviation is about 2.0 MPa and the maximum deviation is 5.6 MPa. Over all, a good conformity of the calculated and the measured values are shown.

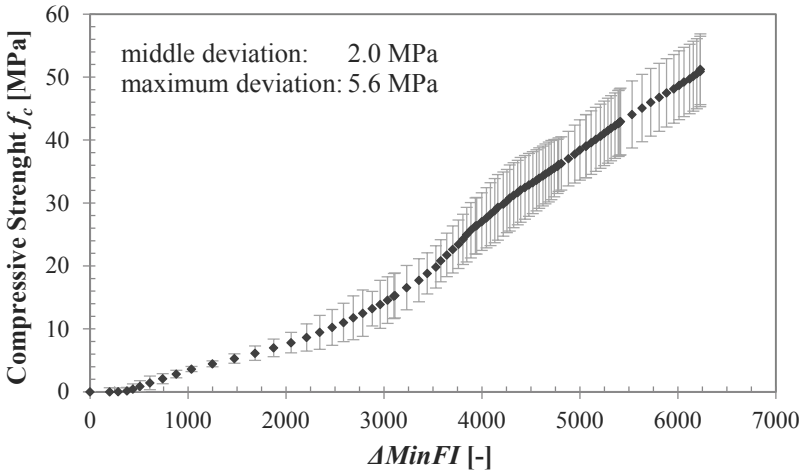

Figure 3: Development and deviation of the calculation model

6. INVESTIGATION OF DIFFERENT CONCRETE COMPOSITIONS

The investigation of different concrete compositions could show influences of such variations on the calculation model of the microwave monitoring method. Therefore, different

cement types and additives in concrete are used and a comparison between measured data and the calculation model is used.

6.1 Different cement types

To investigate the influences of different cement types in concrete on the microwave monitoring method, three different cement types (CEM I, CEM II and CEM III) were used. For all variations of the concrete compositions two test series were carried out.

Figure 4 shows the results of the investigation of the different cement types in concrete. The results of the test series with the CEM II (figure 4 a)) and with the CEM III (figure 4 b)) in relation to the calculation model, which based on the investigation of a CEM I, shows a similar progress. It seems that the cement type has no influence on the calculation model and the direct correlation is almost identically.

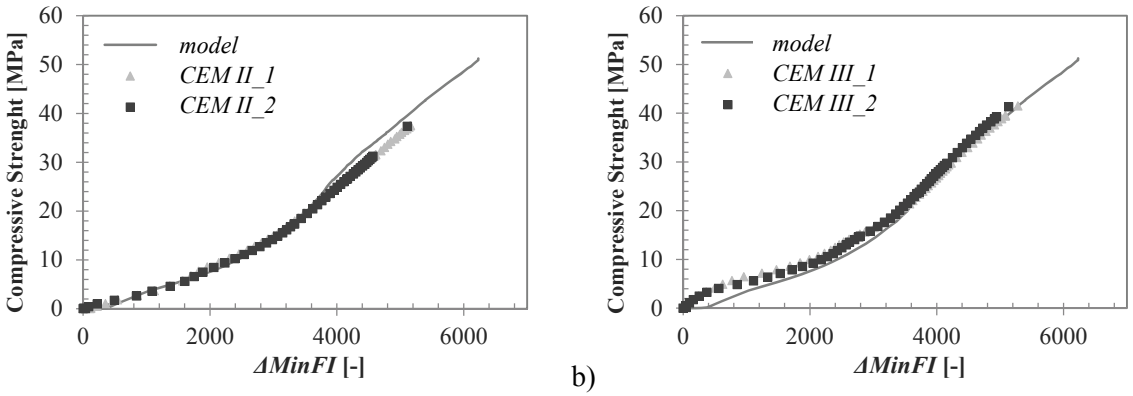

a) b)

Figure 4: Results of the test series with the CEM II a) and the CEM III b)

6.2 Additives in concrete

To investigate the influences of additives in concrete on the calculation model of the microwave monitoring method, a concrete plasticizer and an air entraining agent are used. For all variations of the concrete compositions two test series were carried out.

The name of the test series are:

- concrete plasticizer - CP
- air entraining agent - AEA

In the test series with the air entraining agent two various air pore contents were produced. The air pore contents were circa 5.0 vol.-% (AP_1 & AP_2) and 8.0 vol.-% (AP_3 & AP_4).

Figure 5 shows the results of the investigation. The results of the test series with the concrete plasticizers shows (figure 5 a)), that the development of the measured microwave data is similar to the calculation model. Only a constant shift, to smaller changes in the moisture index can be identified. These smaller changes can be explained by the used concrete plasticizer. A polycarboxylate-ether (PCE) is used, which consists, similar to water, of polarisable molecules and the change in moisture index becomes lower in relation to the calculation model.

The results of the test series with the air entraining agent shows (figure 5 b)), that the progress of the measured microwave data for air pore contents of 5.0 vol.-% is similar to the calculation model. For an air pore content of 8.0 vol.-% the change in moisture index is

greater. These greater changes in moisture index can be explained by the higher content of air in the material. Air have a very low permittivity and the change in moisture index becomes greater.

In summary it can be said, that the use of the concrete plasticizer or an air entraining agent makes adapting the model necessary. Table 1 shows the adapted factors.

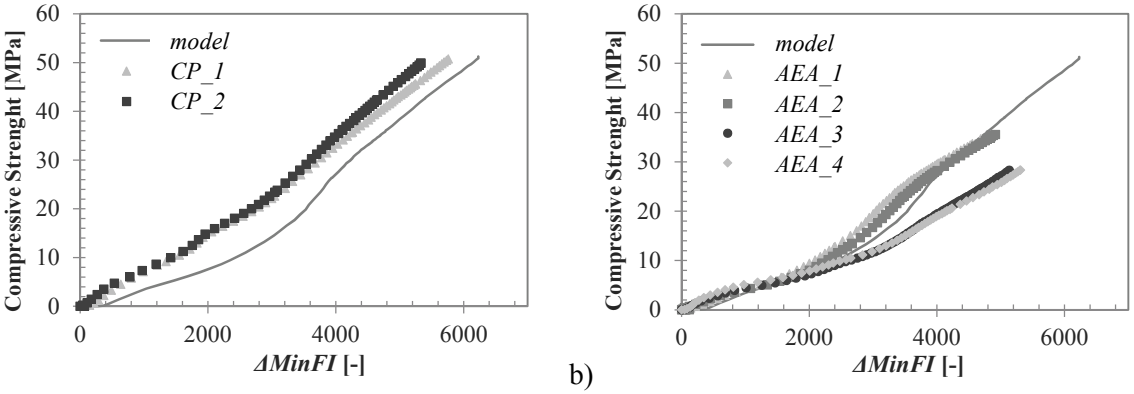

a) b)

Figure 5: Results of the test series with the concrete plasticizer a) and the air entraining agent b)

Table 1: Adapted factors for the calculation model

variations	**factors**		
	A	*B*	*C*
calculation model	38.20	-2.71	0.0038
concrete plasticizers	15.30		0.0071
air entraining agent (>5.0 vol.-% air content)	19.18	-2.58	0.0036

7. CONCLUSIONS

The results of the test series show a very good conformity of the calculated and the reference values for different water cement ratios and cement types. For concrete plasticizer and air pore contents of more than 5 vol.-%, the factors of the calculation model have to be adapted. With the matching of the factors it is possible to determine the compressive strength of concrete continuously and non-destructively by using the microwave monitoring method.

Further tests of the microwave monitoring method directly on the building site or in concrete factories are planned. With these the real-world suitability of the developed method shall be proven.

REFERENCES

[1] Dollase A., Möller U., Nietner L., Göller A. & Jungstand B. (2016): EM HYDRA - Microwave Method for detecting the hydration process of concrete; ISEMA 2016, 11th International Conference on Electromagnetic Wave Interaction with Water and Moist Substances; Florenz (Italien), 23.-27.05.2016
[2] Göller A., Jungstand B., Dollase A. & Möller U. (2016): EM HYDRA - Mikrowellen-Messverfahren zur Erfassung von Hydratationsprozessen in Beton; DGZFP-Fachtagung Bauwerksdiagnose 2016, BAM Berlin, 25.-26.02.2016
[3] Göller A., Jungstand B., Dollase A. & Möller U. (2016): EM HYDRA - Mikrowellen-Messverfahren und -systeme zur Erfassung von Hydratationsprozessen in Beton; 9.Tagung des Competence Center for Material Moisture (CMM), Karlsruhe, 18.-21.09.2017
[4] Rzepecka, M. A. et al. (1972); Monitoring of Concrete Process by Microwave Terminal Measurements; IEEE Transactions on Industrial Electronics and Control Instrumentation, Vol. IECI-19, No. 4
[5] Schmidt, J. (1991); Einsatz der Mikrowellenmesstechnik zur zerstörungsfreien und kontinuierlichen Erfassung der Hydratationskinetik von Mörteln und Betonen; DGZfP Symposium Zerstörungsfreie Prüfung im Bauwesen, Berlin
[6] Mubarark, K. & Bois, K. J. (2001); A Simple, Robust, and On-Site Microwave Technique for Determining Water-to-Cement Ratio (w/c) of Fresh Portland Cement-Based Materials; IEEE Transactions on Instrumentation and Measurement, Vol. 50, No. 5
[7] Röhling, S. et al. (1985): Monolithischer Betonbau. Verlag für Bauwesen, Berlin.
[8] Jonasson, J.-E. (1984): Slipform construction – calculation for assessing protection against early freezing. Swedish Cement and Concrete Research Institute, Stockholm
[9] Rostasy, F. S.; Krauß, M. (2001): Frühe Risse in massigen Betonbauteilen – Ingenieurmodelle für die Planung von Gegenmaßnahmen. Deutscher Ausschuss für Stahlbetonbau, Heft 520, Beuth Verlag, Berlin.

International Conference on Sustainable Materials, Systems and Structures (SMSS 2019)
Novel Methods for Characterization of Materials and Structures
20-22 March 2019 – Rovinj, Croatia

DEVELOPING BETTER UNDERSTANDING OF DETERIORATION PROGRESSION IN CONCRETE BRIDGE DECKS THROUGH ACCELERATED STRUCTURAL EVALUATION

Nenad Gucunski (1), Franklin Moon (1) and Ali Maher (1)

(1) Department of Civil and Environmental Engineering, and Center for Advanced Infrastructure and Transportation (CAIT), Rutgers University, USA

Abstract

Since concrete bridge decks are deteriorating faster than other bridge components, implementation of realistic deterioration, predictive and life cycle cost models for them is of special importance for good bridge management. Bridge deck deterioration is a complex process that is frequently a result of numerous physical, chemical and other actions. Those actions are often connected and deterioration by one process often accelerates deterioration by another. Therefore, to better understand the connectivity of these diverse deterioration processes, it is imperative to use a suite of complementary nondestructive evaluation (NDE) technologies that can capture them at all phases of the life of a deck.

While the development of deterioration and predictive models for bridge decks was previously presented, it was primarily relying on visual inspection results. On the other hand, the same models from NDE surveys were based on limited period data sets. The BEAST (Bridge Evaluation and Accelerated Structural Testing) facility at Rutgers University opens opportunities for accelerated evaluation of full size bridge components, including bridge decks. Accelerated traffic and environmental loading, complemented by periodical NDE surveys, has high potential to enhance our understanding of the deterioration mechanisms in bridge decks and to lead to more realistic deterioration and predictive models.

Keywords: concrete, bridge decks, accelerated testing, NDE, deterioration modelling

1. INTRODUCTION

Reinforced concrete bridge decks are deteriorating faster than other bridge components, in the greatest part due to their direct exposure to traffic, environmental loading, and application of de-icing chemicals. Since the maintenance, rehabilitation and replacement of concrete decks represent the single highest expenditure for any bridge component, good understanding of deterioration processes and accurate assessment of their condition is of special importance

for their effective management. Bridge deck deterioration is a complex process that may be a result of numerous physical factors, like repeated traffic loading, freeze-thaw cycles, thermal effects or shrinkage, or chemical factors, like reinforcement corrosion, carbonation, alkali-silica reaction (ASR), etc. Deterioration processes will lead to defects, like cracking and delamination, and the overall decrease of concrete quality. Therefore, to better understand the connectivity of these diverse processes, it is imperative to use a suite of complementary NDE technologies that would capture deterioration processes and describe generated defects at all phases of the life of a bridge deck. Application of four NDE technologies: electrical resistivity (ER), ground-penetrating radar (GPR), impact echo (IE) and ultrasonic surface waves (USW) methods, is illustrated in Figure 1. In this case, the data collection by the four NDE methods is done using a fully autonomous robotic system RABIT [1]. The ER provides information about the concrete's corrosive environment and to it related anticipated corrosion rate, while the GPR provides a qualitative assessment of the condition of deck, with respect to corrosion and delamination potential. The IE method detects and characterizes delamination, while the USW method provides a quantitative assessment of concrete quality through a measurement of concrete's elastic modulus.

Figure 1: RABIT (Robotics Assisted Bridge Inspection Tool) surveying a deck.

The results from NDE data analysis are quantitative. Therefore, the condition can be objectively described. Equally important, the progression of deterioration can be objectively assessed and presented. One of the ways to summarize the condition of a deck is through a condition index [2] for deterioration characterized by any applied NDE technology, or for the

overall deck condition. The condition index (CI) describes a weighted average of percentages of deck area in various states (conditions), with 100 representing the best, and 0 the worst condition. As an example, deterioration progression of a bridge deck in Haymarket, Virginia, during the 2009 to 2015 period, described in terms of CI is shown in Figure 2. The deck deterioration in this case was clearly captured through four ER, GPR, IE and half-cell potential (HCP) surveys. On the other hand, there are two missing parts in the presented deterioration curve. The first missing information is the initial condition at the time of construction, which could have been obtained from the baseline measurement at the time of completion of construction. The second missing part is the shape of the deterioration curve, since there were no NDE surveys conducted between 1979 and 2009, and there was no information about maintenance and rehabilitation procedures applied during the same period. The BEAST (Bridge Evaluation and Accelerated Structural Testing) facility at Rutgers University opens opportunities to fill those gaps through accelerated full life-span evaluation of full size bridge decks.

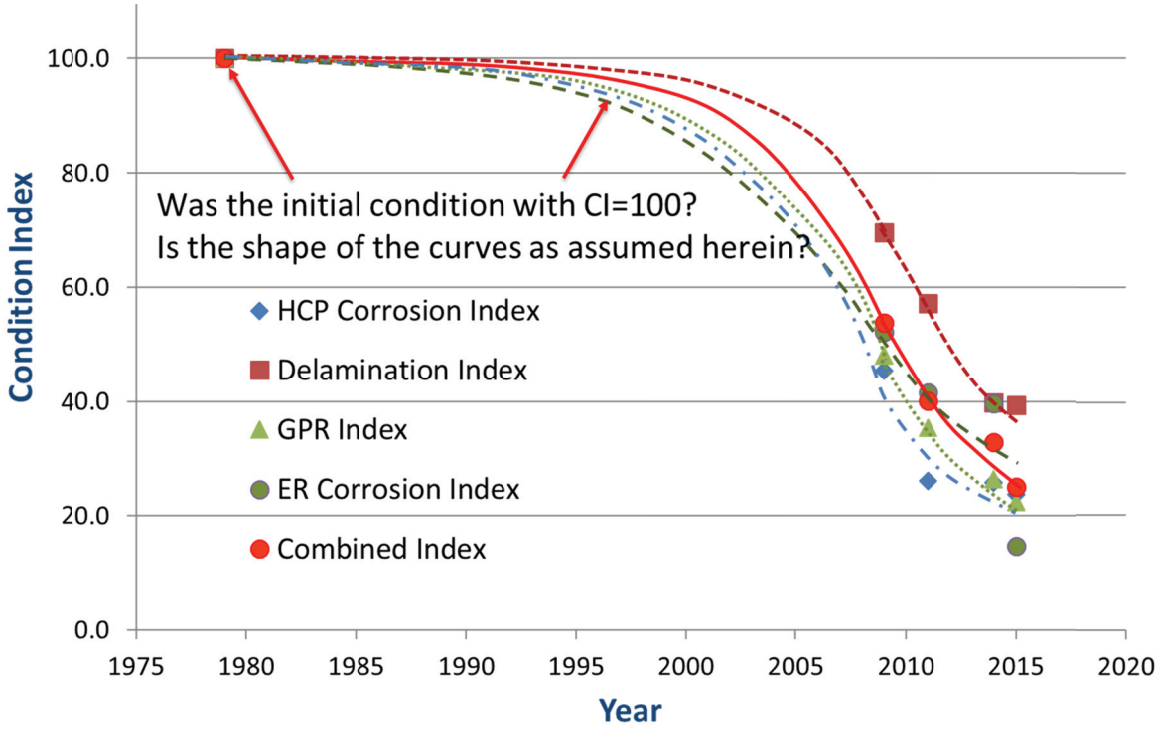

Figure 2: Deterioration curves for the Haymarket Bridge deck.

2. BEAST FACILITY

The Bridge Evaluation and Accelerated Structural Testing (BEAST) Laboratory is a one-of-a-kind testing facility capable of expediting the aging of full-scale bridge superstructures through controlled application of a realistic suite of demands (Figure 3). The ability to both control inputs and accelerate their influences on full-scale bridge systems is a potential game-changer for long-term bridge performance research. More specifically, these unique capabilities will allow researchers, for the first time, to:

(1) Observe the full life cycle of bridge performance (deterioration, initiation, and propagation) in a highly condensed time, and quantify the performance through high-resolution (both spatial and temporal) data collection efforts, and
(2) Quantitatively decouple the influence of different demands on various deterioration of bridges through controlling the levels of live load, environmental, and maintenance exposure.

Figure 3: BEAST facility during construction (top), and completed (bottom).

This facility can accommodate bridge structures 15 m long, 8.5 m wide and 1.5 m deep. It is capable of applying realistic demands to a full-scale bridge superstructure in an accelerated manner, which include:

(a) Live load applied through rolling wheel loads (Figure 4) to simulate the wear-and-tear on deck surfaces (as opposed to stationary actuators). The load configuration is equivalent to the rear carriage of a tractor trailer that moves at speeds up to 32 km/hr, and can impose forces from 45 kN up to 270 kN to simulate live load demands on primary components (e.g. deck, girders). At its maximum capacity, the BEAST is capable of inducing 17,500 cycles of live load per day, which corresponds to an Average Daily Truck Traffic (ADTT) of approximately 900, if an acceleration ratio of 20 is assumed.

(b) Temperature fluctuations applied to simulate both freeze-thaw and hot-dry cycles to the bridge specimen. The tests are expected to impose at least 280 freeze-thaw cycles (-20^0C to 10^0C) and at least 120 hot-dry cycles (10^0C to 40^0C) during a 9-month duration of the experiment.

(c) Application of de-icing agents to the bridge specimen to simulate common winter maintenance practices. A brine solution with up to 18% NaCl can be deployed during any phase of the accelerated testing.

The roof truss portion of the environmental chamber is designed to allow the BEAST to be located at different load lines across the test specimen, while keeping the chamber environmentally contained. Specimens can be either delivered by truck (precast slabs) or fabricated on-site (cast-in-place).

Figure 4: Dual-axle carriage for application of live loading and de-icing agents.

3. SCOPE OF ACTIVITIES

The installation of first specimen will be completed in November of 2018. Therefore, the following paragraphs will describe the specimen being constructed, planned activities, and some of the main goals stemming from the NDE data collection.

The specimen will be 8.1 m wide and 15 m long. These dimensions allow for four girders spaced 2.1 m on center, with about 0.9 m overhangs along each edge. A span-to-depth ratio of L/25 for the girders is used. Two internal diaphragms, in addition to those over the supports will be installed. The girders are sized as per the AASHTO LRFD Bridge Design Specifications based on the simplified single-line girder modeling approach, and are designed to be composite (using standard shear stud connectors and spacing) with the RC deck. This approach is the most commonly used in practice and will result in the most realistic girder and superstructure stiffness and strength characteristics. The reinforced concrete deck will be constructed using high performance concrete (HPC) and will be 20 cm thick, with a specified top cover of 6.3 cm. To allow for the influence of reinforcement coating to be assessed, the specimen will be constructed using two different types of deck reinforcement: epoxy-coated and galvanized reinforcement.

To achieve objectives of the study, live loading, environmental loading, and winter maintenance loading protocols were designed. The loading protocol will allow the effects of truck weights on the localized deterioration of the deck to be investigated. To accomplish this, four tracks on the bridge are proposed for the live loading, as shown in Figure 5. These tracks correspond to the least and most significant demands on the deck. In addition to varying the spatial location of the live load to simulate realistic force effects, the live load protocol will also vary the magnitude to allow the influence of truck weight to be assessed.

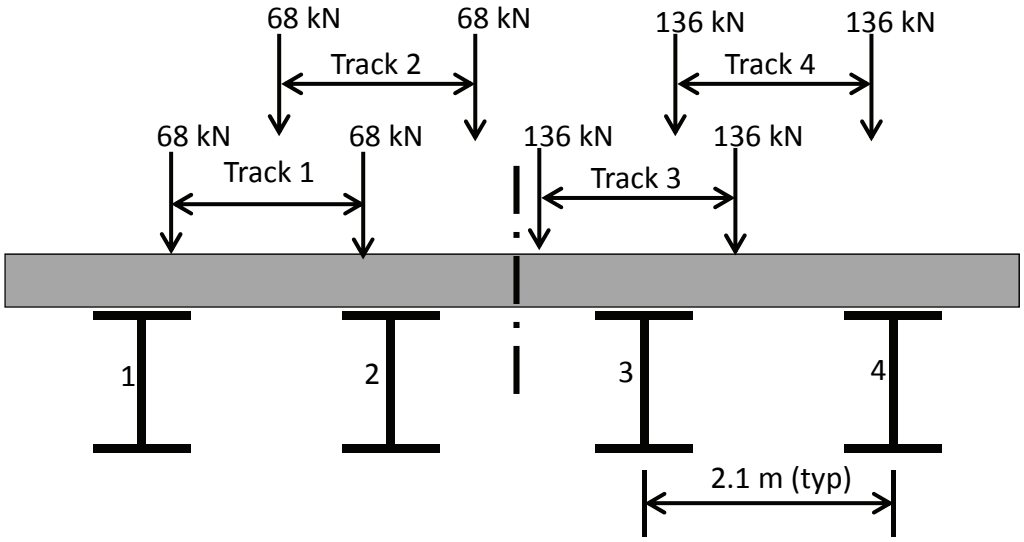

Figure 5: Elevation view illustrating the proposed live load location and magnitude

The proposed environmental loading protocol provides seven freeze-thaw cycles and three hot-dry cycles during every week of testing (with 8.5 hours of dwell time following each temperature change). Over the anticipated nine month testing period, this translates into approximately 280 freeze-thaw cycles. In order to introduce chlorides into the bridge specimen to simulate the effects of winter maintenance practices, during the Freeze Exposure

Cycles, a 10% brine solution will be constantly sprayed onto the deck of the specimen by the live load carriage. Since the location of the live load track defines the application region for the brine solution, the solution will be applied so that each track receives equal brine solution during each exposure cycle.

To evaluate effects of live, environmental and maintenance loading on the deterioration processes in the deck, the NDE surveys will be conducted on a bi-weekly basis using five technologies: ER, HCP, GPR, IE and USW. Other NDE technologies, like ultrasonic tomography, will be deployed once the first defects, or other anomalies, are detected for their more detailed evaluation. The data collection will be conducted on a permanently marked 0.3 m by 0.3 m grid. The following specific long-term goals will be pursued as a part of the NDE data collection and analysis, to develop or enhance:

- Fundamental understanding of deterioration progression in concrete decks,
- Master deterioration curves and, thus, predictive relationships as a function of traffic and environmental loading, maintenance activities and superstructure characteristics,
- Correlations between NDE technologies, and between NDE technologies, physical sampling and other results, for NDE technology optimization,
- Optimized NDE data collection with respect to the frequency of data collection and spatial data distribution,
- Understanding of the effects of local deterioration on the global structural response, and vice versa, and
- Understanding of the effectiveness of protective systems and maintenance procedures.

4. CONCLUSIONS

The newly constructed BEAST facility opens opportunities for accelerated evaluation of full size bridge components, including bridge decks. Accelerated live, environmental and maintenance loading, accompanied by periodical comprehensive assessment using an array of NDE technologies, will provide valuable data regarding the full life-cycle performance of bridge decks. Most importantly, it will enhance our understanding of the deterioration mechanisms in concrete bridge decks and development of more realistic deterioration and predictive models.

REFERENCES

[1] Gucunski, N., Basily, B., Kim, J., Dinh, K., Duong, T., Kee, S.H., and Maher, A., 'RABIT: implementation, performance validation and integration with other robotic platforms for improved management of bridge decks', *International Journal of Intelligent Robotics and Applications,* 1(3) (2017) 271-286.

[2] Gucunski, N., Pailes, B., Kim, J., Azari, H., and Dinh, K., 'Capture and quantification of deterioration progression in concrete bridge decks through periodical NDE surveys,' ASCE *Journal of Infrastructure Systems,* 23(1) (2016): B4016005.

International Conference on Sustainable Materials, Systems and Structures (SMSS 2019)
Novel Methods for Characterization of Materials and Structures
20-22 March 2019 – Rovinj, Croatia

POST-EARTHQUAKE DAMAGE EVALUATION OF CONCRETE STRUCTURES USING ULTRASONIC MONITORING: A PROOF-OF CONCEPT LABORATORY STUDY

Ali Hafiz (1), Thomas Schumacher (2), Peter Dusicka (2) and Ernst Niederleithinger (3)

(1) PhD Candidate, Civil and Environmental Engineering, Portland State University, Portland, OR, USA

(2) PhD, PE (DE), Associate Professor, Civil and Environmental Engineering, Portland State University, Portland, OR, USA

(3) PhD, Bundesanstalt für Materialforschung und -prüfung (BAM), Berlin, Germany

Abstract

In earthquake-prone regions such as the Pacific Northwest, damage assessment tools are needed to enable safety evaluations to support recovery. Currently, damage assessment is performed primarily by visual inspection and is often impossible for structural members that are inaccessible, such as deep foundations or interior members hidden by cladding. This study explores the possibility of using embedded ultrasonic transducers to monitor reinforced concrete members for damage progression under earthquake loading. A novel methodology is proposed where changes in the member condition due to an increase in the earthquake-type loading of a full-scale column-foundation specimen are correlated with changes in the recorded ultrasonic waveforms. The discussed preliminary analysis of the ultrasonic signals is based on wave propagation velocity, changes in the coda wave portion, and maximum amplitude of the signals. Three embedded transducers were used to continuously monitor the laboratory specimen during destructive testing. This paper provides an overview of the proposed methodology, outlines the laboratory experiment, and discusses some preliminary observations.

Keywords: Damage evaluation, Structural health monitoring, Ultrasound, Coda wave, Embedded transducers, Earthquake, Reinforced concrete, Column.

1. INTRODUCTION

Structures such as buildings and bridges begin to deteriorate as soon as they are built and taken into service [1]. This paper focuses on structural concrete, which represents the most widely used construction material. In addition to deterioration due to aging and environmental effects, structures have to withstand natural hazards such as earthquakes, which can introduce both small and large-scale damage in the structures. Generally, the term “damage” can be

defined as a change in the structure that affects its performance in the present or future [2]. Therefore, evaluating a structure's integrity, or health, is of greatest importance and structural health monitoring (SHM) can be used as a tool for this purpose.

SHM can be defined as a process of determining and tracking structural integrity [2] at frequent intervals during the life (or partial life) of a structure [1]. It is also used to assess the nature of damage in a structure by determining the location and severity of the damage [1]. Generally, a comparison between two different condition states is used in structural health monitoring by comparing the current state with a reference (typically undamaged) state [2]. SHM is a passive process whereby the response of the structure is monitored over time.

Many types on sensors are used for SHM of concrete structures such as accelerometers, strain gauges, displacement sensors…etc. [3]. Ultrasonic waves have an advantage over traditional sensors, since the waves travel through the body of a member, as opposed to the former sensors, which represent surface measurements. Additionally, ultrasonic signals from concrete are complex since the wave experiences multiple scattering during propagation due to the heterogeneous nature of concrete [4]. Generally, an ultrasonic signal can be divided into two portions: coherent and diffuse (or coda). The coherent portion includes the initial, i.e. p-wave arrival, whereas the coda wave includes the later portion of a recorded ultrasonic signal [5]. The coherent portion is only affected if significant discontinuities such as cracks and voids lying in the direct wave propagation path are present. The coda wave, however, has been found significantly more sensitive to small changes in the material, even when it is not in the direct wave propagation path. For example, changes in the internal stress of a member have been characterized using a number of analysis techniques [5][6][7][8]. Additionally, approaches using the coda wave have also been developed to detect cracks in concrete members [9][10].

In this study, ultrasonic signals were used for earthquake damage assessment. For this purpose, ultrasonic transducers were embedded in a full-scale laboratory column-foundation specimen that was subjected to subduction-earthquake-type loading [11]. This paper discusses the test setup and some preliminary observations focusing on the early loading phase to demonstrate the feasibility of the proposed approach.

2. EXPERIMENT SETUP

2.1 Specimen Details and Loading Protocol

A full-scale reinforced concrete column-foundation subassembly was used for this study. The column has a square cross-section (0.61 x 0.61 m) and a height of 2.6 m. The column was cast on a square slab footing with a side length of 1.82 m and a depth of 0.61 m, as shown in Fig. 1. The concrete compressive strength at test day was 44.1 MPa and 40.5 MPa for the foundation and the column, respectively. The specimen and reinforcement details are representative of reinforced concrete bridges in Oregon, USA prior to the 1970s.

Commonly, a cyclic loading protocol is used in order to evaluate the seismic performance of reinforced concrete bridge columns [12]. The loading protocol used in this study was developed by Bazaez and Dusicka [13] to represent a Cascadia subduction-zone earthquake, and is shown in Fig. 2. An axial and a lateral force were applied to the column top by means of two hydraulic actuators (see Fig. 1.b). The axial and lateral forces were applied in force- and displacement-controlled mode, respectively.

The column was instrumented with displacement sensors, strain gages, and monitored with digital cameras to capture the response throughout the loading process. Acoustic emissions (AE) were also monitored to capture ongoing fracture processes, but are not discussed here.

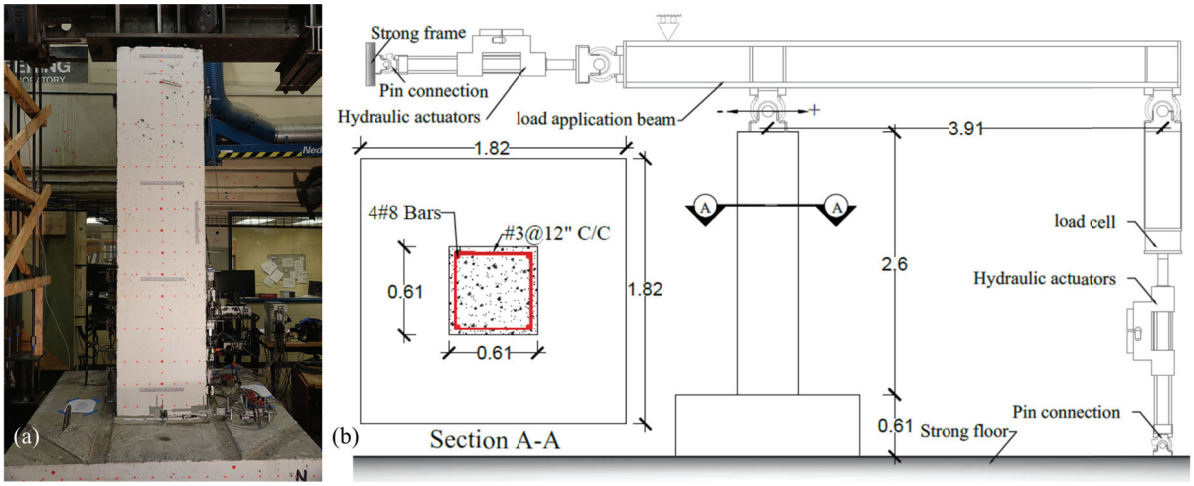

Figure 1: (a) Photo of instrumented specimen and (b) elevation view showing laboratory test.

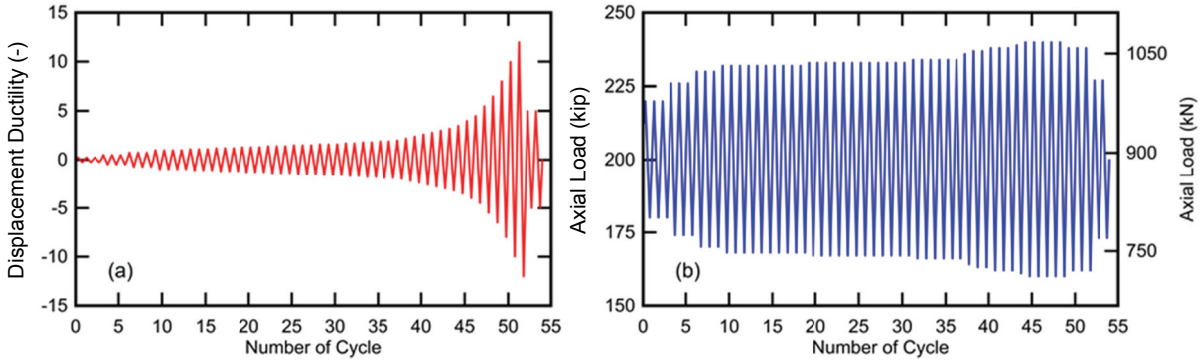

Figure 2: Subduction earthquake-type loading protocol: (a) Lateral loading and (b) axial loading.

2.1 Ultrasonic Wave Test

Three embeddable ultrasonic transducers [10][14] were fixed on the formwork before casting, as shown in Fig. 3.a. Two of these transducers were placed at the center of the column cross-section at a height of 0.76 and 1.67 m from the upper face of the slab. The third transducer was placed at a depth of 0.15 m in the slab, as shown in Fig. 3.b. The transducers are referred as the top, middle, and bottom transducers. The middle transducer was used as a transmitter (T) and the other two as receivers (R). This configuration provided information about condition changes in the column for two zones. The first zone (see orange box in Fig. 3.b) is between the bottom and middle transducer, which is where the plastic hinge was expected to form. The second zone lies between the middle and upper transducer. The first zone was expected to experience more significant damage compared to the second zone.

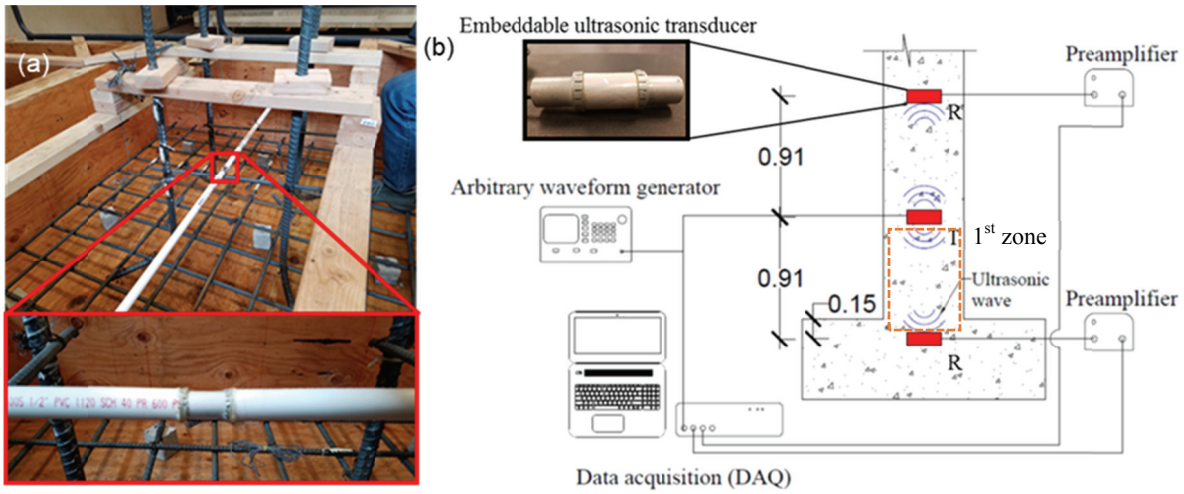

Figure 3: (a) Photo of embeddable ultrasonic transducer before concrete casting and (b) illustration of ultrasonic monitoring setup.

Throughout the loading process, a 60 kHz Morlet-type pulse was sent to the transmitting transducer by an arbitrary waveform generator (Manufacturer: BK Precision) using a pulse repetition frequency (PRF) of 1 Hz. Using an output of 20 V-p-p from the waveform generator was sufficient to produce a measurable ultrasonic stress wave. The receiving transducers were connected to preamplifiers to intensify the signal (Model: Olympus 5660B). Finally, a high-speed data acquisition system (Model: Elsys TraNET 204s) was used to record the transmitted pulse as well as the received signals using a sampling frequency of 1 MHz. Low-pass anti-aliasing filters were set to 500 kHz.

3. RESULTS AND DISCUSSION

The received signals at the bottom transducer are discussed here (first zone) and exhibited significant changes due to increases in the lateral displacement as well as the resulting increase in damage in form of cracking. These changes could be observed in the coda wave portion, propagation velocity, and maximum amplitude. In this paper, preliminary observations of the experimental test are presented and discussed and are limited to 17 mm of lateral displacement, as shown in Fig. 4. For reference, the specimen failed at a lateral displacement of 137 mm. Focusing on early damage, the changes in the ultrasonic wave could be attributed qualitatively to three different phases, named PH I, PH II and PH III, as shown in Fig. 4. These phases were categorized according to the type of the changes observed in the recorded ultrasonic signals as well as to the condition state of the specimen.

Phase I lies between the initial condition (= unloaded specimen) and approximately 4 mm of applied lateral displacement. This phase corresponds to the highest applied lateral displacement that did not result in any changes in the wave propagation velocity, which is associated with the time-of flight of the coherent wave. Fig. 5 shows two sample signals: one in the initial (= unloaded) condition (red) and the other at the end of Phase I (blue), at an applied lateral displacement of 4 mm. A notable difference in the coda wave portion between the two signals can be observed (Fig. 5.a), which can be associated with differences in the

internal stress in the column. On the other hand, no measurable difference in the coherent portion can be observed, as highlighted in Fig. 5.b. For reference, in a previous study the authors have found that increases in the axial stress in concrete cylinders of up to 50 to 70% from ultimate stress were not found to result in measurable changes in the time of flight [5][6][15].

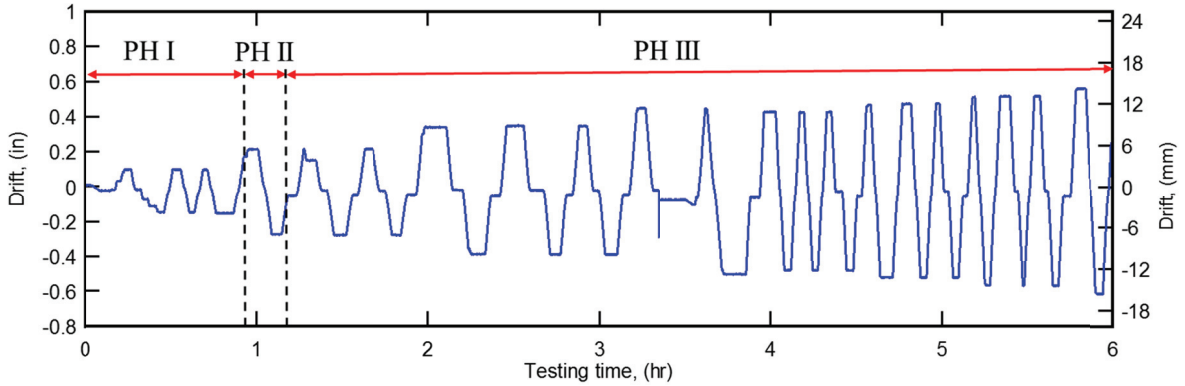

Figure 4: Measured applied column top lateral displacement vs. test time.

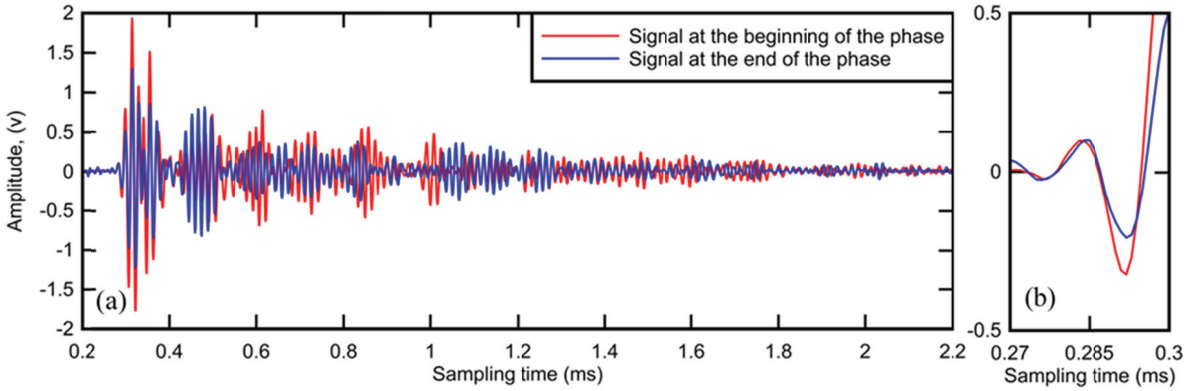

Figure 5: Two samples of recorded ultrasonic signals for Phase I: (a) Entire signal and (b) p-wave arrival (coherent portion) of the signal.

Phase II is situated between approximately 4 and 7 mm applied lateral displacement. Fig. 6 shows two sample signals: at the beginning and end of Phase II. In addition to the effect of changes in the internal stress on the coda wave portion, the generated stress had a small but measurable influence on the ultrasonic wave propagation velocity by changing the time of flight (TOF), as shown in Fig. 6 b. In this phase, the wave propagation velocity showed a relationship with the applied lateral displacement where the propagation velocity of the ultrasonic wave decreased with increasing applied lateral displacement. It is speculated that this phenomenon occurred because of a change in the propagation path of the ultrasonic wave due to the opening of micro cracks. In Phase 1, no visually observable (macro) cracking had occurred. In Phase II, however, cracks appeared on the specimen surface. This was also observed by the authors in two of their previous studies [5][15]. In conclusion, changes in the propagation velocity (or the coherent portion of the signal) can be used as an indicator for crack initiation, which can be used to estimate the condition of the member.

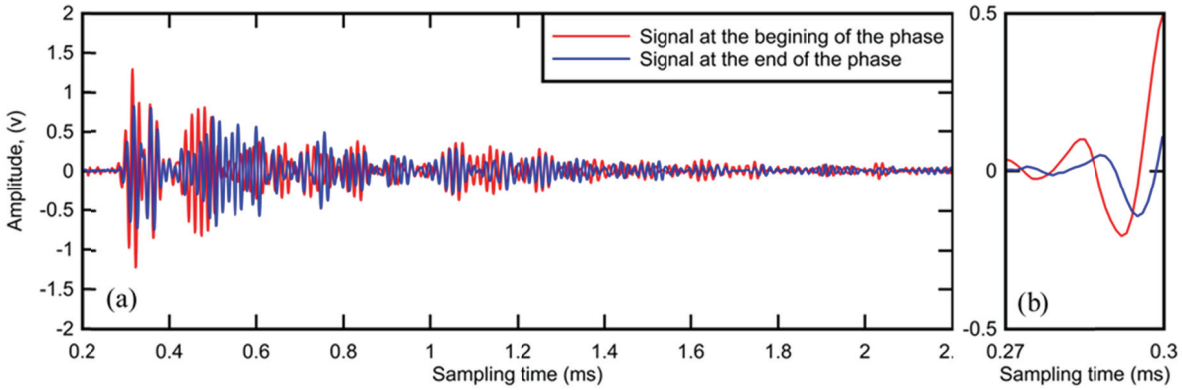

Figure 6: Two samples of recorded ultrasonic signals for Phase I: (a) Entire signal and (b) p-wave arrival (coherent portion) of the signal.

Phase III begins when visible cracking had developed in the column near reaching the direct path of the wave. In our experiment, these cracks appeared on both sides of the column when the applied lateral displacement exceeded 7 mm, as shown in Fig. **4**. Due to the nature of cyclic loading, the cracks closed and opened according to the direction of the applied lateral displacement. This phenomenon is sometimes referred to as crack breathing [16]. Crack breathing had a serious effect on the ultrasonic waves because the propagation path became much longer when the cracks were open. This phenomenon can be observed in two ways. First, the propagation velocity decreases with increasing propagation path length. Fig. 7 shows two signals for open and closed cracks. It can be observed that the phase shift (change in time of flight) is on order of the signal period. In contrast, the phase shift was comparatively small during Phase II. Second, attenuation of the maximum signal amplitude increases with increasing applied lateral displacement, as shown is illustrated in Fig. 8. It can be observed that there is a significant reduction in the maximum amplitude by approximately 75% due to the effect of crack breathing. Additionally, this figure demonstrates the column's symmetric response, i.e. the cracks developed on both sides having comparable levels of severity. Finally, Fig. 8 suggests that the threshold-level for the applied lateral displacement for fully-opened cracks is approximately 5 mm for both sides of the column, as indicated by the green dash line.

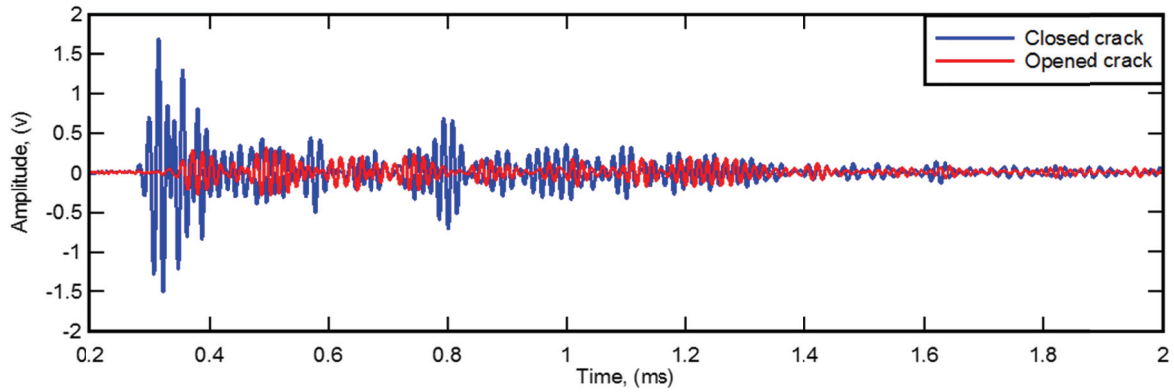

Figure 7: Two samples of recorded ultrasonic signals for Phase III.

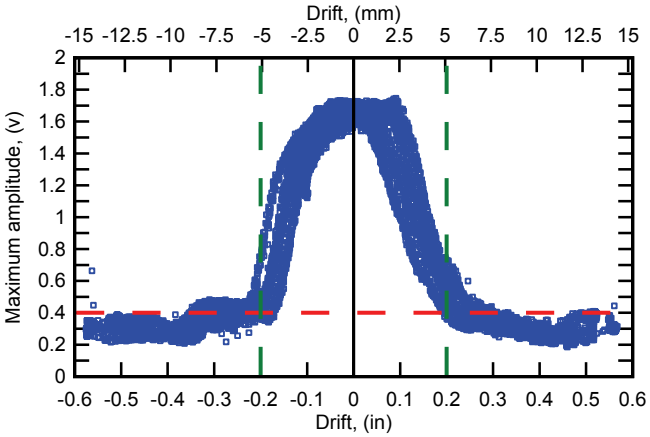

Figure 8: Maximum signal amplitude vs. applied lateral displacement.

4. SUMMARY AND CONCLUSIONS

A novel methodology for damage evaluation of concrete members under earthquake loading using embedded ultrasonic sensors is proposed. Based on the presented preliminary results, the observed changes in the recorded ultrasonic signals were divided into three phases, corresponding to the level of observed deterioration in terms of visible cracking on the column. The three phases were distinguished according to the following observed changes they had on the recorded ultrasonic signals:

Phase I: Only the coda portion of the signals is affected, which can be associated with low stress changes in the linear-elastic range. While there might be some opening and closing of micro-cracks, no macro-level cracking has occurred.

Phase II: The coherent portion of the signals is affected, i.e. there is a visible delay of the p-wave arrival, which results in an increased time-of-flight. First visible cracks appeared on the column surface.

Phase III: The delay of the p-wave arrival is on the order of several time periods, which indicates that the direct travel path for the signal has increased. In this phase, a relationship between lateral drift and maximum signal amplitude was found.

To conclude, the findings demonstrate the proposed methodology's potential for damage condition assessment in the context of earthquake loading. Future work includes analyzing all available data, and correlating it with other available physical measurements.

ACKNOWLEDGEMENTS

The sponsorship of the experiment by the Oregon Department of Transportation, Project SPR-802, is greatly appreciated. Furthermore, funding for the first author was provided by the Higher Education Commission of Iraq. BAM provided the embeddable sensors. Finally, the help of the laboratory personnel as well as other graduate and undergraduate students is greatly appreciated.

REFERENCES

[1] Chang, P. C.; Flatau, A.; Liu, S. C. Review paper: Health monitoring of civil infrastructure. *Structural Health Monitoring* 2003, *2*, 257–267.

[2] Farrar, C. R.; Worden, K. An introduction to structural health monitoring. *Philosophical transactions. Series A, Mathematical, physical, and engineering sciences* **2007**, *365*, 303–315, doi:10.1098/rsta.2006.1928.
[3] Wang, K. L.; Lynch, J. P.; Sohn, H. Sensor Technologies for Civil Infrastructures, Volume 1. *Woodhead Publishing*. **2014**, ISBN: *9780857094322*.
[4] Snieder, R. The theory of coda wave interferometry. *Pure and Applied Geophysics* **2006**, *163*, 455–473, doi:10.1007/s00024-005-0026-6.
[5] Hafiz, A.; Schumacher, T. MONITORING OF STRESSES IN CONCRETE USING ULTRASONIC CODA WAVE COMPARISON TECHNIQUE. *Journal of Nondestructive Evaluation*.
[6] Hafiz, A.; Schumacher, T. Characterizing the effect of applied stress in concrete by magnitude-squared coherence of ultrasonic full-waveforms. In *Structural Health Monitoring 2017: Real-Time Material State Awareness and Data-Driven Safety Assurance - Proceedings of the 11th International Workshop on Structural Health Monitoring, IWSHM 2017*; 2017; Vol. 2.
[7] Planès, T.; Larose, E. A review of ultrasonic Coda Wave Interferometry in concrete. *Cement and Concrete Research* **2013**, *53*, 248–255, doi:10.1016/j.cemconres.2013.07.009.
[8] Larose, E.; Hall, S. Monitoring stress related velocity variation in concrete with a 2× 10− 5 relative resolution using diffuse ultrasound. *The Journal of the Acoustical Society of America* **2009**, *125*, 1853–1856.
[9] Planès, T.; Larose, E.; Margerin, L.; Rossetto, V.; Sens-Schönfelder, C. Decorrelation and phase-shift of coda waves induced by local changes: Multiple scattering approach and numerical validation. *Waves in Random and Complex Media* **2014**, *24*, 99–125, doi:10.1080/17455030.2014.880821.
[10] Niederleithinger, E.; Wang, X.; Herbrand, M.; Müller, M. Processing ultrasonic data by coda wave interferometry to monitor load tests of concrete beams. *Sensors (Switzerland)* **2018**, *18*, doi:10.3390/s18061971.
[11] Dusicka, P.; Knoles, S. Subduction megathrust earthquake demands on ductile bridge columns. In *7NSC), Seventh National Seismic Conference on Bridges and Highways*; 2012.
[12] Mehary, S.; Dusicka, P.; Bazaez, R. Effect of Subduction Earthquake-Based Loading History on Substandard RC Square Columns. *Journal of Bridge Engineering* **2017**, *23*, 4017146.
[13] Bazaez, R.; Dusicka, P. Cyclic Loading for RC Bridge Columns Considering Subduction Megathrust Earthquakes. *Journal of Bridge Engineering* **2016**, 1–13, doi:10.1061/(ASCE)BE.1943-5592.0000891.
[14] Niederleithinger, E.; Wolf, J.; Mielentz, F.; Wiggenhauser, H.; Pirskawetz, S. Embedded ultrasonic transducers for active and passive concrete monitoring. *Sensors (Switzerland)* **2015**, *15*, 9756–9772, doi:10.3390/s150509756.
[15] Hafiz, A.; Schumacher, T. Monitoring of applied stress in concrete using ultrasonic full-waveform comparison techniques. In *Nondestructive Characterization and Monitoring of Advanced Materials, Aerospace, and Civil Infrastructure 2017*; International Society for Optics and Photonics, 2017; Vol. 10169, p. 101692Z.
[16] Giannini, O.; Casini, P.; Vestroni, F. Nonlinear harmonic identification of cracks in structures. In *Conference Proceedings of the Society for Experimental Mechanics Series*; 2014; Vol. 4, pp. 207–217.

International Conference on Sustainable Materials, Systems and Structures (SMSS 2019)
Novel Methods for Characterization of Materials and Structures
20-22 March 2019 – Rovinj, Croatia

RHEOLOGICAL BEHAVIOUR OF LOW-CO_2 CONCRETE MIXTURES

Mayra T. de Grazia (1), Leandro F. M. Sanchez (1), Jose A. F. S. de Mesquita (2), Heitor M. Bernardo (2), Roberto C. de O. Romano (2) and Rafael G. Pileggi (2)

(1) Department of Civil Engineering, University of Ottawa, Canada

(2) Department of Civil Engineering, University of São Paulo, Brazil

Abstract

Concrete has a huge environmental impact producing about 7% of the global carbon dioxide (CO_2). Portland cement (PC), which is the primary component of concrete is responsible for more than 90% of its total carbon footprint. Given the rapid growth of CO_2 emissions and concerns related to global warming, a number of studies have been focusing on distinct approaches aiming to reduce the environmental impact of PC's use; among others the improvement of concrete mix-design techniques aiming to reduce concrete porosity. Although the latter was proven to be effective, there is currently a lack of literature results on the effect of reducing PC content on the concrete fresh state properties. While there is a current misconception in the concrete industry that single point tests such as slump are capable of evaluating the concrete fresh behaviour, this project emphasizes that a full rheological characterization is needed to assess concrete fresh state performance. The current project aims to investigate the influence of two physical parameters (maximum paste thickness and interparticle space) on the fresh and hardened state properties of concrete mixtures designed with reduced PC content (54, 159, and 260 kg/m^3).

Keywords: low cement content, eco-efficient concrete, maximum paste thickness, interparticle distance, rheological behaviour

1 INTRODUCTION

Nowadays, the construction industry is not only focusing on the performance and economic benefits of the materials used but rather on their environmental impact. Although concrete is one of the most energy-efficient construction materials currently used worldwide, it produces approximately 7% of the global carbon dioxide (CO_2) emission annually. Portland cement (PC), which is the primary component of concrete is responsible for more than 90% of its total carbon footprint.[1]. It is worth noting that a ton of PC produces approximately one ton of CO_2, which justify the global pressure to reduce PC content in concrete [2–4]. In order to assess concrete environmental impact, Damineli et al. (2010) proposed the use of an index,

the so-called binder intensity index (BI), which correlates the amount of binder required to develop one unit of concrete property, for instance, the compressive strength.

Although supplementary cementing materials (SCMs) and or inert fillers (IF) may be used to mitigate concrete environmental impact, SCMs global availability is not enough to overcome the increasing PC's demand. Therefore, recent studies demonstrated that IF might be used to reduce PC content, hence enhancing concrete eco-efficiency [6–8]. Another novel technique used to reduce the amount of PC in concrete is through the use of advanced mix-design techniques that aim to increase the material's packing density, lowering its porosity and amount of cement paste required [9,10]. Yet, although the above strategies are widely known, low-CO_2 concrete mixtures with reduced porosity (and low PC content) is currently not used for important structural applications since concerns regarding their fresh state performance were raised by the technical society.

2 BACKGROUND

2.1 Mobility Parameters

The amount of PC is, on the one hand, the most important cause of concrete carbon footprint. On the other hand, there is a need of a minimum amount of cement paste to ensure flow in concrete mixtures. Hence, highly packed and low porosity systems may present some issues in the fresh state. It has been found that two parameters must be studied to assess the mobility of granular systems: the interparticle separation distance (IPS – Equation 1) and the maximum paste thickness (MPT - Equation 2) [11,12]. IPS is considered as the average distance between adjacent fine particles (≤ 125 μm) [12]. Since these particles are normally separated by water, IPS is directly proportional to the water content in the mix [12,13]. Literature suggests that the lower the IPS, the lower the flowability of granular systems (i.e. the higher the viscosity and particles collisions). Conversely, high IPS yields less viscous, more flowable mixes [9,14].

$$IPS = \frac{2}{VSA}\left[\frac{1}{V_s} - \frac{1}{(1 - P_{of})}\right] \quad (1)$$

Where IPS is the interparticle spacing, VSA is the calculated volume surface area per cubic centimetre of powder, V_s is the volume fraction fine solids (particles smaller than 125 μm), and P_{of} is the pore fraction assuming the densest packing of the fine particles.

Likewise, MPT is the maximum paste thickness among adjacent aggregate particles greater than 125 μm [11,15,16].

$$MPT = \frac{2}{VSA_c}\left[\frac{1}{V_{sc}} - \frac{1}{(1 - P_{ofc})}\right] \quad (2)$$

Where MPT is the distance between aggregates, VSA_c is the calculated volume surface area of aggregate (particles greater than 125 μm) fraction, V_{sc} is the volumetric aggregate solid fraction, and P_{ofc} is the pore of aggregate fraction assuming the densest packing.

Previous studies highlight that the greater the IPS and MPT, the higher the flowability of the mixes due to the decrease in friction amongst the particles for the same water content [7,12].

3 EXPERIMENTAL PROGRAM

3.1 Materials

Three concrete mixtures containing the same slump flow (i.e. 615 mm) and with distinct cement contents (i.e., 54, 159 and 260 kg/m³) were designed and evaluated in the fresh and hardened states. The PC used in all mixes was a type HE "high early strength" from the Brazilian market (i.e. CPV-ARI), which is similar to ASTM C150 type III cement [17]. Moreover, the distinct concrete mixtures also contain two types of limestone fillers: performance fillers (composed of particles smaller than PC) and replacement fillers (composed of particles similar to PC). Natural sand, manufactured sand, and two types of limestone coarse aggregates were used with specific gravity of 2.64, 2.68, 2.67 g/cm^3, respectively. In order to achieve the required slump flow, chemical admixtures were used (1% of the fines mass; i.e. particles < 125 μm), wherein ½ was a lignosulfonate-based mid-range plasticizer and ½ was a polycarboxylate-based superplasticizer.

3.2 Concrete Mixtures

Based on preliminary experimental works, ratios of 1/3 for coarse (i.e. coarse 1 to coarse 2) and 3/2 for fine (i.e. fine 1 to fine 2) were selected aiming to lower the friction among the particles. The mix-design of all tested mixes are shown in Table 1. The mixes were designated according to their cement content; i.e. mix C260 contains 260 kg/m^3 of PC.

Table 1: Mix-design of three low-CO_2 concrete mixtures

Mixture Name	**Cement (kg/m³)**	**F.A. (kg/m³)**	**C.A. (kg/m³)**	**Filler (kg/m³)**	**Water (kg/m³)**	**W/C**
C54	54	833	1059	356	115	2.13
C159	159	820	1041	244	133	0.84
C260	260	810	1029	138	146	0.56

3.3 Fabrication of samples and testing procedures

Fifteen litres of the three distinct concrete mixtures were mixed and evaluated using a planetary rheometer. The fresh state analyzes were divided into two measurements: mixing energy and rheological behaviour. For the first test, the raw material was mixed and the maximum and final torques required to enable flow and the mixing energy of each mixture were determined. The second fresh state test was performed to appraise each concrete rheological behaviour and profile. The test protocol consisted of shear-controlled time-step cycles with acceleration and deceleration process. The shear rate increased until 1380 rpm and decreased at the same stepwise down to 35 rpm. It is important to note that the rotation speed was maintained constant for eight seconds in each step. Thus, several rheological parameters (i.e. viscosity, yield stress, and shear rate) were determined for each concrete mixture.

Then, cylinders of 100 mm diameter x 200 mm long were fabricated from each mix to test concrete compressive strength at 14, 28, and 56 days, according to ASTM C 39 [18].

4 RESULTS AND DISCUSSION

4.1 Fresh state properties

Although all the three mixtures were designed for an equal initial consistency (i.e. 620 mm; Table 2), the rheological test demonstrates their noteworthy difference. Analyzing Figure 1, one may notice that the lower the cement content, the higher the maximum and final torques achieved while mixing. Therefore, the higher mixing energy was obtained in C54 equal to 15824 N·m·s, while C159 and C260 achieved mixing energy equal to 7455 and 3620 (N.m.s), respectively.

Table 2: Fresh state characteristics of low-CO_2 concrete mixtures

Concrete	**C54**	**C159**	**C260**
IPS (μm)	0.13	0.17	0.20
MPT (μm)	1.60	1.70	1.90
Temperature after mixing (°C)	29	27.5	24.9
Slump Flow (mm)	620	620	615

Figure 2a displays the relationship between torque and rotation of the low-CO_2 mixtures studied. The three mixtures presented an initial torque approximately equal to zero, as expected since they presented a slump-flow of 615 ± 5 mm. Regarding their rheological behaviour, C54 and C159 presented a shear thinning behaviour (i.e. decrease of viscosity as a function of torque), while C260 showed a quite linear relationship between torque and rotation. Figure 2b demonstrates the relationship between rotation and viscosity of the three mixtures studied. C159 and C260 presented an extremely low viscosity equal to 0.11 and 0.07 Nm/rpm, respectively throughout the distinct rotation regimes studied, whereas C54 presented a high viscosity for low rotation regimes, decreasing as a function of the rotation applied and achieving similar values to C159 and C260 at high rotation regimes.

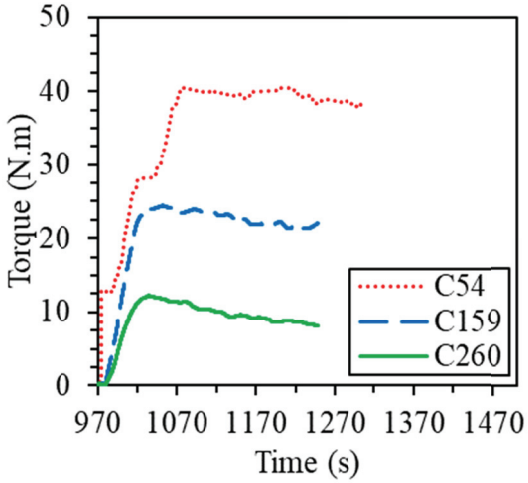

Figure 1: a) Rheological analysis of low-CO_2 mixtures.

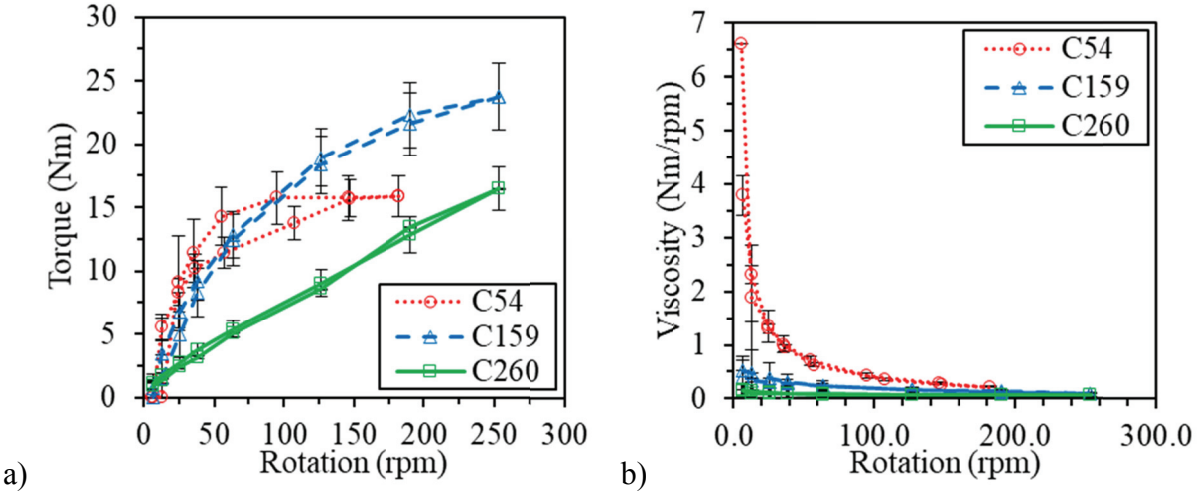

a) b)

Figure 2: Relationship between rotation and a) torque b) viscosity

Figure 3 presents a relationship of IPS, MPT, mixing energy, maximum and final torque clarifying the importance of studying the mobility parameters (IPS and MPT) while evaluating the fresh state properties of concrete mixtures. Although the three low-CO_2 mixtures studied presented the same slump-flow, each mixture required a different mixing energy to reach the maximum torque. As shown in Figure 3, the higher the IPS and MPT, the lower the mixing energy, the maximum and final torque. It occurs due to the greater distance between the particles which allows them to move easily without considerable interference. Table 3 shows the temperature of the mixtures studied after mixing. One may notice that the C54 is the mixture with higher temperature after mixing and it may have occurred due to the lower IPS and MPT; i.e. higher collision among particles.

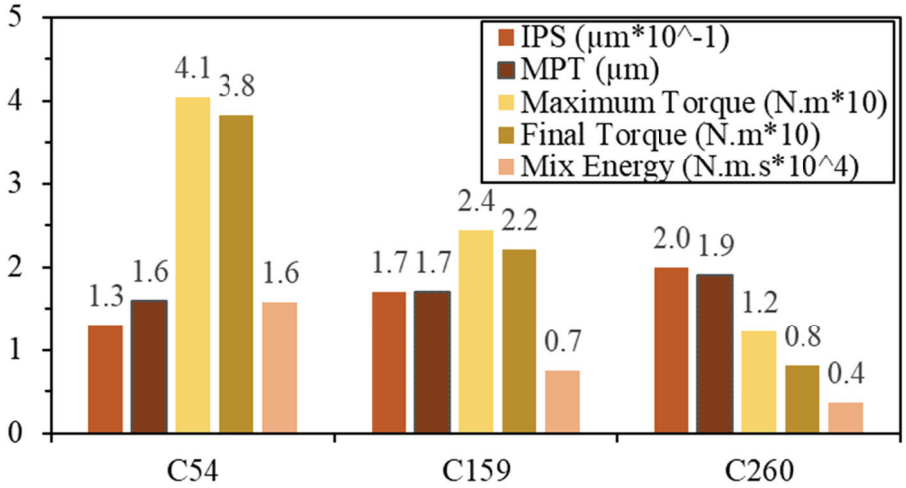

Figure 3: Comparison between mobility parameters and rheological responses

4.2 Hardened state properties

The 14, 28, and 56-day compressive strength values of the three low-CO_2 mixtures are shown in Figure 4a. It is worth noting that the difference in compressive strength found are due the distinct water-to-cement ratios (w/c; C54 - w/c = 2.13, C159 – w/c = 0.83, and C260 –

w/c = 0.56) of the mixes and not due to their PC content. Abrams' law is a widely well-known relationship that predicts concrete compressive strength accounting for the w/c of conventional concrete mixtures [19–21]. However, for highly packed low porosity mixtures with low PC content, the w/c from Abrams' law may not be the only parameter influencing the mechanical properties of the material such as compressive strength. Analyzing the three concrete mixtures studied in this research, the ordinary Abrams' law was found to be unsuitable to predict their compressive strength results. Figure 4b shows that the best fit for A and B parameters in Abrams law to represent the compressive strength values obtained for the different mixes was 136.4 and 3.35 respectively. It is important to notice that conventional concrete mixtures with moderate to high PC contents and porosity present A and B values of around 100 and 10, respectively. The 14 and 28-day compressive strength values do not present significant variance because mixtures were developed with a high early strength PC.

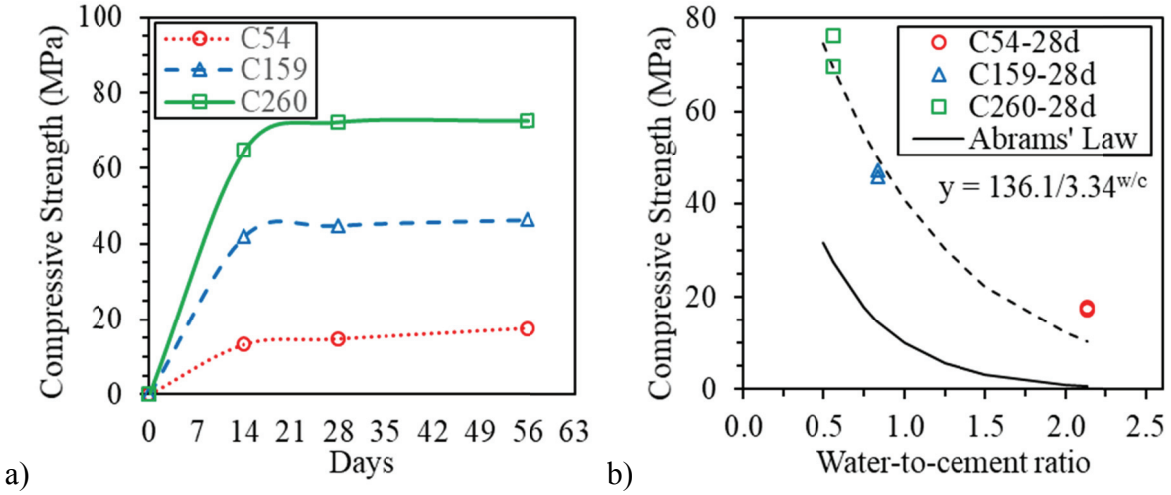

Figure 4: a) Compressive strength of low-CO_2 mixtures b) Evaluation of Abrams' law

5 CONCLUSION

This study appraises the fresh (rheological behaviour) and hardened (compressive strength) state properties of distinct low-CO_2 concrete mixtures. Although all mixtures studied presented the same initial condition (i.e. slump-flow of 620 mm), the different rheological profiles show that each mixture actually presents a different fresh state performance (i.e. viscosity) for distinct torque regimes. The three low-CO_2 mixtures presented a shear-thinning behaviour, also known as pseudoplastic behaviour that is normally recommended for pumped and/or vibrated concrete (high torque over pouring). Moreover, the two mobility parameters studied (IPS and MPT) confirmed their major impact on concrete rheological characteristics of the materials. The increase of these factors results in a greater distance among particles, and consequently reduces the particle's friction and thus energy required to mix the material. It is worth noting that when the PC content increases in a pace around 100 kg/m^3, the IPS and MPT grow in an average rate of 0.04 and 0.15, respectively. As a result of the mix-design and low porosity system, concrete mixtures with low PC content and high w/c showed high compressive strength values, for example, C54 - w/c = 2.13 achieved compressive strength

equal to 14.7 MPa at 28-days. While C159 – w/c = 0.83 and C260 – w/c = 0.56 reached compressive strength results of 44.9 and 72.4 MPa, respectively, at 28-days.

REFERENCES

[1] M. Limbachiya, S.C. Bostanci, H. Kew, Suitability of BS EN 197-1 CEM II and CEM V cement for production of low carbon concrete, Constr. Build. Mater. 71 (2014) 397–405.
[2] N. Makul, G. Sua-Iam, Effect of granular urea on the properties of self-consolidating concrete incorporating untreated rice husk ash: Flowability, compressive strength and temperature rise, Constr. Build. Mater. 162 (2018) 489–502.
[3] J. Zachar, M. Asce, Sustainable and Economical Precast and Prestressed Concrete Using Fly Ash as a Cement Replacement, J. Mat. Civ. Eng. 23 (2011) 789–792.
[4] M.C.G. Juenger, R. Siddique, Recent advances in understanding the role of supplementary cementitious materials in concrete, Cem. Concr. Res. 78 (2015) 71–80.
[5] B.L. Damineli, F.M. Kemeid, P.S. Aguiar, V.M. John, Measuring the eco-efficiency of cement use, Cem. Concr. Compos. 32 (2010) 555–562.
[6] Y. Knop, A. Peled, Setting behavior of blended cement with limestone: influence of particle size and content, Mater. Struct. 49 (2016) 439–452.
[7] C. Varhen, I. Dilonardo, C. Romano, R.G. Pileggi, A. Figueiredo, Effect of the substitution of cement by limestone filler on the rheological behaviour and shrinkage of microconcretes, Constr. Build. Mater. 125 (2016) 375–386.
[8] B.L. Damineli, V.M. John, B. Lagerblad, R.G. Pileggi, Viscosity prediction of cement-filler suspensions using interference model: A route for binder efficiency enhancement, Cem. Concr. Res. 84 (2016) 8–19.
[9] A.K. Castro, V.C. Pandolfelli, Review: Concepts of particle dispersion and packing for special concretes production, 18 CerâMica. 55 (2009) 18–32.
[10] M. Noël, L. Sanchez, G. Fathifazl, Recent Advances in Sustainable Concrete for Structural Applications, in: Sustain. Constr. Mater. Technol. 4, 2016: p. 10.
[11] F. De Larrard, A. Belloc, The influence of aggregate on the compressive strength of normal and high-strength concrete, ACI Mater. J. 94 (1997) 417–426.
[12] M. T. de Grazia, L. F. M. Sanchez, R. C. O. Romano, R. G. Pileggi, Investigation of the use of continuous particle packing models (PPMs) on the fresh and hardened properties of low-cement concrete (LCC) systems, Constr. Build. Mater. 195 (2019).
[13] D. Dinger, J. Funk, Predictive process control of crowded particulate suspensions, 1st ed., New York, 1994.
[14] I.R. Oliveira, A.R. Studart, R.G. Pileggi, V.C. Pandolfelli, Dispersão e Empacotamento de Partículas, Fazendo Arte Editorial, São Paulo, 2000.
[15] P. Bonadia, A.R. Studart, R.G. Pileggi, V.C. Pandolfelli, Maximum paste thickness (MPT) principle applied to high alumina refractory castables, CerâMica. 45 (1999) 24–28.
[16] M.D.M. Innocentini, R.G. Pileggi, F.T. Ramal, V.C. Pandolfelli, PSD-Designed refractory castables, Am. Ceram. Soc. Bull. 82 (2003) 9401–9406.
[17] ASTM C150, Standard Specification for Portland Cement, 2018.
[18] ASTM C39, Standard Test Method for Compressive Strength of Cylindrical Concrete Specimens, 1999.
[19] C.F. Ferraris, P. Billberg, R. Ferron, D. Feys, J. Hu, S. Kawashima, E. Koehler, Role of Rheology in Achieving Successful Concrete Performance, ACI Comm. 238. 39 (2017) 43–51.
[20] D. Han, R.D. Ferron, Influence of high mixing intensity on rheology, hydration, and microstructure of fresh state cement paste, Cem. Concr. Res. 84 (2016) 95–106.
[21] P.K. Mehta, P.J.M. Monteiro, Concrete: Microstructure, Properties, and Materials, McGraw-Hill, 2006.

International Conference on Sustainable Materials, Systems and Structures (SMSS 2019)
Novel Methods for Characterization of Materials and Structures
20-22 March 2019 – Rovinj, Croatia

COMPARISON OF METHODS FOR IN SITU CONCRETE COMPRESSIVE STRENGTH ASSESSMENT

Marijan Skazlić (1), Ivan Gabrijel (1)

(1) Univeristy of Zagreb, Faculty of Civil Engineering, Materials Department

Abstract

Paper presents a case study made during construction of two high-rise buildings in Zagreb, the capital of Croatia. Concrete compressive strength assessment was determined by two different non-destructive test (NDT) methods (pull-out testing and schmidt hammer). Parallel with NDT concrete strength tests cube testing was also done.

An analysis of the results obtained show a correlation between pull-out and schmidt hammer strength and concrete cubes strength at various ages. According to the results obtained, a comparison of different NDT methods for early age strength assessment was made. It is recommended that a pull-out testing method can be successful used for early age determination of concrete compressive strength in structure.

Keywords: concrete strength, non-destructive test methods, pull-out testing, schmidt hammer

1. INTRODUCTION

Compressive strength is a basic concrete property. Early age concrete compressive strength is determined mainly to achieve greater process efficiency and overall speed of construction. It is required that the concrete should have certain compressive strength necessary for striking of props and for pre-stressing; additionally, compressive strength is used to define the quality of the protective layer and assess durability properties. When concrete is placed in extreme winter temperatures, knowledge of an actual increase in compressive strength is of crucial importance. There are also different examples when it is important for accurate determination of concrete compressive strength due to lack of technical documentation or in the case of doubt in actual concrete compressive strength.

Early age concrete strength in a structure can be determined by testing control concrete specimens, i.e. cubes 150x150x150 mm or cylinders 150x300 mm, or by using non-destructive (NDT) test methods. Testing of compressive strength on control specimens is performed using the same technique as is applied for the proof determination of the class of the compressive strength at 28 days according to standard HRN EN 12390-3. The main disadvantage of this test method is the fact that compressive strength is tested on the ideal shape of a specimen and consequently does not indicate actual compressive strength of the

concrete in the structure. Additionally, a large number of test specimens, apart from those necessary for the determination of the compressive strength class, put the contractor to an extra expense. [1, 2]

Several different non-destructive test methods are available for testing early age concrete compressive strength in a structure; those most commonly used are schmidt hammer and pull-out testing. Non-destructive determination of concrete compressive strength by schmid hammer is proposed in standard HRN EN 12504-2, and pull-out testing of concrete compressive strength is done in standard HRN EN 12504-3. Compressive strength testing with the schmidt hammer represents a very fast and cheap testing method, but this method is not reliable enough in all cases. For this reason, pull-out test methods are generally used recently, and the pull-out testing method named Lok-test is the most often employed one. In such a test, the force required to extract an expanded metal disc embedded in fresh concrete is measured. An insert is extracted by the load applied onto the stem on which a disk is placed. During the insert extraction, a conic portion of concrete is extracted together with the disk. The extraction force in the pull-out Lok-test has a producer correlation with the compressive strength measured on conventional concrete specimens. [1-4]

This paper presents the test results of early compressive strength employing different test methods, that is to say parallel determinations of compressive strength using conventional specimens, the schmidt hammer and the pull-out test method. Experimental work was done in two steps. In first step laboratory correlation between concrete compressive strength and parameters of non-destructive test (rebound hammer and pull-out force) was done. After that, on-site experimental investigation was made during construction of two high-rise buildings (Fig. 1). Both high-rise buildings have eight storeys above ground.

Figure 1: The experimental work was carried out on high-rise building in Zagorska Street (left) and Radnicka Street (right) in Zagreb, Croatia

2. EXPERIMENTAL LABORATORY WORK

Considering that the test results obtained by schmidt hammer and pull-out test are most affected by the type of aggregate incorporated in the concrete mix, previous tests were carried out on concrete containing the aggregate from the same part of the country. Pervious tests were made in laboratory by parallel testing of concrete compressive strength on control

specimens and NDT test methods (schmidt hammer and pull-out). Figure 2 shows steps in determination of correlation curves in laboratory. Figure 3 shows the test results obtained from the pull-out test and the correlation between these results and the curves defined by Germann Instruments, the manufacturer of the pull-out Lok-test system used. An analysis of the results shows that the correlation curves of the extraction force in the Lok-test, concrete compressive strength obtained in the laboratory and the manufacturer's recommended correlations correspond at satisfactory level.

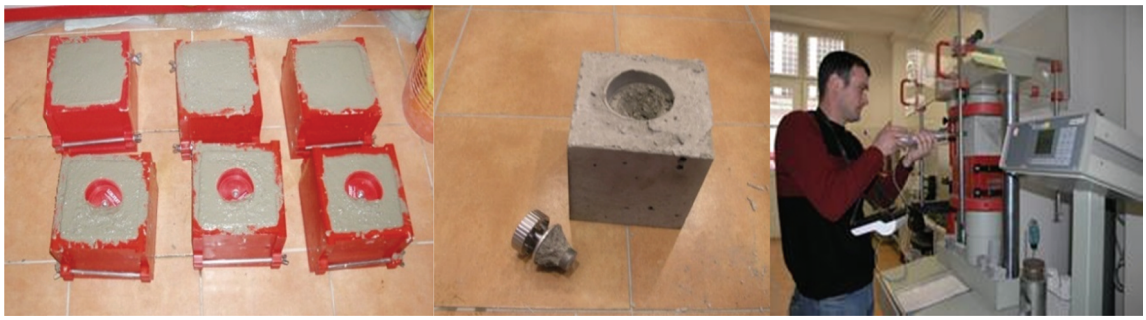

Figure 2: Fresh concrete samples with pull-out inserts (left), hardened concrete sample after pull-out test (middle), and determination of concrete strength with schmidt hammer on 150 mm cube (right)

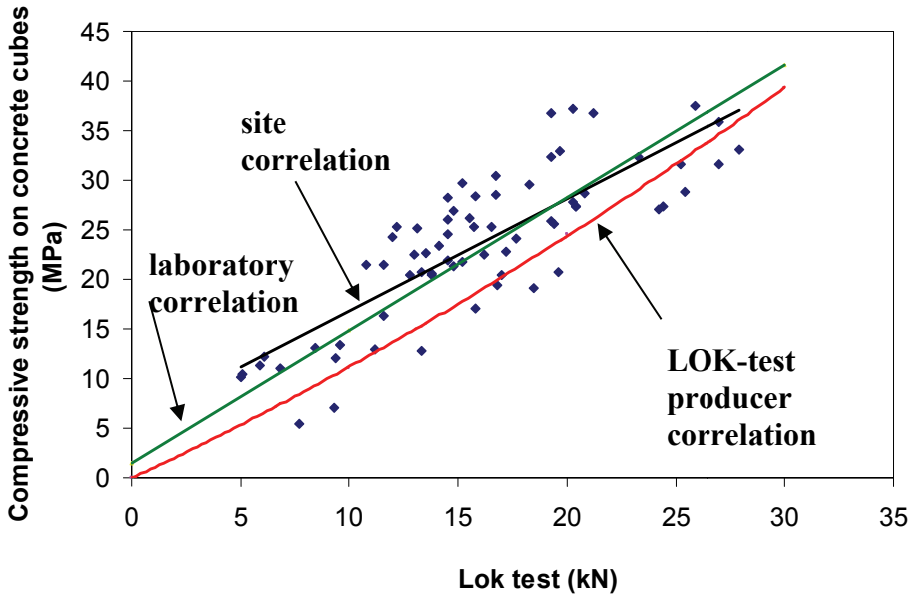

Figure 3: The results obtained from testing with the pull-out test method name Lok-test in laboratory and on-site and the agreement with the correlation curves obtained from the equipment manufacturer

3. ON-SITE COMPRESSIVE STRENGTH ASSESSMENT

The experimental on-site work was carried out on floor slabs of two high-rise buildings in Zagreb. The testing performed is aimed at analysing reliability of various non-destructive test methods (pull-out Lok-test and schmidt hammer) for assessment of early age compressive strength. [5, 6]

Early compressive strength was tested at different ages up to 28 days. All tests were carried out in the summer period, i.e. from April to July.

Parallel compressive strength testing was performed with the pull-out Lok-test, schmidt hammer and 150 mm cubes cast during concrete placement (Fig. 4 and Fig. 5). Tests were carried out only on floor slabs of the structures mentioned above. A total number of 70 parallel compressive strength tests were done on cubes, and with the pull-out Lok-test and with schmidt hammer.

To perform testing with the pull-out Lok-test, plastic inserts were installed in each about 15 m^3 of the concrete slab (Fig.4). During installation, care was taken to avoid the reinforcement and the formation of possible bubbles beneath the insert, which could affect the test results. On the plastic inserts a small quantity of concrete was placed to avoid the action of buoyancy forces that could eject them. The inserts were inclined at 10^o to 15° to the vertical.

Figure 4: The appearance of the floor slab just after concrete placement (left) and that of a plastic insert placed in fresh concrete for the Lok-test (middle), determination of pull-out concrete strength (right)

Figure 5: Testing of concrete compressive strength in the floor slab with the the Schmidt hammer (left), and on 150 mm cubes (right)

Schmidt hammer testing is carried out on clean, plane and dry concrete surfaces. Estimated in-situ compressive strength is an average value of 12 test results. Concrete compressive strength obtained by schmidt hammer was computed from a schmidt hammer rebound index based on an expression obtained from previous tests.

The results illustrated in Fig. 6 show the comparison between different methods for testing concrete compressive strength.

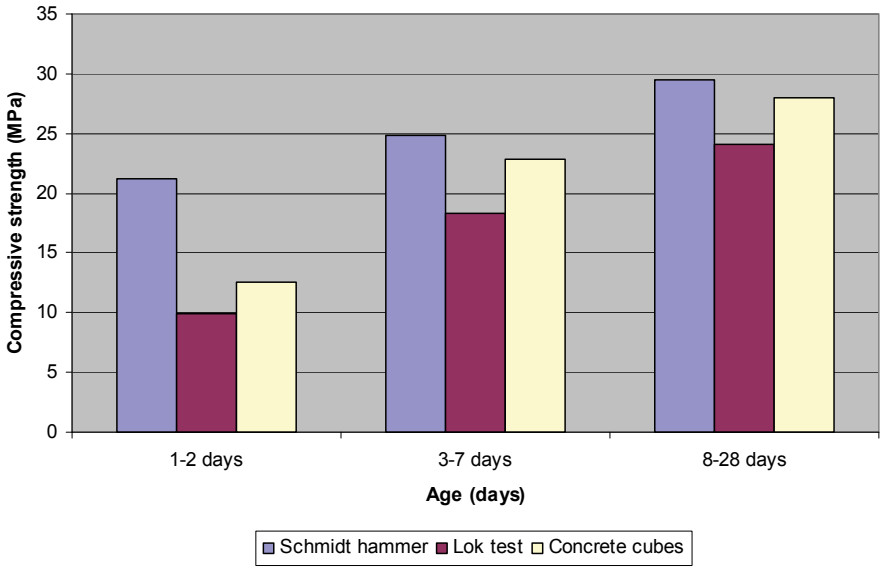

Figure 6: Testing results of parallel determination of compressive strength using concrete cubes, pull-out Lok-test and schmidt hammer on the floor slabs in the high-rise buildings

It is well known that compressive strength in concrete structure is mostly because of curing condition approximately 15 % lower than concrete cube compressive strength. Results present in Fig. 6 show that pull-out Lok-test strength results are 21 %, 19 % and 18 % lower than concrete cubes compressive strength results at concrete age of 1-2 days, 3-7 days and 8-28 days. Testing results from Fig. 6 show that schmidt hammer strengths are 69 %, 9 % and 5 % higher than concrete cubes compressive strength at the concrete age of 1-2 days, 3-7 days and 8-28 days.

Getting results show that pull-out Lok-test method is much more accurate for determining concrete compressive strength than schmidt hammer method. Beside that, Lok-test pull-out method is a good indicator of actual compressive strength of the concrete in structure.

Experience from these tests show that general producer correlation for the Lok-test defined by the manufacturer could be used for testing of concrete strength in structure. The pull-out Lok-test proved to be a very time saving testing method for estimating the concrete compressive strength gain in the structure. Knowledge of in-situ concrete compressive strength at an early age may in high-rise buildings affect the construction procedures by early striking of formwork and props. In this manner the contractor can directly contribute to construction process efficiency and potential savings in the work schedule. In the pull-out Lok-test, it is recommended that the number of inserts and location of tests should be well-

planned whereby the type and importance of the structure should be taken into account since this affects the reliability of testing.

4. CONCLUSIONS

In this paper the results are presented of testing early age compressive strength carried out on the floor slabs in two high-rise buildings. Parallel testing with the pull-out Lok-test, schmidt hammer and 150 mm cubes in the laboratory was performed. On the basis of the test results obtained, the conclusions can be made as follows:

- Prior to starting in-situ testing with a pull-out Lok-test or schmidt hammer, correlation curves obtained from the manufacturer should be verified.
- The reliability of testing can be influenced by planning the number and location of the tests carried out using the pull-out Lok-test and schmidt hammer method depending on the type and importance of the structure.
- The results of concrete compressive strength estimation with the pull-out Lok-test are much more reliable than those obtained with the schmidt hammer.
- Pull-out Lok-test method is a good indicator of actual compressive strength of the concrete in structure.
- In building construction, early compressive strength can be estimated by using the non-destructive test methods. In this way, early striking of props and formwork can contribute to faster and more economical construction.

REFERENCES

[1] Bungey, J.H., Millard, S.G. (1996) "Testing of concrete in structures", Blackie Academic & Professional, Glasgow
[2] Malhotra, V.M., Carino N.J. (2004) "Handbook on Nondestructive testing of concrete", CRC Press, Boca Raton, London, New York,Washington
[3] Petersen, C.G., "'LOK-TEST and CAPO-TEST pullout testing, twenty years experience", http:// www.germann.org
[4] Bungey, J.H., Long, A.E., Soutsos, M.N., Henderson, G.D. (2000) "Early age acceptance of concrete", BRE Report 387, CRC Ltd.
[5] Krnjak, Z. (2007) "NDT testing of concrete strength" (in croatian), Diploma Thesis, Faculty of Civil Engineering, University of Zagreb, Zagreb, Croatia
[6] Baluban B. (2007) "NDT testing of concrete compressive strength by pull-out test method" (in croatian), Diploma Thesis, Faculty of Civil Engineering, University of Zagreb, Zagreb, Croatia

International Conference on Sustainable Materials, Systems and Structures (SMSS 2019)
Novel Methods for Characterization of Materials and Structures
20-22 March 2019 – Rovinj, Croatia

WHAT CAN DROP IMBIBITION INTO GEOMATERIALS TELL US ABOUT THEIR PORE STRUCTURE?

J.-B. d'Espinose de Lacaillerie (1), C. Davy (2), M. Marinova-Atanassova (3), A.-M. Blanchenet (4), F. Lequeux (1), Y. Du (1), Q. H. Nguyen (1)

(1) Soft Matter Science and Engineering laboratory, UMR CNRS 7615, ESPCI Paris, PSL Research University, Paris, France

(2) Centrale Lille and UCCS UMR CNRS 8181, Villeneuve d'Ascq, France

(3) Fédération Chevreul, FR CNRS/Lille1/ENSCL ECL/Lille2/Artois n. 2638, France

(4) UMET, UMR CNRS 8207, Université de Lille, 59655 Villeneuve d'Ascq, France

Abstract

Water ingress into porous materials has a considerable impact on their usage properties. Unfortunately, kinetics of water imbibition into complex porous networks, e.g. Portland cement or geopolymers, are extremely slow, thus precluding characterization of the pore network through usual equilibrium methods. This situation is particularly delicate in the case of geopolymer (GP) cements. They are reputed both mesoporous and macroporous, with a porosity on the order of 15%. It is currently unclear which part of the GP pore network drives fluid imbibition and transport, and hence, their durability.

Useful understanding can be obtained by following the kinetics of spontaneous imbibition of a liquid drop on the surface of a porous material. From simple physical considerations, we show that when the motor for imbibition is capillary suction, imbibition speed is governed more by pore network geometry than by its whole pore size distribution. This allows a certain level of prediction as will be illustrated on a GP paste. Another originality of this contribution is to image the GP pore network at the nanoscale, by using 2D Scanning TEM (STEM) on thinned bulk paste. The two characteristic pore sizes of GP paste are identified and provide insights into pores driving fluid transport.

Keywords: geopolymer, imbibition, pore structure, Scanning Transmission Electron Microscopy (STEM)

1. INTRODUCTION

Water ingress into porous materials has a considerable impact on their usage properties. It can lead to chemical degradation or fluid transfer detrimental to their durability, or to their

efficiency as barriers for contaminants. Unfortunately, the kinetics of water imbibition into complex porous networks, as can be found in Portland cement, geopolymers or natural claystones, are extremely slow [1–4], thus precluding the characterization of the pore network through usual equilibrium methods such as gas adsorption or differential vapor sorption. This is a major obstacle to the fundamental understanding of the mechanism of water ingress. This situation is particularly delicate in the case of geopolymer (GP) cements [5–7]. They are reputed mesoporous and macroporous materials, with two main pore sizes of between 5 and 15 nm and around 2 microns, respectively [3,8–10]. Their porosity is significant, with values up to between 39-46%. It is currently unclear which part of the GP pore network drives fluid imbibition and transport, and hence their durability.

A surprisingly high level of understanding can be obtained by simply following the kinetics of spontaneous imbibition of a liquid drop on the surface of a porous material. From simple physical considerations, we show in this contribution that when the motor for imbibition is capillary suction, the speed of imbibition is governed more by the geometry of the network (e.g. by its tortuosity) than by its whole pore size distribution. This allows a certain level of prediction as will be illustrated on a geopolymer made of pure metakaolin (MK). Aside from the water drop imbibition experiment, one originality of this contribution is to provide novel insights into the pore network of geopolymers at the nanoscale, by using 2D Scanning TEM (STEM) on thinned bulk paste samples. To our knowledge, the only existing imaging data on geopolymer pastes at the nanoscale use 2D full frame bright field TEM [9,10], which tends to damage samples more easily than STEM, due to strong beam interactions.

2. MATERIALS AND METHODS

2.1 Materials

Table 1: X-ray fluorescence results for MK commercial metakaolin

Oxide name	**MK1 (%mass)**	**MK1 (%mol)**
SiO_2	58.4	71.2
Al_2O_3	33.6	24.1
Fe_2O_3	2.2	1.0
K_2O	1.3	1.0
TiO_2	2.89	2.7

A GP paste is made at a stoichiometry of (1 Al_2O_3 . 3.6 SiO_2 . 1 Na_2O . 12 H_2O), with a metakaolin (MK) powder Argical M-1000 (AGS Minerals, France, of nominal chemical formula $2SiO_2{\cdot}Al_2O_3$). The MK powder is alkali-activated with a Betol 52T sodium silicate solution provided by Wöllner (Germany). Table 1 provides X-Ray fluorescence results for the MK powder. The chemical composition of Betol 52T is 2.12 $SiO_2{\cdot}Na_2O{\cdot}12.9\ H_2O$.

Specific preparation protocols are followed to generate the GP samples. The paste preparation consists of two steps. Firstly, stoichiometric amounts of raw materials - Milli-Q water, NaOH pellets and sodium silicate solution- are mixed for 1 h. After obtaining a homogenous solution, the required amount of MK to reach the targeted geopolymer composition is added gradually while mixing manually. The homogenous geopolymer slurry

is then transferred into plastic Petri dishes (Φ=5.5 cm) using a 5 ml syringe. Sample pastes are cured at ambient temperature under autogenous conditions for different durations of 3 days, 10 days and 16 days before drying at room temperature for 18 h. The disk-like geopolymer samples are demoulded so that their size is of about 5 cm in diameter and 2 mm in thickness. The samples are separated into small pieces and conserved individually in sealed storage vessels at 43% RH until used in characterization experiments.

For TEM and STEM imaging, the GP paste is taken after 16 days and further dried by lyophilization. Part of this lyophilized paste is subjected to a nitrogen sorption experiment using an ASAP 2020 apparatus by Micromeritics, with a mass of 1.9g. Prior to conducting the sorption experiment, the powder is degassed at 60°C. First, temperature is increased from the ambient up to 60°C at a rate of 1°C/h, and then let for 4h at 60°C. The equilibration interval between two relative pressure (P/P_0) steps of 0.05 is of 10s. This provides a total pore volume of 0.17 cm^3/g +/- 0.05, so that with an estimated density of 1.1 g/cm^3 [11], this leads to a porosity on the order of 15%.

2.2 Imbibition experiment

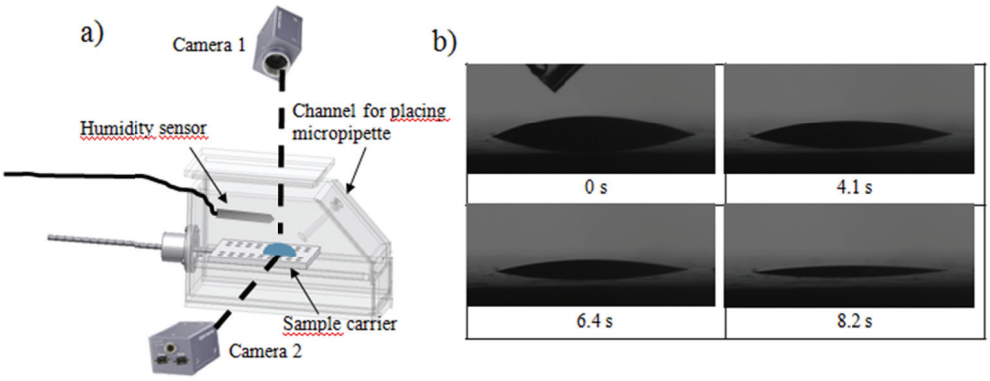

Figure 1: (a) Experimental setup diagram for liquid imbibition tests; (b) a sequence of images showing a droplet impinged on geopolymer.

Liquid imbibition is carried out in a transparent testing box as shown in Figure 1 (a). Relative humidity (RH) is controlled a salt-saturated water solution placed at the bottom of the sealed box. Two different RH are used: 43% and 11%. The samples are placed on a moving sample carrier. At the right side of the box, a channel is designed to lead in a micropipette, that performs the liquid dropping. By adjusting the position of the sample carrier, microliter-sized distilled water droplets can be placed at different spots on the sample surface. The whole process of drop penetration is monitored using a high speed imaging system with two cameras, one above the sample (camera 1) and the other in front of the sample (camera 2). The camera above the sample is used to check that the droplet section remains circular during the experiment duration. The camera on the side is used to measure the droplet radius and contact angle. From the latter, the droplet surface and volume are calculated at each time step (Figure 1 (b)). It is noted that the surface actually does not vary significantly during the experiment duration. It is well known that the disappearance of liquid droplets on a permeable substrate involves liquid evaporation and liquid imbibition. As a

reference, the evaporation rate is quantified by dropping liquid on impermeable silicon wafers. Hence, the imbibition volume can be expressed as:

$$V_{imb}(t) = V_{droplet\ initial} - V_{droplet}(t) - V_{evapo} \quad (1)$$

As a complementary experiment, dynamic water sorption (DVS) is carried out in VTI-SA+ Vapor Sorption Analyzer (TA Instruments) at room temperature. Only one step in RH change is probed, from RH = 43% to RH = 53%. This aims at estimating the necessary time to reach equilibrium, and thus determining the Fickian diffusivity of water vapor within the pore structure. A geopolymer sample cured for 10 days and dried at room temperature is prepared in the form of a cube of side length of 2 mm. The DVS software is programmed to stay at 43% RH for 1 h and then to switch to 53% RH. The measurement criterion dm/dt is selected as 0.0001 % min^{-1}.

2.3 2D Scanning Transmission Electron Microscopy (STEM)

STEM (Scanning Transmission Electron Microscopy) is performed on a Tecnai G2 20 apparatus (FEI, now Thermo Fisher Scientific, NH, USA), at 200kV acceleration voltage. Imaging is performed on the MK powder, simply deposited on the sample holder surface after cryo-slicing. The lyophilized GP paste is and thinned down manually down to about 300 microns, and finished by ion thinning on a Duomill Gatan (CA, USA) apparatus operated under liquid nitrogen with a cold stage sample holder. The final GP sample thickness is below 100nm to achieve electron transparency. Image analysis (cropping, binarization) is performed with the Image J software (by W. Rasband, NIH and LOCI, University of Wisconsin, USA).

3. RESULTS AND DISCUSSION

3.1 Water imbibition

According to Lucas-Washburn model of capillary suction, water imbibition can be modelled according to [12]:

$$\left(\frac{V_{imb}(t)}{S_g}\right)^2 = R_W \frac{\phi^2}{\tau}\frac{\sigma}{2\eta}t = G\, v_i\, t \quad (2)$$

where S_g is the surface of the water drop, R_W is an effective pore radius, Φ is the pore volume fraction, τ tortuosity or retardation factor, σ surface tension and η viscosity. This allows to define a dimensionless geometrical factor G for the porous solid, and a characteristic imbibition speed v_i for the fluid. The surface tension and viscosity being known, geometrical factor G are obtained from the imbibed volume at each time step (Figure 2). This analysis is validated by the expected fact that geometrical factor G does not vary with time. Furthermore, replacing water by dodecane, which is an imbibition liquid of different surface tension and viscosity than water, did not significantly affect the results.

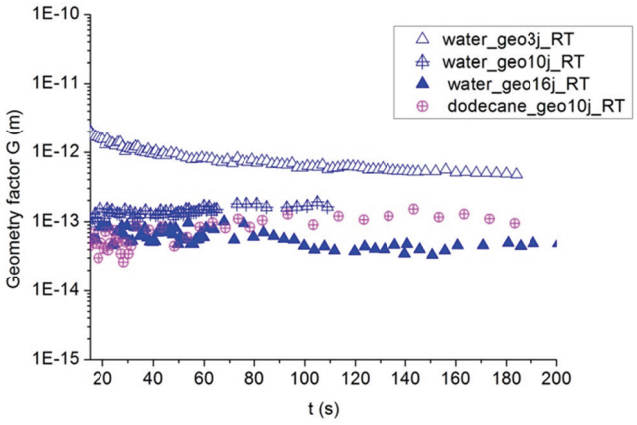

Figure 2: Geometrical factor G calculated from water or dodecane imbibition tests for geopolymer samples with different curing times.

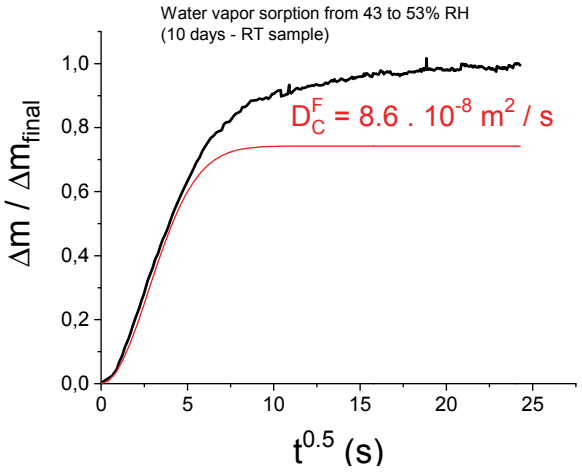

Figure 3: Relative mass variation as a function of square root of time during water vapour sorption from 43 to 53%RH, performed by DVS (in black) for a sample cured for 10 days at room temperature (RT), compared to a Fickian model (in red).

Geometrical factor G in our geopolymers is thus determined to range between 10^{-3} and 10^{-2}. From DVS experiment (Figure 3), and considering that the early part of adsorption follows a Fickian regime, the ratio of porous fraction ϕ to tortuosity τ can be obtained by comparison with water vapour diffusion coefficient (see for example [13]):

$$\frac{D_C^F}{D_{VAP}} = \frac{\phi}{\tau} = 3.6 \cdot 10^{-3} \qquad (3)$$

Combining this value to the geometrical factor from the imbibition experiment, one estimates the product of the effective pore radius to the pore volume fraction, as within the following range:

$$R_W\phi = \frac{G}{\frac{\phi}{\tau}} \approx \frac{10^{-13} - 10^{-12}}{3.6 \,.\, 10^{-3}} m \approx 3.10^{-2} - 3.10^{-1} nm \tag{4}$$

3.2 GP pore structure supporting the water imbibition results

The MK powder used to manufacture the GP paste is presented in Fig. 4 below. The two main noticeable features of this MK are its significant proportion of amorphous shapeless matter, combined with stacked platelets of varying thickness, up to more than one micron.

In relation to these observations, the first general views of the GP paste show the presence of a continuous dense paste surrounding isolated elongated pores (Fig. 5). These isolated pores are up to four microns length and three microns width, i.e. they are macroporous. They are also consistent with the macropores identified by Benavent et al. [3] on similar GP paste formulations (1 Al_2O_3 . 3.6 SiO_2 . 1 Na_2O . 13 H_2O), which were not connected together, i.e. these pores were not percolating. When selecting a square of 2 microns size inside these elongated macropores (this is called cropping, see Fig. 6 left), a proportion of 10.5% of the area is obtained after binarization (Fig. 6 right).

More interestingly, the macropores are surrounded by a continuous paste, which pores are observed in Fig. 7 at a much higher magnification of x320k. The image shows qualitatively the presence of pores several tens of nm diameter, and even pores of only a few nm size. As analyzed by Benavent et al. in bright field TEM (i.e. without any actual surface relief) [3], the morphology of these mesopores is wormlike, with a cylindrical form (i.e. with a quasi-spherical cross section). On an area of about 100 nm x 200 nm, their proportion is significant, and of around 13.8% (Fig. 8). Being the only percolating (i.e. connected) porosity, these mesoscale pores are bound to drive fluid transport, and particularly imbibition. They represent a very close porosity to that found by nitrogen adsorption.

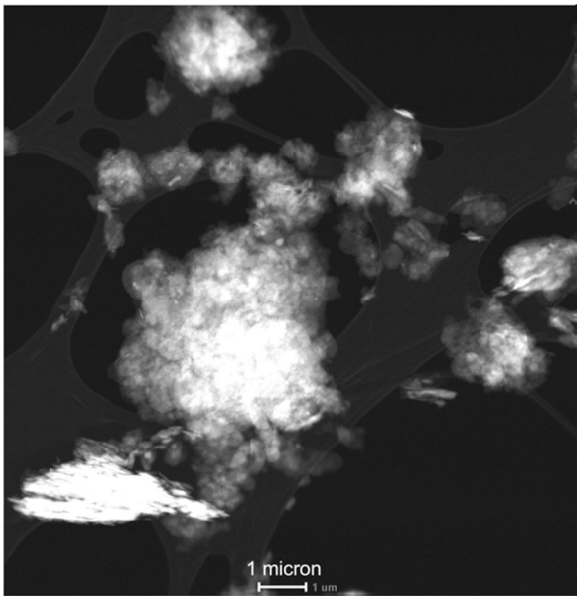

Figure 4: Observation by 2D STEM (at a magnification of x10k) of the MK used to manufacture the GP presented in Fig. 2. A particle made of stacked platelets of more than 1 micron thickness is seen at the bottom left of the image.

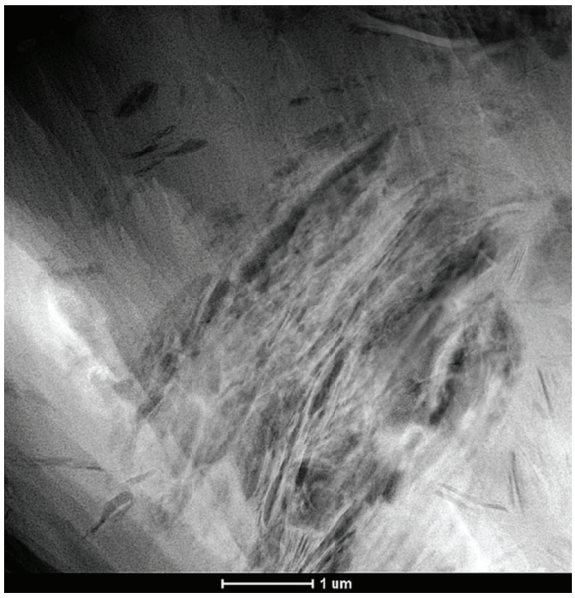

Figure 5: General view of a geopolymer paste by 2D STEM (at a magnification of x10k).

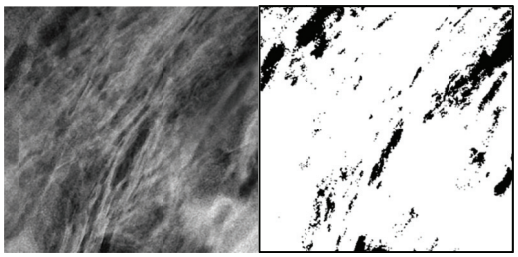

Figure 6: Crop (left) and binarization (right) of the image presented in Fig. 2, aiming to extract a lower limit of pore proportion (it represents 10.5% of the image area).

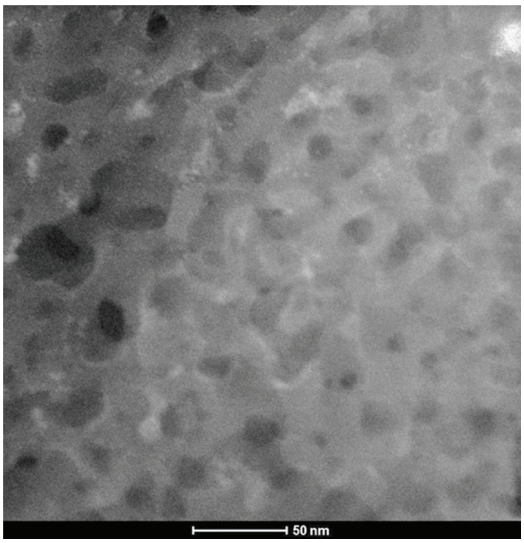

Figure 7: Observation of the dense GP structure seen in Fig. 2 by 2D STEM (at a magnification of x320k).

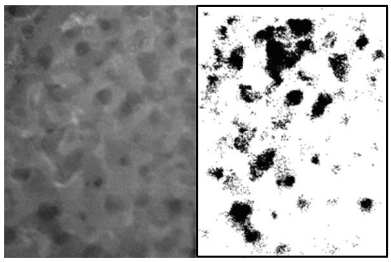

Figure 8: Crop (left) and binarization (right) of the image presented in Fig. 4, aiming to extract a lower limit of pore proportion (it represents 13.8% of the image area).

4. CONCLUSIONS

2D STEM images (Figures 5 and 7) give a lower limit of the pore volume fraction Φ around 0.10-0.138, in good agreement with nitrogen adsorption results. From imbibition data, this leads to a higher limit for the effective pore radius of $R_W \approx \frac{3.10^{-2} — 3.10^{-1}}{\phi} nm \approx 0.2 — 2\ nm$.

Looking at STEM images, this value is obviously too small to correspond to an average pore value and highlights the fact that capillary imbibition cannot be determined by the pore size itself but by constrictions, which delay capillary suction by interface pinning at pore openings [14]. If needed, this is further demonstration that large mesopores do not contribute significantly to water ingress into multiscale porous materials.

ACKNOWLEDGEMENTS

The SEM and TEM national facilities available at the Centre Commun de Microscopie de Lille (France) are supported by the Conseil Régional du Nord-Pas de Calais, and by the European Regional Development Fund (ERDF).

REFERENCES

[1] Chen W., Liu J., Brue F., Skoczylas F., Davy C. A., Bourbon X., Talandier J., Cem Concr Res, **42** (2012) 1001-1013.
[2] Davy C. A., Hauss G., Planel B., Lambertin D., Journal of the American Ceramic Society, doi: 10.1111/jace.16142, in press, 2018.
[3] Benavent V., Frizon F., Poulesquen A., Journal of Applied Crystallography **49** (2016) 2116-2128.
[4] Davy C. A., Skoczylas F., Barnichon J.-D., Lebon P., Phys Chem Earth **32** (2007) 667-680.
[5] Provis J.L., and Van Deventer J.S.J., eds,, Woodhead Publishing in Materials: Cambridge, UK, 2009.
[6] Davidovits J., J Therm Anal. **37**(8) (1991) 1633-1656.
[7] Duxson P., Fernandez-Jimenez A., Provis J. L., Lukey G. C., Palomo A., van Deventer J. S. J., J. Mater. Sci. **42**(9) (2007) 2917-2933.
[8] Thommes M., Kaneko K., Neimark A. V., Olivier J.P., Rodriguez-Reinoso F., Rouquerol J., Sing K.S.W., IUPAC Technical report, Pure Appl. Chem., 19p., 2015.
[9] Duxson P., Mallicoat S. W., Lukey G. C., Kriven W. M., van Deventer J. S. J., Colloids and Surfaces A: Physicochem. Eng. Aspects **292** (2007) 8–20.
[10] Lee S., Jou H. T., van Riessen A., Rickard W. D. A., Chon C. M., Kang N. H., Construction and Building Materials, **52** (2014) 221-226.

[11] Nguyen Q. H., Lorente S., Duhart-Barone A., Lamotte H., Construction and Building Materials **191** (2018) 853–865.
[12] Gruener S., Hofmann T., Wallacher D., Kityk A.V., Huber P., Phys. Rev. E. **79** (2009) 067301.
[13] Saeidpour M., Wadsö L., Cem. Concr. Res. **69** (2015) 88–95.
[14] Wiklund H. S., Uesaka T., Phys. Rev. E. **87** (2013) 023006.

International Conference on Sustainable Materials, Systems and Structures (SMSS 2019)
Novel Methods for Characterization of Materials and Structures
20-22 March 2019 – Rovinj, Croatia

MEASURING RATE EFFECTS ON INTERNAL DAMAGE AND FRACTURE OF ULTRA HIGH-PERFORMANCE CONCRETE

Yi Peng (1), Dmitry Loshkov (1) and Eric N. Landis (1)

(1) Advanced Structures and Composites Center, University of Maine, USA

Abstract

Ultra-high-performance concrete (UHPC), with appropriate fiber reinforcement, is proving to be a versatile material for applications in which the added cost can provide much needed benefits. Adding sufficient quantities of ductile fibers into a brittle matrix such as concrete has long been known to transform a brittle material to a relatively ductile one. That transformation is made possible by a number of well-known toughening mechanisms including, fiber-matrix debonding and pull-out, additional matrix cracking, as well as fiber bending and fracture. In this project, UHPC specimens were loaded in a split-cylinder configuration. Prior to loading, all specimens were scanned using x-ray computed tomography (CT) so that fiber alignment, as well as other internal features could be mapped. Specimens were then subjected to either quasi-static loading or drop-weight impact loading. Post-test CT scans were conducted so that internal cracking and damage could be measured along with any other changes in internal structure. The experimental results show the effect on loading rate and the corresponding shifts in energy dissipation mechanisms.

Keywords: Ultra high-performance concrete, fracture, impact

1. INTRODUCTION

Fiber reinforced cementitious composites have long been known to have added ductility and toughness compared to traditional portland cement concrete. The fibers effectively provide energy dissipation, or toughening mechanisms that are not available to the unreinforced counterparts. These mechanisms include not only the pullout and stretching of the fibers, but the additional matrix cracking that result from the fibers bridging cracks.

While these toughening mechanisms have been qualitatively well know for many years, quantitative analysis has been limited. Previous work has focused on measuring the relative contributions of the different toughening mechanisms to the overall energy absorption capacity of the material in both bending [1] and split cylinder [2]. In the prior work, all loading was done under quasi-static conditions. In the work presented here, we extend our analysis to specimens tested under impact conditions as well. The specific objective is to

examine differences in how the material dissipates energy under impact versus quasi-static loading. The hypothesis to be tested is that there is a shift in internal toughening from a fiber pullout dominated mechanism under the quasi-static loading, to a matrix cracking dominated mechanism under impact loading.

2. MATERIALS

Materials used for this study were developed by the US Army Corps of Engineer Research and Development Center (ERDC). Table 1 shows the mixing proportion by weight [3]. Two types of reinforcing steel fibers were used: one is hooked end Dramix (ZP 305) steel fiber with 30 mm length and 0.55 mm diameter; the other is straight brass-coated steel fiber with 12 mm length and 0.20 mm diameter. Specimens with hooked end fibers, with brass coated fibered, and without reinforcing fibers are called Z specimens, B specimens, and U specimens, respectively. Twelve cylinders were cast, including five hooked end fiber reinforced, five brass coated fiber reinforced, and two unreinforced. The cylinders were nominally 50 mm diameter and 100 mm length.

Table 1: Mix proportions for UHPC cylinders

Materials	Proportion by Weight
Cement	1.00
Sand	0.97
Silica Flour	0.28
Silica Fume	0.39
Superplasticizer	0.018
Water	0.21

Prior to any mechanical testing, cylinders were scanned using x-ray Computed Tomography (CT) to measure internal structure. Specifically, the CT images were analyzed to measure fiber alignment, which has been shown to be critical to specimen performance [4] [5]. 3D renderings of CT data is shown in Fig. 1. Each cylinder was then cut into two specimens, each 43 mm in length. Both the top and bottom of the cylinder were trimmed off to eliminate boundary effects due to casting. The CT images were also cropped so that they consisted of only the volumes in the 43-mm long specimens.

For each shortened reinforced specimen, fiber orientation analysis was used to evaluate the optimum and pessimum orientation for the particular loading condition. The optimum and pessimum orientations represent the position in which the fibers will have the maximum and minimum resistance to tensile stresses [2]. If the fibers orientations were perfectly random, there would be no difference between optimum and pessimum orientation, but since real specimens tend to have a slight preferential alignment, the optimum and pessimum can be used to bound the effects of fiber alignment.

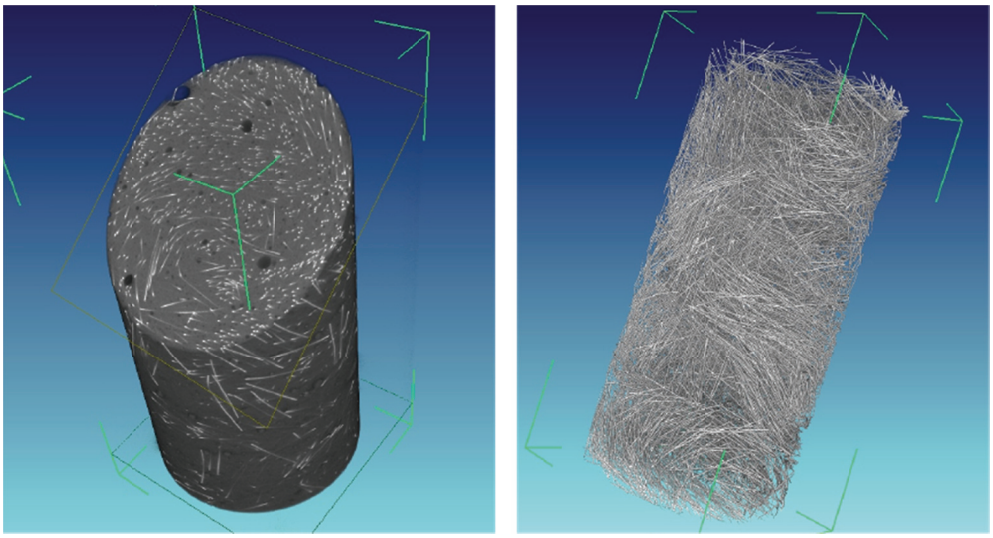

Figure 1: Renderings of CT data, showing UHPC matrix (left) and fibers only (right).

3. EXPERIMENTS

3.1 Quasi-static testing

Quasi-static split cylinder testing was performed following ASTM496/C496M-17, Standard Test Method for Splitting Tensile Strength of Cylindrical Concrete Specimens [6]. Small test fixture modification was made to match the quasi-static and impact testing needs.

A full testing setup is shown in Fig. 2 on the left, where two Linear Variable Differential Transformers (LVDTs) and mounted on either side of the testing plane to account for a more accurate deformation. The top loading plate is mounted on a ball joint to allow self-alignment during loading. A detail of the test setup modification is shown in Fig. 2 on the right, where the specimen was placed in between a set of angles which secure its position. A set of rubber pads were glued on the angle faces to minimize any potential added stiffness in the lateral direction during loading.

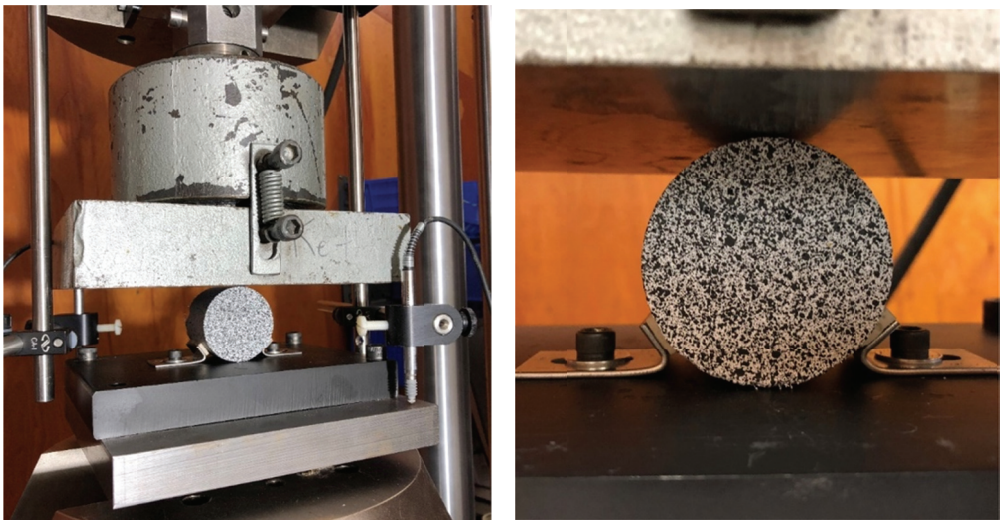

Figure 2: Overall (left) and detail (right) of quasi-static test setup.

Prior to testing a random speckle pattern was applied to one side of the specimen to facilitate DIC full field strain measurements.

The test was conducted on an Instron frame with maximum capacity of 55 kip (245 kN). The testing was program through WaveMatrix platform. The test used position control at loading rate of 0.01 mm/s, load until 10% reduction from peak load, then unload with rate of 0.03 mm/s. The test was terminated once the specimen was no longer in contact with loading plate. All specimens were under loading for approximately 3 minutes with designed loading and unloading rates, which minimized the creep effects.

3.2 Drop-weight impact test

All impact testing was performed with an Instron CEAST 9350 drop-weight impact system, and CEAST DAS 64 K data acquisition system. Total of seven cylinders (14 specimens) were tested. Among these cylinders, three were reinforced with Z fibers, three with brass coated fibers. One cylinder without reinforcement was also tested.

Test parameters and configuration of impact system includes: a two-inch diameter flat face tup insert, where tup mass of 1.4 kg with additional mass of 2.0 kg, and along with tup nominal mass of 1.29 kg, for a total of 4.49 kg impact mass was used. Pretrigger was set to 500, with data collection frequency of 4000 kHz, and total data point limit of 12000 which is 3 micro seconds. Automatic offset points of 100, with a trigger type of rise global. Input energy varied among specimens, and the test matrix is summarized in Table 2.

The testing setup includes a custom-made steel plate with angles covered by rubber as shown in Fig. 3. The rubber padded angle provides guidance for each specimen to be place at the right location for loading and also to prevent specimen form moving before loading. Clear tape was used to prevent specimen from bouncing off the loading plate after impact.

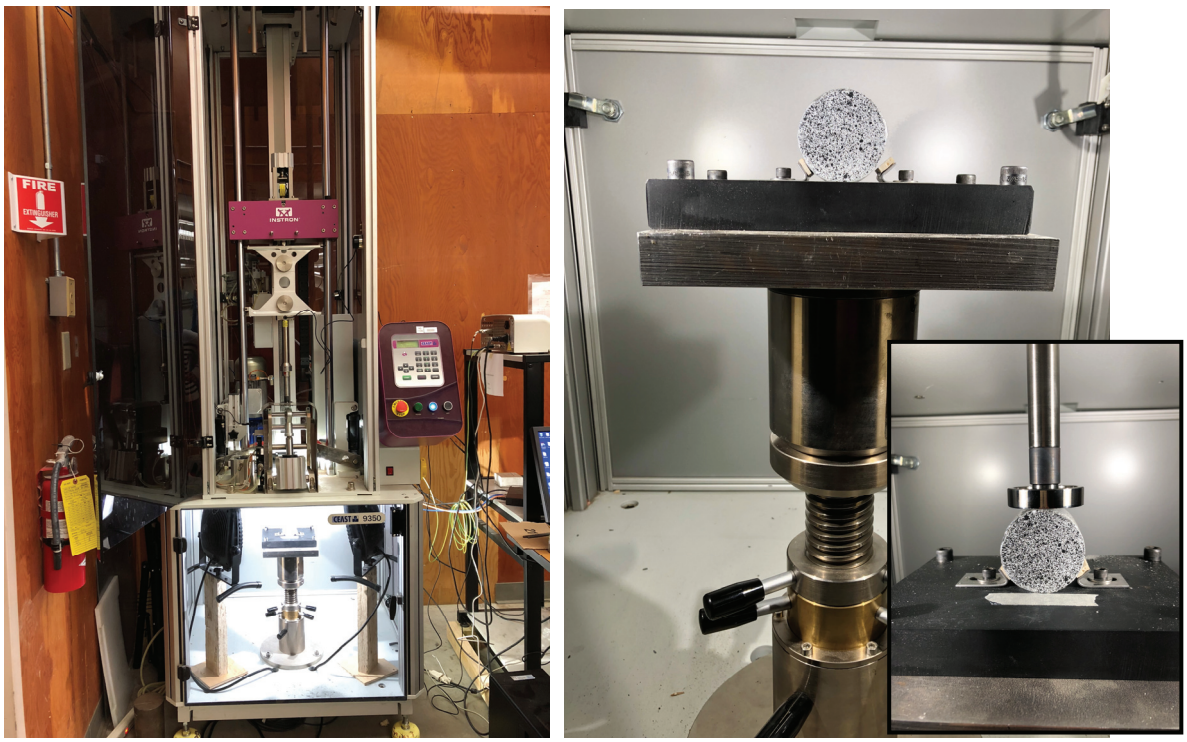

Figure 3: Overall and details of impact test setup.

Table 2: Test matrix

Specimen Type		Input Energy (J)	Input Energy (J)	Input Energy (J)
Z fiber	Optimum	35	50	60
	Pessimum			
B fiber	Optimum	35	50	60
	Pessimum			
Unreinforced		15		

4. RESULTS & DISCUSSION

A sample load-deformation plot for a quasi-static test is shown in Fig. 4. The test protocol was established such that the specimen would continue to be deformed until the load dropped to roughly 90% of peak load, then the specimen would be unloaded. Of greatest interest for the work here is the total energy dissipated by the specimen during loading, which can be defined by the area under the load-deformation curve, less the area of elastic unloading. (The net energy dissipated is shown as the shaded area in Fig. 4.

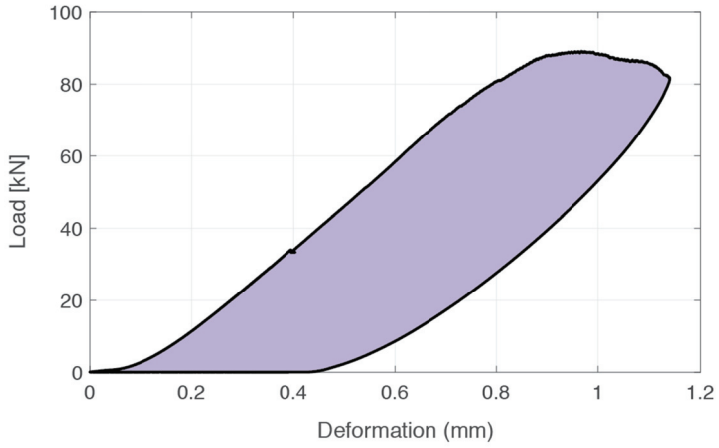

Figure 4: Typical load-deformation plot with net energy dissipated (shaded area).

Table 3 summarizes the net energy dissipation for all specimens tested. As expected, specimens loaded in the optimum orientation dissipated more energy than those loaded in the pessimum orientation. Typically the added energy was due to higher peak loads for the optimally oriented specimens, as is indicated in the table.

Table 3: Quasi-static split cylinder test results

Specimen Type	Net Energy Dissipated (J)		Peak Load (kN)	
	Optimum	Pessimum	Optimum	Pessimum
B	30	29	79	78
	31	20	85	72
Z	38	37	89	85
	55	41	86	79
U	16		36	

It should be noted that the results shown in Table 3 reflect to a certain degree, the degree of fiber randomness. In both the B and Z specimen series, one specimen optimum/pessimum pair had very similar energy dissipation, and one specimen pair had very different energy dissipation. For the specimens in which the optimum and pessimum are very similar, the fibers are more randomly oriented, while for the specimens in which the optimum and pessimum are very different, the fibers are more aligned.

The net energy results from the quasi-static loading were used in part to inform the choice of impact energy for the drop weight testing. As displayed in Table 2, specimens were loaded with three different impact forces sufficient to bound the net energy dissipation of the quasi-static tests. However, it should be noted that not all of the impact energy is dissipated by the specimen. The estimated absorbed energy values were determined from recorded impact force data. In this analysis, energy values were calculated as the area under force curve in force vs deformation graph, and the dissipated energy also considered the deformation velocity and force at a given time. As the striker tip bounces off the specimen, the velocity is in the upwards (negative) direction, which can be understood as the recovery of elastic deformation. The permanent deformation or the damage of the specimen represents the results of absorbed energy during the impact event. Table 4 illustrates the difference between the energy of the impact and the energy absorbed by the specimen.

Table 4: Estimated absorbed energy

Specimen Type		Input Energy (J)	Absorbed Energy (J)	Input Energy (J)	Absorbed Energy (J)	Input Energy (J)	Absorbed Energy (J)
Z fiber	Optimum	35	31	50	45	60	53
	Pessimum		31		44		54
B fiber	Optimum	35	31	50	43	60	51
	Pessimum		31		44		51
Unreinforced		15	15	15	14		

All tested specimens, whether quasi-static or impact, were re-scanned with the x-ray CT system to evaluate internal damage. Example results for two B series specimens are shown in Figs. 5 and 6. The images in these figures are cross sectional slices taken through both a specimen loaded quasi-statically (Fig. 5) and impact (Fig. 6). The images are oriented such that the split cylinder loading is along a vertical axis at the center of the specimens. Of particular interest here is that both specimens dissipated nominally the same energy, around 30 J. However, the internal damage is quite different.

In the quasi-static specimen, (Fig. 5), a major crack is clearly visible in the cross section, with several branches at both the top and the bottom. Whereas in the impact specimen, (Fig. 6), there is only a faint hairline crack visible in the image. This indicates differences in internal energy dissipation since both specimens absorbed the same energy. An initial qualitative conclusion is that there must be a shift in internal energy dissipation between the quasi-static and the impact loading. If this is indeed the case, we could accept the hypothesis presented in section 1.

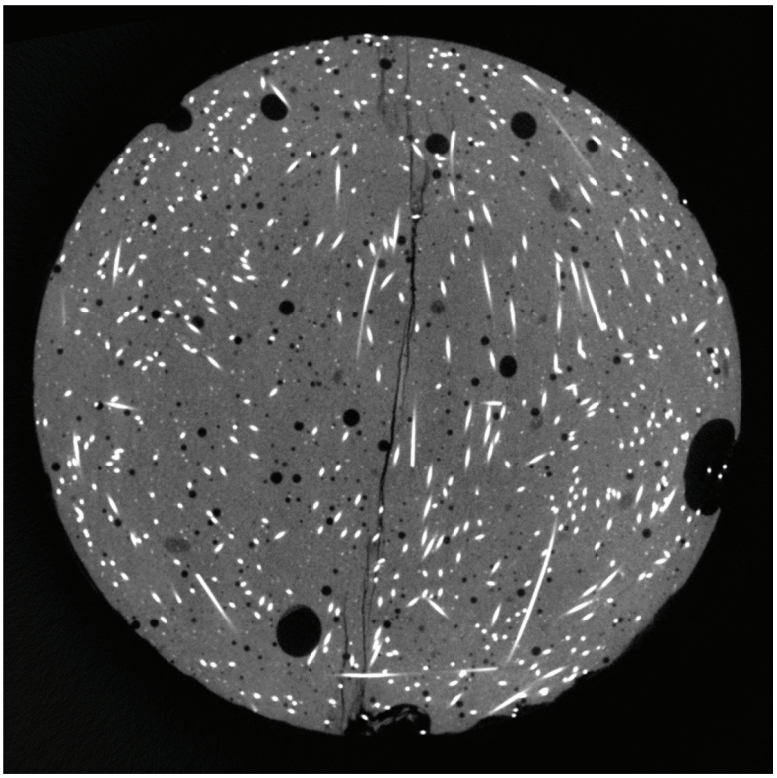

Figure 5: Slice image of quasi-static loaded specimen.

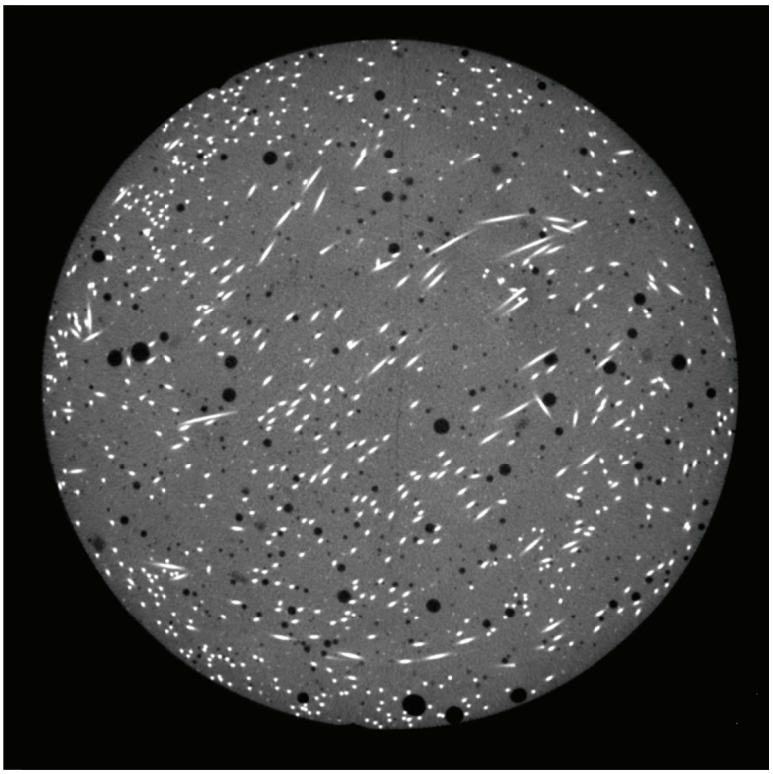

Figure 6: Slice image of impact loaded specimen.

The shift in internal energy dissipation is most likely as follows. In the quasi-static tests, the deformation process is slow enough so that beyond matrix cracking, the specimen can mobilize the additional energy dissipation of fiber pullout, which requires larger crack openings to be significant. In the impact tests, the specimen is not able to deform as quickly, and as a result, crack openings are smaller and fiber pullout less significant. However, in order for the specimen to actually dissipate the energy, we must assume that there are many more smaller cracks that unfortunately are below the resolution of the CT instrument.

5. CONCLUSIONS

The work presented here demonstrates a qualitative shift in the internal energy dissipation mechanisms for specimens subjected to different loading rates. From x-ray CT scans of undamaged and damaged specimens, it is clear that quasi-static load rates produce larger, more highly visible cracks, while a higher loading rate produces smaller crack sizes. Such a shift suggests that fiber pullout contributes more to internal energy dissipation in the former than it does in the latter. While this conclusion is based only on qualitative assessment, current work is underway to emply 3D digital volume correlation (DVC) to measure residual deformations in the CT images as a way to potentially identify cracks that are below the resolution of the instrument.

REFERENCES

[1] K. J. Trainor, B. W. Foust, and E. N. Landis, "Measurement of Energy Dissipation Mechanisms in Fracture of Fiber-Reinforced Ultrahigh-Strength Cement-Based Composites," *J. Eng. Mech.*, vol. 139, no. 7, pp. 771–779, Jul. 2013.

[2] E. N. Landis, R. Kravchuk, and D. Loshkov, "Experimental investigations of internal energy dissipation during fracture of fiber-reinforced ultra-high-performance concrete," *Front. Struct. Civ. Eng.*, Jun. 2018.

[3] E. M. Williams, S. S. Graham, P. A. Reed, and T. S. Rushing, "Laboratory Characterization of Cor-Tuf Concrete With and Without Steel Fibers," U.S. Army Engineering Research and Development Center, technical ERDC/GSL TR-09022, Jul. 2009.

[4] T. S. Oesch, E. N. Landis, and D. A. Kuchma, "Demonstration of Fiber Anisotropy in Fiber-Reinforced Concrete Structures using X-Ray CT," *Mater. Struct.*, vol. 51, no. 3, 2018.

[5] A. B. Groeneveld, T. M. Ahlborn, C. K. Crane, C. A. Burchfield, and E. N. Landis, "Dynamic strength and ductility of ultra-high performance concrete with flow-induced fiber alignment," *Int. J. Impact Eng.*, vol. 111, pp. 37–45, Jan. 2018.

[6] "C496C496M-17 Standard Test Method for Splitting Tensile Strength of Cylindrical Concrete Specimens." ASTM International, 2017.

International Conference on Sustainable Materials, Systems and Structures (SMSS 2019)
Novel Methods for Characterization of Materials and Structures
20-22 March 2019 – Rovinj, Croatia

ROUGHNESS MEASUREMENT OF COARSE NATURAL AGGREGATES BY INTERFEROMETRY AND ITS VARIABILITY

Paulo H. F. Loz (1), Sérgio C. Angulo (1) and Vanderley M. John (1)

(1) University of Sao Paulo, Escola Politécnica, Brazil

Abstract

The aggregates roughness increases the fracture energy in the interfacial cement paste-aggregate region of concrete. However, it reduces workability of concrete, due to high internal friction of particles on the cement paste. Although a relevant parameter, most techniques evaluate roughness qualitatively, or it is not performed in a multi-scale analysis. Therefore, in this paper, we aimed to evaluate the roughness of natural coarse aggregates (granite and quartzite) quantitatively. Internal microstructure images of the aggregates were also used to support roughness results analyzes. Surface indexes of the natural aggregates presented significant variation, even when measured in just one particle. The indexes of the two aggregate types were not statistically different; however, granite particles presented slightly variable results, due to heterogeneous microstructure. Aggregate particles with high surface indexes presented a wider range of crystals sizes and types on the microstructure whereas aggregate particles with low surface indexes were more homogeneous in both microstructural aspects. The natural aggregates roughness seems to be related with its microstructure.

Keywords: roughness, interferometry, coarse aggregates, microstructure.

1. INTRODUCTION

The roughness of aggregates enhances the bonding forces in the interfacial transition zone (ITZ) between the cement paste and the aggregate, resulting in a higher fracture energy composite [1–4]. On the other hand, rough aggregates create more friction between particles, increasing concrete viscosity and reducing workability [1,5,6]. The increase on water demand (or additive consumption) is necessary to ensure similar workability of concrete. There is no consensus on which factor (positive or negative) prevails in the performance of the cementitious materials.

The geometric property that describes the aggregate surface texture is the roughness [1]. Many factors influence of the surface roughness of aggregates, such as the crushing process

(compression, impact, shear, etc.) [1,7], the hardness of the parent rock and its internal microstructure.

Surface roughness evaluation can be carried out by qualitative or quantitative methods [8,9]. Qualitative methods define roughness by visual and tactile observation of the surface [5,10,11]; those results are not numerical and strongly affected by the practitioner. Quantitative methods measure surface features such as height, spacing, and position of peaks, valleys, craters, grooves, and steps, at millimeter-micrometric and even nanometric scales [8,12]. Data obtained by 3D techniques seems to be more representative than those obtained by a 1D (profilometry) or 2D (image) techniques [13].

Most quantitative techniques employed in aggregates have several limitations. Stylus profilometry, the classic one-dimensional method, is strongly affected by tip size, pace and surface irregularities [12]. Various published results on aggregate roughness used this technique [3,14,15]. The University of Illinois Aggregate Image Analyzer (UIAIA) [16] and Aggregate Imaging System (AIMS) [17] methods can be considered the most comprehensive ones, even though they have limitations on the scale (due to the camera resolution). Those methods quantify roughness and this information is simultaneously considered in shape and angularity analyses of the particles. This makes hard to separate the specific contribution of each one of these parameters [3,18].

In this context, the laser interferometry is a suitable alternative technique since it provides 3D data and determines roughness by a multi-scale analysis (from nm to μm). So, the roughness parameter can be separated according to the scale, in macro (mm), micro (μm) and even nano-roughness (nm). In the interferometry technique, a light beam is pointed to a surface that reflects in a specular way, when this surface is smooth, or, in a diffused way appearing as fringes through the camera lens, when the surface is rough. The camera captures these fringes and generates surface characterization data [19]. However, this technique can be only applied to reflective surfaces.

This paper aims to evaluate quantitatively the roughness of two types of coarse natural aggregates (granite and quartzite), using the interferometry technique. The technique generates 3D surfaces of the particles. These results were compared to the particle parent rock internal microstructure; thus, allowing us a better understanding of how both parameters are associated.

2. MATERIALS AND METHODS

2.1 Coarse aggregates types

Two types of natural aggregates were studied, a granite and quartzite-type, collected at the metropolitan region of São Paulo. Granite is the most used aggregate type in Brazil (85%) [20]. Granite is an igneous rock, composed mainly of quartz, feldspar, and mica. Quartzite, although less used gives useful information about how quartz microstructure can influence roughness. Quartzite is a metamorphic rock that contains interlocked quartz crystals, obtained from the recrystallization of sandstone. Both aggregates were crushed by jaw or rotary crushers, both through a compression mechanism. So, the crushing process is not a relevant factor for analysis in this work. Samples were collected and their mass reduced representatively using proper quartering technique [21].

2.2 Measuring roughness by Interferometry

The experimental procedure to measure the roughness of aggregates by interferometry was developed by our research group - the Laboratory of Microstructure and Eco-efficiency of Construction Materials (LME) - University of Sao Paulo, being published in reference [22].

Surface topography of aggregates was generated with a Bruker NPFlex 3D Optical Microscope, using vertical scanning interferometry (VSI) modulus and an anti-vibration system. A green light laser and a Mirau [23] objective of 5x and a multiplier of 0.55x were used. The reachable resolution in this configuration is 3.642 µm/pixel. 3D image stitching was used to generate surface area bigger than that observed by the field of view of the lens (2.331 x 1.748 mm²). For each particle of aggregate analyzed, we produce a 3D surface of 5 x 5 mm².

To reduce the measurement time for each particle, measurement of corners and edges were avoided. These regions present the highest roughness values, probably due to its sharp angles and being more related to shape or angularity parameters of the particles. The data interpretation was performed using built-in software (Bruker Vision64). A gaussian robust filter of 0.25mm was applied to remove the waviness of the surface. The measurement of each particle took about 30 minutes.

There is a great diversity of roughness parameters available on the Vision64 software, but the one that is usually adopted for the study of the roughness of brittle and cementitious materials is the surface index (S_I), also called roughness number (RN) [24,25]. This parameter is obtained by fitting triangles between the measured points that provide the actual surface area (A_A) (Figure 1). Then a dimensionless ratio is formed by this area and a flat projection area of the same surface (P_A) (equation 1). The software calculates both areas excluding all non-detected points. S_I value is ≥ 1, where 1 is a smooth surface. The greater the spatial complexity of the surface is, the larger S_I will be, being affected by both the roughness and the spacing between peaks and valleys [26].

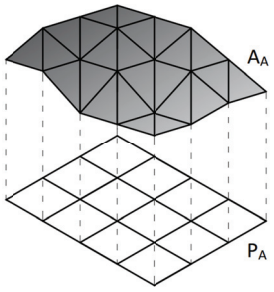

$$S_I = \frac{A_A}{P_A} \qquad (1)$$

Figure 1: 3D Visual representation of the fitted triangles in the actual surface area (A_A) and surface index (S_I) equation.

Eight particles of each type of aggregate (size between 19 and 25 mm) were randomly selected and their roughness was measured on four different arbitrary areas of 5x5 mm² of the surface of each particle, totaling 64 measurements. The surface index (S_I) was determined and mean and standard deviation values were defined for each group.

The resulting parameters were statistically tested to verify normality with Shapiro-Wilk test, using the software Origin. When normality was confirmed, a two-way ANOVA was performed to verify if the variability of data is influenced by the particle or the type of aggregate.

2.3 Microscopic image analysis

A proof-of-concept test was performed to verify if roughness results had any correlation with the internal microstructure of the aggregates; those observed by microscope. Two particles of each aggregate type were selected: the highest and lowest S_I results. The particles had a thin surface layer (1-2 mm) cut off by a diamond blade. The internal surface was embedded in resin and finally polished. The polished surface was then visualized in a Carl-Zeiss Axioplan 2 electronic microscope, with 5x objective, 1x zoom, 0.5x camera adapter, resulting in a 2.5x total magnification and 0.88 µm/px resolution. A filter that enhances the contrast of the images was used in the microscope to improve the visualization of the microstructure. Several superimposed images were captured, then automatically combined to form images of 5x5 mm. These images were visually compared to the surface roughness results to check if exists any correlation between the surface parameters and the internal microstructure of the aggregates.

3. PRELIMINARY RESULTS AND DISCUSSION

3.1 Roughness variability of aggregates types

The roughness of each aggregate particle (average – middle bar, and its standard variation - top and bottom bars) was measured in four randomly selected areas located at the surface. Results of eight arbitrarily selected particles of each aggregate type are also shown in Figure 2 and Figure 3. The average surface indexes for granite and quartzite particles were 1.57 ± 0.19 and 1.61 ± 0.20, respectively.

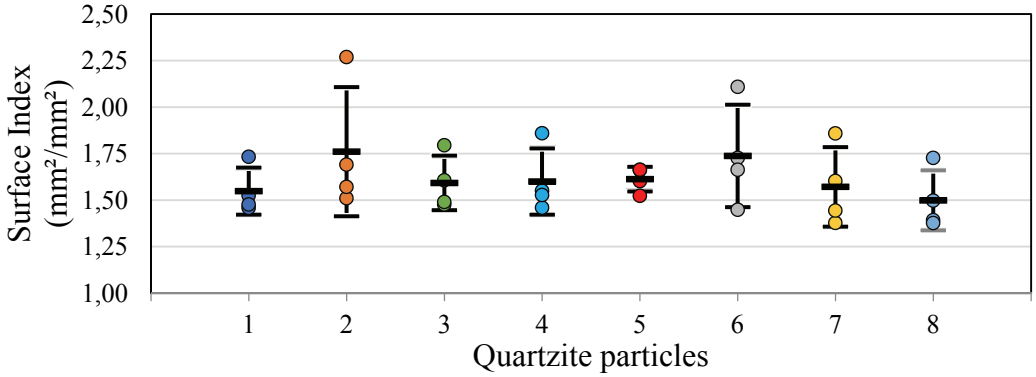

Figure 2: Variability of the surface index – mm²/mm² of 8 random quartzite particles.

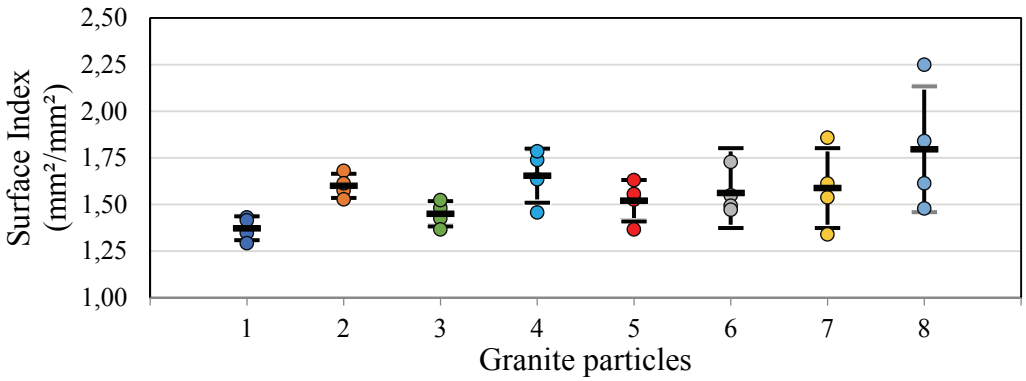

Figure 3: Variability of the surface index – mm²/mm² of 8 random granite particles.

All distributions fitted to Gaussian distributions (with a significance level of 5%). Neither the aggregate type nor the specific particle presented statistical differences between them according to the two-way ANOVA test (with a significance level of 5%). Roughness results for granite or quartzite coarse aggregates can be considered roughly the same.

3.2 Mineral influence on the roughness

Figure 4 shows the overall comparison of the surface index for both aggregates. Typical surface indexes from other products (glass, ceramic, concrete, roughcast concrete) were added in the chart. A Grubb's test was performed to identify the outliers (cross-line icon). These outliers were deep valleys or peaks that significantly increase the surface index (S_I). The average surface indexes of granite and quartzite were rather similar, 1.54 ± 0.15 and 1.57 ± 0.13, respectively. Granite presented a high standard deviation. Both surface index results are in the range of ceramic materials and smooth concrete (as reference).

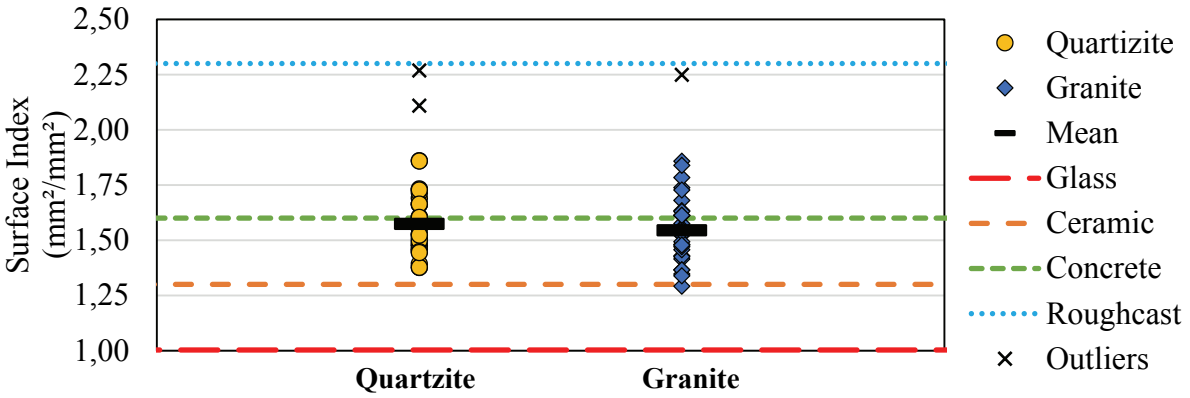

Figure 4: Roughness of four points at the surface in each of the 8 particles of aggregate types.

A visual inspection could somehow explain the variability of the results. Quartzite is mainly formed by small-size quartz grains; thus, it is expected to have less variable surface roughness. Granite is composed of different crystalline phases, with large grains visible at naked eye. Surfaces characteristics are more variable, with large plots of crusted quartz (Figure 5).

Figure 5: Typical appearance of Quartzite and Granite samples.

3.3 Microstructure analysis

The crystalline microstructures of the aggregate particles selected accordingly to the surface index results (the largest and smallest roughness values) were then evaluated by optical microscopy (Figure 6 and Figure 7). The internal microstructure image captured at the same location as the interferometry measurements was presented in the left of the figure. The surface data collected by 3D interferometry was presented in the right of the figure. Both groups of images have the same area, 5x5 mm².

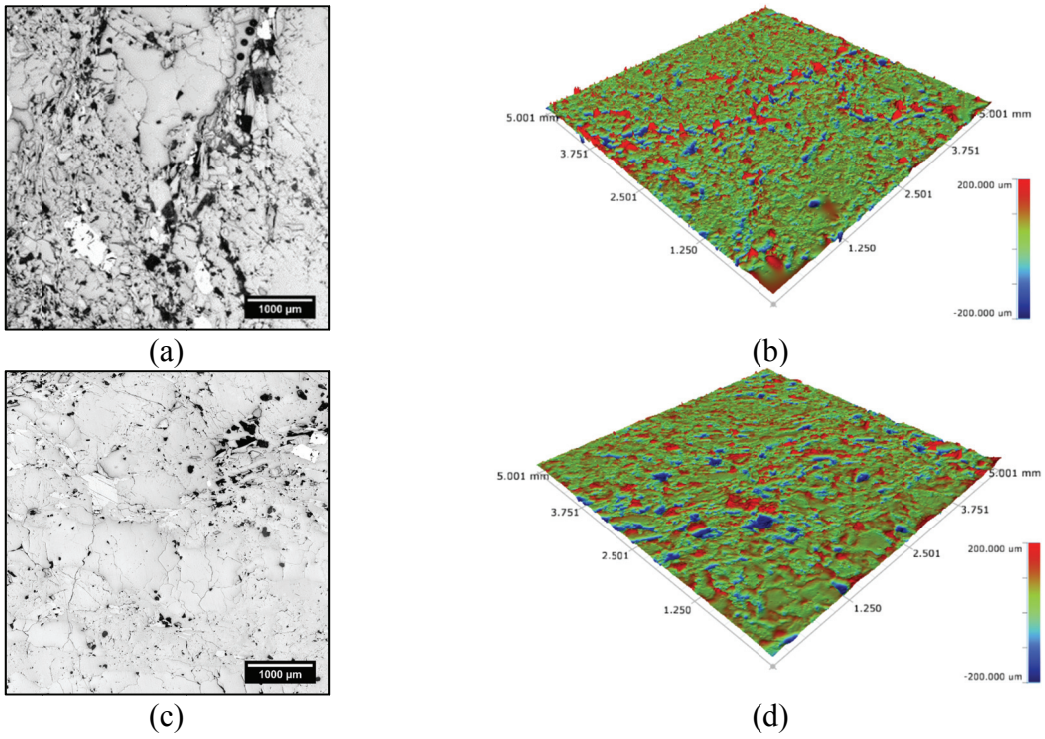

Figure 6: Internal microstructure (a) and surface index - S_I = 2.25 - (b) of granite particle P8. Internal microstructure (c) and surface index – S_I = 1.49 (d) of granite particle P6.

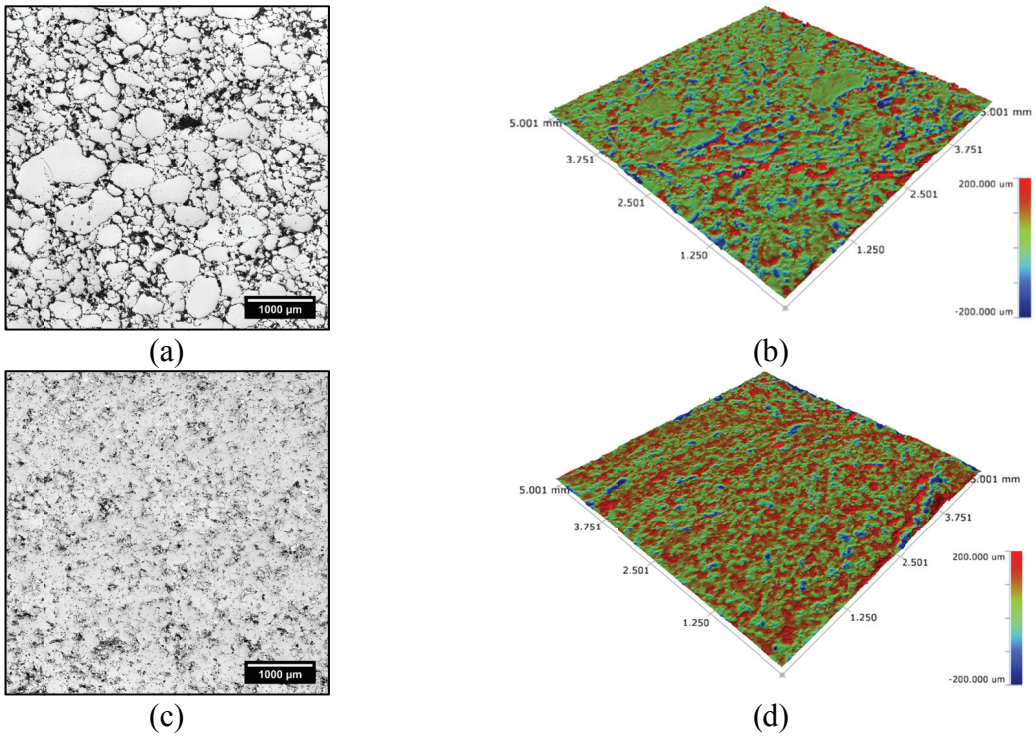

Figure 7: Internal microstructure (a) and surface index – SI = 1.79 (b) of quartzite particle P3. Internal microstructure (c) and surface index - SI = 1.36 (d) of quartzite particle P8.

Granite P8 had the highest S_I=2.25. This is the result of a complex assemblage of crystals, particularly at the bottom left region. The Granite P6 had the lowest S_I=1.49; most of the area contained grains of quartz. We observed more peaks and valleys in granite P8 than in granite P6, which contained larger flat regions. Lower roughness seems to be associated with more homogeneous mineral composition.

In quartzite particles, a difference in mineral grain sizes is noticeable, probably due to metamorphism. Quartzite P3, with S_I=1.65, shows a microstructure with large quartz grains visible in micrography; these large grains show smooth sub-regions with deep valleys at the interface, which may increase the surface index. On the other hand, mineral grains were not identified at P8, which has the lowest surface index (S_I=1.38). for the quartzite, the metamorphism level seems to be an influential factor of S_I.

4. CONCLUSION

Interferometry is a promising technique to measure surface roughness of coarse aggregates, being able to acquire precise 3D quantitative data in a multi-scale way (nm-µm). Crystalline phases sizes and concentration seem to increase the aggregates roughness.

The surface index (S_I) was used to characterize roughness of natural aggregates. We did not find statistical differences between the average roughness of the quartzite and that of the granite. Granite particles presented slightly higher variability than quartzite particles, due to quartz incrustations.

S_I showed somehow coherence with the microstructure of the aggregates. Higher S_I particles presented a microstructure composed of different crystals sizes and types. Lower S_I

particles had greater homogeneity in both microstructural parameters. The metamorphism level seems to be a determining factor to enhance the S_I of quartzite aggregates.

Thus, the roughness of natural aggregates seems to be related to the multi-crystallinity of the phases inside the particle, needing a more comprehensive investigation to better explain the high variability of this parameter.

ACKNOWLEDGMENTS

Authors thanks São Paulo Research Foundation (FAPESP), processes #2014/50948-3 CEMtec, #2016/20420-2, and #2017/25826-0. S.C. Angulo thanks Conselho Nacional de Desenvolvimento Científico e Tecnológico (CNPq), process #311125/2015-8. The information and views set out in this study are those of the authors and do not necessarily reflect the opinion of FAPESP or CNPq.

REFERENCES

[1] Alexander MG, Mindess S. Aggregates in concrete. London; New York: Taylor & Francis; 2008.
[2] Hong L, Gu X, Lin F. Influence of aggregate surface roughness on mechanical properties of interface and concrete. Constr Build Mater 2014;65:338–49. doi:10.1016/j.conbuildmat.2014.04.131.
[3] Jamkar SS, Rao CBK. Index of Aggregate Particle Shape and Texture of coarse aggregate as a parameter for concrete mix proportioning. Cem Concr Res 2004;34:2021–7. doi:10.1016/j.cemconres.2004.03.010.
[4] Rao GA, Prasad BKR. Influence of interface properties on fracture behaviour of concrete. Sadhana Acad. Proc. Eng. Sci., vol. 36, Indian Academy of Sciences; 2011, p. 193–208.
[5] Aïssoun BM, Hwang S-D, Khayat KH. Influence of aggregate characteristics on workability of superworkable concrete. Mater Struct 2016;49:597–609. doi:10.1617/s11527-015-0522-9.
[6] Larrard F de. Concrete mixture proportioning: a scientific approach. London ; New York: E & FN Spon; 1999.
[7] Neville AM, Brooks JJ. Concrete technology. 2. ed. Harlow: Prentice Hall; 2010.
[8] Myshkin N, Grigoriev AY. Roughness and texture concepts in tribology. Tribol Ind 2013;35:97–103.
[9] Santos PMD, Júlio ENBS. A state-of-the-art review on roughness quantification methods for concrete surfaces. Constr Build Mater 2013;38:912–23. doi:10.1016/j.conbuildmat.2012.09.045.
[10] Alexander MG, Mindess S, Diamond S, Qu L. Properties of paste-rock interfaces and their influence on composite behaviour. Mater Struct 1995;28:497–506. doi:10.1007/BF02473154.
[11] Rao AG, Prasad BKR. Influence of type of aggregate and surface roughness on the interface fracture properties. Mater Struct 2004;37:328–34. doi:10.1007/BF02481679.
[12] Elton NJ. An Introduction to the Surfoptic Imaging Reflectometer. Reflectometry Tech Pap 2004:1–10.
[13] Lonardo PM, Trumpold H, De Chiffre L. Progress in 3D Surface Microtopography Characterization. CIRP Ann 1996;45:589–98. doi:10.1016/S0007-8506(07)60513-7.
[14] Al-Rousan T, Masad E, Tutumluer E, Pan T. Evaluation of image analysis techniques for quantifying aggregate shape characteristics. Constr Build Mater 2007;21:978–90. doi:10.1016/j.conbuildmat.2006.03.005.
[15] Masad E, Al-Rousan T, Button J, Little D. Test Methods for Characterizing Aggregate Shape, Texture, and Angularity. Washington, D.C.: Transportation Research Board; 2007. doi:10.17226/14017.

[16] Tutumluer E, Pan T, Carpenter SH. Investigation of aggregate shape effects on hot mix performance using an image analysis approach. 2005.
[17] Masad E, Fletcher T. Aggregate imaging system (AIMS): Basics and applications. Texas Transportation Institute, Texas A & M University System; 2005.
[18] Wang L, Wang X, Mohammad L, Abadie C. Unified method to quantify aggregate shape angularity and texture using Fourier analysis. J Mater Civ Eng 2005;17:498–504.
[19] de Groot P. Principles of interference microscopy for the measurement of surface topography. Adv Opt Photonics 2015;7:1. doi:10.1364/AOP.7.000001.
[20] Quaresma LF. Agregados para Construção Civil. Ministério de Minas e Energia - MME; 2009.
[21] Petersen L, Minkkinen P, Esbensen KH. Representative sampling for reliable data analysis: Theory of Sampling. Chemom Intell Lab Syst 2005;77:261–77. doi:10.1016/j.chemolab.2004.09.013.
[22] Santos WF, Quattrone M, John VM, Angulo SC. Roughness, wettability and water absorption of water repellent treated recycled aggregates. Constr Build Mater 2017;146:502–13. doi:10.1016/j.conbuildmat.2017.04.012.
[23] Mirau AH. Interferometer. US2612074 A, 1952.
[24] Ficker T, Martišek D, Jennings HM. Roughness of fracture surfaces and compressive strength of hydrated cement pastes. Cem Concr Res 2010;40:947–55. doi:10.1016/j.cemconres.2010.02.002.
[25] Lange DA, Jennings HM, Shah SP. Relationship between Fracture Surface Roughness and Fracture Behavior of Cement Paste and Mortar. J Am Ceram Soc 1993;76:589–97. doi:10.1111/j.1151-2916.1993.tb03646.x.
[26] Michigan Metrology. Surface Texture Parameters Glossary. Mich Metrol LLC 2014. https://www.michmet.com/texture_parameters_index_by_name.html (accessed November 28, 2017).

International Conference on Sustainable Materials, Systems and Structures (SMSS 2019)
Novel Methods for Characterization of Materials and Structures
20-22 March 2019 – Rovinj, Croatia

PROBABILISTIC STRENGTH DISTRIBUTION OF NATURAL COARSE AGGREGATES BY POINT LOAD TEST

Natalia V. Silva (1), Sérgio C. Angulo (1) and Amanda A. Bastos (1)

(1) University of Sao Paulo, Escola Politécnica, Brazil

Abstract

The control of the aggregates strength is a relevant factor to ensure the structural performance of middle-high strength concretes (> 50 MPa). The scarcity of aggregates near metropolitan regions has been leading to a decrease of aggregates quality, supporting the need for this kind of control. The strength of single irregular particles of aggregates can be obtained by the Point Load Test (PLT) method; despite its relevance, there is no similar standardized method for civil construction aggregates. This paper uses an adaption of the PLT method, described in the ASTM D 5731 standard, to investigate the strength of granite aggregates collected in the Metropolitan Region of Sao Paulo from two different places: a construction material store (G-CMS) and a concrete plant (G-CP). The variability of the strength among aggregates from both places was discussed based on the Weibull probabilistic analysis. The preliminary results showed differences between both types of granite. G-CMS aggregates, which present less control in terms of quality, showed higher tensile strength variability and presented 10% of the population of particles with tensile strength lower than 5 MPa. This might be a limiting factor to concrete with strength higher than 50 MPa.

Keywords: tensile strength, coarse aggregates, point load test, Weibull distribution.

1. INTRODUCTION

Coarse aggregates represent approximately 45 percent of the concrete volume and influence several of its mechanical properties [1,2]. Regarding concrete structural performance, aggregates may be a limiting factor for their mechanical strength, especially in concrete with compressive strength higher than 50 MPa [3,4]. When the strength of the aggregate is attained, the increase in the cement consumption of the paste (and reduction of the water/cement ratio) does not imply gains in the compressive strength of concrete [5], which leads to side effects in its technical and environmental performance. There is some evidence that the lack of control of the mechanical properties of the aggregates may also result in an increase in the variability of the concrete strength [6].

Natural aggregates originate from rock crushing. In the last decades, the intensive use of aggregates close to the metropolitan regions has resulted in shortage and reduction of supply [7], promoting the use of more porous or weathered rocks [8], compromising the quality of the aggregates. In several regions of the world, it is possible to observe the depletion of coarse aggregates deposits, as in the Netherlands[9], France (Paris) [7], Belgium, Switzerland and Denmark [10].

Currently, the methods that are commonly used to characterize natural coarse aggregates have limited applications. Existing tests applied directly in particles of aggregates, such as crushing value test (BS 812-111:1990 [11]) and ten percent fines value test (EN 1097-2:2010 [12]), only provide indirect information on how strong the material can be. The ASTM 2938-95:2002 [13] is another existing standard, where the mechanical characterization of the aggregates is performed by the mean results of the axial compression tests of its parent rock. This test is expensive, time-consuming, and can be applied only in a few samples. Furthermore, it cannot fulfill the quality control role and does not allow the variability of the properties between particles of aggregates to be well-known.

The distribution of size, volume, shape, and orientation of flaws vary within brittle material, such as particles of aggregates [1], and even if they are of identical sizes, their strength results are quite variable [14,15]. Therefore, to determine these mechanical properties with reliability it is not enough to present only the average value obtained experimentally, but it is essential to consider the dispersion of the results through a probabilistic function. The best way to directly obtain mechanical properties of aggregates may be by testing individual particles [16] and displaying the variability of the results using probabilistic statistical distributions.

Although there is no standard or direct method to determine the mechanical properties of aggregates, there is a standard procedure currently used to estimate the point load strength index of irregular rocks fragment(ASTM D 5731: 2016 [17]), such as aggregates. This standard has been used in the areas of mining, oil and specific civil engineering fields, such as quality control of rail ballast aggregates [18,19]. Moreover, it is based on the point load test method (PLT), which uses two semi-spherical ends of tungsten carbide (radius=5 mm) to apply a compressive load on a rock sample with an external diameter between 30-85 mm. In this method, only specific rupture types are considered valid [17,20].

In the present work, the strength of natural coarse aggregates particles of Brazilian granites collected from two different places (construction material store and a concrete plant) are investigated using an own mechanical testing apparatus (developed based on the PLT method described in the ASTM D 5731). The variability of the strength between the aggregates of the two places is discussed based on the Weibull model.

2. MATERIALS AND METHODS

3kg of natural coarse granite aggregates were collected from two different places in the Metropolitan Region of Sao Paulo. The selected places were a concrete plant (G-CP) and a construction material store (G-CMS). The aggregates were collected from different points of the stockpiles trying to maintain, somehow, its representativeness. It is worth mentioning that during concrete production, aggregates are collected from the stockpiles without any concerns about strength variability. The correct size fraction interval of the material is the only condition considered.

Each aggregate sample was sieved to obtain the granulometric fraction below the 25.0 mm mesh aperture sieve and above 9.5 mm (-25.0+9.5 mm). The average values of density (NM 53 [21]) of G-CP and G-CMS were quite similar (2.70 g/cm³ and 2.72 g/cm³, respectively). However, the average water absorption of G-CMS was higher (NM 53 [21]) than that of G-CP (0.44% and 0.29%, respectively).

The G-CP and G-CMS aggregates are originated from an igneous rock. The XRD patterns in Figure 1 (carried out in the Philips XPERT-MPD Goniometer=PW3050/60) showed that both aggregates have the same mineralogical composition. Basically, the diffraction patterns presented peaks of quartz, feldspar (albite and orthoclase) and mica (phlogopite, muscovite and biotite). However, G-CMS aggregates presented higher peaks intensities that are mostly related to the phase of mica which derives from weathered feldspar. Therefore, this estimation of a higher quantity of mica may allow considering that G-CMS particles are weathered and more porous than the G-CP.

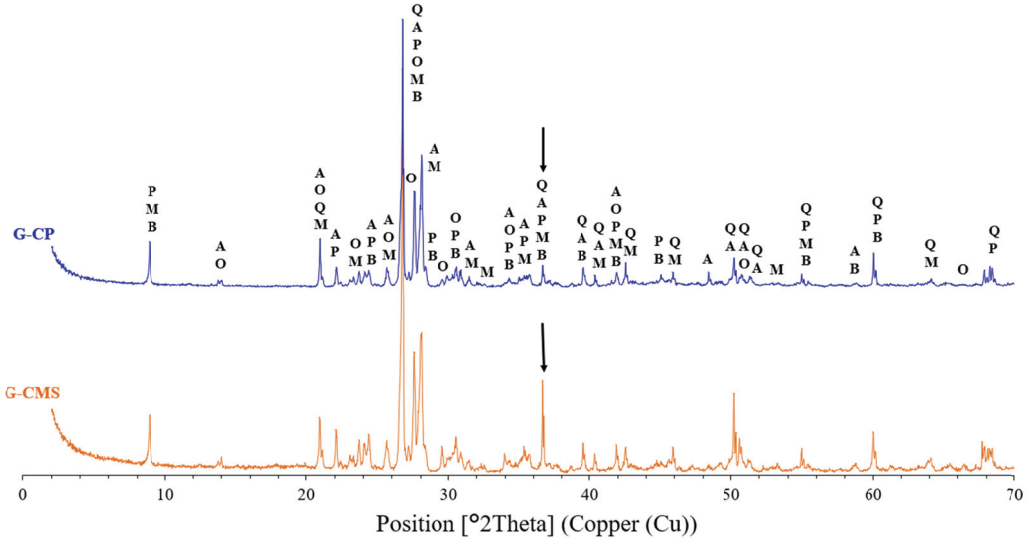

Figure 1: X-ray diffraction patterns of G-CP and G-CMS aggregates. Peaks of quartz - Q, albite - A, orthoclase - O, biotite - B, muscovite - M and phlogopite – P are observed.

The mechanical test was applied to 50 particles randomly selected from each granite sample (G-CP and G-CMS). The test apparatus was developed based on the PLT method and ASTM D 5731: 2016 standard [17]. The mechanical test was carried out in the Instron double-column electronic universal test machine (model 5569) with 50 KN load cell and 0.2 mm / min deformation rate, Figure 2-a.

For the load application, a device with two semi-spherical endings of tungsten carbide (d=14mm) was coupled to the load cell, Figure 2-b. Rings of sponge and brass were used to provide a better placement of the sample and both had a greater diameter than the particles, Figure 2-c. As the compressive load was applied during the test, the sponge ring was compressed providing a contact between the sample and the bottom semi-sphere.

These adaptations in the experimental conditions were tested and validated using a reference material [22]. As a result of this test, the breakage force (F_b) of the aggregate particles was obtained.

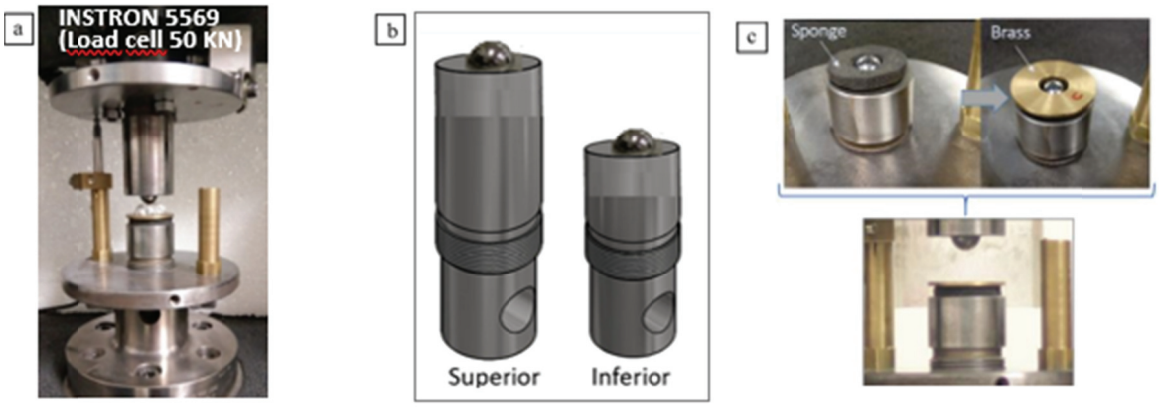

Figure 2: (a) Test apparatus set-up in the Instron double-column electronic universal test machine (model 5569) with 50 KN load cell, (b) semi-spherical tungsten carbide endings (d=14mm) and (c) the placement particles details.

2.1. Determination of the Strength

The determination of the tensile strength by the principle of the PLT method was developed by Hiramatsu and Oka [23]. They proved by photo-elasticity analysis that the tensions formed in the particles around of the axis of the point load are similar, independent of the particle shape. Based on this, they carried out a mathematical analysis of the tension which an element is submitted (through polar coordinates). They concluded that the tensile strength of the particles (σ_t) does not depend on the shape of the particles, but on the concentrated compressive breakage force (F_b) and the distance between the load (D), according to equation (1).

$$\sigma_t = \frac{0.9\ F_b}{D^2} \tag{1}$$

Brook [20] and ASTM 5731:2008 [17] proposed another equation (2) taking into account the equivalent diameter (D_e - Equation (3)) of the particle. This diameter is represented by the circle that has the same minimal transversal section area (A_c - minimum width × distance between the point loads, in mm^2) of the irregular particle. In this work, this equation was used to determine the tensile strength in MPa of the aggregates particles, since the test with the reference material this approach provided more accurate results [22].

$$\sigma_t = \frac{F_b}{D_e{}^2} \tag{2}$$

$$D_e = \sqrt{\frac{4A_c}{\pi}} \tag{3}$$

2.2. Weibull statistical analyses

It is reasonable to represent the strength variability of brittle particles by statistical distributions since the strength values are influenced by the variance, distribution, shape, and orientation of cracks inside the particle [24]. It has been theoretically and experimentally

verified that the Weibull distribution can be used to describe the tensile strength probabilistic distributions of brittle materials [25–27].

Weibull distribution function can be represented by Equation (4) [19,25,28–30]. The function describes the probability of the survival (P_s), or of the failure ($F=1-P_s$) of a fixed volume specimen (V_o), at one given strength (σ_t) and $\sigma_{t,0}$ is the characteristic strength. The survival probability of 0.37 (37%) is used. The variable m is the Weibull modulus and it expresses the variability (dispersion) of the material strength. The lower m is, the more variable the strength of the material is. This function can be transformed into a linear one using log functions. The survival probabilities of the particles can be expressed by Equation (5).

$$P_s(V_0) = \exp\left[-\left(\frac{\sigma_t}{\sigma_{t,0}}\right)^m\right] \quad (4)$$

$$\ln\left[\ln\left(\frac{1}{P_s}\right)\right] = m\left[\ln(\sigma_t) - \ln(\sigma_{t,0})\right] \quad (5)$$

To calculate the parameters of Weibull probabilistic distribution functions, the result of the tensile strength of 50 particles, from each selected place, were arranged in ascending order and the survival probability of the particles was calculated by Equation (6) [25].

$$P_s = 1 - \left(\frac{n}{N+1}\right) \quad (6)$$

P_s survival probability
N total number of samples
n the position of the sample (in ascending order of the strength)

The Weibull parameters were directly obtained by fitting a straight line to $\ln\{\ln[1/(P_s)]\}$ as a function of $\ln \sigma_t$. The Weibull modulus (m) was established from the slope of the plot and the scale factor ($\sigma_{t,0}$) as the value of σ_t when $\ln\{\ln[1/(P_s)]\}=0$. The linear regression fitting results and the main Weibull parameters for the strength at different failure probabilities ($F=1- P_s$) were analyzed. The discrete histograms of the tensile strength and the failure probability versus tensile strength curve were also plotted.

3. PRELIMINARY RESULTS

Figure 3 presents the particles of aggregates after the mechanical test with the semi-sphere endings (diameter 14 mm). Most of the samples (80%) were broken in two plans and according to ASTM D 5731: 2016 [17] and Brook [20], which is a valid type of rupture.

Figure 3: Particles of aggregates after the mechanical test.

The Weibull linearized equations for the strength results are shown in Figure 4-a. As can be seen in Table 1, the Weibull modulus of the aggregates G-CMS and G-CP were 4.3 and 3.0, respectively. These values show higher strength variability of the G-CMS aggregates than

the G-CP. As shown in Figure 4-b, c, the results of the strength for G-CP varied from 5.7 to 16.6 MPa while the G- CMS varied from 2.9 to 19.6 MPa, the latter having a larger amplitude (16.7 MPa). 10% of the aggregate population showed tensile strength lower than 4.5 MPa for G-CMS aggregates and lower than 6.7 MPa for G-CP aggregates.

The major dispersion of the strength results and the lower strength of the G-CMS aggregates were already expected because aggregates sold in packages are commonly used in small-scale civil constructions sites (mostly for informal construction market), being more likely to present more porous and less controlled particles in terms of quality.

From these results, it is suitable to consider that concretes produced with the same paste and same type of aggregates but from different locations may result in concretes with different strength. Besides, considering that coarse aggregates can represent close to 40% of the volume of concrete, a concrete produced with G-CMS may be composed with ~4% of particles with compressive strength lower than 50 MPa. Thus, it is quite reasonable to admit that the aggregate nature will start to influence negatively the compressive strength of concretes higher than 50 MPa, as seen in data from literature [3,31,32].

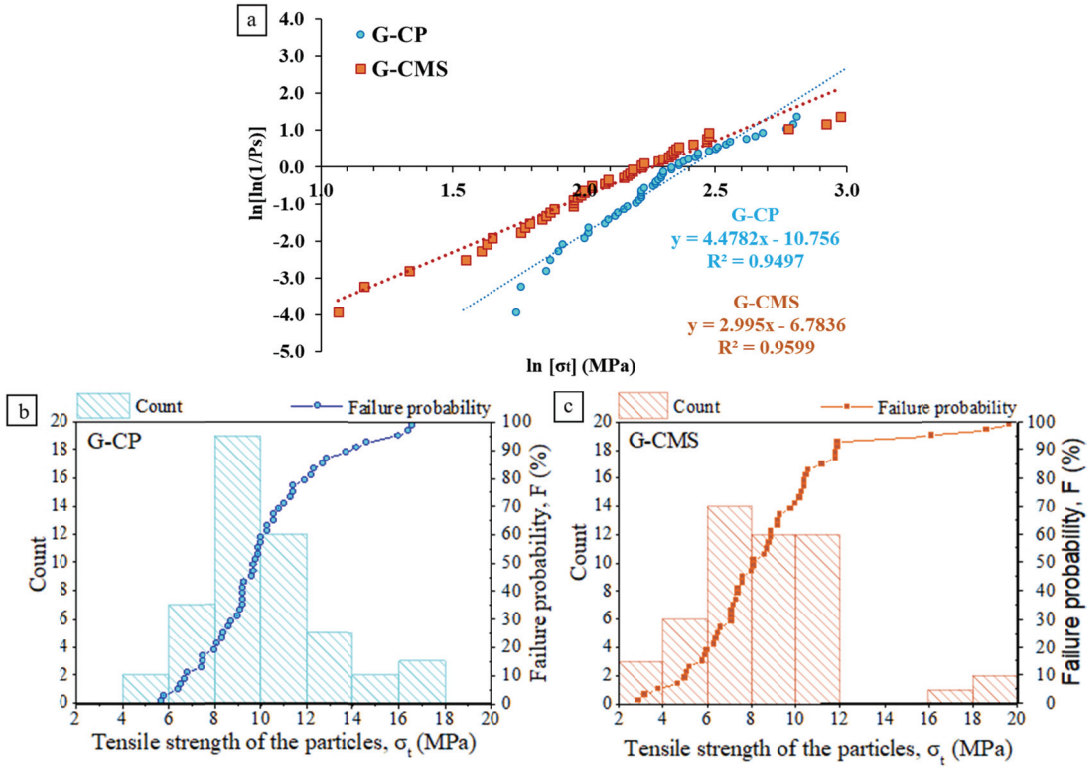

Figure 4: (a) Linear Weibull equations of the strength results (σ_t) of aggregates G-CMS and G-PC, tensile strength histogram (left axis) and failure probability versus tensile strength curve (right axis) of the (b) G-CP and (c) G-CMS.

Table 1: Weibull modulus (m) values, confidence interval of the strength (σ_t -MPa) at different levels of failure probability (F) for G-CP and G-CMS and total amplitude.

Aggregates	m	F=10% (MPa)	F=50% (MPa)	F=63% (MPa)	F=90% (MPa)	Total amplitude
G-CP	4.5	6.7	10.2	11.0	13.3	10.9
G-CMS	3.0	4.5	8.5	9.6	12.7	16.7

4. CONCLUSIONS

A PLT method was used to determine the strength of single particles of granite from two different places and a statistical analysis of the results was performed using Weibull distribution.

From the results, a significant variability in the strength values presented in each sample of aggregate was observed. Notably, granite aggregates from construction material store (G-CMS) presented higher variability and a probability of 10% of its population to have strength lower than 4.5 MPa; this might be a limiting factor for concrete with strength higher than 50 MPa. This emphasizes the need for further investigation and control of granite aggregates used in the concrete production in Brazil.

ACKNOWLEDGMENTS

This work was funded by São Paulo Research Foundation (FAPESP), processes nº 2016/02902-0, 2016/19974-3 and 2016/20420-2. C. Angulo thanks Conselho Nacional de Desenvolvimento Científico e Tecnológico - CNPq, process nº 311125/2015-8. The authors gratefully thank the financial support of InterCement S.A and of the thematic project "Advanced Eco-efficient Cement-Based Technologies (CEMtec), process FAPESP nº 2014/50948-3.

REFERENCES

[1] D. R. Askeland and P. P. Fulay, *Essentials of materials science and engineering*, 2nd ed. Australia ; United States: Cengage Learning, 2009.

[2] P. K. Mehta and P. J. M. Monteiro, *Concrete: microstructure, properties and materials,* 3ª. New York: McGraw-Hill, 2006.

[3] H. Beushausen and T. Dittmer, "The influence of aggregate type on the strength and elastic modulus of high strength concrete," *Constr. Build. Mater.*, vol. 74, pp. 132–139, Jan. 2015.

[4] M. S. Meddah, S. Zitouni, and S. Belâabes, "Effect of content and particle size distribution of coarse aggregate on the compressive strength of concrete," *Constr. Build. Mater.*, vol. 24, no. 4, pp. 505–512, Apr. 2010.

[5] F. de Larrard and A. Belloc, "The Influence of Aggregate on the Compressive Strength of Normal and High-Strength Concrete," *Mater. J.*, vol. 94, no. 5, pp. 417–426, Sep. 1997.

[6] M. De Stefano, M. Tanganelli, and S. Viti, "On the variability of concrete strength as a source of irregularity in elevation for existing RC buildings: a case study," *Bull. Earthq. Eng.*, vol. 11, no. 5, pp. 1711–1726, Oct. 2013.

[7] G. Habert, Y. Bouzidi, C. Chen, and A. Jullien, "Development of a depletion indicator for natural resources used in concrete," *Resour. Conserv. Recycl.*, vol. 54, no. 6, pp. 364–376, Apr. 2010.

[8] A. Lang, P. Range, D. Fowler, and J. Allen, "Prediction of Coarse Aggregate Performance by Micro-Deval and Other Soundness, Strength, and Intrinsic Particle Property Tests," *Transp. Res. Rec. J. Transp. Res. Board*, vol. 2026, pp. 3–8, Dec. 2007.
[9] M. J. Van der Meulen, S. F. Van Gessel, and J. G. Veldkamp, "Aggregate resources in the Netherlands," *Neth. J. Geosci.*, vol. 84, no. 04, pp. 379–387, 2005.
[10] R. Bleischwitz and B. Bahn-Walkowiak, "Sustainable Development in the European aggregates industry," *Wupp. Inst. Clim. Environ. Energy*, 2006.
[11] British Standards Institution, "Testing aggregates. Part 111: Methods for determination of ten per cent fines value (TFV)." British Standards Institution, 1990.
[12] "BS EN 1097-2:1998 - Tests for mechanical and physical properties of aggregates. Methods for the determination of resistance to fragmentation – BSI British Standards." [Online]. Available: http://shop.bsigroup.com/ProductDetail/?pid=000000000030146298. [Accessed: 06-May-2017].
[13] American Society of Testing and Materials, "ASTM Standard D 2938-95 - Standard Test Method for Unconfined Compressive Strength of Intact Rock Core Specimens." 2002.
[14] B. Basu, D. Tiwari, D. Kundu, and R. Prasad, "Is Weibull distribution the most appropriate statistical strength distribution for brittle materials?," *Ceram. Int.*, vol. 35, pp. 237–246.
[15] S. Lobo-Guerrero and L. E. Vallejo, "Application of Weibull statistics to the tensile strength of rock aggregates," *J. Geotech. Geoenvironmental Eng.*, vol. 132, no. 6, pp. 786–790, 2006.
[16] M. G. Alexander and S. Mindess, *Aggregates in concrete*. London; New York: Taylor & Francis, 2008.
[17] American Society of Testing and Materials, "ASTM Standard D 5731 - Determination of the Point Load Strength Index of Rock and Application to Rock Strength Classifications." 2008.
[18] E. Ahmadi Sheshde and A. Cheshomi, "New method for estimating unconfined compressive strength (UCS) using small rock samples," *J. Pet. Sci. Eng.*, vol. 133, pp. 367–375, Sep. 2015.
[19] S. Lobo-Guerrero and L. E. Vallejo, "Application of Weibull Statistics to the Tensile Strength of Rock Aggregates," *J. Geotech. Geoenvironmental Eng.*, vol. 132, no. 6, pp. 786–790, 2006.
[20] N. Brook, "The equivalent core diameter method of size and shape correction in point load testing," in *International Journal of Rock Mechanics and Mining Sciences & Geomechanics Abstracts*, 1985, vol. 22, pp. 61–70.
[21] Norma Mercosur, *NM 53: Agregado graúdo - Determinação de massa específica, massa específica aparente e absorção de água*. 2009.
[22] N. V. Silva, "Método de determinação de resistência à tração e módulo de elasticidade de partículas de agregados graúdos naturais," Dissertação de Mestrado, Universidade de São Paulo, São Paulo, 2018.
[23] Y. Hiramatsu and Y. Oka, "Determination of the tensile strength of rock by a compression test of an irregular test piece," in *International Journal of Rock Mechanics and Mining Sciences & Geomechanics Abstracts*, 1966, vol. 3, pp. 89–90.
[24] W. D. Callister and D. G. Rethwisch, *Materials science and engineering: an introduction*, 8th ed. Hoboken, NJ: John Wiley & Sons, 2010.
[25] W. L. Lim, G. R. McDowell, and A. C. Collop, "The application of Weibull statistics to the strength of railway ballast," *Granul. Matter*, vol. 6, no. 4, pp. 229–237, Dec. 2004.
[26] R. Danzer, P. Supancic, J. Pascual, and T. Lube, "Fracture statistics of ceramics – Weibull statistics and deviations from Weibull statistics," *Eng. Fract. Mech.*, vol. 74, no. 18, pp. 2919–2932, Dec. 2007.
[27] D. R. Askeland and W. J. Wright, *Essentials of materials science and engineering*, Third edition. Stamford, CT: Cengage Learning, 2014.
[28] M. Koohmishi and M. Palassi, "Evaluation of the Strength of Railway Ballast Using Point Load Test for Various Size Fractions and Particle Shapes," *Rock Mech. Rock Eng.*, vol. 49, no. 7, pp. 2655–2664, Jul. 2016.

[29] B. Basu, D. Tiwari, D. Kundu, and R. Prasad, "Is Weibull distribution the most appropriate statistical strength distribution for brittle materials?," *Ceram. Int.*, vol. 35, no. 1, pp. 237–246, Jan. 2009.
[30] G. R. Mcdowell, W. L. Lim, and A. C. Collop, "Measuring the strength of railway ballast," *Ground Eng.*, no. jan, pp. 25–28, 2013.
[31] K.-R. Wu, B. Chen, W. Yao, and D. Zhang, "Effect of coarse aggregate type on mechanical properties of high-performance concrete," *Cem. Concr. Res.*, vol. 31, no. 10, pp. 1421–1425, 2001.
[32] F. de Larrard, *Concrete mixture proportioning: a scientific approach*. London ; New York: E & FN Spon, 1999.

International Conference on Sustainable Materials, Systems and Structures (SMSS 2019)
Novel Methods for Characterization of Materials and Structures
20-22 March 2019 – Rovinj, Croatia

SULFATE RESISTANCE OF CONCRETE BASED ON CEM III WITH RECYCLED AND NATURAL AGGREGATES

Vesna Bulatović (1), Miroslava Radeka (1), Mirjana Malešev (1), Vlastimir Radonjanin (1), Mirjana Laban (1) and Ivan Lukić (1)

(1) University of Novi Sad, Faculty of Technical Sciences, Department of Civil Engineering and Geodesy, Serbia

Abstract

The paper presents the results of the resistance to sulfate attack of two types of concrete: the one that contains CEM III, water/cement ratio 0.55 and natural river aggregate - NA as well as the one composed of CEM III, water to cement ratio 0.55 and recycled concrete aggregate - RCA as coarse aggregate (4/8,8/16). RCA was tested conforming to the standards for aggregate quality specified in EN 12620 and it was in accordance with the recommendations given in EN 206-1. The amount of adhered mortar was 40%. The concrete specimens were submerged up to 365 days in saturated lime water (referent specimens), or in 5% Na_2SO_4/5% $MgSO_4$ solutions. For the evaluation of sulfate resistance of concretes, the testing methods were used: compressive strength, length changes and mineralogical analyses (XRD, FTIR, TGA-DTA).

Compressive strengths of referent specimens made with NA or RCA were similar. In terms of length change, the greatest value was obtained for both concrete specimens immersed in 5% $MgSO_4$ solution. All specimens exposed to either 5% Na_2SO_4 or 5% $MgSO_4$ solutions satisfied the criteria defined by Mehta (25% strength loss limit for sulfate resistance concrete) and Miller and Manson (0.2‰ of expansion-limit for sulfate resistance of concrete).

Key words: recycled concrete aggregate, sulfate attack, CEM III, mineralogical analyses

1. INTRODUCTION

One of the most important issues of sustainable development is the use of aggregates obtained from crushed concretes (RCA), for replacing natural aggregates as well as the limitation of demolished concrete disposal. RCA contain not only the original aggregates but also adhered hydrated cement paste making RCA concrete more susceptible to absorption, diffusion and permeation of fluids. RCA are generally regarded to be weaker than corresponding virgin aggregate in terms of mechanical, physical and chemical action [1]. However, a major problem with the use of RCA in concrete is increase in creep and water sorptivity, drying shrinkage, chloride penetration, the carbonation depth and decrease in the compressive strength, modulus of elasticity, freeze-thaw resistance [2].

There are several studies suggesting that the shortcoming of using recycled aggregate can be moderated by using the double mixing approach in concrete mixing [3], or equivalent mortar volume RCA mixing approach [4], as well as by adding mineral admixtures to concrete mixture [5]. Several publications have reported that the concrete with RCA resistant to external sulfate attack could be obtained adding minerla admixtures [6][7].

External sulfate attack is caused by the interaction between sulfate rich water or soil and cement paste in concretes. The microstructure of the concrete is changed under this attack. These changes may vary in the type of severity, but they commonly include chemical sulfate attack and physical attack caused by salt crystallization in pores [8][9]. Cracking, expansion and loss of bond between the cement paste and aggregate are common damages. The attack of Na_2SO_4 solution triggers typical changes of paste composition, i.e. monosulfate phase conversion to ettringite and, in later stages, gypsum formation. The additional calcium necessary for ettringite and gypsum formation is provided by portlandite and calcium silicate hydrate (C-S-H) in the cement paste [9]. $MgSO_4$ solution could be more aggressive due to the formation of brucite and magnesium silicate hydrates (M-S-H). M-S-H is formed by replacing calcium in C-S-H with magnesium. The displaced calcium takes part in gypsum formation.

The composition of cement plays an important role in sulfate resistance of concrete. Namely, the expansion of mortars/concrete containing conventional cement blended with supplementary cementitious materials (SCMs) such as blast furnace slag is lower than the expansion of plain Portland cements. The pozzolanic reaction of SCMs lowers the availability of CaO, which leads to the formation of a smaller quantity of ettringite and gypsum, as well as to lower crystallization pressures [8]. In addition, more aluminum is bound in the low Ca/Si C-S-H phases present in these binders and thereby reduces the availability of aluminum for additional ettringite formation [9].

The paper presents the results of the resistance to sulfate attack of concrete that combined sulfate-resistant cement type CEM III, and two types of coarse aggregate (natural river (NA) and recycled concrete (RCA)). For the evaluation of sulfate resistance of these concretes, the following testing methods were used on laboratory specimens immersed in sulfate solutions (5% Na_2SO_4 or 5% $MgSO_4$) for 365 days: compressive strength, length change, phase compositions (XRD, Fourier Transform Infrared Spectroscopy-FTIR) and thermogravimetric analysis (TGA-DTA).

2. EXPERIMENTAL INVESTIGATION

2.1 Materials and mixture proportion

The following component materials were used for the preparation of concrete: cement (Low heat/sulfate-resistant cement CEM III/B 32.5N LH/SR), aggregate (fine aggregate 0/4mm - river aggregate and coarse aggregate 4/8 and 8/16mm - NA and RCA); admixture (HRWRA - "SikaViscoCrete 3070" , "Sika"- Switzerland) and tap water.

The basic physical properties of cement were tested according to standards EN 196-1[10], EN 196-3 [11] and EN 196-6 [12]. Recommendations and benchmark values for aggregate quality are given in standards EN 206-1[13] and EN 12620 [14]. The origin of concrete used to obtain RCA was unknown. The content of mortar attached to the original natural aggregate in our recycled aggregate was 40% of the total mass of RCA.

Designed compositions of concrete mixtures are shown in Table 1.

Table 1: Labels and mixture proportions of concrete in kg/m^3

Concretes (mixture)	m_c CEM III	m_v	$m_{v,ad}$	$m_{a,f}$	$m_{a,c}$	m_{spk}	w/c
NMC	338	186	-	936	864	0.7	0.55
RMC	338	186	20.5	881	813	-	0.55

m_c-quantity of cement; m_v-quantity of water; $m_{v,ad}$-additional quantity of water that was calculated on the basis of RCA water absorption (2.5%); $m_{a,f}$-quantity of fine aggregate; $m_{a,c}$-quantity of coarse aggregate; m_{spk}-quantity of super-plasticizer (0.2%); w/c-water-cement ratio

2.2 Experimental programs

Two concretes were prepared and their resistance to sulfate attack was determined by immersing specimens in 5% Na_2SO_4 and 5% $MgSO_4$ solutions. The concrete specimens were completely immersed in sulfate solutions and lime-saturated water (referent solution) and tested according to a previously determined testing program.

2.3 Curing, specimen preparation and labels

Initially all specimens were cured in lime-saturated water for 28 days. After that period, compressive strength was determined by testing three specimens from each mixture. One third of the remained specimens were transferred to containers with 5% Na_2SO_4 and another third in 5% $MgSO_4$ solutions where they were stored until testing was done (90, 180, 365 days). The last third of specimens were submerged in lime-saturated water for 90, 180 and 365 days (reference specimens). For testing compressive strength, the following types of concrete specimens were prepared from each mixture: 150mm cubes for compressive strength at the age of 28 days (designated as 0) and cylinders (D=100mm, H=100mm) for compressive strength at 90, 180 and 365 days for reference and specimens immersed in sulfate solutions (designated as 90, 180 and 365 days). For each compressive strength, 3 specimens were used. Length change (prisms 100x100x500mm^3) was determined according to the procedure given in UNI 11307. For each mixture and each solution, three prisms were measured once a week until the above-mentioned observed periods.

Labelling was done in three series in the following way: those with the first letter "E" were cured in lime-saturated water solution, those with "N" were immersed in 5% Na_2SO_4 solution and those with "M" were stored in 5% $MgSO_4$ solution. The second letter in the label indicates the type of aggregate: "N" is NA and "R" is RCA. The third letter refers to the type of cement: "MC" stands for CEM III. The value of compressive strength at the age of 28 days was taken as the initial value labelled as 0, meaning that the time of exposure to different conditions (sulfate and lime-saturated solutions) started from this point.

2.4 Methods

Compressive strength was tested according to EN 12390-3 before the specimens were immersed in sulfate solutions and after storing them in these solutions for 90, 180 and 365 days. For eachcompressive strength test was used 3 specimens. The length change was measured continuously. Phase composition (XRD and FTIR) and TGA-DTA were determined on CEM III paste and on the pieces of mortars cut from the surface of specimens ENMC, ERMC, MNMC and MRMC at 365 days. Mortar specimens were granulated and sieved in order to separate fine aggregate from hydrated cement paste. For further testing of

microstructure, hydrated cement powder used. XRD patterns were recorded on Philips PW1710 device under the following experimental conditions: monochromatic Cu Kα radiation with 1.5418 Å wavelengths in 10–65° of 2θ range, scan rate 0.02° and 0.5s per step, operating at 40 kV, 30 mA. FTIR (Thermo-Nicolet Nexus 670 FTIR spectrometer) analyses included: KBr pellet technique, spectral resolution of 4 cm^{-1}, range of 4000 – 400 cm^{-1}, 32-averaged scans per one measurement. TGA-DTA tests (Setaram, Labsys Evo) with a balance accuracy of 0,1µg, were performed on the specimens of ~30mg, crushed material, by heating in alumina crucible, 20-1000°C, at 5°C/min heating rate under argon atmosphere.

3. RESULTS

3.1 Compressive strength

The average values of concrete compressive strength after 90, 180 and 365 days of immersion in $MgSO_4$, Na_2SO_4 and lime-saturated water, as well as the strength values prior to the exposure to sulfate solutions (28 days) are presented in Table 2.

Table 2: Compressive strength (MPa) of specimens

Concrete series	0 days	90 days	180 days	365 days	Concrete series	0 days	90 days	180 days	365 days
ENMC	31.8	45.3	46.4	49.7	ERMC	31.3	39.7	45.9	48.8
NNMC		43.4	46.1	45.1	NRMC		43.2	46.7	48.8
MNMC		43.3	42.5	44.3	MRMC		41.6	42.5	43.5

The comparison results of the specimens exposed to Na_2SO_4 or $MgSO_4$ solutions for 90, 180 and 365 days and corresponding 28-day referent specimens (Table 2), clearly show that an increase in compressive strength after these periods of exposure occurred in all concretes.

Relative compressive strength values are illustrated in Figure 1. These values present the relation between the compressive strength of specimens immersed in selected sulfate solution and their corresponding referent values of the same age. After 90, 180 and 365 days of storing in both sulfate solutions, all specimens showed differences in compressive strength compared to corresponding lime-saturated water stored specimens.

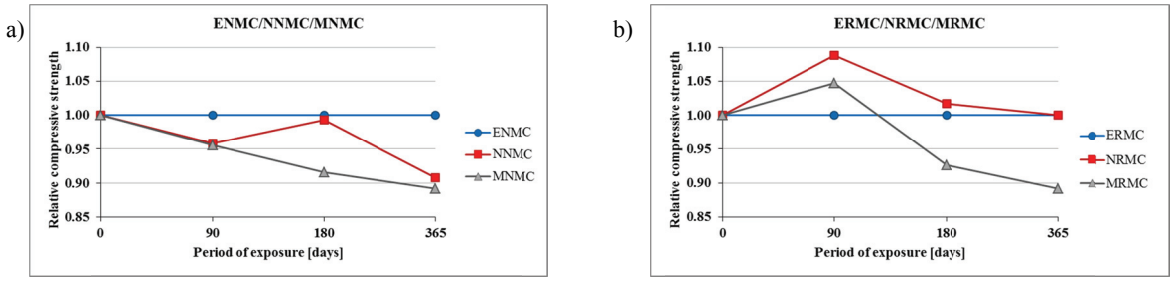

Figure 1: Changes of compressive strength of concretes exposed to sulfate solutions in relation to corresponding strength of referent specimens: a – NA; b – RCA

After 90 days of exposure to sulfate solutions, concrete series with NA showed a small decrease in compressive strength which did not exceed 10% compared to the corresponding

reference value, while the series with RCA showed a small increase in compressive strength (up to 10%). After that period, all series had a continuous decrease in compressive strength up to 10%, with a subtle difference observed for the series with NA in sodium sulfate (Figure 1a). To evaluate sulfate resistance of tested concretes, the calculated values of compressive strength decrease were compared to 25% strength loss limit for sulfate resistant concrete given by Mehta [15]. Based on that criterion, all series had satisfactory sulfate resistance at the observed periods of time.

3.2 Length change

Length change results are shown in Figure 2. A comparison of linear expansion values for the concrete specimens stored in sulfate solutions reveals that those containing RCA have lower values of expansion than the specimens with NA. For both mixtures (with RCA and NA), the series exposed to the attack of magnesium sulfate have larger values of expansion compared to the specimens immersed in sodium sulfate.

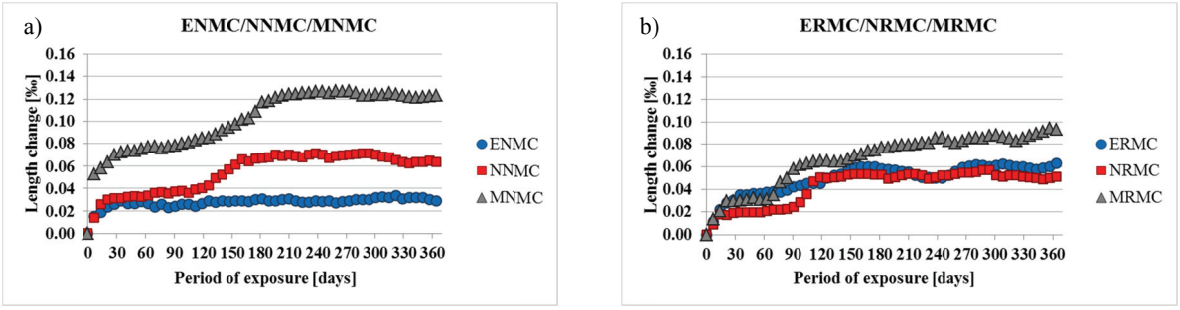

Figure 2: Length change of concretes exposed to sulfate solutions and lime - saturated water: a –NA, b – RCA

The calculated values of length changes were compared to the expansion limit given by Miller and Manson [15] in order to evaluate sulfate resistance of tested concrete mixtures. They proposed a 0.2‰ of expansion as the limit for sulfate resistance of concrete. Based on that criterion, all series have satisfactory sulfate resistance for observed period.

3.3 XRD, FTIR and TGA analyses

The results of mineralogical tests are presented through a comprehensive comparison of the most deteriorated specimens results (MRMC and MNMC) with those of reference series (ERPC and ENPC) as well as CEM III paste.

XRD - Mineralogical investigation demonstrated important differences between the specimens exposed to sulfate solutions and hydrated CEM III, Figure 3. Namely, relative peak intensities of portlandite for specimens exposed to sulfate solution significantly decreased, indicating the reaction of sulfate ions with calcium ions. Additionally, the decrease of portlandite content could be partly influenced by carbonation process since calcite was identified in all examined specimens except in CEM III paste.

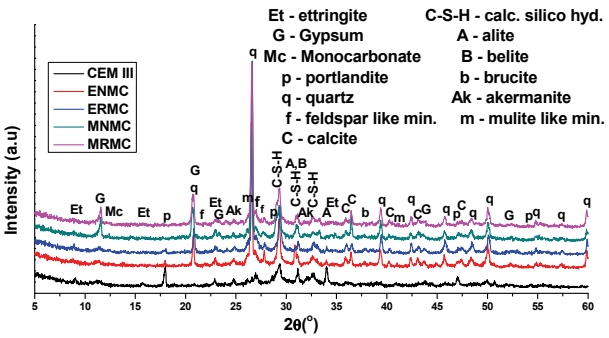

Figure 3: XRD data of CEM III and specimens exposed to sulfate solutions for 365 days

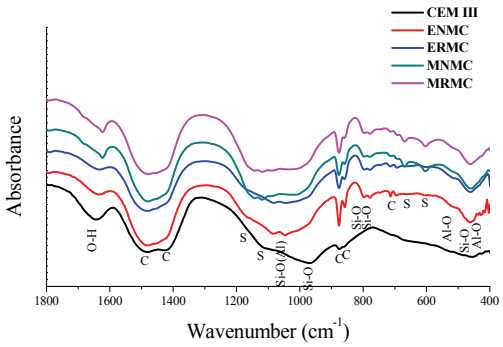

Figure 4: FTIR data of CEM III and specimens exposed to sulfate solutions for 365 days (400-1800cm^{-1})

Also, all specimens showed the presence of sulfate phases (mainly gypsum, then ettringite), apart from the hydration products such as C-S-H phase. The intensities of gypsum peaks were noticeable for specimens exposed to $MgSO_4$ solution. Quartz and feldspate as aggregate remnants were found in all analyzed specimens. Additionally, brucite was identified in the specimens treated with $MgSO_4$. Traces of alite were also found, indicating the presence of a certain amount of clinker remnants in hydrated products.

FTIR – Diagrams are given in Figure 4 and Figure 5.The peak at 3641cm^{-1} was assigned to OH^- group stretching of $Ca(OH)_2$ [16] and it was present only in CEM III. The broad bands at ~3400cm^{-1} were assigned to the stretching of OH^- in water molecules and the band at 1620-1650cm^{-1} presented HOH bending vibrations of the absorbed molecular water. All specimens, except CEM III, were subjected to carbonation, as suggested by the presence of peaks at ~2980cm^{-1},~2930cm^{-1}, 1790cm^{-1} and 714cm^{-1}.The peak at ~2500cm^{-1} was attributed to the carbonation from air. The peaks at 1480cm^{-1}, 880cm^{-1} and at ~ 860cm^{-1} could be assigned to carbonate in the form of vaterite. Therefore, the existence of carbonation peaks in all specimens, except CEM III, implies a synergetic deterioration under sulfate and carbonate ions. The observed bands at ~ 1080-1090cm^{-1} and at ~ 1040-1050cm^{-1} may be related to the presence of Si-O(Al) vibration of C-A-S-H tetrahedra, respectively. This is typical of all specimens, except CEM III, since its peak at 970cm^{-1} was related to Si-O vibrations of C-S-H tetrahedra. Other specimens did not have a clearly defined peak position associated with Si-O vibrations of C-S-H tetrahedra. Their position requires further analysis through deconvolution. The observed shoulder at ~ 1100cm^{-1} - 1145 cm^{-1} was assigned to vibration of SO_4^{2-} of ettringite [16] or some other sulfate salts (in case of MNMC and MRMC), since inorganic sulfate ions were strongly absorbed at 1145–1090 cm^{-1} due to asymmetric SO_4 stretching. The bands at ~780-800cm^{-1} were attributed to Si-O-Si vibrations [17]. The bands at ~ 650-670cm^{-1} and 600cm^{-1}, assigned to sulfate forms (gypsum or ettringite), were present in specimens exposed to sulfate attack (MNMC and MRMC). The bands at ~1140cm^{-1}, and ~1118cm^{-1} (related to the existence of sulfate products) and band at ~1028cm^{-1} were present in the specimens exposed to $MgSO_4$ solution. For those specimens, XRD analyses identified gypsum as the main sulfate phase.

The bands at 460-465 cm^{-1} and at 520-560 cm^{-1} were attributed to in plane Si-O in plane bending and Al-O linkages, respectively. Additionally, the bands observed in the range 400-450cm^{-1} were related to the deformation of SiO_4 tetrahedra.

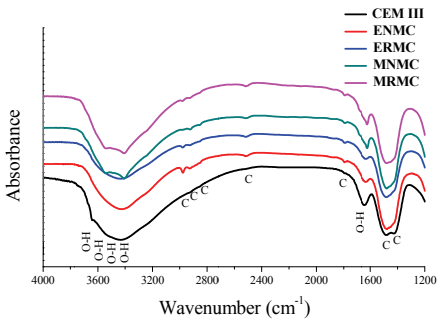

Figure 5: FTIR data of CEM III and specimens exposed to solutions for 365 days (1200-4000cm^{-1})

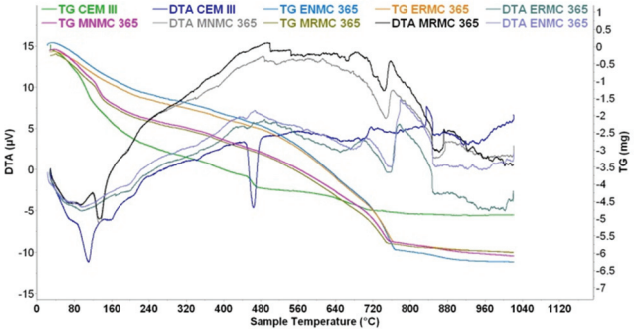

Figure 6: TGA/DTA of CEM III and specimens exposed to solutions for 365 days

TGA–DTA analysis: The results show the prevalent weight loss in CEM III occurred at the temperature of 100°C (corresponding to the loss of water absorption and water from calcium aluminate hydrate) and at 460°C (assigned to portlandite), Figure 6. While hydrated CEM III showed the largest weight loss up to 200°C (8.3 %), specimens ENMC, ERMC, MNMC and MRMC showed the greatest weight loss in the range 500-920°C (8.6-10.8 %). The weight loss in the range 500-920°C could be related to: the weight loss of structural OH^- groups from C-S-H gel (DTG at ≈540°C), weight losses due to the decomposition of amorphous carbonated phases (DTG at ≈640°C) and crystalized calcite (DTG at ≈740°C). DTG peak at 920°C was present in all specimens, while portlandite was present only in CEM III. The specimens exposed to $MgSO_4$ solution showed a more intensive peak at 120°C (related to gypsum). Specimens labelled as MRMC, in comparison to the specimens labelled as MNMC, showed a lower content of gypsum (MRMC=1.9%, MNMC= 2.2%). All specimens had small peak at≈360°C, suggesting the presence of hydrogarnet / hydrotalcite.

4. DISCUSSION

XRD, FTIR and TGA-DTA analyses of CEM III after 28 days of hydration confirmed the formation of C-S-H gel and portlandite as main components. This suggests the hydration process of slag in CEM III did not make a considerable progress after 28 days. Due to page restrictions, results of FTIR spectra deconvolution at wavenumbers ≈970 cm^{-1} were not presented in this paper. Namely, these results could demonstrate the possibility of C-A-S-H gel formation as a result of slag hydration. Gypsum, AFm and Aft phases were less pronounced in XRD diagrams. On the other hand, FTIR analysis confirmed the presence of sulfate ions. In comparison to CEM III (28 days old), XRD, FTIR and TGA-DTA analyses of other specimens (365 days old) showed carbonates were formed and portlandite was not identified. This was evident for both reference and the specimens exposed to sulfate solutions. The disappearance of portlandite in reference specimens implies that carbonation was the reason for this phenomenon, not sulfate attack. Compressive strength and length change results indicate the lowest values of compressive strength and the highest length change values were typical of both types of concrete specimens exposed to $MgSO_4$ solution for 365 days. Length change values can be related to weight loss of these concretes up to 200°C (corresponding to the loss of water absorption, decomposition of gypsum, ettringite, C-S-H and water from other calcium aluminate hydrates) in comparison to the Na_2SO_4 solution.

5. CONCLUSION

The paper studies the sulfate resistance of concretes containing sulfate-resistant cement (CEM III) and natural or recycled coarse aggregates. The results show that all studied concretes have good quality. They satisfied the criterion given by Mehta for compressive strength and expansion limit given by Miller and Manson for periods up to 365 days of exposure to sulfate solutions. XRD, FTIR and TGA-DTA analyses confirmed substantial microstructure changes (formation of gypsum) for the most deteriorated concretes (exposed to $MgSO_4$ solution).

REFERENCES

[1] Parekh, D.N and Modhera, D.C.D., 'Characterization of recycled aggregate concrete', *Inter. Journal of Adv. Eng. Tech.* October-december 2011; Vol. II, Issue IV; 321-330.
[2] Hwang, J.P., Shim, H.B., Lim, S., Ann, K.Y., 'Enhancing the durability properties of concrete containing recycled aggregate by the use of pozzolanic materials', *Journal of Civ. Eng.* 17 (1) (2013) 155-163.
[3] Tam, V.W.Y, Gao, X.F., Tam, C.M,. 'Microstructural analysis of recycled aggregate concrete produced from two-stage mixing approach', *Cem Concr Res* 35 (2005) 1195–203.
[4] Abbas, A., Fathifazl, G., Isgor, O.B., Razaqpur, A.G., Fournier, B., Foo, S., 'Durability of recycled aggregate concrete designed with equivalent mortar volume method', *Cem Concr Compos* 31 (2009) 555–63.
[5] Ann, K.Y., Moon, H.Y., Kim, Y.B., Ryou, J., 'Durability of recycled aggregate concrete using pozzolanic materials', *Waste Manage* 28 (2008) 993–999.
[6] Limbachiya, M. C., 'Recycled Aggregates: Production, Properties and Value-added Sustainable Applications', *Journal of Wuhan University of Technology-Mater. Sci. Ed.*, 2010.
[7] Shayan, A. and Xu, A., 'Performance and Properties of Structural Concrete Made with Recycled Concrete Aggregate', *Materials Journal*, Vol 100 (2003) 371-380
[8] Manu, S., Menashi, C., Olek Jan, D., 'Mechanism of sulfate attack: A fresh look Part1: Summary of experimental results', *Cem Concr Res* 32 (2002) 915-921.
[9] Skalny, J.P.,Marchand, J., Odler, I.,'Sulfate attack on concrete'.Spon press, Taylor & Francis e-Library; 2003.
[10] SRPS EN 196-1. Methods of testing cement - Part 1: Determination of strength. Institute for standardization of Serbia; 2008
[11] SRPS EN 196-3. Methods of testing cement - Part 3: Determination of setting times and soundness. Institute for standardization of Serbia; 2010.
[12] SRPS EN 196-6. Methods of testing cement - Part 6: Determination of fineness. Institute for standardization of Serbia; 2011.
[13] SRPS EN 206-1. Concrete: Specification, performance, production and conformity. Institute for standardization of Serbia;2011.
[14] SRPS EN 12620. Aggregates for concrete. Institute for standardization of Serbia; 2010
[15] Ghafoori, N., Diawara, H., Beasley, S., 'Resistance to external sodium sulphate attack for early-opening-to-traffic Portland cement concrete', *Cem. Concr. Comp*. 30 (2008) 444-454.
[16] Ylmén, J., Jäglid, U., Steenari, B., Panas, I., 'Early hydration and setting of Portland cement monitored by IR, SEM and Vicat techniques', *Cem. and Concr. Res* 39 (2009) 433-439.
[17] Ismal, I., Bernal, S.A., Provis, J.L., Hamdam, S., Deventer J. S.J., Microstructural changes in alkali activated fly ash/slag geopolymers with sulfate exposure', *Mater. and Struct*. 46 (2013) 361-373

International Conference on Sustainable Materials, Systems and Structures (SMSS 2019)
Novel Methods for Characterization of Materials and Structures
20-22 March 2019 – Rovinj, Croatia

CHARACTERIZING THE 3D MESOSTRUCTURE OF HIGH PERFORMANCE CONCRETE BY COMPUTED TOMOGRAPHY

Thorsten Leusmann (1), Gauravdatt Basutkar (1), Matteo Lunardelli (1) and Dirk Lowke (1)

(1) Institute of Building Materials, Concrete Construction and Fire Safety, TU Braunschweig, Germany

Abstract

Among others, size distribution and arrangement of aggregate particles and binder matrix affect the performance of concrete. A dense microstructure with a high packing density is a basic prerequisite for the production of high-performance concretes. The arrangement and the geometry of the aggregate particles strongly affect the crack formation and fracture behaviour of high strength concrete. Therefore, the crack formation is investigated with so-called mesostructural models that distinguish aggregate particles, cementitious matrix, and air voids. For this purpose, it is necessary to map the three mentioned phases in the concrete structure geometrically and to characterize their mechanical properties.

The following paper shows the methods for the geometric characterization of aggregate particles and the three-dimensional geometrical mapping of the concrete phases by computed tomography. Furthermore the development of a mortar representative for the high performance concrete matrix material is adressed.

Keywords: high performance concrete, computed tomography, aggregate segmentation

1. INTRODUCTION

High-performance concrete (HPC) allow slender cross sections and lighter structures for buildings such as wide-span bridges, wind turbines or industrial machine foundations exposed to high load cycles. Due to the reduced weight, these structures are more susceptible to vibrations. Thus, the fatigue behaviour of HPC is critical for the design and implementation of such concrete applications [1].

The fatigue damage occurs in form of cracks, whereby the arrangement and the geometry of the aggregate particles strongly affect the crack pattern and the fracture energy [2]. Computed tomographic scans allow the mapping of the internal aggregate structure of concrete, the observation of crack formation and the verification of simulations on so-called mesomodels.

The mesoscale distinguishes aggregates and air voids above a suitable defined size threshold, bulk cement mortar and the material within the interfacial transition zone (ITZ) between aggregates and bulk cement mortar as concrete phases. Since it is computationally unfeasible to resolve aggregates and pores of all sizes, the cement mortar representing the bulk material includes those below the aforementioned size threshold.

2. CONCRETE EQUIVALENT MORTAR (CM)

In order to determine the mechanical parameters of bulk material, a concrete equivalent mortar representative for the bulk material is developed with the same excess paste thickness as the reference concrete following the procedure described in [3, 4]. The procedure comprises in substituting the coarse aggregate fraction by an amount of sand having an equivalent surface area. As a result, the total aggregate surface to be enclosed with paste will then be equal for the mortar as it was with the coarse aggregates.

For the development of CM, concrete and mortar are regarded as a two-phase structure, in which the aggregates are distinguished as solid phase and the paste as fluid phase. The solid-fluid interactions or the solid-solid interactions are governed by the so-called excess paste thickness $t_{Paste,ex}$ which corresponds to the half distance of two adjacent aggregates and the distance is characterized to be independent of the aggregate size (Figure 1). The excess paste thickness $t_{Paste,ex}$ can be determined by enclosing the surface area of the aggregates A_A with the excess paste volume $V_{Paste,ex}$, which remains after filling the voids between the aggregates V_{void} with paste. The surface area A_A is calculated with equation (1):

$$t_{Paste,ex} = \frac{V_{Paste,ex}}{A_A} = \frac{V_{Paste} - V_{Void}}{A_A} \tag{1}$$

The volume V_{Void} is calculated from the packing density φ_{max}, determined with the compaction test by De Larrard [5], and the surface area of the aggregates A_A, determined with the help of CT-Scans.

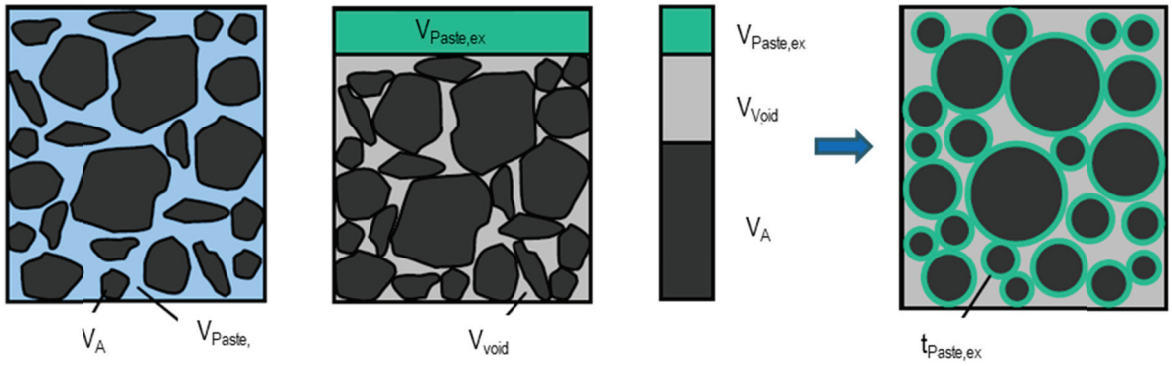

Figure 1: Schematic representation of the excess paste volume $V_{Paste,ex}$ and the excess paste thickness $t_{Paste,ex}$ [3, 4]

2.1 Packing density

A concrete mixture is considered as a dry packing of aggregate particles, filled up with cement paste and its performance is significantly affected by the type and degree of packing of its constituents. In the current study, De Larrard's compaction packing model has been incorporated [5]. The compaction packing density is nothing but the maximum packing density attainable with a specified grain mixture that results from the maximum compaction of the aggregate mixture. During the De Larrard test, the maximum packing density is achieved at a certain compaction level, by applying external energy such as vibration and top-weight. The maximum packing density φ_{max} is calculated as the ratio of the aggregate particle volume V_A to the volume of aggregates including voids in compacted state V_C.

The maximum packing density of the aggregates is determined according to the following procedure: The aggregates are oven dried for 48 hours at 80°C to discard the moisture content prior to the commencement of testing. The dry aggregates with a predetermined composition are uniformly mixed for 30 seconds in a 5-liter Hobart mixer. The aggregate mix is then poured into a cylindrical metal container with an internal diameter of 160 mm, mounted onto the vibrating table. The surface of aggregates are evenly distributed using a trowel and a cylindrical metal piston weighing 19.57 kg is implanted on the surface of aggregates.

The distance between the upper edge of the cylindrical container and the surface of the rammer is measured prior to compaction with a digital vernier calliper at four pre-marked points and the mean value of depth is taken into account.

The aggregates in the cylindrical container are subsequently compacted for 60 seconds by vibration at a constant frequency of 100 Hz. After each compaction, the penetration depth of the metal rammer h_d is measured every 60 seconds and the process is carried out until the change in penetration depth amounts to less than 0.2 mm. By determining the penetration depth, the volume of aggregates in compacted state is evaluated using the equation (3).

$$V_C = \frac{\pi \cdot d_c^2}{4} \cdot \left(h_c - h_l - h_d \right) \tag{3}$$

The volume of the compacted aggregate particle is determined using the diameter of cylindrical container d_c, the height of cylindrical container h_c, the height of cylindrical metal rammer h_l and the mean value of penetration depth after compaction h_d.

Additionally, the absolute volume of the aggregate particles V_A is calculated as the ratio of the mass of aggregates to their particle density ρ_A using the equation (4).

$$V_A = \frac{m_A}{\rho_A} \tag{4}$$

Thus, the maximum packing density of aggregates is evaluated using the equation and the results are summarized in the following table.

Table 1: Packing density of aggregate for HPC and CM

Aggregate Composition	HPC	CM
Maximum Packing Density, φ_{max} [-]	0.755	0.685

2.2 Surface to volume ratio of aggregate fractions

The surface of the aggregate fractions is measured and evaluated three-dimensionally with computed tomography. For this purpose, the aggregate of the fractions basalt 5/8, basalt 2/5, sand 0/2 and quartz sand 0/0.5 is mixed with a low-density material to keep the aggregate particles at a distance and placed in a specimen container. For each fraction, four specimens are produced. The Phoenix VTOMEXS 240 computed tomography system from GE Sensing & Inspection Technologies GmbH performs the CT-Scans of the specimens. For the reconstruction, 1000 X-ray images with a resolution of 1000 × 1000 pixels are generated. The reconstruction software "phoenix datosx" reproduces the volume as an image stack with a voxel edge length between 10 and 40 µm using automatic scan optimization for correction of drift effects and beam hardening correction.

The greyscale difference between aggregate particles and the surrounding material is sufficient enough to identify the particles with the threshold value method. The CT image stack is segmented with a grayscale threshold using MATLAB. Voxels with a grey level above this threshold are assigned a value of 1 and the backround material a value of 0. The watershed algorithm divides connected particles in the binarized image and the regions are subsequently analysed with the MATLAB function "regionprops3" to calculate the surface and the volume of individual particles.

Table 2: Ratio $R = A_A/V_A$ of the analysed aggregate fractions

Basalt 5/8	Basalt 2/5
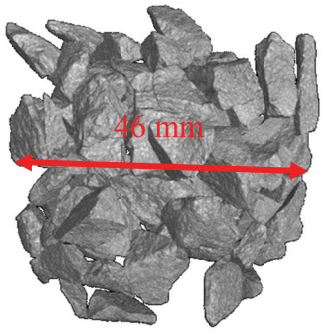	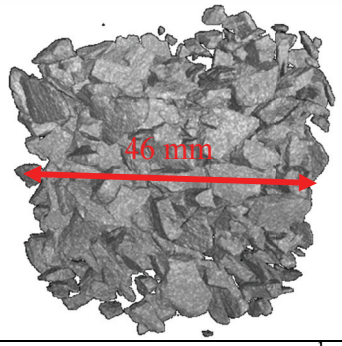
$R = A_A/V_V = 1.30$ mm^{-1}	$R = A_A/V_V = 2.43$ mm^{-1}
Sand 0/2	**Quartz 0/0,5**
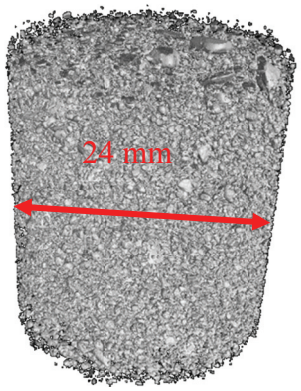	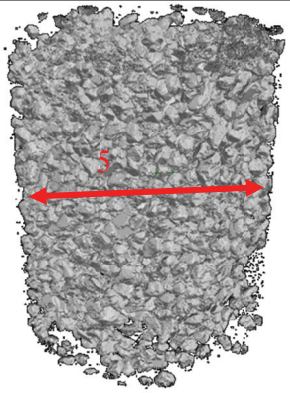
$R = A_A/V_V = 14.7$ mm^{-1}	$R = A_A/V_V = 28.7$ mm^{-1}

2.3 Mix design

The concrete equivalent mortar CM is developed from the HPC listed in table 3. The water/binder ratio w/b is 0.352 for the HPC and the mortar CM. The excess paste thickness $t_{paste,ex}$ of the reference HPC is calculated to 22 µm using equation 5:

$$t_{Paste,ex} = \frac{1000 - V_{AV} - \frac{(1000 - V_{AV})}{\varphi_{\max}} + \frac{V_{Paste}}{\varphi_{\max}}}{A_A}$$
$$V_{Paste} = \frac{m_c}{\rho_c} + {}^{w}\!/_{b} \cdot (1 + {}^{s}\!/_{c}) \cdot m_c + \frac{{}^{s}\!/_{c} \cdot m_c}{\rho_s} + \frac{0.01 \cdot (1 + {}^{s}\!/_{c}) \cdot m_c}{\rho_{sp}} + \frac{0.0057 \cdot (1 + {}^{s}\!/_{c}) \cdot m_c}{\rho_{st}} \quad (5)$$

Therefore, the air void volume V_{AV} of 5 dm³/m³ is considered and the packing density φ_{max} from Table 1 is used. The superplasticizer and the stabilizer depend on the binder mass including silica fume. A proportion of 1% of the binder mass is used for the superplasticizer and 0.57% for the stabilizer. The reference HPC is produced without silica fume. The densities ρ_i can be found in Table 3. The aggregate surface area A_A is calculated from the ratio R_i listed in Table 2 and the aggregate fraction volume V_i for the HPC with equation (6):

$$A_A = \sum_i R_i \cdot V_i = \sum_i R_i \cdot \frac{m_i}{\rho_i} \quad (6)$$

The parameters necessary to solve equation (6) are listed in Table 3, which illustrates the mass of the fractions m_i and the corresponding particle density ρ_i. The cement content m_c is calculated conversely using equation (5). It is varied until the paste thickness of 22 µm is attained. From the HPC without silica fume, a HPC with silica fume with the same paste volume is developed. Therefore, the silica fume to cement ratio s/c is set to 0.1. Accordingly, all cement paste constituents: water, silica fume, superplasticizer and stabilizer can be determined from the cement mass m_c.

Table 3: Concrete composition of HPC and corresponding equivalent Mortar (CM)

Material	Density ρ (kg/m³)	No Silica Fume		Silica Fume	
		HPC (kg/m³)	CM (kg/m³)	HPC (kg/m³)	CM (kg/m³)
Cement c	3.09	500	646	446.8	578
Silica Fume s	2.2	-	-	44.7	57.8
Water w	1.0	176	227	176	223.8
Superplasticizer sp	1.05	5.00	6.46	5.00	5.78
Stabilizer st	1.1	2.85	3.68	2.85	3.29
Quartz sand 0-0.5 mm	2.7	75	118	75	118
Sand 0-2 mm	2.64	850	1336	850	1336
Basalt 2-5 mm	3.06	350	-	350	-
Basalt 5-8 mm	3.06	570	-	570	-

2.4 Mechanical Properties

For concretes and mortars, the compressive strength is determined according to DIN EN 12390-2 and Young's modulus in accordance with DIN EN 12390-5 for cylinders with a diameter of 150 mm and a height of 300 mm. The tensile strength is determined in a direct tensile test on plain cylinders with a diameter of 80 mm and a height of 240 mm. Table 4 summarizes the test results.

Table 4: Mechanical Properties of HPC and CM

Material	No Silica Fume		Silica Fume		Standard Deviation	
	HPC	CM	HPC	CM	HPC	CM
Density [kg/dm³]	2.52	2.33	2.52	2.26	0	0.05
Compressive strength [N/mm²]	112	95.2	116.8	96.4	3.39	0.85
Tensile strength [N/mm²]	5.7	4.9	-	-	-	-
Young's modulus [N/mm²]	44200	39500	44800	33400	424.26	4313.35

3. SEGMENTATION OF CT SCANS

The segmentation of the computed tomography scans allow to generate a real geometry representation. The four concrete phases could be directly used for the mesomodel description: air, basalt aggregate, cement mortar and the interfacial transition zone.

Therefore, the greyscale image stack produced with the CT-Scanner has to be segmented into three phases: air voids, aggregate particles and cement matrix. For the segmentation and classification of the different phases, many methods and procedures are possible [6]. In the case of high performance concrete with crushed basalt aggregate, the following procedure leads to sufficient results:

1. Image acquisition with CT-Scanner
2. Image enhancement with median filter
3. Image segmentation by using a greyscale threshold
4. Separation of connected particles and voids with the Watershed algorithm
5. Mesh generation

The section below describes as an example the procedure for the identification of the basalt aggregate from a cylindrical high performance concrete sample with a diameter of 28 mm and a height of 50 mm. The computed tomography system performs the CT-Scan. For the reconstruction, 1000 X-ray images with a resolution of 1000 × 1000 pixels are generated with the direct-beam tube using a 0.1 mm copper filter with a voltage of 120 kV and a current of 240 A. The reconstruction software "phoenix datosx" reproduces the volume as an image stack with a voxel edge length of 36 µm using automatic scan optimization for correction of drift effects and beam hardening correction.

In the CT image stack, materials with a higher density and materials containing elements with a higher atomic number appear lighter. Basalt has a higher density than sand as well as cement paste and is therefore easy to identify. Furthermore, it contains pyroxene and olivine minerals, which consists of elements with a higher atomic number and are visible as lighter dots within the basalt grains, see Figure 2.

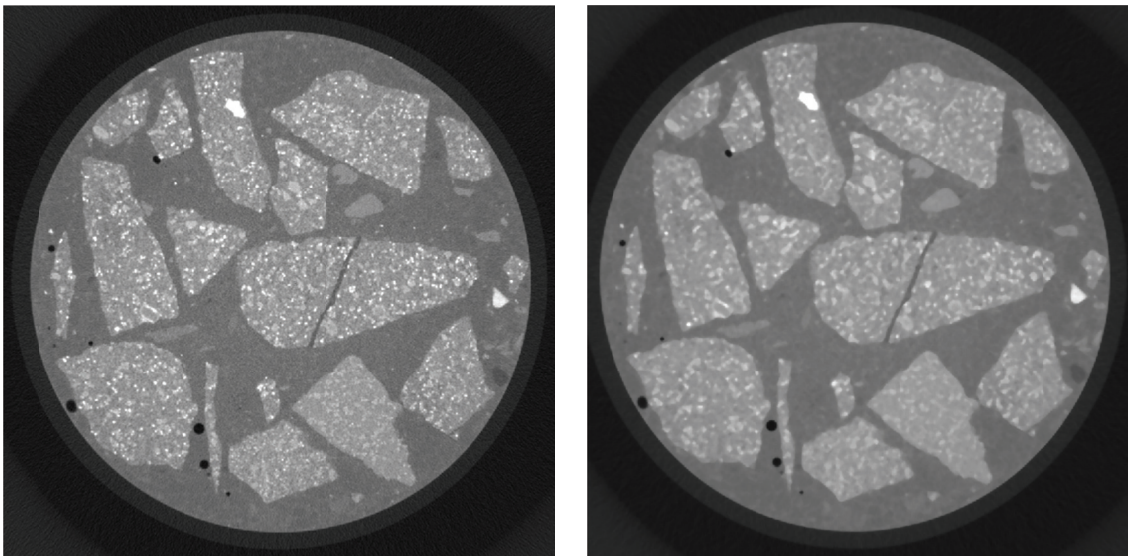

Figure 2: CT-Image (horizontal section) of HPC – Original (left), Filtered (right)

The CT Image stack is enhanced and segmented with the help of the image processing toolbox from MATLAB. First, the median filter function "medfilt3" enhances the image with a pixel mask of 9x9x9 pixels [7]. In this way, the filter produces a smooth image without blurring the contours, see Figure 2 (right).

Subsequently, the segmentation is carried out with the threshold value method. In this case, the threshold value in the histogram is easily determined as the minimum, as shown in Figure 3 (left). On the basis of the grayscale image, it is checked whether the mask generated with the threshold value leads to a meaningful representation of the contours of the aggregate, see Figure 3 (middle). The segmented aggregate grain volume is compared with the aggregate grain volume that is required be present in the sample according to the concrete recipe.

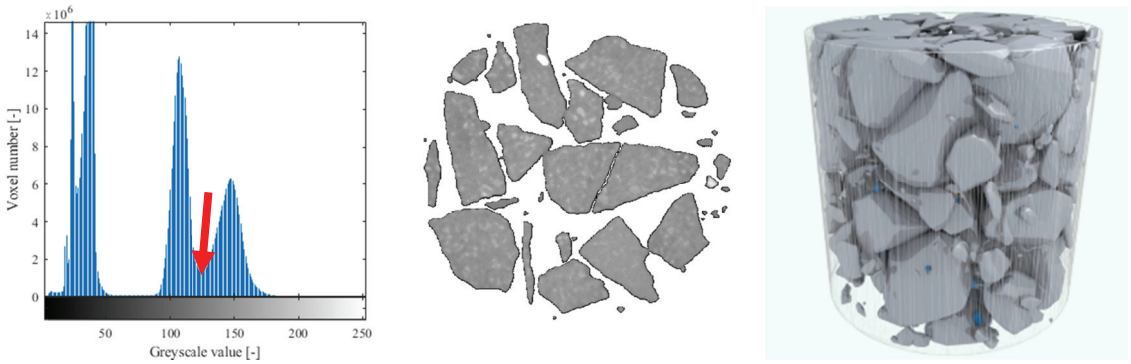

Figure 3: Histogram (left), masked image (middle), 3D aggregate structure (right)

The threshold method binarizes the 3D image. All pixels with a greyscale value above the threshold of 125 are identified as aggregates and receive the value 1, the remaining pixels receive the value 0. The binary image partially contains connected regions, which are separated with the Watershed algorithm [8]. Subsequently, the function "regionprops3" identifies and analyses the regions by determining the surface, volume, barycentre, principal axis orientation, and binary image of each individual rock grain. The smaller components are

removed from the data set and the aggregates with an equivalent diameter above 2 mm are transferred to the meso-model. The mesh for the mesomodel can be built directly from the voxels. Alternatively, a surface mesh can be created for each aggregate grain, which is then transferred to the mesomodel, see Figure 3 (right).

The air voids are segmented and classified analogously to the rock grains. When binarizing, however, the mask has to be inverted in such a way that all voxels with a grayscale value below the threshold for the air voids receive the value 1. In this way, air-filled edge areas are also detected in the CT scan. Due to their large volume, these margins are readily identified and eliminated from the regional analysis data set.

4. CONCLUSIONS

- The theory of excess paste can be used for the preparation of a mortar representative of the bulk material in high performance concrete.
- The Young's modulus of the mortar is reduced in comparison with concrete, as the basalt material is effectively eliminated with a high Young's modulus of 96 kN/mm².
- The compressive strength of the concrete equivalent mortar is also lower than that of concrete. In this case, a reduction of the aggregate interlocking and a lower quality of the ITZ in the mortar are identified as possible reasons.
- The influence of the aggregate interlocking and the ITZ quality on the strength and damage process under fatigue loading of high performance concrete will be studied in further tests.
- The greyscale threshold method delivers sufficient results for the segmentation of basalt grains and air voids within CT images of concrete. Quartz-rich aggregate particles require advanced segmentation techniques like a segmentation based on the variation of grey values [9] or the use of contrast enhancers [10]

ACKNOWLEDGEMENTS

The authors acknowledge support by the German Research Foundation (DFG) through the priority program SPP 2020 “Cyclic deterioration of High-Performance Concrete in an experimental-virtual lab”.

REFERENCES

[1] Oneschkow, N., 'Fatigue behaviour of high-strength concrete with respect to strain and stiffness', Int. J. of Fatigue **87** (2016) 38-49.
[2] Wittmann, F. H., 'Crack formation and fracture energy of normal and high strength concrete', Sadhana **27** (4) (2002) 413-423
[3] Wüstholz, T., 'Experimentelle und theoretische Untersuchungen der Frischbetoneigenschaften von Selbstverdichtendem Beton' (doctoral thesis in German, Universität Stuttgart, Institut für Werkstoffe im Bauwesen, 2005).
[4] Huss, A., 'Mischungsentwurf und Fließeigenschaften von Selbstverdichtendem Beton (SVB) vom Mehlkorntyp unter Berücksichtigung der granulometrischen Eigenschaften der Gesteinskörnung' (Universität Stuttgart, Materialprüfungsanstalt Otto-Graf-Institut (FMPA), 2010).
[5] De Larrard, F., 'Concrete Mixture Proportioning – A Scientific Approach' (E & FN Spon, London, 1999).

[6] Gonzales, R. C., Woods, R. E. , 'Digital Image Processing' (Prentice Hall, New Jersey, 2008).
[7] Marques, O., 'Practical image and video processing using MATLAB' (John Wiley & Sons, Inc., Hoboken, New Jersey, 2011).
[8] Beucher, S., Meyer, F.,. 'The morphological approach to segmentation: The watershed transformation', in 'Mathematical Morphology in Image Processing', (CRC Press, Boca Raton, 1993) 433-481.
[9] Stamati, O., Roubin, E., Andó, E., Malecot, Y., 'Phase segmentation of concrete x-ray tomographic images at mesoscale: Validation with neutron tomography', Cement and Concrete Composites **88,** (2018) 8-16.
[10] Carrara, P., Kruse, R., Bentz, D.P., Lunardelli, M., Leusmann, T., Varady, P.A., De Lorenzis, L., 'Improved mesoscale segmentation of concrete from 3D X-ray images using contrast enhancers', Cement and Concrete Composites **93**, (2018), 30-42.

International Conference on Sustainable Materials, Systems and Structures (SMSS 2019)
Novel Methods for Characterization of Materials and Structures
20-22 March 2019 – Rovinj, Croatia

CHARACTERIZATION OF CURING OF CONCRETE BASED ON COMBINATION OF NDT TECHNIQUES

Evin Dzaye (1,2), Eleni Tsangouri (1), Geert De Schutter (2) and Dimitrios G. Aggelis (1)

(1) Department of Mechanics of Materials and Structures, Vrije Universiteit Brussels, Brussels, Belgium

(2) Magnel Laboratory for Concrete Research, Ghent University, Ghent, Belgium

Abstract

Ensuring the quality of fresh concrete and appropriate curing conditions substantially reduces the likelihood not to perform as expected. In order to obtain control on the curing and hardening process from an age earlier than the age of the standard mechanical tests, this study presents an approach based on different monitoring techniques. Acoustic emission is used to record the numerous events occurring during the first hours when concrete is in liquid form as well as later when hardening starts to take place. Although AE signals carry a great amount of information about the processes occurring in the mix, explaining of their origin is not straightforward due to the different processes that are known to take place in fresh cementitious media like settlement, water and air migration, formation of hydrates as well as shrinkage cracking. To explain the sources of the activity an arsenal of additional monitoring techniques is used. Digital Image Correlation is applied, and a pair of cameras are used to measure both the shrinkage and settlement of fresh concrete in a non-contact way for the first time in literature. Capillary pressure sensors indicate the moment of air entry into the porous system and the measurements are complemented with temperature sensors and mechanical measures of displacement. The information gathered from the multi-attribute setup sheds light in the complex processes and helps to explain the origin of the different sources. Apart from the better control of curing, efforts to correlate early age activity with final mechanical properties are also unfolding with promising results.

Keywords: Cementitious media, Acoustic Emission, Digital Image Correlation, Capillary pressure, Shrinkage, Setting, Monitoring

1. INTRODUCTION

Monitoring of the early stage of concrete is important as it defines the final properties of the hardened material. Acoustic emission (AE) has been increasingly used for this purpose as it shows sensitivity to wave signals during the setting of the material and as early as from the moment of mixing [1-5]. Many processes occur like settlement, formation of bubbles and

hydrates, mobility of bubbles and water, emptying of capillary pores and shrinkage cracking, among others. Since all of them may overlap in time, it is in general a very difficult task to explain the origin of AE populations without the aid of other techniques. At the same time 3D shrinkage occurs in fresh concrete which is conventionally measured by contact and point displacement sensors. Therefore, a non-contact and global methodology is highly sought for. Digital Image Correlation has shown potential of monitoring the 3D movement of a surface but usually after the material has set [6-7]. Additional measurements like capillary pressure can also enlighten us about the moment of air entry and the potential of cracking [8]. Herein, an attempt to combine many techniques in order to monitor fresh cementitious material is made with the use of the aforementioned techniques among others since real time accurate monitoring can provide a tool to characterize the curing process of concrete.

2. OVERVIEW OF TECHNIQUES AND MATERIALS

The AE technique detects stress waves emitted by irreversible processes within a material. These processes may be damage propagation of any form like cracking, other specific processes, like leakage from a pipe or activities occurring in fresh concrete. In a general case, piezoelectric transducers are applied on the surface of the material to transform pressure changes on their surface in electric waveforms. These signals are amplified and led to the acquisition board where they are stored in a digital form [9]. A representation of an AE setup tuned to the current application is given in Figure 1(a) and a photograph of the current setup in Figure 1(b).

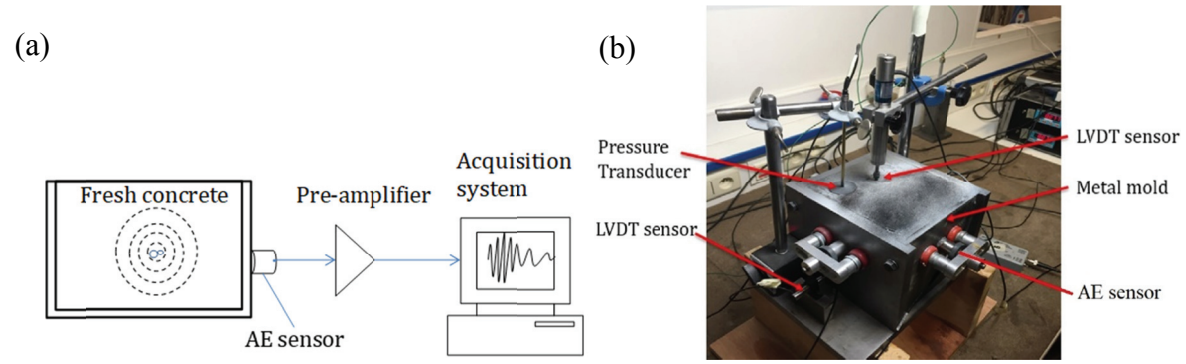

Figure 1: (a) Typical AE setup. (b) photograph of the actual setup [10].

The basic parameters of a recorded waveform are the amplitude, the duration, the energy (area under the rectified envelope), the frequency content measured by the threshold crossings over the duration and others [9]. The AE system of this study is a Micro-II express of Mistras Group that allows recording of the full AE waveform. AE monitoring was applied by means of five piezoelectric sensors (R15, resonant at 150 kHz, Mistras) mounted on the metallic mold. The mold is 150x150x150 mm and the sensors were applied on the center of each side, except the top which was the free surface of concrete.

Concerning the DIC measurements, the concrete top surface was covered by a black and white pattern through spraying. A pair of digital cameras (AVT Stingray with resolution of 2504x2056 pixels) were placed above the mortar surface building a stereovision system that periodically capture images of concrete surface each 2 minutes. The measurement and the

post-processing analysis were conducted by means of VIC-Snap and VIC-3D software respectively. As a result, the 3D displacement vector over the free surface of the specimen were obtained, namely vertical settlement and horizontal shrinkage. Conventional LVDTs were also applied for the settlement and horizontal displacement for comparison purposes. In addition, a pressure sensor was connected to the pore system by a 150 mm long brass tube having an inside diameter of 4 mm, in order to measure the capillary pressure development of the specimen. This brass tube was placed in the specimen and was filled with de-ionized and degassed water. The capillary pressure transducer was attached vertically 30 mm deep into the material from the top surface.

Specimens of cement mortar were prepared using normal Portland cement (cement CEM I 52.5N and water). The mortar mix design was performed with 1 part of cement, 2 parts of sand and with a water to binder ratio of 0.45. The material was prepared in the laboratory concrete mixer and was mixed for 3 min at low speed. After that, the material was poured into a metallic mold and consolidated on the vibration table at high frequency for 20 s. Curing occurred in a temperature and humidity-controlled laboratory room. The temperature was set at 20 ±1 ^{O}C and was controlled by air-conditioning installation and relative air humidity at 50%. The mixing and casting of the cement mortar were completed in approximately 10 min. At a next step, the mold was placed at the experimental setup and the surface was covered in black-white speckle pattern. The preparation of the surface for the DIC measurements lasted approximately 10–15 min. More details on the setup can be found in [10,11].

3. RESULTS

Figure 2 shows the elevation of the concrete surface (W) in two moments, one at reference time 0 min (corresponding to 25 minutes after mixing) and one after approximately 2 h. It is seen that even from a very early age, there is a certain surface morphology with lower elevation in the middle of the specimen. Later this becomes even more evident with the effect of settlement, where at 130 min the maximum settlement in the middle of the specimen is of the order of 1.2 mm. It is obvious that the settlement is not uniform and that only a global measurement tool could indicate such a distribution.

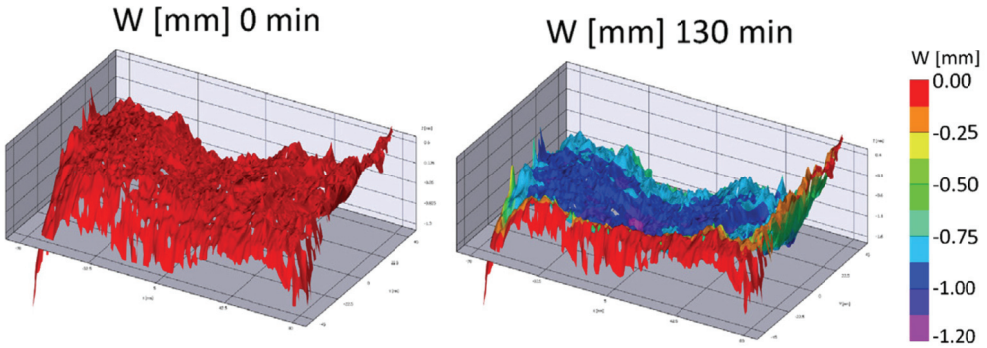

Figure 2: 3D vertical displacement (W) maps at two different ages.

The settlement development as monitored by traditional LVDT is shown in Figure 3. In the same graph the settlement obtained as the average of the DIC values in the total monitored surface area is also depicted and compared with the settlement at the highest and the lowest points. All lines follow the same trend showing a steep decrease until 200 min, while later the

fluctuations are smaller. However, there is strong difference in absolute values as points near the center of the specimen exhibit much stronger settlement (« maximum ») than points near the interface with the mold (« minimum »). Correspondingly, the average DIC value lies in between, being quite close to the LVDT. Considering the range between minimum and maximum settlement on the same surface, it is obvious that a point measurement cannot be considered representative.

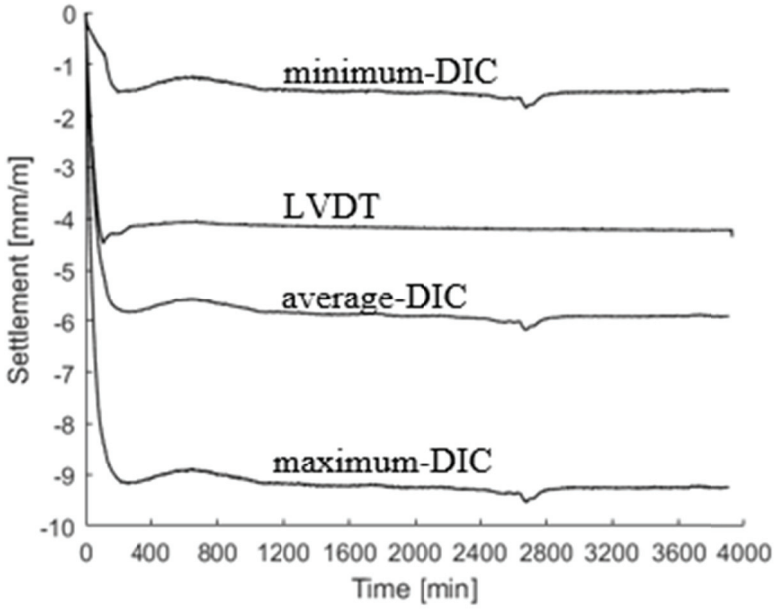

Figure 3: Settlement as measured by LVDT and DIC at different points.

As seen from the above figure, most of the mobility of concrete occurs in the first two hours. Reasonably, this is the period with the highest rate of registered AE activites. This is shown in Figure 4 where the cumulative AE is presented along with the capillary pressure curve. The AE acquisition rate is strong from the start, something related with the high rate of settlement. The capillary pressure started to increase at approximately 100 min until 200 min in the pore system when menisci form between the solid particles at the surface [8]. At that moment, the pressure instantly dropped indicating the air entry point into the system. This moment is also connected to the setting point of concrete. After that period, the mobility of the cementitious medium is reasonably restricted something affecting all the measurements. Indeed AE rate gradually drops to a minimum and the settlement is essentially saturated, see Figure 3. The temporary reversal in settlement that occurs around 600 min coincides with the temperature peak and should be attibuted to the thermal expansion due to hydration.

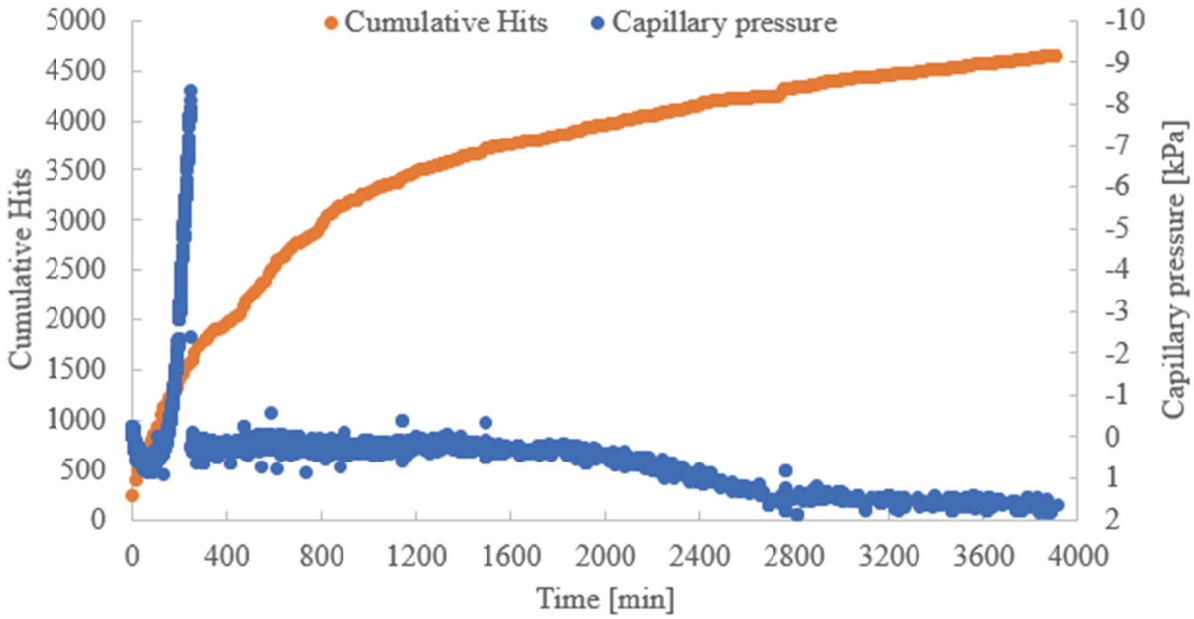

Figure 4: AE cumulative activity and capillary pressure vs. curing time.

4. DISCUSSION

DIC application is very promising as it enables a non-contact, global view on the settlement and shrinkage. However, there are two points where improvement is possible. One is the onset time for the measurement that now may reach even 20 min after mixing, until the material is fixed in the setup. This means that some amount of settlement may have already occurred and therefore is not registered, which of course may apply for the LVDT measurement as well. In addition, excess bleed water interferes with the black and white pattern possibly inducing some extra mobility to the black and white dots interfering with the final results. Concerning AE, it is possible that, as concrete shrinks, a sensor is detached from one of the mold sides, resulting in less acquisition for the corresponding position. In response to that, the sensor at the bottom was placed, which is a side of the mold that will never be detached. Finally, wave propagation characteristics are of great importance. The mechanical properties and viscosity of fresh cement alter throughout the curing period strongly affecting the propagation of waves. A certain difference in frequency and amplitude is expected in the received waveform if a certain excitation propagates through highly attenuative viscous fresh paste, or through hardened concrete. Currently, numerical simulations are under way to enlighten this aspect which is equally important as the source mechanisms themselves.

5. CONCLUSIONS

The present study occupies with AE behavior, DIC and capillary pressure development of concrete samples at very early age. To do this, a combination of non-destructive techniques was combined on the metallic mold. AE sensors applied on the mold proved to be very sensitive and registered thousands of AE signals from few minutes after mixing. Besides, capillary pressure monitoring was applied recording the pressure development. The classical LVDT measurement and DIC measurement followed the same trend indicating the

effectiveness of DIC methods to monitor displacement and strain evolution during the early drying process in a non-contact manner. Three-dimensional DIC technique allows an improved assessment of the non-uniform deformation distribution on the specimen surface when concrete shrinks and settles, which is not possible with classical point LVDT measurements. Further work is necessary mainly in the direction of interpretation of the data in order to firmly connect AE signals to the exact process occurring in fresh concrete.

ACKNOWLEDGEMENTS

Financial support of the Research Foundation Flanders (FWO-Vlaanderen) through Projects No 28976 and G012315N is gratefully acknowledged.

REFERENCES

[1] K. Van Den Abeele, W. Desadeleer, G. De Schutter, and M. Wevers, Active and passive monitoring of the early hydration process in concrete using linear and nonlinear acoustics, Cement and Concrete Research 39(5) (2009) 426–432.
[2] T. Shiotani, J. Bisschop, and J. G. M. Van Mier, Temporal and spatial development of drying shrinkage cracking in cement-based materials, Engineering Fracture Mechanics 70(12) (2003) 1509–1525.
[3] Pietro Lura, Jon Couch, Ole Mejlhede Jensen, Jason Weiss, Early-age acoustic emission measurements in hydrating cement paste: Evidence for cavitation during solidification due to self-desiccation, Cement and Concrete Research 39 (2009) 861–867.
[4] Libor Topolár, Luboš Pazdera, Barbara Kucharczyková, Jaroslav Smutný and Karel Mikulášek, Using Acoustic Emission Methods to Monitor Cement Composites during Setting and Hardening, Applied Science 7(5) (2017) 451; doi:10.3390/app7050451
[5] Iliopoulos, S.N., Khattabi, Y.E., Aggelis, D.G. Towards the Establishment of a Continuous Nondestructive Monitoring Technique for Fresh Concrete, Journal of Nondestructive Evaluation, 35 (3) (2016) article no. 37.DOI: 10.1007/s10921-016-0355-7
[6] T. Mauroux, F. Benboudjema, P. Turcry, A. Aït-mokhtar, O. Deves, Study of cracking due to drying in coating mortars by digital image correlation, Cement Concrete Res. 42 (7) (2012) 1014–1023.
[7] I. Maruyama, H. Sasano, Strain and crack distribution in concrete during drying, Mater. Struct. 47(3) (2014) 517–532.
[8] V. Slowik, M. Schmidt, R. Fritzsch, Capillary pressure in fresh cement-based materials and identification of the air entry value, Cement Concrete Composites 30 (7) (2008) 557–565.
[9] Grosse, C.U., Ohtsu, M.: Acoustic Emission Testing. Springer, Berlin (2008)
[10] Evin Dildar Dzaye, Eleni Tsangouri, Karel Spiessens, Geert De Schutter, Dimitrios G. Aggelis, Digital image correlation (DIC) on fresh cement mortar to quantify settlement and shrinkage, Archives of Civil and Mechanical Engineering, 19 (1) (2019) 205-214.
[11] Evin Dildar Dzaye, Geert De Schutter, Dimitrios G. Aggelis, Study on mechanical acoustic emission sources in fresh concrete, Archives of Civil and Mechanical Engineering, 18 (2018) 742-754.

International Conference on Sustainable Materials, Systems and Structures (SMSS 2019)
Novel Methods for Characterization of Materials and Structures
20-22 March 2019 – Rovinj, Croatia

CHARACTERIZATION AND MODELING OF THE THERMAL AND MECHANICAL PROPERTIES OF SELF-COMPACTING CONCRETE AT EARLY AGES

María D. Crespo (1), Climent Molins (2) and Antonio R. Marí (2)

(1) Department of Structures, School of Civil Engineering, FCEIA, Universidad Nacional de Rosario, Riobamba y Berutti, 2000, Rosario, Argentina

(2) Department of Civil and Environmental Engineering, Universitat Politècnica de Catalunya, Jordi Girona 1-3, 08034, Barcelona, Spain

Abstract

Cracking of concrete at early ages, that may affect the structure durability and even its safety, can be simulated by means of models based on the concepts of degree of hydration and equivalent age, which require the characterization of the concrete during the hydration process of cement. This paper presents the results of the characterization tests of self-compacting concrete and its modeling at early ages according to different models available in the literature. The tests included measurements of developments of the degree of hydration, compressive strength, indirect tensile strength, elastic moduli, creep at loads corresponding to 30% of the strength at 2, 3 and 7 days and autogenous shrinkage. It is concluded that both the maturity method and the degree of hydration concept are valid to predict the evolution of material properties during the hardening process of the tested self-compacting concrete. In addition, best fitting models for most properties are highlighted.

Keywords: concrete at early ages, self-compacting concrete, modeling concrete properties, degree of hydration, maturity

1. INTRODUCTION

Cement hydration not only increases the strength and stiffness of concrete, but also generates heat and causes volume changes (thermal deformations and autogenous shrinkage). When these volume changes are constrained, stresses arise, which in turn are reduced by the effect of relaxation. If the stresses achieved at some point of the structure exceed tensile strength, concrete will crack, which can drastically reduce its durability.

Although the mechanical properties of self-compacting concrete (SCC) are comparable to those of conventional concrete at mature ages [1], significant autogenous shrinkage may arise in SCCs. Furthermore, in a way equivalent to what occurs in conventional compacting

concrete, high cement content will lead to higher hydration heat, consequent dilatation and subsequent thermal deformation, which could lead to significant cracking.

Since SCCs are so widely used today, the possibility of predicting –and if possible avoiding or controlling by means of reinforcement- early age cracking in SCC members, is a topic of major interest.

Early-age cracking of concrete can be simulated using models based on the concept of degree of hydration [2] and on the maturity method or equivalent age [3]. Even though these two approaches are different, both methods take into account the heat-activated nature of cement hydration and lead to the same results when using appropriate functions [4].

The use of either method requires the characterization and modeling of concrete properties at early ages, i.e., the heat of hydration development, the mechanical properties evolution, creep, and autogenous shrinkage strains. The correct evaluation of temperatures and stresses fields and the cracking risk requires accurate input data, so every intervening property needs to be correctly modeled [5].

In order to collect reliable and representative data of the materials used in Spain to simulate the behavior of concrete members with restrained strains, an experimental campaign on a SCC of 60 MPa of strength at 28 days was conducted [5], and the different properties were modeled as a function of both degree of hydration and equivalent age.

This article firstly summarizes the experimental results of the tests performed on a SCC. Then, models specifically developed for concrete at early ages available in the literature are used to adjust the measured properties. Finally, the accuracy of the different models applied is assessed, particularly in terms of the required parameters.

2. EXPERIMENTAL CAMPAIGN

Tests were performed on fresh SCC (slump flow, initial temperature and specific weight) and during the hardening process of four batches.

The SCC was designed to obtain mean 28-day strength of 60 MPa. Table 1 shows the mix proportion and Table 2 shows the fresh concrete properties of three batches.

2.1 Thermal Characterization

Semi-adiabatic tests were performed on two batches and measured temperatures were turned into adiabatic ones according to the RILEM TC 119-TCE [6] recommendations.

After obtaining adiabatic temperatures, degree of hydration is calculated from [7], [8]:

$$\alpha(t) = \frac{Q(t)}{Q_{pot}} = \frac{\Delta T_{ad}(t)}{máx \Delta T_{ad}} \quad (1)$$

where $Q(t)$ is the heat released until time t; Q_{pot} heat potential of hydration, calculated as the sum of the heat released by each reactive component in the hypothetical case of complete hydration. The reactive phases of the Portland cement are calculated based on the percentages of the different oxides in its composition by using the method proposed by Bogue [9].

The liberated heat of hydration in an adiabatic test is computed based on the measured temperatures as:

$$Q(t) = \Delta T_{ad}(t) \,.\, \rho \,.\, c \quad (2)$$

where $\Delta T_{ad}(t)$ is the adiabatic temperature rise and ρ and c are the specific weight and the heat capacity of concrete, respectively.

The development curve of degree of hydration is expressed in terms of equivalent age, calculated according to Freiesleben Hansen and Pedersen [7]:

$$t_{eq} = \int_0^t \exp\left[\frac{E_a}{R}\left(\frac{1}{293} - \frac{1}{273+T(t)}\right)\right]dt \quad (3)$$

where R is the universal gas constant (=8.315 J/mol°C) and E_a is the activation energy (=33.5 kJ/mol for Portland cement). Table 3 lists the thermal properties of concrete.

Table 1: Mix proportion

Material	Proportion	Characteristics
Cement	425 kg/m^3	CEM I 52.5 R
Water	180 l/m^3	
Limestone filler	22.3 kg/m^3	
Fine aggregate 0/5	950 kg/m^3	Limestone
Coarse aggregate 5/12	600 kg/m^3	Limestone
Coarse aggregate 12/20	200 kg/m^3	Limestone
Additive	8.5 kg/m^3	Superplasticizer Glenium Sky 511-R

Table 2: Fresh concrete properties

Batch	1	2	3
Slump flow [mm]	625	570	500
Time T50 [sec]	3:50	2:07	2:95
Initial temperature [ºC]	20.4	21.4	-
Specific weight [kg/m^3]	2 310	2 350	2 330

Table 3: Thermal properties of the concrete (batch 2)

ρ [kg/m^3]	c [J/(kg.K)]	Ea [kJ/mol]	Q_{pot} [kJ/kg]	max ΔT_{ad} [ºC]	ΔT_{ad}^{max} [ºC]	α_{max} [-]
2 386	1 086	33.5	460.9	75.6	59.6	0.788

2.2 Mechanical Characterization

A number of indirect tensile and compressive strengths and elastic moduli tests at the ages of 12 hours, 1, 2, 3, 7, 14 and 28 days were performed. Experiments to measure both autogenous shrinkage and creep were performed on pairs of cylindrical specimens (150 x 300 mm). The autogenous shrinkage deformation was obtained by subtracting the thermal deformation from the strains measured on unloaded specimens, considering a thermal expansion coefficient $\alpha = 10 \times 10^{-6}$ 1/ºC.

The creep tests were performed at ages 2, 3 and 7 days, with loads corresponding to 30% of the strength measured on twin specimens. The two test specimens were serially placed in racks, according to the standard ASTM C 512 [10].

3. MODELING CONCRETE PROPERTIES

3.1 Degree of hydration development

The degree of hydration evolution curve was adjusted with the following models (Table 4): the three-parameter model developed by Freiesleben Hansen and Pedersen [11] and the two-parameter models (modified Jonasson and Danish [7]).

It can be seen in Fig. 1 that both modified Jonasson and Danish models overestimate the degree of hydration at early hours and at the end of the trial, while the Freiesleben model achieves a very good correlation, due to the fact that it is a 3-parameter model that considers the ultimate degree of hydration in the formulation.

Table 4: Models for the development of degree of hydration

Freiesleben Hansen and Pedersen [11]	$\alpha(t_e) = \alpha_u . \exp\left[-\left(\frac{\tau}{t_e}\right)^{\beta}\right]$ τ , β: hydration time and hydration shape parameters; α_u : ultimate degree of hydration
Modified Jonasson [7]	$\alpha(t_e) = \exp\left\{-\left[\ln\left(1+\frac{t_e}{t_k}\right)\right]^{c_1}\right\}$ t_k and c_1 : fitting parameters
Danish [7]	$\alpha(t_e) = \exp\left[-\left(\frac{a}{t_e}\right)^{b}\right]$ a and b : fitting parameters

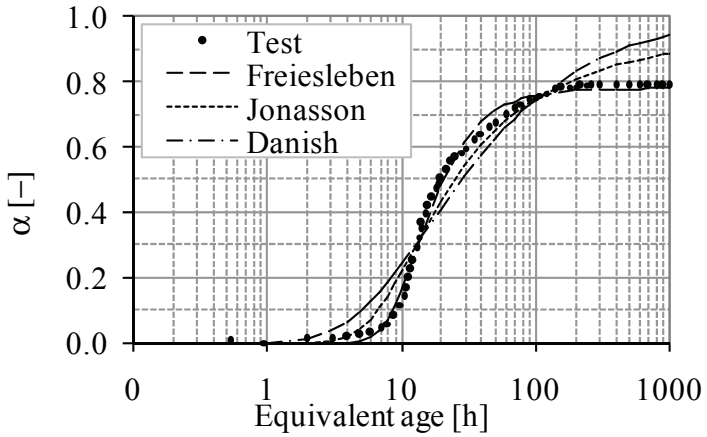

Figure 1: Comparison of the adjustments of the hydration degrees for batch 2

3.2 Mechanical properties

Mechanical properties evolution is adjusted based on equivalent age (Table 5) with the models of the *Japan Concrete Institute* (*JCI)* [12] and the *Norwegian University of Science*

and Technology (*NTNU)* [13], which are modifications of the formulas of the Model Code 90 (*MC90*) [14].

Table 5: Models for the evolution of the mechanical properties as a function of equivalent age

JCI [12]
$f_c(t) = f_{c28} \times \exp\left[s_f \times \left(1 - \sqrt{\frac{28 - a_f}{t - a_f}} \right) \right]$; $E_c(t) = E_{c28} \times \exp\left[s_E \times \left(1 - \sqrt{\frac{28 - a_E}{t - a_E}} \right) \right]$
f_{c28} , E_{c28} : compressive strength and elastic modulus at 28 days ; s_f , s_E : fitting shape parameters ; a_f , a_E : fitting setting time parameters
NTNU [13]
$f_c(t_e) = f_{c28} \times \exp\left[s \times \left(1 - \sqrt{\frac{28}{t_e - t_0}} \right) \right]$; $f_t(t_e) = f_{t28} \times \left\{ \exp\left[s \times \left(1 - \sqrt{\frac{28}{t_e - t_0}} \right) \right] \right\}^{nt}$ $E_c(t_e) = E_{c28} \times \left\{ \exp\left[s \times \left(1 - \sqrt{\frac{28}{t_e - t_0}} \right) \right] \right\}^{nE}$
f_{c28}, f_{t28} , E_{c28} : compressive, tensile strengths and elastic modulus at 28 days ; *s* and t_0 : common parameters; nt and nE : fitting parameters of tensile strength and elastic modulus

The *JCI* incorporates the effect of the setting time in the expressions of compressive strength and elastic modulus to make them applicable to concrete with ages under one day. In turn, the *NTNU* expressions introduce an age parameter t_0 below which stiffness and strength are null. To determine the evolution of tensile strength and elastic modulus, it is only necessary to determine the exponents *nt* and *nE* since t_0 and *s* are parameters common to all three equations and are determined from compression tests.

Fig. 2 shows the experimental results of the different properties evolution overlapped with the models adjustments. It can be seen that both models fit very well the compressive strength evolution. The same applies to the tensile strengths obtained with the *NTNU* model.

Regarding the moduli of elasticity, the values at 28 days are also very similar for both models, but the fitting setting time parameter of the *JCI* model *aE* is very low compared *af*, which may be due to the fact that there were no data of the elastic modulus during the early hours. If the modulus of elasticity is fitted with the *JCI* model considering *aE* = *af* = 11.41 hours (obtained for the compression test), the curve fitting practically coincides with the model of the *NTNU*.

According to Gutsch [8] and De Schutter and Taerwe [15], the different properties evolution can be expressed depending on the degree of hydration as:

$$X_i(\alpha) = X_{il} \times \left(\frac{\alpha - \alpha_0}{1 - \alpha_0} \right)^{ni} \quad (4)$$

For the Gutsch model X_{i1} is a hypothetical value of each property at $\alpha = 1$, whereas for the model of De Schutter X_{i1} is the maximum value of the property. In this paper, the Gustch model is used.

Compressive strength evolution was used to adjust the initial degree of hydration α_0. In Fig. 3, mechanical properties evolutions as a function of hydration degree are shown.

It is noteworthy that there are no measures of strengths for hydration degrees between 0.25 and 0.56, which can be explained by the fact that since the cement is rapid-hardening, the degree of hydration was 0.55 at 24 hours. This should be taken into account when programming the experiments and tests should be conducted between 0.5 and 1 day.

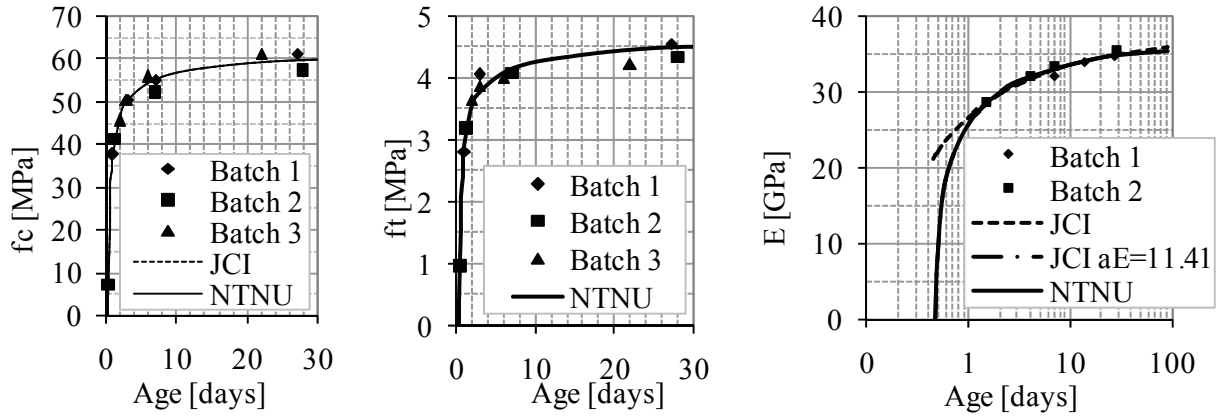

Figure 2: Evolution of compressive strength (a), indirect tensile strength (b) and elastic modules (c) as a function of age

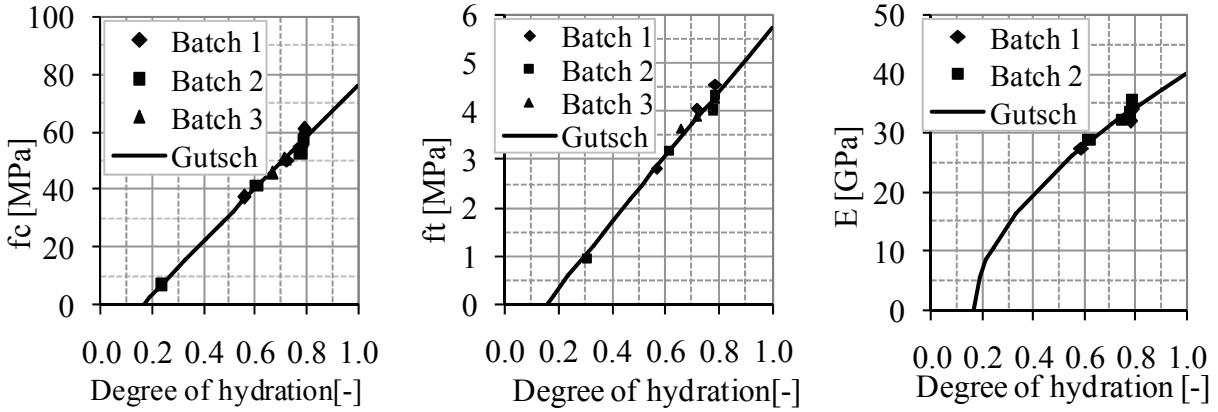

Figure 3: (a) Evolution of compressive and (b) tensile strength and (c) modules of elasticity as a function of degree of hydration

3.3 Autogenous Shrinkage

The autogenous shrinkage deformations modeled are those that occur after "time zero", as these strains are the ones that generate stresses. These strains were adjusted by nonlinear regression with the expressions of *JCI* [12] and Rostásy *et al*. [16] (Table 6), considering initial setting time t_0 =11.41 hours, which is the value found in the characterization of compressive strength. The values obtained by means of non linear regression were: $\varepsilon_{as\infty} = -223.10^{-6}$, $a = 0.193$ and $b = 0.547$.

Table 6: Models for the evolution of autogenous shrinkage

JCI [12] and iBMB [16]
$\varepsilon_{as}(t) = \gamma \cdot \varepsilon_{as\infty} \cdot \beta(t)$; $\beta(t) = 1 - e^{-a \cdot (t-t_0)^b}$
γ : parameter takes into account cement type (= 1 for Portland cement) ; *a* and *b* : constants obtained from a table as function of *w/b* ; t_0 : initial setting time [days] ; *t* : age of the concrete [days] ; *w/b* : water/binder ratio ; $\varepsilon_{as\infty}$: final value of the autogenous shrinkage: *JCI [12]:* $\varepsilon_{as\infty}(w/b) = 3070\ e^{-7.2\ a/b} \times 10^{-6}$; *Rostásy et al. [16]:* $\varepsilon_{as\infty} = 1300\ e^{-5.9\ a/b} \times 10^{-6}$
Fib [17]
$\varepsilon_{as}(t) = \beta_{as}(t) \cdot \varepsilon_{as\infty}$; $\beta_{as}(t) = 1 - \exp\left(-0.2\ t^{0.5}\right)$; $\varepsilon_{as\infty} = -\alpha_{as}\left(0.1 f_{cm} / 6 + 0.1 f_{cm}\right)^{2.5} \times 10^{-6}$
$\varepsilon_{as\infty}$: final value of the autogenous shrinkage; *t* : age of the concrete or equivalent age t_e [days]; f_{cm} : mean compressive strength at 28 days [MPa]; α_{as} : coefficient dependent on cement type (= 600 for rapid hardening high strength cements)

In addition, the final value of autogenous shrinkage was calculated as a function of the w/b ratio (equal to 0.42) with the expressions proposed by the *JCI* [12] and Rostásy *et al*. [16], resulting $\varepsilon_{as\infty} = -170.10^{-6}$ and $\varepsilon_{as\infty} = -121.10^{-6}$, respectively. Autogenous shrinkage was also calculated according to *Fib* model [17] as a function of the mean compressive strength at the age of 28 days, obtaining $\varepsilon_{as\infty} = -109.10^{-6}$.

The experimental and predicted evolution of the autogenous shrinkage strain is shown in Fig. 4. It can be seen that all models underestimate autogenous shrinkage strain.

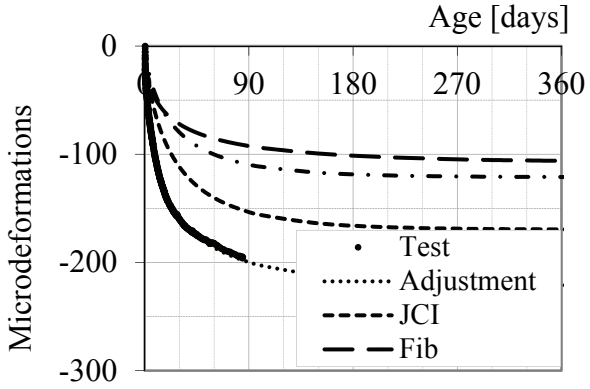

Figure 4: Autogenous shrinkage evolution

3.4 Creep

Two models were used to adjust creep [5], (Table 7): creep compliance was approached as a function of equivalent age with the Jonasson and Larson model ([18], [19]) and creep function $\varphi(t - t_1, t_1)$ (ratio between the creep strain $\varepsilon_{cr}(t - t_1)$ to the elastic strain at loading $\varepsilon_{el}(t_1)$) was approached with the Gutsch model [20] as a function of degree of hydration at loading.

Table 7: Models for the evolution of creep strains

As a function of the equivalent age*: Larson and Jonasson* [20,21]
$$J(\Delta t_{load}, t_0) = \frac{1}{E(t_0)} + \Delta J(\Delta t_{load}, t_0)$$ $\Delta t_{load} = t - t_0$; $\Delta J(\Delta t_{load}, t_0)$: creep associated with the initial modulus of elasticity definition: $E(t_0) = \frac{1}{J(\Delta t_0, t_0)}$; $\Delta(t_0)$=0.001d. When creep is modeled with two lines: $$\Delta J(\Delta t_{load}, t_0) = \begin{cases} a_1(t_0) \cdot \log\left(\frac{\Delta t_{load}}{\Delta t_0}\right) & (1) \\ a_1(t_0) \cdot \log\left(\frac{\Delta t_1}{\Delta t_0}\right) + a_2(t_0) \cdot \log\left(\frac{\Delta t_{load}}{\Delta t_1}\right) & (2) \end{cases}$$ (1) for $\Delta t_0 \le \Delta t_{load} < \Delta t_1$ and (2) for $\Delta t_{load} > \Delta t_1$. The slopes a_1 and a_2 are adjusted with: $$a_i(t_0) = a_i^{min} + \left(a_i^{max} - a_i^{min}\right)\exp\left[-\left(\frac{t_0 - t_s}{t_{ai}}\right)^{n_{ai}}\right]$$ t_s : apparent setting time ; a_i^{max} and a_i^{min} : maximum and minimum values of the slopes (recommended by the authors) ; n_{ai} and t_{ai} : fitting parameters
As a function of hydration degree*: Laube-Gutsch* [22]
$$\varphi(t - t_1, t_1) = \frac{\varepsilon_{cr}(t - t_1)}{\varepsilon_{el}(t_1)} = P_{1c}(\alpha_1) \cdot \left[\frac{t - t_1}{1h}\right]^{P_{2c}(\alpha_1)}$$ α_1 : degree of hydration at loading age t_1 [hours]; $P_{1c}(\alpha_1)$, $P_{2c}(\alpha_1)$: parameters depending on degree of hydration α_1: $P_{1c} = a_1 + b_1 \cdot \alpha_1$, $P_{2c} = a_2 + b_2 \cdot \alpha_1$ which are calibrated from tests

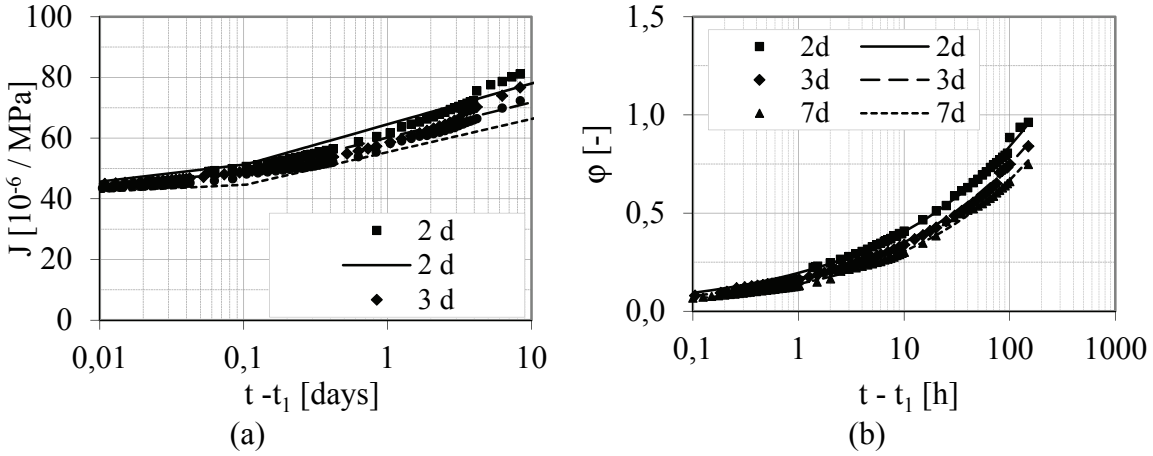

Figure 5: (a) Creep compliances approximated with Larson-Jonasson model. (b) Creep functions approximated with the Laube-Gutsch model

The *Linear Logarithmic Creep Model* of Larsson and Jonasson defines the creep compliance by piecewise linear curves in the logarithmic time scale. When two lines are used, the first line of slope a_1 from t_0 until $\Delta t_{load} = \Delta t_1$ defines the "short-term creep", and the second line of slope a_2 from t_1 forward defines the "long term creep", considering $\Delta t_0 = 0.001$d, $\Delta t_1 = 0.1$d. The parameter t_s is the apparent setting time expressed in days ($t_s = 11.41$ h $= 0.475$d).

Fig. 5a shows the experimental and calculated creep compliances and Fig. 5b compares the creep functions measured and estimated according to Gutsch. Very good correlation between the measured and calculated values are obtained with both models.

4. CONCLUSIONS

The following conclusions can be stated regarding the models used in this paper:

- Freiesleben-Hansen model is the one that best fits the development of the degree of hydration, due to the fact that it is a 3-parameter model that considers the ultimate degree of hydration in the formulation.
- The adjustment of the compressive strength as a function of equivalent age is very good with both *JCI* and *NTNU* models. For the elastic modulus, the approximation of the *JCI* model is not good since no data are available for low degrees of hydration. Considering the setting time parameter for the elastic modulus equal to the one obtained for compression (aE = af) seems to be a good option when data of modules at early hours are not available.
- The Gutsch model depending on the degree of hydration provides a close approximation of the mechanical properties evolution.
- The magnitude of the autogenous shrinkage measured in the SCC is much higher than the one predicted by the different models. According to the results, these large differences in the estimates of the autogenous shrinkage in SCC deserve further research.
- The *JCI* expression as a function of the w/b ratio is the one that best approximates the measured autogenous shrinkage, and the Fib expression as a function of the mean compressive strength at 28 days, is the one that produces the smallest final value of autogenous shrinkage.
- The adjustments of creep strain are very precise, both with Larson-Jonasson model as a function of equivalent age, and with Gutsch-Laube model, depending on the degree of hydration. The Larsson-Jonasson model has the advantage of having a clear physical meaning. However, its use requires the adjustment of many parameters, which entails large amount of experimental data. In turn, the Gustch model requires prior adjustment of degree of hydration.

Given the findings above, both the maturity method and degree of hydration concept are valids to predict the evolution of material properties during hardening of the tested SCC concrete. However, modeling as a function of the degree of hydration is somewhat more complicated since prior adjustment is required.

ACKNOWLEDGEMENTS

This work was performed under a research contract C-05467 between Infraestructures de la Generalitat de Catalunya (GISA) and the Universitat Politècnica de Catalunya (UPC) for research and innovation on Line 9 of the Barcelona Metro. The authors acknowledge the support of all those without whom this study would have been impossible, particularly Mr. Tomas Garcia, Mr. Camilo

Bernard and Mr. Robert Mc-Aloon from the Structural Technology Laboratory of the UPC. The first author would like to gratefully acknowledge the support provided by the School of Exact Sciences and Engineering, Universidad Nacional de Rosario, for making her Ph.D. work at the UPC possible.

REFERENCES

[1] Persson, B., 'A comparison between mechanical properties of self-compacting concrete and the corresponding properties of normal concrete', *Cem. Concr. Res.* **31** (2) (2001) 193-198.
[2] De Schutter, G., 'Fundamental study of early age concrete behaviour as a basis for durable concrete structures', *Mater. Struct*. **35** (1) (2002) 15-21.
[3] Waller, V., d'Aloïa, L., Cussigh, F. and Lecrux, S., 'Using the maturity method in concrete cracking control at early ages', *Cem. Concr. Comp.* **26** (5) (2004) 589-599.
[4] De Schutter, G., 'Applicability of degree of hydration concept and maturity method for thermo-visco-elastic behaviour of early age concrete', *Cem. Concr. Comp*. **26** (5) (2004) 437-443.
[5] Crespo, M.D., 'Behaviour of reinforced concrete at early ages. Structural effects of the imposed strains'. (In Spanish). PhD Thesis. Universitat Politècnica de Catalunya. Escola Tècnica Superior d'Enginyers de Camins, Canals i Ports, Barcelona, (2011).
[6] RILEM TC 119 –TCE, 'Avoidance of thermal cracking in concrete at early ages', *Mater. Struct*. **30** (202) (1997) 451-464.
[7] Krauß, M., Rostásy, F.S. and Gutsch, A.-W., 'Modelling of degree of hydration on basis of adiabatic heat release', IPACS Report BE96-3843/2001:13-3, TU Lulea, (2001).
[8] Gutsch, A.-W., 'Properties of early age concrete – Experiments and modelling', *Mater. Struct*. **35** (2) (2002) 76-79.
[9] Bogue R. H. 'The chemistry of Portland Cement', (Reinhold Publishing Co., New York, 1947).
[10] ASTM C512, 'Standard test method for creep of concrete in compression', (2002).
[11] Freiesleben Hansen, P. and Pedersen, E.J., 'Curing of concrete structures. Draft DEB – Guide to durable concrete structures', Comité Euro - International du Béton, Switzerland, (1985).
[12] JCI: 'Committee report of technical committee on autogenous shrinkage of concrete', in: E.I. Tazawa (Ed) 'Autogenous shrinkage of concrete: proceedings of the international workshop on autogenous shrinkage of concrete', (Hiroshima, E & SPON, 1998), 1-62.
[13] Kanstad, T., Hammer, T.A., Bjontegaard, O. and Sellevold, J., 'Mechanical properties of young concrete: Part II: Determination of model parameters and test program proposals', *Mater. Struct*. **36** (4) (2003) 226-230.
[14] CEB-FIP, 'Ceb-Fip Model Code 1990', Comité Euro-international du béton, (Thomas Telford, London, 1993).
[15] De Schutter, G. and Taerwe, L., 'Degree of hydration-based description of mechanical properties of early age concrete', *Mater. Struct.* **29** (6) (1996), 335-344.
[16] Rostásy, S., Krauß, M. and Gutsch, A.-W., 'Computation of stresses and cracking criteria for early age concrete – Methods of iBMB', IPACS Report BE96-3843/2001:35-4, TU Lulea, (2001).
[17] FIB: 'Model Code 2010 - Final draft, Volume 2', FIB Bulletin **66**, Fédération Internationale du Béton, (2012).
[18] Larson, M. and Jonasson, J.-E., 'Linear Logarithmic Model for Concrete Creep: I. Formulation and Evaluation', *J. Adv. Concr. Tech.*, **1** (2) (2003) 172-187.
[19] Larson, M. and Jonasson, J.-E., 'Linear Logarithmic Model for Concrete Creep: II. Prediction Formulas for Description of Creep Behaviour', *J. Adv. Concr. Tech*. **1** (2) (2003) 188-200.
[20] Gutsch, A.-W., 'Viscoelastic behaviour of early age concrete', IPACS Report BE96-3843/2001:38-9, TU Lulea, (2001).

International Conference on Sustainable Materials, Systems and Structures (SMSS 2019)
Novel Methods for Characterization of Materials and Structures
20-22 March 2019 – Rovinj, Croatia

DEFECT DETECTION IN CONCRETE USING PRINCIPLE COMPONENT THERMOGRAPHY

Bojan Milovanović (1)

(1) Faculty of Civil Engineering, University of Zagreb, Croatia

Abstract

In order to increase the service life of structures, Nondestructive Testing (NDT) methods are being used as an important characterization tool. Usually, two issues are relevant when inspecting concrete structures using NDT. The first one being the detection of defects, while the second issue is to reliably estimate the defect parameters like size and depth.

The aim of this paper is to enhance the defect detection capability of Infrared Thermography (IRT) in concrete, where cooling down IRT will be used to identify subsurface defects. Defect/non-defect contrast for smaller and/or deeper defects will be increased using Principle component thermography (PCT) on data acquired using active thermography technique. As a statistical analysis tool Principal Component Analysis (PCA) is being used for identifying patterns in data and expressing the data in a manner which allows to accentuate the similarities and differences in patterns. PCA applied to the data in the form of thermogram sequence is called principal component thermography (PCT) where the results of the PCT are given as empirical orthogonal functions (EOF). The presented research proved that by using PCT proposed approach, one can significantly enhance the contrast of the defective area in concrete also for small and thin defects.

Keywords: Nondestructive testing, Infrared thermography, Principle component analysis, Reinforced concrete, defect detection

1. INTRODUCTION

In recent years, advances in signal processing, combined with the development of efficient numerical algorithms for post processing of raw data have made it practical to implement imaging technology into non-destructive testing (NDT) of concrete structures. Temperature distribution at the surface of any concrete element can be recorded as an image (thermogram) using infrared thermography (IRT). The use of IRT for structural health monitoring has increased, due in large part to the advancement of IR cameras and the considerable reduction in their cost [1]. The development of IRT for NDT of concrete structures is slow due to its highly inhomogeneous nature on a macroscopic level as well as low thermal conductivity and high thermal inertia compared to for example metals for which IRT is widely used. Low

thermal conductivity and high thermal inertia of concrete require an input of a large amount of energy to initiate heat flow which would enable the use of active IRT to detect defects in concrete. Additionally, the dimensions of concrete structures and defects occurring in concrete have to considered when using IRT [2], [3].

IRT techniques are based on the principle that subsurface defects in concrete affect heat flow through the material, which then cause localized variations of surface temperature. It can thus be concluded that subsurface anomalies in concrete can be located by measuring surface temperatures under transient heat flow through the material, [4].

The preconditions for defect detection is that one uses adequate thermography equipment and that defects cause sufficient temperature difference compared to bulk material [5]. IRT has limitations when low thermal conductivity materials containing deep defects are tested, but it has to be said that IRT was proven useful when combining it with other NDT methods which can detect deeper objects [6].

The so-called passive IRT, has been used in civil engineering for identification of voids, delaminations, and cracks in concrete bridge decks, highway pavements, parking garages, etc. [6]–[9]. Passive IRT is cheap and an environment-friendly technique which provides a perfectly even thermal stimulation of an object. On the other hand, dependence to surface orientation, weather conditions and the surface colour variations are the main disadvantages of passive IRT. Passive IRT is possible on the surfaces with direct sunlight during the period of transient heat flow. If transient conditions are not achieved, it was proved difficult to detect subsurface defects in concrete using passive IRT [10].

The challenge of using IRT presents the inspection of shaded concrete elements which typically exist under a bridge, and in these cases application of passive IRT is very difficult [11]. These situations require the use of active IRT techniques, where energy is imported into the object using an artificial external heat source such that significant heat transfer occurs within the material. This artificial heat source needs to be with significant power if the targeted object is distant, if the defects are small and/or if they are deep in the structure.

The restricted depth of penetration of IRT in most cases limits its application to relatively thin components, and depth of concrete cover. This restriction is caused by an exponential rate of attenuation of defect signature with depth [12], which results with subtle defect signatures, i.e. temperature variations are within tenths of a degree or less. From the standpoint of remote IR detection, this amounts to a difficult technical challenge.

Post-processing techniques for IRT are developed and used in order to enhance the contrast between defect and sound area. In civil engineering, impulse-thermography (IT) and pulse phase thermography (PPT), proved to be useful for the investigation of shallow defects [13], while a few research groups used lock-in technique [14]. This paper presents the use of principle component thermography (PCT), as post-processing technique for defect detection in concrete.

2. PRINCIPLE COMPONENT THERMOGRAPHY

Statistical analysis tool called Principal Component Analysis (PCA) is used for identifying patterns in data and expressing the data in a way to highlight the similarities and differences in patterns. The pattern matching of the data becomes very difficult when data dimension is very high [12]. In such situations PCA comes in handy for analysing and graphically representing of data, where the method of empirical orthogonal functions (EOF) constructs a

set of orthogonal statistical modes that provide the strongest variability projection for the data. Regardless of variance-type, PCA techniques are simply used for compressing the variability of the data into the fewest possible number of modes.

Once the patterns are found, data is compressed by reducing its dimensions without much loss of information [15]. PCA applied to the data in the form of thermogram sequence is called PCT. The thermogram data consists of undesirable signals and noise along with the IR image data. These thermogram sequences are processed in order to eliminate the undesirable signals and enhance the useful information. The PCT used for processing IR sequences is based on thermal contrast evaluation in time, while the PCT analysis is based on the 2nd order statistics of thermogram data. The sequence of thermograms containing the information about the targeted object is processed using PCT based on the singular value decomposition (SVD). When studying thermal response data, the first two EOFs normally provide an adequate description of the relevant systematic spatial variations, which amounts to a remarkably compact representation [12]. Each EOF is associated with a characteristic time behaviour. Conversion of 3D image matrix into 2D matrix is described in in detail in [12], [15], [16].

3. EXPERIMENTAL WORK

The research presented in this paper was conducted by using reflecting method while the experimental setup consists of a thermal excitation unit, an infrared camera and a computer system which enables digital data recording in real time, Figure 1a. Thermal excitation period was performed during 60 minute period while the cooling period lasting additional 60 minutes. Surface temperature was monitored during both heating and cooling periods.

Halogen lamp (1000 W) was used as thermal excitation, and was placed 1.5; 2.0 and 3.0 m from the surface of concrete specimens, respectively. Specimen size is determined by the need of specimen relocation and conditioning, while at the same time they need to be large enough to simulate real defects, without the influence of edges or defects interfering each other‘s temperature field.

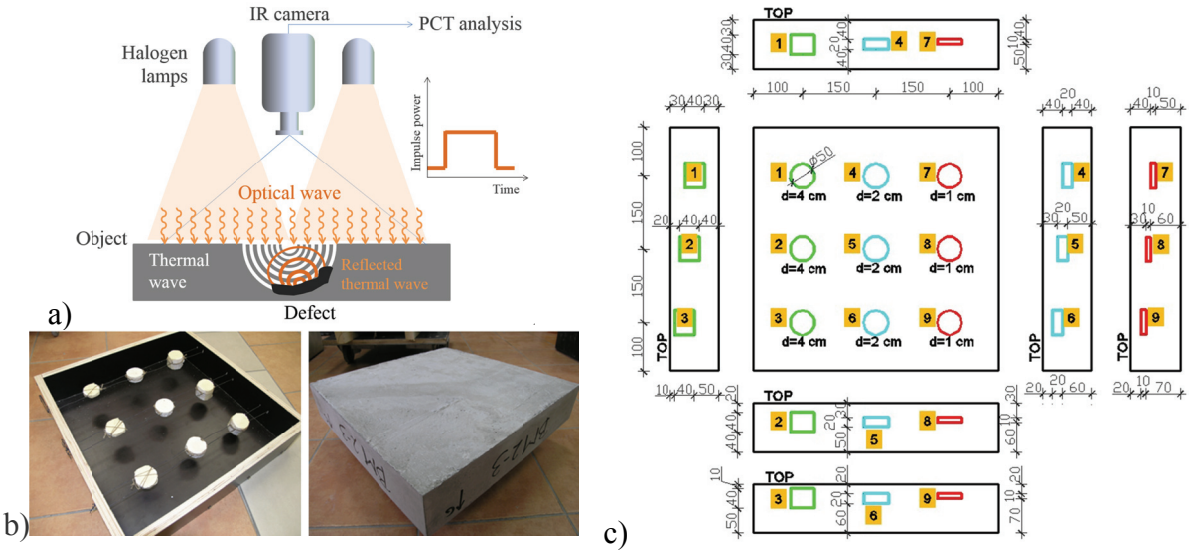

Figure 1: a) Schematic representation of thermal excitation of the object using IRT; b) photos of polystyrene defects placement and finished test specimen; c) Schematics of the specimens BM x-2, dimensions in mm

Within the presented research, concrete specimens with known defects were prepared, Figure 1b. The detectability of defects in concrete using active IRT is determined by their size and depth. As shown in Figure 1c defect size, embedment depth and thickness were varied in order to determine defect detectability in respect to these defect properties by using IRT. Three concrete mixtures (Table 1) with the properties shown in Table 2 were used.

Table 1: Concrete mixture compositions (dolomite aggregates D_{max}=16 mm)

Concrete ID	Cement type	Cement [kg/m^3]	w/c ratio	Admixture type and amount
BM 1-2	CEM III 32.5	271	0.70	Air-entraining agent (0.1%)
BM 2-2	CEM I 42.5R	345	0.55	Air entraining plasticizer (0.5%)
BM 3-2	CEM I 52.5N	425	0.40	Superplasticizer (1%) Silica fume (7%)

These concrete mixtures were created with intention to simulate three concrete classes which can be found in real structures, differing in their thermal conductivities and thermal diffusivities as well as in compressive strength and air content, Table 2. The testing procedures and methods used to determine concrete properties (Table 2) are published elsewhere [10].

Table 2: Properties of concrete used for creating specimens

Property tested	Concrete mixture		
	BM 1-2	BM 2-2	BM 3-2
Concrete density [kg/m^3]	2194.0	2382.7	2545.6
Air content [%]	10.5	4.6	1.4
Compressive strength [MPa]	18.93	40.99	89.05
Thermal conductivity [W/mK]	1.73	2.21	2.80
Thermal diffusivity [m^2/s]	7.996×10^{-7}	9.074×10^{-7}	1.114×10^{-7}
Emissivity	0.928	0.957	0.958

Here, the biggest influence was expected to have the thermal conductivity and thermal diffusivity of the concrete and the variations were caused primarily by the concrete's air content. The focus of the paper is not to study concretes with variable air entrainment, but concretes with variable thermal properties, where the most effective way to do this was to vary air content. Other parameters could also influence thermal properties but were not studied here.

Polystyrene foam was used to simulate compaction defects and voids in concrete, where foam discs have been fixed and carefully implanted into fresh concrete in order to obtain the designed depth in finished specimens. Specimens were tested from both sides, with the aim of gathering data for maximum number of embedment depths.

To perform the presented experiment, IR camera FLIR ThermaCAM P640 was used, with spectral range from 7.5 - 13 μm, thermal sensitivity (NETD) 60 mK and the Focal Plane

Array (FPA) detector with the resolution of 640×480, while 1000 W halogen lamp was used as a thermal excitation source. Active thermography electronic interface was used to connect the IR camera with the computer and the thermal excitation source. FLIR ThermaCAM^{TM} Researcher Pro 2.9 software, and MatLab were used to perform pre-processing of raw data, where a series of more than 700, 2D thermograms were converted into a sequence. As a result, an array i.e. 3D matrix was created, where rows and columns are rows and columns of the thermograms and the third dimension gives the pixel's temporal temperature change. Step heating (SH) thermography (60 min long heating period) was used to collect sequences of thermograms and the same SH duration was performed for all three different thermal excitation distances. Figure 2 shows optimal thermograms extracted from the thermogram sequence after the heating period.

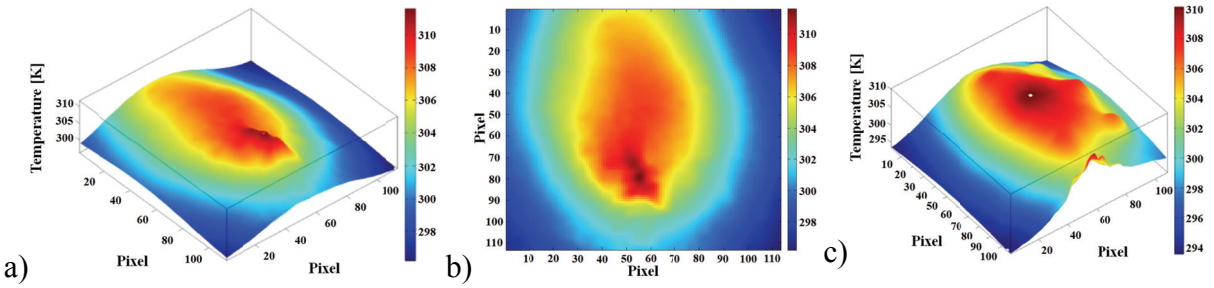

Figure 2: Optimal thermograms of selected specimen configurations, a) b) BM 2-2 bottom surface, distance 1.5 m, 3D and 2D representation, c) BM 3-2 top surface, distance of 1.5 m, 3D representation

It is evident from presented thermograms (Figure 2) that no or only certain defects can be located in specimens, and the same pattern occurred for all specimens and test configurations. This is due to the fact that the measurements are influenced by uneven heating, and reflectance. It is evident (Figure 2) that thermograms, even the optimal thermogram (the best one) cannot be used for location of the defects (especially not for small defects). Thus, some post-processing of the data acquired needs to be performed. In this paper PCT was used as post-processing technique on thermogram sequences for the defect detection in concrete specimens.

4. RESULTS OF EXPERIMENTAL RESEARCH

The figures presented in this chapter (Figure 3 - Figure 6) are selected representative EOF's. In order to depict trends that were identified during the research, and due to paper length limitation, only few representative figures are shown in this paper. These figures represent specific specimen configuration, as shown in captions, but the presented trends can be generalised to other specimen configurations.

Considering the PCT, it proved to be quite useful post-processing technique for detecting small defects in concrete specimens. Never the less, it has to be said that multiple EOFs need to be analysed when trying to interpret the results of the PCT. This is because PCT technique can produce EOF's with perfect contrast between defected and sound area, while the following EOF can provide only noise, which can mislead into the false conclusions if analysed individually, Figure 3. EOFs are showing variability over all frequency bands

(colour scale and/or z-axis, Figure 3 - Figure 6) and since EOF analysis is a strictly statistical method, it is irrelevant how the variance is derived.

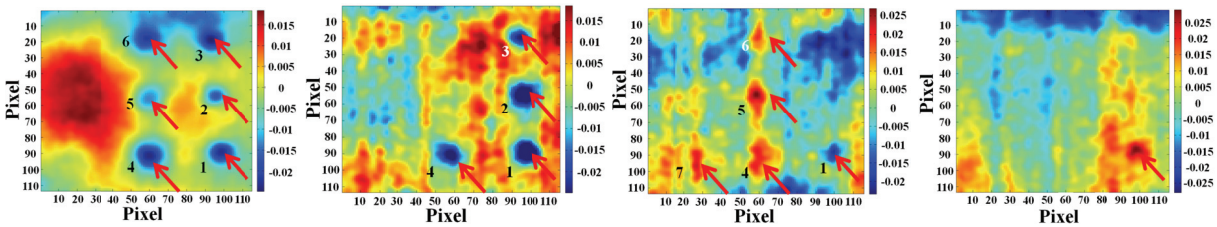

Figure 3: PCT BM 1-2 top surface, distance 1.5 m: a) EOF2; b) EOF3; c) EOF4; d) EOF6;

Additionally, it was noticed that the reflection is not being removed from certain EOF's by the PCT, which means that EOFs containing reflection from excitation source can be misinterpreted. This is understandable since PCT is a statistical method used for identifying patterns, and surface reflection is a pattern occurring in a short period or during the whole testing period. This means that basic IRT good practice procedures still have to be followed in order to identify and if possible avoid reflection.

Nevertheless, when reflection cannot be avoided, it can also be identified by looking at the sequence of EOFs where reflection pattern will change significantly in different EOFs while at the same time defect pattern will change only slightly. It was noticed that when smaller defects are observed one can detect defects in a larger number of EOFs, unlike the situation when larger defects are being identified. Since by analysing more EOFs, one can rule out the reflections and uneven heating of specimens, larger number of usable EOFs certainly proved to be advantage.

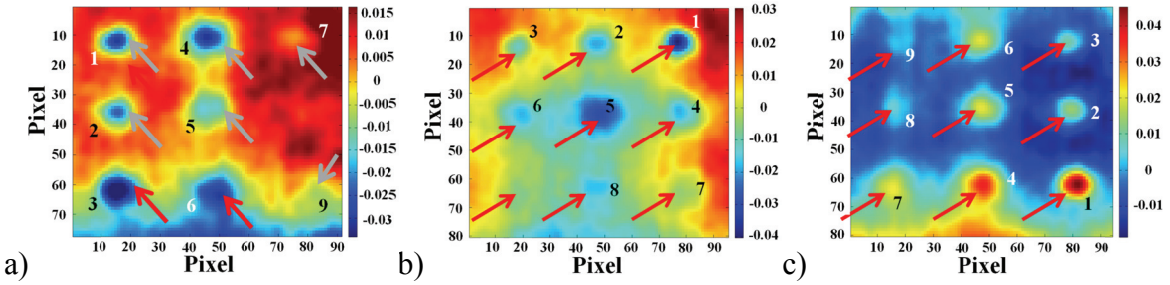

Figure 4: PCT, top surface, distance of 2 m: a) BM 1-2; b) BM 2-2; c) BM 3-2

Concrete quality, has an influence on detectability of defects when using PCT. Concrete of better quality has higher thermal conductivity and lower thermal diffusivity. For lower quality concrete, due to its low thermal conductivity, thermal waves could not reach the defect and return back to the surface in the time faster than the duration of thermal excitation of the specimen. On the other hand, for very good quality concrete, due to its high thermal conductivity, lateral diffusion on the specimen's surface is dominant and it masks the thermal wave reflecting from the defect inside the specimen and consequently prevents the defect detection. Examples of the test results acquired for different concrete qualities by using the PCT as a post-processing technique are shown in Figure 4.

When the results of the PCT analysis are being compared, it can be concluded that with the increased distance, the detectability of defects decreases, Figure 5. This effect was expected, and is occurring due to significantly reduced energy introduced into the specimen when the heat source distance is 3 m from the specimens. In order to increase the detectability from larger distances, one could use more powerful heat source to introduce greater amount of energy.

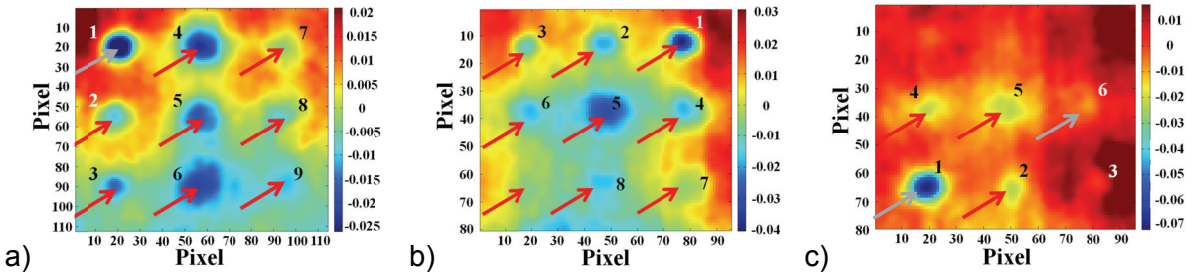

Figure 5: PCT BM 2-2, top surface: a) EOF2 distance of 1.5 m; b) EOF2 distance of 2 m; c) EOF2 distance of 3 m

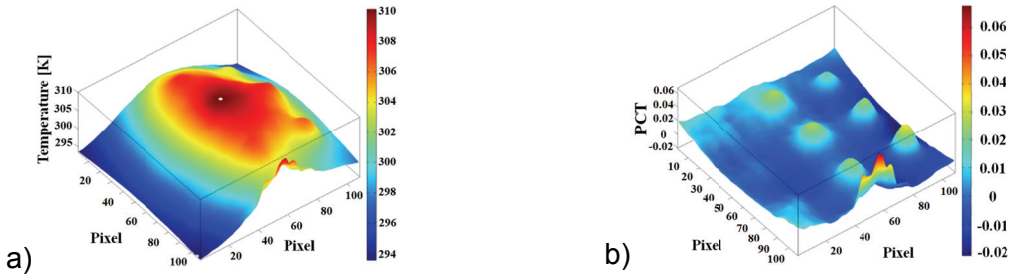

Figure 6: BM 3-2 top surface, distance of 1.5 m: a) Optimal thermogram 3D; b) PCT (EOF2)

EOFs are practically unaffected by non-uniform heating, (Figure 7). Since the non-uniform surface heating is an inherent source of uncertainty in IRT, it can be concluded that elimination of non-uniform heating is one of the most important result of the post-processing using PCT.

5. CONCLUSIONS

The following conclusions can be derived from the results of the research using the method of active IRT and PCT post-processing technique presented in this paper. Active IRT is a suitable tool to be used for NDT of concrete structures only if post-processing techniques like PCT are applied on the raw data, otherwise active IRT can provide false negative or false positive results due to un-uniform heating or reflection issues, respectively. It was shown in this paper that active IRT in combination with PCT post-processing can be used for detection of defects with the diameter as little as 50 mm up to the depth of the concrete cover, or larger defects at greater depths. The detectability of the defects depends on its thickness and embedment depth. The test results are influenced by the quality of concrete since with the quality of concrete thermal conductivity and thermal diffusivity of concrete vary and those are the properties that mostly define the heat flux through concrete. Even though physical properties of concrete influence the test results, it was shown in the paper that defect detection is still possible if one adapts the measurement system, test configuration and post-processing.

PCT is still relatively new in terms of detecting the existence of defects by using IRT, especially in concrete structures, since there are only few research papers published on this topic. To be able to characterize defects using PCT, additional research needs to be performed.

REFERENCES

[1] M. Scott *et al.*, "Passive infrared thermography as a diagnostic tool in civil engineering structural material health monitoring," in *Concrete Repair, Rehabilitation and Retrofitting III: 3rd International Conference on Concrete Repair, Rehabilitation and Retrofitting*, 2012, pp. 760–765.

[2] M. Nahant, S. Paez, and J. Van Leeuwen, "DEFBETIR Detection by infrared thermography of the heat signature of diseases and defects in concrete structures of civil engineering," in *QIRT 2010 - 10th International Conference on Quantitative InfraRed Thermography*, 2010.

[3] F. Weritz, R. W. Arndt, M. Röllig, C. Maierhofer, and H. Wiggenhauser, "Investigation of concrete structures with pulse phase thermography," *Mater. Struct.*, vol. 38, no. 283, pp. 843–849, Mar. 2005.

[4] G. J. Weil, "Infrared thermographic techniques," in *Handbook on Nondestructive Testing of Concrete*, Second Edi., V. M. Malhotra and N. J. Carino, Eds. CRC Press LLC, 2004, pp. 1–14.

[5] C. Maierhofer, R. W. Arndt, and M. Röllig, "Influence of concrete properties on the detection of voids with impulse-thermography," *Infrared Phys. Technol.*, vol. 49, no. 3, pp. 213–217, Jan. 2007.

[6] B. Milovanović and I. Banjad Pečur, "Determination of material homogeneity using infrared thermography," in *Proceedings of the 5th Pan American Conference for NDT*, 2011.

[7] G. J. Weil, "Infrared Thermographic Techniques," in *Handbook on Nondestructive Testing of Concrete*, V. M. Malhotra and N. J. Carino, Eds. Boca Raton, Florida: CRC Press, 1991, pp. 305–316.

[8] F. B. Holt and D. G. Manning, "Infrared Thermography for the Detection of Delaminations in Concrete Bridge Decks," in *Proceedings Fourth Biennial Infrared Information Exchange*, 1978, pp. 61–71.

[9] M. R. Clark, D. M. McCann, and M. C. Forde, "Application of infrared thermography to the non-destructive testing of concrete and masonry bridge," *NDT&E Int.*, vol. 36, pp. 265–275, 2003.

[10] B. Milovanović, "Application of Infrared Thermography for Defect Characterization in Reinforced Concrete," University of Zagreb, 2013.

[11] G. A. Washer, R. Fenwick, and S. Nelson, "Guidelines for the Thermographic Inspection of Concrete Bridge Components in Shaded Conditions." Department of Civil and Environmental Engineering, University of Missouri, Columbia, pp. 1–14, 2013.

[12] N. Rajic, "Principal component thermography for flaw contrast enhancement and flaw depth characterisation in composite structures," *Compos. Struct.*, vol. 58, no. 4, pp. 521–528, 2002.

[13] RILEM Technical Committee 207-INR, *Non-Destructive Assessment of Concrete Structures: Reliability and Limits of Single and Combined Techniques*, 1st ed. Dordrecht: Springer Netherlands, 2012.

[14] T. Sakagami and S. Kubo, "Development of a new non-destructive testing technique for quantitative evaluations of delamination defects in concrete structures based on phase delay measurement using lock-in thermography," *Infrared Phys. Technol.*, vol. 43, no. 3–5, pp. 311–316, Jun. 2002.

[15] R. Parvataneni, "Principal component thermography for steady thermal perturbation scenarios," Clemson University, 2009.

[16] N. Rajic, "Principal component thermography," Fishermans Bend, Victoria, Australia, 2002.

International Conference on Sustainable Materials, Systems and Structures (SMSS 2019)
Novel Methods for Characterization of Materials and Structures
20-22 March 2019 – Rovinj, Croatia

AN EMBEDDED YIELD DESIGN APPROACH WITHIN A NON-LINEAR ANALYSIS FOR STRUCTURAL MODELING OF PROGRESSIVE COLLAPSE

Mohammad El Hajj Diab (1), André Orcesi (1), Cédric Desprez (1) and Jérémy Bleyer (2)

(1) Université Paris-Est, MAST, EMGCU, IFSTTAR, F-77447 Marne-la-Vallée, France

(2) Université Paris-Est, Laboratoire Navier (UMR 8205), CNRS, Ecole des Ponts ParisTech, IFSTTAR, F-77455 Marne-la-Vallée, France

Abstract

Dealing with structural robustness concept requires to investigate whether or not a structure can prevent a disproportionate collapse after the occurrence of a local failure due to an exceptional event. Numerical models can be used to simulate progressive collapse and help quantify the robustness level at a design stage. Non-linear static or dynamic finite element analyses are commonly used tools for structural performance assessment. However, computational time might be in most cases too large for complex structures where several local failure scenarios need to be investigated, and one may encounter convergence issues if the loads applied are close to the limit ones.

In this context, this study proposes a framework for studying the progressive collapse of framed structures, which combines both the yield design approach and the non-linear analysis method. This proposed framework is applied to a steel-framed multi-storey building submitted to column(s) loss.

Keywords: Structural robustness, local failure, progressive collapse, non-linear analysis, yield design approach.

1 INTRODUCTION

Many catastrophic events of structural progressive collapse highlight the importance of the structural design not to be limited to safety under normal conditions, but also to structural integrity under an exceptional event, not necessarily identified during design [1,2,3]. One of the first historical failures that led to a growing interest in structural robustness is the progressive and partial collapse of the Ronan Point tower in London (UK) in 1968. A gas explosion in a corner apartment on the 18th floor of this 22-storey precast concrete building dislodged one of the exterior walls, which led to the collapse of one entire corner of the

building [4]. Very recently, the Genoa Bridge collapse in Italy in August 2018, shed light on complex issues linked with structural robustness.

Therefore, several design codes [5,6,7] mention that structures must be sufficiently robust to prevent localized damage leading to disproportionate and unacceptable collapse. In this respect, the Eurocodes define the structural robustness as "the ability of a structure to withstand events like fire, explosions, impact or the consequences of human error, without being damaged to an extent disproportionate to the original cause" [5].

To assess the level of robustness, a structural modeling can be used to simulate the propagation of failure. In a context of high uncertainty about the initial local failure, it is envisaged to study a large number of local failure scenarios, in order to identify the maximum capacity of the structure to withstand a local failure. The structural analysis of a large number of scenarios requires a simplified structural modeling method.

Non-linear finite element analyses are popular tools to investigate the structural capacity, but some difficulties may arise on the non-convergence of the calculation (when one reaches ultimate limit states), and on the high computation cost especially for studying a large number of scenarios.

This paper presents an original structural modeling method, which combines both the yield design approach and the non-linear analyses method, to analyze the progressive collapse of framed structures. The proposed approach is illustrated on a steel-framed multi-storey building.

2 STRUCTURAL MODELING OF PROGRESSIVE COLLAPSE

The progressive collapse analysis of structures exposed to an exceptional action involves complex phenomena, such as geometrical and material non-linearities due to large displacements and large strains, dynamic effects, and the propagation of failure.

The finite element method is a widely used method in the numerical simulation of structures. The discretization in finite element can be considered at three different levels: local, global, and semi-global [8]. Choosing the level of discretization basically depends on the dimensions of the structure and the level of precision required. In a local approach, the elements are discretized with solid elements, and each material has a specific constitutive law. This approach gives a detailed representation of the structure, with local information on the state of plastification and damage of materials. Significant computation time is requested, especially when dealing with geometrical non-linearities. In a global approach, the structure is modelled with beam/shell elements, and each element has its own constitutive law depending on its geometry and materials. This method can significantly save some computation time, but there might be some difficulties to simulate the material non-linearities and to identify the state of damage in the element sections, especially in case of heterogeneous sections. The semi-global approach is an intermediate scale of discretization between local and global approaches, where the element section is discretized on multi-layer or multi-fiber elements. The constitutive law used for each layer or fiber insures local information of materials state, and the fields of displacements calculated by formulations of classic beam element. This approach integrates the benefits of local and global approaches: saving on computation time and ability to describe geometrical and material non-linearities.

In addition to the issues linked with the choice of discretization, one needs to tackle non-linearities phenomena and dynamic effects [9]. Non-linear analyses are often very time-

consuming and vulnerable to non-convergence issues [10]. To prevent using full dynamic analyses, the structural response can be estimated from a non-linear static response under amplified gravity loading using a dynamic amplification factor [11] or a pseudo-static method [12], which estimates the non-linear dynamic response by a non-linear static analysis through the balance of energy against work done.

With the aim of evaluating the capacity of structure to withstand actions, it is useful to identify the resistance capacity of the structure. In this context, the yield design approach is a good compromise, as it is a direct method, which avoids the non-linear analysis and thus the step-by-step computation of the structure along the full loading path [13]. In fact, only the compatibility between the equilibrium equations and the yield criterion is checked in every point of the structure. This method identifies the ultimate loads, as well as the failure mechanism and the most critical areas of the structure. Moreover, one can dramatically save on computing time compared to a non-linear analysis, and avoid problems of non-convergence [14]. The essential assumptions of the process of yield design approach are that the materials are elastic perfectly plastic, and the assumption of small strains. Therefore, the main challenges to use this method is to take into account the geometrical non-linearities and to simulate the progressive collapse.

3 PROPOSED STRUCTURAL MODELING STRATEGY

An iterative yield design based approach is proposed to follow the propagation of failure. Furthermore, a non-linear static analysis is applied to calculate large displacements if a second line of defence can become effective when frames devolve from a flexure dominant system to a tensile membrane or catenary dominant system. This procedure is illustrated in Figure 1, with the following steps :

1) yield design calculation is applied to identify the ultimate load and the failure mechanism,
2) ultimate and applied loads are compared,
3) in case the ultimate load is larger than the applied load, the current structural configuration can support the applied load, and the failure stops at this stage,
4) in the opposite case, the current configuration of structure cannot support the applied load, and the failure propagates,
5) the failure mechanism identified by the yield design calculation allows to identify the affected part, and to estimate if there is either a loss of stability or the possibility of a second line of defence,
6) in case the failure mechanism indicates the mechanical instability of some elements, these elements are removed for the next iteration,
7) in the opposite case, the failure mechanism indicates that the affected part may develop an alternative functioning stage after large displacement. A non-linear analysis is then applied to the affected part, in order to calculate the geometric displacements under the applied load. Then, a new iteration of yield design calculation is performed with the new geometric configuration,
8) this iterative procedure continues until the end of collapse, for which the ultimate load on remaining elements is larger than the applied load, or until total collapse of the structure.

Thus, the proposed method consists of a coupling between the yield design approach and the non-linear analysis with an iterative procedure. Also, a dynamic amplification factor is used to take into account the dynamic effect. This strategy of structural modelling enables to simulate the progressive collapse.

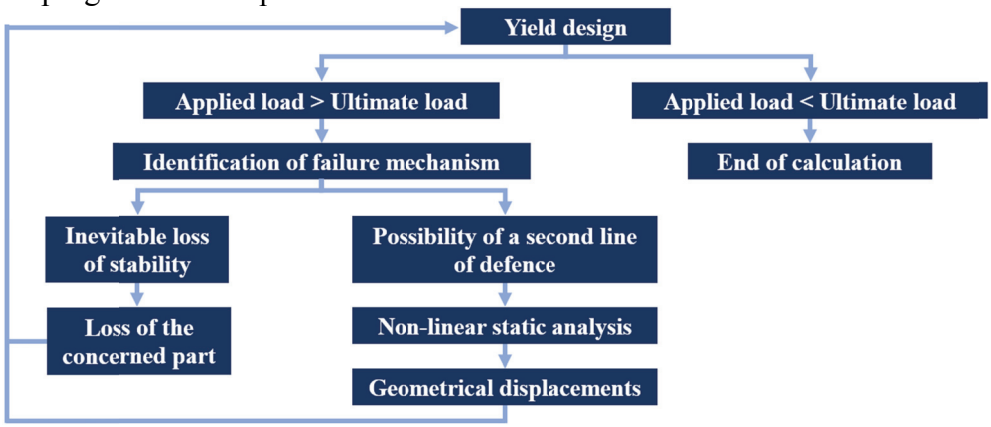

Figure 1: Proposed structural modeling strategy

4 ILLUSTRATIVE APPLICATION

This section presents the application of the proposed method on a steel-framed five-storey building, in order to study the structural response against some local failure scenarios.

4.1 Structural configuration

The structure is a 2D typical five-storey steel-framed building consisting of beams with section IPE360, and columns with section HED500, where Figure 2 presents the layout with dimensions and numbers of columns.

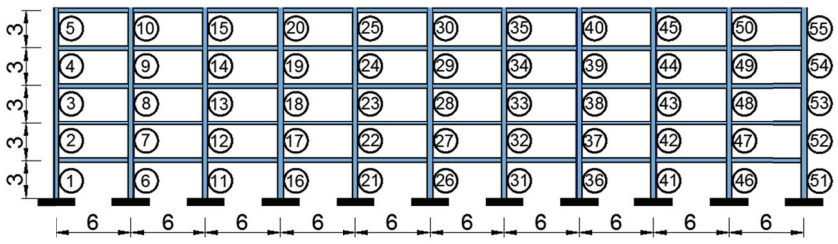

Figure 2: Layout (dimensions in meter).

The steel material of beams and columns is considered as elastic perfectly plastic, where the young modulus E and the yield strength are equal to 210 GPa and 355 MPa, respectively. The connections column/beam and column/footing are considered as rigid joints.

4.2 Applied loads

The beams are exposed to uniform loads, where the values of dead loads (DL) and live loads (LL) are 20 KN/m and 10 KN/m, respectively. The combinations of actions refer to ultimate states, according to Eurocodes EN1990 [11], as follows:

– Normal situation: W=1.35 DL + 1.5 LL (1)

– Accidental situation: W=DL + 0.5 LL (2)

As the analysis is an accidental situation, the combination of loads is equal to 25 KN/m. The self-weight of structural members is 77 KN/m3.

According to Marchand and Alfawakhiri [15], the appropriate dynamic amplification factor for the non-linear elasto-plastic response is between 1.3 and 1.5, in this example the used value is 1.5. The load amplification is applied only on the directly affected part, which normally contains all the beams, columns and beam-to-column joints located just above lost column(s).

4.3 Numerical modeling

The model proposed by Bleyer and de Buhan [16] for yield design calculation of frame structure is used on MATLAB R2017a. This method consists of two main steps. Firstly, yield surfaces of element sections are approximated using a sum of ellipsoids, which identifies the ultimate strength domain of the section in the space of axial force (N) and bending moments (M_y, M_z) as shown in Figure 3 (this approach does not take into account the yield by shear and torsion efforts), with $n=N/N_0$, $my=M_y/M_{y0}$ and $m_z=M_z/M_{z0}$ where $\Sigma_0=(|\min(\Sigma)|+|\max(\Sigma)|)/2$ for Σ=N, M_y or M_z. Secondly, the structure is discretized using beam elements, and the limit load is identified by two approaches (static and kinematic).

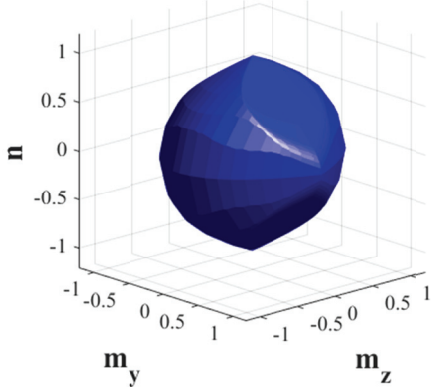

Figure 3: Yield surface in the (n, m_y, m_z) non-dimensional space.

The static approach determines a lower bound of ultimate load according to the optimisation problem (3). The applied loads are decomposed as $\lambda.F + F_0$ where F_0 represents a dead load and $\lambda.F$ is the multiplicative load for which we are interested in finding the limit value at failure through the multiplier λ.

$$\lambda_{static} = \max(\lambda), \text{ such that } \begin{cases} H.\Sigma = \lambda.F + F_0 & \text{global equilibrium} \\ \sigma \in G & \text{local yield criterion} \end{cases} \quad (3)$$

where λ_{static} is the multiplier value identified by static approach, H is the global equilibrium matrix, Σ is global vector of stress parameters, σ is the local vector of stress parameters and G represents the local yield criterion.

Regarding the kinematic approach, one determines an upper bound limit of ultimate load according to the optimisation problem (4), where $\lambda_{kinematic}$ is the multiplier value identified

by the kinematic approach, P_{ext} is the power of external loads, U is the displacement vector, P_{rm} is the maximum resisting work, and $d[U]$ is the strain vector related to U at point χ.

$$\lambda_{kinematic} = \min(\lambda), \text{ such that } P_{rm}(U) \leq P_{ext}(U) \begin{cases} P_{ext}(U) = \lambda.F.U + F_0.U \\ P_{rm}(U) = \int_{\Omega} \Pi(d[U];\chi)d\Omega \\ \Pi(d[U];\chi) = \sup\{\sigma: d[U];\ \sigma \in G\} \end{cases} \quad (4)$$

Concerning the static nonlinear analysis, the MATLAB toolbox FEDEASLab [17] is used, where the multilayer approach is applied to model the structural elements. This toolbox enables to take into account the geometrical non-linearities using co-rotational formulations [18].

4.4 Local failure scenarios

In this example, the local failure scenarios are limited to the total loss of one or several column(s), provided that the damaged columns are always adjacent, that the maximum extent of local failure is in two bays and that the maximum number of damaged columns is three adjacent columns. There are consequently 150 scenarios to investigate.

4.5 Structural response

The structural response is presented with two main indicators:

- directly affected zone: length of the beams within the area directly affected, represented by the affected part of the first iteration of yield design approach, this value presents the area initially affected.
- collapsed zone: length of the beams within the area that collapsed (loss of stability).

These two values enable to evaluate if the local failure has consequences, when the directly affected part is larger than zero, and if it leads to collapse, when the collapsed part is larger than zero. Moreover, these two values present the initial stage and the final stage of the progressive collapse, which allows to quantify the degree of failure propagation, and provide an effective structural robustness index.

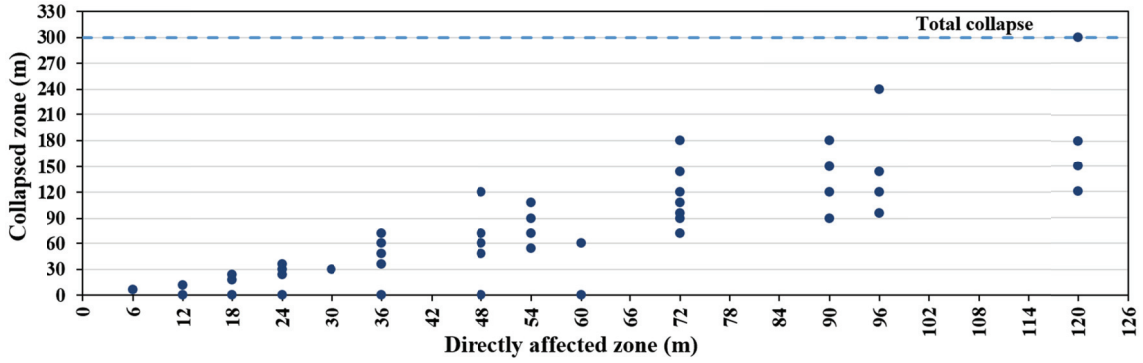

Figure 4: Results of structural response

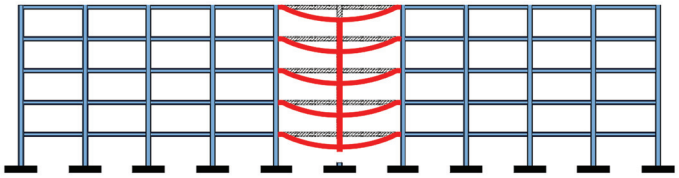

(a) Failure mechanism identified by the first iteration of yield design calculation

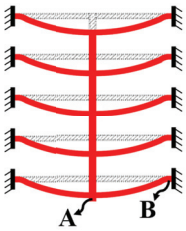

(b) Non-linear analysis of the directly affected part

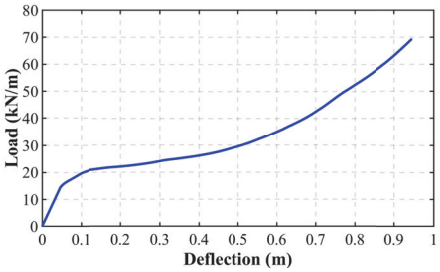

(c) Load-Deflection curve (at point A)

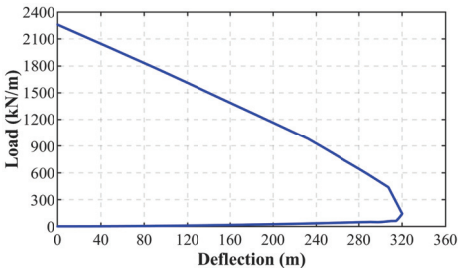

(d) Normal force – Bending moment curve (at point B)

Figure 5: Catenary action (loss of column 26, see Figure 2).

Figure 4 presents the different structural responses against the local failure scenarios taken into consideration in this example. The directly affected zone is larger than zero in all cases, so there is no scenario without consequences. Some scenarios have no collapsed zone, thus the structure has succeeded to find a second line of defence by the catenary action developed in the beams of the directly affected part. Figure 5 represents the non-linear static analysis of the affected part in the case of the loss of column 26. It shows the catenary action where after large deflection there is an increase of tensile stress in beams and decrease of bending moment effort, which helps the structure reaching an alternative equilibrium configuration. Besides, there are one hundred scenarios that lead to a partial/full collapse of the structure, and the extent of failure differs from one scenario to an other, but one of them leads to a total collapse of structure, which is the loss of the central columns 21, 26 and 31 (see Figure 2).

4.6 Robustness index

The goal of robustness indices is to be used as design decision support. Their validity and usefulness depend on the following general requirements: expressiveness, objectivity, simplicity, calculability, and generality [19]. In order to assess the structural robustness, the main aspect that has to be investigated is the extent of failure propagation compared to the local failure. For this purpose, a robustness propagation failure index ($RPFI$) is proposed, which identifies the maximum degree of failure propagation among the N applied scenarios, where the degree of failure propagation (DFP_i) of each scenario i is the collapsed zone after propagation of failure (CZ_i) divided by the initial damaged zone (IDZ_i). This index is expressed as:

$$RPFI = max\,\{DFP_i\,, i \in [1, N]\} \tag{5}$$

$$\begin{cases} DFP_i = \dfrac{CZ_i}{IDZ_i} & if\ IDZ_i \neq 0 \\ DFP_i = 0 & if\ IDZ_i = 0 \end{cases} \tag{6}$$

Based on the applied local failure scenarios, $RPFI$ is equal to 2.5, so the most critical scenarios, with the largest extent of failure propagation, are [21 26 31], [22 27 32], [23 28 33] and [24 29 34], i.e. three central columns located on a given floor, where the collapse propagates to an area 2.5 times larger than the directly affected part.

5 CONCLUSIONS

The structural modeling method proposed in this paper enables to simulate the progressive collapse with saving in computation time and mitigation convergence issues due to the adoption a direct approach by means of the yield design method. The illustrative case study shows the capability of this method to study a large number of local failure scenarios, which allows a general assessment of structural robustness, and to identify the maximum capacity of the structure to withstand exceptional events. Besides, a structural robustness index is proposed ($RPFI$) and allows to evaluate the capacity of structures to prevent the propagation of failure, which accurately responds to the definition of structural robustness.

To enhance the description of progressive collapse, further developments are still needed, to deal with aspects such as the 3D structural response, including the effects of slabs, and to adapt for a large range of materials and structures under different types of exceptional loads.

Furthermore, a strong assumption in this paper has been made, where the materials are considered as elastic perfectly plastic (yield design approach). Therefore, to provide a more realistic behavior of materials, it is important to take into account the ultimate strain of materials, as it can dramatically change the results of the analysis.

REFERENCES

[1] NIST, National Institute of Standards and Technology, 'Final Report on the Collapse of the World Trade Centre Towers', (Gaithersburg, MD, 2006).
[2] El Kamari, Y., Raphael, W. and Chateauneuf, A., 'Reliability Study and Simulation of the Progressive Collapse of Roissy Charles de Gaulle Airport', *Case Studies in Engineering Failure Analysis*. **76** (3) (2015) 88-95.
[3] Sétra, Service d'études sur les transports, les routes et leurs aménagements, 'Maîtrise des risques, Application aux ouvrages d'art', (2013).
[4] Pearson, C. and Delatte, N., 'Ronan Point Apartment Tower Collapse and its Effect on Building Codes', *Journal of Performance of Constructed Facilities*. **19** (2) (2005) 172-177.
[5] CEN, European Committee for Standardization, 'EN 1991-1-7: eurocode 1 – actions on structures – part 1–7: general actions – accidental actions', *European standard*, (2006).
[6] DoD, Department of Defence, 'Design of buildings to resist progressive collapse (UFC 4-023-03)', (Unified Facilities Criteria, Washington, DC, 2013).
[7] British Standards Institution, 'BS 5950-1:2000. Structural use of steelwork in building-Part 1: Code of practice for design - rolled and welded sections', (London, 2001).
[8] Franz-Josef, U.L.M., 'Un modèle d'endommagement plastique: application aux bétons de structure', (Laboratoire central des ponts et chaussées, 1996).
[9] GSA, General services administration, 'Alternate path analysis & design guidelines for progressive collapse resistance', (2013).
[10] Vidalis, C.A., 'Improving the resistance to progressive collapse of steel and composite frames', *PhD Thesis*, (Imperial College London, 2014).
[11] CEN, European Committee for Standardization, 'EN 1990: Basis of structural design', *European standard*, (2003).

[12] Izzuddin, B.A., Vlassis, A.G., Elghazouli, A.Y. and Nethercot, D.A., 'Progressive collapse of multi-storey buildings due to sudden column loss – Part 1: simplified assessment framework', *Engineering Structures*. **30** (5) (2008) 1308-1318.
[13] Salençon, J., 'Yield Design', *ISTE-Wiley*, (2013).
[14] De Buhan, P., 'Plasticité et calcul à la rupture', *presses of university Ecole Nationale des Ponts et Chaussées*, (2007).
[15] Marchand, K.A. and Alfawakhiri, F., 'Facts for Steel Buildings-Blast and Progressive Collapse', *American Institute of Steel Construction, Inc*, (United States of America, 2005).
[16] Bleyer, J. and de Buhan, P., 'Yield surface approximation for lower and upper bound yield design of 3D composite frame structures', *Journal of Computers and Structures*. **129** (2013) 86–98.
[17] Filippou, F.C. and Constantinides, M., 'FEDEASLab getting started guide and simulation examples. Technical report NEESgrid-TR22', (2004).
[18] Spacone, E., Filippou, F.C. and TAUCER, F.F., 'Fiber Beam-Column Model for Nonlinear Analysis of R/C', *Earthquake Engineering & Structural Dynamics*. **25** (7) (1996) 711-725.
[19] Starossek, U. and Haberland, M., 'Measures of Structural Robustness – Requirements & Applications'. Proceedings of an International Conference, Vancouver, 2008 (structures congress-crossing borders, Vancouver, 2008).

International Conference on Sustainable Materials, Systems and Structures (SMSS 2019)
Novel Methods for Characterization of Materials and Structures
20-22 March 2019 – Rovinj, Croatia

NANOINDENTATION ASSISTED SMALL SCALE TENSILE PROPERTIES OF HYDRATED CEMENT AND AAFA PASTES

Jiří Němeček (1), Jiří Němeček (1), Jitka Němečková (1), Jan Maňák (2)

(1) Czech Technical University in Prague, Faculty of Civil Engineering, Prague, Czech Republic

(2) Institute of Physics, Academy of Sciences, Prague, Czech Republic

Abstract

Nanoindentation is a well established experimental method used for characterization of small scale material properties. Here, nanoindentation is employed as a precise loading tool on samples prepared with Focused Ion Beam (FIB) milling technique. Micrometer sized beam specimens were prepared. Subsequently, they were bent with the aid nanoindenter and fracture characteristics acquired. Evaluation is performed for elastic properties, tensile strength and fracture energy of individual small scale microstructural constituents of cement paste like C-S-H rich phases and CH and N-A-S-H gels in alkali-activated fly ash (AAFA). Very high tensile strengths at the micrometer scale were observed for cement paste hydration products (200-700 MPa) as well as for N-A-S-H gel (340 MPa). The results are consistent with atomistic simulations and multi-scale modeling from available literature. The scaling factor of the tensile properties is caused by the multi-level character of the studied composites that consist of multiple defects in the form of pores, cracks and crystalline inclusions at higher (meso- and macro-) levels and that are not present at the micrometer scale.

Keywords: nanoindentation, FIB, cement, fly ash, microbending

1. INTRODUCTION

Tensile strength and fracture toughness are crucial characteristics of concrete and cement based materials that are widely used in the building industry. Under unconfined conditions, the strength of ordinary lab samples (cm dimensions) is typically very low, in the order of a few MPa. Cementitious composites are based on cement matrix which is characterized by a brittle failure and the ductility of the whole composite specimen depends very much on the its size, volume content and shape of defects that are present in the form of cracks and voids. From the macroscopic point of view the size dependence and strength scaling has been studied by fracture mechanics for a long time. Energetic size effect on strength was derived

by Bažant [1]. However, the mechanisms of the fracture and related micromechanical characteristics in the fracture process zone remained unknown until recently. It is now clear that the initiation of the fracture happens on scales much smaller than the lab specimens, i.e. on the microscale. Thus, advanced material models (usually multi-scale) must take into account intrinsic strength and fracture properties of individual small scale constituents of the cementitious matrix.

With the development of novel experimental techniques like electron microscopy, nanoindentation [2] and focused ion beam milling (FIB) [3] it is now possible to extract properties on scales as low as 1 μm. While microscopy enables visualizing morphology and chemical composition of microstructural features of cement matrix nanoindentation allows micromechanical characterization of the small material volumes. Works on elastic and some inelastic properties of small scale constituents including C-S-H gels and Portlandite (CH) and N-A-S-H gels in AAFA utilizing nanoindentation have been proved in many cases [4], [5]. But until recently, it was not possible to access fracture properties of the constituents. Němeček et al. developed a methodology based on bending of FIB prepared micrometer sized specimens [6] where FIB allows preparation of geometrically precise microscopic samples and nanoindenter allows precise measurement of the bending response of the micro-beams.

The work presented in this paper focuses of the strength and fracture properties of individual constituents of cement paste at micrometer scale (1-100 μm). Intrinsic fracture properties are shown for C-S-H phases and CH. Since many structural composites are based also on supplementary materials, the paper concentrates also on alternative binders. Basic building blocks of alkali-activated fly ash samples, the N-A-S-H gel, are characterized with the common methodology as used for cement samples.

2. EXPERIMENTAL PROGRAM

2.1 Samples and microstructure

Two kinds of samples were prepared. First, cement paste from CEM-I 42.5R with water to binder ratio 0.4 were produced and stored in water for 8 years. Thus, they were fully hydrated. Based on SEM imaging and microstructure modeling with Cemhyd 3D model [6], an approximate volumetric content of individual microstructural phases included inner and outer products (~50%), Portlandite (CH) (~20%), other hydrates (~15%), unhydrated clinker (3%) and capillary porosity (12%), see [6] for details. The second part of samples was prepared from alkali-activated fly ash. Raw fly ash originated from brown coal power plant Opatovice (Czech Republic). The fly ash was mixed with an alkali-activator which was prepared by dissolving NaOH pellets in tap water and by adding sodium silicate (water glass). Resulting mixture was characterized by mass oxide ratio of an activator and activator-to-solid mass ratio as: $Na_2O/SiO=0.881$, $H_2O/Na_2O=3.068$, activator/solid=0.456. After mixing, samples were cured at 80°C for 12 h and then stored in laboratory conditions (~22°C) until testing.

Prior to further analyses samples were cut into 5 mm thick slices and prepared with a metallographic procedure [4]-[6] to get a flat and smooth surface with small roughness of several tens of nm.

2.2 Methods

First, samples were scanned in SEM and locations of individual microstructural phases detected. An example of sample microstructure as seen in SEM-BSE is shown in Fig. 1

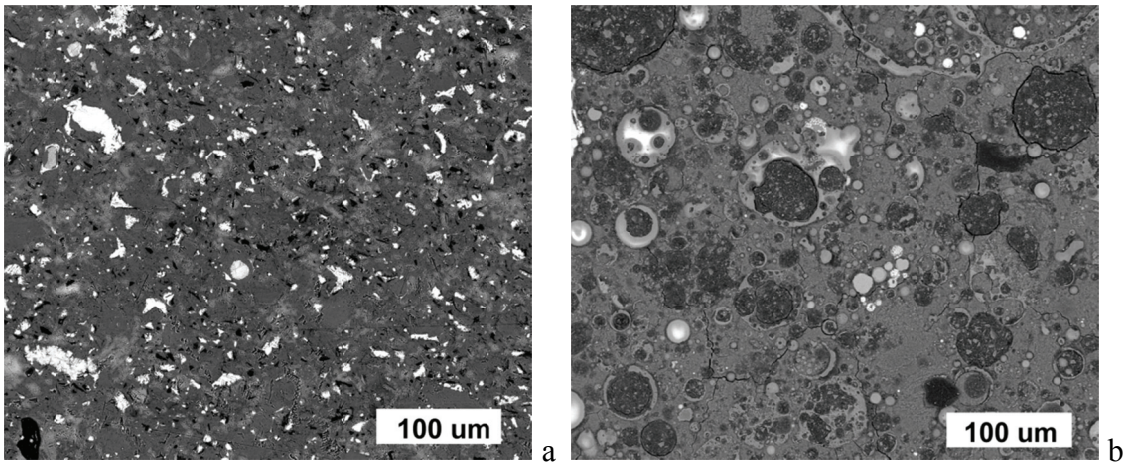

a b

Figure 1: SEM-BSE images with microstructures of (a) cement paste, (b) AAFA.

Then, micro-beams were milled with FIB (FEI Quanta 3D FEG) in the phases. The cantilevers were about 15-20 μm long with triangular cross-section (3-4 μm). FIB milling procedure was optimized to suppress the redeposition of sputtered material on the micro-beam surface and the final milling step was done at an accelerating voltage of 30 kV and low current of 1 nA [6] on cement samples and 0.1 nA on AAFA samples.

As the next step, micro-beams were loaded at the free end by nanoindenter (Hysitron TI-700) and bent. Bending response of the beams was tested in several elastic cycles. Young modulus was calculated as

$$E = \frac{FL^3}{3wI_y}, \tag{1}$$

where F and w are the force and deflection reached in the elastic regime, respectively, L is the micro-beam length, I_y the second moment of inertia of the cross section. Then beams were bent until break and tensile strength and fracture energy calculated. according to the methodology used in [6]. From load-deflection curves measured by nanoindenter tensile strength, f_t, and fracture energy, G_f, were calculated using beam theory as

$$f_t = \frac{F_{\max} L}{W_h}, \tag{2}$$

$$G_f^{\sup} = \frac{1}{A_f} \int_0^{w_{\max}} F dw, \tag{3}$$

where F_{max} is the maximum measured force, W_h is the section modulus, w_{max} is the peak deflection and A_f is the nominal fracture area (i.e. $A_f = ½bd$ for the triangle $b \times d$). Measurement of the load-displacement curve was done in the displacement controlled regime. However, current capabilities of the instrument do not allow to capture softening and the descending branch of the curves is not stable. Thus, the fracture energy was, in accordance with [6] assessed as supremum energy assuming that micro-beam behavior shows neither snap-back nor softening.

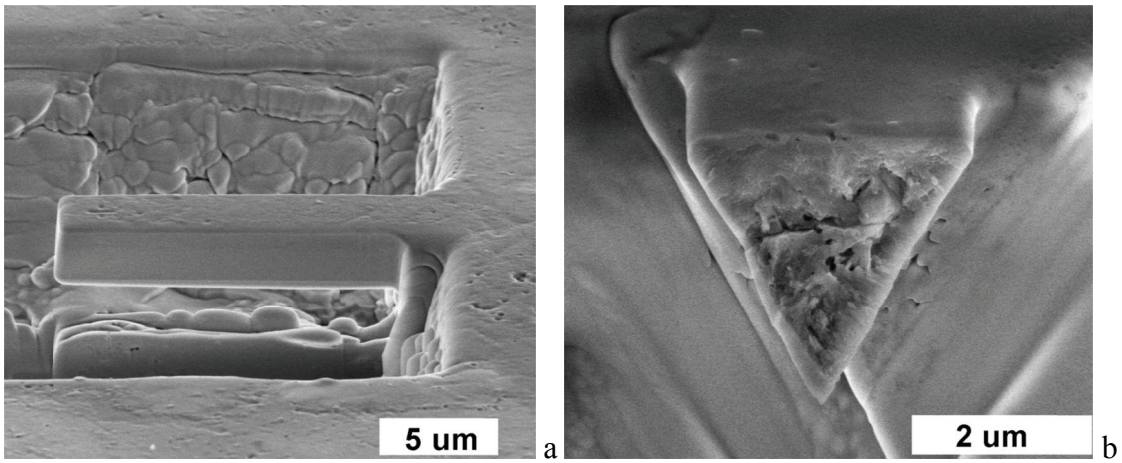

a b

Figure 2: Examples of micro-beams in cement paste. (a) CH before loading. (b) inner product after the break.

3. RESULTS AND DISCUSSION

Load-deflection curves were obtained on 7-10 micro-beams for each studied phase. Mechanical parameters of the phases are summarized in Tab. 1. Fig. 3 depicts loading diagrams normalized with respect to beam length. Behavior of all phases was mostly linear upto the break with sudden descending branch which is a manifestation of their brittle nature and unability of the instrument to capture softening, as mentioned before. In some limited number of cases softening was measured as shown for N-A-S-H gel in Fig. 3. The results of elastic properties are in good agreement with literature data of specific microscale constituents. Tensile strengths are much higher than macroscale values of cement paste showing a high scaling factor. The discrepancy between the scales is explained by multiscale models that take into account defect present at higher composite levels [7]. The defects are voids, crakcs or inclusions. Strength calculation at C-S-H level provided by molecular dynamics models yields tensile strength for low density and high density C-S-H as 550-720 MPa [8]. AFM measurements revealed 930 MPa [9]. The values are comparable with microbending tests in Tab. 1. MD simulations give fracture energies in the range of 0.4-3 J/m^2 [10],[11] which is a bit less than our supremum energies. Tensile strength and fracture energy of N-A-S-H gel is comparable with low density C-S-H phases, i.e. with outer product of cement paste.

Table 1: Results of nanoindentation and micro-beam bending.

	Cement paste			**AAFA**
	Outer product	**Inner product**	**CH**	**N-A-S-H gel**
E (GPa)	24.9 ± 1.3	33.6±2.0	39.0±7.1	25.5±4.24
f_t (MPa)	264.1 ± 73.4	700.2±198.5	655.1±258.3	340.8±124.1
G_f^{sup} (J/m^2)	4.4±1.9	19.7±3.8	19.9±14.4	4.5±1.8

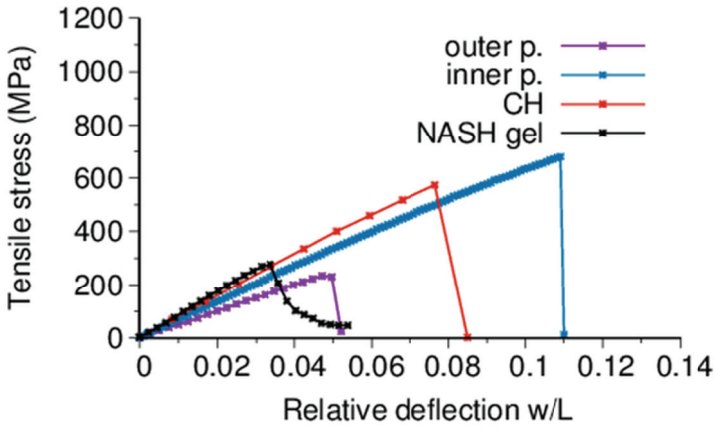

Figure 3: Examples of load-deflection curves measured by nanoindeter.

4. CONCLUSIONS

The paper shows results of microscale experiments performed on individual phases of hydrated cement paste phases and main reaction product of alkali-activated fly ash, the N-A-S-H gel. Micro-beams were fabricated with the aid of FIB milling and samples loaded by nanoindenter. Quantitative results of tensile strength and fracture energy were obtained. It was found that the tensile strength is two orders of magnitude higher than the macroscopic value. results are in relation with molecular dynamics simulations available from literature. The strength scaling corresponds to multi-scale character of the composite in which defects occurs at higher levels as suggested by corresponding models [7].

ACKNOWLEDGEMENTS

Financial support of the Czech Science Foundation (project 17-05360S) and the Czech Technical University in Prague (SGS18/114/OHK1/2T/11) is gratefully acknowledged.

REFERENCES

[1] Bažant, Z. P., 'Scaling of Structural Strength', second ed., (Elsevier Ltd., 2005).
[2] Fischer-Cripps A.C., 'Nanoindentation', (Springer, 2002).
[3] Gianuzzi, L. and Stevie, F., 'Introduction to Focused Ion Beams. Instrumentation, Theory, Techniques and Practice', (Springer, 2005).
[4] Němeček, J., Králík, V. and Vondřejc, J., 'Micromechanical analysis of heterogeneous structural materials'. *Cem Concr Comp* **36** (2013), 85–92.
[5] Němeček, J., Šmilauer V., Kopecký, L., 'Nanoindentation characteristics of alkali-activated aluminosilicate materials', *Cem Concr Comp* **33** (2011), 163–170
[6] Němeček, J., Králík, V., Šmilauer V., Polívka L., Jager, A., 'Tensile strength of hydrated cement paste phases assessed by microbending tests and nanoindentation', *Cem Concr Comp* **73** (2016), 164-173.
[7] Němeček, J., Šmilauer V., Němeček, J., Kolařík, F., 'Fracture properties of cement hydrates determined from microbending tests and multiscale modeling', *Proceedings of EURO-C 2018*, (Taylor and Francis, 2018).

[8] Davie, C. and Masoero, E., 'Modelling damage from the nano-scale up'. In 10th International Conference on Mechanics and Physics of Creep, Shrinkage, and Durability of *Concrete and Concrete Structures*, 2015.
[9] Plassard, C., Lesniewska, E., Pochard, I. and Nonat A., 'Nanoscale experimental investigation of particle interactions at the origin of the cohesion of cement'. *Langmuir* **21**(16) (2005), 7263–7270.
[10] Ghebrab, T., Soroushian, P. 'Mechanical properties of hydrated cement paste: development of structure-property relationships', J. *Concr. Struct. Mater.* 7 (4) (2010), 37-43.
[11] Bauchy, M., Laubie, H., Qomi, M.A., Hoover, C., Ulm, F.-J., Pelenq, R.-M., 'Fracture toughness of calcium-silicate-hydrate from molecular dynamics simulations', *J. Non Cryst. Solids* **419** (2015), 58-64.

International Conference on Sustainable Materials, Systems and Structures (SMSS 2019)
Novel Methods for Characterization of Materials and Structures
20-22 March 2019 – Rovinj, Croatia

MECHANICAL AND MICROSTRUCTURAL EVALUATION OF BIO-BASED BUILDING BOARDS – PRELIMINARY STUDY

L. Korat (1), V. Ducman (1) and S. Medved (2)

(1) Slovenian National Building and Civil Engineering Institute, Dimičeva 12, 1000 Ljubljana, Slovenia
(2) Department of Wood Science and Technology, Biotechnical Faculty, University of Ljubljana, Jamnikarjeva ulica 101, SI-1000 Ljubljana, Slovenia

Abstract

The development of building materials which include bio-based materials is an area of rapid development. In particular, the combined use of bio-based and other materials allows the formation of different composites, such as fibre boards, sandwich panels etc. [1]. In the present study different bio-based composite internal building boards, based either on cement or an alkali activated precursor, were prepared in the laboratory and characterised. Standard X-ray fluorescence (XRF) and X-ray diffraction (XRD) were used to examine the chemistry and mineralogy of input materials (cement, fly ash). The density and standard mechanical properties of the laboratory-prepared boards were later analysed. Preliminary results showed the flexural strength to be 5-10 MPa for cement-based materials and around 3 MPa for alkali activated materials. The density was 1-2 g/cm^3 for both types of material.

Keywords: bio-composite, building boards, fibres, cement, alkali activated materials

1. INTRODUCTION

The use of bio-based or cellulose-based materials in construction is an area of rapid development. In particular, the use of bio-based substances combined with other materials allows the formation of different composites, such as fireboards, sandwich panels etc. In addition to being extremely environmentally-friendly (one of the lowest amounts of embodied CO_2 per kilogram), such materials, especially cellulose-based materials, possess excellent thermal and acoustic properties. Cellulose materials, however, only account for a minor share of materials on the European insulation market, primarily because they are highly hygroscopic, flammable and prone to mould. Improving these shortcomings would facilitate the usage of cellulose for insulation purposes in the building sector, and help reduce the effects of built environments and restoration procedures on the environment. This is the scope of the project "Potential of biomass for development of advanced materials and bio-based products" [2]. Within this project the focus of the present research is the development of products with a higher proportion of bio-based components and improved functionalities for

construction. Two types of building boards were produced; building boards based on cement, and building boards based on an alkali activated precursor.

2. EXPERIMENTAL PROCEDURE

2.1 Materials

Cement (CEM I), fibres and fly ash were analysed and their use for the preparation of building boards, based on either cement or an alkali activated precursor, was investigated. Fibres used in both building boards were wood fibres with λ_D: 0.038 W/(m·K), a BET surface area of 16.7 m^2/g and diameters of 10 µm up to 200 µm, as shown in Figure 1.

Figure 1: Fibres, presented by optical microscopy and FE-SEM

Building boards based on cement were prepared from the afore-mentioned fibres and cement CEM I. As seen from Table 1, the primary compounds of CEM I are CaO and SiO_2, largely related to the content of C_3S and C_2S minerals, followed by Al_2O_3 and Fe_2O_3, related to the C_3A and C_4AF minerals. LOI value was 3.1%, mainly attributed to the presence of organic matter and carbonates, and the BET surface area was 1.95 m^2/g.

Table 1: Chemical and physical properties and qualitative phase composition of CEM I and fly ash used in the investigation

Chemical analysis	CEM I	Fly ash	CEM I	Fly ash
Oxide	wt. %	wt. %	Phase	
SiO_2	20.51	39.37	C_3S	Anhydrite
Al_2O_3	5.14	17.01	C_2S	Gehlenite
Fe_2O_3	2.71	8.62	C_3A	Hematite
CaO	60.39	18.63	C_4AF	Lime
MgO	1.81	1.79	Gypsum	Periclase
K_2O	0.77	3.92	Bassanite	Plagioclase
Na_2O	0.53	0.78	Calcite	Quartz
SO_3	2.24	2.73		
P_2O_5	0.12	0.40		
LOI	3.10	5.01		
BET [m^2/g]	1.95	16.7		

Building boards based on an alkali activated precursor were prepared from fibres, fly ash (originated from coal combustion), an activating sodium silicate solution, and NaOH. As seen from Table 1, the proportion of SiO_2 is high. According to standard EN 197-1 [3], fly ash can be classified as a siliceous fly ash (< 10 % CaO). The concentrations of Fe_2O_3 and Al_2O_3 are also high, likely due to the presence of hematite and gehlenite (Table 1). The LOI value was 5.01 % and the BET surface area 16.7 m^2/g. According to the standard EN 450-1 [4], the content of sulphate (< 3 %), alkalis (Na_2O < 5 %) and phosphate (< 5 %), were all below the limits.

2.2 Preparation of samples

Building boards based on cement were prepared from dry fibres and cement CEM I. The preparation of building boards based on cement was divided into two parts, firstly the preparation of smaller boards (dimensions 12x16x10 cm, designated as sCBB), and secondly the preparation of larger building boards (dimensions 50x50x10 cm, designated as lCBB). A cement mixture for sCBB was prepared regarding the appropriate water-solid ratio (preliminary testing of several mixtures with w/s ratio ranging from 0.4 to 0.6) and a fibre-cement ratio of 1:50 (Table 2). The sCBB were first compressed (5 KPa) and exposed to laboratory conditions (temperature 21 °C and relative humidity ≤ 53 %) for 24 hours. For the following 24 hours they were cured in a humidity chamber (temperature 20 °C and relative humidity ≤ 90 %). The sCBB were then returned to laboratory conditions in order to investigate their compressive strength after 7, 14 and 28 days of hydration (from sCBB_A to sCBB_E). The cement mixture for the large boards (lCBB) was prepared similarly to that for the small boards (Table 2), where the amount of material was higher. Two different temperatures (20 °C and 70 °C) were applied during the compression process (8 KPa). After compression the lCBB boards were exposed to laboratory conditions in order to investigate their compressive strengths after 7 and 35 days of hydration (lCBB_A and lCBB_B).

Table 2: Composition of the investigated CBB mixtures by weight

Designation	Solid compounds			Compression	
	CEM I [g]	Dry fibers [g]	w/s	Time	Temperature [°C]
sCBB_A	300	15	0.4	24 h	21
sCBB_B	300	15	0.5	24 h	21
sCBB_C	300	15	0.6	24 h	21
sCBB_D	300	20	0.7	24 h	21
sCBB_E	300	20	0.8	24 h	21
lCBB_A	6000	300	0.4	30 min	20
lCBB_B	6000	300	0.4	30 min	70

w - the amount of mixing demineralized water
s - solid material

Building boards based on an alkali activated precursor (ABB) were prepared from fibres, fly ash, an activating sodium silicate solution (sodium silicate Crystal 0112; produced by Tennants Distribution, Ltd., SiO_2:Na_2O = 1.97, 54.2 mass % aqueous solution) and NaOH (produced by Donau Chemie, 41.7 mass % aqueous solution). These boards were designated as smaller boards (dimensions 12x16x1 cm, designated as sABB). Foaming and stabilizing agents were later added to create alkali activated foams. The influence of both agents was

initially tested on prisms (4x4x16 cm) and the best mixture was later used in the preparation of larger building boards (dimensions 60x40x1 cm, designated as lABB). The moulds were then placed in an oven for 24 hours at a temperature of 70 ^{o}C. The resulting hardened test specimens were removed from the moulds and stored for a further 3 days at a controlled temperature of 20 ± 2 °C.

Table 3: Composition of the investigated ABB mixtures by weight

Designation	Solid compounds [g]				Liquid compounds [g]	
	Fly ash	Dry fibers	FA	SA	Water glass	NaOH
sABB_A	300	10	0	0	180	90
sABB_B	300	25	0	0	180	90
lABB	3000	50	150	150	1800	900

*FA is foaming agent and SA is stabilizing agent

2.3 Techniques

The chemical composition of materials was determined using a Thermo Scientific ARL PERFORM'X Wavelength Dispersive X-Ray Fluorescence Spectrometer with Rh-target x-ray tube. Prior to the measurements, samples were dried at 105 °C and heated at 950 °C. A fused bead was then prepared with lithium tetraborate 50 %/lithium metaborate 50 %, with a 1:10 mixture of the sample and flux heated at 1025 °C. Loss on ignition (LOI) was determined in accordance with EN 196-2. The total specific area or Brunauer-Emmet-Teller (BET) surface area of the samples was determined via nitrogen adsorption at 77 K, using a Micromeritics ASAP 2020 instrument.

The phase composition of the samples was determined via PANalytical Empyrean with CuKα radiation. Data was collected at 45 kV and a current of 40 mA, over the 2θ range from 4 to 70°. Mineral phases were determined using X´PertHighScore Plus diffraction software from Panalytical with PAN-ICSD powder diffraction files.

Densities of boards were determined using "geometrical density", obtained by dividing the measured weights by their dimensions. Reported values of density were obtained using the average of 10 test specimens per mixture, and the average of 3 separate measures per sample size.

Determination of the consistency of fresh mortar (by flow table) of the studied materials was determined according to EN 1015-3 [5].

The flexural and compressive strength of the test specimens were determined at different time points (7, 14 and 28 days) by means of a Toninorm testing machine (Toni Technik, Germany). The reported values of mechanical strength were obtained from the average of 3 sample measures per mixture.

The thermal conductivity of samples was measured at 7 days and 35 days using a heat flow meter LM305 and a sample thickness of 10 mm.

The back-scattered electrons (BSE) image mode of a low vacuum scanning electron microscope (JEOL 5500 LV equipment) was chosen as a complementary method to examine the microstructure (to determine ITZ between the matrix and the fibres).

X-ray computed microtomography ('Xradia μCT-400' tomograph, Concord, California, USA) was selected for detailed analysis of the inner structure (pores and fibres). The beam energy was set to 80 kV. Two thousand projection images were acquired on the CCD camera,

which was equipped with a 0.39X magnification optical objective, and samples were scanned at a resolution of 5 microns per pixel. Avizo Fire 3D-image analysis software was used to reconstruct the three-dimensional internal pore structure of the samples.

3. RESULTS

3.1 Building boards based on cement (CBB)

Building boards based on cement with fibres (sCBB) are presented in Figure 2, where the differences in internal structure according to the proportion of fibres added can be seen. XRD analysis revealed mineral phases within the material: C_3S, C_2S, C_4AF, calcite, ettringite and calcium hemicarboaluminate hydrate. For detailed analysis of the inner structure (pores and fibres), X-ray computed microtomography was selected. X-ray computer microtomography is mainly used for the detection of dislocations, inclusions, and cracks, and for porosity determination [6], but lately it has also been used as a method for the determination of fibre distribution [7]. Conventional techniques such as SEM are not appropriate because the size distribution of phases with complex shapes in the material cannot be obtained from a 2D section. In such cases only X-ray computer microtomography is an adequate technique, although SEM is still useful for giving an insight into the zone between the fibres and the matrix. The zone between the fibres and the matrix is presented in more detail in Figure 3 (a), as determined by SEM. The uneven fibre distribution and occurrence of larger air voids within the structure can also be seen in Figure 3(b).

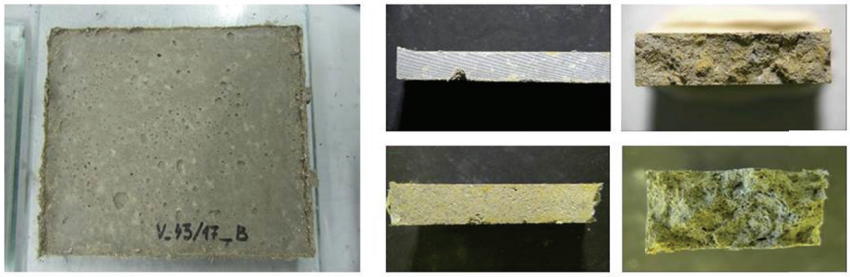

Figure 2: Building boards based on cement with fibers (sCBB), sCBB_A and sCBB_E shown

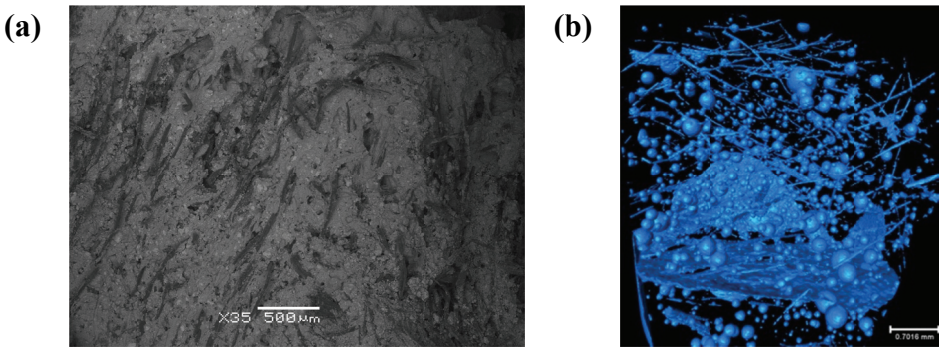

Figure 3: Building boards based on cement with fibres (sCBB), (a) determined by SEM, and (b) by X-ray computed microtomography (3D view)

The measured density and flexural strength of the sCBB, after hydration times of 7, 14 and 28 days are presented in Table 4. The table shows that the density of the investigated sCBB decreased by approximately 15 % between 7 and 28 days, and that the density is influenced by the water-solid ratio. The water-solid ratio also affects the flexural strength; samples with a lower water-solid ratio have a higher flexural strength, and properties of sCBB increased by approximately 37 % at 28 days.

Table 4: Density and flexural strength of CBB investigated at different time points (standard deviations of measures are shown in brackets)

Designation	Density [g/cm^3]			Flexural strength [MPa]		
	7 days	14 days	28 days	7 days	14 days	28 days
sCBB_A	1.46 (±0.03)	1.21 (±0.03)	1.23 (±0.02)	4.84 (±0.25)	4.42 (±1.05)	5.75 (±0.87)
sCBB_B	1.57 (±0.03)	1.51 (±0.00)	1.50 (±0.01)	6.90 (±0.20)	6.90 (±0.62)	7.91 (±1.03)
sCBB_C	1.74 (±0.05)	1.67 (±0.00)	1.66 (±0.02)	8.71 (±0.78)	8.42 (±0.59)	9.17 (±0.82)
sCBB_D	0.93 (±0.04)	-	0.91 (±0.06)	3.03 (±0.33)	-	3.15 (±1.73)
sCBB_E	0.95 (±0.08)	-	1.04 (±0.06)	2.08 (±1.06)	-	4.07 (±1.14)
Designation	Density [g/cm^3]			Flexural strength [MPa]		
	7 days		35 days	7 days		35 days
lCBB_A	1.44 (±0.01)		1.49 (±0.01)	8.21 (±2.17)		8.33 (±1.31)
lCBB_B	1.45 (±0.03)		1.48 (±0.01)	7.93 (±2.61)		7.92 (±1.01)

Figure 4 shows larger building boards based on cement with fibres (lCBB), in which a fairly even distribution of fibres can be seen, although some fibres are still joined in particular locations. The contact between the fibres and the cement matrix is good. Determination of consistency of fresh mortar (by flow table) for lCBB was 144 mm and the results of the density and flexural strength of lCBB are reported in Table 4. There are not huge differences in density between lCBB_A and B, but small changes are seen regarding the flexural strength, especially for lCBB_A. Thermal conductivity after 7 and 35 days respectively was 0.184 W/m·K and 0.168 W/m·K for lCBB_A, and 0.178 W/m·K and 0.148 mW/m·K for lCBB_B. The difference could be attributed to the presence of water in the system which after a certain period is either consumed for hydration or evaporated.

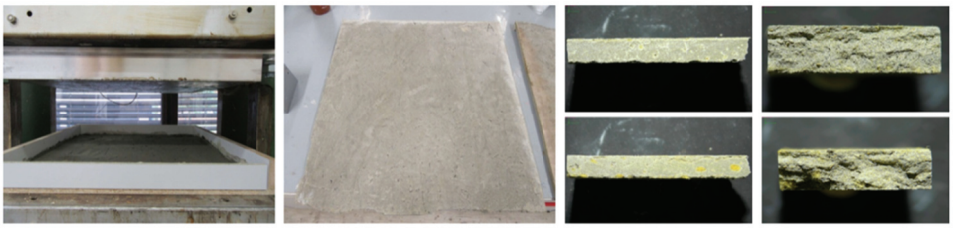

Figure 4: Building boards based on cement with fibres (lCBB), lCBB_A and B

Some commercial cement based boards were taken from the market and analysed for comparison. Wooden particle cement boards of density 1350 kg/m^3, for example, exhibit a bending strength of > 9 MPa, and thermal conductivity of 0.26 W/mK.

4.2 Building boards based on an alkali activated precursor (ABB)

Building boards based on an alkali activated precursor (ABB) are presented in Figure 5, where the difference in inner structure according to the amount of fibres added can be seen. The density and flexural strength of sABB are reported in Table 5. Sample sABB_A has a higher density but lower flexural strength than sample sABB_A, indicating that a greater amount of fibre increased the flexural strength.

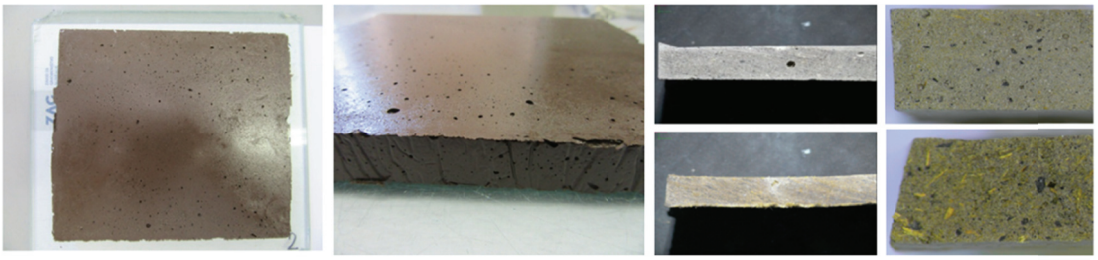

Figure 5: Building boards based on an alkali activated precursor (sABB); samples sABB_A,B

Table 5: Density and flexural strength of ABB investigated at different time points (the standard deviations of measures are shown in brackets)

Designation	Density [g/cm^3]	Flexural strength [MPa]	Compressive strength [MPa]
sABB_A	1.53 (±0.02)	3.08 (±0.61)	-
sABB_B	1.38 (±0.03)	3.48 (±0.24)	-
lABB	0.27 (±0.01)	0.17 (±0.01)	0.25 (±0.01)

Larger building boards based on an alkali activated precursor with fibres and foaming agent (lABB) are presented in Figure 6. The distribution of the fibres can be seen in Figure 7, where it is evident that the contact between the fibres and the matrix is good. The thermal conductivity for lABB was 0.119 W/m·K.

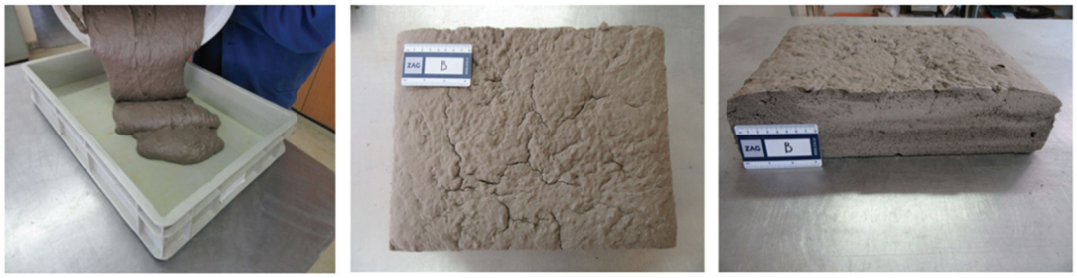

Figure 6: Building boards based on an alkali activated precursor (lABB)

(a) **(b)**

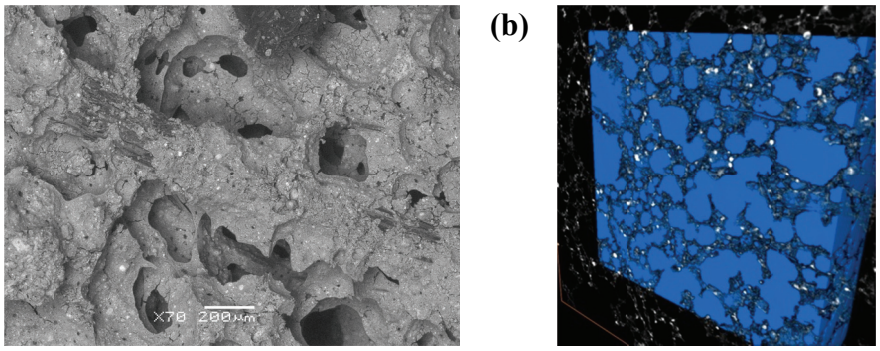

Figure 7: Building boards based on an alkali activated precursor (lABB), (a) determined by SEM and (b) by X-ray computed microtomography (3D view)

5. CONCLUSIONS

- Within the present study, different bio-based composite internal building boards, based on cement or an alkali activated precursor, were prepared in the laboratory and characterized. Their properties were compared to commercially available insulation boards.
- Cement based boards exhibit similar properties (bending strength, thermal conductivity) to those that are commercially available, while boards based on alkali activator precursors still require further optimisation.

ACKNOWLEDGEMENTS

The work was carried out within the RDI project Cel.Cycle: “Potential of biomass for development of advanced materials and bio-based products”and co-financed by the Republic of Slovenia, Ministry of Education, Science and Sport and the European Union under the European Regional Development Fund. 2016-2020. The Metrology Institute of the Republic of Slovenia is acknowledged for the use of XRF. The authors would like to thank Dr. Erika Švara Fabjan (ZAG) for the FE-SEM images.

REFERENCES

[1] Jones, D. and Brischke, C., Performance of Bio-based Building Materials, abstract of Journal Publication –COST Action FP1404. Sterman, S. and Marsden, J.G., 'Silane coupling agents', *Ind. Engng. Chem.* **58** (3) (1966) 33-77.
[2] Potential of biomass for development of advanced materials and bio-based products http://celkrog.si/o-projektu/?lang=en
[3] EN 197-1, Cement - Part 1: Composition, specifications and conformity criteria for common cements.
[4] EN 450-1, Fly ash for concrete - Part 1: Definition, specifications and conformity criteria.
[5] EN 1015-3, Methods of test for mortar for masonry - Part 3: Determination of consistence of fresh mortar (by flow table).
[6] Korat, L. and Ducman, V., The influence of the stabilizing agent SDS on porosity development in alkali-activated fly-ash based foams. *Cement & Concrete Composites* 80 (2017) 168-174.
[7] Westenberger, P., Estrade, P., Lichau, D., Fiber Orientation Visualization with Avizo Fire®. Conference on Industrial Computed Tomography (ICT) 2012 – Wels. Austria.

International Conference on Sustainable Materials, Systems and Structures (SMSS 2019)
Novel Methods for Characterization of Materials and Structures
20-22 March 2019 – Rovinj, Croatia

A NEW APPROACH TO QUANTIFICATION OF RESIDUAL FLEXURAL STIFFNESS OF REINFORCED CONCRETE

Viktor Gribniak (1), Aleksandr Sokolov (1) and Arvydas Rimkus (1)

(1) Laboratory of Innovative Building Structures, Vilnius Gediminas Technical University, Vilnius, Lithuania

Abstract

Residual stiffness of reinforced concrete elements is closely related with structural integrity of cracked sections. A plenty of various evaluation procedures, however, does not enable the comparative analysis of different reinforcement schemes, since they are tested in different manner. To solve this problem, a new quantification procedure of the tension stiffening effect is introduced. It employs a new testing layout designed with the purpose to form multiple cracks in a small laboratory specimen. This enables to reduce scatter of the results due to the crack formation peculiarities. The corresponding analytical model, representing the average equivalent stress-strain behaviour of the tensile concrete, is proposed. The model is based on the following simplifications: smeared crack approach; linear strain distribution within the section depth; elastic behaviour of reinforcement and compressive concrete; and rectangular distribution of stresses in the tensile concrete. The latter assumption enables obtaining a closed-form analytical solution of the constitutive modelling problem. That makes the analysis results independent on the loading history: the analysis is performed in a uniform manner for the cases of short-term, sustained, or cyclic load applications. Furthermore, the proposed methodology could be acceptable for estimating residual stiffness of elements with various reinforcement combinations. The application of the proposed technique is illustrated experimentally. Several specimens with composite reinforcement are subjected to monotonic and cyclic load patterns.

Keywords: concrete, composite reinforcement, tests, analytical model, tension stiffening

1. INTRODUCTION

Residual stiffness of reinforced concrete elements is closely related with structural integrity of cracked sections. Tension stiffening models can estimate the stiffness decay in an averaged manner. Numerous studies have investigated the tension stiffening issue. However, only several works investigated the flexural effects. Fundamental studies by *Kaklauskas & Ghaboussi* [1] and *Torres et al.* [2] can be mentioned in this context. Several approaches to the constitutive modelling problem have been developed [1-7]. Elaborate numerical

procedures are intrinsic attribute of the "exact" approaches [1, 3, 7]. Iterative nature of the corresponding procedures often complicates the analysis [3, 7]: the calculation errors are accumulated following the load history. The development of more reliable algorithms employed the reinforcement-related tension stiffening concept was a consequence of the further improvements [4-6]. Such models, however, are not useful for the analysis of the elements reinforced with a combination of different types of internal bars and/or external sheets.

This study introduces a simplified approach to the flexural stiffness analysis. It employs a new testing layout designed with the purpose to form multiple cracks in a small laboratory specimen that reduces scatter of the results due to the cracking peculiarities. Representing a closed-form solution of the tension stiffening problem, the proposed analytical model requires neither iterative calculations nor description of the loading history. The application of the proposed technique is illustrated experimentally. Several flexural elements with composite reinforcement are considered. The specimens are subjected to monotonic and cyclic loadings.

2. THE PROPOSED TEST PROCEDURE

The previous studies [8, 9] have indicated that different number of cracks formed in small-size elements has a primary effect on the constitutive modelling results. Since laboratory conditions limit size of the specimens, design of the testing layout was focused to ensure the cracking process, i.e. induce multiple cracks, of a small-size sample. *Williams* [10], *Purainer* [11] and *Gilbert* [12] revealed that a slab-shaped geometry of concrete specimens enables formation of multiple cracks with narrow crack spacing. Such geometry of the specimens is used in this study. The analysis is based on monitoring results of the pure bending zone. The specimens were designed ensuring maximum length of the monitoring zone. Such design fits the *Eurocode 2* condition for elements not requiring design of shear reinforcement, i.e. $a \leq 2d$, where a is the shear span, d is the effective depth of the cross-section.

The proposed slab-shaped 1000 mm long specimen has a rectangular 100×200 mm cross-section. Three series of concrete specimens with different reinforcement are used for the tension stiffening analysis. The first three specimens (designated to as *B1-GFRP*, *B2-GFRP* and *B3E-GFRP*) were reinforced with 8 mm *ComBar* GFRP bars. Two beams (*B4* and *B5*) were reinforced with 8 mm steel bars. The remaining five specimens had only external reinforcement (CFRP sheets). Three externally reinforced beams (*B6-CFRP*, *B7-CFRP* and *B8E-CFRP*) were subjected to monotonic load (in the same manner as previously described elements), while the specimens *B9C-CFRP* and *B10C-CFRP* were subjected to cyclic load. Letter *E* in the beam notation indicates beams with external shear reinforcement, while *C* marks elements subjected to cyclic loading. The loading scheme is shown in Figure 1. To prevent shear failure of the beams with composite reinforcement, two specimens subjected to monotonic load (*B3E-GFRP*, *B8E-CFRP*) and both elements subjected to cyclic load are strengthened with CFRP wrap as shown in Figure 2. Single layer of the unidirectional *MapeWrap C UNI-AX* sheet was used as the external reinforcement. The equivalent thickness of the dry layer is equal to 0.166 mm.

All specimens were produced in one batch. The composition of the concrete (for one cubic meter) are following: 356 kg of cement CEM I 42.5 R, 163 l of water, 177 kg of limestone powder, 890 kg of 0/4 mm sand and 801 kg of 4/16 mm crushed aggregates; 1.97% (by the cement weight) of the superplasticizer *Mapei Dynamon XTend* and 3.5 kg of the admixture

SCP 1000 Optimizer. The concrete also contained synthetic fibres: 4.2 kg of the *Durus EasyFinish* macro-fibres and 0.9 kg of the *Crackstop M Ultra* micro-fibres. Strength of the ∅150×300 mm compressive concrete cylinders at the beam testing day was found equal to 46.0 MPa.

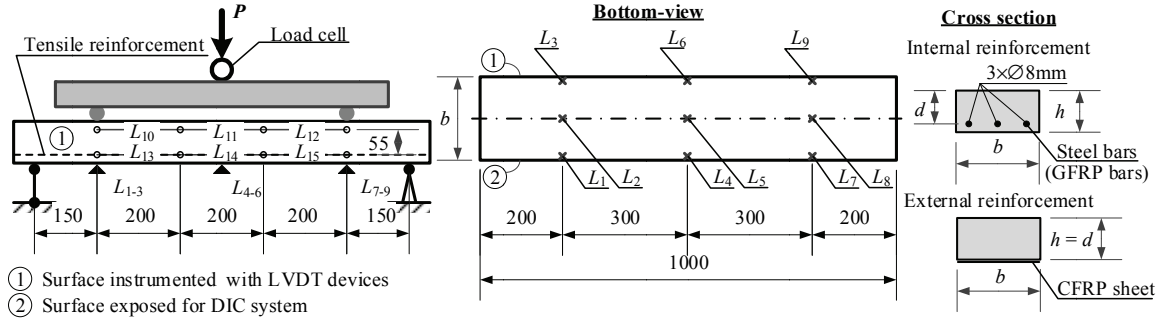

Figure 1: Monitoring devices, loading scheme and cross-sections of the tested elements

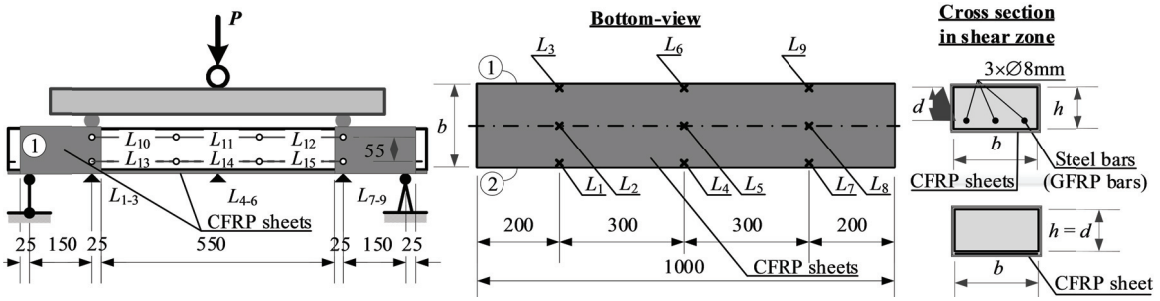

Figure 2: Loading scheme and cross-section of beams with CFRP shear strengthening

Figure 3: Test setup and monitoring devices

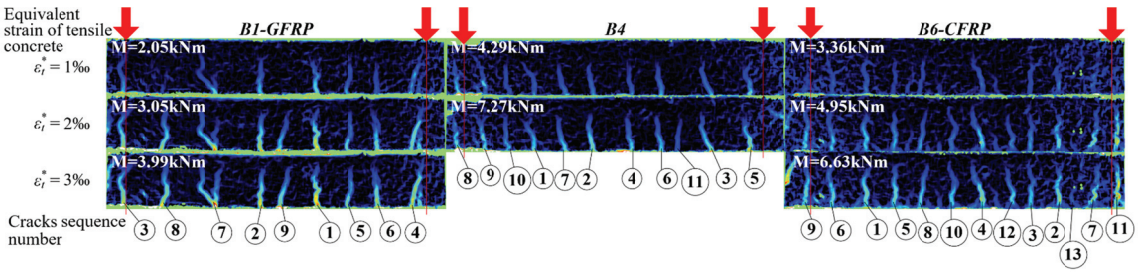

Figure 4: Cracking of the pure bending zone of selected beams corresponding different equivalent strain of tensile concrete (DIC results)

Main parameters of the test specimens are presented in Table 1. In this table, h, b and d are the height, width and effective depth of the cross-section; A_r and E_r are the area and elasticity modulus of reinforcement, respectively.

Table 1: Main parameters of the beams

Beam	h [mm]	b [mm]	d [mm]	A_r [mm^2]	E_r [GPa]
B1-GFRP	101	199	75	150.8	64.4
B2-GFRP	101	200	76	150.8	64.4
B3E-GFRP	100	200	76	150.8	64.4
B4	104	199	79	150.8	196
B5	105	200	79	150.8	196
B6-CFRP	110	204	110	23.2	230
B7-CFRP	104	196	104	23.2	230
B8E-CFRP	99	202	99	23.2	230
B9C-CFRP	106	195	106	23.2	230
B10C-CFRP	106	194	106	23.2	230

The tests are carried out using a 5 MN capacity servo-hydraulic machine. The monotonic load is applied with a rate of 0.4 mm/min. The cyclically loaded specimens are subjected to the monotonically increased load with rate of 1.68 kN/min until it reaches 40 kN. After that, the sinusoidal load cycles start with amplitude approximately equal 15 kN and the frequency of 0.167 Hz. The number of cycles (100) was the same in both tests. A load cell is used for the load measurements. Linear variable displacement transducers (LVDT, L_{10}-L_{15}) attached in two continuous lines to side surface No. 1 (see in Figures 1-3) of the specimen monitor the surface deformations. Nine LVDT (L_1-L_9, Figures 1, 2) measure the vertical displacements in pure bending zone. The data logger Almemo 5690-2 collects the output results of all LVDT and the load cell. Deformations and crack pattern of the opposite side No. 2 (see in Figures 1-3) are fixed with the help of digital image correlation system (DIC). Two cameras Imager E-lite 5M are used for this purpose. The cameras are placed on a tripod at the 3.0 m distance from the specimens; the distance between the cameras is equal to 0.4 m. The cameras, incorporating a charge-coupled device (CCD) detector, have a resolution of 2456×2085 pixel at the 12.2 fps rate. The DIC application example is presented in Figure 4. The cracking schemes are related to the average equivalent deformations of tensile concrete ε_t^*.

3. ANALYTICAL MODEL

The stiffness analysis is based on the moment-curvature response of the pure bending zone. The analytical model proposed for the analysis of residual stiffness considers an average stress-strain behaviour of the tensile concrete. The model employs the following assumptions: smeared crack model; linear strain distribution within the section depth; elastic behaviour of reinforcement and compressive concrete; and rectangular distribution of stresses in the tensile concrete. The latter assumption enables obtaining a closed-form analytical solution of the tension stiffening modelling problem. The Figure 5 shows the modelling scheme. Based on the equilibrium equations of internal forces and bending moments in respect to the centroid of the equivalent tensile stress diagram (Figure 5), the equivalent average stress in the tensile concrete and the corresponding strain can be expressed as

$$\sigma_t^* = \kappa \frac{y_c^2 b E_c - 2(d - y_c) E_r A_r}{2(h - y_c) b}, \tag{1}$$

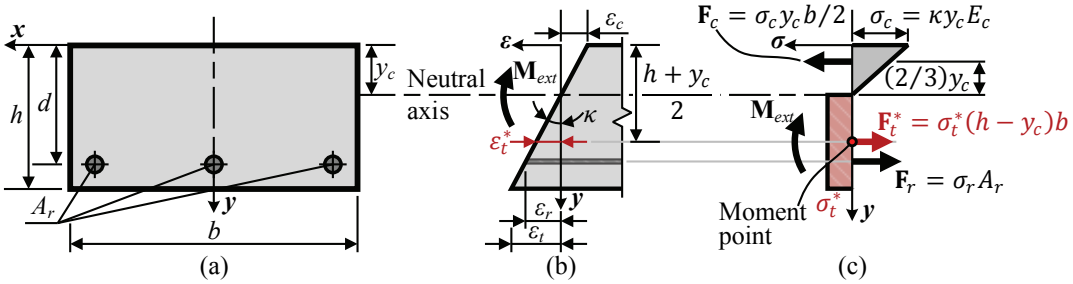

Figure 5: Analytical model of the element subjected to external bending moment $\mathbf{M}_{ext}$: RC section (a); strain profile (b); stresses and internal forces acting in section (c)

$$\varepsilon_t^* = \kappa(h - y_c)/2\,, \tag{2}$$

where E_c and E_r are the elasticity moduli of concrete and reinforcement, respectively, A_r is the reinforcement area; other notations are evident from Figure 5a. Position of the neutral axis is estimated as

$$y_c = \frac{1}{3C_3}\left\{2\Lambda \cos\left(\frac{1}{3}\cos^{-1}\{\Psi\}\right) - C_2\right\}, \tag{3}$$

where

$$\Psi = -(27C_3^2 C_0 - 9C_3 C_2 C_1 + 2C_2^3)/2\Lambda^3\,, \quad \Lambda = \sqrt{C_2^2 - 3C_3 C_1}. \tag{4}$$

The corresponding coefficients are following:

$$C_0 = \kappa d^2 E_r A_r \left(1 - \frac{h}{2d}\right) - \mathbf{M}_{ext};$$
$$C_1 = \frac{\kappa E_r A_r}{4}(h - 3d); \quad C_2 = \frac{\kappa}{4}(2E_r A_r + E_c b h); \quad C_3 = \frac{\kappa E_c b}{12}. \tag{5}$$

The application of the proposed simplified approach to the tension stiffening problem causes a very similar result (tension stiffening diagram) as the exact solution of the inverse analysis problem [3, 7]. An example of such analysis is presented in Figure 6. The moment-curvature diagram shown in Figure 6a is used to determine the tension stiffening models in Figure 6b. It can be observed that the exact and the simplified models are agreed well. Since the exact inverse procedure [3, 7] considers deformation behaviour of the most tensioned layer of the section, it enables determining the stress-strain response of the tensile concrete at more advanced deformation levels than the analytical procedure. However, more stable results (in the terms of the diagram oscillations) characterize the application of the analytical approach; furthermore, it represents a closed-form solution of the inverse problem, which does not require any iterative calculations as well as description of the loading history.

4. TENSION STIFFENING ANALYSIS

The monitoring scheme (Figures 1, 2) enables the curvature estimation in different ways: from vertical displacements of LVDT L_1-L_9 and from surface deformations identified using the LVDT L_{10}-L_{15} or DIC system. References [3-4, 6] describe the data processing algorithms. Analysis of the alternative curvature diagrams enables avoiding errors due to measurement interruptions or other inaccuracies.

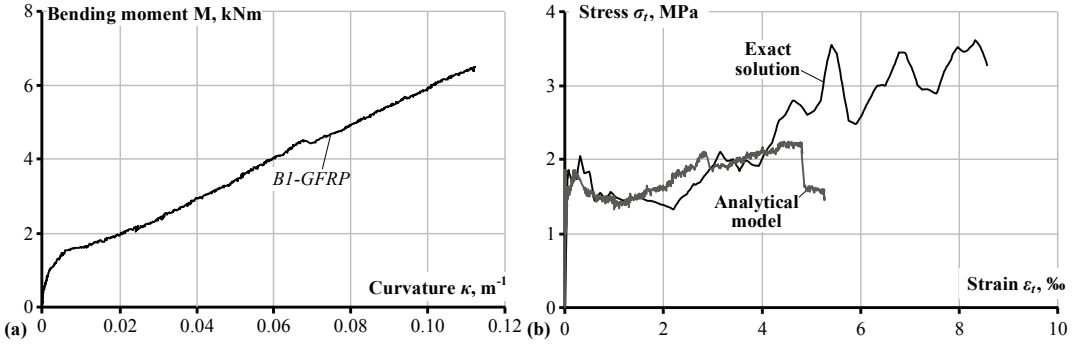

Figure 6: Comparison of the analytical and exact modelling results: moment-curvature diagram (a) and the corresponding tension stiffening models (b)

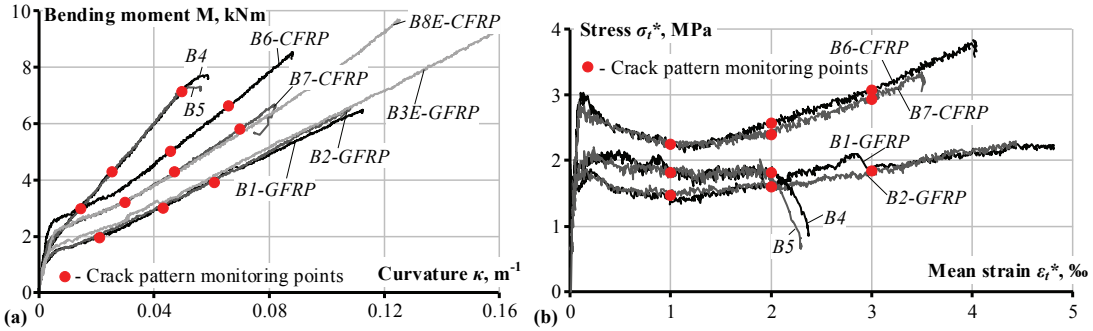

Figure 7: Moment-curvature diagrams (a) and the corresponding tension stiffening models (b)

Figure 7a shows the moment-curvature diagrams of the beams subjected to the monotonic load. These diagrams are constructed using the surface deformations captured by the DIC system. The differences between the diagrams of nominally identical beams (*B6-CFRP* and *B7-CFRP*) can be related with variation in the cross-section height. The corresponding tension stiffening models are shown in Figure 7b. These diagrams are derived using the concept of the equivalent average stress of tensile concrete (Section 3). Red points in the diagrams shown in Figure 7 correspond to the cracking patterns presented in Figure 4. As can be observed in Figure 7b, the diagrams of the nominally identical specimens are practically coincident. Analysis of the tension stiffening models reveals significant efficiency of the external CFRP reinforcement system concerning the internal reinforcing schemes. This effect is the object of further research.

Failure character of the beam specimens is another topic that is requiring analysis. As can be observed in Figure 8, formation of a critical shear crack has caused failure of specimens with composite reinforcement. That is a consequence of a low resistance of fibre reinforced bars or external sheets to transverse load.

To improve this situation, shear zone of two specimens with composite reinforcement is strengthened with CFRP sheets. Figure 2 shows the corresponding testing scheme. These sheets were glued to the concrete surface in the same manner as the longitudinal reinforcement sheets. As it can be observed from Figure 7a, the ultimate curvature of the strengthened specimens (*B3E-GFRP* and *B8E-CFRP*) increase by 40% to 50% concerning the counterparts without CFRP sheets in the shear zone. The ultimate load bearing capacity increases as well. The strengthening procedure also changes the failure character as shown in Figure 8 (compare ultimate behaviour of the specimens *B1-GFRP* and *B3E-GFRP*). The failure signs become evident only after the cyclic load (see the result of the beam *B9C-CFRP* in Figure 8). These results are in good agreement with the previous findings analysing the ultimate behaviour of beams with external reinforcement [13]. Hence, the additional shear strengthening is recommended for the analysis of the beam specimens (Section 2) without steel reinforcement.

One of the most important beneficial feature of the proposed analytical model is that it enables analysis of the tension stiffening effect in elements subjected to a cyclic loading. Figure 9a demonstrates the moment-curvature diagrams of the beam specimens subjected for cyclic load. The tension stiffening analysis is related to an arbitrarily set reference bending moment. The dashed line in Figure 9a indicates the reference load. Figure 9b demonstrates increase of the curvature under cycling load. The curvature evolution is estimated by using one curvature value at each loading cycle that corresponds to the ascending of diagrams shown in Figure 9a. The application of the proposed analytical model for the tension stiffening analysis generates diagrams shown in Figure 9c. The tension stiffening decay tendency is evident.

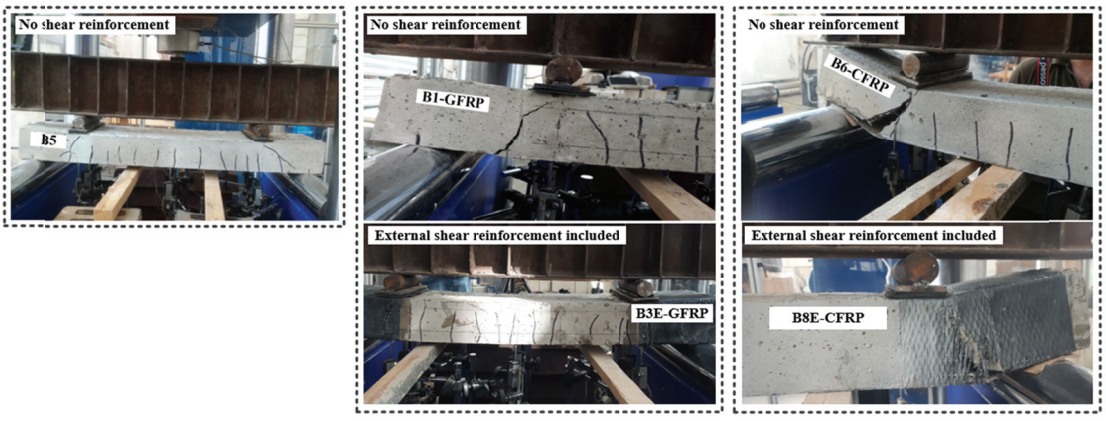

Figure 8: Failure character of the beam specimens

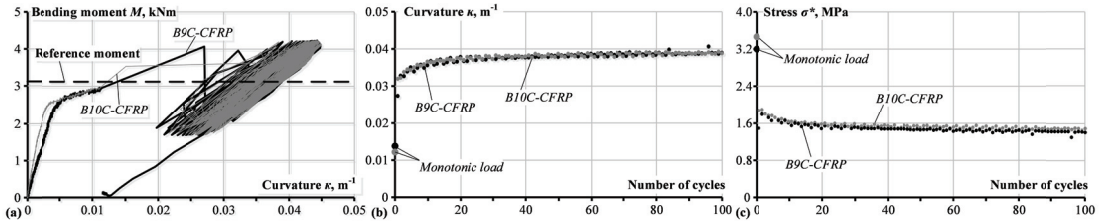

Figure 9: Cyclic loading results: moment-curvature diagrams (a); the reference curvature variation with loading cycles (b); and the corresponding tension stiffening response (c)

5. CONCLUSIONS

The proposed analytical model represents a closed-form solution of the tension stiffening problem requiring neither iterative calculations nor description of the load history.

The proposed methodology, employing a new test layout, is acceptable for comparative analysis of the tension stiffening effect of different reinforcement layouts. The residual stiffness of elements reinforced with any combinations of internal bars, dispersed fibres and external sheets can be estimated in the unified manner.

Test results demonstrate that external reinforcement (CFRP sheets) is the most efficient structural system among the analysed reinforcement layouts for ensuring flexural stiffness. However, shear resistance of elements with FRP reinforcement is not sufficient requiring additional means for improvement.

Decay of tension stiffening due to cyclic load has been estimated for elements with composite reinforcement. After cracking, the elements reinforced with external CFRP have demonstrated almost constant flexural stiffness after 100 loading cycles.

ACKNOWLEDGEMENT

The authors wish to express their sincere gratitude to the financial support by the *Research Council of Lithuania* (Research Project S-MIP-17-62).

REFERENCES

[1] Kaklauskas G. and Ghaboussi J., 'Stress-strain relations for cracked tensile concrete from RC beam tests', *ASCE Journal of Structural Engineering* **127** (1) (2001) 64-73.
[2] Torres L., López-Almansa F. and Bozzo L.M., 'Tension-stiffening model for cracked flexural concrete members', *ASCE Journal of Structural Engineering* **130** (8) (2004) 1242-1251.
[3] Gribniak V., Kaklauskas G., Juozapaitis A., Kliukas R. and Meskenas A., 'Efficient technique for constitutive analysis of reinforced concrete flexural members', *Inverse Problems in Science and Engineering* **25** (1) (2017) 27-40.
[4] Kaklauskas G., Gribniak V., Salys D., Sokolov A. and Meskenas A., 'Tension-stiffening model attributed to tensile reinforcement for concrete flexural members', *Procedia Engineering* **14**: (2011) 1433-1438.
[5] Torres L., Barris C., Kaklauskas G. and Gribniak V., 'Modelling of tension-stiffening in bending RC elements based on equivalent stiffness of the rebar', *Structural Engineering and Mechanics* **53** (5) (2015) 997-1016.
[6] Kaklauskas G. and Gribniak V., 'Hybrid tension stiffening approach for decoupling shrinkage effect in cracked reinforced concrete members', *ASCE Journal of Engineering Mechanics* **142** (11) (2016) Paper ID: 04016085, 1-11.
[7] Gribniak, V., Kaklauskas, G., Kacianauskas, R. and Kliukas, R., 'Improving efficiency of inverse constitutive analysis of reinforced concrete flexural members', *Scientific Research and Essays* **7** (8) (2012) 923-938.
[8] Sokolov A., Kaklauskas G., Jakubovskis R., Juknys M., Kliukas R., Ng P. L. and Gribniak V., 'Experimental investigation of tension stiffening in RC ties', *Advances in Materials Science and Engineering* **2016** (2016) Paper ID: 6965932, 1-8.
[9] Rimkus A. and Gribniak V., 'Experimental investigation of cracking and deformations of concrete ties reinforced with multiple bars', Construction and Building Materials **148** (2017) 49-61.
[10] Williams A., 'Test on Large Reinforced Concrete Elements Subjected to Direct Tension', Technical Report **562** (Cement and Concrete Association, Wexham Springs, 1986).

[11] Purainer R., 'Last- und Verformungsverhalten von Stahlbetonflächentragwerken unter zweiaxialer Zugbeanspruchung', PhD Thesis (University of the Federal Armed Forces, Munich, 2005, in German).
[12] Gilbert R. I., 'Tension stiffening in lightly reinforced concrete slabs', *ASCE Journal of Structural Engineering* **133** (6) (2008) 899-903.
[13] Gribniak, V., Tamulenas, V., Ng, P.-L., Arnautov, A., Gudonis, E. and Misiunaite, I., 'Mechanical behavior of steel fiber-reinforced concrete beams bonded with external carbon fiber sheets', *Materials* **10** (6) (2017) Paper ID: 666, 1-18.

International Conference on Sustainable Materials, Systems and Structures (SMSS 2019)
Novel Methods for Characterization of Materials and Structures
20-22 March 2019 – Rovinj, Croatia

EXPERIMENTAL LOCATION OF MATERIAL INCLUSIONS IN BUILDING PARTITION MODELS THROUGH ACTIVE THERMOGRAPHY AND INVERSE CONTRAST

P. Noszczyk (1), H. Nowak (1)

(1) Faculty of Civil Engineering, Wroclaw University of Science and Technology, Poland

Abstract

Active thermography is widely used in many branches of industry, also in construction, to examine the material structure of elements. This paper describes experiments carried out on building partition (gypsum board) models containing material (steel, styrofoam and granite) inclusions with considerably different thermal parameters. A long continuous heat pulse was used for thermal excitation and subsequently thermograms were periodically recorded simultaneously in the reflection mode and the transmission mode. A phenomenon, referred to as inverse contrast, was discovered during the experiment. An area first visible as cooler in the thermogram, after some time begins to be seen as a warmer area (and vice versa). The inverse contrast phenomenon was discovered owing to the long (30 minutes) heating of the investigated element and to the extended time (amounting to at least a few hours) of recording thermograms.

Key words: materials testing, thermography, active thermography, detection of inclusions, inverse contrast

1. INTRODUCTION

In recent years great advances have been made in thermographic methods of materials testing. This is owing to, among other things, the increased accuracy (higher infrared detector resolution and higher thermal sensitivity) of thermal imaging cameras and their greater availability (lower prices and a wider choice). Thermography is used in practically every branch of science and economy. Also in materials testing it has found numerous applications. A special kind of thermography is active thermography. It consists in the thermal excitation of the tested element and the periodic recording of the thermograms as the thermal response to the applied controlled excitation. Thanks to this method one can investigate all kinds of discontinuities in the material structure, which are visible in the thermograms as disturbances in temperature field distribution. There are several types of active thermography (differing in

the excitation and in the method of analysing the thermograms) [1-4]. In the literature on the subject one can find many applications of this method. In materials testing it is used to, e.g., determine the depth at which material inclusions occur in the tested elements [5], examine the material structure of historic buildings [6, 7, 8], locate the reinforcement in reinforced concrete members [9, 10] and test the strengthening of structural members with reinforcing strips [11]. Active thermography is used to test materials in practically every field of science, the food industry, the aerospace industry, the materials industry and in medical diagnostics.

A survey of current thermographic investigations of reinforced concrete members conducted by researchers all over the world can be found in paper [12] by Milovanović and Pečur. The Russian scientist V. P. Vavilov summed up and described the limitations of the thermographic method in nondestructive testing, due to (noise) interference [13]. In another paper [14] Vavilov and Burleigh carried out a review of the world achievements in active thermography testing, described the created commercial measuring systems and presented the advantages and disadvantages of the particular testing methods. Other review papers summing up active thermography research and indicating the latest trends in this testing method are, e.g., [15] by Vavilov, [16] (dealing with vibrothermography) by Umar et al. and [17, 18] by Ibarra-Castanedo et al.

The first attempts at standardizing materials active thermography testing have already been made. The BAM (Federal Institute for Materials Research and Testing – Bundesanstalt für Materialforschung und - Prüfung) research group proposed to use a reference steel sample for tests with flash lamp excitation, Maierhofer at al. [19] and developed a methodology for such testing, Maierhofer et al. [20].

In the research on thermography a tendency to conduct experiments in which thermograms are recorded only in the initial phase of element cooling was noticed. In the literature on the subject one can find no experiments in which the time over which thermograms are recorded is extended until a thermal equilibrium between the tested element and the environment is reached. This paper presents a description of such an experiment. When analysing the obtained thermograms an interesting phenomenon, which probably had not been noticed and described in scientific publications before, was discovered. This phenomenon was called "inverse contrast" and it is described further in this paper.

2. DESCRIPTION OF EXPERIMENT

2.1 Test stand

The main component of the test stand was a building partition model. The partition was made of a homogenous material (4 gypsum boards in turn 22, 10, 10 and 22 mm thick, together forming a 64 mm thick partition) with 3 holes cut out in it. Material (styrofoam, granite and steel) inclusions, differing considerably in their thermal properties, were put into the holes. The 2 cm thick 20×10 cm inclusions were inside the partition model, under the surface (on both sides) of the 22 mm thick homogenous material. Figure 1 shows the partition model structure and the arrangement of the material inclusions inside it.

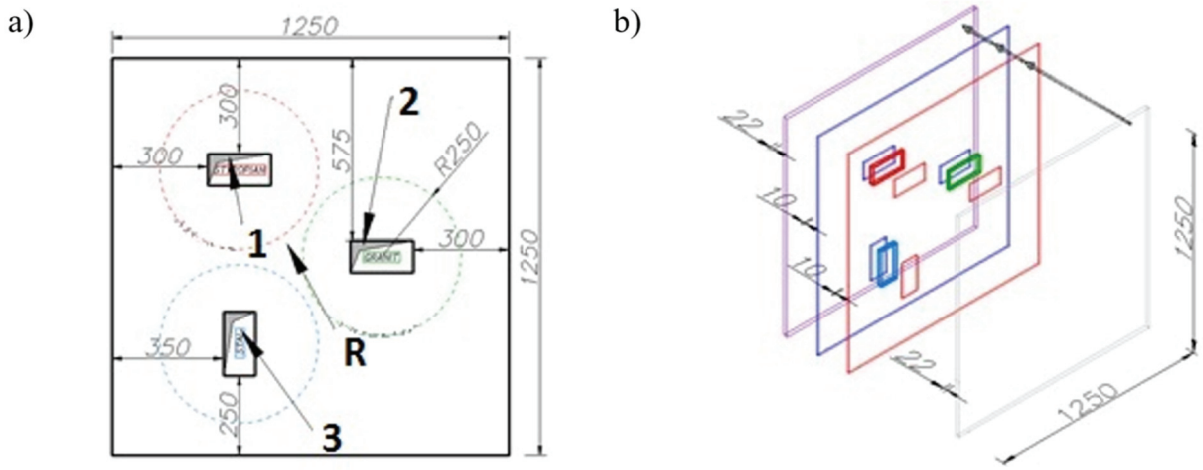

Figure 1: Structure of tested partition model: a) arrangement of material inclusions, b) view of partition inside; 1-styrofoam inclusion, 2-granite inclusion, 3-steel inclusion, R-homogenous cross section without inclusion

Besides the tested model, the test stand included 2 thermal imaging cameras (located on both sides of the model), a heat source and an air temperature and humidity sensor. A FLIR P65 camera with a resolution of 320×240px and an OPTRIS PI400 camera with a resolution of 382×288px (both cameras with a thermal resolution of 80 mK) were used in the experiment. The source of thermal excitation was a FOBO infrared radiator with a power of 6×1.2kW.

A schematic of the test stand is shown in Figure 2.

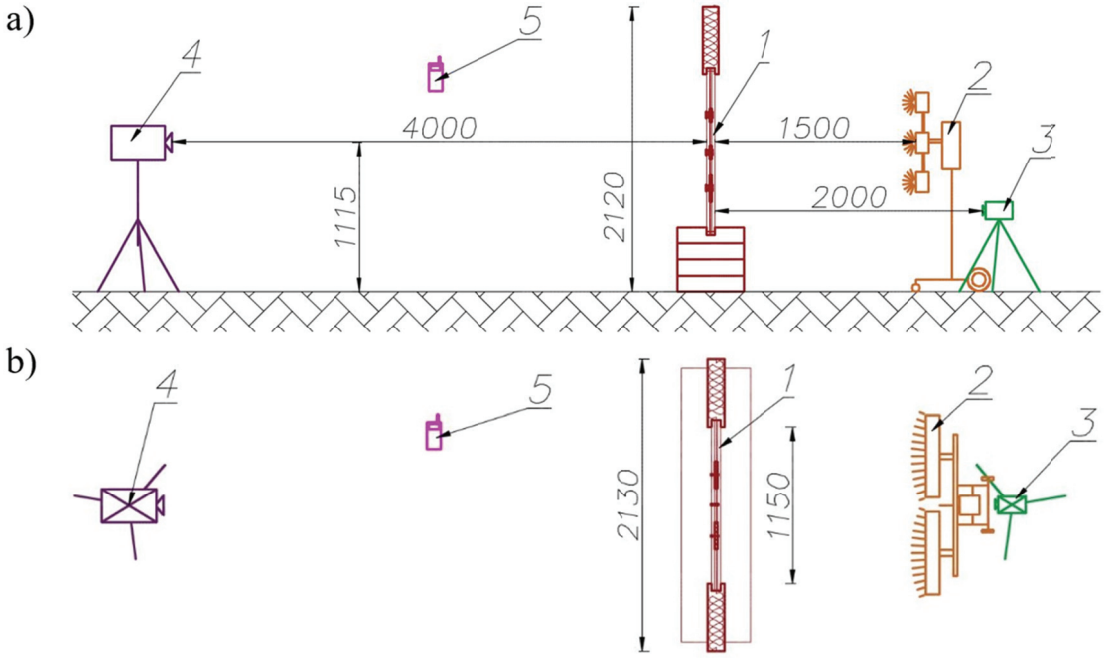

Figure 2: Schematic of test stand: a) side view, b) top view: 1- tested partition model; 2- infrared radiator; 3- thermal imaging camera OPTRIS PI400; 4- thermal imaging camera FLIR P65; 5- air temperature and relative humidity sensor.

The thermal parameters of the tested materials were found to have the strongest influence on the test results. The homogenous material and the material inclusions were matched to make it possible to compare the effect of the differences in the thermal parameters on the recorded temperature field distribution. The thermal parameters of the materials are presented in Table 1.

Table 1: Thermal parameters of tested materials

1	2	3	4	5	6
Kind of material	Bulk density	Specific heat	Heat capacity	Thermal conductivity	Thermal diffusivity
[-]	ρ_{bulk} [kg/m^3]	c_w [J/(kg·K)	C_{bulk} [J/(m^3·K)]	λ [W/(m·K)]	a [m^2/h]
Material inclusions					
Styrofoam	30	1460	$0.04 \cdot 10^6$	0.033	$0.75 \cdot 10^{-6}$
Granite	2600	920	$2.39 \cdot 10^6$	2.80	$1.17 \cdot 10^{-6}$
Steel	7900	500	$3.95 \cdot 10^6$	17.0	$4.30 \cdot 10^{-6}$
Homogenous material					
Gypsum board	1000	1000	$1.0 \cdot 10^6$	0.23	$0.23 \cdot 10^{-6}$

2.2 Research methodology

The experiment can be divided into two main parts. In the first part the temperature field distribution was measured simultaneously on both sides of the tested element, i.e. on the heated side, where the heat source was located (the reflection mode), and on the opposite (unheated) side (the transmission mode). The tested element was heated using the infrared radiator from a distance of 1.5 m for about 30 minutes. After the 30 minute long uninterrupted heat pulse the lamp was switched off and thermograms were recorded at every 20 s for up to 8 h.

In the second part of the experiment the obtained periodic thermograms were analysed. Temperature values were measured in four points in the characteristic places on the partition surface, i.e. in the centre of each of the three material inclusions and in the cross section containing only the homogenous material. The measuring point size was 3×3px. Using the obtained temperature values the absolute contrast was calculated from formula 1.

$$C_a(t) = T_p(t) - T_{pj}(t) \quad [^oC] \tag{1}$$

where: $T_p(t)$ – the temperature in the surface point in the cross section containing a material inclusion [^{o}C],
$T_{pj}(t)$ – the temperature in the surface point over the defect-free homogenous area [^{o}C].

3. SELECTED TEST RESULTS

3.1 Thermograms

Selected test results are presented as thermograms in Figure 3. The temperature field distributions in the reflection mode are in the first row, while the ones in the transmission mode are in the second row. The time which elapsed since the beginning of the element cooling down phase is given over the thermograms.

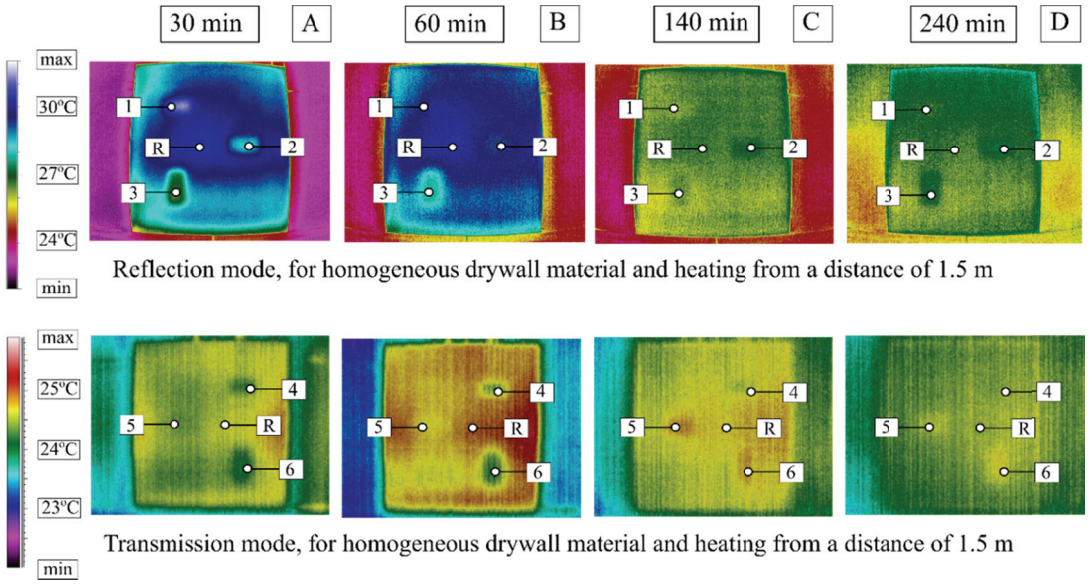

Figure 3: Thermal imaging photos taken at selected instants during respectively reflection and transmission mode measurement. Column letters A-D and measuring point numbers 1-6 correspond to those in Figures 4 and 5.

3.2 Absolute contrast

Absolute contrast in the characteristic points (points 1-6 in Figure 3) of the thermograms was calculated from formula 1. Figure 4 shows the measurement results for respectively the reflection mode and the transmission mode. The semitransparent line (on graph as 1-6) was determined directly on the basis of the average temperature value measured for the 3×3 pixels area – each points. The measuring points (1-6) were in the centre of the material inclusions, while point "R" was in the centre of the homogenous (without any inclusion) cross section of the tested element. The two thick broken lines and the one solid line mark the trend lines approximating the change of temperature over time.

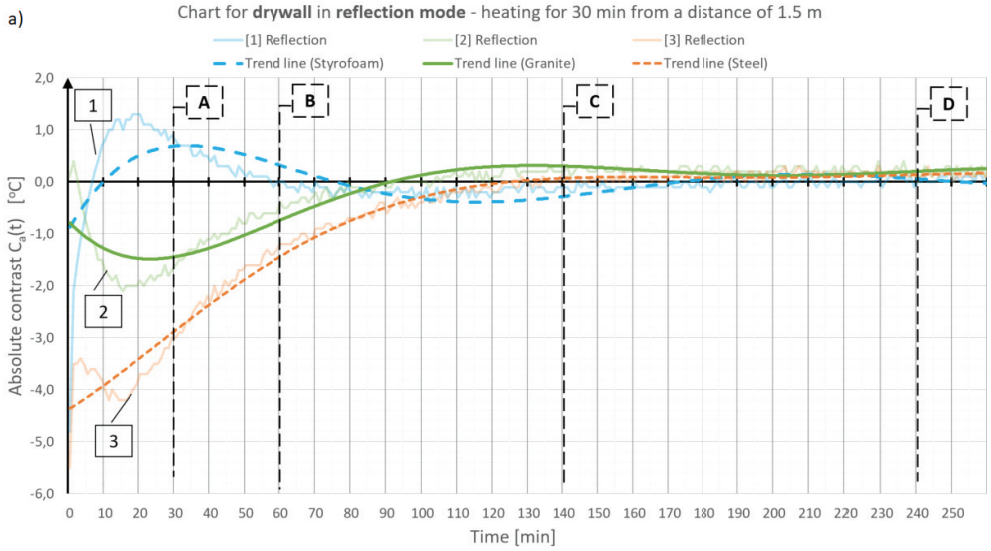

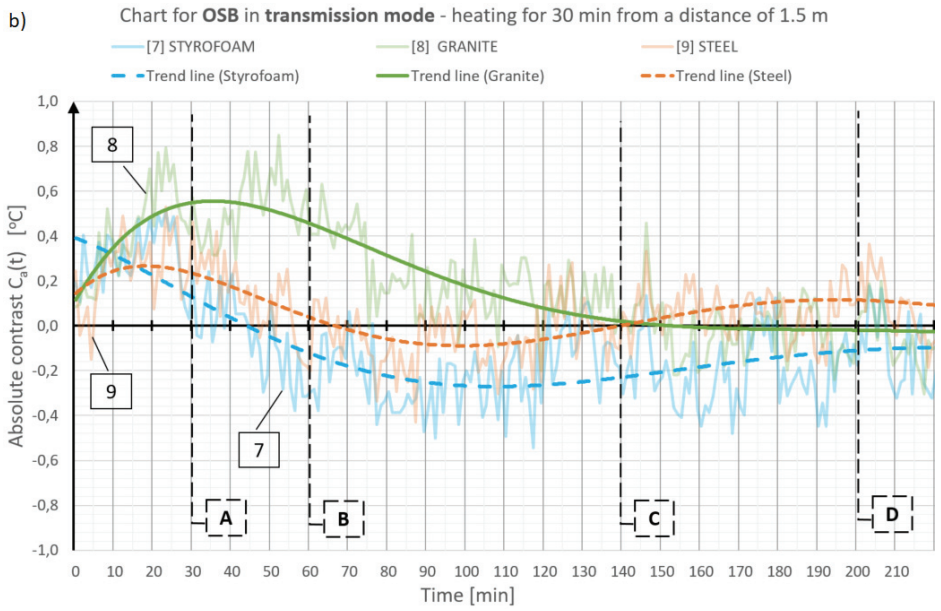

Figure 4: Graphs of absolute contrast in characteristic cross sections with three different inclusions for respectively a) reflection mode and b) transmission mode.

4. DISCUSSION

As part of the experiment the distribution of the temperature field over time during the cooling down of the previously excited surface was analysed. Through the measurement it was possible to locate material inclusions "hidden" under a 22 mm thick layer of gypsum board. All the inclusions began to appear after about 10 minutes since the switching off the heat source. The highest temperature contrast occurred in the interval of 10-60 minutes. On the heated side the maximum differences in surface temperature between the homogenous cross section and the cross section with an inclusion would reach +1.5 °C for styrofoam, -2.0 °C for granite and over -4.0 °C for steel. On the unheated side the respective values amounted to -1.0 °C, -0.6 °C and -1.2 °C. On the unheated side the inclusions would begin to become visible after about 20 minutes. The "+" sign at a temperature value means that the inclusion was visible in the thermogram as an area warmer than the homogenous cross section, whereas the "-" sign means that the inclusion was visible as a cooler area. In both the reflection mode and the transmission mode the inclusions were best visible in the thermograms after 10-60 minutes, but in the transmission mode a time shift (due to the flow of heat through the cross sections characterized by different thermal diffusivity (Tab. 1)) was visible. The best visible inclusion was the steel one – its location and shape could be easily seen from both sides of the partition. In Figures 3-4 one can see that the absolute contrast intersects the time axis and its sign changes. This point was called "inverse contrast instant". After this instant, the inclusion which previously was visible as a cooler area in the thermogram begins to be seen as a warmer area (and vice versa). The absolute contrast after the "inverse contrast instant" passes was called "inverse contrast". In order to see inverse contrast one should heat the tested surface appropriately long (supply a large amount of thermal energy) and then record thermograms for at least a few hours. The absolute contrast and the corresponding inverse contrast (for granite defect) are marked in Figure 5. One can notice that on both the heated side and the unheated side the inverse contrast does not exceed 0.5 °C.

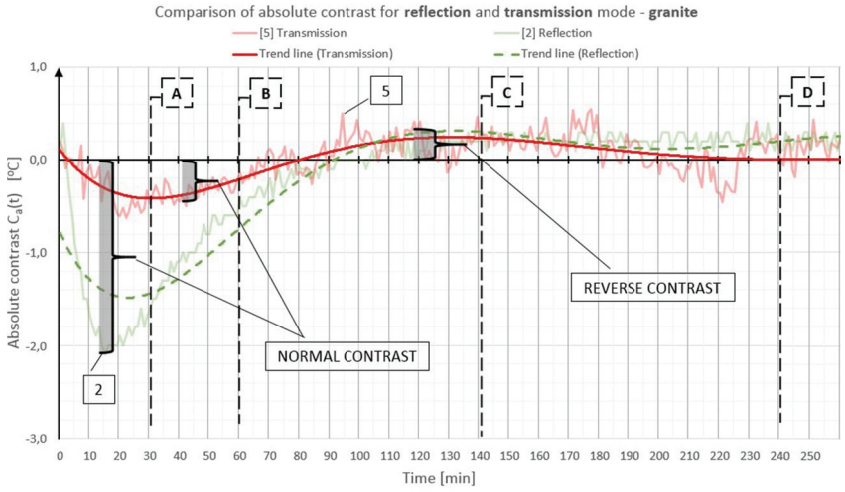

Figure 5: Comparison of absolute (normal and inverse) contrast in reflection mode and in transmission mode for granite inclusion.

5. CONCLUSION

In the literature on the subject the occurrence of inverse contrast during materials testing by means of active thermography has not been described before. This phenomenon has not been noticed before probably because the thermographic measurement was not sufficiently long. The present research has shown that inverse contrast occurs in the measurement conducted in both the reflection mode and the transmission mode. The values of this contrast change from positive values to negative ones and vice versa. The discovered phenomenon can be exploited to increase the effectiveness of locating material inclusions in materials testing. The authors hope that the findings of their further research will find application in the detection of material inhomogeneities in massive building partitions. Thanks to the nondestructive character of such testing, active thermography has a chance to become a new tool for diagnosing building structures [22]. The authors' further research will focus on the effect of heating duration and the distance of the heat source from the surface on absolute contrast and inverse contrast values in building partition models, and on the application of the obtained results to solve inverse heat conduction problems.

ACKNOWLEDGEMENTS

The authors thank Prof. Jacek Kasperski – the head of the Department of Construction and Flow Machines – for lending the thermographic camera used in the experiment.

REFERENCES

[1] Maldague X. and Marinetti S., "Pulse phase infrared thermography", J. Appl. Phys., vol. 79, no. 5, pp. 2694-2698, 1996.
[2] Wu D., Karpen W. and Busse G., "Lock-in thermography for multiplex photothermal nondestructive evaluation", presented at QIRT 1992, Paris, 1992.
[3] Keo S. A., Brachelet F., Breaban F., and Defer D., "Steel detection in reinforced concrete wall by microwave infrared thermography", NDT E Int., vol. 62, pp. 172-177, March 2014.
[4] Maldague X., Ziadi A. and Klein M., "Double pulse infrared thermography", NDT E Int., vol. 37, no. 7, pp. 559-564, October 2004.

[5] Dudzik S., "Analysis of the accuracy of a neural algorithm for defect depth estimation using PCA processing from active thermography data", *Infrared Phys. Technol.*, vol. 56, pp. 1-7, January 2013.
[6] Arndt R. W., "Square pulse thermography in frequency domain as adaptation of pulsed phase thermography for qualitative and quantitative applications in cultural heritage and civil engineering", *Infrared Phys. Technol.*, vol. 53, no. 4, pp. 246-253, July 2010.
[7] Ibarra-Castanedo C., Sfarra S., Klein M. and Maldague X., "Solar loading thermography: Time-lapsed thermographic survey and advanced thermographic signal processing for the inspection of civil engineering and cultural heritage structures", Infrared Phys. Technol., vol. 82, pp. 56-74, May 2017.
[8] Nowak H., Noszczyk P., "Applying active thermography in the non-destructive investigation of historical objects", Civil and Environmental Engineering Reports, vol. 17, no. 2, pp 105-115, 2015.
[9] Maierhofer C., Brink A., Röllig M. and Wiggenhauser H., "Detection of shallow voids in concrete structures with impulse thermography and radar", *NDT E Int.*, vol. 36, no. 4, pp. 257-263, June 2003.
[10] Noszczyk P., Nowak H., "Active thermography as a modern method of testing reinforced concrete members" (in Polish), Journal of Civil Engineering, Environment and Architecture, vol. 33, iss. 63, no. 3, pp. 279-286, 2016.
[11] Liu B., Zhang H., Fernandes H. and Maldague X., "Experimental evaluation of pulsed thermography, lock-in thermography and vibrothermography on foreign object defect (FOD) in CFRP", *Quantitative evaluation of pulsed thermography, lock-in thermography and vibrothermography on foreign object defect (FOD) in CFRP*, May 2016.
[12] Milovanović B. and Banjad Pečur I., "Review of Active IR Thermography for Detection and Characterization of Defects in Reinforced Concrete", *J. Imaging*, vol. 2, no. 2, p. 11, April 2016.
[13] Vavilov V., "Noise-limited thermal/infrared nondestructive testing", *NDT E Int.*, vol. 61, pp. 16-23, January 2014.
[14] Vavilov V. and Burleigh D. D., "Review of pulsed thermal NDT: Physical principles, theory and data processing", *NDT E Int.*, vol. 73, pp. 28-52, July 2015.
[15] Vavilov V., "Thermal NDT: historical milestones, state-of-the-art and trends", *Quant. InfraRed Thermogr. J.*, vol. 11, no. 1, pp. 66-83, January 2014.
[16] Umar M. Z., Vavilov V., Abdullah H. and Ariffin A. K., "Ultrasonic infrared thermography in non-destructive testing: A review", *Russ. J. Nondestruct. Test.*, vol. 52, no. 4, pp. 212-219, April 2016.
[17] Ibarra-Castanedo C. et al., "Comparative Study of Active Thermography Techniques for the Nondestructive Evaluation of Honeycomb Structures", Res. Nondestruct. Eval., vol. 20, no. 1, pp. 1-31, January 2009.
[18] Ibarra-Castanedo C. and Maldague X., "Pulsed phase thermography reviewed", Quant. InfraRed Thermogr. J., vol. 1, no. 1, pp. 47-70, June 2004.
[19] Maierhofer C., Reischel M., Steinfurth H., Röllig M., Myrach P. and Ziegler M., "Development of reference test specimens for the standardisation of active thermography with flash excitation", presented at QIRT 2012, Naples, 2012.
[20] Maierhofer C., Myrach P., Steinfurth H., Reischel M. and Röllig M., "Development of standards for flash thermography and lock-in thermography", presented at QIRT 2014, Bordeaux, 2014.
[21] Weritz F., Arndt R., Röllig M., Maierhofer C. and Wiggenhauser H., "Investigation of concrete structures with pulse phase thermography", Materials and Structures 38, pp. 843-849, 2005.
[22] Foudazi A., Mehdipour I., Donnell K., Khayat K., "Evaluation of steel fiber distribution in cement-based mortars using active microwave thermography", Materials and Structures 49, pp. 5051-5065, 2016.

International Conference on Sustainable Materials, Systems and Structures (SMSS 2019)
Novel Methods for Characterization of Materials and Structures
20-22 March 2019 – Rovinj, Croatia

THE INTERPRETATION OF EXAFS DATA WITH CHEMICAL REACTIVITY IN ACTIVATED SLAG

Yeonung Jeong (1), Sung-Hoon Kang (2) and Juhyuk Moon (1)

(1) Department of Civil and Environmental Engineering, Seoul National University, Republic of Korea

(2) Department of Architectural Engneering, Seoul National University, Republic of Korea

Abstract

This study investigated mechanical properties and local Ca structure of various alkali-activated slag (AAS) activated by MgO, $Mg(OH)_2$, CaO, $Ca(OH)_2$, $Ba(OH)_2$, and $Ba(OH)_2 \cdot 8H_2O$. The heavier main element in activators produced higher compressive strength and low chemically bound water in the same element type of activators contributed to better strength development. An average pore diameter measured by mercury intrusion porosimetry would be a better indicator to predict AAS pastes rather than total pore volume. While Mg-based activator did not change local Ca structure of raw slag, Ca- and Ba-based activator increased radial distance of Ca-O path. In addition, as atomic number of main elements in activators increased, Ca-O distance of AAS pastes increased, while coordination number of core Ca atoms decreased.

Keywords: alkali-activation, slag cement, local Ca structure, X-ray absorption spectroscopy, EXAFS

1. INTRODUCTION

Alkali-activated slag (AAS) has been considered as a potential alternative to ordinary Portland cement (OPC) because the use of AAS can significantly reduce carbon dioxide emissions, comparing production of OPC, and AAS possesses good mechanical properties if proper types and amounts of activators are used. The AAS produces not only amorphous calcium aluminosilicate hydrate (C-A-S-H) gels as a main reaction product but small amount of crystalline phases such as hydrotalcite-like phases, zeolite and AFm phases depending on compositions of raw slag [1, 2].

The atomic structure of C-A-S-H gels in AAS has been studied, mainly using ^{29}Si and ^{27}Al nuclear magnetic resonance (NMR) spectroscopy [3, 4]. Thus, its silicon and aluminium structures are relatively well investigated as a model of poorly crystallized tobermorite with substitution of bridging tetrahedral silicon by tetrahedral aluminium [5]. However, local

calcium structure of the C-A-S-H gels is not well informed due to some limitations of experimental facilities.

This study explored mechanical properties and local calcium structure of AAS with various activators such as MgO, $Mg(OH)_2$, CaO, $Ca(OH)_2$, $Ba(OH)_2$, and $Ba(OH)_2{\cdot}8H_2O$. Compressive strength tests, porosimetry and synchrotron-based X-ray absorption spectroscopy (XAS) were applied.

2. MATERIALS AND EXPERIMENTAL DETAILS

Commercial ground granulated blast-furnace slag and reagent grade chemicals for activators (i.e. MgO, $Mg(OH)_2$, CaO, $Ca(OH)_2$, $Ba(OH)_2$, and $Ba(OH)_2{\cdot}8H_2O$) were obtained. Chemical oxide composition of raw slag is shown in Table 1 and the raw slag did not contain any crystalline phase.

Table 1: Oxide composition of raw slag.

Formula	CaO	SiO_2	Al_2O_3	MgO	SO_3	TiO_2	Fe_2O_3	K_2O	MnO	SrO
Weight(%)	43.4	35.2	14.1	3.2	2.1	0.7	0.5	0.5	0.2	0.1

AAS cement was prepared by mixing raw slag and powder forms of activators, including MgO, $Mg(OH)_2$, CaO, $Ca(OH)_2$, $Ba(OH)_2$, and $Ba(OH)_2{\cdot}8H_2O$. The amounts of water and activators were set as 40 wt.% and 10 wt. % of raw slag, respectively, and were adjusted for preparing a comparison sample which has identical molar ratio. The detailed mix proportion is shown in Table 2.

Table 2: Mixture proportions of AAS cement in mass

Sample	Prepared AAS							water
	Slag	MgO	$Mg(OH)_2$	CaO	$Ca(OH)_2$	$Ba(OH)_2$	$Ba(OH)_2{\cdot}8H_2O$	
MgO 10%	100	10	0	0	0	0	0	40
MgO 6.9%	100	6.9	0	0	0	0	0	43.1
$Mg(OH)_2$ 10%	100	0	10	0	0	0	0	40
CaO 10%	100	0	0	10	0	0	0	40
CaO 7.6%	100	0	0	7.6	0	0	0	42.4
$Ca(OH)_2$ 10%	100	0	0	0	10	0	0	40
$Ba(OH)_2$ 10%	100	0	0	0	0	10	0	40
$Ba(OH)_2$ 5.4%	100	0	0	0	0	5.4	0	44.6
$Ba(OH)_2{\cdot}8H_2O$ 10%	100	0	0	0	0	0	10	40

The pastes were cured in fog room with 23 ± 2°C for 28 days. Compressive strength of prepared AAS pastes was evaluated at 28 days and fractured pieces were collected to prepared powder forms of XAS samples and MIP experiments. The hydration of all samples was stopped, using isopropyl alcohol and diethyl ether at 28 days of curing.

3. EXPERIMENTAL RESULTS

3.1 Compressive strength

Figure 1 presents the results of compressive strength tests, which implies that the heavier elements in activators used, the better compressive strength was achieved i.e., Ba > Ca > Mg. In addition, as the activators with low chemically bound water used, mechanical properties of AAS was improved, but those effects became weak as atomic number of the main elements in activators increased.

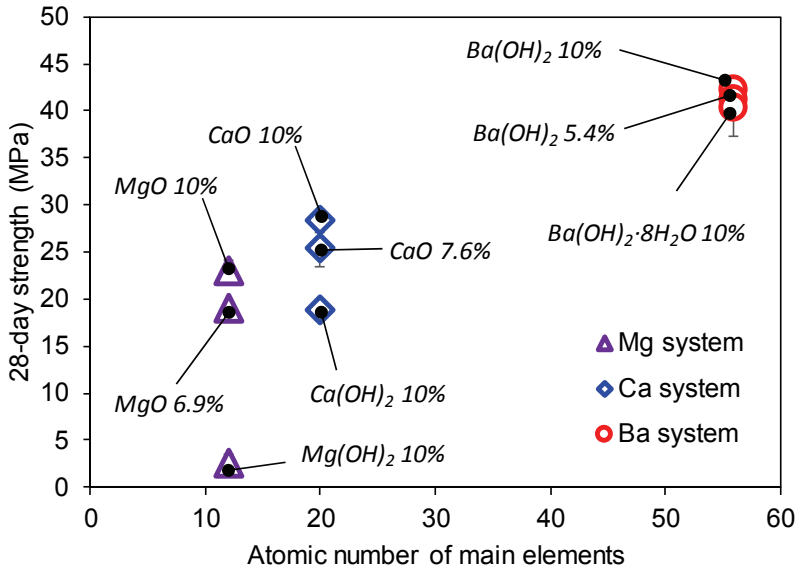

Figure 1: Compressive strength of AAS pastes at 28 days

3.2 Mercury intrusion porosimetry

Although total pore volume of cementitious materials has an inverse relationship with those mechanical properties [6], Figure 2 clearly presents that average pore diameter can be a better indicator to predict mechanical properties of AAS pastes. In the case where the degree of slag dissolution in AAS system had a significant difference between the samples, average pore diameter would have the inverse relationship with compressive strength than total pore volume because residual slag particles were denser than binding products [7].

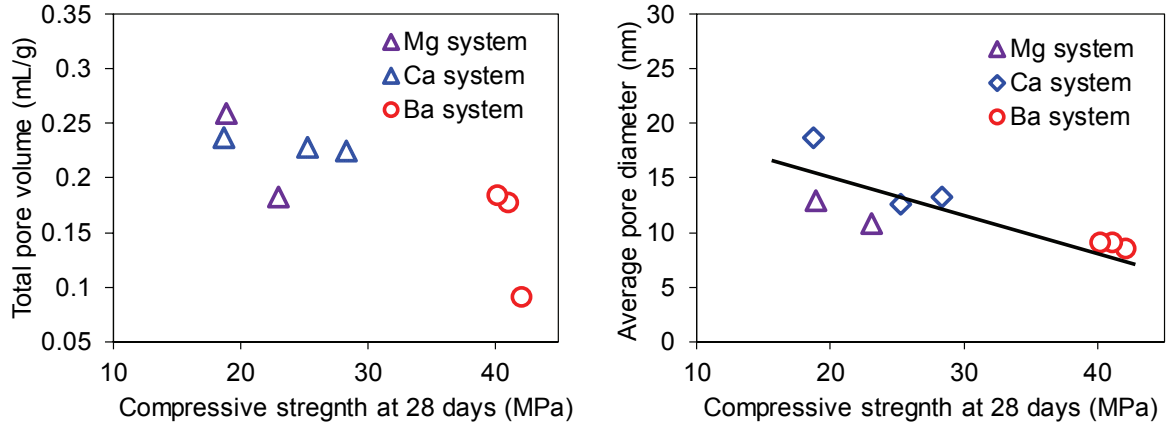

(a) (b)

Figure 2: Relationship between pore structure and compressive strength of AAS cements: (a) pore volume versus strength, and (b) average pore diameter versus strength.

3.3 X-ray absorption spectroscopy

The XAS experiments were conducted using an X-ray absorption fine structure for catalysis (XAFCA) beamline [8] at Singapore Synchrotron Light Source (SSLS), Singapore. Background of measured data was removed and Fourier transformation (FT) was carried out, by using Athena software [9] to obtain radial distance function (RDF) of each sample. Quick first shell (QFS) fitting of FT-extended X-ray absorption fine structure (EXAFS) spectra was conducted, using Artemis software [9] to calculate actual bond length of Ca-O path and coordination number of the core Ca atom. Figure 3 presents FT-EXAFS spectra of each pastes, implying that Ca-O bond length of Mg system is not changed from that of raw slag, but that of Ca and Ba system is lengthened. This result suggests that as activators with heavy main elements used, Ca-O bond length increased.

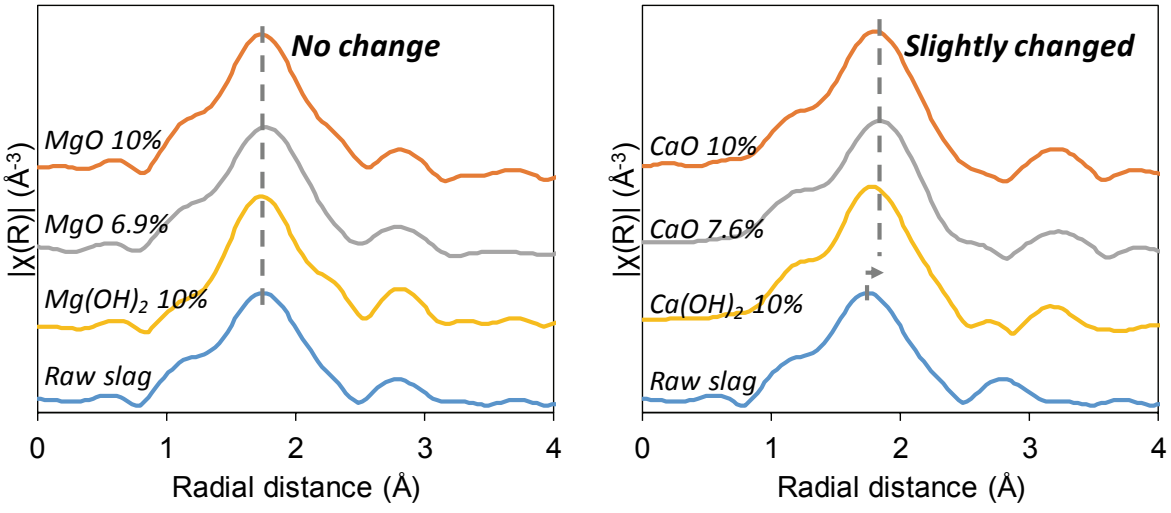

(a) (b)

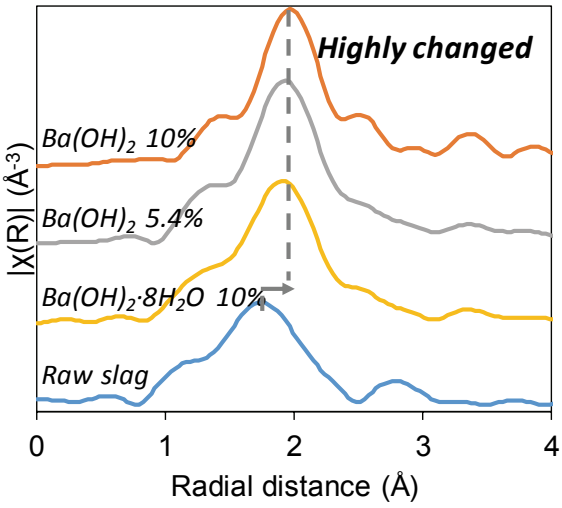

(c)

Figure 3: Radial distance function (RDF) of (a) Mg-based AAS, (b) Ca-based AAS, and (c) Ba-based AAS.

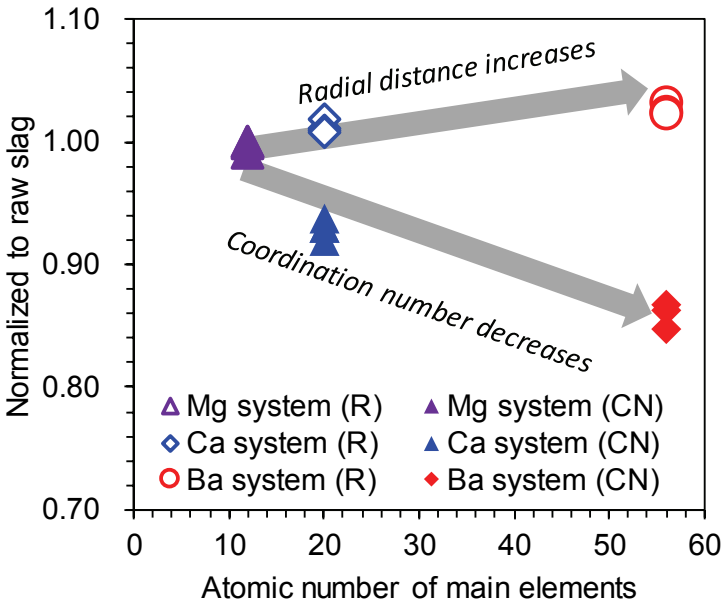

Figure 4: Normalized radial distance and coordination number of each pastes; R indicates normalized radial distances, and CN indicates normalized coordination numbers.

Calculated radial distances of Ca-O path and coordination number of core Ca atom were normalized to those of raw slag. As presented in Figure 4, radial distances increase, but coordination numbers decreased as atomic number of main elements in activators increase. This results can be due to differences in degree of slag dissolution.

4. CONCLUSIONS

- Compressive strength of AAS cements increased as main element of activators became heavier and low chemically bound water content in the same element type of activators contributed to strength development.
- Average pore diameter of AAS pastes would be a better indicator to predict mechanical properties of the pastes rather than total pore volumes measured by MIP, likely due to significant difference of residual slag particle amount.
- Mg-based activators did not change local Ca structure, but Ca- and Ba-based activators increased radial distance of Ca-O bond length.
- As main elements in activator increased, radial distance of Ca-O path increased and coordination numbers of core Ca atoms decreased.

ACKNOWLEDGEMENTS

This study was supported by the Basic Science Research Program through the National Research Foundation of Korea (NRF) funded by the Ministry of Education, Republic of Korea (NRF-2018R1C1B6003058).

REFERENCES

[1] Ben Haha, M., Lothenbach, B., Le Saout, G., Winnefeld, F., 'Influence of slag chemistry on the hydration of alkali-activated blast-furnace slag – Part I: Effect of MgO', *Cem. Concr. Res.* **41** (9) (2011) 955-963.
[2] Myers, R. J., Bernal, S. A., Provis, J. L., "Phase diagrams for alkali-activated slag binders', *Cem. Concr. Res.* **95** (2017) 30-38.
[3] Bernal, S. A., Provis, J. L., Rose, V., Mejia de Gutierrez, R., 'Evolution of binder structure in sodium silicate-activated slag-metakaolin blends', *Cem. Concr. Compos.* **33** (1) (2011) 46-54.
[4] Wang, S.-D. and Scrivener, K. L., '^{29}Si and ^{27}Al NMR study of alkali-activated slag', *Cem. Concr. Res.* **33** (5) (2003) 769-74.
[5] Richardson, I. G., Brough, A. R., Groves, G. W., Dobson, C. M., 'The characterization of hardened alkali-activated blast-furnace slag pastes and the nature of the calcium silicate hydrate (C-S-H) phase' *Cem. Concr. Res.* **24** (5) (1994) 813-829.
[6] Mehta, P. K. and Monteiro, P. J., 'Concrete: Microstructure, Properties, and Materials', 3rd Edn (McGraw-Hill, New York, 2006).
[7] Jeong, Y., Park, H., Jun, Y., Jeong, J. H., Oh, J. E., 'Influence of slag characteristics on strength development and reaction products in a CaO-activated slag system' *Cem Concr Compos.* **72** (2016) 155-167.
[8] Du, Y., Zhu, Y., Xi, S., Yang, P., Moser, H. O., Breese, M. B. H., 'XAFCA: A new XAFS beamline for catalysis research' *J. Synchrotron Radiat.* **22** (3) (2015) 839-843.
[9] Ravel, B. and Newville, M. 'ATHENA, ARTEMIS, HEPHAESTUS: Data analysis for X-ray absorption spectroscopy using IFEFFIT' *J. Synchrotron Radiat.* **12** (4) (2005) 537-541.

International Conference on Sustainable Materials, Systems and Structures (SMSS 2019)
Novel Methods for Characterization of Materials and Structures
20-22 March 2019 – Rovinj, Croatia

INFLUENCE OF THE MIXTURE COMPOSITION OF CEMENTITIOUS MATRICES ON ULTRASOUND INVESTIGATIONS AT EARLY AGE

Markus Krüger (1), Rok Bregar (1), Gheorghe Alexandru David (1), Joachim Juhart (1)

(1) Institute of Technology and Testing of Building Materials, Graz University of Technology, Graz, Austria

Abstract

Ultrasonic methods have been developed in the past to study properties of cement-based materials in the fresh and hardening state. Especially by combined shear and compressional wave measurements, several possibilities exist for better describing the changing properties of cementitious materials at very early age, e.g. by calculating dynamic elastic properties from ultrasound wave velocities. Within the paper, test results from ultrasound investigations on different cementitious paste, mortar and concrete are presented and discussed. A special focus is on the quantification of the effects of material composition on the wave propagation. This is for example the air content and the matrix composition, the viscous fluid/solid ratio and the heat of hydration. Some analytical models are presented that will correlate the results from ultrasound measurements with the composition of the cementitious matrixes, which either helps to better understand the early age hydration or helps to better interpret the test results from ultrasound investigations.

Keywords: US testing, maturity, elastic properties, early age hydration

1. INTRODUCTION

The properties of cement-based materials in the fresh and hardening state are currently measured with rather conventional methods. Ultrasonic methods have been developed in the past using through-transmission techniques and analysing the whole waveform. Today ultrasound is accepted as a very useful tool to continuously investigate the setting and hardening process of cementitious materials [1-4]. With respect to new concrete mixture concepts that especially focus on the optimization of the matrix composition by using a well-defined amount of fillers and supplementary cementitious materials, many traditional concrete mix design methods to predict workability, setting and hardening as well as strength development fail. This is especially true for mixes, at which ordinary Portland cement (OPC) or clinker is partly substituted by combined mineral fillers, which enhance packing density and reduce the water demand of the mix for certain workability [5].

In the current study, properly selected limestone powders of different size are used, which we call eco-filler (EF) when they have a similar particle size compared to the used OPC and micro-filler (MF) when their mean particle diameter d_{50} is significantly lower than that of OPC (d_{50} < 3 µm). The combined fillers ensure that the water demand is reduced while keeping the workability and strength development almost constant compared to matrices with pure OPC. This is mainly achieved by packing optimization, which corresponds to a physical filler effect of MFs placed into voids instead of interstitial water. Additionally a significant amount of EF, which have a high sensitivity to water addition, can lower the water demand for certain flowability of a mix (see Tab. 1). Such optimized matrices provide lower environmental impact at equivalent functional properties (workability, strength) compared to pure OPC matrices [5].

However, it is also the setting and hardening behaviour as well as the strength development, which is strongly influenced. In the following study, two types of cementitious mixes are investigated, one with pure OPC and the other with a combination of OPC and EF and MF in an optimized ratio. The latter mixes, if properly optimized, typically have the same or an even higher w/c-ratio as pure OPC-mixes, but have a decreased w/p-ratio (water/powder-ratio, "powder" = OPC/EF/MF) at equal flowability.

2. MATERIALS AND MIX DESIGN

2.1 Materials

Powder materials referred to in this study are classified into a group of micro-filler (MF) and eco-filler (EF) according to their mean particle diameter d_{50}. The used micro-filler has a d_{50} < 3 µm that is significantly smaller than that of OPC. The eco-filler shows slightly smaller mean particle size but similar Blaine value like the cement. Details on the particle size distribution of the materials and the corresponding mixes determined by laser diffraction (HELOS) are presented in [3].

Table 1: Characteristic properties of the used materials.

type	true density ρ_0	grain size d_{50}	Blaine-value	water demand (void content) $V_{w,s}/V_p$	ϕ_{exp}	water demand for spread flow 190mm $V_{w,190}/V_p$
	[g/cm³]	[µm]	[cm²/g]	[-]	[-]	[-]
CEM I 52.5 R (OPC)	3.14	6.3	4656	0.83	0.57	1.57
$Limestone_{ECO}$ (EF)	2.72	6.9	4032	0.62	0.61	0.68
$Limestone_{MICRO}$ (MF)	2.73	2.2	9314	0.61	0.62	0.65
Sand 0.1/1	2.65	460	(n.m.)	0.65	(n.m.)	
Gravel 1/4	2.73	2700	No measurement (n.m.)			
Gravel 4/8	2.65	not relevant				
Gravel 8/16	2.67					
SP (PCE)	1.06	not relevant				

As the amount of water to achieve a certain workability of a water/powder-mix plays a major role, table 1 show also the values for water demand $V_{w,s}/V_p$, where $V_{w,s}$ is the volume of water at saturation point and $V_{w,fi}/V_p$, where $V_{w,fi}$ is the volume of water for a certain

flowability (here spread flow fi = 190 mm) and V_p,which is the volume of powder of the water-powder mixes. These values were determined by a method (MEM-ST) presented by Juhart et al. [5].

2.2 Concrete and mortar mix design

Table 2 contains the mix proportions, the recipe parameters and some selected properties of tested pastes, mortars und concretes in terms of workability, strength, Vicat initial setting, elastic dynamic modulus and dynamic shear modulus (according to ultrasound measurements performed with FreshCon device). While the *REF* mixes are based on Portland cement OPC (95% cement clinker), for the development of *ECO* mixes 50% of the OPC was replaced by limestone filler EF and micro-filler MF considering the paste optimization.

The granular *ECO* paste mix was optimized to achieve a higher packing density and thus a lower w/p-ratio than the paste of the reference mortars and concretes. The *OPC* pastes and *ECO* pastes from Table 2 were used to produce mortars and concretes of similar workability with similar volume of paste, air content and sieve line of the aggregates. The consistency of mortar and concrete was adjusted to an equivalent value (160 mm for mortar and 500 mm for concrete) by adding superplasticizer (see Table 2). Despite a significantly higher w/c-ratio of *ECO* than *REF*, flowability and strength were nearly the same.

3. TESTING AND EVALUATION METHODS

3.1 Ultrasound experimental setup for simultaneous p- and s-wave measurements

The FreshCon-system was used for the ultrasound measurements. The test setup is similar to that proposed by a RILEM recommendation worked out by RILEM TC 218-SFC **Error! Reference source not found.**. However, besides the usage of a container equipped with p-wave transducers with a center frequency of 500 kHz an additional container with two broadband s-wave transducers with a center frequency of 250 kHz was used. A sensor distance of 50 mm was found to be sufficient for both containers. A more detailed system description is given in Krueger et al. [3], [6].

To study the setting and hardening time at very early age in the following a test time of 24 hours was considered. In a post processing procedure the measurements were analysed and dynamic elastic parameters were calculated with equations (1) and (2) according to Krueger et al. [6].

3.2 Calorimetry and heat of hydration

The heat of hydration was determined with an ASTM C1679 compliant isothermal calorimeter (Calmetrix I-Cal 4000 HPC) at isothermal conditions (20°C), in which an amount of appr. 50-100 g was filled in right after mixing (≈10 – 40 min). The measuring interval was 1/min. The results are presented as specific heat per g of cement and do not consider the limestone filler as binder.

In addition to that, the temperature evolvement during hydration was determined within the US test containers as well.

3.3 Standardized functional parameters

For the pastes the spread flow (fi) was determined on a dry glass plate with a Hägermann cone (according to EN 1015-3 but without any shocks), for mortars the spread was tested accordingly with shocks. Additionally the corresponding water demand ($V_{w,fi}/V_p$) was recorded. From paste and mortar mixes prisms 40/40/160 mm were cast to test the

compressive strength (n=3 specimen) after 24 hours ($f_{cm,1d}$) and 7 days ($f_{cm,7d}$) acc. to EN 196-1. Vicat needle test according to EN 196-3 was conducted to determine initial setting time of pastes and mortars.

For concrete the flow-table spread (acc. to EN 12350-5: 2009) of the mix was determined 10 min after water addition. The compressive strength was tested on concrete cubes (150 mm, n = 3) acc. to EN 12390-3:2009 cured first 24 hours ($f_{cm,1d}$) in moulds covered with plastic sheet at a temperature 20 - 23°C and then stored under water until testing at an age of 7 days ($f_{cm,7d}$).

Table 2: Composition and selected properties of the investigated mixtures.

		P ref	**P eco**	**P eco SP**	**M ref**	**M eco**	**C ref**	**C eco**
CEM I 52.5 R (OPC)		1186	774	774	468	303	356	233
$Limestone_{ECO}$ (EF)			391	391	-	153	-	118
$Limestone_{MICRO}$ (MF)			391	391	-	153	-	118
sand 0/1	[kg/m³]	-	-	-	739	739	552	552
gravel 1/4			-	-	835	835	624	624
aggregate 4/8		-	-	-	-	-	320	320
aggregate 8/16		-	-	-	-	-	322	322
w/c		0.52	0.59	0.59	0.52	0.59	0.52	0.59
V_w/V_p	[-]	1.63	0.928	0.928	1.348*	0.747*	1.334*	0.740*
V_w/V_c		1.63	1.86	1.86	1.63	1.86	1.63	1.86
superplasticizer content	[kg/m³]	-	-	4.75	1.85	4.75	1.69	5.2
Workability**	mm	192.5	205	285	162.5	160	495	465
Vicat initial set	[h]	5.5	2.7	5.3	-	-	-	-
G_{dyn} (t_e=Vicat initial set)	[GPa]	0.12	0.08	0.06	-	-	-	-
t (G_{dyn} = 0.1 GPa)	[h]	4.73	3.00	4.93	3.1	3.5	3.25	2.75
t (G_{dyn} = 0.2 GPa)	[h]	5.28	3.5	5.5	3.5	4.0	3.71	3.17
$E_{dyn\text{-}24\ hours}$	[GPa]	11.6	15.6	16.2	25.5	30.3	31.6	33.6
$f_{cm,1d}$		31.8	36.7	33.2	36.2	35.7	31.0	35.8
$f_{cm,7d}$	[MPa]	50.2	56.2	49.0	56.6	63.8	47.0	65.0
E_{dyn} (sand+gravel)		-	-	-	48000	48000	52000	52000
air content	[%]	1.1	0.8	0.8	6.0	4.2	5.6	4.0
fresh density mix	[kg/m³]	1846	2019	2016	2273	2356	2270	2382

* powder = PC+EF+MF (fines of the sand/aggregates are considered)
** paste: spread flow without shocks, mortar: spread with shocks, concrete: flow-table spread

4. TEST RESULTS AND EVALUATION OF THE MIXES

4.1 Dynamic elastic properties obtained from US testing during early age hydration

If it is assumed that the material to be tested is homogeneous and isotropic the dyn. elastic modulus can be calculated from the shear wave velocity v_s, the compressional wave velocity v_p and the materials density ρ_c by using the following equations:

$$\sigma_{dyn} = \frac{\frac{1}{2} \cdot v_p^2 - v_s^2}{v_p^2 - v_s^2} \tag{1}$$

$$E_{dyn} = \frac{(1 + \sigma_{dyn}) \cdot (1 - 2\sigma_{dyn})}{(1 - \sigma_{dyn})} \cdot v_p^2 \cdot \rho_c = (2 + 2\sigma_{dyn}) \cdot v_s^2 \cdot \rho_c \tag{2}$$

4.2 Effect of aggregate content and SP on dynamic elastic modulus and heat release

It is expected that the evolution of dyn. elastic modulus during early hydration is dominated by the changing mechanical properties of the matrix and that the influence of the elastic properties of the aggregates remain constant. For the prediction of the elastic modulus of concrete many different models exists [7]. Most of the models are two-phase models separating the influence of matrix and particles. Hansen presented a model for estimating dynamic moduli of concrete, mortar and cement paste phases by consideration of the stiffness constant of the particular phases [9]. His work is based on Maxwell´s approach on electrical resistivity of multiphase systems. Nwokoye evaluated the approach for pulse velocity tests on cement pastes and mortars later on and has shown its principle applicability on cementitious materials [8]. The practical equation for predicting the elastic modulus of concrete resp. mortar $E_{cal,dyn}$ from the stiffness parameters of binder paste and aggregates according to Hansen can be given as

$$E_{cal,dyn} = \frac{2E_{p,dyn} + E_a - 2V_a(E_{p,dyn} - E_a)}{2E_{p,dyn} + E_a + V_a(E_{p,dyn} - E_a)} \cdot E_{p,dyn} \tag{3}$$

where V_a is the volume fraction and E_a the weighted elastic modulus of the aggregates within the mix. $E_{p,dyn}$ represents the time dependant dyn. elastic modulus of the binder (paste) mix calculated from the US testing. It is to be noted that the air content is not explicitly considered in the volume fractions of binder or aggregate. However, wave velocities and thus calculated dyn. elastic moduli are directly affected by air content, which results in some uncertainty in the results from the mathematical equations (1) and (2). Another aspect is that US pulse velocity is mainly determined by the material´s elasticity, which does not comply to the assumption of concrete being a (homogeneous) visco-elastic material.

Hence, it has also to be considered that hydration heat strongly influences the setting and hardening process, which makes it difficult to compare tests on concrete with tests on paste, as paste show higher temperature during hydration. In addition to that, the use of superplasticizer can influence the setting behaviour as well. For that reason the temperature of the mix in the US testing device and calorimetric measurements have been conducted. Fig. 1 shows the calorimetric heat of hydration of *REF* and *ECO* mixes. The earlier and higher peak of heat release and also higher total heat release after 24 hours indicates that the addition of limestone powder enhances the silicates hydration. In addition, the retarding effect of the superplastizer can be observed especially at the ECO paste mixes with and without SP.

Compared to the calorimetric measurements, the temperature measurements conducted within the US container (see Fig. 2) show a slightly different temperature evolution as expected. However, the peak temperatures of the ECO pastes (with and without SP) are significantly lower compared to the REF paste and the retarding effect of the SP is observable.

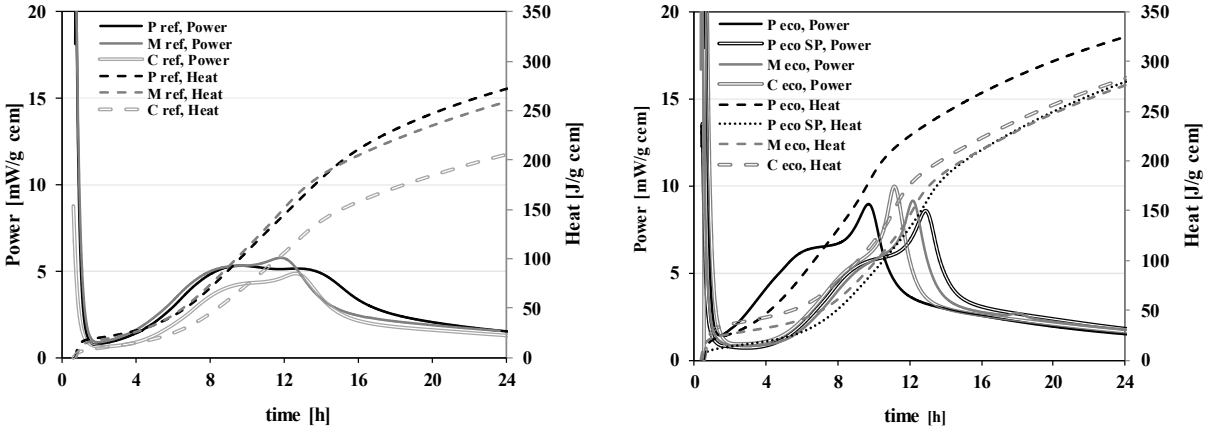

Figure 1: Heat of hydration of *REF* (left) and *ECO* mixes (right).

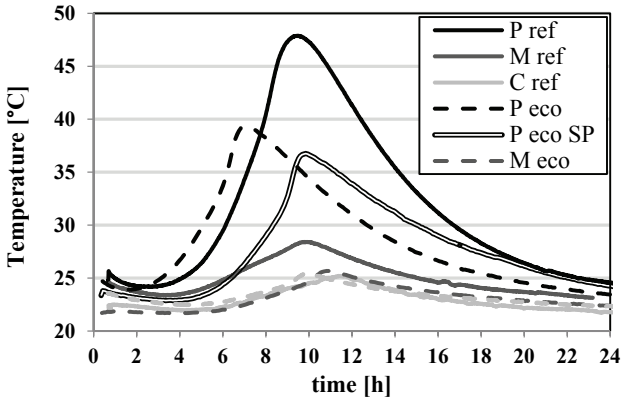

Figure 2: Temperature evolution in US-FreshCon device.

For better comparing the evolution of dyn. elastic properties from the different mixes the temperature from the US test container have been used to calculate the maturity of each mix. In principle the maturity can be estimated by the following equation [10]

$$t_e = \sum \Delta t_i \cdot k(t) \quad \text{with} \quad k(t) = [(T + 15)/35]^m \tag{4}$$

where t_e is the temperature adjusted concrete age, which replaces t in the corresponding real time, Δt_i is the time where a temperature T prevails and *k(t)* is a function that depends on the activation energy for cement hydration. The activation energy does not only depend on the type of the cement, but also on the *w/p* ratio, admixtures and additional supplementary materials like the used limestone. For that reason there are many different formulations of *k(t)* used in practice [10], [11]. A relatively simple empirical formula is used for the actual investigation, at which *m* is a binder dependant constant (Röhling suggests *m=2* for CEM I and *m=2.5* for CEM III/B) [10]. As there is so far no information on the impact of the limestone available, a value of *m=2* was chosen for the *REF* mixes and the *ECO* mixes.

Fig. 3 shows the evolution of the dyn. elastic modulus calculated from the ultrasound measurements for the first 24 h of hydration of the reference mixes *(REF)* and the packing density optimized mix *ECO* for the temperature adjusted age t_e. As there is some missing data from concrete temperature between time of water addition and start of the US measurements a constant mix temperature of 21 to 23°C was assumed for the first minutes for t_e calculation of all mixes. In addition, the results from the predicted elastic modulus for mortar and concrete based on the paste mix using the mathematical equation (3) are visualised in Fig. 3. It can be seen that the evolution of E_{dyn} of mortars and concrete at early age can predicted from paste measurement quite well, although there is some deviation at very early age (e.g. C eco). That is mainly the result of the retarding effect of the used superplastizer, which can be seen by the two curves prognosed for concrete with SP in the paste or without.

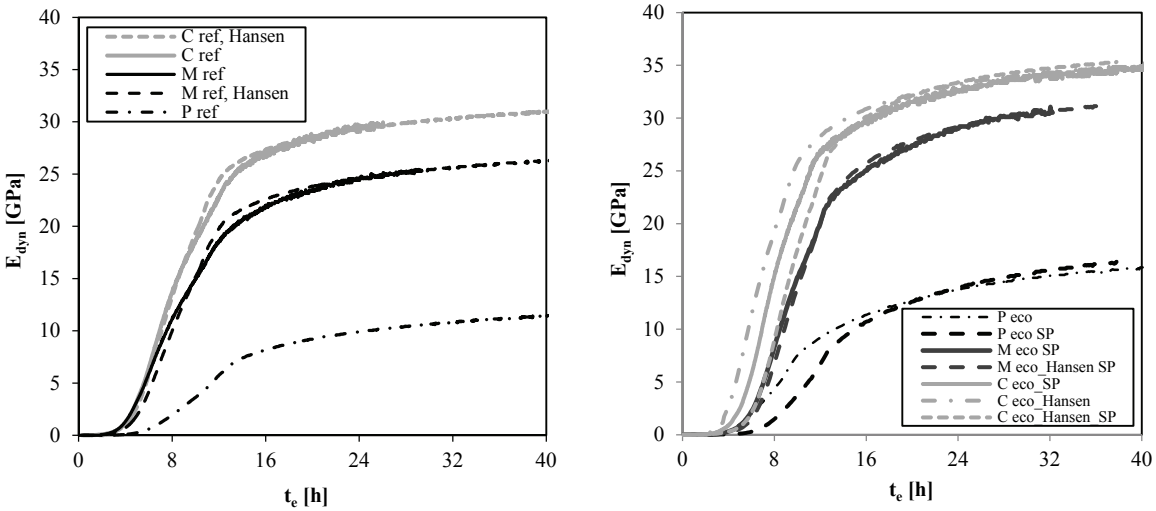

Figure 3: Comparison of dynamic elastic modulus from US testing and calculated ones acc. to Hansen [9] based one E_{dyn} of paste at temperature adjusted age t_e.

4.3 Effect of w/p ratio and matrix composition on early age hydration

Tab. 2 lists the results from the Vicat tests and also a certain time for which a specific dyn. elastic modulus (at 0.1 GPa) resp. a specific shear modulus (at 0.1 GPa and 0.2 GPa) was determined by the ultrasound testing. It is obvious that for pastes G_{dyn} of approximately 0.1 GPa determined at the temperature adjusted age t_e corresponds roughly to the initial setting according to Vicat. But for mortar and concrete higher values for G_{dyn} must be considered. In this context, it is worth to note that the *ECO* mixes with optimized packing density show earlier setting times. Main reason for this is the smaller mean distance of the particles, which allows hydration products to earlier build bridges between particles. Nevertheless, it is also the larger specific surface area that increases the speed of hydration as it can be seen from the calorimetric measurements. The calorimetric measurements show, that the evolution of heat of hydration of the optimized *ECO* mixes starts earlier and also total heat release is higher per unit weight of cement. However, overall heat release of the *ECO* mix is less compared to the reference mixes if the limestone powder is considered as binder. Berodier and Scrivener have already published similar results [12]. It was shown that independent from the nature of the particles a smaller particle distance lead to an accelerated hydration rate. Several interpretations of the relation of smaller particle distance and early age hydration have been

proposed by different researchers, among which are chemical effects, mechanical effects (esp. increased shearing during mixing [12], [13]) or just the above mentioned geometrical effects, i.e. smaller particle distance allows the hydration products to earlier bridge the opposite particles. Consequently, the traditional approach using the w/c-ratio or an equivalent w/c-ratio in combination with an activity index (k-value) for SCM is not considering the effects of enhanced packing density and reduced w/p-ratio on early age matrix properties. Thus, further research is needed.

4. CONCLUSIONS

From the test series and the results presented in this paper some conclusions can be drawn:

- The dynamic elastic properties (E_{dyn} and G_{dyn}) derived from the ultrasound compressional and shear wave velocities show good correlation with the strength development at early age independently from the mixture composition. However, early age strength cannot be directly deduced from the absolute values of elastic modulus, as aggregates strongly influence the elastic modulus but have minor effect on early strength.
- The initial setting time of a cementitious paste can be estimated from the temperature compensated G_{dyn} calculated from ultrasound testing. However, for mortars and concrete sand and aggregate content has to be considered, i.e. higher amount of sand and aggregate results in higher G_{dyn} at initial setting.
- Ultrasound tests on pastes can be used to calculate the evolvement of elastic modulus of mortar and concrete at early age, if constant mixture proportion of the matrix (powder composition and w/c ratio). For this calculation, the degree of hydration resp. the maturity of the mixes according to the released heat during hydration has to be considered.

REFERENCES

[1] Carette, J., Staquet, S.: Monitoring the setting of mortars by ultrasonic P-wave and S-wave transmission velocity measurement, Constr. Build. Mater. 94 (2015) pp. 196-208.
[2] Carette, J., Staquet, S., Monitoring the setting process of eco-binders by ultrasonic P-wave and S-wave transmission velocity measurement: Mortar vs. concrete, Constr. Build. Mater.110 (2016) pp. 32-41.
[3] Reinhardt, H.-W., Grosse, C.U., Aggelis, D., De Belie, N., Krüger, M., Ohtsu, M., Robeyst, N., Shah, S.P.; and Tatarin, R.: Recommendation of RILEM TC 218-SFC: Sonic methods for quality control of fresh cementitious materials. Testing of fresh concrete by ultrasound transmission. RILEM TC 218-SFC, In: Materials and Structures (2011) 44:1047–1062. DOI 10.1617/s11527-011-9734-9.
[4] Krüger, M., Bregar, R., David, G.A., Juhart, J.: Non-destructive evaluation of eco-friendly cementitious materials by ultrasound. International RILEM Conf. on Materials, Systems and Structures in Civil Engineering Vol. 2, (2016), pp. 503-512
[5] Juhart, J., David, G.A., Nickel, C., Fischer, G., Mittermayr, F.: A new combined filler concept for eco-concrete, Proc. of 14th International Congress on the Chemistry of Cement (ICCC 2015), Beijing, 2015
[6] Krüger, M., Grosse, C.U., Lehmann, F.: Automated shear-wave techniques to investigate the setting and hardening of concrete in through-transmission. International Symposium on

Nondestructive Testing of Materials and Structures, May 15-18, 2011, Istanbul, Turkey, RILEM Book series, Springer, Dordrecht, The Netherlands, 2012
[7] Meyer, L.: Zum Einfluss der Kontaktzone bei der Modellierung des Elastizitätsmoduls von Beton. Dissertation, Zugl. ersch.: Aachen: Mainz, 2018
[8] Nwokoye D.N.: Assessment of the elastic moduli of cement paste and mortar phases in concrete from pulse velocity tests cement and concrete research. Vol. 4, pp. 641-655, 1974
[9] Hansen, T.C.: Thermal and electrical conductivity and modulus of elasticity of two-phase composite materials. RILEM Bulletin N. S. (1966) Nr. 31
[10] Röhling, S.: Zwangsspannungen infolge Hydratationswärme. 2., durchges. und erw. Aufl. Düsseldorf: Verlag Bau + Technik, 2009
[11] De Vree, R.; Tegelaar, R.: Gewichtete Reife des Betons. beton 48 (1998) Nr. 11, S. 674 – 678
[12] Berodier, E., Scrivener, K.: Understanding the filler effect on the nucleation and growth of C–S–H. J Am Ceram Soc 97(12):3764–3773, 2014
[13] Berodier, E.: Impact of the supplementary cementitious materials on the kinetics and microstructural development of cement hydration. Doctoral thesis, Switzerland, 2015

International Conference on Sustainable Materials, Systems and Structures (SMSS 2019)
Novel Methods for Characterization of Materials and Structures
20-22 March 2019 – Rovinj, Croatia

ESTIMATING RATE OF HYDRATION IN ULTRASONIC TESTS FROM TEMPERATURE MEASUREMENTS

Ivan Gabrijel (1), Marijan Skazlić (1)

(1) University of Zagreb, Faculty of Civil Engineering, Croatia

Abstract

Temperature of the mixture has a very large influence on the rate of hydration in cement-based materials. Therefore, temperature is often measured during experiments if there is the need to compare properties of material which undergoes different temperature history. Broadly accepted approach for considering influence of temperature on the rate of hydration is maturity principle. Different maturity functions are used which require at least one parameter which characterizes temperature sensitivity of the mixture.

In this paper a numerical modelling approach in used for evaluation of hydration rate which is based on the heat flow within the sample being tested. Temperature measured within the sample serves as an input parameter for modelling and the temperature field throughout the specimen is reconstructed. Calculation procedure also evaluates amount of heat generated at each time step. An example calculation is presented which deals with the heat generation in cement paste sample during ultrasonic pulse velocity test.

Keywords: hydration, cement, heat generation, ultrasonic

1. INTRODUCTION

Ultrasonic testing methods are often used to monitor setting and hardening processes in cement-based materials. Microstructural build-up during early ages gradually enables better transfer of ultrasonic wave energy which on the macro-level reflects as an increase of the wave velocity and increase in the quantity of wave energy transferred. Linking of macrostructural changes to microstructure requires quantification of hydration process.

Progress of hydration is often quantified through a degree of hydration. The extent of the hydration process is usually indicated with the term degree of hydration [1]. Degree of hydration (α) is defined as the ratio between the amount od cement that has reacted until time t to the initial amount of cement (Eq. 1).

$$\alpha(t) = \frac{amount\ of\ cement\ that\ has\ reacted\ untill\ time\ t}{total\ amount\ of\ cement\ at\ time\ t = 0} \quad (1)$$

All hydration reactions are accompanied by release of heat and monitoring the rate of heat evolution is a widely accepted method for monitoring hydration. Degree of hydration from calorimetric measurement is than estimated as the ratio of heat liberated until time t ($Q(t)$) to the total amount of heat that would be liberated if all cement would hydrate (Q_{max}) (Eq. 2):

$$\alpha(t) = \frac{Q(t)}{Q_{max}} \tag{2}$$

Linking the changes in ultrasonic signal to the degree of hydration requires performing calorimetric measurement in parallel to the ultrasonic measurement but these two measurements expose the sample under test to the different temperature conditions. Since temperature of the sample has a very large influence on the rate of hydration in cement-based materials, temperature is often measured during experiments.

Broadly accepted approach for considering influence of temperature on the rate of hydration is maturity principle [2]. Different maturity functions are used which require at least one parameter which characterizes temperature sensitivity of the mixture. Maybe the most common method used for this purpose is the Arrhenius equation, which requires the selection of activation energy E_a. For cementitious materials, E_a is typically computed using the isothermal calorimetry but there is a disagreement in literature as to the proper method to compute E_a from measured data [3].

In this paper a numerical modelling approach in used for evaluation of hydration rate which is based on the heat flow within the sample being tested. Temperature measured within the sample serves as an input parameter for modelling and the temperature field throughout the specimen is reconstructed. Calculation procedure also evaluates amount of heat generated at each time step. An example calculation is presented which deals with the heat generation in cement paste sample during ultrasonic pulse velocity test.

2. DESCRIPTION OF THE NUMERICAL MODEL

2.1 Numerical algorithm

Temperature distribution throughout the mould for ultrasonic testing is modelled using equation 3:

$$\lambda \nabla^2 T + \Phi_G = \rho c \frac{\partial T}{\partial t} \tag{3}$$

Where λ, ρ and c are thermal conductivity, density and specific heat capacity, T is temperature, t is time and Φ_G is heat generation. The above equation is converted into a system of linear equations using the finite difference method. After discretization of the space domain with uniform space steps in all three directions ($\Delta x = \Delta y = \Delta z$) implicit formulation of equation 1 for interior nodes becomes:

$$T_{i,j,k}^{l+1}(1 + 6F_0) - F_0\left(T_{i+1,j,k}^{l+1} + T_{i-1,j,k}^{l+1} + T_{i,+1j,k}^{l+1} + T_{i,j-1,k}^{l+1} + T_{i,j,k+1}^{l+1} + T_{i,j,k-1}^{l+1}\right) = T_{i,j,k}^{l} + \Delta T_G$$

$$\Delta T_G = \frac{\Delta Q m_c}{\rho c} \qquad F_0 = \frac{\lambda}{\rho c}\frac{\Delta t}{\Delta x^2} \tag{4}$$

Where i, j, k are node notations in x, y and z direction and l is a node notation in time domain. ΔQ is the heat liberated during time interval Δt and m_c is the mass of cement per 1 m^3 of the mixture. In matrix notation the above system of equations can be written as:

$$[A]\{T^{l+1}\} = \{T^{l}\} + \{\Delta T_G\} \tag{5}$$

Where $[A]$ is a matrix of coefficients, $\{T^{l+1}\}$ is the vector of unknown temperatures at a time step l+1, $\{T^{l}\}$ is a vector of known temperatures at a time step l and ΔT_G is a temperature increase due to heat generated during interval Δt. When heat generation is a known quantity than vector of unknown temperatures from equation 5 can be simply calculated as:

$$\{T^{l+1}\} = [A^{-1}](\{T^{l}\} + \{\Delta T_G\}) \tag{6}$$

Since in the present case heat liberation is also not known solving equation 3 requires iterations within each time step. Calculation begins by guessing a value for a ΔT_G and temperatures in all nodes in time step l+1 are calculated. Then a condition is checked in which calculated temperature in a certain node in time step l+1 is compared to a measured temperature in a time step l+1 at that node. If the difference between calculated and measured temperature is within the specified range, calculation proceeds to a next time step. If the difference between calculated and measured temperature is outside the specified range a new value of ΔT_G is used and the calculation is repeated. Described algorithm is searching ΔT_G for each time step required to reconstruct measured temperature is a certain node.

2.2 Geometry and material properties

In Figure 1-a mould for ultrasonic pulse velocity (UPV) test on cement paste is shown. Dimension of the sample are 150×150×70 mm where 70 mm is the distance between the transducers. Inner walls of the mould are made of 20 mm thick extruded polystyrene (XPS) supported by 20 mm thick plywood plates connected with bolts. Transducers are 50 mm in diameter with resonant frequency of 54kHz.

a) b)

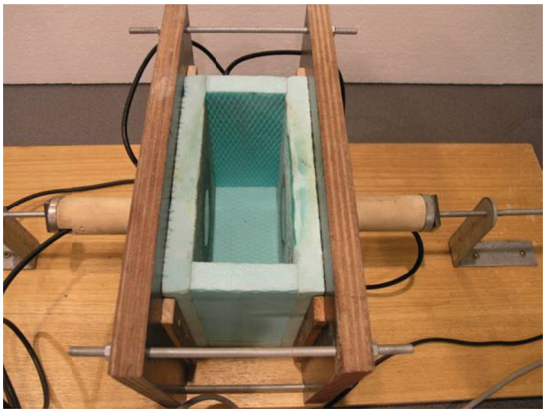

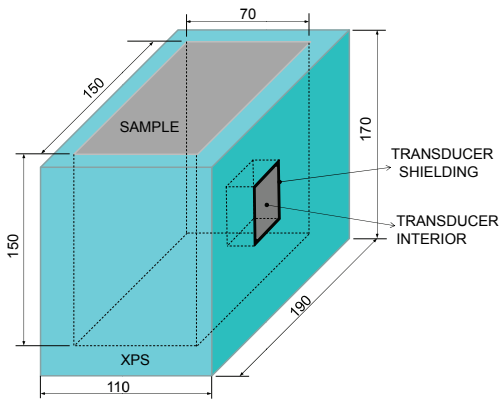

Figure 1: a) mould for UPV test; b) geometry of the numerical model

In Figure 1-b geometry of the numerical model is presented. In numerical model transducers are modelled with rectangular cross section with dimensions 40×50 mm. In the model transducers are composed of exterior part and interior part. Exterior part represents transducer

casing which is made from stainless steel and is very thermally conductive compared to interior. Interior of a typical piezoelectric transducer contains piezoelectric element, backing material, electrodes and wiring but it also contains air which reduces the heat conduction rate through the interior. In the model presented transducer interior is treated as homogenous. Its density and specific heat capacity were calculated as the average density and specific heat capacity of piezoelectric material, backing material (steel) and air. Thermal conductivity of the transducers interior is determined during calibration of the model described in the following section. Properties of the materials used in the model are listed in Table 1.

Table 1: Properties of materials used in numerical model

Material	Density, ρ (kg/m^3)	Specific heat capacity, c (J/(kg·K))	Thermal conductivity, λ (W/(m·K))
XPS	40	1450	0,04
Transducer exterior	8000	450	15
Transducer interior	5500	580	0,2
Cement paste*			
w/c= 0,3	2091	1615	1,0
w/c= 0,4	1939	1800	1,0
w/c= 0,5	1824	1960	1,0
*density of cement ρ_C = 3140 kg/m^3, density of water ρ_W = 1000 kg/m^3 specific heat capacity of cement c_{cem} = 840 J/(kg·K), specific heat capacity of water c_{wat} = 4200 J/(kg·K)			

Properties of the cement paste are dependent on the mix composition. In Table 1 an example calculation of density and specific heat capacity of cement pastes in the range on w/c ratio from 0.3 - 0.5 is given. Literature values for specific heat capacity of cement range from 750 J/(kg·K) [4, 5] to 1140 J/(kg·K) [6]. In Table 1 specific heat capacity is calculated using the simple law of mixtures taking into account mass of cement and water in the mixture.

Bentz reported thermal conductivity values for cement paste with w/c ratio of 0.3 and 0.4 between 0.9 and 1.05 W/(m·K) during the entire hydration period [4]. Qomi et al. reported values of thermal conductivity of cement paste with w/c ratio of 0.3 and 0.5 in the range from 0.8-1.2 [5]. Increasing the w/c ratio decreases the value of thermal conductivity of cement paste [4, 5].

In the model presented thermal conductivity was set equal to 1 W/(m·K) for all w/c ratios. All properties were considered constant during hydration.

2.3 Boundary conditions

Two boundary conditions are used in the model. On the bottom surface temperature is kept constant and equal to the temperature of the environment (T_a). On all other surfaces heat flux (q) is calculated according to equation 7:

$$q = h_c(T_s - T_a) \tag{7}$$

where h_c is convection coefficient, T_s is temperature of the surface a T_a is temperature of air surrounding the surface. Convection coefficient of 25 W/m^2 was found to give best agreement of measured and calculated temperatures.

3. EXPERIMENTAL WORK

3.1 Calibration of the model

An experiment was conducted which is used to calibrate the model. In the experiment 7 thermocouples was installed inside of the mould for UPV test (Figure 2). Locations of the thermocouples are given on two vertical cross-sections through the centre of the mould (Figure 2-b). Thermocouples are designated as T2 to T8. Thermocouple designated T1 was used to measure temperature of the surrounding air.

Cement paste made with a w/c ratio 0.3 is placed inside of the mould and temperatures were recorded. Measured temperatures are shown in Figure 3. Highest temperature is measured at positions T5 and T2 which are closest to the bottom of the mould while lowest temperature increase is recorded at positions T4 and T7 which are closest to the top surface. In Figure 3 calculated temperatures are also plotted. It can be seen from the figure that there is a good agreement between calculated and measured temperatures.

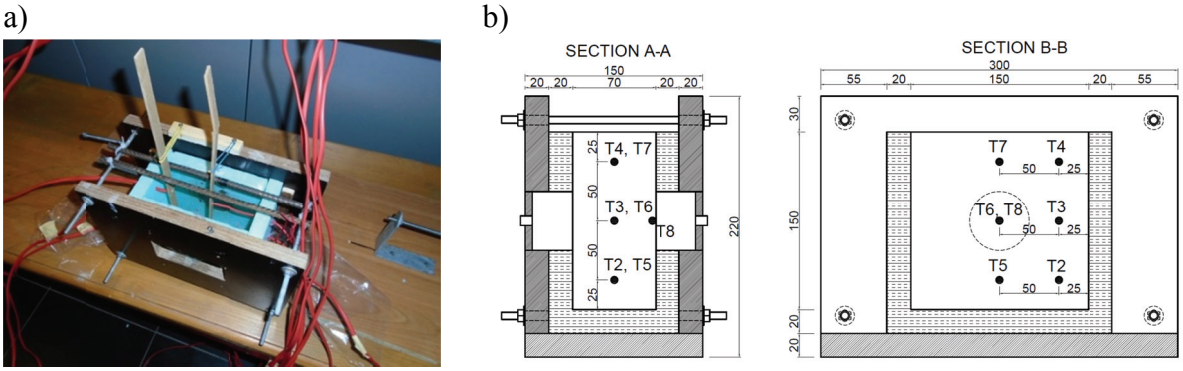

Figure 2: a) Photo of the UPV mould with thermocouples installed; b) two vertical cross sections of the mould with locations of thermocouples.

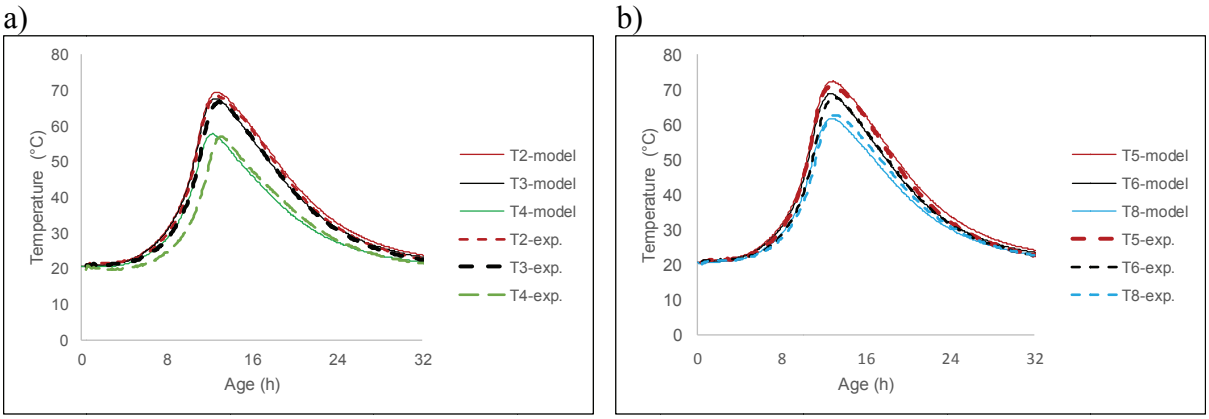

Figure 3: Comparison of measured and calculated temperatures for a) at the location of thermocouples T2, T3 and T4; b) at the location of thermocouples T5, T6 and T8

In Figure 3-a there is a shift in the peak temperature at position T4 between measured and calculated temperature. In calculation results presented in Figure 3 temperature measured at location T3 has been used for searching a value of ΔT_G. Since at the location T3 temperature is always higher than at the location T4 peak value of heat generation rate will be reached within shorter time period at location T3 than at location T4. The model described in section 2 assumes the same rate of heat generation in all points within the cement paste sample i.e. heat generation is not temperature dependant. This is a most probable cause of shifted temperature peak at position T4. To overcome this heat generation rate should be modelled as temperature dependant.

Temperature distributions in two vertical cross sections through the centre of the mould are plotted in Figure 4. In Figure 5-a heat generation rate calculated by numerical model is plotted while in Figure 5-b generated heat is plotted which is obtained by integration of heat generation rate.

a) b)

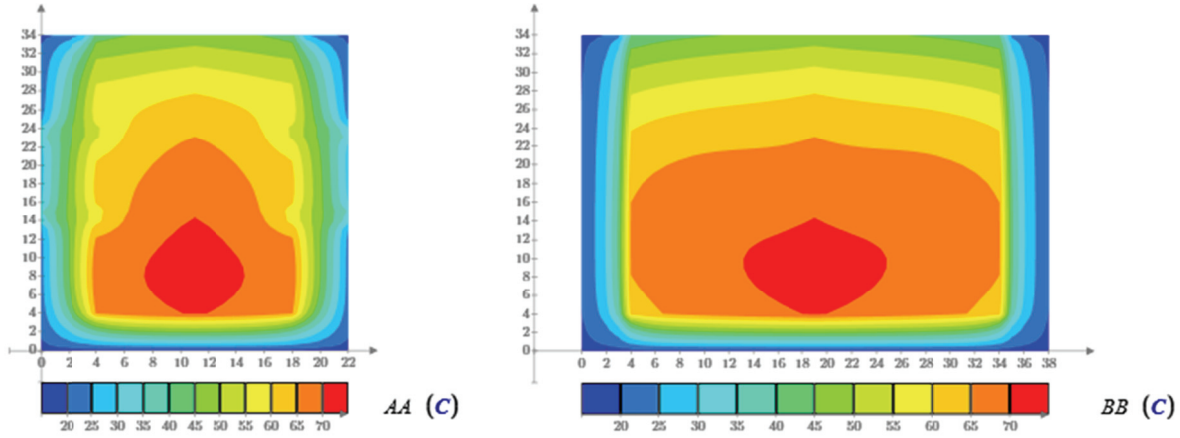

Figure 4: Temperature distribution in two vertical cross sections through the centre of the mould at age of cement paste 13,3 h: a) section A-A; b) section B-B

a) b)

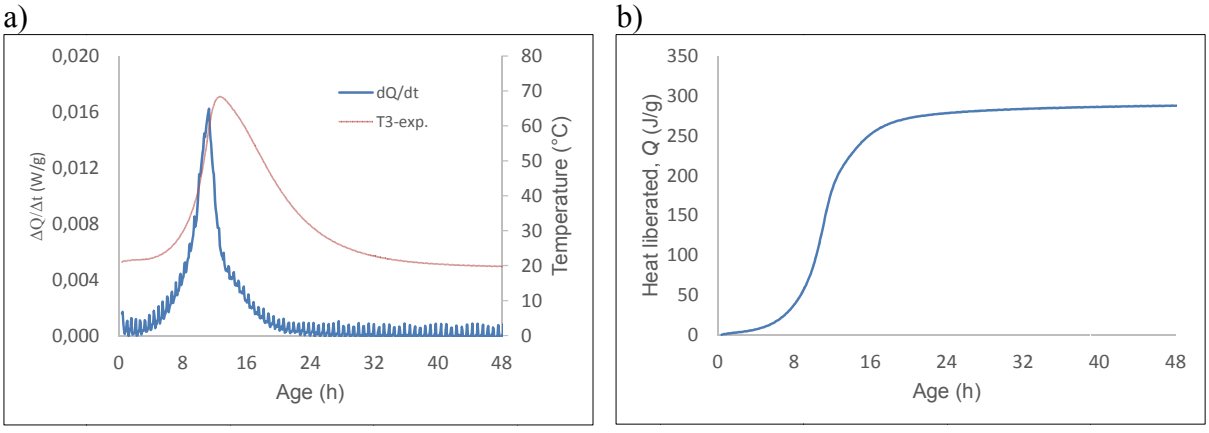

Figure 5: Calculated values of a) rate of heat generation; b) generated heat $Q(t)$

3.2 Comparison with isothermal calorimetry results

In this section heat generation estimated numerically from temperature measurement is compared with results of isothermal calorimetry on different temperatures (20°C, 30°C, 40°C, 50°C and 60°C). Mix composition of cement paste and properties used in numerical model are given in Table 2.

Total amount of heat $Q_{\max}$ is calculated according to equation 8 form data on mineral composition and oxide content given in Table 3:

$$Q_{max} = 500p_{C_3S} + 260p_{C_2S} + 866p_{C_3A} + 420p_{C_4AF} + 624p_{SO_3} + 1186p_{N-CaO} + 850p_{MgO} \quad (8)$$

where p_i is the mass ratio of the i-th component [7]. Total amount of heat Q_{max} = 471,5 J/g.

Table 2: Properties of cement paste used in numerical model

Material	Density, ρ (kg/m^3)	Specific heat capacity, c (J/(kg·K))	Thermal conductivity, λ (W/(m·K))
Cement paste*			
w/c= 0,4	1946	1800	1,0
*cement: CEM I 52.5 N-SR3 CE PM-CP2 NF HRC admixtures - Plasticizer SIKAPLAST Techno 80 (0,45%)			

Table 3: Composition of cement CEM I 52.5 N-SR3 CE PM-CP2 NF HRC

Compound	C_3S	C_2S	C_3A	C_4AF	MgO	SO_3
Quantity (%)	67	12	2	13	1,9	2,7

In Figure 6-a temperature measured in UPV mould is presented. Initial temperature of cement paste is around 20°C during the first 20 hours of hydration. After that a steep increase in temperature follows with a peak temperature of 62°C. Temperature measured in UPV mould is used as an input parameter for numerical estimation of heat generation (Q(t)) during UPV test. Estimated heat generation from UPV test is presented in Figure 6-b and compared with isothermal calorimetry measurements.

a) b)

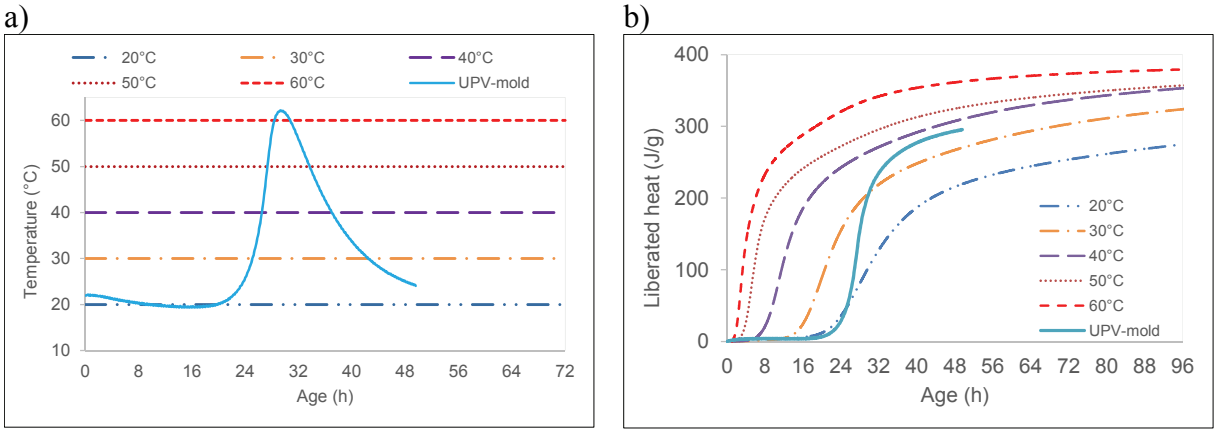

Figure 6: Measurement on MCP mixture a) temperature in the UPV mould during test; b) liberated heat during UPV test compared with results of isothermal calorimetry

Since $Q(t)$ and Q_{max} are known degree of hydration can now be calculated from equation 2. Measured UPV on cement paste during first 48 hours of hydration is presented in Figure 7 as a function of age (7-a) and as a function of degree of hydration (7-b).

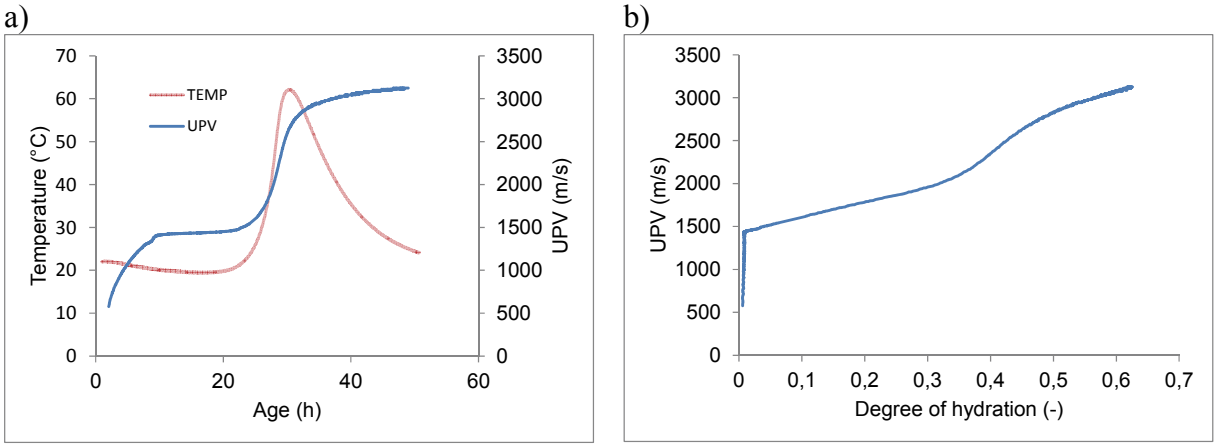

Figure 7: Measurement on MCP mixture: a) UPV and measured temperature vs. age; b) UPV as a function of degree of hydration

4. CONCLUSION

Based on a comparison with measurements made with isothermal calorimetry it seems that presented approach can provide a reasonable estimate of generated heat from a sample under test. Benefit of the methodology is that it does not require additional calorimetry measurements or information about activation energy to link the changes in ultrasonic signal to the degree of hydration.

ACKNOWLEDGEMENTS

The authors would like to thank Fragkoulis Kanavaris and Queens University of Belfast for providing isothermal calorimetry measurements on MCP paste which were made within the Extended Round Robin Testing Programme of Cost action TU1404.

REFERENCES

[1] Van Breugel, K. *Simulation of Hydration and Formation of Structure in Hardening Cement-Based Materials*, Delft Univ.Press, Delft, 1991.
[2] Carino, N. J. *The maturity method: From theory to application*, Proceedings of the 2001 Structures Congress & Exposition, Chang, P.C. ed., Washington, D.C., May 21-23, 2001.
[3] Jonathan L. Poole, Kyle A. Riding, Kevin J. Folliard, Maria C. G. Juenger, and Anton K. Schindler *Methods for Calculating Activation Energy for Portland Cement*, ACI Materials Journal, V. 104, No. 1, January-February 2007, pp. 303-311.
[4] Bentz, D.P. *Transient plane source measurements of the thermal properties of hydrating cement pastes*, Materials and Structures (2007) 40:1073-1080
[5] M.J.A. Qomi, F.-J. Ulm and R.J.-M. Pellenq *Physical Origins of Thermal Properties of Cement Paste*, Physical Review Applied 3, 064010 (2015)
[6] Young, J.F. and Mindess, S. *Concrete*, Prentice-Hall, New Jersey (1981)
[7] Schindler, A. K. *Effect of Temperature on Hydration of Cementitious Materials*, ACI Materials Journal, V 101 , No 1, 2004.

International Conference on Sustainable Materials, Systems and Structures (SMSS 2019)
Novel Methods for Characterization of Materials and Structures
20-22 March 2019 – Rovinj, Croatia

THIXOTROPIC STRUCTURAL BUILD-UP OF CEMENT PASTES AT LOW SHEAR RATES

Mareike Thiedeitz (1), Thomas Kränkel (1), Bianca Bauer (1) and Christoph Gehlen (1)

(1) Technical University of Munich, centre for building materials (cbm), Germany

Abstract

This study presents examinations on the thixotropic structural build-up of cement pastes owing to various low shear rates as preliminary investigation for the form filling ability of fresh concrete, which is highly affected by its rheological properties. In particular, highly viscous systems exhibit a strong thixotropic structural build-up, which aggravates a precise prediction of the flow behaviour of concrete according to standardized test methods.

At low shear rates, structural build-up, dependent on the thixotropic behaviour of the used material takes place. The thixotropy rate at low shear rates is almost not predictable due to the huge amount of interfering factors like solid and superplasticizer content which affects interparticle forces as well as external factors like shear history and current shear rate. Hence, for the determination of the rate of thixotropy, cement pastes with different w/c ratios and superplasticizer contents were analysed at different low shear rates. For every paste, the dynamic yield stress and viscosity as well as the time dependent evolution of the static yield stress at different low shear rates were investigated. The evolution of the static yield stress of each sample was analysed on a dependence of thixotropy on viscosity and shear rate.

Keywords: Thixotropy, low shear rates, static yield stress, structural build-up

1. INTRODUCTION

For the development of robust concretes with required workability properties, knowledge on the rheological properties of their basic cementitious suspension is necessary. The workability of concrete is normally expressed by the rheological values dynamic yield stress $\tau_{0,D}$ and plastic viscosity μ. The rheological properties are dependent on different chemical and physical factors, e.g. particle size distribution, solid content and chemical composition of the suspension [1–4]. In cementitious systems, the rheological properties are shear-rate dependent: Due to colloidal interactions, the viscosity can either decrease or increase, which is called shear thinning or shear thickening behaviour [3]. A stress response of a matter, that is proportional to the applied shear rate is called as Newtonian behaviour. At high shear rates,

the rheological properties are evaluated very precisely because Newtonian as well as shear thinning and shear thickening behaviour can be described according to mathematical functions. According to that, dynamic rheological measurements are a good tool for the prediction of rheological properties during flow. At low shear rates, interfering forces and hydration nucleation effects between the particles produce structural build-up which complicates the prediction of the flow behaviour, wherefore measurements at low shear rates or static measurements during the rest of a paste produce inaccurate results [5]. The structural build-up takes places as soon as the applied stress or strain is too low to break interparticle forces. This behaviour is called thixotropy: Thixotropy therefore produces an increasing viscosity over the time and moreover is dependent from the yield stress and viscosity of the colloidal suspension.

For a precise prediction of the flowability of a cementitious suspension, the thixotropy has to be known. In the present study, rheological measurements were therefore performed on cement pastes with different yield stresses and viscosities to measure the effect of these parameters on thixotropy. For the required adjustment of these rheological parameters the superplasticizer amount and the solid/water content were varied.

The use of superplasticizer produces good flowability and workability of pastes due to a lower yield stress as a result to electrostatic repulsion or steric effects and thus less flocculation of the particles. A change of yield stress for a given cement paste therefore was achieved by an adjustment of the superplasticizer content. A variation of the paste viscosity was reached by a variation of the water/cement-ratio and thus the solid content of the paste: With a decreasing solid content in a suspension, the distance between particles increases and the magnitude of interparticle forces decreases which results in a lower viscosity.

2. RHEOLOGICAL BACKGROUND

Yield stress and viscosity

Generally, fluids are divided into Newtonian and Non-Newtonian fluids. Newtonian Fluids exhibit a flow resistance which is proportional to the flow velocity [6–8]. The dynamic viscosity is the proportionality factor between the resulting shear rate and shear stress:

$$\tau = \eta * \gamma \tag{1}$$

Some materials exhibit as well a linear relationship between the resulting shear rate and shear stress but need to overcome shear stress to start flowing. This shear stress is called yield stress. The so-called Bingham-materials behave like elastic solids until the yield stress is obtained. Beyond the yield stress Bingham-materials behave like Newtonian Fluids with a constant viscosity. Non-Newtonian fluids however do not have a linear dynamic viscosity. The viscosity is a function of the shear rate: Fluids can be either shear thinning or shear thickening [9, 10]. There exist many regression functions for the yield behaviour. The so-called Hershel-Bulkley model implements this behaviour in the following regression equation:

$$\tau = \tau_0 + k * \dot{\gamma}^n \tag{2}$$

With the exponent n=1, the fluid behaves like a Bingham-Material. With changing exponent, the shear thinning or shear thickening of a material is taken into account.

Thixotropy

Thixotropy is the time and shear dependent change of viscosity of colloidal systems and occurs due to the interparticle forces in a suspension [11]. Thixotropic structures break down when shear occurs to the colloidal system and rebuild their structure at rest, see Fig.1. The viscosity of the system changes due to the structural change. The thixotropic structural breakdown and build-up is dependent of the presence and magnitude of interparticle forces: With higher interparticle forces, the system is more robust and thixotropy increases [6, 12, 13]. The thixotropic structural build-up is said to be fully reversible [10, 11, 14, 15].

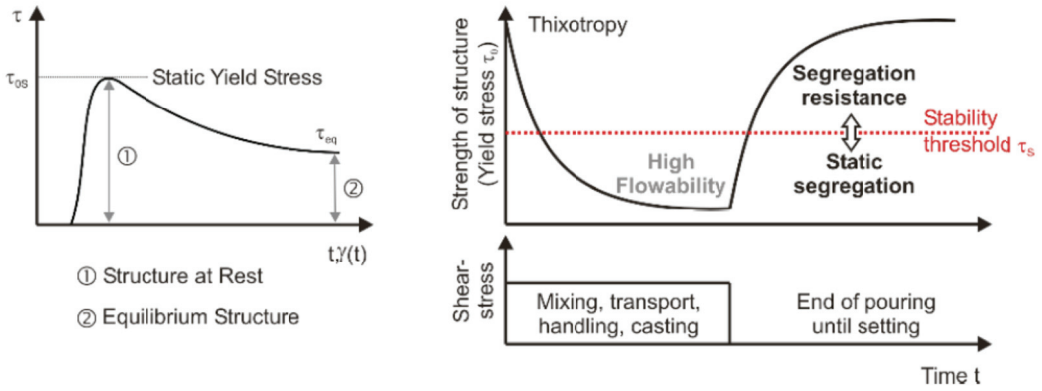

Figure 1: Evolution of static yield stress during low shear (left) and time and shear dependent change of viscosity: decrease during shear and recovery at rest (right), acc. to [6]

Rheological behaviour of cementitious suspensions

Cementitious suspensions are Non-Newtonian fluids. They exhibit a yield stress and a certain viscosity. The Hershel-Bulkley model shows the flow behaviour of most cement pastes well. Furthermore, they behave thixotropic. The thixotropy in cementitious suspensions is difficult to investigate: Due to the ongoing early hydration (formation of ettringite) and thus the change of the chemical composition of the suspension which affects the interparticle forces between the particles, the reversible part of thixotropic structural build-up in cementitious systems cannot be fully distinguished from the irreversible. Nevertheless, following the influence of ettringite formation and its influence on the thixotropy is not further discussed [16].

3. MATERIALS AND METHODS

3.1 Materials and mix design

An Ordinary Portland Cement CEM I 42,5 R according to EN 197-1, demineralized water and a PCE-type superplasticizer were used to produce cement pastes. Two water/cement ratios, i.e. 0.3 and 0.4 were chosen for a targeted variation of the paste viscosity. The viscosity changes with the variation of water content: Decreasing particle distances caused by lower water contents and thus higher solid contents cause smaller particle distances. Due to that,

interparticle forces increase as well as colloidal particle interactions, which cause higher viscosities.

The further intention was a systematic variation of the dynamic yield stress This was realized by a proper adjustment of the content of the superplasticizer and thus a variation of the slump flow diameter. The paste mix design is shown in Table 1. It has to be noted that the PCE has a water content of 70%, which has to be subtracted from the water addition.

Table 1 : Paste mix design

w/c-ratio [-]	Cement [kg/m³]	PCE [M-% o.C.]	PCE [kg/m³]]	Water amount [kg/m³]
0.4	1393.81	0.000-0.480	0.0-6.69	558.00
0.3	1619.54	0.350-0.526	5.67-8.52	486.00

The cement pastes were prepared using a mortar mixer "ToniMix 6210" with a mix program according to EN 196-1. The rheological measurements were performed using an Anton Paar Rheometer MCR 502. For the dynamic measurements, a parallel plate geometry with a plate diameter of 50 mm and a gap width of 1 mm was used. This configuration enables the calculation of absolute values for the dynamic yield stress and viscosity respectively. Sandpaper, fixed on the top of both plates, was used to prevent wall slip. The static measurements were performed with a six-bladed vane device. Due to the very low rotational velocities in the static experiments, shear was assumed to only occur at the circumference of the vane in order to simplify the calculation of the related shear rates.

3.2 Experimental procedure

The time of water addition was set as start time. The mixing acc. to the program EN 196-1 with a total time of 04:00 min then started without delay. After mixing, the temperature of the paste was measured. At a total time of 06:30 min after water addition, the paste for the rheological measurements was remixed for 10 sec. Following, a sufficient amount of paste was placed between the parallel plates. The rheological measurements thus started at a time of 07:45 min after water addition. At a total time of 07:50 min, the slump flow was measured; thus the dynamic rotational rheometer measurements were executed simultaneously to mini slump flow tests in order to investigate both the dynamic yield stress and viscosity of the pastes as well as its relationship between dynamic yield stress and mini slump flow diameter acc. to [17]. The dynamic shear profile is shown in figure 2. After a constant pre-shear with a shear rate of $40s^{-1}$, the shear rate was stepwise decreased from 80 s^{-1} to 0.02 s^{-1}.

For the static measurements, a sufficient amount of paste was placed in the Vane cup and remixed for 10 sec at a total time of 11:00 min after water addition. After passing the parallel plate measurement, the vane cup was installed in the Rheometer and a static rheometric measurement was passed to investigate the time and shear rate dependent development of the static yield stress and thus the thixotropy rate.

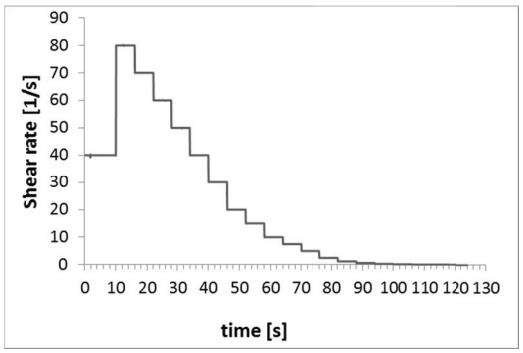

Figure 2: Shear profile for the determination of dynamic yield stress and viscosity of the pastes

For this reason, in a first test series during 360 sec of resting time, four steps from resting state to an immediate shear rate of 0.055 rpm were performed: During 360 sec of measurement, the cement paste rested for 55 sec until an apparent shear rate of 0.055 rpm was set for five seconds. Another 'time at rest' of 55 sec followed, thus the next shear rate of 0.055 rpm was set at 120 sec. This step was repeated twice for 240 sec and 360 sec with a resting time of 115 sec, respectively During the resting time the cement paste rebuilt its structure due to thixotropic behaviour, thus the measured peak of yield stress increased over the time. The peak of measured shear stress during shear was evaluated as static yield stress and the slope of static yield stress over the time was calculated as thixotropy.

In the second test series the paste again was measured during 360 sec of resting time. Instead of total rest, different low shear rates were set and time dependent evolution of static yield stress was measured to analyse the effect of low shear on the thixotropic structural build-up.

4. RESULTS AND DISCUSSION

4.1 Relationship between dynamic yield stress and mini slump flow diameter

The yield stress was calculated according to the Hershel-Bulkley regression. In Fig. 3 a relationship between the slump flow diameter and the dynamic yield stress is shown for cement pastes with a w/c ratio of 0.3 and 0.4. It can be pointed out that there is dependence between the yield stress and the flowability of a system measured by the slump flow diameter. An analytical prediction for the mathematical function was given in [17].

There is a correlation between the results of the dynamic yield stress and the mini slump flow. The analytical results of yield stress in dependence of the slump flow acc. to [17] are lower than the measured values. In general, a correlation between the slump flow and the dynamic yield stress could be shown. Moreover, there was almost no difference of yield stress for a given slump flow diameter between the cement pastes with different w/c-ratios and thus viscosities.

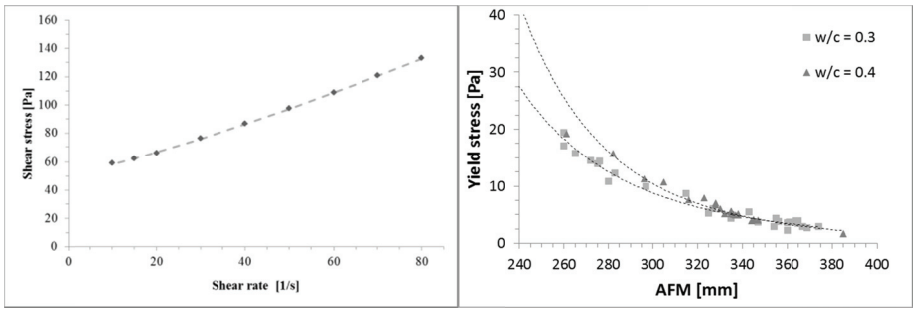

Figure 3: Flow curve after dynamic measurement with a R^2 of 1.0 (left) and correlation of yield stress and mini slump-flow acc. to [17] with R^2=0.95 (right)

4.2 Structural build-up during rest

The evolution of static yield stress for the cement paste is shown in Fig. 4 with a w/c-ratio of 0.3. For the static yield stress only the linear increase from sec. 120 to sec. 360 was taken into account. The first measured static yield stress after 60 sec did not reach its maximum peak during the applied shear, thus is can be considered that the structure of the paste was not broken during the 6 sec of shear. According to this, the static yield stress could not be calculated correctly. Nevertheless, the applied shear at the following steps produced a structural break so static yield stress could be considered as the peak. Moreover, the static yield stress has a linear incline from sec. 120 to sec. 360. The slope of the linear incline was calculated as the thixotropy A_{thix} [Pa/s] and again compared to the results of the mini slump flow measurements to point out the effect of yield stress and viscosity on the thixotropy.

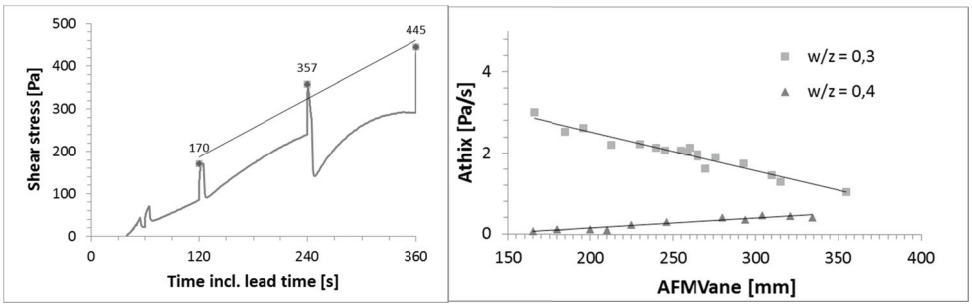

Figure 4 Static yield stress measurement (left) and correlation between mini slump flow and thixotropy with R^2 = 0.92 for w/c = 0.4 and R^2 = 0.92 for w/c = 0.3(right)

Fig. 4 shows that a change of w/c-ratio causes a change in the thixotropy: The cement paste with a w/c-ratio of 0.4 and thus a lower viscosity has a lower thixotropy than the cement paste with a w/c-ratio of 0.3. Obviously, a lower solid content causes more space between the cement particles. In fact, less interparticle forces can be built and thus, the thixotropy is lower.

Meanwhile, the change of the thixotropy with the slump flow and thus the change of the yield stress is higher for a cement paste with the w/c ratio of 0.3: At a higher solid content, superplasticizers have a bigger effect on particle interactions. Hence, with increasing superplasticizer amount, thixotropy decreases due to the steric effects of superplasticizers. At a w/c ratio of 0.4, the particle space is too high for the effect of superplasticizers on particle surface interactions.

4.3 Structural build-up depending on low shear rates

With the first test series (see figure 4, right), it could be shown that thixotropy decreases with increasing w/c-ratio (and thus decreasing viscosity), for a fixed slump flow, caused by enlarged distances and therefore lower interparticle forces between the cement particles. A lower thixotropy with decreasing yield stress caused by a higher superplasticizer amount was measured for cement pastes with a w/c ratio of 0.3, which can be explained by the steric effects of the superplasticizers between the cement particles.

In the second experimental series, the static yield stress was measured for cement pastes with different low shear rates during the 'time at rest'. The thixotropy at rest was set as the total amount of thixotropy. With increasing shear during 'time at rest', lower thixotropy was measured. The remaining thixotropy in dependence of the apparent shear rate for two different w/c-ratios and thus viscosities is shown in Fig. 5. A good correlation of a power function with the decreasing thixotropy in dependency of the shear stress during rest. The decrease of thixotropy with an increasing shear rate is caused by the break of the interparticle forces between the cement particles. Thus, a simultaneous structural breakdown takes place during structural build-up.

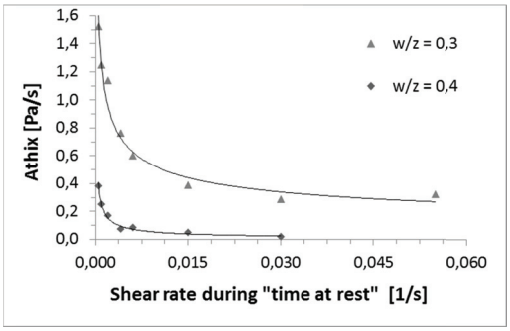

Figure 5 : Effect of shear rate during 'time at rest' on the thixotropy of cement pastes with w/c = 0.3 and w/c = 0.4 ($R^2 = 0.97$)

5. CONCLUSION

Thixotropic structural build-up was shown in dependence of the rheological parameters yield stress and viscosity and different low shear rates during resting time. It could be shown that the thixotropy is strongly dependent on the viscosity of a system, which is caused by the distance between the cement particles in the colloidal suspension and thus the number and amount of interparticle forces. However, dependence between the yield stress and the thixotropy only was measured for cement pastes with a w/c ratio of 0.3 because of the low distance between the cement particles and thus the effect of steric forces caused by superplasticizer. The superplasticizer amount did not change the behaviour of interparticle forces between cement particles for higher water content and thus a higher distance between the cement particles. Hence, further research should investigate cementitious suspensions with a higher viscosity to monitor the chemical and physical impact of superplasticizers on the development of structural build-up.

Furthermore, the investigations points out a strong effect of the shear rate of a cement paste on the thixotropic structural build-up during very low flow. The higher the shear rate, the less structure is rebuilt and thus the thixotropy decreases. Investigations that are more detailed

have to be performed for a better understanding of the physical and chemical background of this behaviour to better predict the thixotropic structural build-up during very low shear rates.

REFERENCES

[1] BANFILL, P. F. G.: *The Rheology of Fresh Cement and Concrete - A Review* (11th International Cement Chemistry Congress). Durban, 2003

[2] ROUSSEL, Nicolas ; LEMAÎTRE, Anael ; FLATT, Robert J. ; COUSSOT, Philippe: *Steady state flow of cement suspensions* : *A micromechanical state of the art*. In: *Cement and Concrete Research* 40 (2010), Nr. 1, S. 77–84

[3] CONTE, Théau ; CHAOUCHE, Mohend: *Rheological behavior of cement pastes under Large Amplitude Oscillatory Shear*. In: *Cement and Concrete Research* 89 (2016), S. 332–344

[4] FLATT, Robert J. ; BOWEN, Paul: *Yodel* : *A Yield Stress Model for Suspensions*. In: *Journal of the American Ceramic Society* 89 (2006), Nr. 4, S. 1244–1256

[5] MEWIS, Jan ; WAGNER, Norman J.: *Current trends in suspension rheology*. In: *Journal of Non-Newtonian Fluid Mechanics* 157 (2009), Nr. 3, S. 147–150

[6] LOWKE, Dirk: *Sedimentationsverhalten und Robustheit Selbstverdichtender Betone* : *Optimierung auf Basis der Modellierung der interpartikulären Wechselwirkungen in zementbasierten Suspensionen*. München, Technische Universität München. Dissertation. 2013

[7] MEZGER, Thomas: *Das Rheologie Handbuch* : *Für Anwender von Rotations- und Oszillations-Rheometern*. 5., vollständig überarbeitete Auflage : Hannover: Vincentz, 2016

[8] BARNES, Howard A.: *The yield stress - a review or panta rei - everthing flows?* . In: *Journal of Non-Newtonian Fluid Mechanics* (1999), Nr. 81, S. 133–178

[9] STRUBLE, Leslie ; SUN, Guo-Kuang: *Viscosity of Portland cement paste as a function of concentration*. In: *Advanced Cement Based Materials* 2 (1995), Nr. 2, S. 62–69

[10] RUCKENSTEIN, E. ; MEWIS, J.: *Kinetics of structural changes in thixotropic fluids*. In: *Journal of Colloid and Interface Science* 44 (1973), Nr. 3, S. 532–541

[11] BARNES, Howard A.: *Thixotropy—a review*. In: *Journal of Non-Newtonian Fluid Mechanics* 70 (1997), 1-2, S. 1–33

[12] ROUSSEL, Nicolas: *A thixotropy model for fresh fluid concretes* : *Theory, validation and applications*. In: *Cement and Concrete Research* 36 (2006), Nr. 10, S. 1797–1806

[13] ROUSSEL, N. ; OVARLEZ, G. ; GARRAULT, S. ; BRUMAUD, C.: *The origins of thixotropy of fresh cement pastes*. In: *Cement and Concrete Research* 42 (2012), Nr. 1, S. 148–157

[14] BARNES, Howard A. ; HUTTON, John F. ; WALTERS, Kenneth: *An introduction to rheology*. 3. impression. Amsterdam : Elsevier, 1993 (Rheology series 3)

[15] GOODEVE, C. F.: *General theory of thixotropy and viscosity* (1938)

[16] BAUER, Bianca: *Untersuchungen zum thixotropen Strukturaufbau von Zementsuspensionen unter geringer Scherbelastung*. München, TU München. Master's Thesis. 2018

[17] ROUSSEL, N. ; STEFANI, C. ; LEROY, R.: *From mini-cone test to Abrams cone test* : *Measurement of cement-based materials yield stress using slump tests*. In: *Cement and Concrete Research* 35 (2005), Nr. 5, S. 817–822

International Conference on Sustainable Materials, Systems and Structures (SMSS 2019)
Novel Methods for Characterization of Materials and Structures
20-22 March 2019 – Rovinj, Croatia

CIRIA GUIDE C766: AN OVERVIEW OF THE UPDATED CIRIA C660 GUIDANCE ON CONTROL OF CRACKING IN REINFORCED CONCRETE STRUCTURES

Fragkoulis Kanavaris (1)* and Sarah Kaethner (1)

(1) Advanced Technology & Research, Arup, London, UK

Abstract

This paper provides a brief overview of the updated version of the CIRIA C660 guide on control of thermal cracking, which has been used extensively in the UK and is also popular across Europe. The updated guide is entitled CIRIA C766 – Control of cracking caused by restrained deformation in concrete. It aims towards designing reinforced concrete structures subjected to restrained thermal and shrinkage deformations in a more efficient and sustainable manner, as well as less conservatively while maintaining an adequate degree of safety.

The primary updates present a design approach more closely aligned with BS EN 1992-1-1+A1:2014 and BS EN 1992-3:2006. Revisions include limiting cracking widths, calculation of restraint considering early age and long-term effect and viscoelasticity, models to predict temperature histories of concretes containing mineral additions, as well as a more sustainable selection of parameters relevant to the estimation of crack inducing strains and minimum steel required to control crack widths. Nonetheless, there are still aspects of design that may have not been adequately addressed, potentially requiring further improvements.

Keywords: Early age/Long term cracking, crack control, restraint, thermal and shrinkage cracking

1. INTRODUCTION

Cracking due to restrained volumetric changes in reinforced concrete (RC) structures has long been a recognised problem. This cracking occurrence is predominately associated with imposed deformations due to thermal and shrinkage (autogenous and drying) related effects, at both early ages and long-term, and it is often desired to control them in terms of the resulting crack width [1]. The primary reasons that crack control in RC structures is of great importance for the serviceability limit state design quoted in C766 are: a) ensuring adequate durability of concrete depending on exposure conditions throughout a specified design service

life, b) achieving and maintaining different degrees of "leak-tightness" depending on performance requirements and c) aesthetics.

Several guidance documents with respect to crack control in RC structures are consulted by engineers [2]-[11]. Amongst the most popular, certainly in the UK, and in parts of Europe, is the CIRIA C660 guide [6] on controlling early age thermal cracking in concrete. This guide was released in 2007 and it has been one of the most frequently used design guides in the UK; however, there were several aspects of the design process and assumptions that required updating. The design solutions were considered unsustainable and over-conservative in terms of cracking width calculation and the amount of steel required to control cracking. Thus, a collective of subject-matter experts from different institutions has been working for several years, together with the leading author of the CIRIA C660 guide, towards updating it. The finally updated guide, now entitled C766 - "Control of cracking caused by restrained deformation in concrete", is released by CIRIA in late 2018 [12]. Arup had an instrumental role in evaluating, updating, assessing and developing further the guide and this paper aims to provide an overview of some, mainly primary, changes issued in the updated C660 guide, which is of interest and benefit of structural engineers in both academia and practice.

2. OVERVIEW OF MAJOR UPDATES

The primary updates were concerned with presenting a design approach more closely aligned with BS EN 1992-1-1+A1:2014 [2] and BS EN 1992-3:2006 [3]. Updates were also mindful of the Annex D of the new Eurocode 2 which is currently being drafted (expected 2023), where cracking risk will be evaluated in terms of stress histories [13]. Updates in C766 regarding limiting cracking widths, calculation of restraint and temperature histories, as well as selection of parameters relevant to the estimation of minimum steel required to control crack widths, will be briefly discussed in this section.

2.1 Limiting cracking width criteria for self-healing to occur

Self-healing (or autogenous healing) of cracks in concrete in the presence of water is a recognised phenomenon, with great relevance to water-retaining structures. BS EN 1992-3:2006 provides suggestions of limiting cracking widths for self-healing to occur as a function of the pressure gradient. However, on the basis that crack movement (live and dormant cracks) is a decisive factor with respect to self-healing (following [14]), CIRIA C766, suggests a relaxation in crack width limit, provided that crack movement (Δw) remains equal or less than 10%, as shown in Figure 1.

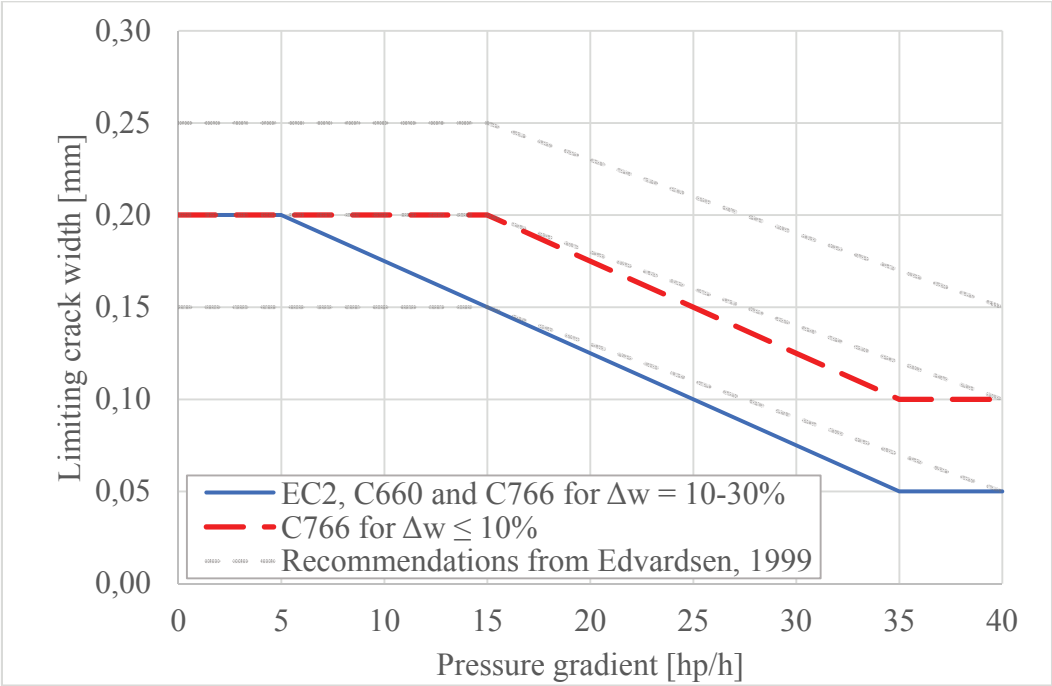

Figure 1: Recommendations on limiting crack width for self-healing to occur

2.2 Calculation of the restrained strain

Modifications were also applied in the analytical formulation of the restrained strain. These aimed to account for the contribution of individual components of strain on the restrained strain, ε_r. This also considers stress relaxation due to creep under sustained loading at both early ages and long-term. The restrained strain is now formulated as follows:

$$\varepsilon_r = K_{c1}[\alpha_c T_1 + \varepsilon_{ca}(3)]R_1 + K_{c1}[\varepsilon_{ca}(28) - \varepsilon_{ca}(3) + \alpha_c T_2]R_2 + K_{c2}\varepsilon_{cd}R_3 \quad (1)$$

Where ε_r is the restrained strain, $\varepsilon_{ca}(t)$ is autogenous shrinkage at time t, ε_{cd} is the drying shrinkage strain, R_1 is the restraint factor that applies during early thermal cycle, R_2 and R_3 are restraint factors applying to medium- and long-term deformations, T_1 is the maximum temperature differential, T_2 is temperature drop after early age, α_c is the coefficient of thermal dilation of concrete and K_{c1} and K_{c2} are coefficients that account for viscoelasticity and stress relaxation at early ages (taken as 0.65) and long-term (taken as 0.5) respectively. For the calculation of the early age thermal restrained contraction, i.e. 3 days, the last two components of Equation (1) may be disregarded. This formulation for restrained strain includes a number of simplified assumptions which, in combination, it has been estimated provide a safety margin of 10-15%.

2.3 Characteristic tensile strength of concrete

The value of tensile strength used in design in the calculation of crack inducing strain is of paramount importance as it dictates the magnitude of crack inducing strain, particularly in end restraint condition ($\varepsilon_{sm} - \varepsilon_{cm}$), as described in Annex M of BS EN 1992-3:

$$(\varepsilon_{sm} - \varepsilon_{cm}) = (0.5 k_c \alpha_e f_{ct,eff} k) / E_s \times [1 + 1/(\alpha_e \rho)] \quad (2)$$

Where k is a coefficient for non-uniform and self-equilibrating stresses, k_c is a coefficient accounting for stress distribution within the section immediately before cracking, $f_{ct,eff}$ is the effective tensile strength at the time of cracking, E_s is the elastic modulus of steel reinforcement, α_e is the modular ratio (steel to concrete) and ρ is the ratio of the total reinforcement area to the area of concrete in tension.

BS EN 1992-1-1 and C660 recommend the value for $f_{ct,eff}$ to be equal to the mean tensile strength of concrete, f_{ctm}. However, C766 recognises reductions in tensile strength arising from the combinations of weakest link and scale effects, tension stiffening and early age and long-term sustained load effects, and recommends that $f_{ct,eff}$ is replaced by a characteristic tensile strength ($f_{ct,r}$) equal to $0.7*f_{ct,eff}$, as also recommended in [8] and [10].

2.4 Calculation of minimum area of steel required

Controlling the crack spacing and hence the cracking width, requires sufficient steel such that when cracking occurs the reinforcement will not yield. Similarly to the calculation of the crack inducing strain, the tensile strength selected in the design affects significantly the amount of reinforcement required to control cracking. While the originally recommended value of tensile strength was f_{ctm}, C766 recommends a value of $0.7*f_{ctm}$ (as previously described in section 2.3). In addition, a coefficient, k_{Redge}, is introduced to account for the transfer of part of the load in the concrete before cracking to the (edge) restraining element when the crack occurs. Thus, factor k_{Redge} varies from 0.5 to 1 depending on the degree of restraint. Consequently, the calculation of the minimum area of reinforcement required, $A_{s,min}$, is performed as follows:

$$A_{s,min} = (k_{Redge} k_c k A_{ct}) \times (f_{ct,r}/(f_y)) \quad (3)$$

With A_{ct} being the area of concrete in the tensile zone and f_y the yield strength of steel.

2.4 Crack spacing and consideration of bond characteristics

C766 and C660 recognise the importance of bond characteristics in crack spacing and consider the risk of poor bond occurrence at early ages. This is accommodated through a modification in the k_1 coefficient for bond in expression 7.2 in BS EN 1992-1-1 for crack spacing calculation. It is, however, suggested in C766 that the definition of poor bond should only be applied at early ages for elements thicker than 300 mm, and which also have a cover ≤ 50 mm.

2.5 Cover to reinforcement used in calculations

The value of reinforcement cover is influential in the calculation of crack spacing and cracking width. What was initially suggested, was that for the purpose of this calculation, c_{nom} should be considered. For cracking from restrained strain, where limits are not governed by aesthetic considerations, C766 recommends that the full crack width calculation is conducted based on c_{min}. This is an alternative to the simplified adjustment in UK national documents. By using the full formula from the code this will account for the non-linear nature of the crack width opening whilst c_{min} includes sufficient cover to account for non-linear bond effects as well as additional crack opening in the durability cover zone and fire resistance, as also discussed in [15]. Such adaptation can result in steel reinforcement savings even as high as 77% [12].

2.6 Hydration model for concrete containing GGBS (slag)

The hydration model in C660 for concretes containing particularly high cement replacement with GGBS, i.e. above 50%, had reportedly been overestimating the actual adiabatic temperature rise [16]0 and consequently, the temperature generated in structural elements containing such concrete. The model has been recalibrated in C766 with additional data; temperature estimates for high GGBS contents are now lower than those of C660. The differences between the adiabatic temperature estimates of the models are shown in Figure 2, for a typical 70% GGBS (by mass of total binder content) concrete with a binder content of 380 kg/m^3.

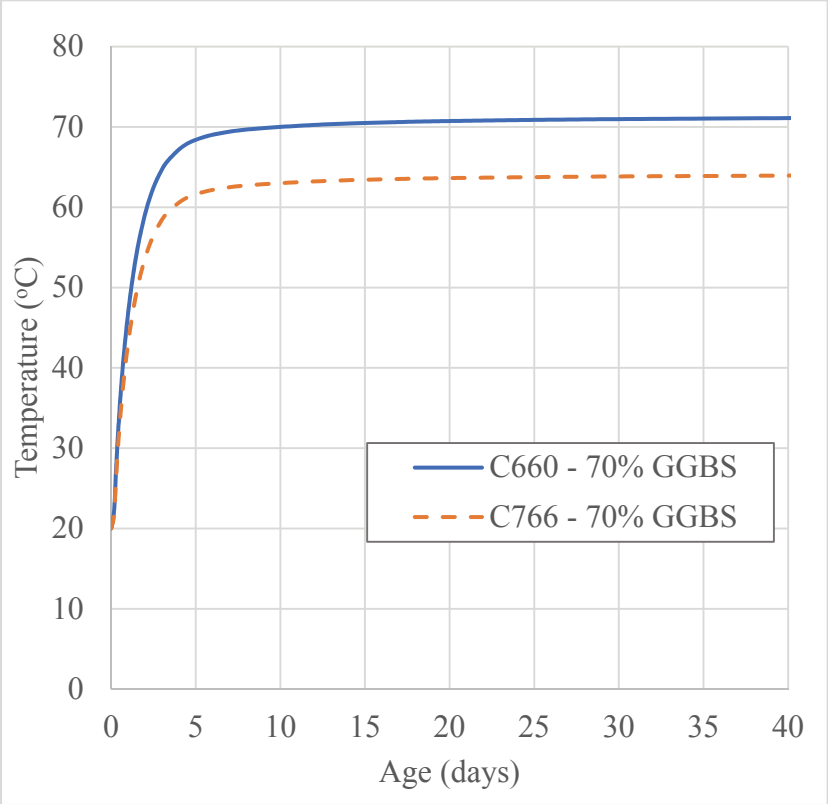

Figure 2: Estimated adiatbatic tempreature rise of a typical 70% GGBS concrete based on C660 and C766.

4. FURTHER IMPROVEMENTS AND CONSIDERATIONS

Although significant improvements were made in the original C660 with respect to more accurately calculating restrained strains and defining minimum amounts of reinforcement more sustainably, there is certainly more to explore in the topic of cracking due to restrained deformations. Further updates on this topic will be introduced by the new Eurocode 2 (currently being drafted and expended to be published in 2023) which will include a stress history-based design approach for crack control/mitigation.

5. SUMMARY

In this paper, a brief overview of the updated version of the CIRIA C660 guide on control of thermal cracking, which has been used extensively in the UK and is also popular across Europe, has been presented. The updated guide (now entitled CIRIA C766 – Control of cracking caused by restrained deformation in concrete) intends to provide more sustainable and pragmatic solutions for designing reinforced concrete structures subjected to restrained thermal and shrinkage deformations while also still being in agreement with the current versions of BS EN 1992-1-1 and BS EN 1993-3, as well as in view of the new Eurocode 2.

ACKNOWLEDGEMENTS

The authors would like to thank Dr B.K. Marsh (Arup) for his fruitful comments on the manuscript and Dr A. Delahunty (Arup) for her contributions in evaluating parts of the C660 guide.

REFERENCES

[1] Gilbert, R.I. and Ranzi, G. 'Time-dependent behaviour of concrete structures', *CRC Press*, 2010.
[2] BS EN 1992-1-1: +A1:2014: Eurocode 2 – Design of concrete structures, Part 1-1: General rules and rules for buildings, 2014.
[3] BS EN 1992-3: Eurocode 2 – Design of concrete structures, Part 3: Liquid retaining and containment structures, 2014.
[4] *fib* Model Code for concrete structures 2010.
[5] American Concrete Institute, 'ACI 224R-01: Control of cracking in concrete structures', 2001.
[6] Bamforth, P.B., 'Early age thermal crack control in concrete', CIRIA C660, 2007.
[7] Japan Concrete Institute, 'Guidelines for control of cracking of mass concrete', 2016.
[8] Barre et al., 'Control of cracking in reinforced concrete structures', *John Wiley & Sons*, 2016.
[9] Fairbairn, E.M.R. and Azenha, M. (eds) 'Thermal cracking of massive Concrete Structures: State of the Art Report of the RILEM Technical Committee 254-CMS', *Springer*, 2019.
[10] Concrete Society, 'Movement, restraint and cracking in concrete structures', Technical Report 27, London, 2008.
[11] Forth, J.P. and Martin, A.J., 'Design of liquid retaining concrete structures', 3rd ed., *Whittles Publishing*, 2014.
[12] Bamforth, P.B., 'Control of cracking caused by restrained deformation in concrete', CIRIA C766, 2018.
[13] Kanstad, T. and Klausen, A.E., 'Background for a new Eurocode 2-Annex: Evaluation of early age and long term cracking due to restrained deformations', in: Synercrete18' – Interdisciplinary approaches for cement-based materials and structural concrete (Azenha, M., Schlicke, D., Bendoudjema, F. and Jedrzejewska, A. (eds)), pp. 86-92.
[14] Edvardsen, K. 'Water permeability and autogenous healing of cracks in concrete', *ACI Mat. J.*, **96**(4), 1999, pp. 448-455.
[15] Kathner, S. 'Have EC2 cracking rules advanced the mystical art of crack width prediction?', *The Struct. Eng.* **89**(19) (2011) 14-22.
[16] Kanavaris, F. 'Early age behaviour and cracking risk of concretes containing GGBS', *PhD Thesis*, Queen's University Belfast, UK, 2017.
Vollpracth, A., Soutsos, M. and Kanavaris, F. 'Strength development of GGBS and fly ash concretes and applicability of fib model code's maturity function - A critical review', *Con. Build Mat.*, 162, 2018, pp. 830-846.

International Conference on Sustainable Materials, Systems and Structures (SMSS 2019)
Novel Methods for Characterization of Materials and Structures
20-22 March 2019 – Rovinj, Croatia

A MODIFIED PYCNOMETER METHOD TO DETERMINE THE WATER ABSORPTION OF COMBINED CRUSHED CONCRETE AGGREGATE FRACTIONS

Madumita Sadagopan (1), Katarina Malaga (2) and Agnes Nagy (1)

(1) Department of Resource Recovery and Building Technology, University of Borås, Sweden

(2) Department of Resource Recovery and Building Technology, University of Borås, Sweden. RISE, CBI Swedish Cement and Concrete Research Institute

Abstract

Crushed Concrete Aggregates (CCA) as fine and coarse aggregates in new concrete helps achieve closed-loop recycling. Assessment of workability, mechanical properties and durability of concrete demands knowledge of the water absorbed by the CCA. The EN 1097-6 standard method is difficult to execute due to the presence of entrapped air and CCA sedimentation while performing water absorption experiment for fine CCA. Additionally, the assessment of Saturated Surface Dry (SSD) state seems operator specific and non-reproducible; moreover, giving water absorption measurement only at 24 hours. However, findings from this paper show measurements at 15 minutes is influential for concrete workability.

The modified pycnometer method analyses the water absorption of a combined fraction consisting of coarse and fine CCA as proportioned in a given concrete recipe. Furthermore, sedimentation and entrapped air are prevented by pre-soaking the CCA in a solution of distilled water and poly-carboxylate based superplasticizer before commencing the experiment. Ultimately, the combined fraction is drained to SSD condition by vacuum filtration, which is easy to handle by professional operators. In this way, the water absorption development is measured from starting point to 24 hours for the combined fraction to determine the appropriate water amount to saturate CCA during concrete mixing.

Keywords: crushed concrete aggregate, water absorption, pycnometer, SSD, sustainability

1. INTRODUCTION

Crushed Concrete Aggregates (CCA) as fine and coarse aggregates in new structural concrete helps achieve closed-loop recycling. Satisfying the workability requirements of new structural concrete containing CCA demands knowledge of water absorption of the included CCA. Moreover, the cement mortar adhered at the CCA surface causes it to be more porous

than other aggregates [1, 2]; it is even more necessary to determine the water absorbed by the CCA to optimize mixing water added to the concrete.

Practical issues such as sedimentation and air entrapment are encountered when the water absorption of fine CCA is tested using the EN 1097-6 standard pycnometer method. The sedimentation of CCA is also problematic because of the difficulty in removing the CCA specimen from the pycnometer for saturated surface dry state assessment. Also observed, is the fine CCA do not meet the assessment requirements prescribed by the European standard for Saturated Surface Dry (SSD) condition, performed by the sand absorption cone. Earlier research attributed the issues with sedimentation and SSD assessment to the angular shape and presence of excessive fines in the crushed aggregates [3, 4].

2. MATERIALS

To determine the water absorption as it would happen during the concrete mixing, the modified pycnometer method tests a combined fraction CCA consisting of coarse and fine CCA fractions in the same proportions as they occur in the concrete recipe. Combined aggregate fractions are used as specimens for water absorption and particle density investigations in transportation and infrastructure research [5, 6].

This study investigates three CCA fractions namely 0/4 mm, 0.5/4 mm and 8/11.2 mm, which appear in the concrete recipes in the ratio 20, 35 and 45% respectively. The fine CCA fractions 0/4 mm and 0.5/4 mm are used together to satisfy the fines content of the concrete recipe. The combined grading curve for the aggregate fractions are shown in figure 1.

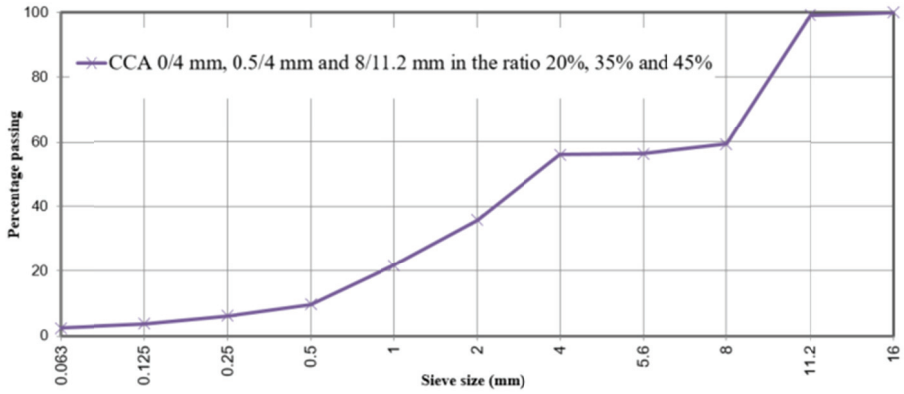

Figure 1: Combined grading curve of the fine and coarse CCA fractions

The CCA fractions are acquired from prefabricated concrete rejects and are crushed to size by a jaw crusher. The combined fractions as suitable test specimen instead of individual aggregate fractions is verified by comparing the apparent densities of the individual CCA fractions and the combined fraction CCA seen in table 1. The apparent density of the combined fraction lies within the interval of the apparent densities of the 0/4 mm fine fraction and 8/11.2 mm coarse fraction. Thus, the combined fraction is used instead of individual fractions for water absorption investigations.

Table 1: Comparison of the apparent densities of individual and combined CCA fractions

CCA Fraction (mm)	Apparent density ρ_a(g/cm^3)
0/4	2.94
0.5/4	2.72
8/11.2	2.66
Combined fraction - 0/4, 0.5/4 and 8/11.2 in the ratio 20%, 35%, 45%	2.81

3. METHOD

The modified pycnometer is different from the standard pycnometer methods [7, 8] since it consists of a pre-processing step where the CCA is pre-soaked in a superplasticizer solution which acts like a particle dispersant and prevents sedimentation. The water absorption test is carried out in the same super plasticizer solution instead of distilled water as in the case of the standard method. Finally, the SSD state assessment is performed using a physical device such as the vacuum filtration set up to drain the excess water from the wet aggregates. This is done instead of the oven drying or wiping which are the standard techniques. The flow chart of the modified pycnometer method is shown in figure 2.

Figure 2: Flowchart of the modified pycnometer method

3.1 Pre-processing the combined fraction CCA

The combined CCA fraction weighing 200g is pre-soaked momentarily in a solution of polycarboxylate-based superplasticizer and distilled water in the concentration 6.35g/l; solution is poured to cover the surface of the aggregates. To drain away the excess solution, the pre-soaked CCA is oven-dried at 110±5℃ before it is introduced in the pycnometer containing the same superplasticizer solution. Oven drying the crushed concrete aggregates can be compared to boiling technique performed by Schouenborg et al. [9] where CCA were soaked in boiling water before water absorption test to remove the air obstructing the absorption of water in the CCA pores.

3.2 Water absorption of combined fraction CCA

The pre-processed CCA is poured into a pycnometer containing the superplasticizer solution to measure the water absorption development from starting point to 24 hours. The SSD assessment is performed at three time intervals namely starting point, 15 minutes and 24 hours to receive the water absorption values at the specific duration.

3.3 SSD assessment by vacuum filtration technique

The vacuum filtration technique uses vacuum to drain out the excess water from the wet CCA until they have reached the SSD state. The contents of the pycnometer are directly poured into a Büchner Funnel containing a qualitative filter paper made of cellulose that can retain particles of size less than 10µm. The water from the funnel drains into a flask by vacuum, created by an adjoining tap with flowing water, connected to the flask by a hose

arrangement as shown in figure 3. An additional moist filter paper is placed on top of the CCA to prevent any possible evaporation. The contents of the funnel are stirred once every two minutes to ensure uniform draining.

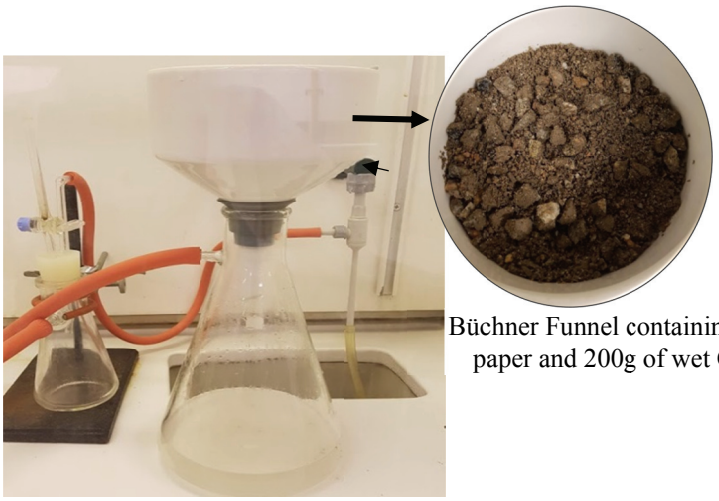

Figure 3: SSD assessment by vacuum filtration technique

This technique uses an ocular assessment just as the standard pycnometer method [8] in the case of coarse aggregates which after wiping are considered as SSD when they lose the shiny and wet appearance. In this new technique, during the filtration it is observed that the coarser particles drain faster than the finer ones meaning that the coarse are in SSD state before the fines. Therefore, for the combined fraction to reach SSD state the majority fraction being the 8/11.2 mm should be in SSD. However, from experiments it is observed that when the coarse appear SSD, the finer fractions are still wet. The fines seem to appear surface dry when the coarse just begin to change colour and appear light grey as shown in figure 4.

Figure 4: SSD assessment by vacuum filtration technique

The effectiveness of the vacuum filtration technique is verified on coarse CCA namely the 8/11.2 mm fraction. The water absorption results performed by the standard pycnometer method [8] followed by the SSD assessments by the standard method and vacuum filtration are compared. The water absorption values shown in figure 5 reveal that both the techniques yield almost similar results for starting point and 15 minutes water absorption. However, there

is a slight difference in the results at 24 hours, which could be due to variations in the composition of the CCA samples investigated.

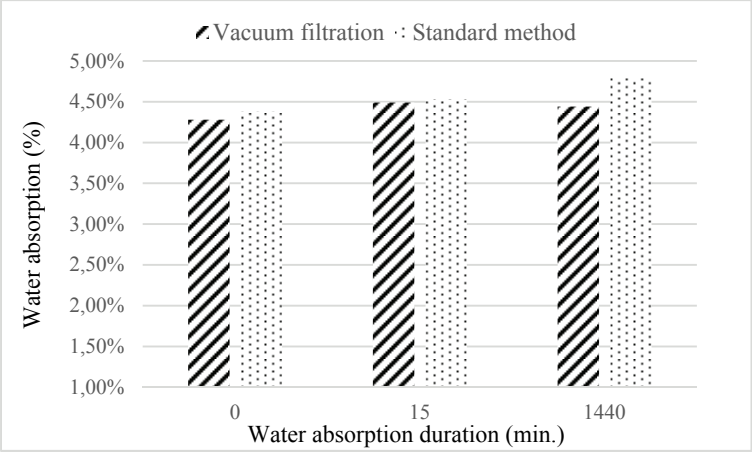

Figure 5: Water absorption of coarse CCA- comparison of the standard [8] and vacuum filtration SSD assessments techniques

4. RESULTS

The water absorption by the modified pycnometer method has been performed at three different time durations to receive a development as shown in figure 6. It is observed that the water absorption at starting point is at least 90% of the water absorption at 24 hours. The water absorption is almost constant after the first 15 minutes until 24 hours, showing that almost all the water absorption happens within the first 15 minutes.

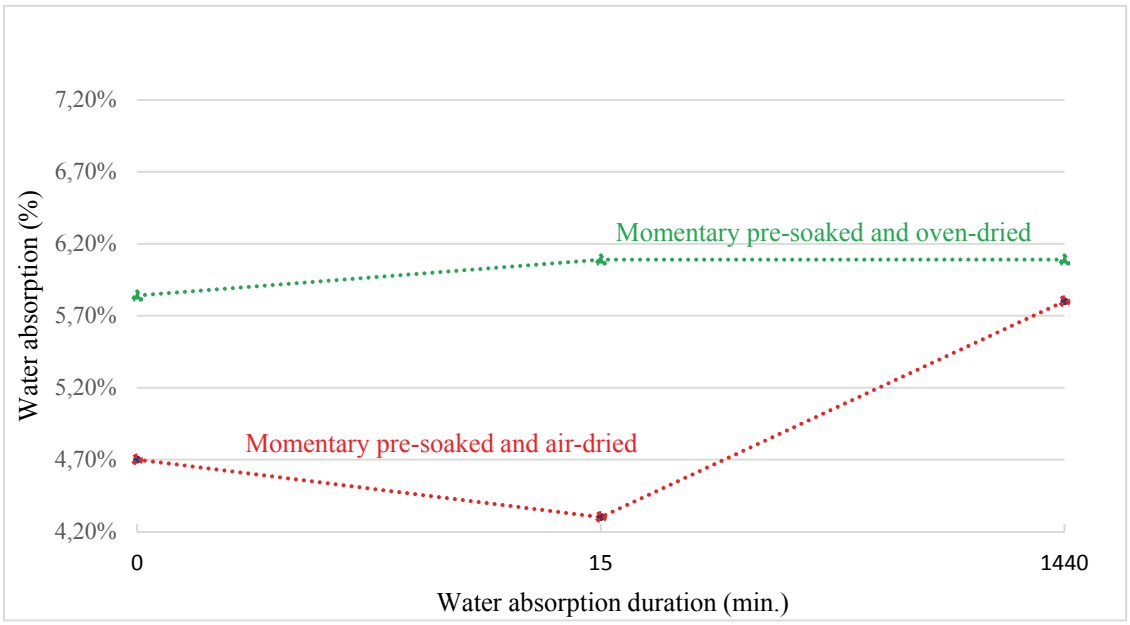

Figure 6: Water absorption of combined CCA using modified pycnometer method

The water absorption development is used to determine the amount of water required to pre-soak the crushed concrete aggregates before concrete mixing. Since the CCA are in air-dry condition when they are mixed in the concrete, a water absorption development for such air-dry aggregates is required. The combined fraction CCA is left to air-dry (approx. 72 hours) after pre-processing and the water absorption is determined by the modified pycnometer method. The results in figure 6 show that the water absorption of air-dry CCA is less than the oven-dried CCA over the entire duration. The air-dry CCA at 24 hours is at the same level as the oven dry water absorption value at the starting point. This could mean that air-dry CCA is not reaching the maximum water absorption in 24 hours- a fact, which already reported in earlier research [9, 10]. Alternatively, oven drying the CCA before water absorption can reduce the water absorption duration to receive maximum water absorption in comparatively lesser time.

5. CONCLUSIONS

- The modified pycnometer method with the vacuum filtration technique for SSD assessment is a robust method and can be used for testing in the field.
- The initial condition of the oven drying the CCA is so strict that the development of water absorption with time is considerably even. Whereby, the water absorption at starting point of the oven-dried combined fraction CCA can be assessed as 80% of the 24-hour value and used in practical applications.

ACKNOWLEDGEMENTS

This research was funded by Gunnar Ivarson's board for Sustainable Built Environment. We would like to thank SIKA Sverige AB, CEMENTA and Hedareds Sand och Betong AB for providing materials for the experiments in this study.

REFERENCES

[1] de Juan, M.S. and P.A. Gutiérrez, Study on the influence of attached mortar content on the properties of recycled concrete aggregate. Construction and Building Materials, 2009. **23**(2): p. 872-877.
[2] Padmini, A.K., K. Ramamurthy, et al., Influence of parent concrete on the properties of recycled aggregate concrete. Construction and Building Materials, 2009. **23**(2): p. 829-836.
[3] Kim, J., G. Zi, et al., Measurement of Water Absorption of Very Fine Particles Using Electrical Resistivity. ACI Materials Journal, 2017. **114**(6).
[4] Naël-Redolfi, J., E. Keita, et al., Water absorption measurement of fine porous aggregates using an evaporative method: Experimental results and physical analysis. Cement and Concrete Research, 2018. **104**: p. 61-67.
[5] Hall, K., Using a single test to determine specific gravity and absorption of aggregate blends. Transportation Research Record: Journal of the Transportation Research Board, 2004(1874): p. 3-10.
[6] Cross, S.A. and M.K. Mgonella, Evaluation of test methods for determination of aggregate specific gravity. 2005, Oklahoma Department of Transportation.

[7] ASTM International, ASTM C128-15, Standard Test Method for Relative Density (Specific Gravity) and Absorption of Fine Aggregate. 2015, ASTM International: West Conshohocken, Pennsylvania.
[8] Swedish Standards Institute, SS-EN 1097-6:2013 Tests for mechanical and physical properties of aggregates - Part 6: Determination of particle density and water absorption. 2013, Swedish Standards Institute: Stockholm.
[9] Schouenborg, B., J. Aurstad, et al., Test methods adapted for alternative and recycled, porous aggregate materials. Part 3-Water absorption. Nordtest project 1531-01. 2004, Nordic Innovation Centre: Oslo, Norway.
[10] Tam, V.W.Y., X.F. Gao, et al., New approach in measuring water absorption of recycled aggregates. Construction and Building Materials, 2008. **22**(3): p. 364-369.

International Conference on Sustainable Materials, Systems and Structures (SMSS 2019)
Novel Methods for Characterization of Materials and Structures
20-22 March 2019 – Rovinj, Croatia

ASSESING REACTIVITY OF SUPPLEMENTARY CEMENTITIOUS MATERIALS IN TERENARY BLENDED CEMENTS

Ruben Snellings (1)

(1) Flemish Institute of Technological Research, Belgium

Abstract

The development of low clinker ternary cements ties to a further intensification of industrial symbiosis systems and targets a further reduction of the environmental impacts of our present-day production system such as climate change, primary resource consumption and waste management.

One of the main technical challenges for low clinker cements is to meet early age strength requirements. The supplementary cementitious materials (SCMs) used to replace Portland clinker are less reactive and therefore contribute later to the strength development. Finding ways to increase the reactivity of SCMs therefore also opens up opportunities to further reduce clinker factors.

Assessing the reactivity of SCMs in hydrating ternary blended cements is important as is it sheds light on synergetic or competitive among different SCMs, or between the SCM and the clinker phases. There are two main approaches to assess the reactivity as SCM, either directly as part of the hydrating blended cement, or indirectly through measurement of the SCM reactivity in a simplified model system. The former direct approach is arguably closer to reality, but is fraught with experimental difficulties requiring advanced characterization techniques and data analysis methods. The latter indirect approach is farther removed from the final application but has the advantage of enabling to obtain relevant information by less complicated, more widely available measurement techniques.

This contribution relates results of both approaches on a ternary blended cement composed of clinker, slag and limestone. Hydration kinetics and product development over time were established by isothermal calorimetry, XRD Rietveld-PONKCS and Electron microscopy image analysis. The results were compared to a benchmarked calorimetry based R3 reactivity test for SCMs developed in RILEM TC-267 TRM.

Author index

SPONSORS AND SUPPORT

UNIVERSITY OF ZAGREB
FACULTY OF CIVIL ENGINEERING

100 Years

1919-2019

www.grad.unizg.hr

Mision, Vision and Strategy

Mission

The Faculty of Civil Engineering of the University of Zagreb is the oldest civil engineering faculty in Croatia conducting university education at an undergraduate, graduate and postgraduate level in all branches of civil engineering. It is continually developing and advancing higher education, scientific research activities and overall education, and actively participates in the development of the profession and implementation of new technologies.

Vision

- to retain and strengthen the leading position as a university and scientific-research centre in the country, which covers all branches of civil engineering
- to achieve international recognisability by developing a culture of quality higher education and research work by implementing the best European and world practices, promoting the mobility of students and researchers, and by becoming one of the regional centres of excellence in individual disciplines, as well as a "cooperation bridge" for countries of the European Union and the region
- to retain and strengthen cooperation with the business sector in high-expertise tasks and developmental projects, specialised life-long higher education, and the development of an alumni network for mutual support and progress

Objectives

- further harmonisation of the outcome of learning with the demands of the profession and market, with continual modernisation of the teaching process and content
- connecting and expanding cooperation with related university institutions and scientific institutions, primarily in the European Union, along with promoting the international mobility of students and researchers
- participation in joint research projects and joint studies with partners from EU countries and the region
- founding individual study programmes in the English language, and organising life-long learning and non-formal education in the English language
- development and modernisation, and certification of laboratories
- increasing spatial and personnel capacities for teaching and research needs
- further ties with the business sector and searching for adequate organisational forms

BE SURE. BUILD SURE.

ENABLING BETTER CONSTRUCTION AND REPAIR

Each individual product can have a critical effect on an entire structure or its repair. Choosing the wrong solutions or applying them incorrectly can lead to component and structural damage and, in extreme cases, even endanger life.
Planners, engineers and applicators therefore have a significant responsibility to bear, of which we are only too aware.
It is not only your own good name that is at stake; businesses and people also have to be protected.
Hence – through reliable and sound technical advice and product solutions – we dedicate our fullest efforts, care and attention to ensuring that each project performed by our customers is executed to their enduring satisfaction and peace of mind. Because part of being MC really does mean accepting responsibility for lives and reputations.

We take building seriously.
BE SURE. BUILD SURE.

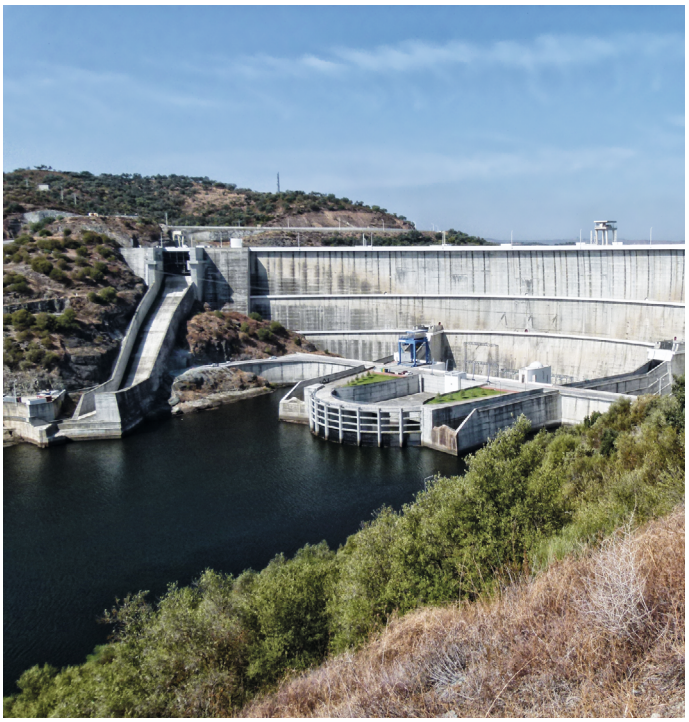

Injection systems

Admixtures for precast concrete

Admixtures
Concrete cosmetics
Grouting mortar

Admixtures
Concrete cosmetics

Floor coatings
Epoxy, Polyurethane

Injection systems
Concrete repair

Floor coatings
Waterproofing
Surface protection

MC solutions in demand throughout the world

MC solutions have been used in major construction and repair projects around the world for more than 50 years now. Developers, promoters, architects, planning engineers and applicators know they can rely both on the advice of our experienced consultants and on the high quality of our product systems.

MC – Building Chemicals d.o.o.
Kovinska 4a, 10090 Zagreb
Tel. +385 (1) 5587 797

www.mc-bauchemie.hr
infocro@mc-bauchemie.com

MASTER® BUILDERS SOLUTIONS

I WANT TO GET THE MOST OUT OF MY QUARRY

MasterSuna SBS: The solution for fine aggregates containing clay

QUANTIFIED SUSTAINABLE BENEFITS – REDUCE YOUR FOOTPRINT AND BOOST YOUR BOTTOM LINE

Clay containing fine aggregates were once regarded as unsuitable for the production of high-quality concrete. But this is no longer the case. With the new MasterSuna SBS sand blocker from BASF, it is even possible to convert difficult sands into a valuable resource. Thanks to MasterSuna SBS, the concrete producer BRONZO PERASSO in Marseille, France, no longer needs to transport sand from remote sites. That reduces sand and transportation costs, and saves up to 25 tons of CO_2 per year.

Discover more about this success story:
sustainability.master-builders-solutions.basf.com

BASF
We create chemistry

*Figures provided are based on an actual case from the concrete producer BRONZO PERASSO in Marseille, France

CONFERENCE EXHIBITORS

CORTEC CORPORATION
Environmentally Safe VpCI®/MCI® Technologies

challenge. create. care. KNAUF INSULATION

BeTon učko

PermeaTORR ACTIVE CELL

METTLER TOLEDO

RO-TEHNOLOGIJA
RO - TECHNOLOGIES AG

Toni Technik TEBE BERT

ISSN: 0350-2465 (print)
ISSN: 1333-9095 (on-line)

GRAĐEVINAR

Journal of the Croatian Association of Civil Engineers

Scientific and Professional Papers
Professional news items

The journal is published regularly
12 times a year since 1949.

Indexed in:
Science Citation Index Expanded

Papers are published in Croatian language and, all papers in the online edition are entirely in Croatian and English

The biggest scientific & professional journal of civil engineering in Croatia

Journal published monthly
(12 issues/year)

Circulation: 3500 copies

Editorial address:
Berislavićeva 6, Zagreb, Croatia
phone: +385 1 4872-502
fax: +385 1 4872-526
e-mail: gradjevinar@hsgi.org
www.casopis-gradjevinar.hr

ISSN: 0350-2465 (print)
ISSN: 1333-9095 (on-line)

GRAĐEVINAR

Journal of the Croatian Association of Civil Engineers

Editor-in-Chief
Prof. **Stjepan Lakusic**
University of Zagreb
Faculty of Civil Engineering

stjepan.lakusic@grad.hr

Journal GRADEVINAR (eng. CIVIL ENGINEER) is a scientific/professional journal with a strong focus on all aspects of Civil Engineering

12 issues/year
3500 copies/issue

The journal GRADEVINAR is a monthly publication that has been regularly appearing **12 times a year** without interruption for three decades now. As the journal is published each month, the publication process of reviewed and accepted papers is relatively fast. The Journal uses the **double blind review** process for evaluation of papers. All papers are printed in Croatian language, but the online edition of the journal features full versions of all papers in English language as well.

The journal GRADEVINAR encourages submission of good papers, not only to help disseminate technical information useful in the field of civil engineering, but also to provide authors with the opportunity to have their paper reviewed by peers and, when published, receive proper recognition for their efforts. The scientific/professional papers are grouped into four categories, depending on their contribution to the advancement of research or professional work.

According to its circulation (3,500 copies), GRADEVINAR is the biggest scientific/professional journal in the field of technical engineering in Croatia and wider region, and is **Indexed in Science Citation Index Expanded.**

On the homepage of Journal GRADEVINAR you can:

- **Find all information about the journal**
- **Acquire information about the journal's most read papers**
- **Read all papers free of charge**
- **Find submission information**

For more information and for submission guidelines, please visit us at www.casopis-gradjevinar.hr

Editorial address:
Berislavićeva 6, Zagreb, Croatia
phone: +385 1 4872-502
fax: +385 1 4872-526
e-mail: gradjevinar@hsgi.org
www.casopis-gradjevinar.hr

International Conference on Sustainable Materials, Systems and Structures (SMSS2019) – 20-22 March 2019 – Rovinj, Croatia
Novel Methods for Characterization of Materials and Structures

Edited by Ivan Gabrijel, Christian Grosse, Marijan Skazlić

RILEM Proceedings PRO 128
ISBN: 978-2-35158-217-6
VOL 5. ISBN: 978-2-35158-227-5
e-ISBN: 978-2-35158-218-3
2019 Edition

As part of the RILEM SMSS 2019 conference, the segment Novel Methods for Characterization of Materials and Structures aimed to gather a compendium of papers which are primarily oriented on promoting approaches that provide new insight into material properties or structural behaviour. Contribution to the segment deal with methods for characterisation of materials at microstructural level, methods for monitoring of age-dependant processes in cement based materials, experimental techniques supported by numerical analysis, new applications of existing methods, non-destructive testing methods, methods for on-site inspection and monitoring and novel approaches in design of concrete structures.

RILEM Publications S.a.r.l.
4 avenue du Recteur Poincaré
75016 Paris - FRANCE
Tel: + 33 1 42 24 64 46 Fax: + 33 9 70 29 51 20
E-mail : dg@rilem.net